Sphingolipide in der entzündlichen Kanzerogenese

Dissertation zur Erlangung des Doktorgrades
der Naturwissenschaften

vorgelegt beim
Fachbereich Biochemie, Chemie und Pharmazie
der Johann Wolfgang Goethe-Universität
in Frankfurt am Main

von
Khadija EL-HINDI
aus Fulda

Frankfurt am Main 2022
(D 30)

Diese Arbeit wurde vom Fachbereich Biochemie, Chemie und Pharmazie
der Johann Wolfgang Goethe-Universität als Dissertation angenommen.

Dekan: Prof. Dr. Glemens Glaubitz

1. Gutachter: Prof. Dr. Dr. Achim Schmidtko

2. Gutachter: Prof. Dr. Sabine Grösch

Datum der Disputation: 30.01.2023

Declaration of Authorship

Except where stated otherwise by reference or acknowledgment, the work presented was generated by myself under the supervision of my advisors during my doctoral studies.
The figures and tables listed below were obtained in the context of collaborative research:

- Figure 3.8: Disease progression of AOM/DSS induced CAC, Sebastian Brachtendorf (Institute of Clinical Pharmacology) collected the data of CerS4 Vil/Cre mice, I performed the statistical analysis
- Table 3.5: Flow cytometry analysis of immune cells in the IEL after AOM/DSS treatment, Stephanie Örtel (Institute of Clinical Pharmacology) stained the cells and performed the flow cytometry measurement, I performed flow cytometry analysis and statistics
- Table 3.6: Flow cytometry analysis of immune cells in LP of control mice and after AOM/DSS treatment, Stephanie Örtel (Institute of Clinical Pharmacology) stained and performed the flow cytometry measurement, I performed flow cytometry analysis and statistics
- Figure 3.16: Immune cell profile in blood after AOM/DSS treatment determined by flow cytometry, Sebastian Brachtendorf (Institute of Clinical Pharmacology), Jennifer Christina Hartel (Institut of Clinical Pharmacology) and I performed the staining and flow cytometry measurement, and the flow cytometry analysis and statistics were performed by me
- Figure 3.17: Immune cell profile in blood after AOM/DSS treatment determined by flow cytometry, Sebastian Brachtendorf (Institute for Clinical Pharmacology), Jennifer Christina Hartel (Institut of Clinical Pharmacology) and I performed the staining and flow cytometry measurement, and the flow cytometry analysis and statistics were performed by me
- Table 3.7: Flow cytometry analysis of immune cells in the blood of control mice and after AOM/DSS treatment, Sebastian Brachtendorf (Institute for Clinical Pharmacology), Jennifer Christina Hartel (Institut of Clinical Pharmacology) and me performed the staining and flow cytometry measurement, the flow cytometry analysis and statistics were performed by me
- Table 3.8: Flow cytometry analysis of immune cells in the spleen in control mice and after AOM/DSS treatment, Sebastian Brachtendorf (Institute for Clinical Pharmacology), Jennifer Christina Hartel (Institut of Clinical Pharmacology) and I performed the staining and flow cytometry measurement, the flow cytometry analysis and statistics were performed by me.

- Table 3.9: LC-MS/MS in colon tissue after acute DSS treatment, Sandra Trautmann (Analytic department, Institute of Clinical Pharmacology) performed the measurement with LC-MS/MS and the analysis, I did the sample pre-preparation and statistical analysis
- Table 3.10: Sphingolipid levels in small intestine of control mice and after AOM/DSS treatment, Sandra Trautmann (Analytic department, Institute of Clinical Pharmacology) performed the measurement with LC-MS/MS and the analysis, I did the sample pre-preparation and statistical analysis
- Table 3.11: Sphingolipid levels in the liver of control mice and after acute DSS treatment, Sandra Trautmann (Analytic department, Institute of Clinical Pharmacology) performed the measurement with LC-MS/MS and the analysis, I did the sample pre-preparation and statistical analysis
- Table 3.12: Sphingolipid levels in the plasma of control mice and after acute DSS treatment, Sandra Trautmann (Analytic department, Institute of Clinical Pharmacology) performed the measurement with LC-MS/MS and the analysis, I did the sample pre-preparation and statistical analysis
- Table 3.13: LC-MS/MS measurements of the plasma after acute DSS treatment in CerS4 LCK/Cre mice, Sandra Trautmann (Analytic department, Institute of Clinical Pharmacology) performed the measurement with LC-MS/MS and the analysis, I did the sample pre-preparation and statistical analysis
- Table 3.14: LC-MS/MS in spleen after acute DSS treatment in CerS4 LCK/Cre mice, Sandra Trautmann (Analytic department, Institute of Clinical Pharmacology) performed the measurement with LC-MS/MS and the analysis, I did the sample pre-preparation and statistical analysis
- Table 3.15: Sphingolipid profile in the thymus after acute DSS treatment in CerS4 LCK/Cre mice, Sandra Trautmann (Analytic department, Institute of Clinical Pharmacology) performed the measurement with LC-MS/MS and the analysis, I did the sample pre-preparation and statistical analysis
- Table 3.16: Sphingolipid profile of the colon after AOM/DSS treatment, Sandra Trautmann (Analytic department, Institute of Clinical Pharmacology) performed the measurement with LC-MS/MS and the analysis, I did the sample pre-preparation and statistical analysis
- Table 3.17: Sphingolipid profile of the liver after AOM/DSS treatment, Sandra Trautmann (Analytic department, Institute of Clinical Pharmacology) performed the measurement with LC-MS/MS and the analysis, I did the sample pre-preparation and statistical analysis

- Table 3.18: Sphingolipid profile of the plasma after AOM/DSS treatment, Sandra Trautmann (Analytic department, Institute of Clinical Pharmacology) performed the measurement with LC-MS/MS and the analysis, I did the sample pre-preparation and statistical analysis
- Figure 3.49 B: Luciferase activity assay with CerS4 promoter deletion constructs can be amplified with HDACS inhibitors, CerS4 promotor and 3'UTR activity in HCT116 cells and HCT15 cells, Christiane Mack (Institute of Clinical Pharmacology) performed the luciferase assay and analysis, I performed the statistical analysis.
- Figure 3.49 B: Luciferase activity assay with CerS4 promoter deletion constructs can be amplified with HDACS inhibitors, Christiane Mack (Institute of Clinical Pharmacology) performed the luciferase assay and analysis, I performed the statistical analysis.

Whenever a figure, table or text is identical to a previous publication, it is stated explicitly in the thesis that copyright permission and/or co-author agreement has been obtained. The following parts of the thesis have been previously published in El-Hindi et al., Int J Mol Sci. 2022:

- Figures: Figure 3.1 B1, Figure 3.2 A, Figure 3.4 A, C, Figure 3.8 B, Figure 3.11 II, IV, Figure A.1, Figure A.2, Figure A.3
- Tables: Table 3.9, Table 3.10,Table 3.11,Table 3.12, Table 3.14, Table 3.15, Table 3.13 Table 3.16, Table 3.17, Table 3.18, Table 2.11

Frankfurt am Main,

.....

Khadija EL-HINDI

Contents

List of Figures

List of Tables

Index of abbreviations

ADP	adenosine diphosphate
AFB1	aflatoxin B1
AJ	adherens junctions
ALPI	alkaline phosphatase
ANOVA	analysis of variance
AOM	azoxymethane
AOM/DSS	azoxymethane/dextran sulfate sodium
AP-1	activating protein-1
APC	adenomatous polyposis coli
APS	Ammonium persulfate
ATCC	American Type Cell Culture Collection
ATP	adenosine triphosphate
AUC	area under curve
bp	base pair
BMP	bone morphogenetic protein
BSA	bovine serum albumin
CAC	colitis associated cancer
CA	carbone anhydrase
C_{Cl}	capacitance
CD	Crohn's disease
CDase	ceramidase
cDC	conventional DCs type
CDK	cyclin-dependent kinase
cDNA	complementary DNA
Cer	Ceramides
CerS	ceramide synthase
CI95	95% confidence interval
CLDN	claudin
CKM	Cdk8 kinase module
CRC	colrectal cancer
CRP	C-reactive protein
CT	threshold cycle
DAG	diacylglycerol
DAPI	4',6-diamidin-2-phenylindol
DC	detergent compatible
DCs	Dentritic cells
DTT	dithiothreitol
DEGS	dihydroceramide desaturase
dhCer	dihydroceramides
DMSO	dimethyl sulfoxide
DNA	deoxyribonucleic acid
DPBS	dulbecco's phosphate-buffered saline
Drp1	dynamin-related protein 1

DSS	dextran sulfate sodium
E2F	E2 factor
EDTA	ethylenediaminetetraacetic acid
EGF	epidermal growth factor
ELovl6	ELPVL fatty acid elongate 6
EMT	epithelial-mesenchymal transformation
EN	organoid culture medium (EGF, Noggin)
ENO1	Enolase 1
ENR	organoid culture medium (EGF, Noggin, R-spondin)
ENR+CV	organoid culture medium supplemented with CHIR99021 and valporic acid
EPHB2	ephrin type-B receptor 2
ER	endoplasmatic reticulum
ESI	electrospray ionization
FA	fatty acyl-CoAs
FABP1	fatty acid binding protein
FACS	fluorescence-activated cell sorting
FC	fold change
FCS	fetal calf serum
FDR	False Discovery Rate
FIS1	mitochondrial fission 1 protein
FITC	fluorescein isothiocynate
FTY720	fingolimod
GlcCer	glucosylceramide
GLUT	Glucose transporter
GSK3-β	glycogen synthase kinase-3-β
HAT	histone acetyltransferases
HBSS	Hanks' Balanced Salt Solution
HDAC	histone deacetylase
HE	Hematoxylin-Eosin
HEPES	2-(4-(2-hydroxyethyl)-1-piperazinyl)-ethansulfon acid
HFD	high-fat diet
HIF	Hypoxia inducible factors
HIF1α	Hypoxia inducible factor 1α
HK	hexokinase
HRP	horseradish peroxidase
HPLC	high performance liquid chromatography
I2PP2A	inhibitor 2 of protein phosphatase 2A
IBD	intestinale bowel disease
ICC	immunocytochemistry
IEL	Intraepithelial lymphocytes
IHC	Immunohistochemistry
IL	interleukin
IFN-γ	interferon γ
KDM5	JmjC lysine demethylase 5
KO	knockout mice

KRT	keratins
KSR	ketosphinganine reductase
KTM	lysine methyltransferases
LacCer	lactosylceramide
LASS	longevity-assurance homolog
LC-MS/MS	high performance liquid chromatography – tandem mass spectrometry
LCK-Cre	Cre-recombinase gene driven by the distal promoter of the lymphocyte protein tyrosine kinase (Lck) gene
LDHA	lactate dehydrogenase A
Lgr	leucine-rich repeat-containing G-protein coupled receptor
LP	lamina propria
luc+	firefly luciferase gene
MAPK	p38 mitogen-activated protein kinase
MCTs	monocarboxylate transporters
MDVs	mitochondria derived vesicles
MEM	Minimum Essential Medium
Mfn	mitofusion
MMR	mismatch repair genes
MOI	Multiplicity of infection
MS	mass spectrometry
mTORC1	mammalian target of rapamycin complex 1
MUC	mucin
MXI1	MAX interactor 1
NAD^+	adenine dinucleotide
NADH	nicotinamide adenine dinucleotide hydrogen
NGS	Normal goat serum
NFκB	nuclear factor 'kappa-light-chain-enhancer' of activated B-cells
NK cells	natural killer cells
NP-40	nonyl phenoxypolyethoxylethanol
Olfm4	olfactomedin-4
OPA	optic atrophy 1
OXPHOS	oxidative phosphorylation
PARK	Parkin
PCR	polymerase chain reaction
PBS	phosphate buffered saline
PDHA	pyruvate dehydrogenase
PDK	PDH kinase
PFA	paraformaldehyde
PHD	prolyl hydroxylase domain
PINK1	phosphatase and tension homolog-induced kinase 1
PM	plasma membrane
PK	pyruvate kinase
PKB	protein kinase B (AKT)
PKC	protein kinase C
PKM	pyruvate kinase isoform

PP2A protein phosphatase 2A
PPIA peptidylprolyl isomerase A
PPP pentose phosphate pathway
PTK7 tyrosine-protein kinase-like 7
qRT-PCR quantitative real-time polymerase chain reaction
RFU relative fluorescence units
RISC RNA-induced silencing complex
RPL37A 60S ribosomal protein L37a
RLU relative light units
ROCK Rho-associated kinase
ROS reactive oxygen species
RT room temperature
RT buffer reverse transcription buffer
RT-PCR real time polymerase chain reaction
S1P sphingosine-1-phosphate
SAHA Suberoylanlilide hydroxyamic acid
SDS sodiumdodecylsulfat
SEM standard error of the mean
shRNA short hairpin RNA
siRNA short interfering RNA
SM sphingomyelin
SMase sphingomyelinase
SMOC-2 Secreted modular calcium-binding matricellular protein-2
SMS sphingomyelin synthases
SP1 specificity protein 1
SPHK sphingosine kinase
SPL S1P lyase
SPT serine palmitoyl transferase
TA transit amplifying
TCA tricarboxylic acid
TEER Transepithelial/-endothelial electrical resistance
TEMED Tetramethylethylenediamine
TFF trefoil factor family
TGF-β transforming growth factor-β
TH helper T cells
TIP60 tat-interactive protein-60
TJs tight junction
TKT transketolase
TKTL1 transketolase-like 1
TLR Toll-like receptors
TNF-α tumour necrosis factor β
TMP transcripts per kilobase million
T_{reg} regulatory T cells
Tris tris(hydroxymethyl)-aminomethan
TSA trichostatin A

TSP-1	thrombospodin-1
TSS	transcription start site
3'UTR	3'-untranslated region
5'UTR	5'-untranslated region
UC	ulcerative colitis
UGCG	UDP-glucose:ceramide glucosyltransferase
UICC	Union for International Cancer Control
Villin-Cre	transgenic mice, in which Cre recombinase is expressed in villus and crypt epithelial cells of the small and large intestines
v/v	volume per volume
WBCs	white blood cells
WB	Western Blot
Wnt	Wingless-related integration site
WT	wildtype mice
w/v	weight per volume
Z	impetance
ZO	zonula occludens

Summary

The incidence of intestinale bowel disease (IBD) has been increasing worldwide since the end of the last century, with the highest incidences in North America and Northern Europe. The etiology is complex and based on an interplay of genetic and environmental factors. Relapsing intestinal inflammation strongly affects their life quality of patients and elevates the risk of developing colrectal cancer (CRC). Disturbed homeostasis of the intestinal barrier or a disproportion between proinflammatory and anti-inflammatory responses are not only causative for disease progression, but also targets for therapy. Regeneration of the intestinal epithelial after inflammation is possible through proliferation and differentiation of pluripotent adult stem cells into different intestinal cell types. Continuous renewal requires higher energy metabolism, which is challenging in the colon due to low oxygen availability. However, cell metabolic adaptation and mitochondrial dynamics are key factors that maintain intestinal cell homeostasis. Alterations in various sphingolipid concentrations have been observed in both inflammatory bowel tissue and colon tumors. Ceramides (Cer) are the central molecules for complex sphingolipids and depending on their chain length, can influence the physicochemical properties of membranes. They influence membrane composition and are enriched in microdomains called lipid rafts, which are important for the accumulation and activation of receptors and integral membrane proteins. Ceramides and other sphingolipids also act as "second messengers" involved in various signaling pathways. Ceramides are synthesized by ceramide synthase (CerS), a family of 6 isoforms that exhibit substrate specificity for distinct fatty acid chain lengths and are differentially expressed in tissues.

The aim of this thesis was to explore the influence of CerS4 on the progression of inflammatory CRC. To understand the effects of CerS4 on the progression of acute colitis and colitis associated cancer (CAC), CerS4 was knocked out globally and in a tissue-specific manner in mice. Mice global CerS4 KO and mice in which CerS4 depletion was restricted to T cells (CerS4 LCK/Cre) or intestinal cells (CerS4 Vil/Cre) were then compared with CerS4 wild-type (WT) mice in the dextran sulfate sodium (DSS) induced colitis and azoxymethane/dextran sulfate sodium (AOM/DSS)-induced CAC. CerS4 KO mice suffered more from DSS-induced colitis than WT and CerS4 LCK/Cre mice. The lipid profile changed after acute colitis: Cer d18:1/16:0, Cer d18:1/20:0, d18:1/24:1, and glucosylceramide (GlcCer) d18:1/16:0, GlcCer d18:1/24:1 increased in the colon and other tissues including the lymphoid organs spleen and thymus. This suggests that inflammation induced by DSS alters sphingolipid levels not only locally in colonic tissues but also in other tissues. Mechanistically, global CerS4 depletion did not affect the intestinal barrier, but these mice showed markedly increased neutrophils in blood and colon tissue, contributing to an enhanced inflammatory response. In the AOM/DSS model, CerS4 WT mice developed the largest tumors, and tissue specific gene knockout of CerS4 led to opposite results: CerS4 Vil/Cre mice had fewer tumors, whereas LCK/Cre mice suffered from pan colitis and had a higher tumor incidence. CerS4 LCK/Cre mice also had more regulatory T cells (T_{reg}) and fewer

cytotoxic T cells, which may have contributed to the increased tumor incidence. The protective role against tumorigenesis by specific CerS4 depletion in intestinal cells in CerS4 Vil/Cre mice indicates a key function of CerS4 in early tumorigenesis.

Therefore, the CerS profile was analyzed in organoids from patients that showed different expression of CerS4 depending on tissue origin and CRC stage. When paired sample were analyzed, organoids from tumor biopsies had higher CerS4 levels than control organoids from the same patient. Correlation between CerS level, stem cell markers, and differentiation markers, as well as analysis of two other studies showed that the CerS profile changes with differentiation. CerS4 correlates with a stem cell marker leucine-rich repeat-containing G-protein coupled receptor (Lgr) and appears to be dependent on the physiological level of the signaling molecule Wingless-related integration site (Wnt). Further studies are required for a comprehensive understanding of the role of CerS4 in this important signaling pathway.

The Wnt signaling pathway is a critical driver of tumor growth in CRC. During the late stages of tumor progression in the colon, colon cancer cells must also respond to potential oxygen starvation (hypoxia) in order to survive. Therefore, CRC cell lines exposed to chronic hypoxia in 2D and 3D cultivation were examined for the changes in CerS expression. This showed that the expression of CerS4 decreased in all CRC cell lines in 2D and 3D, and in HCT116 cells, the expression of CerS5 also decreased. Further studies, such as promoter studies and treatment of cell lines with histone deacetylase (HDAC) inhibitors showed not only differential transcriptional regulation of CerS4 in CRC cell lines, but also that hypoxia is a possible mechanism for downregulation of CerS4. However, this downregulation is independent of HIF1α and appears to be epigenetically regulated. Therefore, future studies should further investigate the epigenetic regulation of CerS4. To further investigate the effects of CerS4 and CerS5 downregulation, CerS4 and CerS5 were downregulated in HCT116 cells and Caco-2 cells and exposed to chronic hypoxia for $24\,\mathrm{h}$ to $72\,\mathrm{h}$. The metabolic cell response to hypoxia as well as mitochondrial dynamics was analyzed by quantitative real-time polymerase chain reaction (qRT-PCR). The results indicated that CerS may be involved in the regulation of metabolic signaling pathways, but this remains to be confirmed at the protein expression level. Hypoxia exposure of colon cancer cell lines also altered mitochondrial dynamics. In this regard, CerS5 appears to play an important role in mitochondria. Thus, the data suggest that CerS4 and CerS5 play a role in intestinal homeostasis through mitochondrial dynamics as well as metabolism.

In summary, I demonstrated in this thesis that the sphingolipid profile in colitis changes not only locally but also systemically and therefore represent a suitable biomarker for inflammation but not for CRC. In CRC progression, CerS4 plays a critical role. Tissue-specific depletion of CerS4 differentially affected colorectal cancer progression and expression of CerS4 in colorectal cells also appears to vary by tumor stage. In this regard, hypoxia may be a potential driver of CerS4 downregulation. In addition, the data point to the important role of CerS4 in T-cell regulation. To consider CerS4 as a therapeutic target in colorectal cancer patients, this would need to be tissue specific: Specifically, upregulation of CerS4 in T cells could be a potential therapeutic target and, in contrast, at the onset of colorectal

cancer development, downregulation of CerS4 in intestinal cells could provide a benefit to patients.

Zusammenfassung

Die Inzidenz von entzündlichen Darmerkrankungen steigt seit dem Ende des letzten Jahrhunderts weltweit an – mit den höchsten Inzidenzen in Nord-Amerika und Nord-Europa. Die Ätiologie ist komplex und beruht auf einem Zusammenspiel von genetischen Faktoren und Umweltfaktoren. Vor allem rezidivierende Darmentzündungen, in der Fachsprache Kolitis genannt, beeinträchtigen die Lebensqualität der Patienten stark und erhöhen das Risiko, an Darmkrebs zu erkranken. Eine gestörte Homöostase der Darmbarriere oder ein Missverhältnis zwischen entzündungsfördernder und antiinflammatorischer Reaktion sind nicht nur ursächlich für das Fortschreiten der Krankheit, sondern auch Angriffspunkte für die Therapie.

Die Regeneration des Darmepithels nach einer Entzündung ist durch die Proliferation und Differenzierung von pluripotenten adulten Stammzellen in verschiedene Darmzelltypen möglich. Die kontinuierliche Erneuerung erfordert einen höheren Energiestoffwechsel, der im Dickdarm aufgrund der geringen Sauerstoffverfügbarkeit eine Herausforderung darstellt. Die metabolische Anpassung der Zellen und die Dynamik der Mitochondrien sind jedoch wichtige Faktoren, welche die Homöostase der Darmzellen aufrechterhalten.

Sowohl in entzündlichem Darmgewebe als auch in Dickdarmtumoren wurden Veränderungen in verschiedenen Sphingolipidkonzentrationen beobachtet. Ceramide (Cer) sind die zentralen Moleküle für komplexe Sphingolipide und können in Abhängigkeit ihrer Kettenlänge, die physikochemischen Eigenschaften von Membranen beeinflussen. Sie beeinflussen die Membranzusammensetzung und sind in Mikrodomänen, den sogenannten Lipid Rafts, angereichert, welche für die Akkumulation und Aktivierung von Rezeptoren und integrale Membranproteine wichtig sind. Cer und andere Sphingolipide agieren außerdem als „second messengers“, die an verschiedenen Signalwegen beteiligt sind. Je nach Kettenlänge der Cer können sie zelluläre Signalwege wie Proliferation, Apoptose oder Autophagie unterschiedlich beeinflussen. Cer können durch die Hydrolyse von komplexen Sphingolipiden oder durch *de novo* Synthese gebildet werden. Die *de novo* Synthese wird von Ceramidsynthasen (CerS) im endoplasmatischen Retikulum durchgeführt. Bei diesem Prozess fügen CerS Fettsäuren unterschiedlicher Kettenlänge an das Sphingosin-Rückgrat an, um Cer zu bilden. CerS umfassen eine Familie von 6 Isoformen, die eine Substratspezifität für verschiedene Fettsäurekettenlängen aufweisen und in verschiedenen Geweben unterschiedlich exprimiert werden. Eine ubiquitär exprimierte CerS Isoform ist CerS4, die langkettige Cer (Cer d18:1/18:0 und Cer d18:1/20:0) bildet.

Patientendaten zeigen, dass das Gleichgewicht von Sphingolipiden mit unterschiedlichen Fettsäurekettenlängen und die Expression von CerS-Isoformen bei Dickdarmkrebs verändert sind. CerS spielen daher eine Rolle bei der Veränderung des Sphingolipids-Gleichgewichts während der Tumorprogression. Der Einfluss der kettenlängenspezifischen Cer auf

das Fortschreiten des Dickdarmkrebses ist trotz mehrerer Studien nicht ausreichend geklärt.

Das Ziel dieser Arbeit war es, den Einfluss der CerS4 auf die Progression von entzündlichem Dickdarmkrebs zu erforschen. Um die Effekte von CerS4 auf das Fortschreiten der akuten Kolitis und des kolitisassoziierten Krebs (CAC) zu verstehen, wurde CerS4 bei Mäus-en global und gewebespezifisch ausgeschaltet. Mäuse mit globalem CerS4-Knockout (CerS4 KO) und Mäuse, bei denen die CerS4-Depletion auf T-Zellen (CerS4 LCK/Cre) oder Darmepithelzellen (CerS4 Vil/Cre) beschränkt war, wurden anschließend hinsichtlich des Krank-heitsverlaufs bei Dextransulfat-Natrium (DSS) und Azoxymethan/Dextransulfat-Natrium (AOM/ DSS) induzierter CAC mit Wildtyp Mäusen (WT) verglichen. CerS4 KO-Mäuse litten stärker unter DSS-induzierter Kolitis als WT- und CerS4 LCK/Cre-Mäuse. Das Lipidprofil veränderte sich nach der akuten Kolitis: Cer d18:1/16:0, Cer d18:1/20:0, Cer d18:1/24:1 und GlcCer d18:1/16:0, GlcCer d18:1/ 24:1 stiegen im Dickdarm und in anderen Geweben einschließlich der lymphatischen Organe Milz und Thymus an. Dies deutet darauf hin, dass eine durch DSS ausgelöste Entzündung den Sphingolipidspiegel nicht nur lokal im Dickdarmgewebe, sondern auch in anderen Geweben verändert.

Mechanistisch gesehen beeinträchtigte die globale CerS4-Depletion nicht die Darmbarriere. Dies konnte daraus abgeleitet werden, dass sowohl die histologische Analyse der „tight junction"-Proteine im Dickdarm von CerS4 KO-Mäusen als auch die *in vitro*-Analysen mit Caco-2-Zellen keinen Unterschied in der Barrierefunktion zeigten. Caco-2-Zellen sind eine Dickdarmkrebs-Zelllinie, die ein gängiges Darmbarrieremodell darstellt. Die Barrierefunktion wurde durch den transepithelialen elektrischen Widerstand (TEER) und die Durchlässigkeit eines fluoreszierenden Zuckers bestimmt. Die Herabregulierung von CerS4 in Caco-2-Zellen veränderte weder den Widerstand noch die Permeabilität in Caco-2-Zellen, erhöhte jedoch die Zellkapazität. Diese Ergebnisse deuten darauf hin, dass CerS4 die Barrierfunktion nicht beeinträchtigt, aber möglicherweise an Transportprozesse in der Zelle wie der Vesikelbildung beteiligt ist.

Der Grund für die erhöhte Sensitivität von CerS4 KO-Mäusen bei DSS induzierten Kolitis ist daher auf die Immunreaktion zurückzuführen. CerS4 KO-Mäuse wiesen deutlich erhöhte Neutrophile im Blut und im Dickdarmgewebe auf, die zu einer verstärkten Entzündungsreaktion beitragen.

AOM/DSS induzierte CAC löste Dickdarmkrebs bei Mäusen aus. Dabei entwickelten WT-Mäuse die größten Tumore, und der gewebespezifische Gen-Knockdown von CerS4 führte zu entgegengesetzten Ergebnissen. CerS4 Vil/Cre-Mäuse hatten weniger Tumore, während CerS4 LCK/Cre-Mäuse an Pan-Kolitis litten und eine höhere Tumorinzidenz aufwiesen. CerS4 LCK/Cre-Mäuse hatten auch mehr regulatorische T-Zellen und weniger zytotoxische T-Zellen, was zu der erhöhten Tumorinzidenz beigetragen haben könnte.

Die Analyse weiterer Studien ergab, dass das Fehlen von CerS4 in T-Zellen deren Funktion beeinträchtigt. Die CerS4-Defizienz in T-Zellen verlängerte die Zytokinsekretion und führte zu einer konstitutionellen Aktivierung des CD28 Signals. Diese Dysregulation der Immunantwort erklärt die beobachtete Pan-Kolitis in CerS4 LCK/Cre-Mäusen im AOM/

DSS induzierten CAC. Mechanistisch gesehen ist außerdem der TGFβ-Signalweg von Bedeutung, da Cer d18:1/18:0 und Cer d18:1/20:0 die inhibitorische Regulation des TGFβ-Signal-wegs in Zilienzellen mitregulieren. Die fehlende Hemmung dieses Signalwegs könnte zu der verlängerten Immunreaktion geführt haben.

Im Gegensatz zu CerS4 LCK/Cre-Mäusen, zeigten CerS4 Vil/Cre-Mäuse weniger Tumorbildung nach AOM/DSS induzierter CAC. Die spezifische CerS4-Depletion in Darmzellen deutet auf eine Schutzfunktion gegen die Tumorentstehung hin und weist auf eine Schlüsselfunktion von CerS4 in der frühen Tumorentstehung hin.

Um zu überprüfen, ob die gleiche Beobachtung auch für Patienten gilt, wurde im zweiten Teil dieser Arbeit das CerS-Profil in Organoiden von Patienten analysiert. Es zeigte sich, dass die Expression von CerS4 je nach Gewebeursprung und Darmkrebsstadium unterschiedlich ist. Die höchste Expression von CerS4 wurde in Organoiden aus Divertikulitis-Proben gefunden. Bei der Analyse von gepaarten Proben wiesen Organoide aus Tumorbiopsien höhere CerS4-Werte auf als Kontrollorganoide desselben Patienten. Die Korrelation zwischen CerS-Expression, Stammzellmarkern und Differenzierungsmarkern zeigte, dass sich das CerS-Profil mit der Differenzierung verändert. CerS2 korrelierte mit einigen Differenzierungsmarkern, während CerS4 mit dem Stammzellmarker Leucine-rich repeat-enthalten-den G-protein gekoppelten Rezeptor 5 (Lgr5) korrelierte. Dies wurde auch bei der Analyse weiterer Studien mit humanen Darmorganoiden bestätigt und zeigte auf, dass die Korrelation von CerS4 und Lgr5 vom physiologischen Gehalt des Signalmoleküls Wingless/ Int-1 (Wnt) abhängig ist. Andere Arbeiten zeigten auch, dass die CerS4 abhängigen Ceramide-Zusammensetzung das Schicksal adulter Stammzellen in der Epidermis bestimmt. Daher deuten die Ergebnisse dieser Arbeit darauf hin, dass CerS4 auch bei der Regulierung der intestinalen Stammzellhomöostase eine wichtige Rolle spielt. Weitere Studien sind jedoch notwendig, um zu klären, ob CerS4 abhängige Cer als potenzielle Liganden von Lgr5 am Wnt-Signalweg beteiligt sind.

Der Wnt-Signalweg ist ein entscheidender Treiber des Tumorwachstums bei Dickdarmkrebs. Während der späten Phasen der Tumorprogression müssen Darmkrebszellen auch auf möglichen Sauerstoffmangel (Hypoxie) reagieren, um zu überleben. Daher wurden im dritten Teil dieser Arbeit Dickdarmkrebs-Zelllinien (HCT116-Zellen, HCT15-Zellen und Caco-2-Zellen) in 2D- und 3D kultiviert und chronischer Hypoxie ausgesetzt. Nach Hypoxie wurden die Dickdarmzellinien auf Veränderungen in der CerS-Expression untersucht. Dabei zeigte sich, dass die CerS4-Expression in allen Dickdarmkrebs-Zelllinien abnahm und die Expression von CerS5 in HCT116-Zellen zurückging. Die Untersuchungen des CerS4-Promotors zeigten nicht nur eine unterschiedliche Transkriptionsregulierung von CerS4 in Dickdarmkrebs-Zelllinien, sondern auch, dass Hypoxie ein möglicher Mechanismus für die Herabregulierung von CerS4 auf der Transkriptionsebene ist. Die unveränderte Proteinexpression des Hypoxie-induzierbaren Faktors 1α (HIF1α) in CerS4 herunterregulierten Zellen deutet darauf hin, dass die Hypoxie induzierte Herabregulierung von CerS4 unabhängig von HIF1α ist. Diese Beobachtung wurde auch in anderen Studien gemacht.

Dabei zeigte die Transkriptomanalyse von HIF1α-defizienten HCT116-Zellen, dass nicht der Transkriptionsfaktor HIF1α für die Transkription von CerS4 entscheidend ist, sondern der Co-Transkriptionsfaktor CDK8 Kinase Modul. Die Epigenetik ist ein weiterer Mechanismus zur Herabregulierung von CerS4. Die Behandlung von Dickdarmkrebs-Zelllinien mit Histondeacetylase-Inhibitoren deutete darauf hin, dass CerS4 in HCT15-Zellen epigenetisch herunterreguliert sein könnte. Diese Beobachtung kann auch in anderen Studien gemacht werden, die gezeigt haben, dass nach epigenetischen Veränderungen in Leberzellen oder Fibroblasten, CerS4 mitbetroffen ist. Da Hypoxie auch epigenetische Ereignisse auslösen kann, sollten die durch Hypoxie aktivierte Histon-Methyltransferase und Lysin-Methyltransferase in zukünftigen Studien zur epigenetischen Regulierung von CerS4 weiter analys-iert werden.

Um die Auswirkungen der Herabregulierung von CerS4 und CerS5 weiter zu untersuchen, wurden CerS4 und CerS5 in HCT116-Zellen und Caco-2-Zellen herunterreguliert und 24 bis 72 Stunden lang einer chronischen Hypoxie ausgesetzt. Die beiden Darmkrebs-Zelllinien unterscheiden sich hinsichtlich des Tumorstadiums. Während die Caco-2-Zellen in einem frühen Stadium des Krebses isoliert wurden, repräsentieren die HCT116-Zellen ein spätes Stadium des Dickdarmkrebses. Die Ergebnisse zeigten, dass CerS4- oder CerS5-Herunterregulierung je nach Zelllinie an der Regulierung von Stoffwechsel-Signalwegen beteiligt sein könnte, was jedoch auf der Ebene der Proteinexpression und des Zellstoffwechsels noch bestätigt werden muss. Nach Hypoxie stieg die Expression von Glutamin-Transporter 1 und die Laktatdehydrogenase in HCT116-Zellen und Caco-2-Zellen an, wobei die höchste Expression nach 48 Stunden Hypoxie auftrat. Die größten Unterschiede wurden zwischen CerS4- und CerS5-herunterregulierten HCT116-Zellen festgestellt. Die Expression der an der Glykolyse beteiligten Proteine in CerS4- und CerS5-herunterregulierten Caco-2-Zellen änderte sich nicht. Daher deuten die Ergebnisse darauf hin, dass eine CerS4- oder CerS5-Defizienz in Dickdarmkrebszellen je nach Tumorstadium unterschiedliche Auswirkungen auf den Stoffwechsel haben kann.

Die Hypoxieexposition von Dickdarmkrebs-Zelllinien veränderte auch die mitochondriale Dynamik. Insgesamt nahm die Expression mitochondrialer Fusionsproteine und mitochondrialer Fissionsproteine in HCT116-Zellen und Caco-2-Zellen ab. Je nach Zelllinie wurde die Transkription dieser Proteine in CerS4- oder CerS5-herunterregulierten Zellen signifikanter verringert. Diese Herabregulierung der mitochondrialen Dynamik wurde auch in Transkriptomdaten aus einer anderen Studie bestätigt. In diesem Zusammenhang scheint CerS5 eine wichtige Rolle in Mitochondrien zu spielen. Gestresste Mitochondrien werden durch die Phosphatase-Kinase PINK1 und der Ubiquitin-Ligase PARK markiert. Nach Hypoxie stieg die Expression von PARK in CerS5-defizienten Caco-2-Zellen deutlich an. Im Gegensatz dazu beeinträchtigte die Herabregulierung von CerS4 die Hochregulierung der PARK-Expression nach Hypoxie sowohl in HCT116-Zellen als auch in Caco-2-Zellen. Nach Hypoxie nahm die Expression von PINK in CerS5-herunterregulierten HCT116-Zellen und Caco-2-Zellen signifikant ab. Diese Beobachtungen und eine weiterer Studie

legen nahe, dass CerS5 eine wichtige Rolle bei der Mitophagie spielt. Da andere Studien zeigen, dass defiziente Mitochondrien die Metastasierung von Tumoren vorantreibt und die CerS5-Expression in den letzten Stadien des Dickdarmkrebses bei Patienten abnimmt, sollte in weiteren Studien der Einfluss von CerS auf die Metastasierung weiter untersuchen werden.

Zusammenfassend konnte diese Arbeit zeigen, dass sich das Sphingolipidprofil bei einer Dickdarmentzündung nicht nur lokal, sondern auch systemisch verändert. Diese Veränderung waren nach einer akuten Darmentzündung deutlicher als nach einer AOM/DSS indudzierten CAC bei Mäusen zu beobachten. Daher ist das Sphingolipidprofil ein geeigneter Biomarker für Entzündungen, nicht aber für Dickdarmkrebs. Bei der Progression von Darmkrebs spielt CerS4 eine entscheidende Rolle. Die gewebespezifische Depletion von CerS4 in Mäusen beeinflusste die Darmkrebsprogression unterschiedlich. Während die Depletion von CerS4 in Darmepithelzellen die Tumorentwicklung reduziert, fördert die CerS4-Depletion in T-Zellen die Tumorinzidenz. CerS4 spielt also eine entscheidende Rolle bei der Regulierung der T-Zellen-Reaktion. Daher stellt CerS4 ein interessantes therapeutisches Ziel bei Patienten dar. Basierend auf diesen Mausdaten müsste dies jedoch gewebespezifisch erfolgen: Konkret könnte die Hochregulierung von CerS4 in T-Zellen ein potentielles Therapieziel darstellen, während die Herunterregulierung von CerS4 in Darmkrebszellen zu Beginn der Entwicklung von Dickdarmkrebs den Patienten einen Nutzen bringen könnte. Schließlich deuten die Ergebnisse der Organoide darauf hin, dass CerS4 die intestinale Stammzellhomöostase über Lgr5 regulieren kann. Inwieweit CerS4 die Tumorprogression über den Wnt-Signalweg beeinflusst, muss in zukünftigen Studien noch geklärt werden. Es scheint nämlich, dass diese Regulation nur unter physiologischen Bedingungen, nicht aber bei onkogenen Prozessen stattfindet. Die Ergebnisse sowohl aus Organoiddaten als auch aus Dickdarmkrebs-Zelllinien zeigten, dass die CerS4-Expression je nach Tumorstadium variiert. In diesem Zusammenhang scheint Hypoxie ein Ereignis zu sein, das die CerS4- und teilweise CerS5-Expression herunterreguliert. Insgesamt deuten die Daten zur Stoffwechsel- und Mitochondrienregulation darauf hin, dass CerS4 und CerS5 über die mitochondrielle Dynamik und den Stoffwechsel eine Rolle bei der intestinalen Homöostase spielen und die Tumorprogression vorantreiben können. Ein möglicher Therapieansatz sollte nach Dickdarmkrebsstadium differenzieren und möglicherweise die CerS4-Expression durch epigenetische Medikamente regulieren.

Chapter 1

Introduction

1.1 Inflammatory bowel disease (IBD)

IBD is a hypernym for non-infectious inflammatory diseases of the gastrointestinal tract that is chronic or recurrent. Both disease picture Crohn's disease (CD) and ulcerative colitis (UC) fall within this hypernym [1]. "In UC, the inflammation is restricted to the colon and the rectum", while CD can affect any part of the digestive system from the mouth, through the esophagus, the stomach, the small intestine, large intestine to the anus [2, 3, 4].

The incidence and prevalence of IBD differ geographically and is increased in high-income countries and newly industrialized countries. This shows that apart from genetic predispositions environmental and lifestyle factors influence IBD development. Changes in diet, lifestyle, microbiota and environmental factors are putative risk factors [5]. About 15% to 40% of IBD patients are obese, this indicates that the incidence of IBD increases in parallel with obesity. It is suggested, that obesity contributes to development of IBD through disruption in microbiota homeostasis (dysbiosis), bacterial influx caused by mucosal barrier dysfunction and the activation of adipocytes [6]. The activation of adipocytes increases inflammatory cytokines and affects lipid and glucose metabolism [6]. Metabolic consequences of obesity are also associated with IBD disease severity. Patients with metabolic syndrome (diabetes mellitus, high levels of circulating triglycerides and low levels of circulating HDL cholesterols) have a higher incidence of CD-related hospitalization[7]. Beyond the intestinal manifestation, IBD patients suffer from extraintestinal complications proceed from the intestinal inflammation and others are independent from it. Further, disease treatment can cause extraintestinal manifestations such as iron-deficiency anemia or osteoporosis that strongly affect life quality of patients. There are controversial studies about the risk of colorectal cancer in UC, while a meta-analysis from 2001 did not reveal significant increase in risk of CRC in UC patients [8], other studies emphasis a higher risk of persistent inflammation and clarifies that not all UC patients have the same incidence for CRC. Disease severity (extensive UC) and duration of colorectal inflammation elevates the neoplasia risk [9, 10]. The increased incidence of UC patients that develops CRC is higher and such patients are younger than sporadic CRC patients and more likely have multiple cancer lesions [11].

1.1.1 Colorectal cancer

CRC arises in the colon or rectum. The high incidence and mortality of CRC pose a major health burden worldwide. In 2017, CRC was projected to be the third most frequently diagnosed cancer in both sexes and the second common death caused by cancer in men and third in women at 8% [12]. CRC is an age associated risk, meaning that its incidence rate grows with age. Through increased CRC screening the incidence declined in adults ages $\geq$50 years but increased among persons ages <50 years [13]. In parallel with incidence statistics, CRC mortality rates declined by 3% between 2000 to 2014 among adults aged $\geq$50 years and increased by 13% among individuals younger than 50 years [13].

CRC is etiologically a heterogeneous disease, which can either be predisposed by germline mutations or epigenetic silencing of mismatch repair genes (MMR) or adenomatous polyposis coli (APC) genes or occur sporadically [14, 15, 16]. The majority of CRC cases are sporadic cancer and ascribed to various lifestyle factors such as western diet, smoking, physical inactivity, high alcohol consumption or obesity as putative risk factors for CRC development [17, 18]. During pathogenesis, successive and multiple genetic mutations and epigenetic alterations in epithelial cells lead to an uncontrolled and hyper-proliferation, which sometimes cannot be reversed causing a dysplastic growth. The dysplasia forms a polyp shape, and with accumulating more mutations and hypermethylation of MMR genes, an adenoma develops. Larger adenomas are more likely to become malignant adenocarcinomas, which finally become invasive and metastatic [19]. This episodic accumulation of specific mutations and alterations is thought to occur over a period of 20-40 years [20].

Although each individual CRC is unique, classifying the cancers of patients help to define prognosis and treatment. Cancer stages describes the cancer spread by evaluating the anatomic extent of the primary tumor invading the intestinal wall (T), or the lymph nodes (N) and the metastasis spread (M) (TNM classification) [21, 22, 23]. This classification system is revised continuously by the Union for International Cancer Control (UICC) and American Joint Committee on Cancer [24] and describes the pathological stage (surgical staging) after examination of the tissue after operative removing. UICC stage 0 is the earliest stage, in which cancer is locally restricted to the inner mucosa. As soon as the cancer crosses the submusoca, it is defined as UICC I stage. The outgrowth through the colon wall but not into nearby organs or tissue is termed as UICC II stage. In the later stages tumor cells spread into lymph nodes (UICC III) or distant organs (UICC IV) [24].

1.1.2 Anatomy of colon and epithelial cell integrity

The intestinal tract is the largest organ opposed to the environment; it consists of three layers. The outer layer carries out the rhythmic peristaltic movements through many smooth muscle layers (submucosa). The connective tissue between the outer muscle layer and inner epithelial cells, harbors the stroma, connective tissue traversed with blood and lymph vessels, nerve fibers and immune cells (lamina propria (LP)). Only a single layer of epithelial cells is located on the apical side of the luminal surface. This layer is called mucosa and

consists of four different cell types, that process and absorb nutrients and compact the stool [25, 26].

The mucosa renews every four to five days [27]. The intestinal crypts harbor adult stem cells, which are long-living and multipotent [26]. They are defined by the expression of Lgr5 and a olfactomedin-4 (Olfm4), which competes with Wnt ligand. It acts as a negative regulator of Wnt signaling and downregulates β-catenin signaling [28, 29, 30]. Secreted modular calcium-binding matricellular protein-2 (SMOC-2) is also expressed in the bottom of the crypts in stem cells expressing Lgr5 [31] and is a matricellular protein that promotes matrix assembly and stimulates angiogenesis [32]. Adult intestinal stem cells divide into transit amplifying (TA) cells, which proliferate before they differentiate in one of four cell types. Paneth cells, which protect stem cells by secreting antimicrobial molecules (defensins, lysozymes or cryptdins) and provide the niche signals for stem cells by secreting epidermal growth factor (EGF), transforming growth factor-β (TGF-β), Notch ligand and Wnt. [33, 34]. These factors are crucial for the maintenance of stem cell renewing, proliferation and differentiation [27]. Enterocytes are enriched in the small intestine and are absorptive cells that secrete a diverse hydrolytic enzymes like alkaline phosphatase (ALPI) or carbone anhydrase (CA) [35, 27, 36]. All intestinal epithelium cells express several types of keratins (KRT) to support the function of intermediate filaments. KRT20 is highly expressed in enterocytes and on the basal site of enteroendocrine cells [37]. Enteroendocrine cells are hormone and hormone-like secreting epithelial cells, which are key regulators for appetite, digestion, gut-motility, and metabolism [38, 39]. The fatty acid binding protein (FABP1) is not only expressed in hepatocytes, but also in enterocytes and enteroendocrine cells [40]. Nagatake et al. (2014) also showed that the tight junction (TJs) claudine 4 is diffusely and highly expressed on the surface of enteroendocrine cells. [39]. In parallel to the increased compactness of the stool, the frequency of goblet cells rises from proximal to distal bowel [26]. Goblet cells secrete mucus and is encoded by 20 mucin (MUC) genes to produce glycoproteins and mucopolysaccharides. MUC2 is expressed primarily in intestinal goblet cells and is secreted together with the trefoil factor family (TFF), which not only reinforces the defense of the mucus function but also support the repair of lesions [41].

1.2 Intestinal epithelial barrier integrity

Intestinal barrier is a precisely regulated system, which needs to maintain a mucosal immune homeostasis to prevent uncontrolled inflammation causing intestinal lesions induced by environmental foreign antigens and microorganisms. The interaction of mucus production, epithelial cell integrity with its paracellular permeability and a robust innate immune response regulates intestinal barrier [42]. Alterations in any of these components disrupts intestinal immune homeostasis and leads to subsequent inflammation [42]. The mucus acts as a first line defense against microbiota plays a crucial role in strengthening the intestinal barrier. On the surface of the apical epithelial, enterocytes, Paneth and goblet cells secrete large, highly glycosylated proteins, mucin and phospholipids that form a jellylike layer covering the colon by two layers: an inner attached mucus layer, which is impenetrable for

bacteria and an outer lose mucus which harbors the symbiotic bacteria [43]. Mucus attached to the epithelial layer is negatively charged, harbors antimicrobial molecules as IgA, lactoferrin and defensins [44, 42, 45, 46]. One model for pathogenesis of UC is that any defects in inner mucus layer enable the penetration of bacteria to the epithelium and subsequently will trigger immune reaction by the subepithelial immune system [43].

However, the epithelium is a tight barrier that regulates molecule passage through paracellular spaces [42]. The maintenance of cell-cell interaction is maintained by adherence junction (adherens junctions (AJ)) and desmosomes., but the intestinal permeability is regulated by tight junctions (TJs), which seal intercellular space of epithelial cells [42]. TJs composite of transmembrane proteins, scaffolding cytosolic proteins and regulatory proteins. Among the transmembrane proteins, claudins include 24 members and regulate pore pathways by either decreasing paracellular permeability or forming ion channel pores and thereby increase paracellular permeability [47, 48]. The first identified transmembrane TJ protein was occludin, which plays a critical role in intestinal epithelial permeability. The interaction of the extracellular loops of occludin with adjacent cells creates a barrier against macromolecules, but is selective for small ions [49, 47]. The leak permeability is regulated through phosphorylation, localization, and its interaction with scaffold proteins. zonula occludens (ZO) family members are cytosolic scaffolding protein that consist of various domains, which interact directly with transmembrane TJs, other ZO protein, but also with the actin cytoskeleton and regulatory elements [48]. Hence, it anchors transmembrane proteins with the actin cytoskeleton. The contractility of the actin cytoskeleton is regulated by the phosphorylation of myosin light chain by serine-threonine specific protein kinases, which increases the paracellular permeability [47].

The binding of cytokines and growth factors on its respective receptor on epithelial cells regulates the permeability. During pathogenesis, the activated immune cells release (tumour necrosis factor β (TNF-α)) and interleukin (IL)-13, which increase paracellular pathway. Whereas TNF-α activates myosin light chain kinase activity and occludin endocytosis, IL-13 increases claudin 2 expression and increase the leak and pore pathways. Many cytokines, such as interferon γ (IFN-γ), IL-4, IL-6, increase the intestinal permeability [50, 51, 52, 53], but glucocorticoids and IL-10 can restore the barrier integrity [54, 55].

Cytokine secretion explains the interdependence of the intestinal barrier function and inflammation and how the attaching LP, which harbors the immune cells, influence the intestinal barrier and allows the intestinal luminal content to influx [56]. However, immune cells are not restricted to the LP, through occludin-occludin interaction lymphocytes can move dynamically to the epithelium and are called Intraepithelial lymphocytes (IEL) [57]. IELs do not only protect the intestinal barrier by hosting the defense to pathogens, but also by stimulating tissue repair [58]. Resident macrophages also regulate intestinal epithelial barrier, by clearing apoptotic cells and stimulating the proliferation of TA [59]. Hence, immune cells play an important role and may contribute to barrier dysfunction, if either the stimulation or the initiation of the immune cells is dysregulated. To sum up, already a defective intestinal barrier enables pathogen influx and the inflammatory response

initiate an inflammation cycle, in which the recruited immune cells increase intestinal barrier permeability, which in turn cause a higher pathogen antigen influx and increases the inflammatory response [56].

1.3 Immune cell homeostasis

The intestinal homeostasis maintains a balance between proinflammatory and immunosuppressive response and distinguishes between harmful antigens and pathogens and harmless ones. Dentritic cells (DCs) in the LP interact with the luminal environment through trans-epithelial extension (dendrites). Thereby, DCs open epithelial TJs to protrude their dendrites, but similar to the IELs, DCs express TJ proteins and preserve the epithelial barrier integrity [60, 61]. Hence, DCs can induce tolerance or orchestra immune response upon activation of the pattern recognition receptors (including Toll-like receptors (TLR)) [62]. TLR signaling activate the transcription factor nuclear factor 'kappa-light-chain-enhancer' of activated B-cells (NFκB), which induces the transcription of several cytokines [63]. The cytokine secretion modulates T cell differentiation to T helper cells such as helper T cells (TH)1, TH2 or TH17. TH1 subset support cellular immunity to get rid of intracellular pathogens, while TH2 and TH17 eliminates extracellular pathogens [64]. During acute inflammation, pro-inflammatory innate immune cells as monocytes, macrophages, mast cells, eosinophils and neutrophils are recruited to clear pathogens [65]. The release of reactive oxygen species (ROS), destructive proteases along with inflammatory cytokines by neutrophils antagonizes pathogens but also damages the tissue [66]. Hence, for an adequate immune response the proinflammatory milieu needs to be suppressed. The suppression of effector T cells is facilitated by the IL-10 secretion by T_{reg} [66]. But also some tissue resident macrophages can secrete IL-10 and further limit the inflammation by secreting lipid mediator prostaglandin E2, which inhibits neutrophils [66]. Neutrophils are also directly downregulated by natural killer cells (NK cells) [67]. Hence, the crosstalk between immune cells leads to activation but also inhibition of immune response.

Mucosal inflammation is not only locally restricted, but it also interplays with the systemic immune compartments. This crosstalk can either be driven by the innate immune system. DCs and specific monocytes/macrophages migrate to mesenteric lymph node and spleen and induce through their antigen presenting activity a systemic response [60, 68]. As the spleen has an open circulatory system, which means that the blood passes through spleen without endothelial cells, the resident macrophages filter blood. Thereby, they recycle the iron from aged red blood cells, but also remove antigens, encapsulated pathogens or apoptotic cells and initiate antigen specific immune responses [69, 70]. Besides these non-lymphatic DCs that migrate to the spleen, the spleen hosts subtypes of lymphoid-resident DCs, which induce different responses depending on the stimulus [71]. Resident conventional DCs type (cDC)1 expresses CD8a and are crucial for cytotoxic response to viral infections and tumor. They cross-present effectively extracellular antigens to $CD8^+$ T cells, secrete IL-12 and induce in NK cells an TH1 cells responses [72]. Resident cDC2

express $CD4^+$ and upon extracellular bacterial stimulation they induce TH17 immune response [73]. With their ability to present antigen, DC subtypes activate not only circulating T and B cells but also follicular B an T cells in the splenic white pulp. Also B cells promote T cell dependent and independent immune response with their antigen-sensing function [70]. Splenocytes exits the spleen and relocates into peripheral sites or tumor stroma [70]. The egress of the secondary lymphoid organs is mediated through sphingosine-1-phosphate (S1P) gradient [74, 75, 76].

Monocytes entering the intestinal tissue can either uptake antigens and transport them to lymph nodes or differentiate to macrophages, which do not return to the lymphoid systems, but remain highly phagocytic after antigen uptake [77]. Macrophages take an important role in the initiation of inflammation by eliminating pathogens and directing T cell activation, but also execute resolution by eliminating injured cells, promoting angiogenesis and cell proliferation. Especially the feature of resolution is critical for tumor progression. Tumor progression undergoes a progress called cancer immunoediting [78, 79, 80, 81, 82, 76]. Nascent transformed cells are recognized and eliminated by effective cytotoxic immune cells. IFN-γ promotes tumor progression, by driving the polarization of TH cells to TH1 phenotype, inducing cytotoxic T cells and inhibiting Tregs [79]. Tumor cells that survived the anti-tumor response maintain in equilibrium. This phase is marked by a balance between anti-tumor (IL-12, IFN-γ) and tumor promoting (IL-10, IL-23) cytokines, in which transformed cells are under constant immune pressure and undergo genetic and epigenetic alterations, that resist immune recognition or drive them into senescence through a long lasting growth arrest [83, 78]. Through diverse mechanisms immune recognition can be reduced within a tumor and the tumor can outgrowth. Many molecular mechanisms have to occur to establish an immunosuppressive tumor microenvironment [78, 79]. The secretion of M2-like macrophages and DCs immunosuppressive cytokines as IL-10 or TGF-β, reduced CD8 proliferation and promote Treg polarization. Adaptive Tregs that arise from inflammatory process inhibit effector T cells and the function of NK cells and B cells [84, 85]. Depending on tumor milieu TH17 cells secrete IL17 and induce angiogenesis, which promotes tumor growth [86, 87]. Tregs also promote angiogenesis more strongly in a hypoxic tumor environment [88]. Hence, factors that promote resolution of inflammation and tissue repair also benefits tumor progression.

1.4 Bioenergetic requirements for proliferation

The continues renewal of the intestine under physiological conditions, the tissue repair after inflammation and the strong tumor proliferation require higher energy metabolism, nutrient uptake and biosynthetic activity as the biomass is doubled for the daughter cell [89]. Hence, a cell that wants to respond to a proliferative stimulus must met the metabolic challenge. Under resting conditions, cells produce low level of adenosine triphosphate (ATP) by taking up sufficient nutrients such as glucose or amino acids. Glucose transporter (GLUT)

provide the glucose supply for the glycolysis. In this process, glucose is catalyzed to pyruvate by the pyruvate kinase (PK), which converts adenosine diphosphate (ADP) and phosphoenolpyruvate to ATP and pyruvate. Pyruvate is then transported to the mitochondrial matrix through the conversion to acetyl-CoA and CO_2 by pyruvate dehydrogenase (PDHA). Thus, PDHA is the gateway to the usage of acetyl-CoA for oxidative phosphorylation (OXPHOS) in tricarboxylic acid (TCA) cycle. The activity of PDHA is regulated by phosphorylation, free CoA levels and the ration of adenine dinucleotide (NAD^+) to nicotinamide adenine dinucleotide hydrogen (NADH). In response to a proliferative stimulus, cells increase the nutrients influx and distribute them among metabolic pathways to increase the cellular biomass and form a daughter cell [89]. In the cytoplasm of proliferating cells, the glycolysis increases and generates rapidly ATP. Hence, the ratio of NAD^+/NADH decreases, which drives the cell to convert a part of the pyruvate to lactate by the lactate dehydrogenase A (LDHA) to regenerate NAD^+ from NADH [89]. With the regenerated NAD^+ level, glycolysis persists, but as the high levels of lactate are cytotoxic, "lactate is transported out of the cell through monocarboxylate transporters (MCTs)" [90, 91, 92]. Hence, the residual pyruvate can enter the TCA cycle to produce further ATP. The produced ATP is used for biosynthetic pathway, such as the lipid synthesis which also uses the intermediates of TCA cycle citrate for fatty acid and cholesterol synthesis [89].

Glucose is not only used for glycolysis, during glycolysis the pentose phosphate pathway (PPP) branches already from the first intermediate glucose 6-phosphate to maintain the redox homeostasis by generation of NADH (oxidative PPP) and produce ribose 5-phosphate for nucleic acid synthesis (non-oxidative PPP). Thereby, depending on the cellular needs, either the oxidative branch for NADH generation is accelerated or in proliferating cells the non-oxidative PPP. The reversible reactions of the transketolase (TKT) regulates the carbon flux between both branches and regulates the flux of glycolysis by providing respective metabolites [93, 94, 95].

However, tumor metabolism differs from the metabol-ism of proliferating cells. Many tumor cells have an increase in glycolytic flux [96] but harbor defects in the oxidative metabol-ism [97], which causes that 90% of glucose carbon is converted to lactate [89]. Moreover, the glycolytic flux surpasses the capacity of PDHA, so LDHA activity uses the accumulated pyruvate and enables by generating NAD^+ a continuous glycolytic flux [89]. The increased glycolysis provides the tumor with intermediates as ribose for nucleotide synthesis or glycerol and citrate for synthesis of lipids and non-essential amino acid [89]. Hence, some cancers avoid oxidative phosphorylation even if oxygen supply is sufficient. This is known as the Warburg effect [89].

1.5 Hypoxia

A further challenge for solid tumors is the oxygen availability. Through the intensive growth of tumor cells the oxygen supply from existing vasculature cannot reach the neoplastic regions in the inner of the tumor, causing a need for oxygen, since the oxygen demand exceeds the oxygen availability [98]. Cells sense cellular oxygen level and respond

to changes in oxygen level. Hypoxia inducible factors (HIF) levels increases when cellular oxygen concentration is reduced [99]. The HIF subunit is constantly expressed in the cell but is destabilized under aerobic conditions by prolyl hydroxylase domain (PHD) protein. In humans, three oxygenases, PHD1, PHD2, and PHD3 hydroxylate HIFα subunit oxygen-dependently and causes a subsequent polyubiquitination and proteasomal degradation of HIF [100, 101, 102]. In most cultured cells, PHD2 expression is highest and functions as the main cellular oxygen sensor under normoxia [103, 102]. Under hypoxia, the substrate oxygen is missing for hydrolysis of HIFα subunit, so HIFα is stabilized and can translocate to the nucleus to induce the transcription of several targets. Thereby, it also regulates PHD transcription. PHD1 remains unchanged or decreases, but PHD2 and PHD3 levels increase upon hypoxia [100, 104, 101]. HIF1α does not alone control transcriptional response to hypoxia, it activates further transcription factors directly and indirectly like NFκB, activating protein-1 (AP-1), p53 or specificity protein 1 (SP1) [105]. However, it also needs other co-factors, which mediate the pre-initiation complex assembly and recruitment of RNA polymerase II, like the mediator-associated cyclin-dependent kinase (CDK)8 [106]. HIF1α regulates the metabolic adaptation [107]. It increases the glycolysis through upregulation of GLUT1 and glycolytic enzymes as the hexokinase (HK). It further increases the transcription of LDHA and PDH kinase (PDK)). Thereby, the generated pyruvate is used mainly for lactate production and inhibits the entrance to the TCA cycle as PDK1 inhibits PDHA1 [107].

1.6 Mitochondrial dynamics

Without HIF1α response, cells would still be able to produce ATP through mitochondrial respiration, but under hypoxic conditions, electron transfer is insufficient, resulting in increased ROS production that cannot be detoxified [108]. Abundance of ROS production causes cell damage that leads to cell death. To prevent ROS accumulation under hypoxia, mitochondria change their morphology [109]. Mitochondria are highly dynamic and constantly fuse and divide, to form interconnected intracellular networks or numerous mitochondrial fragments [110]. Mitochondrial dynamics changes during the cell cycle but also upon DNA damage and hypoxia [111]. Under normoxia, they favor the formation of tubular networks, but under hypoxia mitochondria fragmentation occurs [111, 109]. This division is called fission and is mediated by the interaction of GTPase dynamin-related protein 1 (Drp1) in the mitochondrial inner membrane with dynamin-related protein mitochondrial fission 1 protein (FIS1) in the mitochondrial outer membrane. Two observations lef to the conclusion that FIS, in particular, is a limiting factor in mitochondrial fission, first its overexpression promotes mitochondrial fragmentation [112] and second its depletion causes 'interconnected net-like mitochondria', which is the result of excessive fission [110],[113]. The fission of mitochondria is regulated by interaction of GTPase mitofusion (Mfn)1 and Mfn2 in the outer mitochondrial membrane with the organizer of the inner mitochondrial membrane GTPase optic atrophy 1 (OPA) [114]. Through mitochondrial dynamics the mitochondrial content is exchanged and distributed. In addition, it allows the release of cytochrome

C during apoptosis [115]. Hence, any dysfunction or inhibition in mitochondrial dynamics reduce respiratory capacity or delay apoptosis [115]. Distressed mitochondrial are sensed by the phosphatase and tension homolog-induced kinase 1 (PINK1), which flags them and recruits the ubiquitin ligase Parkin (PARK) to the outer mitochondrial membrane to induce mitophagy [116, 117]. Once mitophagy is induced, Mfn1 and Mfn2 are ubiquitinated [118] and PINK and PARK recruit cooperatively Drp1 for mitophagy [119, 120]. Under some circumstance, PARK can also mediate the Drp1-dependent fission [119, 120], or remove damaged mitochondrial protein complexes and lipids through mitochondria derived vesicles (MDVs) via peroxisomes and lysosome to maintain the integrity of the organelle [121, 122]. Pink and Park do not only manage the removal of damaged mitochondria but are also involved in regeneration by inducing the biogenesis of new mitochondria or only individual protein complexes or protein import[123].

1.7 Sphingolipids

1.7.1 Structure

Sphingolipids are ubiquitous class of lipids that affect physiology and pathophysiology. They share a sphingoid base as a backbone as a common structure. In mammalians, the most common sphingoid base is sphingosine, a lipid containing 18 carbon-atoms (C18), two hydroxyl groups (d) and one double bound (:1), designated as d18:1, and its saturated form sphinganine (d18:0) [124]. In small amount free sphingoid bases can be detected and in even lesser amounts as a phosphorylated molecule, S1P, but the majority is bound to a second fatty acyl-CoAs (FA) forming Cer. Cer (N-acetyl-sphingosine) are generated by an amide cross-linking of FA to a sphingoid base[125, 126]. The respective FA of the Cer can differ in saturation and chain length. Cer with an FA chain from C14 to C20 is termed as long chain Cer, and Cer with a FA starting from C22 is defined as very long chain Cer. Hence, the nomenclature describes the backbone and the attached FA (e.g saturated C16 Ceramide is d18:1/16:0). If sphinganine is the backbone, then it is designed as a dihydroceramides (dhCer), which is the precursor for Cer. Cer is a central molecule in the sphingolipid class, as it is the backbone for many other complex sphingolipids. On the primary hydroxyl group of the sphingoid base backbone a hydrophilic head groups as hexose (glucose or galactose) or disaccharide or complex carbohydrates can be attached, resulting in the generation of GlcCer or lactosylceramide (LacCer) or gangliosides. Cer can also be modified by a phosphocholine headgroup to sphingomyelin, which is the most largest class of sphingolipids in the plasma membrane (PM) [125, 127, 128].

1.7.2 Metabolism

Although most sphingolipids are incorporated in the plasma membrane, their synthesis begins in the endoplasmatic reticulum (ER). Serine and palmityl-CoA are condensed to 3-ketodihydrosphingosine by serine palmitoyl transferase (SPT) (gene name SPTLC) [129]. Its activity resembles the first step in the *de novo* generation of sphingolipids and is rate limited

[130]. After a further condensation step by ketosphinganine reductase (KSR), sphinganine is synthesized and resembles the substrate for CerS (gene name LASS) which attach covalently a FA of different chain lengths to it and generate dhCer. Subsequently the dhCer is desaturated to Cer by the dihydroceramide desaturase (DEGS) [131]. The precursor of the further complex sphingolipids Cer is then transported from the ER to the Golgi apparatus. In different compartments of the Golgi apparatus further metabolic steps occur: either the synthesis of sphingomyelin (SM) by sphingomyelin synthases (SMS) (gene name SMPD) or GlcCer by UDP-glucose:ceramide glucosyltransferase (UGCG), which can further be modified to LacCer and then to complex glycosphingolipids. Finally, the *de novo* synthesized sphingolipids are transported to the PM [132]. Lipids in the PM are very dynamic, not only in their movements but also in switching class. SM is hydrolyzed by sphingomyelinase (SMase) (gene name SGMS) to Cer and phosphocholine, but in the PM, SMS can resynthesize SM from Cer and phosphatidylcholine, while producing diacylglycerol (DAG). This turnover between Cer and SM is termed as sphingomyelinase pathway [133, 134].

Besides the *de novo* synthesis as a main source for Cer production, the salvage pathway provides recycled sphingosine, which can be used by CerS to synthesize new Cer molecules without dhCer intermediates. SM and glycosphingolipids are degraded to Cer, which is deacetylated to a FA and sphingosine by the acid ceramidase (CDase) (gene name ASAH) [135]. Sphingosine does not only act as a Cer substrate, it "can be phosphorylated to S1P by sphingosine kinase (SPHK)" [136, 137]. S1P is considered as the product of sphingolipid breakdown [135]. Back in the ER, it is irreversibly cleaved by S1P lyase (SPL) (gene name SGPL) [138, 139]. The complex sphingolipid metabolism is a continues turnover and only the SPL activity enables the removal from the sphingolipid metabolism [140].

1.7.3 Ceramide synthase

Cer is the center of the sphingolipid metabolism and as CerS generates Cer via *de novo* and salvage pathway they are key enzymes for the regulation of complex sphingolipids [141]. CerS consists of six mammalian isoforms (CerS 1-6), which differ in tissue expression and in substrate specificity. CerS1 has a high selectivity to stearoyl-CoA (C18:0), it is mainly expressed in the brain and skeletal muscle [141]. CerS2 is a ubiquitously expressed and has a preference for very long chain FA as (C22:0 to C26:1) [142, 143]. CerS3 plays also an important role in the testis with a preference for middle to very long chain FA-CoAs [144] and it also acetylates ultra-long chain FA (<C22:0), which is very important for the barrier formation in the epidermis [145, 146]. In contrast to the restricted CerS3 expression in few particular tissues, CerS4 is more broadly expressed with a higher expression in skin, liver, heart and leukocytes and has a substrate preference for C18:0 and C20:0 [141]. Both CerS5 and CerS6 prefer palmitoyl-CoA (and additionally myristoyl-CoA for CerS5) but have slightly different tissue expression [141].

Tissue expression of CerS is regulated through trannscriptional, posttranscriptional and posttranslational mechanisms, causing that the produced Cer are not always correlating

with the protein expression It is also assumed that substrate availability influence CerS activity and expression [143]. Besides posttranslational mechanism, such as phosphorylation, that impacts CerS activity [147], different CerS isoforms can form dimers that influence their activity [148, 147, 149].

1.7.4 Function

The interaction of all CerS isoforms provides a pool for the generation of complex sphingolipids from Cer of different FA chains. This variety influences the biophysical function within the membrane by fine tuning the interface of specific domains [150, 151, 152]. The strong impact of ceramide variety on membrane properties may explain the difference of the ceramide distribution in various tissues [142]. Within the plasma membrane, Cer accumulates in specific domains and forms Cer-enriched microdomains also known as lipid rafts. They stabilize the rafts by their tightly packed property and serve as platforms, in which receptors can cluster, and amplifies signal transduction after receptor activation [152, 153].

The function of Cer is not restricted to compositional membrane function. Cer also activates several enzymes such as proteases [154], Cer-activated protein phosphatases [155, 156], or regulates serine/threonine-protein kinases such as protein kinase C (PKC) [157, 158]. In addition, upon receptor activation such as CD95, voltage-gated potassium channel Kv1.3 ion channels can either be localized to lipid rafts or the Cer activated tyrosine kinases can inhibit these channels via phosphorylation [152].

Interference with the membrane also affects cell-to-cell signaling. Exosomes are secreted macrovesicle that enable cell to cell communication [159, 160]. Thereby, Cer are not only enriched in exosomes but are also involved in the release of exosomes [161]. CerS are also known under the designation longevity-assurance homolog (LASS) proteins [162], associating that upon intrinsic stressors or extrinsic stressors survival responses are induced to overcome crises and to extend life spam [163, 164]. Indeed, CerS are involved in apoptosis, implicated in cell differentiation and senescence, autophagy, inflammatory processes, ER stress response, regulating sensitivity to chemotherapeutica, radiation and UV-light [165, 152, 141, 166]. Cer can induce cell death either through clustering of death receptor pathway [167], formation of pores in the outer mitochondrial membrane, or intrinsically by activating Bax/Bak translocation, inducing lethal mitophagy, causing cytochrome c release to induce apoptosis or even necrosis and necroptosis [168, 169, 170, 171, 172, 173, 174].

However, it was shown that in the colon cancer these effects depend on the chain length of Cer, while long chain Cer had pro-apoptotic effects, very long chain Cer had protective effects [166]. Another mechanism in which proliferation is inhibited and apoptosis induced, is the direct binding of Cer d18:1/16:0 and Cer d18:1/18:0 to inhibitor 2 of protein phosphatase 2A (I2PP2A). This interaction reduces the binding of I2PP2A [166], so that PP2A can orchestrate the phosphorylation cascade via glycogen synthase kinase-3-β (GSK3-β) to mediate indirectly the degradation of c-myc and β-catenin, both regulate cell growth and proliferation but also cell death [175, 176, 177, 178].

The various functions of sphingolipids as membrane components or signaling molecules, indicate that any alterations in sphingolipid impacts the cell -to cell communication [150, 179]. In particular, the importance of the equilibrium between long chain Cer and very long chain Cer in normal cell physiology and the disequilibrium in cancer drives the attention to the importance of the various CerS isoforms. [180].

1.7.5 Sphingolipids in intestinal tract

In the intestinal tract sphingolipids constitute up to 40% of the apical site of absorptive cells. Especially glucosylceramides are enriched in mature absorptive cells in the villus of the small intestine. The composition of the sphingolipids alters when cells in the crypts differentiate to mature enterocytes, indicating a relation between sphingolipid synthesis and intestinal epithelial homeostasis [181]. In the crypts of small intestine in rats, more ceramides are detected than GlcCer. However this ratio inverts in differentiated villus cells, which have increased concentrations of GlCer [182, 183]. The major Cer species in small intestine of rats are Cer d18:1/16:0, followed by hydroxylated Cer as Cer t18:0/24:0, Cer t18:0/22:0, Cer t18:0/20:0. Cer d18:0/18:0 and dhCer d18:0/18:1 were more abundant as dhCer than Cer [184, 185]. While mature enterocytes were rich in hydroxylated GlcCer t18:1/24:0, crypts had mostly glycolipids with a C20 non-hydroxy FA [185]. It is possible, that Cer metabolites are involved in cell differentiation. Various studies showed the induction of Cer *de novo* synthesis is associated with cell proliferation and differentiation upon steroid hormone stimulation [186, 187, 188].

In the epithelial cells of the intestine, sphingolipids provide structural integrity. Thereby, the chain length is critical [189, 190], but also the class, in particular GlcCer [191]. Hence, the important function of sphingolipids for barrier formation highlights that disbalance in the sphingolipid equilibrium may be relevant for the pathogenesis of IBD [181]. Further, *de novo* synthesis of sphingolipids plays a crucial role in inflammation. Enhanced levels of Cer d18:1/16:0 through CerS6 overexpression in hepatocytes activates p38 mitogen-activated protein kinase (MAPK) and causes TNF-α secretion [192]. In contrast, depending on the stimulus, Cer d18:1/16:0 reveals anti-inflammatory effects by suppressing activation of neutrophil upon TNF-α stimulus and hampers the migration of leucocytes after G-CSF stimulus, which in turn activates CerS2 to promote migration [193]. Furthermore, activation of TLR in macrophages was shown to induce *de novo* synthesis and increases Cer levels for the autophagosome formation [194]. TLR are not only involved in innate immunity, but is also crucial for adaptive immune response [195, 46]. The *de novo* synthesis is also crucial for lymphocyte function. The CerS6 produced Cer d18:1/16:0 are involved several signaling pathways, that promotes activation of T cell receptor activation, proliferation and migration [196].

In general, Cer and sphingosine are regulators of cell death, growth and differentiation. Dysfunction in apoptosis pathway within CRC may support tumor proliferation. And indeed, in human colon cancer Cer levels are reduced about $50\,\%$ in colon mucosa [197] together with SM levels [198]. Inhibiting ceramidase activity increased Cer level and

promoted fast apoptosis induction [197]. Such anticancer effects are achieved through a reduced alkaline SMase activity in carcinogenesis [199, 200]. Indicating that cancer influence the cell fate through the sphingolipid rheostat, which designates the balance between pro-apoptotic Cer and pro-survival S1P levels [201].

1.8 Questions and objectives

Disbalance in sphingolipid levels is a critical feature in tumor progression. So far, alteration in Cer levels in colon cancer has been achieved through manipulating 'hydrolysis pathway' or salvage pathway. Thereby, the role of the *de novo* synthesis in colon cancer progression needs further investigations, especially because CerS activity is the only way to synthesize Cer of different chain length, which have different function. The aim of this work was to investigate the functional role of sphingolipids in inflammatory induced colon carcinogenesis. Specifically tailored on ceramide chain length specific effects by elucidating the role of CerS in colitis and colon cancer progression. For that purpose, this project was divided into different parts using different models to address more specific aspects of the role of CerS in pathology.

1.8.1 Part I

The impact of Cer in barrier integrity and inflammation, but also cell death and proliferation questions: which role do CerS play in the pathogenesis of IBD and CRC? In CerS2 KO mice, it was previously shown that the lack of very long chain Cer was compensated by long chain Cer [189, 192]. Therefore, the focus of this part, was on the impact of CerS4 in colitis and CAC by using CerS4 deficient mice. As CerS isoforms show different tissue expression, the question arises whether CerS4 had tissue specific impact on disease progression of colitis and CAC. Following objectives were investigated:

1. Compare disease progression of WT, CerS4 global knockout (KO) and T cell specific CerS4 (LCK/Cre) deficient mice in DSS induced colitis to define the tissue specific impact of CerS4 by monitoring disease progression pre-mortem and post-mortem.

2. Examine whether CerS4 deficiency impacts intestinal barrier formation in vitro with human colon cancer cells by comparing the Transepithelial/-endothelial electrical resistance (TEER) and permeability assay in Caco-2 cells after downregulation of CerS4 (shCerS4 Caco-2 cells) with control (shNC Caco-2 cells).

3. Evaluate whether the immune response influenced disease progression by measuring the immune cell profile using flow cytometry in colon, spleen and plasma after DSS treatment of CerS4 WT, KO and LCK/Cre and compare it with control mice.

4. Explore the role of CerS4 in inflammatory induced CRC using azoxymethane (AOM)/ DSS model and thereby differentiate between global CerS4 KO and tissue specific

CerS4 deficiency in CerS4 LCK/Cre or intestinal epithelial cell specific CerS4 deficiency (Vil/Cre). Evaluate disease progression by clinical score and histological analysis of the colon.

5. Compare the immune cell profile via flow cytometry in AOM/DSS treated mice with control mice to understand the inflammatory profile in CAC progression.

6. Analyze disease induced shift in sphingolipid composition of colon and various tissue after DSS induced colitis and AOM/DSS induced colitis to discover disease driven changes in sphingolipid composition.

1.8.2 Part II

To investigate whether animal studies could be transferred to the situation in humans, organoids from patient derived colon tissue were established. In the non-interventional clinical trial, questioning which role sphingolipids play in the carcinogenesis, colon organoids were grown from patient biopsies of control tissue, tumor tissue and occasionally from diverticulitis cases. Diverticulitis is not equitable with colitis: In diverticulitis bulging pouches (diverticula) develops, in which microbiota gets caught and stuck causing an inflammation. Organoids grown from patients demonstrates the epithelial cell integrity from self-renewal of stem cell to the differentiation into mature intestinal cells on a small scale and even customized to the patient. This part was established to give a first overview on the CerS profile in organoids differentiating between organoids derived from control or cancer regions, but also inflammatory regions derived from diverticulitis biopsies. To outline tumor driven changes on CerS profile in organoids following objectives were implemented:

1. Establish patient derived organoid cultivation and staining method to investigate CerS mRNA profile in organoids derived from control, colon cancer and diverticulitis patients.

2. Determine mRNA level of stem cell and differentiation marker of various organoids and assess a possible relation between CerS and mucosal integrity.

3. Compare changes in CerS profile and stem cell and differentiation marker of paired samples and between different tumor from the same patient derived from adenoma carcinoma and colon cancer to discover alterations induced through tumor progression.

1.8.3 Part III

Cell proliferation requires nutrients and oxygen for metabolism. However, early in tumor progression oxygen availability is restricted and cells are exposed to hypoxia. Only tumor cells that overcome this challenge, can survive and expand. As CerS are involved in stress regulation, the questions arises whether hypoxia affects CerS expression and which possible impact the respective CerS may have in this early step in tumor progression. In addition,

mimicking artificial environment for CRC lines enable them to interact and grow with their surroundings in all dimensions. This condition may physiologically be more relevant in cell proliferation and growth conditions [202]. Is hypoxia response in that artificial 3D environment comparable with the response in 2D culture? In unpublished data it was shown that CerS expression in dysregulated in tumor tissue from CRC patients compared to their normal mucosa, especially CerS4 was downregulated early in UICC stages. This questions not only how CerS4 impacts cancer progression, but also how this is achieved in CRC and how CerS4 transcription is regulated? To address all these questions, the following approaches were taken:

1. Summarize CerS expression status in CRC lines HCT116, HCT15 and Caco-2 cells to identify possible differences.

2. Analyze the response of CRC lines HCT116, HCT15 and Caco-2 cells to chronic hypoxia regarding alterations in CerS profile and metabolic adaptation at mRNA level but also in HIF1α expression to confirm the hypoxic response and whether they differ.

3. Culture the CRC cells in Matrigel and compare the cell growth of HCT116 cells, HCT15 cells and Caco-2 cells and their response to chronic hypoxia regarding CerS profile and metabolic adjustment to propose more physiologically important results.

4. Investigate chronic hypoxia response in CerS4 and CerS5 downregulation in HCT116 cells and Caco-2 cells. Thereby, compare hypoxia response and determine whether simple downregulation effects HIF1α expression or its translocation to the nucleus. Further, examine whether CerS4 or CerS5 alters chronic hypoxia response regarding mRNA expression of CerS, metabolic adjustment, PPP, mitochondrial dynamic and quality.

5. Analyze transcriptional regulation of CerS4 in CRC lines with luciferase promotor and 3'-untranslated region (3'UTR) system. Further, test whether epigenetic regulation is involved in CerS4 regulation.

6. Verify whether hypoxia affects CerS4 mRNA regulation already on transcriptional level. Confirm this with the luciferase activity assay of CerS4 promotor and promoter deletion constructs in CRC lines after hypoxia exposure to identify putative transcriptional regulators.

Chapter 2

Material and Methods

2.1 Chemicals and reagents

In the following section the purchased reagents, kits and chemicals are listed (Table 2.1). Table 2.2 and Table 2.3 summarizes the composition of the used buffers except high performance liquid chromatography – tandem mass spectrometry (LC-MS/MS) technique. The manufacturer of devices, important plastics and software is specified in each method description. Used antibodies are also listed in the respective method description.

TABLE 2.1: Chemicals, kits and reagents were purchased from following manufacturer.

Chemicals and Reagents	Manufacturer
2-Propanol	Carl Roth GmbH & Co. KG, Karlsruhe, Germany
2x ReddyMix PCR Master Mix	Thermo Scientific, Waltham, USA
4',6-Diamidino-2-phenylindole (DAPI)	Sigma-Aldrich, Deisenhofen, Germany
A83-01	Tocris, Bristol, UK
Accutase® solution	Sigma-Aldrich, Deisenhofen, Germany
Advanced DMEM/F12	Gibco® by Life Technologies, Carlsbad, USA
Agarose Standard Roti®Agarose	Carl Roth GmbH & Co. KG, Karlsruhe, Germany
Ammonium persulfate (APS)	Carl Roth GmbH & Co. KG, Karlsruhe, Germany
Aqua-Poly/Mount	Polysciences, Inc., Eppelheim, Germany
ATP	PJK GmbH, Kleinblittersdorf, Germany
β-Mercaptoethanol	Sigma-Aldrich, Deisenhofen, Germany
B27-Supplement	Life Technologies, Cralsbad, USA
BD Horizon Brilliant Stain Buffer	BD Biosciences, San Jose, CA, USA
BD FACSFlow™ Sheath Fluid	BD Biosciences, San Jose, CA, USA
Bradford Reagent	Sigma-Aldrich, Deisenhofen, Germany
Bromophenol blue sodium salt	AppliChem GmbH, Darmstadt, Germany
Bovine serum albumin (BSA)	Sigma-Aldrich, Deisenhofen, Germany
Calcium chloride ($CaCl_2$)	Sigma-Aldrich, Deisenhofen, Germany
CellTiter-Blue® Cell Viability Assay	Promega GmbH, Walldorf, Germany
Coelenterazine	PJK GmbH, Kleinblittersdorf; Germany

TABLE 2.1: Chemicals, kits and reagents were purchased from following manufacturer.

Chemicals and Reagents	Manufacturer
Coenzyme A	PJK GmbH, Kleinblittersdorf, Germany
Cultrex® Organoid Harvesting Solution	Trevigen, Gaithersburg, USA
DC protein assay kit	BioRad, Munich, Germany
Dimethyl sulfoxide (DMSO)	Carl Roth GmbH & Co. KG, Karlsruhe, Germany
Dithiothreitol (DTT)	AppliChem GmbH, Darmstadt, Germany
D-Luciferin, free acid	AppliChem GmbH, Darmstadt, Germany
DMEM, high glucose, GlutaMAX™ Supplement	Gibco® by Life Technologies, Carlsbad, USA
Dulbecco's Phosphate-Buffered Saline, 1x (DPBS)	Gibco® by Life Technologies, Carlsbad, USA
Eosin	Sigma-Aldrich, Deisenhofen, Germany
Ethanol, absolute	Sigma-Aldrich, Deisenhofen, Germany
Ethanol, 70 %	Carl Roth GmbH & Co. KG, Karlsruhe, Germany
Ethylenediaminetetraacetate (EDTA)	Sigma-Aldrich, Deisenhofen, Germany
FcR Blocking Reagent	Miltenyi Biotec, Bergisch Gladbach, Germany
fetal calf serum (FCS)	Gibco® by Life Technologies, Carlsbad, USA
fluorescein isothiocynate (FITC) dextran	Sigma-Aldrich, Deisenhofen, Germany
Flow cytometric absolute count standard	Polyscience, Eppelheim, Germany
GeneRuler™DNA Ladder-Mix	Thermo Scientific, Waltham, USA
Gentomycin	Gibco ® by Life Technologies, Carlsbad, USA
Glycerine	Carl Roth GmbH & Co. KG, Karlsruhe, Germany
Glycine	Sigma-Aldrich, Deisenhofen, Germany
Growth Factor Reduced (GFR) Basement Membrane Matrix	Corning®, NY, USA
Hanks' Balanced Salt Solution (HBSS) 1x supplemented with Ca^{2+} and Mg^{2+}	Gibco ® by Life Technologies, Carlsbad, USA
HBSS 1x without calcium and magnesium	Gibco ® by Life Technologies, Carlsbad, USA
HEPES	Sigma-Aldrich, Deisenhofen, Germany
human EGF	Peprotech, Hamburg, Germany
Hydrochlorid acid min 37 %	Sigma Aldrich, Steinheim, Germany
KAPPA Genotyping Kit	Kappa Biosystems, Massachusetts, USA
Lamina propria isolation kit	Milteneyi Biotec, Bergisch Gladbach, Germany
Lipofectamine® 2000 transfection reagent	Invitrogen by Life Technologies, Carlsbad, USA
MACS Tissue Storage Solution	Milteneyi Biotec, Bergisch Gladbach, Germany
Magnesium chloride ($MgCl_2$)	Sigma-Aldrich, Deisenhofen, Germany
Mayer's Hematoxylin Solution	Sigma-Aldrich, Deisenhofen, Germany
McCoy's 5A medium (ATCC® 30-2007™)	Gibco® by Life Technologies, Carlsbad, USA
Minimum Essential Medium (MEM)	Gibco® by Life Technologies, Carlsbad, USA

TABLE 2.1: Chemicals, kits and reagents were purchased from following manufacturer.

Chemicals and Reagents	Manufacturer
MEM Non-Essential Amino Acids	Gibco® by Life Technologies, Carlsbad, USA
Methanol, 100 %	Sigma-Aldrich, Deisenhofen, Germany
$MgCO_3$ x $Mg(OH)_2$ x 5 H_2O	Sigma-Aldrich, Deisenhofen, Germany
$MgSO_4$ x 7 H_2O	AppliChem GmbH, Darmstadt, Germany
MilliQ water	Millipore, Darmstadt, Germany
MycoAlert™ Mycoplasma Detection Kit	Lonza Group Ldt., Basel, Switzerland
N Acetylcystein	Sigma-Aldrich, Deisenhofen, Germany
Normal goat serum (NGS)	Thermo Scientific, Waltham, USA
Nicotinamid	Sigma-Aldrich, Deisenhofen, Germany
nonyl phenoxypolyethoxylethanol (NP-40)	Sigma-Aldrich, Deisenhofen, Germany
Nuclease-free water	Gibco® by Life Technologies, Carlsbad, USA
Odyssey® Intercept blocking buffer (PBS)	LI-COR Biosciences GmbH, Bad Homburg, Germany
Opti-MEM®, Reduced Serum Medium	Gibco® by Life Technologies, Carlsbad, USA
Passive Lysis 5x Buffer	Promega GmbH, Walldorf, Germany
Penicillin-Streptomycin	Invitrogen by Life Technologies, Karlsruhe, Germany
Pertex	Medite, Burgdorf, Germany
paraformaldehyde (PFA)	Sigma-Aldrich, Deisenhofen, Germany
pGL3 Basic vector	Promega, Fitchburg, USA
pGL3 Promotor vector	Promega, Fitchburg, USA
Phenylmethylsulfonyl fluoride (PMSF)	Boehringer Mannheim, Mannheim, Germany
PhosphoSafe™	Extraction Reagent EMD Biosciences Inc., Darmstadt, Germany
Ponceau S	Carl Roth GmbH & Co. KG, Karlsruhe, Germany
Potassium chloride (KCl)	Merck KGaA, Darmstadt, Germany
Potassium dihydrogenphosphate (KH_2PO_4)	Carl Roth GmbH & Co. KG, Karlsruhe, Germany
Potassium hydroxide (KOH)	Merck KGaA, Darmstadt, Germany
Precision Plus Protein™ Standards, Dual Color	Bio-Rad, Munich, Germany
Primocyin	Invivogen, Troulouse, France
Purocyin	Invivogen, Troulouse, France
pRL-SV40 vector	Promega, itchburg, USA
Puromycin	InvivoGen, Toulouse, France
QIAGEN Plasmid Mini Kit	Qiagen GmbH, Hilden, Germany
QIAGEN RNA Midi Kit	Qiagen GmbH, Hilden, Germany

TABLE 2.1: Chemicals, kits and reagents were purchased from following manufacturer.

Chemicals and Reagents	Manufacturer
Recovery-Cell Culture Freezing Medium	Gibco® by Life Technologies, Carlsbad, USA
RNeasy Mini Kit	Qiagen GmbH, Hilden, Germany
RNAqueous® Total RNA Isolation Kit	Invitrogen by Life Technologies, Karlsruhe, Germany
Roche cOmplete™, Mini, Protease Inhibitor Cocktail Tablets	Roche Diagnostics Deutschland GmbH, Mannheim, Germany
Rotiphorese® Gel 30 (37.5:1) acrylamide	Carl Roth GmbH & Co. KG, Karlsruhe, Germany
Roti®-Safe GelStain	Carl Roth GmbH & Co. KG, Karlsruhe, Germany
RPMI 1640 Medium, GlutaMAX™	Gibco® by Life Technologies, Carlsbad, USA
SB202191	LC Laboratories, Woburn, USA
Sodium bicarbonate ($NaHCO_3$)	Sigma-Aldrich, Deisenhofen, Germany
Sodium chloride (NaCl)	Sigma-Aldrich, Deisenhofen, Germany
Sodium Dextran sulfate (DSS)	MP Biomedicals, Illkirch, France
Sodium dodecyl sulfate (SDS)	AppliChem GmbH, Darmstadt, Germany
Suberoylanlilide hydroxyamic acid (SAHA)	Tocris, Darmstadt, Germany
SYBR Select Master Mix	Thermo Scientific, Waltham, USA
Tetramethylethylenediamine (TEMED)	Carl Roth GmbH & Co. KG, Karlsruhe, Germany
Tissue-Tek® O.C.T.	Sakura Finetek, Umkirch, Germany
trichostatin A (TSA)	Tocris, Darmstadt, Germany
tris(hydroxymethyl)-aminomethan (Tris) Base	AppliChem GmbH, Darmstadt, Germany
Tris-HCl	Carl Roth GmbH & Co. KG, Karlsruhe, Germany
Triton X-100	Merck KGaA, Darmstadt, Germany
Trypan Blue solution, $0.4\,\%$	Sigma-Aldrich, Deisenhofen, Germany
Trypsin-EDTA, $0.05\,\%$ (1x)	Gibco® by Life Technologies, Carlsbad, Germany
Tween® 20	AppliChem GmbH, Darmstadt, Germany
Verso cDNA Synthesis Kit	Thermo Scientific, Waltham, USA
Y-27632 Dihydrochloride salt	LC Laboratories, Woburn, USA
Zeocin	Invivogen, Troulouse, France

TABLE 2.2: Composition of different buffers used for various applications.

Buffer	Composition	Application
AK solution	3 % BSA, 1 % NGS in PBS	Antibody buffer for IHC/ICC
Band shift lysis buffer	1,000 mM Tris-HCL, pH 7.4 10 mM NaCl 3 mM $MgCl_2$,1 mM PMSF	Solution for nuclear protein extraction
Blocking buffer	3 % BSA, 10 % NGS in PBS	Blocking solution for IHC/ICC
Eosin	100 mg Phloxine B, 20 mL 5 % Eosin stock solution H_2O 780 mL 95 % EtOH 4 mL glacial acetic acid 90 mL	Solution for HE staining
HIF1α lysis buffer	4 % SDS, 150 mM NaCl, 100 mM Tris/HCL, pH 7.4	Lysis buffer for HIF1α in 3D CRC cells
Nuclear lysis buffer	20 mM HEPES, pH 7.4 600 mM KCL, 0.5 mM EDTA freshly added 2 mM DTT freshly added 1 mM PMSF	Lysis buffer for nuclear protein fraction
Nuclear lysis buffer II	20 mM HEPES, pH 7.4 0.2 mM EDTA freshly added 2 mM DTT freshly added 1 mM PMSF	Lysis buffer for nuclear protein fraction
1 PBS	14 mM NaCl, 1 mM, 0.64 mM Na_2HPO, 0.2 mM KH_2PO_4	Washing buffer for IHC, PBS-T (Tween or Triton)
PhosphoSafe based Lysis	PhospoSafe™Extraction Reagent, Roche Complete™Protease Inhibitor Cocktail, 7x in H_2O, DTT 2 mM	Lysis buffer for whole protein extraction
10x TBE buffer	Tris 108 g, Boric acid 55 g, 40 ml 0.5 M EDTA, pH 8, ad 1 l H_2O	Buffer for agarose gel and gel electrophorese
Tail lysis buffer	100 mM Tris HCL, 5 mM EDTA, 0.2 % SDS, 200 mM NaClF	Tail lysis buffer for genotyping
ProteinaseK buffer	5 ml 1 mM Tris HCL pH 8, 0.15 g $CaCl_2$, 25 ml Glycerol	Buffer for solving of ProteinaseK
Erythrocytes lysis buffer	1.5 M NH_4Cl, 100 mM $NaHCO_3$, 10 mM EDTA, 1 N HCl, 1 N NaOH	Erythrocytes lysis buffer for cell isolation for FACS
10% SDS	30 g TrisBase, 150 g Glycine 10 g SDS, ad 1 L H_2O	SDS page
Laemmli buffer	50 mM Tris, 384 mM Glycinerine, 0.1 %[w/v] SDS, 0.01 % Bromphenolblue, 20 % (v/v) β-Mercaptoethanol	Sample buffer for SDS gel

TABLE 2.3: Buffers composition used for luciferase assay.

Buffer	Composition	Application
Firefly luciferase assay buffer	20 mM Tricin, 2.67 mM $MgCO_3$ x $Mg(OH)_2$ x 5 H_2O 1.07 mM $MgSO_4$ x 7 H_2O, 100 µM EDTA, 33 mM DTT 630 µM ATP 277 µM Coenzyme A 470 µM D-Luciferin, free acid in MilliQ H_2O	Firefly luciferase reagent
Renilla luciferase assay buffer	100 mM NaCl, 25 mM Tris-HCL, pH 7.5, 1 mM $CaCl_2$ + 900 nM Coelenterazine, in MilliQ H_2O	Renilla luciferase reagent

TABLE 2.4: Buffer composition for Lamina Propria kit. HBSS (w/o): HBSS without magnesium and calcium.

Buffer for LP Isolation	**composition**
Predigestion solution	HBSS (w/o), 5 mM EDTA, 5 % FCS, 1 mM DTT
Digestion solution	HBSS, 5 % FCS
PB buffer	PBS, 0.5 % BSA

2.2 Animal models

All animal experiments were in compliance with the ethics guidelines and approved by the local authorities, the Animal Welfare Committee of the Regional Council Darmstadt (Germany) (FK/1082). Three CerS4 deficient strains Lass4$^{-/-}$(KO), CerS4$^{fl/fl}$Vil-Cre^{+} (Vil/Cre) and CerS4$^{fl/fl}$LCK-Cre^{+} (LCK/Cre) were generated. CerS4 complete knockout was obtained by deleting exon 3 of the CerS4 gene and inserting an exon 3 flanking LoxP site (CerS4$^{fl/fl}$ mice). Finally, the CerS4$^{fl/fl}$ mice were crossed with Flp deleted Cre deleter mice. The generation is described in [203]. The two other Lass4 conditional knockout alleles were generated by crossing CerS4$^{fl/fl}$ with either transgenic mice, in which Cre recombinase is expressed in villus and crypt epithelial cells of the small and large intestines (Villin-Cre) (B6.Cg-Tg(Vil1-cre)1000Gum/J) or Cre-recombinase gene driven by the distal promoter of the lymphocyte protein tyrosine kinase (Lck) gene (LCK-Cre) (B6-Cg-Tg(Lck-cre)548Jxm) mice obtained from Jackson Laboratory (by Charles River, Sulzfeld, Germany). The CerS4$^{fl/fl}$ mice were a kindly gift from Prof. Martin Krönke (Institute for Medical Microbiology, Immunology and Hygiene; University of Cologne, Germany) [204]. The breeding of mice was operated by mfd-diagnostics (Mainz, Germany) and the householding and experiment performance at the Zentrale Forschungseinrichtung (ZFE) of the University Hospital Frankfurt. The mice were kept under standard housing conditions with a controlled environment (temperature of 22 °C ± 2 °C, relative humidity of 55 % ±10 %, 12:12 h

light-dark cycle), standard food (fixed formulation diet) and water ad libitum. Before starting with experimental procedures, newly delivered mice were accustomed to housing and feeding for 2-3 weeks. Male and female mice in the age of 6 to 12 weeks were enrolled. CerS4 KO mice had a distinct phenotype: the mice had a progressive hair loss (Figure 2.1). Ebel et al. (2014) described that fur begins to start falling out at about postnatal 50 days, in old age (22 months) the CerS4 KO mice suffered from total loss of back hair [205]. The other mice had no phenotype.

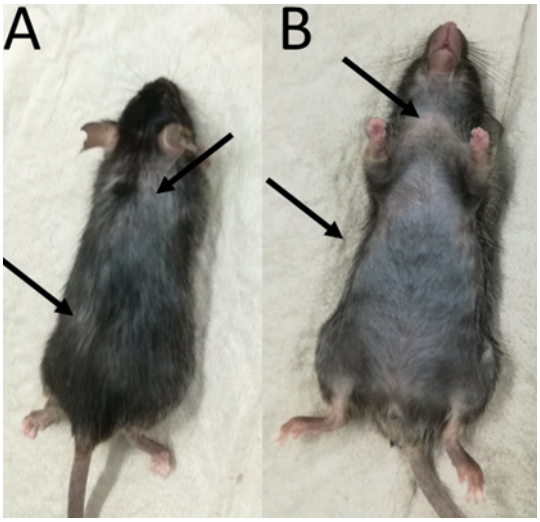

FIGURE 2.1: Representative example of hair loss phenotype of a male CerS4 KO control mice. The belly fur (B) was stronger affected than the back fur (A). Black arrows point at regions affected from hair loss.

In the DSS induced inflammation model the drinking water of the mice was supplemented with $2\,\%$ DSS (colitis grade, M.W. 36,000 - 50,000) for five days and exchanged afterwards. After three days the animal experiment was terminated and further proceeded to tissue processing. In CerS4 LCK/Cre mice the DSS induced colitis was terminated after 4-5 days. The CAC model is based on the inflammation induced by the acute model. However, to accelerate mutagenesis in the colon epithelium, $5\,\mathrm{mg\,kg^{-1}}$ AOM was initially injected intraperitoneally twice at day 0 and 1 and followed by $2\,\%$ DSS application for 5 days. "To induce chronic inflammation the DSS treatment was repeated twice after a recovery of 14 days between each DSS cycle" [204]. After the last DSS cycle, the mice were kept under normal conditions and constant observation for up to 6 weeks and then by CO_2 inhalation and killed by cervical fracture and cardiac puncture. The entire duration of both models was 7-10 days for the acute DSS model and 13 weeks for the CAC model. Based on the Canadian Council on Animal Care 1998 [206], the observation protocol for the mice during the experiments was followed. Thus, disease progression was monitored by body weight, stool consistency, bleeding, and body posture. Changes in body weight and physical condition of the mice were matched with specific scores and used to estimate an overall disease progression score. Once a human endpoint (Score >3) was reached, the pain of the mice was terminated by sacrificing, and at a Score of 2, attempts were made to relieve suffering

by intraperitoneal injection of isotonic sodium chloride solution (0.9 % NaCl) or administration of water-soaked food pellets in the cage. Post-mortem the colon was washed and cut longitudinally and the length was captured with hand camera shots. The colon length was measured in cm with the measurement tool of FIJI software [207] after calibrating the scale.

2.2.1 Genotyping

KAPA Genotyping Kit was used to determine the genotype of the mice. First, ear punch tissue was lysed by 10 % volume per volume (v/v) tail lysis supplemented with 2 % v/v protease K and incubated at 70 °C for 10 min with gently shaking (350 rpm) followed by 5 min shaking (350 rpm) at an incubation temperature of 95 °C. Amplification was performed by Taq deoxyribonucleic acid (DNA) Polymerase with the primer sequence of CerS4 and for conditional knockout additionally with either Vil-Cre or LCK-Cre Primer (Table 2.6) with the following polymerase chain reaction (PCR) programs (Table 2.5). PCR resulted to an amplicon of 1,011 basepair(bp) for the wild-type and an amplicon of 239 bp for the Cers4$^{-/-}$ allele. For the conditional knockout mouse, the wildtype amplicon was 182 bp and 150 bp for the Vil-Cre and 324 bp for the LCK-Cre. Amplicon size was confirmed by gel electrophoresis. Therefore, PCR products were loaded onto a 2 % (3 % for Vil/Cre PCR amplicons) agarose gel supplemented with Roti®-Safe GelStrain DNA-binding fluorescence dye (5 % v/v) and a GeneRuler™ DNA Ladder Mix as DNA standard. PCR products were separated by electrophoresis at 100 V (PowerPac Basic, BioRad, Feldkirchen, Germany). And visualized on a Gel Doc XR+ System with the ImageLab™ software, both obtained by Bio-Rad (Feldkirchen, Germany).

TABLE 2.5: Specification for genotyping PCR in a reaction volume of 20 µL performed in flexid Mastercylcler nexus (Eppendorf, Hamburg, Germany).

Preparation for 1 sample		**PCR program** Lass4 , LCK-Cre			Vil/Cre		
Taq Polymerase Mix	12.5 µL	95 °C	5 min		94 °C	2 min	
Primer forward	1.25 µL	95 °C	30 sec		95 °C	20 sec	
Primer reverse	1.25 µL	60 °C	30 sec	35x	65 °C	15 sec	10x
Nuclease free Water	4 µL	72 °C	2.5 min		68 °C	10 sec	
Template DNA	1 µL	72 °C	5 min		94 °C	15 sec	
		4 °C	hold		60 °C	15 sec	28x
					72 °C	15 sec	
					72 °C	2 min	
					10 °C	hold	

2.3 Tissue preparation

For the analysis of sphingolipids, inflammatory response, and tumor development various tissues (colon, small intestine, liver, spleen and blood) were dissected and washed in

TABLE 2.6: Used Oligonucleutide sequence to identify the knockout mice. Primer were used in a concentration of 10 µM and purchased from biomers.net GmbH (Ulm, Germany)

	Sequence (5′-3′)
CerS4 Forward	GCCCTTGAGTAACCTGATGC
CerS4 Reverse	CCCAGAAAGGCTACACAAGG
LCK-Cre Forward	CAGTCAGGAGCTTGAATCCC
LCK-Cre Reverse	CACTAAAGGGAACAAAAGCTGG
Vil-Cre Forward	GCCTTCTCCTCTAGGCTCGT
Vil-Cre Reverse	AGGCAAATTTTGGTGTACGG

cold Dulbecco's phosphate-buffered saline dulbecco's phosphate-buffered saline (DPBS). For sphingolipid analysis of Lass4 KO mice and wildtype mice (WT), the colon and distal part of the small intestine were cleared from feces mechanically with forceps and by rinsing with cold DPBS. 5 mg to 10 mg of tissue was weighted and stored on dry ice. A liver lobe was dissected, weighted (5 mg to 10 mg) and stored on dry ice. Blood samples were obtained by cardiac puncture and stored in small ethylenediaminetetraacetic acid (EDTA) tubes on ice. For plasma collection, blood samples were centrifuged at 500 x g for 10 min at 4 °C. For flow cytometry, blood and spleen were always used for analysis and colon tissue was also processed for acute DSS model (descripted in subsection 2.3.1). To isolate white blood cells (WBCs), the mixture of 100 µL of ice-cold EDTA blood with 1:1 (v/v) 2-(4-(2-hydroxyethyl)-1-piperazinyl)-ethansulfon acid (HEPES) was lysed twice with an erythrocyte's lysis buffer for 10 min at room temperature (RT) and centrifuged at 600 x g at 4 °C. The pellet was resuspended in 100 µL FACS-flow and stored on ice. The spleen was grinded with a stamp and washed once with HBSS through a 70 µm Corning cell strainer (BD Falcon). Splenocytes were collected by centrifugation (5 min, 600 x g at 4 °C), washed with 1x DPBS after 10 min erythrocytes lysis (for 500 x g at 4 °C, 5 min) and resuspended in 300 µL FACS flow.

2.3.1 LP and IEL Isolation

After dissection and cleaning the colon from feces with cold DPBS, it was cut longitudinally and sliced into 0.5 cm pieces. The colon pieces were digested twice in predigestion buffer (Table 2.4) by rotation on a MACS Rotator (Miltenyi Biotec, Bergisch Gladbach, Germany) at 37 °C for 20 min, pooled and filtered through a 70 µm strainer. Using this procedure, IEL were mechanically isolated and pooled by centrifugation at 300 x g for 10 min. For the digestion, the colon pieces were transferred in Gentle MACS C Tubes in digestion solution (Table 2.4) supplemented with a defined enzyme cocktail mix 100 µL of Enzyme D, 50 µL of Enzyme R, 12.5 µL of Enzyme A) and incubated in the Gentle MACS Octo Dissociator (Miltenyi Biotec, Bergisch Gladbach, Germany) at 37 °C for 25 min. The LP cells were spun down and centrifugated at 300 x g for 10 min. After washing the pellet with FACS flow, cells were resuspended in 200 µL FACS flow and 100 µL transferred to a FACS tubes (Falcon® 5 mL polystyrene round-bottom tube (Corning) for staining.

TABLE 2.7: Antibodies coupled with fluorochromes were diluted in 55 µL Brilliant stain buffer to detect specific cell surface markers in the samples by fluorescence-activated cell sorting (FACS).

Antigen	Cell type	Dye	1x (µL)	Manufacturer
CD3	T-cells	PE-CF594	1	BD, Heidelberg, Germany
CD4	CD4 T-cells	BV 711	1	BD, Heidelberg, Germany
CD8	CD8 T-cells	eVolve 655	2	eBioscience, Frankfurt, Germany
CD11b	Monocytes	BV 510	0.5	BD, Heidelberg, Germany
CD11c	DC	AlexaFluor700	0.5	BD, Heidelberg, Germany
CD14	Monocytes	PE	0.5	BD, Heidelberg, Germany
CD19	B-cells	APC-H7	1	BD, Heidelberg, Germany
CD25	Tregs	PE-Cy7	2	BD, Heidelberg, Germany
CD36	Macrophages	APC	2	eBioscience, Frankfurt, Germany
CD45	Immune cells	VioBlue	2	Miltenyi Biotec, Bergisch Gladbach, Germany
CD80	Monocytes, B cells	FITC	2	BD, Heidelberg, Germany
GITR	Tregs	FITC	1	BD, Heidelberg, Germany
F4/80	Macrophages	PE-Cy7	0.5	BioLegend, Fell, Germany
Ly-6G	Neutrophils	APC-Cy7	1	BD, Heidelberg, Germany
Ly-6C	Monocytes	PerCP-Cy5.5	0.5	eBioscience, Frankfurt, Germany
MHC II	Antigen presenting cells	BV 605	0.5	BD, Heidelberg, Germany
NK 1.1	NK-cells	PE	2	BD, Heidelberg, Germany
7-AAD	Dead cells	PE	2	BD, Heidelberg, Germany

2.3.2 FACS analysis of cell surface proteins

To determine immune cell populations, cells were stained with surface immune cell marker. Prior to staining, 100 µL cell suspension of WBCs, spleen, IEL and LP isolated suspensions were blocked with FcR blocking reagent at RT for 15 min protected from light. The antibody cocktail (listed in Table 2.7) was added and incubated for 15 min at RT in the dark. Then the cells were washed with 500 µL FACS flow (500 x g, 4 °C, 5 min) and resuspended in 300 µL FACS Flow. Flow cytometric analysis of fluorescence emission was performed using the BD LSRFortessa™ Cell Analyzer and the BD FACS Diva™ software (BD Biosciences, Heidelberg, Germany), both provided by Prof. Dr. Bernhard Brüne (Institute of Biochemistry I, Faculty of Medicine, Goethe-University Frankfurt). Immune cell populations were analyzed using FlowJo software v10 (Treestar, Ashland, MA, USA). Percentage of the living immune cells ($CD45^+$ and $7AAD^-$ population) was calculated by FlowJo software v10 (Treestar, Ashland, MA, USA). The gating strategy is attached in the Appendix A (Figure A.1, Figure A.2,Figure A.3).

2.3.3 Hematoxylin-Eosin staining

For histological analysis of the colon, the cleaned, longitudinally cut colon was rolled from the proximal part to the distal colon as a Swiss role using two forceps, embedded in "Tissue-Tek® O.C.T.™ compound (Sakura Finetek, Umkirch, Germany) in a Tissue-Tek® Cryomold® intermediate Biopsy Molds (15x15x5 mm, Sakura Finetek, Umkirch, Germany), frozen on dry ice and stored at -80 °C" [204]. $10\,\mu\mathrm{m}$ sections of the colon roles were cut using a LEICA CM 3050S microtome and stored at -80 °C for at least $24\,\mathrm{h}$. Hematoxylin-Eosin (HE) is a standard method for pathology diagnosis, in which two dyes are combined to contrast tissue and cell structures. Hematoxylin is cationic, basic dye, that is achieved through the oxidation of hematein combined with aluminum alum. In contrast, eosin is a the potassium salt of tetrabromfluorescein and an anionic acid dye HE. Applying both dyes subsequently to the tissue causes blue stained nuclei and a pink stained cytoplasm, organelles and extracellular matrix [208]. For staining, the colon sections were thawed, fixed with $4.5\,\%$ PFA and washed twice with distilled water. The HE staining protocol used was as follows: The slices were incubated in hematoxylin solution for $6\,\mathrm{min}$, washed with running tab water for $10\,\mathrm{min}$, rinsed three times briefly in hydrochloride alcohol ($0.625\,\%$ v/v in $100\,\%$ ethanol) and washed under running tab water. The slices were then rinsed three times briefly in ascending concentration of ethanol ($70\,\%$ and $96\,\%$ ethanol) and stained with eosin solution (Table 2.2) for half a minute. After rinsing in distilled water, the slices were dehydrated in an ascending serial ethanol concentration ($70\,\%$, $80\,\%$, $96\,\%$ and $100\,\%$) for $2\,\mathrm{min}$ each and finally in xylene for $2\,\mathrm{min}$ twice. After vaporization of the xylene, the slides were embedded in xylene-based mounting medium Pertex®, evaporated for $24\,\mathrm{h}$ and stored at RT.

2.3.4 Histological Analysis

For histological analysis, the slides stained with HE were viewed using the BIOREVO microscope (Keyence, Neu-Isenburg, Germany) with a 10x/0.3 objective (with z-stack exposure), and the best-fitting z-sections were merged with the merging tool of BZ II Analyzer (Keyence, Neu-Isenburg, Germany). Fiji software was used to measure the length of the entire colon roll, inflamed areas (filled with immune cells), destructive crypts regions, hyperplastic regions, dysplastic regions and neoplastic regions using the freehand line tool on the graphic tablet (XP-Pen Technology CO., USA) (Appendix A Figure A.4).

2.4 Cell culture

2.4.1 Cell lines and culture

Three commercial colon cell lines purchased from American Type Cell Culture Collection (ATCC) were used in this project: HCT116 cell line, HCT15 cell line and Caco-2 cell line. All three cell lines were adherent epithelial cells and suitable for transfection. The cell lines were verified by sequencing and controlled for mycoplasma contamination using the

MycoAlert™ Mycoplasma Detection Kit by luminescence according manufactures instruction. For cultivation, CRC cell lines were cultivated at $37\,^{\circ}\mathrm{C}$ in a humidified atmosphere containing $5\,\%$ CO_2 in a Heracell 240 incubator (Thermo Scientific, Wallthan, USA).

HCT116 (ATCC® CCL-247™) was obtained from colorectal carcinoma of a patient with advanced metastatic disease stage (Dukes Type D) [209]. These adherent epithelial cells were purchased from the ATCC® (Manassas, USA) and cultured in McCoy's 5A Medium supplemented with $10\,\%$ FCS according to ATCC recommendation.

HCT15 (ATCC® CCL-225™) was derived from colorectal adenocarcinoma of a patient with advanced, metastasizing disease stage (Dukes Type D) [209]. The HCT15 intestinal epithelial cells were purchased from ATCC® (Manassas, USA) and cultured in RPMI 1640 medium supplemented with $10\,\%$ FCS according to ATCC® recommendation.

Caco-2 (ATCC® HTB-37™) (Cancer-coli-2) was established from moderate, well differentiated colorectal adenocarcinoma [210, 211]. Human epithelial cells have an epithelial like morphology. They were provided by Susanne Schiffmann (Fraunhofer ITMP, Frankfurt, Germany) and cultured in Eagle's Minimum Essential Medium supplemented with $10\,\%$ FCS, $1\,\%$ MEM Non-Essential Amino Acids and $1\,\%$ HEPES. Caco-2 cells have the feature that they still retain contact inhibition in culture, so they spontaneously differentiate when confluence is reached in long term culture [211]. For passaging, a subconfluent monolayer was maintained, and spontaneous differentiation was undesirable.

2.4.2 Stable CerS knockdown generation

Posttranscriptional gene silencing was used to induce a CerS knockdown in CRC cell lines. Here, a stable CerS knockout cells was generated by lentiviral transduction with short hairpin RNA (shRNA). This enabled a stable integration of shRNA, which are short hairpin structures produced by mammalian cells from a lentiviral plasmid. RNA pol II and III transcribe two short (19-22 bp) complementary RNA sequences joined by a short loop to form a hairpin structure. This structure "is processed by the enzyme Dicer into short interfering RNA (siRNA)" [212]. In the cytosol, a multiprotein complex, the RNA-induced silencing complex (RISC), uses the siRNA to recognize its complementary mRNA and leads to its RNA cleavage [213, 214, 215]. Lentiviral transduction enables continuous shRNA transcription that is stable after cell division and passaging. CerS4 and CerS5 were downregulated in CRC cell lines with specific targeted sequences (shCerS4, shCerS5) and nonspecific, scrambled shRNA was used as a negative control to generate shNC cultures. Stable downregulated cells were generated in house and the procedure described in detail in [189]. In brief, pGIPZ-vector (Figure 2.2) constructs were transfected into HEK293T-cells together with lentiviral packaging vectors (pMD2.G-VSVG, pCMV-dR8.91-Gag/pol) in presence of calcium-phosphate. $48\,\mathrm{h}$ after transduction, viruses were collected and used to infect CRC cell lines with Multiplicity of infection (MOI)10. Stable transduced cell lines were then selected with puromycin. For selection of stable transduced cells, Caco-2 cells were exposed to ($3\,\mu\mathrm{g/mL}$), HCT116 cells to $1\,\mu\mathrm{g/mL}$ and HCT15 cells $1.5\,\mu\mathrm{g/mL}$ puromycin. The pGIPZ plasmid not only allows a selection by its puromycin sequence, but also the GFP cassette

upstream of the target sequence coding for a hairpin structure (Figure 2.2), allows marking of transduced cells by fluorescence microscopy. The knockdown efficiency was detected using real time polymerase chain reaction (RT-PCR) (subsection 2.6.4).

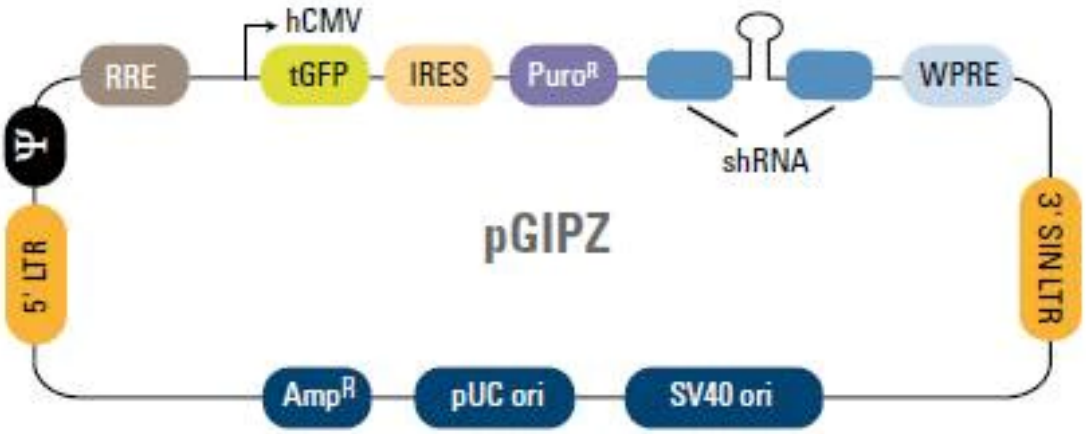

FIGURE 2.2: Vector map of the gipz vector. The lentiviral vector was used to insert shRNA to downregulate CerS4 and CerS5 translation. As a control a scrambled shRNA was inserted into shNC cells. tGFP: turboGFP reporter for fluorescence monitoring, Puro:, puromycin resistance for antibiotic selection pressure, IRES: internal ribosomal entry site to warrant the expression of TurboGFP and PuroR in a single transcript, shRNA: micro-RNA-adapted shRNA for target gene knockdown. Source for picture and further explanation of other vector elements in Supporting Data GIPZ Lentiviral shRNa by horizon (PerkinElmer).

2.4.3 Cell passaging and counting

To maintain a consistent growth of a subconfluent human CRC cell line, HCT116 cells and HCT15 cells were passaged every two to three days and Caco-2 cells every three to four days. Adherent cells were washed with prewarmed DPBS and detached by incubation with pre-warmed $0.05\,\%$ trypsin-EDTA for two to four minutes. Once the cells were detached, the trypsin was neutralized by the same volume of pre-warmed culture medium. Compared to the other cell lines, Caco-2 cells were very adherent, so trypsinization was not sufficient and the cell layer was additionally scrapped off with a cell sharper. Cells were resuspended and collected in conical centrifuge tubes and HCT116 cells and HCT15 cells were pelleted at $1{,}200\,\mathrm{rpm}$ at RT, Caco-2 cells at $800\,\mathrm{rpm}$ for $5\,\mathrm{min}$ in the 5810 R centrifuge (Eppendorf, Hamburg, Germany). Cell pellets were resuspended in fresh culture medium and seeded in fresh culture medium in culture flasks at ratios of 1:5 (HCT15 cells, Caco-2 cells) to 1:10 (HCT116 cells). To determine cell count, cell suspensions were diluted 1:10 with trypan blue solution and manually counted with a Neubauer counting chamber (Marienfeld Superior, Lauda Königshofen, Germany) using a ZEISS Primovert inverted microscope (Carl Zeiss Microscopy GmbH, Jena, Germany) with 10x/0.25 planachromat objective. Trypan blue stained cells were excluded in the viable cell count. The cell count of the original suspension was determined by multiplying the average number of cells in all four large squares by the trypan blue dilution factor and calculation factor 1×10^4 (Equation 2.1) .

$$\text{Cell concentration} = \text{average cell number} \cdot \text{Dilution factor} \cdot 1 \times 10^4 \quad (2.1)$$

The seeding of cells was different for the various assays: For incubation under hypoxia, CRC cells were seeded to extract proteins ($100\,\mathrm{mm}$ dish) or RNA ($60\,\mathrm{mm}$ dish), but also to test the cell viability (48-well plate). For luciferase assays, cells were seeded in a 24-well plate or 96-well plate and for HDAC inhibitor assay in 6-well plates. The seeding density of each cell line is summarized in Table 2.8. Because Caco-2 cells are larger and grow more slowly than HCT116 cells and HCT15 cells, more cells were initially seeded.

TABLE 2.8: Cell density of the CRC lines differed depending on the culture format and CRC line

Culture format	Culture medium per well/dish	Cell number per well/dish HCT116	HCT15	Caco-2
96-well plate	$150\,\mu\mathrm{L}$	0.14×10^5	0.3×10^5	
48-well plate	$500\,\mu\mathrm{L}$	0.1 & 0.2×10^5	0.1 & 0.2×10^5	0.2 & 0.25×10^5
24-well plate	$1\,\mathrm{mL}$	0.75×10^5		0.75×10^5
6-well plate	$2\,\mathrm{mL}$	3×10^5	3×10^5	
$60\,\mathrm{mm}$ dish	$3\,\mathrm{mL}$	1.4×10^5	2×10^5	5×10^5
$100\,\mathrm{mm}$ dish	$10\,\mathrm{mL}$	4×10^5	8×10^5	15×10^5

2.4.4 Cell freezing and thawing

For long term cell line storage, cell line cultures were cryopreserved at low passage numbers. As previously described (2.4.3), cells were centrifuged after counting and resuspended in cryopreservation solution (FCS containing $10\,\%$ [v/v] dimethyl sulfoxide (DMSO)). 4-8×10^6 cells were transferred to CRYO.STM cryotubes (greiner bio-one, Frickenhausen, Germany) and chilled $10\,\mathrm{min}$ on ice. Wrapped in thick layers of paper towels cryomolds were stored at -$80\,^\circ\mathrm{C}$ for at least overnight and for long term storage transferred in liquid nitrogen. The cryopreserved cell cultures were thawed in a water bath at $37\,^\circ\mathrm{C}$ until most of the ice had melted and immediately transferred in $10\,\mathrm{mL}$ prewarmed cultured medium. To remove residual DMSO, cells were centrifuged at $1{,}200\,\mathrm{rpm}$, at RT for $3\,\mathrm{min}$, resuspended in fresh culture medium, and seeded in $75\,\mathrm{cm}^2$ (HCT15 cells, Caco-2 cells) or $175\,\mathrm{cm}^2$ culture flask (HCT116 cells). After $24\,\mathrm{h}$, dead cells and debris were removed by complete medium exchange and cultured as previous descripted (2.4.3).

2.4.5 3D cultured cell lines

To approximate the condition of colon tissue *in vivo*, CRC cell lines were seeded in growth factor reduced basement membrane matrix (Matrigel, #356231). 2×10^4 cells were seeded in $500\,\mu\mathrm{L}$ Matrigel (HCT116 cells, HCT15 cells) or 2.5×10^4 cells (Caco-2 cells), $80\,\mu\mathrm{L}$ were seeded as droplets in the center of a 24-well plate, and as in hanging droplet protocol, the plate was turned upside down in the incubator to solidify the Matrigel. The plate was incubated in the incubator upside down for $25\,\mathrm{min}$, then inverted and $1\,\mathrm{mm}$ of culture medium

was added and incubated for 7 days. For harvesting, the medium was removed and washed once with DPBS. 300 µL Cultrex harvesting solution were used to depolymerizes the Matrigel domes in a 24-well plate in each well with moderate shaking at 4 °C for >90 min. If the domes were not dissolved after shaking, the process was accelerated by pipetting up and down and then transferred to a 2 mL reaction tube. The non-enzymatic Cultrex solution was removed by centrifugation at 4 °C for 5 min at 500 x g. Cells were washed with cold DPBS under the same conditions. After removal of DPBS, the pellet was further used for either RNA isolation or protein isolation or stored at -80 °C.

Phase contrast images were taken with an Axio Primovert invert microscope (Carl Zeiss, Oberkochen, Germany) with an integrated AxioCamERc 5s with a Plan-Achromat 4x/0.10 objective.

2.4.6 Hypoxic incubation

For chronic hypoxia exposure, CRC cells were cultured at 1 % O_2. Therefore, the CRC cell lines were incubated in a hypoxia incubator SciTive Workstation (Baker Ruskinn, Leeds, UK) at 1 % O_2 and 5 % CO_2 for 24 h to 72 h. To ensure a continuous nutrient availableness, fresh medium was equilibrated to the workflow atmosphere and used for media exchange after the first 24 h. CRC cells were seeded for RNA and protein harvest in 6 mm, 10 mm cell culture dishes as described in Table 2.8, cultured in incubator at normoxia and at different time points transferred to the SciTive Workstation (exhibited to hypoxia) and then all harvested once with the control sample. For protein extraction, cell lysis was performed in the SciTive Workstation, while for RNA extraction, cells were lysed on the lab bench. The SciTive Workstation was provided by Prof. Dr. Bernhard Brüne (Institute of Biochemistry I, Faculty of Medicine, Goethe-University Frankfurt).

2.4.7 Cell viability assay

To screen how many cells are viable after an experiment, cell-based viability assays are used. A multitude of indicators can be used to detect metabolically active cells by measuring either ATP content of the cell or protease activity or the ability to reduce a substrate [216]. To exclude cell death due to chronic hypoxia exposure (72 h), cell viability was detected using a fluorescent based method (CellTiter-Blue® assay) in which live CRC cells convert resazurin. Resazurin is a redox dye that penetrates the cell and is reduced to the product resorufin. While viable cells can reduce the dark blue dye to a pink, fluorescent resorufin, dead cells that have lost their metabolic capacity do not generate this fluorescent signal. Thus, the fluorescence signal is proportional to the amount of viable cells [216]. For this assay, CRC cells were seeded as in a 48-well format as described in Table 2.8. Both 2D and 3D CRC cells were seeded in triplicates in two plates. After 24 h, one plate was cultured in the SciTive Workstation (Baker Ruskinn, Leeds, UK) at 1 % O_2 and 5 % CO_2 at 37 °C for 72 h, meanwhile the other was incubated under normoxic conditions at 37 °C. On the third day, cells were stained with CellTiter-Blue® and incubated for 1 h under normoxic conditions at 37 °C. Fluorescence was measured using a Spark Multimode Microplate Reader

(Tecan, Männedorf, Germany). Cell plates were excited with 10 flashes at the wavelength $545\,\mathrm{nm}$, and emission at the wavelength of $590\,\mathrm{nm}$ was measured. relative fluorescence units (RFU) values were referenced to Caco-2 cells $0\,\mathrm{h}$ (set as $100\,\%$) and to determine the viability, protein concentration in each well was determined after washing and cell lysis with either Bradford method or, for 3D cells, the detergent compatible (DC) protein assay (subsubsection 2.7.3.1). To determine viability, RFU was related to the protein concentration. Calculated viability was also referenced to Caco-2 cells $0\,\mathrm{h}$ (set as $100\,\%$).

2.4.8 TEER measurement

A common barrier model *in vitro* is the measurement of TEER, which indicates the integrity of the tight junction dynamics by the paracellular flow. In an epithelial cell layer, molecules and ions can be transported either between cells (paracellular flow) or through cells (transcellular flow)[217, 218]. *In vitro*, barrier functionality was determined by measuring the electric impetance (Z) of a cell system. From the recorded Z both TEER and electric capacitance (C_{Cl}) are extrapolated. These two parameters contribute to the Z spectrum of a cell layer and provide information about the cell layer. TEER correlates directly with the paracellular flow. This parameter indicates the tightness of the barrier. The more cell-to-cell contacts are formed, the higher the Ω resistance will be, the higher the paracellular resistance is [217]. The transcellular resistance can be determined by the electric C_{Cl} ($\mu\mathrm{F\,cm^{-2}}$). It indicates the expression of microvilli or membrane extrusions and is thus an indicator for differentiation [219, 217]. TEER measurements on Caco-2 cells were performed using a cellZcope2 instrument (nanoAnalytics GmbH, Münster, Germany) provided by Fraunhofer IME in Frankfurt, Höchst. CellZscope2 is an automated Z-based cell monitoring system that measures TEER under physiological conditions and a non-invasively [217]. In contrast to HCT116 cells and HCT15 cells, Caco-2 cells form a tight barrier and are more suitable for TEER measurements (determined experimentally, [220]). ShNC and shCerS4 Caco-2 cells, were seeded on $1\,\mu\mathrm{m}$, transparent 24-well ThinCert cell culture inserts (greiner bio-one, Frickenhausen, Germany). For better cell growth of Caco-2 cells, ThinCert inserts were coated with bovine serum albumin (BSA) for $30\,\mathrm{min}$ at RT and washed with culture medium. 3×10^4 Caco-2 cells were seeded in $300\,\mu\mathrm{L}$ culture medium into the inserts and afterwards the bottom chamber of the instrument was filled with $1\,\mathrm{mL}$ culture medium. Half of the medium was replaced every three days, and after 4 days all old medium was replaced with fresh one in the upper inserts and bottom chambers. The CellZscope device set to stimulate the cells with $1\,\mathrm{kHz}$ to $10\,\mathrm{kHz}$ and to measure the Z every hour. The CellZscope software (NanoAnayltics GmbH, Münster, Germany) calculated the capacity ($\mu\mathrm{F\,cm^{-2}}$) and the TEER ($\Omega\,\mathrm{cm^2}$).

2.4.9 Permeability Assay

Another analysis of barrier function is the permeability of acFITC-dextran through a cell barrier [221]. Therefore, the cells for TEER and FITC permeability were seeded on two

separate plates but cultured under the same conditions and at the same time. When Caco-2 cells in the CellZscope2 had reached a plateau and Z was at a saturated constant level, $100\,\mu g\,mL^{-1}$ FITC-dextran (average mol wt $40{,}000$ was added to the top of the Caco-2 cells in the second plate 2.4.8).The epithelial monolayer allows the fluorescent molecule to pass through, in proportion to the permeability of the monolayer. $20\,\mu L$ of the apical medium and $66.7\,\mu L$ of the lateral medium were taken at different time points ($1\,h$ to $8\,h$, $24\,h$, $48\,h$) for fluorescence measurements. Fluorescence was measured with the EnSpire Multimode Plate Reader (PerkinElmer, Rodgau, Germany) in a black polysterol 384-well plate (greiner bio-one, Frickenhausen, Germany) provided by Fraunhofer ITMP in Frankfurt, Germany. A standard curve was used to calculate the FITC content from the emission. The samples were measured at an excitation wavelength of $496\,nm$ and an emission wavelength of $530\,nm$ with 100 flashes.

2.4.10 Luciferase reporter gene assay

Similar to RNA quantification, detection of promotor activity can be used to study transcriptional regulation of a gene of interest. Reporter fusions assays facilitate the investigation of promotor activity in cells [222]. The measurement of the reporter activity, in this case luciferase, reflects the expression of the gene of interest. Firefly luciferase is an enzyme that generates bioluminescence by cleaving a substrate, D-luciferin. This ATP dependent oxidation results in a by-product that is light [223].

The firefly luciferase reporter gene assay quantifies the activity of the produced firefly luciferase in cultured cells and is a tool to investigate among other things, a functional link between cellular events and targeted DNA gene expression [224]. This system was used to determine the transcriptional and posttranscriptional regulation of the full-length CerS4 gene in different CRC cell lines and in response to hypoxia. For this purpose, the CerS4 promotor was flanked in a vector construct adjacent to the luciferase reporter gene (published in [188]). Hence, the transcription of the luciferase reporter was dependent from the specific CerS4 promotor sequence and the luminescence signal is dependent on the level of luciferase expression. The more luciferase was produced in the cultured cells, the higher the luminescence signal is expected to be. A supervised Master thesis was within the scope of this work and included the analysis of promotor deletion constructs, which also were previously published in [188]. Parts of these results were also considered to specify or exclude potential transcription factors that may be relevant for CerS4 regulation. In the following steps, the setup of the constructs, then the transfection of the cells and culture and finally the measurement are briefly descripted.

The full-length CerS4 promotor (1386 bp) and several deletion constructs thereof, construct F 979 bp and construct D 607 bp, were previously generated and cloned into the multiple cloning region of the pGL3 Basic vector [188]. The multiple cloning site was adjacent to the firefly luciferase gene (luc+). The reporter construct tool enables not only transcriptional regulation but also posttranscriptional regulation. By adding a 3'UTR to the reporter gene constructs, the post-transcriptional stability of luciferase mRNA can be modulated

[225]. To analyze post-transcriptional activity of CerS4, CerS4 3'UTR flanked the adjoining SV40 promotor [188]. This promotor allows basic transcription of luc+, so any changes in the transcript levels are caused by the destabilizing for the mRNA. To normalize the firefly luciferase reporter assay, the luciferase construct pRL-SV40-Renilla luciferase control vector was co-transfected. This control construct encodes a Renilla luciferase that catalyzes the oxidation of coelenterazine, generating light as a byproduct [226].Expression of the Renilla luciferase is strong and efficient due to the upstream location of SV40 promotor and the T7 promotor and is used to normalize experimental variations in transfection efficiency or cell number.

The protocol for this dual luciferase system was as follows: Cells were seeded according Table 2.8 and co-transfected on the following day with lipofectamine plasmid mixture. For transfection, $20\,\mathrm{ng}$ of Renilla plasmid and $200\,\mathrm{ng}$ of Firefly plasmid were diluted in reduced serum medium, Opti-Mem. Lipofectamine 2000, was used as a transfection reagent. It is a cationic liposome that mediates the delivery of the DNA to the cells. The electrostatic interaction of different charges of the liposome and the DNA allows this mixture to fuse with the cell membrane and penetrate through the intact nuclear envelops to provide access for the transcription machinery. Such transfection, although transient, causes strong expression of the introduced plasmid. Hence, the plasmid mixture was incubated with Lipofectamine Mix ($0.3\,\mu\mathrm{L}$ Lipofectamine in $15\,\mu\mathrm{L}$ Opti-Mem per well) for $15\,\mathrm{min}$ and little by little added to the freshly changed culture medium. The next day, the medium was refreshed and if treatment was planned, either HDAC inhibitors were added or the plate was incubated in the SciTive Workstation (Baker Ruskinn, Leeds, UK). On day 4, cells were harvested. For this, cells were washed with DPBS and lysed on a rocking table for $10\,\mathrm{min}$ with passive lysis buffer diluted 1:5 and pre-warmed at RT prewarmed. Subsequently, $20\,\mu\mathrm{L}$ of lysed suspension was transferred to a LUMITRAC™ microplate (greiner bio-one, Frickenhausen, Germany) and frozen at -$80\,^{\circ}\mathrm{C}$. Different experiments were performed on the same day with the same substrate.

By adding the substrate D-luciferin and ATP to the cell lysate, the emitted luminescence was measured by a luminometer. For Renilla luciferase, coelenterazine was added to a separate plate and measured. For luminescence measurement, the plates with the cell lysates were thawed at RT for $20\,\mathrm{min}$ on a rocking table. Meanwhile, Renilla buffer supplemented with coelenterazine, and luciferase reagent were prewarmed in water bath ($37\,^{\circ}\mathrm{C}$). Measurements were performed using an Infinite 200 Pro plate reader with injector module or a Spark Multimode Microplate Reader with injector module (both by Tecan, Männedorf, Germany), which allowed automatic injection and luminescence measurement for either luciferase reagent or Renilla buffer as a control Table 2.3. The settings for the measurements were as follows: Injection volume $50\,\mu\mathrm{L}$, Speed: $200\,\mu\mathrm{L/sec}$, Refill speed $200\,\mu\mathrm{L/sec}$, Injection refill volume $50\,\mu\mathrm{L}$, Waiting time 00:00:10, Luminescence with automatic attenuation with $1{,}000\,\mathrm{m\,sec}$ integration time). Prior to measurement, the injection module was cleaned with $70\,\%$ ethanol followed by MilliQ water (wash speed $300\,\mu\mathrm{L/sec}$, position strokes 5) and primed with the substrate (prime volume: $1{,}000\,\mu\mathrm{L}$, prime speed $300\,\mu\mathrm{L/sec}$) and cleaned again with ethanol and MilliQ water after measurements.

Luminescence was determined by relative light units (RLU). RLU of the firefly luciferase activity was divided the Renilla luciferase activity from the same well. In all experiments, an empty pGL3 basic or pGL3 promotor vector was included as a control. Therefore, the luciferase activity was also normalized with respect to this empty vector. For treatment effects of HDAC inhibitors or hypoxia, the detected RLU was also normalized by the respective control.

2.4.11 HDAC Assay

Upstream of transcriptional regulation, epigenetic regulation of CerS4 expression modulates gene transcription. Modification of histone by acetylation by histone acetyltransferases (HAT) increases gene transcription, whereas removal of the acetyl groups on histones by HDAC enhances gene transcription [227]. Acylic hydroxymate molecules as trichostatin A (TSA) and Suberoylanlilide hydroxyamic acid (SAHA) inhibit HDAC and thus increase gene transcription [228]. HCT116 cells and HCT15 cells were seeded in a 6-well plate as described in Table 2.8. The next day, the culture medium was replaced and $50\,\mu M$ and $100\,\mu M$ SAHA or $50\,nM$ and $100\,nM$ TSA were added to the well. As controls, one well was not treated (negative control) and the other was incubated with the $2\,\mu L$ DMSO. HCT116 cells and HCT15 cells were treated with HDAC inhibitors for $4\,h$, then washed and harvested by scrapping with a sharper in PBS. Cells were collected in a reaction tube, centrifuged at $2{,}000\,x\,g$ at $4\,°C$ for $7\,min$ and used for RNA isolation (2.6.1).

2.5 Organoid cultivation

Organoids are self-organizing 3D culture systems. They derive from pluripotent stem cells or adult stem cells and differentiate in a controlled manner to from structures that a closely to human organs [229, 230]. Organoids are an important cell model because colon cell types differentiate from stem cells and yet the stem cell niche is preserved. As part of a clinical study, patient biopsies, including control regions of the colon, colorectal carcinoma, colon carcinoma and adenocarcinomas, and diverticulitis biopsies, were collected to isolate colon primary adult stem-cells for organoid cultivation. Addition of specific factors to the media maintains self-renewal and differentiation capacities, making these organoids self-organizing human 3D primary cultures. The isolation and cultivation protocols were optimized by the Georg Speyer House (AG Farin Henner and AG Florian Greten, Georg Speyer House, Frankfurt, Germany). The term organoid is conveniently also used for pluripotent cells, although the term organoid is the result of the self-renewal system.

2.5.1 Extracellular Matrix

Basement membrane proteins extracted from Engelbreth–Holm–Swarm mouse sarcomas are known as Matrigel [231]. It contains various basement membrane factors such as collagen, laminin, metalloproteinases and many growth factors that support cell attachment and differentiation [231]. Stem cells in particular need a fibroblast layer to support their growth

and survival. They polarize on Matrigel, as in normal tissue. Laminin and collagen promote angiogenic and growth-factors and prevent anoikis, an induced cell death when cells lose contact with the extracellular matrix [232]. Matrigel, free of phenol red and reduced growth factor was used for the organoid cultivation to define growth factors and allow fluorescence detection. It was stored at -20 °C and thawed either overnight at 4 °C or on ice at least 2 h before use. It gelatinizes at temperatures of 24 °C to 37 °C. This property must be taken in account when working with Matrigel. When detaching the cells from Matrigel (e.g., splitting organoids), a cold medium must be used to dissolve the Matrigel and isolate the organoids, and the Matrigel must remain cold so that it does not gel in the pipette. Wetting pipette tips is also important to prevent the organoids from sticking to the plastic.

2.5.2 Patient derived organoid isolation and cultivation

Patient biopsies were provided by the clinic in Wiesbaden and stored MACS tissue storage solution at 4 °C to remain viable and avoid apoptosis or cell activation. Samples were washed with DPBS and cut in small pieces with two scalpels and washed with DMEM. Thereby the collected pieces should settle down to the bottom of the falcon by gravity. After removing the supernatant, the tissue was washed with DPBS and incubated with 4 mM EDTA for 20 min, with occasionally shaking. The tissue-EDTA-mixture was pipetted harshly (50-70 times) to dissolve the cells from the tissue. After waiting some minutes till the tissue pieces settled down, the supernatant was collected with 1 mL pipette and centrifuged at 4 °C at 500 x g for 5 min. For the tissue pieces, the same step was repeated with 10 mM EDTA PBS. After collection of the 10 mM EDTA-tissue supernatant and centrifugation, the pellet was embedded in Matrigel and incubated upside down in the incubator (humidified atmosphere containing 5 % CO_2 at 37 °C) for 20 min to solidify. Primocin 1:500 was added to the medium to prevent contamination, and Rho-associated kinase (ROCK) inhibitor Y27632 (1:1000) was added once to maintain the self-renewal capacity. The culture medium (HS Full medium) consisted of 50 % L-WNT3a -, 20 % Rspol- , 10 % Noggin - conditioned medium and Ad-DF +++ (Advanced Medium supplemented with 1 % Glutamax, 1 % HEPES 1 M, 1 % Penicillin-Streptomycin) and commercial growth factors were added: 2 % B27 Supplement, 1 % HEPES, 1 % Nicotinamide 1 mM, 0.25 % n-Acetyl Cystein, 0.1 % A83-01 (500 nM), 0.032 % SB202190, 0.01 % human Epidermal Growth Factor (hEGF) and to avoid contamination 0.2 % Primocin was added.

Each additive to the organoid culture medium is required for long term culture to enhance stem cell survival (Nicotinamide [233]) or inhibit differentiation (A83-01 [234]) to enhance stem cell self-renewal [34]. Additionally, antioxidants as N-acetylcysteine [235] are added. The main pathways with inhibitors and supplements target the Wnt pathway required for crypt proliferation, such as Wnt3a or the Wnt activator R-spondin, which is a ligand for Lgr5 [236]. Epidermal growth factor (EGF) is important for intestinal proliferation [236] and Noggin induces crypt expansion [236] by regulating bone morphogenetic protein (bone morphogenetic protein (BMP)) [237]. Other inhibitors used targeted TGFβ / ALK (A83-01), p38 MAPK (SB202190 [238]) or the ROCK pathway (Y-27623 [239]). These factors

can differ depending on the type of tissue and whether human or murine cells are cultured [236].

Depending on the organoid density within a Matrigel droplet, organoids were split when the medium was exhausted. For organoid passage, the Matrigel drops were washed with ice cold Ad-DF+++ and mechanically singularized by vigorous resuspension (using wetted $10\,\mu L$ pipette tips in $1\,mL$ pipette tips in $1\,mL$ cold Ad-DF+++). Then, $4\,mL$ of ice-cold Ad-DF+++ medium was added to dissolve the Matrigel, and cells were pelleted at $4\,°C$ at $500\,x\,g$ for $5\,min$. To enrich the crypts, the supernatant was transferred into another conical centrifuge tube and the centrifugation step was repeated before the supernatant was discarded. The singularized cell pellet was embedded in Matrigel. The Matrigel was polymerized upside down at $37\,°C$ for 20-25 min before adding the HS-Full medium. ROCK inhibitor Y27632 (1:1000) was included to the HS-Full culture medium at each passage. Organoids were incubated at $37\,°C$ and $5\,\%$ CO_2, and the culture medium was refreshed every 3 days.

2.5.3 Freezing and thawing of patient derived organoids

For cryopreservation, organoids were mechanically fragmented and washed as described in (2.5.2) and resupended in cold recovery-cell culture freezing medium. Depending on the organoid density the amount of two to three drops were transferred to cryomolds. For a gradual freezing, cryomolds were placed on ice for $10\,min$, then wrapped in thick layers of paper towels and stored in -80 $°C$ and transferred to liquid nitrogen for long-term storage. Frozen organoids were recovered by rapid thawing in a $37\,°C$ water bath in DMEM medium containing $10\,\%$ FCS as descripted in 2.4.4 and embedded in Matrigel as described in 2.5.2 and cultured in HS-Full medium and Y27632 (1:1000).

2.5.4 Preparation of conditioned medium

Fibroblast provides stem cells with important growth and survival factors. Not all factors were commercially obtained but produced in house and added. L-Wnt3a, Noggin and Rspol conditioned media were prepared by either L cells (Wnt3a) or HEK 293T cells (R-Spondin, Noggin). The cells were obtained from AG Greten and AG Henner, Georg Speyer House, Frankfurt am Main, with a permission of Prof. Hans Clevers, Hubrecht Institute, Netherlands. First, cells were thawed and cultured in growth medium (DMEM supplemented with $12\,\%$ FCS and $1\,\%$ Penicillin-Streptomycin) in the presence of a selection antibiotic (Zeocin $300\,\mu g\,mL^{-1}$ for Rspol and $125\,\mu g\,mL^{-1}$ for L-Wnt3a, $500\,\mu g\,mL^{-1}$ Geneticine G418 for Noggin) in a $175\,cm^2$ culture flasks. After reaching confluence, the cells were split and grown without adding antibiotic until confluence was reached. Then, the old medium was replaced with AD-DF+++ conditioning medium and after one-week incubation at $37\,°C$ $5\,\%$ CO_2 the medium was harvested. To harvest the medium with the released growth factors from the cells, the collected medium was spun at $1{,}500\,rpm$ for $5\,min$ to remove floating cells and then filtered through a steritop threated bottle top filter, $0.22\,\mu m$ Pore (Millipore, Darmstadt, Germany), and aliquoted. For L-Wnt3a conditioned medium, the L cells were

also kept in FCS-containing medium for conditioning, so the L-Wnt3a medium was stored at $4\,°C$, whereas Rspol and Noggin were conditioned in FCS-free medium and therefore stored at -$20\,°C$.

2.6 Molecular biology methods

2.6.1 RNA extraction

2.6.1.1 RNA extraction from murine tissue

Total murine RNA was extracted from $5\,mg$ of colon tissue using the RNAqueous™ Total RNA Isolation Kit. "The tissue was homogenized with 20x volumes of lysis buffer in a swing mill (Retsch, Haan, Germany) with 3 zirconium oxide grinding balls per sample by $25\,Hz$ for $2.5\,min$"[204]. For RNA extraction, half volume of $100\,\%$ ethanol lysate was added and bound by centrifugation (high speed, $30\,sec$) with the 5424 R centrifuge (Eppendorf, Hamburg, Germany) in the microfilter cartridge. After three washing steps to remove contaminating molecules, the purified RNA was eluted in $20\,\mu L$ of prewarmed elution solution.

2.6.1.2 RNA extraction from human CRC cell lines

For total RNA extraction from human CRC cell lines, cells were seeded in $60\,mm$ culture dishes (Table 2.8) in $3\,mL$ culture medium. After respective culture time, the medium was aspirated, washed once with $1\,mL$ DPBS, and cells were either lysed directly in RLT lysis buffer of RNAeasy Mini Kit® (Qiagen, Hilden) or harvested with a cell scraper in DPBS, and the pellet was then stored at -$80\,°C$ and lysed at another time point. The RLT buffer is a guanidine-thiocyanate-containing buffer, that supports the binding of RNA to a silica membrane and leads to straight denaturation of RNAses. A volume of $70\,\%$ ethanol was added to the homogenized lysate and the RNA was bound to the microfilter cartridge by centrifugation (high speed, $30\,sec$) with the 5424 R centrifuge (Eppendorf, Hamburg, Germany). After several washing steps to remove contaminating molecules, the purified RNA was eluted in 30 to $50\,\mu L$ RNAse/DNase free water.

2.6.1.3 RNA extraction from organoids and 3D cultured cell lines

For RNA extraction from cell cultured in the Matrigel, the Matrigel had to be removed first, either by dissolving the Matrigel with ice cold medium ($1{,}500\,rpm$, $4\,°C$, $5\,min$) or by using the Matrigel dissolving solution Cultrex® Organoid Harvesting solution. With this non enzymatic solution, Matrigel is depolymerized by adding 10 volumes of solution to a Matrigel dome and shaking for >$90\,min$ at $4\,°C$. Organoids were then transferred into a $2\,mL$ microfuge tube and centrifuged ($500\,x\,g$, $5\,min$, $4\,°C$) and washed again with 10 volumes of DPBS at $500\,x\,g$, $4\,°C$ for $5\,min$. Total RNA was extracted and purified using the RNeasy Mini Kit (Qiagen, Hilden) (as descripted in 2.6.1.2) and eluted in DNase/RNase free water.

2.6.2 Determination of RNA concentration

RNA concentration was determined spectrophotometrically with the Infinite® F200 PRO microplate reader (Tecan, Männedorf, Switzerland), using the NanoQuant Plate and the icontrol™ software (both from Tecan, Männedorf, Switzerland). Elution medium was used for blanking (either DNAse/Rnase-free water or prewarmed elution buffer provided in the kit). The measurement was performed in duplicates and the absorption at wavelengths at $260\,\mathrm{nm}$ and $280\,\mathrm{nm}$ were measured. All measurements of nucleic acid concentrations and the 260/280 ratio were automatically transferred and calculated in MS Excel (Microsoft Corporation, Redmond, WA, USA). Purified RNA is unstable and was therefore stored at -$80\,^{\circ}\mathrm{C}$ or immediately used for cDNA synthesis.

2.6.3 cDNA synthesis

For analysis of mRNA expression levels by quantitative real time PCR(2.6.4), extracted RNA, was transcribed into more stable complementary DNA (cDNA) by RT-PCR. The cDNA was synthesized from $800\,\mathrm{ng}$ total cellular RNA using the Verso cDNA synthesis kit. A 7:3 ratio of random hexamers and anchored oligo dT primers was used as primers for the reverse transcriptase enzyme, and potentially contaminating genomic DNA was degrades by the reverse transcription buffer (reverse transcription buffer (RT buffer)) enhancer (Table 2.9). RT-PCR was performed using the Mastercycler® nexus (Eppendorf; Hamburg, Germany) in a two-step program (Table 2.9). cDNA was subsequently diluted 3:4 with nuclease free water and stored at -$20\,^{\circ}\mathrm{C}$.

TABLE 2.9: Specification for cDNA synthesis in terms of reaction mixture and cycling program performed with Mastercycler® nexus (Eppendorf, Hamburg, Germany).

Preparation for 1 sample		RT-PCR program	
RNA	$200\,\mathrm{ng}$	$30\,\mathrm{min}$	$42\,^{\circ}\mathrm{C}$
5x RT buffer	$4\,\mu\mathrm{L}$	$2\,\mathrm{min}$	$95\,^{\circ}\mathrm{C}$
$20\,\mathrm{mM}$ dNTPs	$2\,\mu\mathrm{L}$	hold	$4\,^{\circ}\mathrm{C}$
Random hexamers	$0.7\,\mu\mathrm{L}$		
Oligodentromers	$0.3\,\mu\mathrm{L}$		
20x RT Enzym mix	$1\,\mu\mathrm{L}$		
RT Enhancer	$1\,\mu\mathrm{L}$		
Nuclease free H_2O	add $20\,\mu\mathrm{L}$		

2.6.4 Quantitative real time PCR

Dye based qRT-PCR was used to detect cellular mRNA expression levels of the genes of interest. This quantification is based on the incorporation of a fluorescent dye into the double-stranded DNA. With each PCR amplification cycle of the target sequence, the fluorescence increases proportionally to the amount of double-stranded DNA. Based on this

fluorescence signal, the PCR cycle at which the fluorescence signal outstrips a gene specific background threshold is deduced as the threshold cycle (CT) value. This is defined by the program and calculated for each primer pair and sample. To normalize the target gene expression, the CT values of a stable, treatment-independent mRNA expression were measured concurrently and set as the housekeeping gene. In this study, qRT-PCR was mainly performed using SYBR® Select Master Mix, which contains SYBR Green ER™ as fluorescent dye. The reagent mixture and the cycling program were set according Table 2.10 and $0.1\,\mu m$ oligonucleotide primers (human primers Table 2.12, murine primer Table 2.11) were used. 60S ribosomal protein L37a (RPL37A) was measured as housekeeping gene for human cells and peptidylprolyl isomerase A (PPIA) for murine cells. For qRT-PCR, 3:4 cDNA dilutions were used, and samples were measured in triplicate in Applied Biosystems Micro™Amp™ Optical 384-Well-Reaction Plates (Thermo Fisher Scientific, Waltham, USA) with the QuantStudio™ 5 Real-Time PCR Systems (Thermo Fisher Scientific, Waltham, USA). Fluorescence emission was monitored using QuantStudio™ Design & Analysis Desktop Software (Applied Biosystems by Thermo Fisher Scientific, Waltham, USA). The basal mRNA expression level of the target gene was determined by normalizing to the housekeeping gene as ΔCT (Equation 2.2), by subtracting the CT values of the housekeeping gene from the CT value of the target gene. By negative CT is proportional to the log (concentration):

$$\Delta\mathrm{CT} = -\mathrm{CT}(\mathrm{Target}) - (-\mathrm{CT}(\mathrm{Ref})) = -\mathrm{CT}(\mathrm{Target}) + \mathrm{CT}(\mathrm{Ref}) = \mathrm{CT}(\mathrm{Ref}) - \mathrm{CT}(\mathrm{Target}). \tag{2.2}$$

Relative mRNA level expression additionally is referenced to an internal reference sample (e.g., untreated cell or control WT line compared with KO or treatment) and was calculated as ΔΔCT:

$$\Delta\Delta\mathrm{CT} = \Delta\mathrm{CT}(\mathrm{Treatment}) - \Delta\mathrm{CT}(\mathrm{Control}). \tag{2.3}$$

TABLE 2.10: Specification of qRT-PCR in terms of reaction mixture and cycling program carried out with QuantStudio 5 Real-Time PCR System (Thermo Fisher Scientific, Waltham, USA).

Preparation for 1 qPCR reaction sample		qPCR program		
SYBR Green ER ™	5 µL	50 °C	2 min	
Forward primer	1 µL	95 °C	15 min	
Reverse Primer	1 µL	95 °C	15 s	45x
Nuclease free H_2O	2 µL	60 °C	1 min	
cDNA template	1 µL			

TABLE 2.11: Oligonucleotide primers used for qPCR for mouse tissue. The annealing temperature was 60 °C. The Oligonucleotide sequence were specific for mouse. All oligonucleotide primers were purchased from biomers.net GmbH, Ulm, Germany and sequences were published in [189]. for = forward; rev = reverse.

Target gene	Oligonucleotide sequence (5'... 3')	Sense
CerS1	GCCACCACACACATCTTTCGG	for
	GGAGCAGGTAAGCGCAGTAG	rev
CerS2	GAAGTGGGAAACGGAGTAGCG	for
	AGTTCACAGGCAGCCATAGTCG	rev
CerS3	CCTGGCTGCTATTAGTCTGATG	for
	CTGCTTCCATCCAGCATAGG	rev
CerS4	CTGTGGTACTGTTGTTGCATGAC	for
	GCGCGTGTAGAAGAAGACTAAG	rev
CerS5	TGGCCAATTATGCCAGACGTGAG	for
	GGTAGGGCCCAATAATCTCCCAGC	rev
CerS6	GCATTCAACGCTGGTTTCGAC	for
	TTCAAGAACCGGACTCCGTAG	rev
PPIA	GCTGGACCAAACACAAACGG	for
	GCCATTCCTGGACCCAAAAC	rev

2.7 Protein biochemical methods

2.7.1 Total protein extraction

For whole protein extraction from human CRC cell lines, cells were seeded in 100 mm culture dishes in 10 mL medium (Table 2.8). After each culture or treatment time, the medium was aspirated, washed once with sterile phosphate buffered saline (PBS), and collected on ice by gentle scraping in PhosphoSafe based lysis buffer (Table 2.2). The lysis buffer was composed of a reagent preserving protein phosphorylation, the PhosphoSafe™ Extraction Reagent (1x v/v), cOmplete™ Protease Inhibitor Cocktail (1x v/v) to prevent protease-mediated protein degradation, and dithiothreitol (DTT) as a reducing agent to prevent endogenous protein conformations like oxidation of sulfhydryl (-SH) groups to disulfide bonds [240]. To solubilize the cellular membrane, cell suspensions were sonicated thrice for 3 sec (30 % intensity, level 3) with a Branson Sonifer 250 (Branson Ultrasonics Corporation, Brookfield, US). Cell debris and nonprotein components were removed by centrifugation (high speed, 4 °C for 30 min) with the 5424 R centrifuge (Epppendorf, Hamburg, Germany). The supernatant containing the proteins was transferred to new microcentrifuge tubes and stored at -80 °C.

3D-grown CRC cells were first removed from the Matrigel with Cultrex Organoid Harvesting solution by shaking for at least 90 min at 4 °C. After washing with DPBS the PhosphoSafe based lysis buffer (Table 2.2) was added and homogenized by pipetting up and down. Cells were sonicated thrice for 3 sec (30 % intensity, level 3) with a Branson Sonifer 250 (Branson Ultrasonics Corporation, Brookfield, US) and spun to purify the protein extraction from debris and cellular non-protein components (high speed, 4 °C, 30 min). The

TABLE 2.12: Oligonucleotide primers designed for human cells used for qPCR. Forward and Reverse Sequence (5′-3′). The primer were synthesized by biomers.net GmbH, Ulm, Germany. Primer sequence of the house keeping gene RPL37A was synthesized by BioSpring GmbH, Frankfurt, Germany

Gene	Forward Sequence (5′-3′)	Reverse Sequence (5′-3′)
CerS1	CCTCCAGCCCAGAGAT	AGAAGGGGTAGTCGGTG
CerS2	CCAGGTAGAGCGTTGGTT	CCAGGGTTTATCCACAATGAC
CerS3	CCTGGCTGCTATTAGTCTGAT	TCACGAGGGTCCCACT
CerS4	GCAAGGATTTCAAGGAGAG	AACAGCAGCACCAGAGAG
CerS5	CAAGTATCAGCGGCTCTGT	ATTATCTCCCAACTCTCAAAGA
CerS6	AAGCAACTGGACTGGGATGTT	AATCTGACTCCGTAGGTAAATACA
Lgr5	CACCTCCTACCTAGACCTCAGT	CGCAAGACGTAACTCCTCCAG
Olfm4	TGCCATTCGCCGAGAAATC	GGACGACAGGGGTGTTTTGAT
SMOC	ATGACGACGGCACCTACAG	TCGCGTTGGGGTAACTTTTCA
TFF1	CACCTCCTACCTAGACCTCAGT	GGGACTAATCACCGTGCTGG
KRT20	GGTGAACTATGGGAGCGATCT	CTAGACGGTCATTTAGGTTCTGC
FABP1	GTGTCGGAAATCGTGCAGAAT	GACTTTCTCCCCTGTCATTGTC
CA2	GGATGGCACTTACAGATTGA	TGAACCAAGTGAAGTTCTGC
ALPI	TACACGTCCATCCTGTACGG	CTCGCTCTCATTCACGTCTGG
Muc2	CACCTCCTACCTAGACCTCAGT	GGCGAAGTTGTAGTCGCAGAG
RPL37A	ATTGAAATCAGCCAGCACGC	AGGAACCACAGTGCCAGATCC
FIS	GATGACATCCGTAAAGGCATCG	AGAAGACGTAATCCCGCTGTT
GLUT1	TCACTGTGCTCCTGGTTCTG	CCTGTGCTCCTGAGAGATCC
LDHA	ATGGCAACTCTAAAGGATCAGC	CCAACCCCAACAACTGTAATCT
MFN1	ATGACCTGGTGTTAGTAGACAGT	AGACATCAGCATCTAGGCAAAAC
MFN2	CACATGGAGCGTTGTACCAG	TTGAGCACCTCCTTAGCAGAC
OPA	TCAAGAAAAACTTGATGCTTTCA-	GCAGAGCTGATTATGAGTACGATT
PARK	GTGTTTGTCAGGTTCAACTCCA	GAAAATCACACGCAACTGGTC
PDH3	AGATCGTAGGAACCCACACG	CAGATTTCAGAGCACGGTCA
PDHA	TGGTAGCATCCCGTAATTTTGC	ATTCGGCGTACAGTCTGCATC
PINK1	CCCAAGCAACTAGCCCCTC	GGCAGCACATCAGGGTAGTC
PK	CGCCTGGACATTGATTCA	GTTCAGACGAGCCACATT
PKM1	CACCTGATAGCTCGTGAGGC	TGGCTTCCATGAGGTCTGTG
PKM2	CAGAGGCTGCCATCTACCAC	GAGGACGATTATGGCCCAC
TKT	TGTGTCCAGTGCAGTAGTGG	ACACTTCATACCCGCCCTAG
TKTL1	AAGCCTTTGGGTGGAACACTTA	CTGAGAAGCCTGCCAGAATACC

supernatant was transferred to a new microcentrifuge tube and stored at -80 °C.

2.7.2 Nuclear protein extraction

To analyze the nuclear translocation of proteins, particularly the transcription factor HIF1α, nuclear extraction was isolated by the band-shift-method. The band shift assay is based on the fact that free DNA moves faster through a native PAGE than DNA-protein-complexes. Hence after electrophoresis, the free DNA segments appears as an upwardly shifted DNA band (Shift). To extract the nuclear fraction, cells cultured in a 10 cm dish plate were washed twice with cold PBS. They were then harvested by scrapping in 1 mL PBS and sedimented

by centrifugation (1 min, 10,000 rpm). The pellet was resuspended on ice for 10 min in band shift lysis buffer (Table 2.2). To break the cell membrane, including the nuclear membrane, 53 µL of 10 % NP-40 was added and incubated 2 min on ice. The lysate was centrifuged at 2,500 rpm at 4 °C for 5 min and the pellet was carefully resuspended with 500 µL band shift- lysis buffer and centrifuged again at 2,500 rpm at 4 °C for 5 min. The nuclear pellet was resuspended in twice the volume of nuclear lysis buffer (Table 2.2). After 30 min incubation on ice, the nuclear extraction supernatant was isolated by centrifugation for 10 min at 14,000 rpm and diluted 1:1 with nuclear lysis buffer II (Table 2.2) and stored at -80 °C.

2.7.3 Photometric determination of protein concentration

Protein concentration was principally determined using a colorimetric dye assay, in which protein-dye binding is detected by a color change at RT. The Bradford assay was generally used to determine protein concentration. However, in the 3D cell viability assay, the 3D cells were lysed with a special HIF1α lysis buffer (Table 2.2), so the protein concentration could not be determined by the Bradford due to incompatibility with the HIF1α lysis buffer.

2.7.3.1 Bradford

For colorimetric protein determination, the Bradford method with Coomassie brilliant blue G-250 was used [241]. The Coomassie blue dye incorporates with basic and aromatic amino acids, causing a shift in absorbance from 465 nm to 595 nm [242]. 1 µL protein sample was diluted 1:10 (v/v) with water in a 96-well plate (flatbottom) and measured in triplicate. A serial dilution of BSA was also used in triplicate for each measurement. The BSA was diluted in distilled water with a total volume of 10 µL to generate a standard dilution of 0 mg mL^{-1} to 0.8 mg mL^{-1} of BSA. 200 µL/well of ready-to-use Bradford reagent was added and absorption was spectrophotometrically measured at the wavelength of 595 nm using the Infinite® F200 PRO microplate reader with the i-control™ software (both by Tecan, Männedorf, Switzerland). To calculate the protein concentration, a calibration curve was calculated with values of the BSA standard absorbance in MS Excel (Microsoft Corporation, Redmond, WA, USA).

2.7.3.2 DC Protein Assay

The DC™ protein assay is another colorimetric method to determine protein concentration and is similar to the Lowry assay. It relies on two reactions that led to color development. The first is the chelation of copper with proteins in an alkaline environment and the second is the detection of reduced copper by the folin reagent [243]. Protein determination was performed according to the manufacturer's instructions. Briefly, reagent S was added to the alkaline copper tartrate solution Reagent A at a ratio of 1:50 because the HIF1α solution contains a detergent [244]. The provided BSA was dissolved as 1.45 mg mL^{-1} and diluted as twofold serial dilution with MilliQ® water. 5 µL of standard and samples were diluted

1:6 in prepared reagent A, reagent B was added and after $15\,\mathrm{min}$ the absorbance at $750\,\mathrm{nm}$ was read.

2.7.4 Sodium dodecyl sulfate polyacrylamide gel electrophoresis (SDS Page)

The sodiumdodecylsulfat (SDS) page is a technique that allows the separation of proteins according to their molecular weight through a polyacrylamide matrix in an electrical field. SDS is a anionic detergent which denatures proteins and provides them a negative charge. Thus, smaller proteins pass through the polyacyralamide matrix faster than larger proteins. Protein extracts from CRC cells were separated by discontinuous SDS-PAGE according to the method by Laemmli [245]. $40\,\mu\mathrm{g}$ proteins ($30\,\mu\mathrm{g}$ for nuclear extracts) were denatured with 1x Laemmli sample buffer (Table 2.2) supplemented with β-mercaptoethanol and boiled at $95\,^{\circ}\mathrm{C}$ for $5\,\mathrm{min}$ before loading onto $10\,\%$ or $12\,\%$ polyacrylamide gels ($7.5\,\%$ SDS polyacrylamide gels for nuclear extraction). Along with the protein samples, Precision Plus Protein™ Standards Dual Color was loaded as a reference protein marker ($2.5\,\mu\mathrm{L/lane}$). Proteins were separated in 1x SDS running buffer (Table 2.2) using the Mini-PROTEAN® 3 chamber system (BioRad, Munich, Germany). Proteins first accumulated in the stacking gel ($80\,\mathrm{V}$, $30\,\mathrm{min}$) and were then separated by the separating gel ($100\,\mathrm{V}$-$120\,\mathrm{V}$, $90\,\mathrm{min}$).

2.7.5 Western Blot

Western Blot (WB) is an analytical method for determining the presence of specific protein in a cell homogenate. It is based on interaction between antibody and antigen. Visualization of this interaction can be achieved using either fluorescence or a chemiluminescence techniques. In the chemiluminescence method, an enzyme reporter generates a colorimetric signal by metabolizing a substrate, which can then be detected. A weak signal indicates a low presence of the protein of interest, while signal saturation is associated with a high protein load [246].

After electrophoretic separation of proteins from cell lysates, proteins on the SDS Page were transferred to a nitrocellulose membrane (Amersham™ Protran™ $0.2\,\mu\mathrm{m}$ NC, GE Healthcare Life Sciences, Freiburg, Germany) by semi-dry electroblotting for $7\,\mathrm{min}$ at $1.3\,\mathrm{A}$ using the Trans-Blot® Turbo™ Transfer System (Bio-Rad, Munich, Germany). Subsequently, protein immobilization on the membrane was verified by reversible protein staining with Ponceau S solution ($0.5\,\%$ [weight per volume (w/v)] in $1\,\%$ acetic acid) for $2\,\mathrm{min}$ with shaking at RT. The Ponceau staining was removed from the nitrocellulose membrane by washing in PBS for $10\,\mathrm{min}$ at RT on a rocking table. The protein of interest was detected by indirect fluorescence. For this purpose, the membrane was first blocked by incubation with a $5\,\%$ milk solution (diluted in PBS-T (PBS containing $0.1\,\%$[v/v] Tween 20)) for $90\,\mathrm{min}$ at RT on a rocking table to prevent non-specific binding of antibodies. The first antibody directed against the protein of interest was incubated in $5\,\%$ milk solution (1:1000 HIF1α, NB100-134, Novus Biologicals, Wiesbaden, Germany) (1:1000 β-actin, [AC-15], Sigma Aldrich, Deisenhofen, Germany) over night at $4\,^{\circ}\mathrm{C}$. After washing the membrane with PBS-T for $5\,\mathrm{min}$ three times at RT, the corresponding fluorescent IRDye®-conjugated secondary antibody

(LI-COR Bioscience, Bad Homburg, Germany) (1:10,000 (v/v) Intercept® blocking solution in PBS-T) was incubated for 2 h at RT at a rocking table. After washing three times with PBS-T (5 min, RT) on a rocking table, proteins were detected using the Odyssey CLx Imaging System including the Image Studio™ Lite Software, version 5.2 (LI-COR Biosciences, Bad Homburg, Germany).

Because the signal was weak with the fluorescent Western detection, a chemiluminescent detection method was used for nuclear HIF1α detection. Chemiluminescent detection was based on the same nitrocellulose membrane, which was also blocked for 2 h at RT in 5 % milk and incubated overnight at 4 °C with anti-HIF1α rabbit (1:1000, NB100-134, Novus Biologicals, Wiesbaden, Germany). However, the secondary antibody was labeled with the enzyme reporter horseradish peroxidase (HRP), (1:1000, 7074s, Cell Signaling Technology, MA, USA) was added to the membrane for 1.15 h and after washing the membrane three times with PBS, 3 mL of WesternSure®Premium Chemiluminescent Substrate (Li-COR Bioscience, Bad Homburg, Germany) was incubated for 5 min. The signal is generated immediately by oxidization of the substrate in the presence of hydrogen peroxide. The light photons were then digitally measured using the C-DiGit® Blot Scanner (LI-COR Bioscience, Bad Homburg, Germany).

For densitometric analysis, the intensity of protein bands was evaluated using Image Studio™ Lite Software, version 5.2 (LI-COR Biosciences, Bad Homburg, Germany). The analyzed area was kept at the same size throughout a blot. The program automatically subtracted the background signals. To account for any differences in protein loading, the protein content was normalized by dividing the signal intensity of the target protein by the corresponding signal of the housekeeping protein, β-actin. For a better comparison, the final calculated protein content was related to the respective untreated reference line (usually shNC HCT116 cells or Caco-2 cells 0 h) by dividing the ratio of sample by the ratio of the reference in MS Excel (Microsoft Corporation, Redmond, WA, USA).

2.7.6 Immunohistochemistry & Immunocytochemistry

Immunohistochemistry (IHC) is a method that allows the detection of antigen localization in tissues and immunocytochemistry (ICC) in cultured cells. After TEER measurement, the cells in the Thincert insert and organoids seeded and cultured on coverslips were also stained for either TJs or CerS. To stain slides, the suspensions were covering the tissue sections, whereas both Thincert inserts and cover slips with Matrigel, were stained and washed in a 24-well plate. To create a snapshot that preserved the original morphology, the slides and cells were fixed in 4.5% PFA and washed three times with PBS. Since chemical fixation results in many cross-links between alkaline amino acids through hydroxymethyl bridges, the antibodies cannot penetrate and bind to the target. Therefore, the permeabilization reagents are used to break the membrane integrity of the PM and facilitate the penetration of antibodies [247]. After washing, slides and cells were permeabilized in PBS supplemented with 0.025 % Triton-X-100 (PBST). To reduce nonspecific staining, the slides and cells were blocked with blocking solution for 90 min (Table 2.2). The blocking solution

was removed and the primary antibody was diluted 1:250 in AK solution (Table 2.2) and was incubated overnight at $4\,^{\circ}\mathrm{C}$ (Table 2.13). After washing the slides or cells to remove excess primary antibody with PBST, the secondary antibody (1:800) (Table 2.14 was added and incubated for $2\,\mathrm{h}$ at RT. The excess secondary antibody was washed, and either for a co-staining, the steps were repeated with other antibodies or the nuclei were stained with 4',6-diamidin-2-phenylindol (DAPI) (1:1000) for 10 min. After washing with PBS, the slides and cells were embedded in Aqua-Poly/Mount. For embedding the TEER Thincert inserts, the edges of the Thincert inserts were cut with a scalpel and the side with the cells was placed on a drop of Aqua-Poly/Mount on a slide and covered with coverslips. For the coverslips, a drop of Aqua-Poly/Mount was also placed on a slide and covered with the stained coverslips. The slides were stored in the dark and at $4\,^{\circ}\mathrm{C}$. Samples were analyzed using an Axio Observer.Z1 microscope with an apoptome unite to minimize scattered fluorescence (Carl Zeiss, Oberkochen, Germany). For TJs images of TEER Thincert inserts, z-stakes images of each channel were optimized to either TJs or nuclei and overlaid together.

TABLE 2.13: Primary antibodies used for ICC or IHC. The dilution was 1:250 in for IHC in $3\,\%$ BSA in PBS, and for ICC, in antibody solution. Specification list either the catalogue number or in square brackets the clone number, if the antibody is monoclonal.

Target	Host species	Manufacturer	Specification	Application
CerS2	rabbit	Atlas Antibodies	HPA027262	ICC
CerS4	rabbit	Elabscience	#E-AB-13375	ICC
CerS6	rabbit	Atlas Antibodies	HPA044683	ICC
Claudin 4	mouse	Invitrogen	[3E2C1]	ICC
Occludin	mouse	Atlas Antibodies	[CL1608]	IHC
Occludin	mouse	Invitrogen	[OC-3F10]	ICC
ZO-1	rabbit	Invitrogen	#61-7300	IHC

TABLE 2.14: Secondary antibodies used for ICC and IHC. The dilution was 1:800 in antibody buffer or for IHC in $3\,\%$ BSA in PBS.

Target	Manufacturer	Coupled dye
mouse	Sigma Aldrich	Cy3
mouse	Invitrogen	Alexa Fluor®488
rabbit	Sigma Aldrich	Cy3
rabbit	Invitrogen	Alexa Fluor®647

For staining, organoids were washed twice with PBS and stained with $4\,\%$ PFA at RT for $30\,\mathrm{min}$. After removing and washing the PFA organoids were blocked with blocking solution and primary antibody (1:250) were incubated overnight at $4\,^{\circ}\mathrm{C}$. Secondary antibodies (1:800) were incubated for $15\,\mathrm{min}$ and stained with DAPI for $10\,\mathrm{min}$ (1:1000) and covered with PolyAqua Mount on a slide.

2.8 LC-MS/MS

Concentrations of cellular sphingolipids in mouse tissues or CRC cell lines, were quantified by high-performance LC-MS/MS. Extraction and quantification of sphingolipids were performed by Sandra Trautmann and Dr. Dominique Thomas from the Analytical Department of Institute of Clinical Pharmacology (Goethe University, Frankfurt, Germany). Therefore, the chemicals used are not listed in Table 2.1 and Table 2.2 but here.

Increasing technical advances in mass spectrometry (MS) facilitate the mapping of cellular and liquid lipids. A fundamental step in this process is lipid extraction using a suitable organic solvent mixture. This solvent solution generates a biphasic system in which the various lipids distribute in the organic phase [248, 249]. For each extraction of sphingoid bases and ceramides from tissue and cell pellets, a different solvent solution was used for the measurements. Tissue was homogenized in water/ethanol 3:1 (v/v) to reach a concentration of $0.05\,\mathrm{mg\,\mu L^{-1}}$. $20\,\mu L$ tissue suspension, $10\,\mu L$ thawed plasma and cell pellets were resuspended in $200\,\mu L$ extraction buffer (citric acid $30\,\mathrm{mM}$, disodium hydrogen phosphate $40\,\mathrm{mM}$ and $20\,\mu L$ internal standard solution was added. The internal standard consisted of SPH d18:1-d7, SPH d18:0-d7, S1P d18:1-d7, S1P d18:0-d7, Cer d18:0/18:0-d3, Cer d18:0/24:0-d7, Cer d18:1/16:0-d7, Cer d18:1/18:0-d7, Cer d18:1/24:0-d4, Cer d18:1/24:1-d7, GlcCer d18:1/18:0-d5, GlcCer d18:1/24:1-d5, LacCer d18:1/16:0-d3, LacCer d18:1/17:0, LacCer d18:1/24:0-d7 all of which were obtained from Avanti Polar Lipids, Alabaster, AL, USA, except for Cer d18:1/24:0-d4, which was obtained from Chiroblock GmbH, Wolfen, Germany. The solvent mixture for the internal standards was chloroform/methanol (2:1, v/v) with $0.1\,\%$ butylated hydroxytoluene [250]. The mixture was again extracted in $600\,\mu L$ methanol/chloroform/hydrochloric acid (15:83:2, v/v/v). The lower organic phase was removed and split into two aliquots that were evaporated at -$45\,^{\circ}\mathrm{C}$ under a mild stream of nitrogen to prevent degradative or oxidative changes in the lipids [251]. Subsequently, both aliquots were reconstituted either in $50\,\mu L$ solvent solution containing methanol/formic acid (95:5, v/v) for the detection of sphingoid base, or tetrahydrofuran/$0.2\,\%$ formic acid and $10\,\mathrm{mM}$ ammonium formate for the detection of ceramide [250]. Calibration standards and quality controls were diluted in methanol, while ceramides were diluted in chloroform/ methanol (2:1, v/v) containing $0.1\,\%$ butylated hydroxytoluene and sphingoid bases in methanol.

The reference standards for sphingoid bases included SPH d18:1, SPH d18:0, SPH d20:1, SPH d20:0, S1P d16:1, S1P d18:1, S1P d18:0 (obtained from Avanti Polar Lipids, Alabaster, AL, USA). The reference standards for ceramides (dhCer, Cer, GlcCer and LacCer) were dhCer d18:0/16:0, dhCer d18:0/18:0, dhCer d18:0/24:0, dhCer d18:0/24:1, Cer d18:1/14:0, Cer d18:1/16:0, Cer d18:1/18:0, Cer d18:0/18:1, Cer d18:1/ 20:0, Cer d18:1/22:0, Cer d18:1/ 24:0, Cer d18:1/24:1, GlcCer d18:1/16:0, GlcCer d18:1/18:0, GlcCer d18:1/18:1, GlcCer d18:1/ 24:1, LacCer d18:1/16:0, LacCer d18:1/18:0, LacCer d18:1/ 18:1, LacCer d18:1/24:0, LacCer d18:1/24:1 (purchased from Avanti Polar Lipids, Alabaster, AL, USA).

Lipids were then measured by LC-MS/MS. To increase the detection sensitivity of MS, the samples were separated by high performance liquid chromatography (HPLC). This

technique allows detection and quantification of the available lipid classes in the samples and was carried out in an Agilent 1290 Infinity UHPLC system (Agilent Technologies, Waldbronn, Germany). In a Zorbax Eclipse Plus LC C8 columns (purchased from Agilent Technologies, Waldbronn, Germany), samples were chromatographically separated in a specific gradient of two solvents. For the sphingoid bases, $0.05\,\%$ formic acid was used as solvent A, and acetonitrile/isopropanol/acetone/formic acid (50:30:19:1, v/v/v/v) was used as solvent B. The gradient of solvent A/B resulted in elution. The ratio between both solvents was initially $55\,\%/45\,\%$ and held for $1.5\,\mathrm{min}$, then changed linearly to $0\,\%/100\,\%$ for $1.5\,\mathrm{min}$ and returned to $55\,\%/45\,\%$ with a constant flow rate of $400\,\mu\mathrm{L}$ and an injection volume of $5\,\mu\mathrm{L}$. Ceramide separation differed from the sphenoid base detection by LC column, solvents and consequently by gradient program and time. Solvent A consisted of $10\,\mathrm{mM}$ ammonium formate diluted in water supplemented with $0.2\,\%$ formic acid, and solvent B consisted of acetonitrile/isopropanol/acetone (50/30/20, v/v/v) supplemented with $0.2\,\%$ formic acid. The same HPLC instrument but a C18 LC column (Zorbax Eclipse Plus C18 obtained from Agilent Technologies, Waldbronn, Germany) was used, the injection volume was $5\,\mu\mathrm{L}$, and at a constant flow rate of $350\,\mu\mathrm{L}$, the gradient program was as follows: for $0.6\,\mathrm{min}$, the ratio of solvent A/B was initially $50\,\%/50\,\%$ and changed linearly to $10\,\%/90\,\%$ after $0.6\,\mathrm{min}$. At $4.0\,\mathrm{min}$, the gradient was $0\,\%/100\,\%$ for $1.5\,\mathrm{min}$ and the column was re-equilibrated with a $50\,\%/50\,\%$ ratio for $1.5\,\mathrm{min}$.

Lipids were detected in a QTrap 5500 mass spectrometer equipped with a Turbo V Ion Source in positive electrospray ionization (ESI) mode (Sciex, Darmstadt, Germany). The instrument for tandem mass spectrometry (MS/MS) was calibrated and the following ESI settings were used: Ion spray voltage $5{,}500\,\mathrm{V}$, ion source temperature $450\,^{\circ}\mathrm{C}$, curtain gas $37.5\,\mathrm{psi}$, collision gas $9\,\mathrm{psi}$, nebulizer gas $45\,\mathrm{psi}$ and heater gas $65\,\mathrm{psi}$ [252]. All spectra were recorded and analyzed in multiple reaction monitoring mode. While the acquisition was performed with Analyst software V 1.6.3, the quantification, MultiQuant Software 3.0.3 (both Sciex, Darmstadt, Germany) was used for quantification. Using the internal standard method of isotope dilution mass spectrometry, the ion transitions of precursor to product (m/z) of the each analyte and standard listed in [250], were used to calculate calibration curves and quantify sphingolipids.

2.9 Statistics

Numerical data were calculated using MS Excel (Microsoft Corporation, Redmond, WA, USA), analyzed and plotted using GraphPad Prim software (version 9.1.0; GraphPad Software, San Diego, CA). Significant differences from grouped data were calculated by two-way analysis of variance (ANOVA) with Tukey's multiple comparison posttest or one-way ANOVA with Sidak's multiple comparison test comparing $95\,\%$ confidence intervals with the mean of all other samples. Sphingolipid data were also analyzed using a multiple comparison test. The p-values were adjusted using either Holm-Sidak method or by False Discovery Rate (FDR). Data from two independent samples were compared by an unpaired, two-tailed t-test with a 95% confidence interval (CI95). Statistical significance of (adjusted)

p-values was presented as follows: * p<0.05; ** p<0.01; *** p<0.001, **** p<0.0001. Data were plotted as mean ± standard error of the mean (SEM)) or box plots, with median value and either CI95 or the smallest and largest value (min/max). To compare differences in data collected over time, area under curve (AUC) were calculated with GraphPad Prism with the following formula:

$$\text{AUC(Body weight)} = \%\ \text{Body weight} \cdot \frac{\text{Time}}{2} \tag{2.4}$$

$$\text{AUC(Score)} = \text{Score} \cdot \frac{\text{Time}}{2} \tag{2.5}$$

Correlation was calculated using GraphPad Prism software (version 9.1.0; GraphPad Software, San Diego, CA) by first computing the means of side-by-side replicates and then analyzing the means. A strong correlation was indicated by a value close ± 1. Only when p-values were significant was the correlation of two factors was accepted and indicated. For a multiple comparison test was used, and the p-values were adjusted by the Holm-Sidak-method or corrected by controlling the FDR using a two-stage linear step-up algorithm of Benjamini, Krieger and Yekutieli with a $5\,\%$ desired FDR.

Mouse data were raised by raw data of Sebastian Brachtendorf and Stephanie Örtel. To get a better picture of the CerS4 tissue specific function, also the raw data of Sebastian Brachtendorf of CerS4 Vil/Cre mice in the AOM/DSS model were analyzed.

Chapter 3

Results

Part I

3.1 Impact of tissue specific CerS4 deficiency on DSS induced colitis

In the DSS induced colitis model, administration of $2\,\%$ DSS in the drinking water of mice induced clinical symptoms comparable to those of patients; the mice lose weight, change stool consistency and had bloody stool. After water replacement, the body weight of the mice dropped over time compared with control mice (Figure 3.1 A1). The AUC of the DSS treated mice exhibited that the body weight loss was greater in CerS4 KO mice than in WT mice or CerS4 LCK/Cre mice (Figure 3.1) A2). The disease score also increased with time; in CerS4 KO mice, the maximum was at day 7, whereas in CerS4 LCK/Cre mice it was delayed until day 8 but reached a value as high as that in WT mice. Because the disease severity was higher in CerS4 KO mice the experiment was terminated at day 8, while in CerS4 LCK/Cre mice disease symptoms were delayed and therefore the experiment terminated at day 10 (Figure 3.1) B1).Comparing the disease progressions independent from the time course, indicated that the AUC did not differ between the DSS treated mice (Figure 3.1) B2). Thus, monitoring of the health condition of the mice showed that CerS4 KO mice were more susceptible to DSS. CerS4 LCK/Cre mice also appeared to respond, but with a time delay compared with CerS4 KO mice.

Another indicator for colonic inflammation is shortening of the colon (Figure 3.2 A). Comparing the colon length exhibited a clear shortening upon DSS treatment. In CerS4 KO mice the colon was reduced by approximately $3\,\mathrm{cm}$, while in the CerS4 LCK/Cre mice the shortening amounted $1.5\,\mathrm{cm}$. This shortening was in CerS4 KO mice significantly increased compared to the CerS4 LCK/Cre mice. In addition, a significant reduction in colon length was observed in WT mice after DSS treatment (Figure 3.2 B).

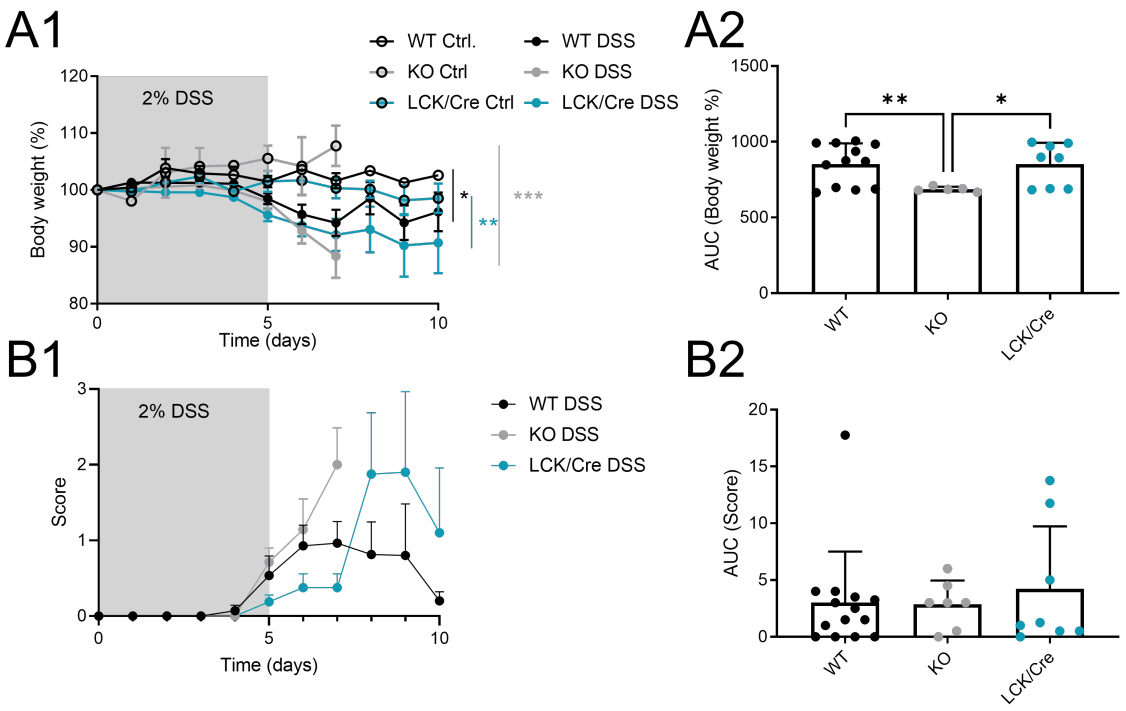

FIGURE 3.1: Disease progression in WT mice (WT), CerS4 KO mice (KO) and CerS4 LCK/Cre mice (LCK/Cre) after DSS treatment for 5 days. (A1) The body weight before the start of the experiment was set at 100 %. (A2) The AUC was calculated for each single DSS treated mice and the mean of the different mice compared statistically. (B1) The score represented the health condition of the mice. Next to the body weight also other parameters such as stool consistency, bloods stool and body posture were included in the assessment. (B2) The AUC between the different DSS treated mice was not significantly different. Data are mean ±SEM. Statistical analysis was performed by one-way ANOVA. Group size of control mice: WT mice n=11, CerS4 KO mice n=6 and CerS4 LCK/Cre mice n=12 and for DSS treated group WT mice n=12, CerS4 KO mice n=7 and CerS4 LCK/Cre mice n=8. Data and B1 previously published in [204].

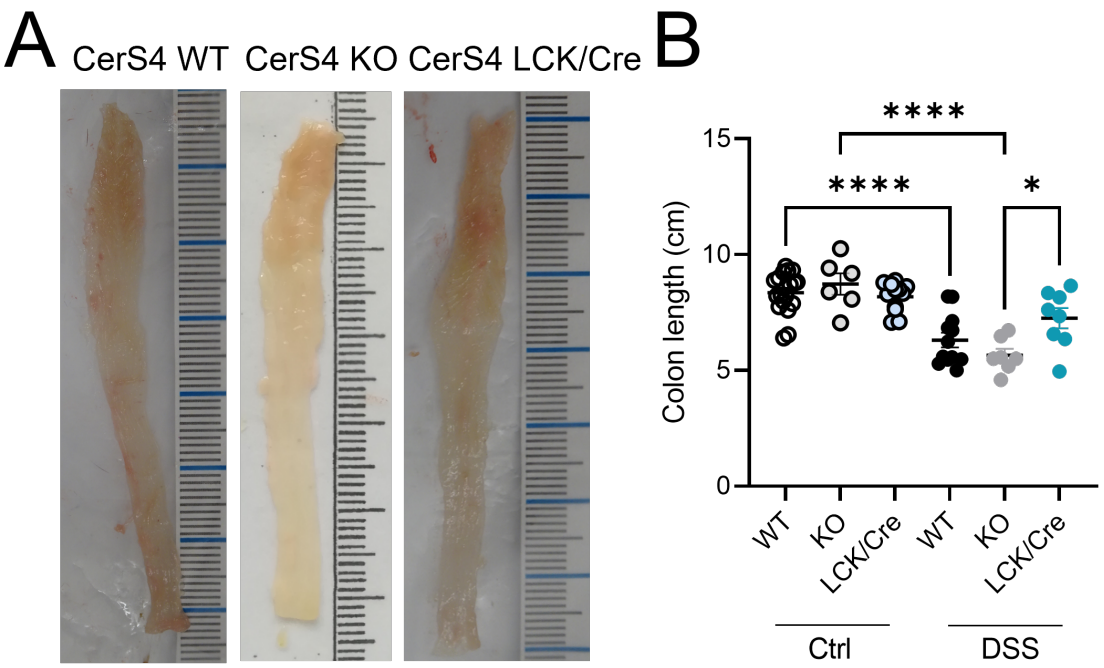

FIGURE 3.2: Shrinking colon size upon DSS treatment. (A) Already, the representative hand shot pictures indicate a higher reduction in CerS4 KO mice (KO) compared to WT mice (WT) and CerS4 LCK/Cre mice (LCK/Cre). (B) Colon length of longitudinal cut colon of control (Ctrl) and DSS treated (DSS) mice were statistically compared, indicating an inflammatory induced reduction of the total colon after DSS treatment. Data are mean ±SEM. Statistical analysis was performed by two-way ANOVA. Group size of control mice WT mice n=11, CerS4 KO mice n=6 and CerS4 LCK/Cre mice n=12 and for DSS treated group WT mice n=12, CerS4 KO mice n=7 and CerS4 LCK/Cre mice n=8. Data and A previously published in [204].

3.1.1 The enhanced sensitivity of CerS4 KO mice is not due barrier integrity defects

Defects in the barrier function was a possible hypothesis for "the higher susceptibility of CerS4 KO mice to DSS induced colitis" [204]. To analyze whether CerS4 deficiency affected barrier function, TJs were stained histologically with anti-ZO-1 and anti-Occludin antibodies. The staining showed no difference in colon of CerS4 KO mouse compared to WT mouse (Figure 3.3). To further confirm this, CerS4 was also downregulated in the human CRC cell line Caco-2. CerS4 expression was downregulated in Caco-2 cells by shRNA and compared to Caco-2 cells that were transduced with a non-coding (NC) shRNA (Figure 3.38 A). Transduction of CerS4-shRNA resulted in a 0.8-fold decrease in CerS4 and, as a compensation, CerS1 mRNA expression increased 1.13-fold. nsThe expression of other CerS were not affected in shCerS4 Caco-2 cells (Figure 3.38 B). These cells were used to analyze barrier function by TEER using the CellZscope instrument, which calculates from the impedance of the cells both capacitance and electrical resistance.

Caco-2 cells reached an electrical resistance of $700\,\Omega\,\mathrm{cm}^2$ to $800\,\Omega\,\mathrm{cm}^2$ (Figure 3.4 A). The AUC was calculated and the median of three independent measurements with at least triplicates in each measurement was $94{,}296\,\Omega\,\mathrm{cm}^2$ for shNC Caco-2 cells and $75{,}269\,\Omega\,\mathrm{cm}^2$ for shCerS4 Caco-2 cells. Although the electrical resistance of the shCerS4 Caco-2 cells was reduced by 0.8-fold, this was not statistically significant compared with the electrical resistance of shNC Caco-2 cells(Figure 3.4 A). This indicates that downregulation of CerS4 does not affect barrier functionality. While the electrical resistance increases with time, the electrical capacitance behaves reciprocally and decreases. Initially, the capacity was higher in shCerS4 Caco-2 cells ($7 \pm 2.2\,\mu\mathrm{F\,cm}^{-2}$) than in shNC Caco-2 cells ($4.7 \pm 2.4\,\mu\mathrm{F\,cm}^{-2}$). Although the capacity of both cell lines reached the same level, the mean of the AUC was significantly higher in shCerS4 Caco-2 cells ($669.5 \pm 182.7\,\mu\mathrm{F\,cm}^{-2}$) than shNC Caco-2 cells ($550.8 \pm 135.4\,\mu\mathrm{F\,cm}^{-2}$) (p=0.04) (Figure 3.4 B). This suggests that CerS4 downregulation does not influence TJs, but it may affect the cell morphology or vesicle formation [253, 254].

The permeability assay of FITC dextran also showed that CerS4 deficiency in Caco-2 cells did not affect barrier function. Already after $2\,\mathrm{h}$, $2.4\,\mu\mathrm{g\,mL}^{-1}$ of FITC dextran was detected in the basal medium of an empty insert. Over 8h, fluorescence increased linearly by a factor of $\sim$1.8. After $24\,\mathrm{h}$, $26.6 \pm 4.2\,\mu\mathrm{g\,mL}^{-1}$ FITC dextran was detected in basal medium without a cell layer, and after $48\,\mathrm{h}$, fluorescence increased 1.3-fold. However, the inclusion of a Caco-2 cell layer affected the FITC dextran permeability through the insert. Only after $24\,\mathrm{h}$, $0.9 \pm 2.5\,\mu\mathrm{g\,mL}^{-1}$ FITC dextran was detected in the basal medium and remained at this level after $48\,\mathrm{h}$.In shCerS4 Caco-2 cells, $0.7 \pm 2.2\,\mu\mathrm{g\,mL}^{-1}$ was the highest concentration of FITC dextran detected in the basal medium (Figure 3.4 C). Overall, the permeability of FITC dextran through shCerS4 Caco-2 cells changed 0.63 times compared with shNC Caco-2 cells (ns), and the permeability of FITC dextran in shNC Caco-2 cells was 34.4-fold lower than the median values of an empty insert. Hence, because of the tight barrier already indicated by the high electrical resistance of the Caco-2 cells, hardly any FITC dextran molecules were detected in the basal medium, indicating that CerS4 deficiency does not alter permeability

(Figure 3.4 C).

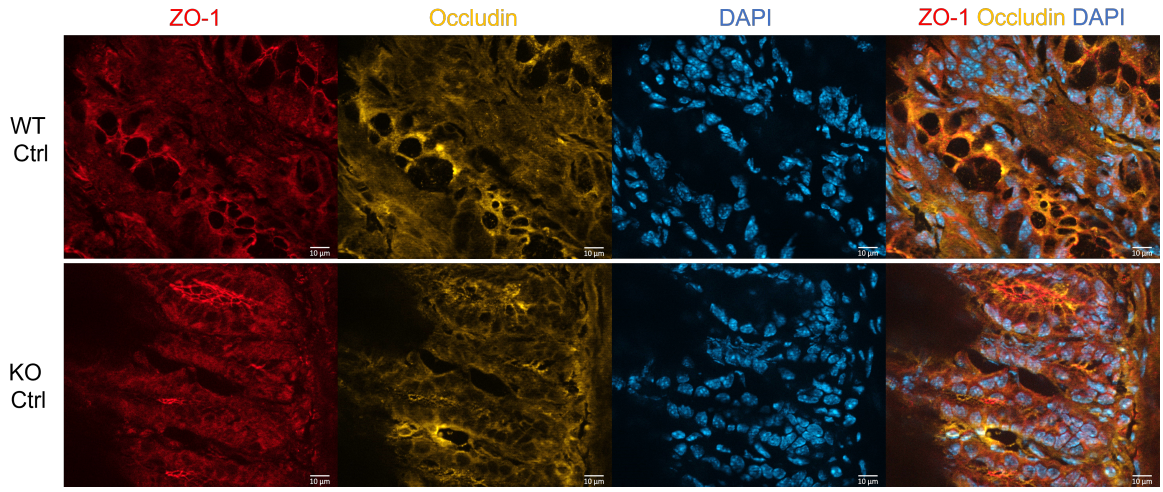

FIGURE 3.3: Immunohistochemical staining of TJs proteins in colon tissue. ZO-1 (Alexa Fluor® 647, red), occludin (Cy3, yellow), and nucleus staining with DAPI (blue) in colon tissue of WT mouse (WT) and CerS4 KO mouse (KO) without DSS treatment. Overlap of ZO-1 and Occludin staining in the tissue resulted in an orange staining. 60x magnifications were taken with an Axio Observer microscope (Zeiss). Scale bar 10 µm.

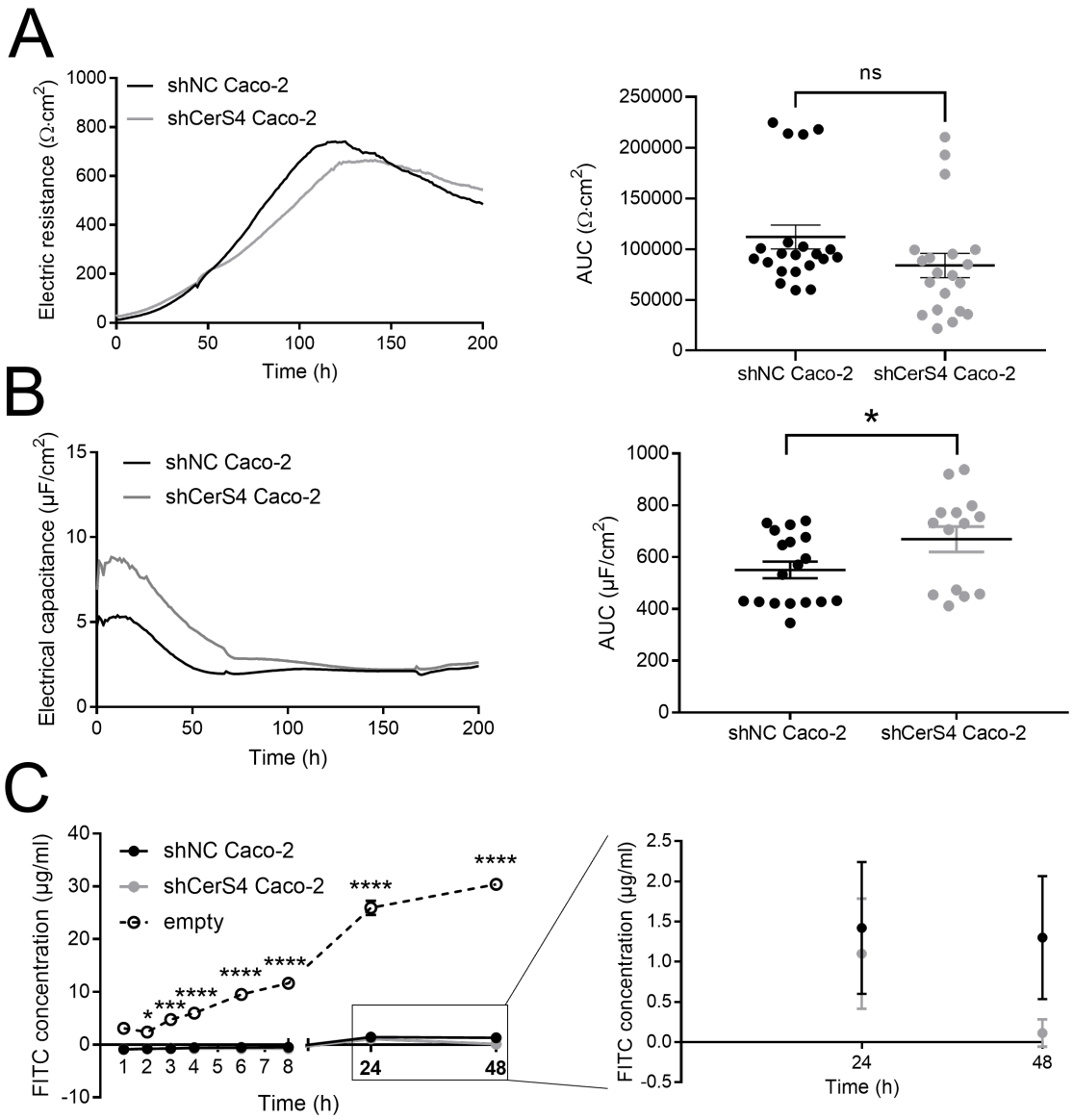

FIGURE 3.4: CerS4 deficiency does not affect barrier function in Caco-2 cells. (A) Transepithelial electrical resistance (TEER) of inserts coated with Caco-2 cells was measured with a CellZscope2 indicated no difference. Exemplary measurement of electrical resistance ($\Omega\,\mathrm{cm}^2$) over time of control Caco-2 cells (shNC Caco-2 cells) and CerS4 downregulated Caco-2 cells (shCerS4 Caco-2 cells). Calculation of the AUC of electrical resistance of the different runs. (B) Higher electrical capacitance ($\mu\mathrm{F\,cm}^{-2}$) measured by CellZscope2 in an exemplary measurement and calculated by the AUC of different runs. (C) Permeability assay of FITC dextran at $100\,\mu\mathrm{g\,mL}^{-1}$ (average size 40,000). Fluorescence in basal medium was measured over $48\,\mathrm{h}$, indicating a strong barrier of Caco-2 cells and no difference between shNC and shCerS4 Caco-2 cells. Data are mean ±SEM of n=3 independent measurements. Statistical analysis was performed by Student's t-test or by a one-way ANOVA. * p<0.05, ** p<0.01, *** p<0.001, **** p<0.0001. Parts of the data (A,C) are published in [204].

3.1.1.1 Increased sensitivity of CerS4 KO mice is associated with increased neutrophils

Analysis of the immune cell homeostasis in the colon indicated an infiltration of immune cell during DSS induced colitis progression. Overall, both IEL and immune cells within the

LP compose the immune cell status in the colon. Analysis of these fractions by flow cytometry confirmed a higher immune cell infiltration in the colon after DSS treatment. Trends were similar in both fractions, IEL and LP, but T cells were more abundant in IEL fraction of the colon and monocytes/macrophages were more in LP fraction. Within the innate immune cells, the increase in neutrophils was remarkable after DSS treatment. While this increase was 4.5-fold higher in CerS4 LCK/Cre mice than in the control mice, neutrophil frequency increased up to $47\,\%$ in both WT mice and CerS4 KO mice after DSS treatment in the IEL fraction. This increase was significantly higher in CerS4 KO mice compared with WT mice and CerS4 LCK/Cre mice in the IEL fraction of the colon. In the LP fraction of the colon, neutrophils increased 8-fold in WT mice, 5.8-fold in CerS4 LCK/Cre mice, but 300-fold in CerS4 KO mice after DSS treatment (Figure 3.5 A, C, Table 3.2, Table 3.1). The frequency of DCs, B cells and NK T cells did not alter significantly. Once undifferentiated monocytes ($Ly6G^+CD11b^+Ly6c^+MHCII^-$) from the blood infiltrate the tissue, they differentiate into macrophages ($Ly6G^+CD11b^+Ly6C^-MHCII^+$). During the switch in the downregulation of LyC6 receptor and upregulation of MHCII receptor, there is a state in which monocytes are double positive for both receptors ($Ly6G^+CD11b^+Ly6C^+MHCII^+$). This population was referred as 'Monocytes differentiating to Macrophages' (Monocytes diff. to MΦ). While there was a tendency for increased levels of 'Monocytes differentiating to Macrophages' in LP fraction of CerS4 KO mice (p=0.086) after DSS treatment, this population was significantly elevated in IEL fraction of the colon not only compared to control CerS4 KO mice but also to WT and CerS4 LCK/Cre DSS treated mice (Figure 3.5 A, C, Table 3.2, Table 3.1). In general, $CD11b^+$ monocytes were increased in CerS4 KO mice after DSS treatment and compared with the other DSS treated mice. However, the 18-fold increase in undifferentiated monocytes in the LP fraction of CerS4 KO mice compared with the 3-fold and 2-fold increase in WT mice and CerS4 LCK/Cre mice, respectively, and the increase in differentiated macrophage population indicate a greater infiltration of monocytes in CerS4 KO mice compared with WT mice and CerS4 LCK/Cre mice, respectively (Figure 3.5 A, C, Table 3.2, Table 3.1).

In addition to the innate immune cells, the intraepithelial T cells contribute to homeostasis and inflammation in the colon [255]. Although the frequency of T cells was higher in IEL-fraction of the colon, no significant changes were observed upon treatment with DSS. However, T cells in the IEL fraction of the colon were already higher in CerS4 LCK/Cre mice than in the CerS4 KO mice under control conditions. The distribution of $CD8^+$ T cells was dependent on the localization: more $CD8^+$ T cells were detected in the IEL fraction of the colon. The tendency of the elevated $CD8^+$ T cell levels in CerS4 LCK/Cre mice compared to CerS4 KO mice (p=0.083) indicated that a large proportion of the increased T cells compared to CerS4 KO mice were $CD8^+$ T cells (Figure 3.5 B, D, Table 3.2, Table 3.1). While $CD8^+$ T cells were largely resident in the IEL fraction, this was not the case for $CD4^+$ T cells. The frequency of $CD4^+$ T cells was lower than that of cytotoxic $CD8^+$ T cells in all mice. In CerS4 KO mice, hardly any $CD4^+$ T cells were found in the IEL fraction ($0.424\ \pm 0.12$) and LP fraction ($2.36\,\% \pm 1.05\,\%$), whereas approximately double the amount was detected in WT mice and CerS4 LCK/Cre mice, demonstrating that $CD4^+$ T cells mainly located in

the LP fraction of the colon. As well as the double amount of $CD4^+$ T cells detected in WT mice and CerS4 LCK/Cre mice, $CD4^-CD8^-$ T cells in CerS4 KO mice were only half the size of those in control WT mice and control CerS4 LCK/Cre mice and mainly located in the IEL fraction (Table 3.1, Table 3.2). Among the T cells, the double positive $CD4^+CD8^+$ T cells were the smallest subpopulation in both in IEL and LP fractions. In the colon, T_{regs} are important cells that maintain immune tolerance in the intestine [256, 257]. In the colon, $30\,\%$ of the $CD4^+$ T cells were $FOXP3^+CD4^+$, and the $CD25^+GITR^{high}$ population accounted for only about $3\,\%$ of $CD4^+$ T cells and did change significantly after DSS treatment in WT mice. Whereas in CerS4 KO mice barely T_{regs} could be detected in both IEL fraction and LP fraction, in CerS4 LCK/Cre mice T_{regs} were mainly located in the IEL fraction (Figure 3.5 B, D, Table 3.2, Table 3.1).

In conclusion, myeloid cells increased predominantly in the inflamed colon induced by DSS, demonstrating a stronger innate immune response than an adaptive response in the acute phase of inflammation. However, CerS4 deficiency played a role in disease pathology. The number of myeloid cells increased in the colon after DSS treatment in CerS4 KO mice that suffered severe inflammation triggered by DSS. Especially neutrophiles were abundant in CerS4 KO mice compared with WT mice and CerS4 LCK/Cre mice, resulting in a 300-fold increase in LP fraction of the colon. The number of infiltrating monocytes was also higher in the CerS4 KO mice compared with WT mice and CerS4 LCK/Cre mice after DSS treatment. The increased frequency of undifferentiated monocytes and "monocytes differentiating into macrophages" indicated a strong infiltration from the blood and lymphatic system into the inflammatory site. However, the adaptive immune system, including B cells and T cells, did not change significantly upon DSS treatment. Among T cells, cytotoxic $CD8^+$ T cells were mainly in the IEL fraction of the colon, while $CD4^+$ T cells were in the LP fraction of the colon.

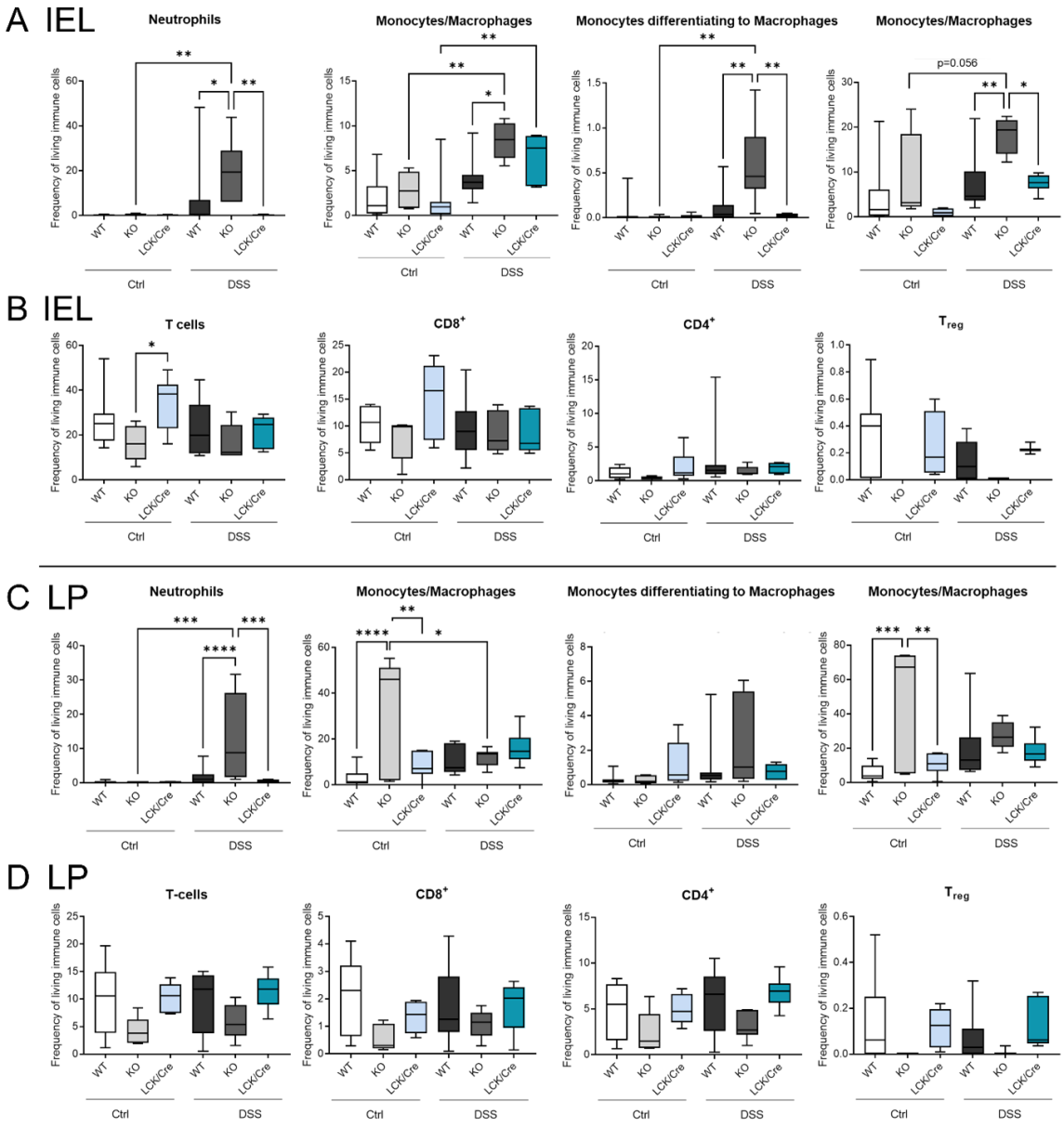

FIGURE 3.5: Flow cytometry analysis of immune cells isolated from the IEL fraction or LP fraction of the colon tissue of control (Ctrl) and DSS treated (DSS) WT mice (WT), CerS4 KO mice (KO) and CerS4 LCK/Cre mice (LCK/Cre). (A) IEL fraction of the colon with the significant alterations in myeloid cells upon DSS treatment. (B) T cells and T cell subtypes detected in the IEL fraction of the colon. (C) Myeloid cells detected in the LP fraction were altered not only compared to the control, but the extend in the increase was also compared to the DSS treated groups different. (D) Detected T cells and T cell subtypes measured in the LP fraction of the colon. Data are plotted as median ±Min to Max in box & whiskers. Statistical analysis was performed by one-way ANOVA. Group size of control mice: WT mice n=11 CerS4 KO mice n=5 and CerS4 LCK/Cre mice n=6; and for DSS treated group WT mice: n=11 CerS4 KO mice n=7 and CerS4 LCK/Cre mice n=6. Parts of Data published in [204].

TABLE 3.1: Flow cytometry analysis of the LP isolated from the colon of control and DSS treated mice. Data are mean ±SEM with distinct group sizes. Statistical analysis was performed by one-way ANOVA, significant differences were highlighted bold and tendencies italic. Abbreviation: MΦ, Macrophages; diff., differentiating; undiff., undifferentiated.

LP	WT Ctrl			WT DSS			KO Ctrl			KO DSS			LCK/Cre Ctrl			LCK/Cre DSS		
	Mean	SEM	n	Mean	SEM	n	Mean	SEM	n	Mean	SEM	n	Mean	SEM	n	Mean	SEM	n
Immune cells	7.87	2.08	11	**11.48**	1.32	11	8.88	2.36	5	**13.94**	1.66	7	5.028	0.68	6	**9**	0.94	6
Single Cells	57.36	3.05	11	74.12	4.10	11	46.08	10.12	5	88.09	6.38	7	51.55	3.91	6	61	4.17	6
Living immune cells	55.86	5.79	11	74.99	3.03	11	66.64	4.09	5	**71.63**	4.41	7	59.78	6.15	6	78	4.36	6
$CD3^+$ T cells	10.17	1.83	11	9.34	1.58	11	4.05	1.18	5	5.80	1.13	7	10.36	1.07	6	11	1.29	6
$CD4^+$ T cells	4.96	0.84	11	5.79	1.01	11	2.36	1.05	5	3.11	0.56	7	4.94	0.68	6	7	0.71	6
$CD25^+GITR^+$ T_{regs}	0.15	0.06	11	0.08	0.03	11	0.00	0.00	5	**0.01**	0.00	7	0.12	0.03	6	0	0.04	6
$CD8^+$	2.11	0.41	11	1.73	0.38	11	0.58	0.22	5	1.10	0.20	7	1.35	0.24	6	2	0.38	6
$CD8^-CD4^-$ T cells	2.93	0.78	11	1.73	0.35	11	1.00	0.26	5	1.35	0.37	7	3.95	0.55	6	3	0.51	6
$CD8^+CD4^+$ T cells	0.18	0.07	11	0.09	0.03	11	0.11	0.05	5	0.24	0.10	7	0.132	0.07	6	0	0.03	6
$NK1.1^+$ T cells	0.75	0.18	11	0.32	0.08	11	0.21	0.06	5	0.75	0.16	7	0.497	0.08	6	0	0.11	6
$CD11b^-MHCII^+CD19^+$ B cells	5.75	2.64	11	7.64	2.65	11	**1.05**	0.62	5	4.53	1.69	7	3.44	1.89	6	6	2.82	6
Monocytes/Macrophages	11.34	6.11	11	**19.20**	5.12	11	45.09	16.30	5	27.39	2.87	7	10.89	2.49	6.	**18**	3.17	6
Monocytes diff. to MΦ	0.27	0.08	11	0.93	0.44	11	**0.28**	0.11	5	2.34	0.92	7	1.175	0.55	6	1	0.18	6
Monocytes/Macrophages	7.84	4.80	11	10.61	1.71	11	30.46	11.77	5	11.75	1.50	7	8.424	2.34	6	16	3.08	6
Undiff. Monocytes	0.21	0.15	11	0.70	0.40	11	0.16	0.08	5	**2.95**	0.36	7	0.061	0.03	6	0	0.07	6
Neutrophils	0.20	0.10	11	1.67	0.66	11	0.17	0.04	5	13.00	4.46	7	0.093	0.06	6	1	0.16	6
$CD11c^+MHCII^+$ DCs	0.19	0.04	6	0.33	0.11	8	0.64	0.283	5	0.47	0.16	7	0.24	0.08	2	0.59	0.20	3

TABLE 3.2: Flow cytometry analysis of the IEL isolated from the colon of control and DSS treated mice. Data are mean ±SEM with distinct group sizes. Statistical analysis was performed by one-way ANOVA. significant differences were highlighted bold and tendencies italic. Abbreviation: MΦ, Macrophages; diff., differentiating; undiff., undifferentiated.

IEL	WT Ctrl			WT DSS			KO Ctrl			KO DSS			LCK/Cre Ctrl			LCK/Cre DSS		
	Mean	SEM	n	Mean	SEM	n	Mean	SEM	n	Mean	SEM	n	Mean	SEM	n	Mean	SEM	n
Immune cells	2.96	0.32	11	**4.65**	0.44	11	3.34	1.11	5	**7.25**	0.65	6	2.3	0.21	9	3.03	**0.2**	6
Single Cells	56.79	7.36	11	76.69	5.07	11	44.69	15	5	83.5	8.48	6	58.3	6.32	9	75.03	6.84	6
Living immune cells	60.44	4.58	11	65.26	4.31	11	67.4	3.77	5	**52.73**	5.29	6	66.09	4.75	9	72.63	2.51	6
$CD3^+$ T cells	26.36	3.2	11	23.38	3.52	11	16.48	3.55	5	16.62	3.26	6	34.6	3.9	9	22.08	2.88	6
$CD4^+$ T cells	1.15	0.25	11	3.45	1.43	11	0.42	0.12	5	1.45	0.29	6	2.18	0.69	9	1.91	0.33	6
$CD25^+GITR^+$ T_{regs}	0.24	0.09	11	0.08	0.04	11	0	0	5	**0**	0	6	0.17	0.07	9	0.12	0.05	6
$CD8^+$ T cells	11.9	1.94	11	10	1.71	11	7.61	1.76	5	8.59	1.53	6	15.1	2.31	9	8.5	1.58	6
$CD8^-CD4^-$ T cells	12.41	1.36	11	9.24	1.49	11	8.19	2.22	5	6.13	1.96	6	16.23	2.29	9	11.39	1.72	6
$CD8^+CD4^+$ T cells	0.98	0.35	11	0.7	0.34	11	0.24	0.08	5	0.47	0.06	6	1.16	0.35	9	0.31	0.09	6
$NK1.1^+$ T cells	1.06	0.11	11	0.68	0.08	11	0.67	0.21	5	0.61	0.06	6	0.91	0.17	9	0.77	0.17	6
B cells	3.44	0.69	11	4.46	0.78	11	**1.96**	0.86	5	3.3	1.01	6	3.85	0.67	9	4.76	1	6
Monocytes/Makrophages	4.15	1.94	11	**7.28**	1.77	11	8.93	4.27	5	18.23	1.63	6	4.3	3.3	9	7.56	**0.82**	6
Monocytes diff. to MΦ	0.05	0.04	11	0.14	0.06	11	**0.01**	0.01	5	0.59	0.19	6	0.01	0.01	9	0.02	0.01	6
Monocytes/Makrophages	1.77	0.66	11	4.35	0.76	11	2.85	0.91	5	8.36	0.9	6	1.61	0.88	9	6.55	1.08	6
Undiff. Monocytes	0.29	0.27	11	0.77	0.46	11	0.01	0.01	5	**2.81**	0.63	6	0.02	0.01	9	0.38	0.33	6
Neutrophiles	0.16	0.08	11	7.27	4.34	11	0.42	0.24	5	19.89	5.71	6	0.06	0.05	9	0.27	0.11	6
$CD11c^+MHCII^+$ DCs	0.48	0.2	6	0.97	0.17	8	1.12	0.49	5	0.86	0.13	5	0.69	0.49	3	1.17	0.43	3

The inflammation at the colon attracted many immune cells. Therefore, circulating immune cells isolated from the blood were analyzed by flow cytometry. In general, CerS4 deficiency had only specific effects on the immune cell status of the control mice. The control CerS4 KO mice had fewer activated monocytes ($CD3^-CD11b^+Ly6G^-Ly6C^-MHCII^-CD14^+$ $CD80^+$), $CD80^+$ monocytes and NK T cells (Figure 3.6 A). T cell specific CerS4 deficiency did not affect the total number of T cells. Of the T cell subpopulation, only $CD8^+$ T cells were decreased in blood of control CerS4 LCK/Cre mice (Figure 3.6 B). DSS induced inflammation led not only to an increase in immune cells in the colon tissue but also to different immune populations circulating in the blood. Among myeloid cells, only the frequency of neutrophils increased in the blood after DSS treatment. While the increase was twofold in WT mice and CerS4 LCK/Cre mice, it was 4.7-fold higher in blood of CerS4 KO mice in comparison to control population and CerS4 LCK/Cre DSS treated mice, respectively (Figure 3.6 A, Table 3.3). Other myeloid cells were not affected, i.e., DCs, monocytes, B cells and circulating NK cells were not altered in the blood upon DSS treatment. In contrast, lymphocyte levels changed with inflammation. B cells did not change, but in DSS treated mice, the amount of T cells was reduced 0.39-fold. $CD4^+$ T cells represented half the proportion of T cells in the blood. The 0.39-fold decrease was also observed in the $CD4^+$ T cells of CerS4 KO mice. A slightly smaller decrease in $CD8^+$ T cells (0.48-fold decrease) was observed in CerS4 KO mice and a significant decrease in WT mice (0.57 fold decrease) whereas the values did not change in CerS4 LCK/Cre mice (Figure 3.6 B, Table 3.3). A much smaller proportion of total T cells were the $CD4^+CD8^+$ and $CD4^-CD8^-$ T cells. In CerS4 KO mice, double-positive T cells show a tendency to rise whereas $CD8^-CD4^-$ T cells show a tendency to decline in the blood after DSS treatment compared to CerS4 LCK/Cre DSS treated mice. This suggested that the infiltrating immune cells are partly derived from the blood, whereas the remaining increased immune cells are likely derived from the lymphatic system (Figure 3.6 B, Table 3.3).

The status of immune cells in the spleen was quite comparable between the different mice strains. The mice differed only in cDC1 resident DCs, which increased after DSS treatment in WT mice (3.4-fold change, p=0.056) and in CerS4 KO mice (2.8-fold change, p=0.0003). The level of cDC1 in DSS treated CerS4 KO mice was twice that level of DSS treated CerS4 LCK/Cre mice (p=0.01). Acute DSS treatment did not alter the DC population and cDC2 level in the spleen (Figure 3.7 A). Regarding T cells, CerS4 LCK/Cre mice had fewer $CD8^+$ T cells than control WT mice but did not differ in the T cells, $CD4^+$ T cells, or even T_{regs}. The percentage of T_{regs} in total $CD4^+$ T cells ranged from $7\,\%$ and $13\,\%$, but did not alter significantly after DSS treatment (Figure 3.7 B). Because DCs activate different immune cells depending on the stimulus, additional myeloid cells were compared (Figure 3.7 C). Although CerS4 LCK/Cre mice had fewer cytotoxic $CD8^+$ T cells, it seems they compensated for this lack with a twofold increase in NK cells compared to WT mice and CerS4 KO mice under control conditions. After DSS treatment, the level of NK cells decreased by half (p=0.091) and was at the same level as in WT mice and CerS4 KO mice. However, distinct myeloid cells were altered upon DSS induced inflammation in the spleen. The frequency of monocytes/macrophages ($CD11^+$ cells) was significantly increased twofold in

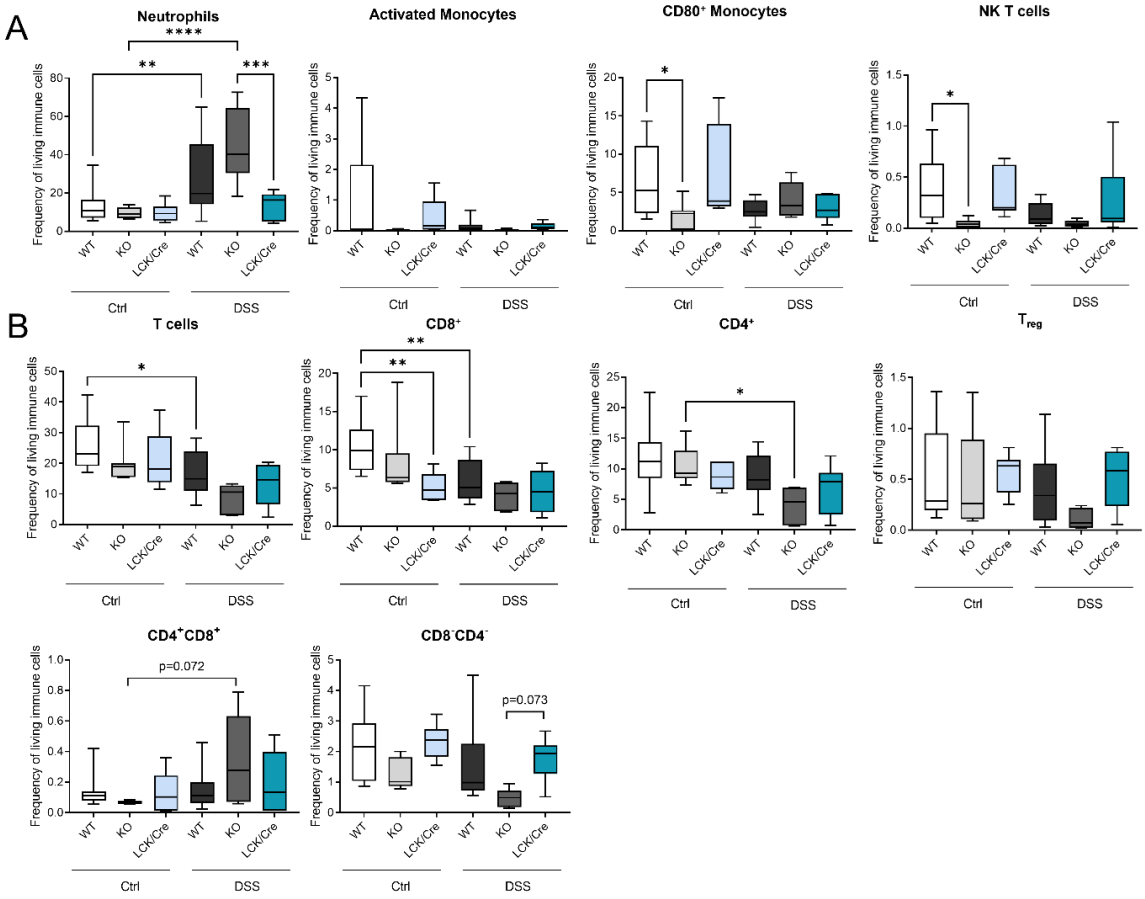

FIGURE 3.6: Flow Cytometry analysis of immune cells isolated from the blood of control (Ctrl) and DSS treated (DSS) WT mice (WT), CerS4 KO mice (KO) and CerS4 LCK/Cre mice (LCK/Cre). The DSS induced acute inflammation also resulted in an abundance of neutrophils in the blood. (A) Different cells in which the immune status on the basal level differed. (B) Circulating T cells and T cell subpopulation in the blood altered upon DSS induced inflammation. Data are median ±Min/Max. Statistical analysis was performed by one-way ANOVA. Group size in different tissue of control mice: WT mice n=18, CerS4 KO mice n=9 and CerS4 LCK/Cre mice n=7 and for DSS treated group WT mice: n=12 CerS4 KO mice n=6 and CerS4 LCK/Cre mice n=8. Data partially published in [204].

WT mice after DSS treatment (2.4-fold increase, p=0.031). In CerS4 KO mice, DSS treatment increased the F4/80$^+$CD36$^+$ macrophages by 9.6-fold (p<0.0001). This level in the spleen was also higher than in DSS treated WT mice (2,75-fold change, p=0.0004) and DSS treated CerS4 LCK/Cre mice (7.7-fold change, p<0.0001). In contrast to the very low F4/80$^+$CD36$^+$ macrophages, DSS treated CerS4 LCK/Cre mice had the highest monocyte level. After DSS treatment, the monocytes frequency increased threefold (p=0.007) and was twice that of DSS treated WT mice (p=0.049) and five times that of DSS treated CerS4 KO mice (p=0.0014). Not only monocyte levels were increased, but neutrophil levels were also increased 2.6-fold in the spleen after DSS treatment in CerS4 LCK/Cre mice (p=0.025), but did not differ between DSS treated WT mice and DSS treated CerS4 KO mice (Figure 3.7 C,Table 3.4).

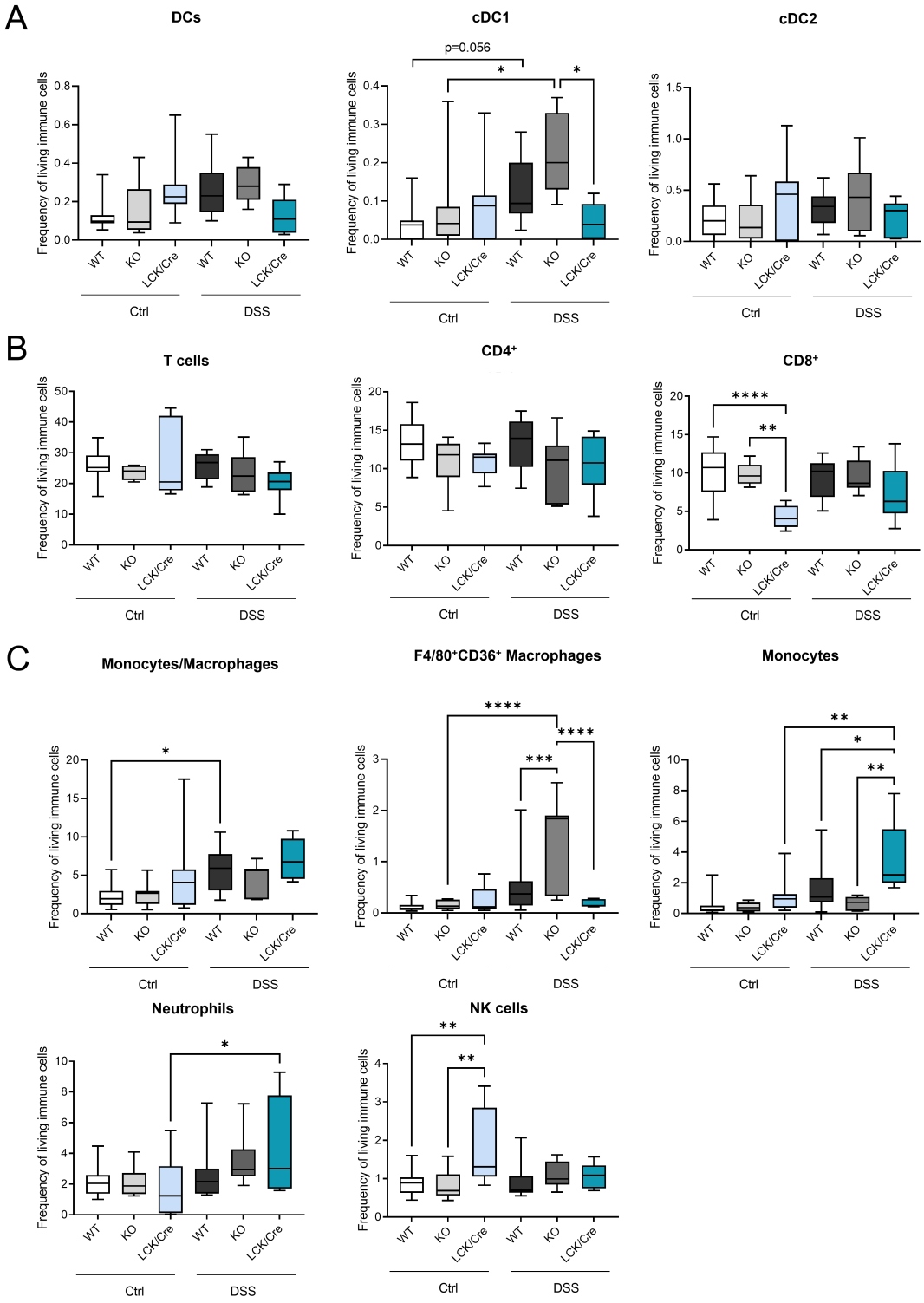

FIGURE 3.7: Flow Cytometry analysis of immune cells isolated from the spleen of control (Ctrl) and DSS treated WT mice (WT), CerS4 KO mice (KO) and CerS4 LCK/Cre mice (LCK/Cre). (A) Resident subpopulations of DCs besides the DCs, namely, cDC1 and cDC2. (B) T cell and T cell subpopulation $CD4^+$ T cells and $CD8^+$ T cells. (C) Further immune cell populations which changed upon DSS treatment. Data are median ±Min/Max. Statistical analysis was performed by one-way ANOVA. Group size in different tissue of control mice: WT mice n=17, CerS4 KO mice n=11 and CerS4 LCK/Cre mice n=9 and for DSS treated group WT mice: n=12 CerS4 KO mice n=6 and CerS4 LCK/Cre mice n=8. Data published in [204].

TABLE 3.3: Flow Cytometry analysis of the white blood cells isolated from the blood of control (Ctrl) and DSS treated (DSS) WT mice (WT), CerS4 KO mice (KO) and CerS4 LCK/Cre mice (LCK/Cre). Data are mean ±SEM with distinct group sizes. Statistical analysis was performed by one-way ANOVA, significant differences were highlighted bold and tendencies italic.

Blood	WT Ctrl			WT DSS			KO Ctrl			KO DSS			LCK/Cre Ctrl			LCK/Cre DSS		
	Mean	SEM	n	Mean	SEM	n	Mean	SEM	n	Mean	SEM	n	Mean	SEM	n	Mean	SEM	n
Single cells	80.18	5.46	18	86.98	6.73	12	89.41	4.12	9	99.22	0.09	6	82.23	6.08	7	88.58	5.33	8
Living immune cells	67.14	8.96	18	38.98	11.53	12	42.35	13.05	9	64.87	17.35	6	62.25	17.16	7	42.48	16.75	8
$CD3^+$ T cells	27.46	2.05	18	16.48	2.05	12	22.99	3.75	9	*8.86*	1.95	6	16.13	1.25	7	13.35	2.43	8
$CD4^+$ T cells	11.53	1.25	18	8.79	1.06	12	10.56	0.97	9	4.09	1.17	6	8.7	0.76	7	6.79	1.4	8
T_{regs}	0.55	0.1	18	0.42	0.1	12	0.46	0.16	9	0.11	0.04	6	0.57	0.07	7	0.51	0.1	8
$CD8^+$ T cells	10.49	0.79	18	6	0.81	12	8.19	1.51	9	3.98	0.71	6	5.02	0.7	7	4.64	0.98	8
$CD8^-CD4^-$ T cells	4.74	1.51	18	1.56	0.34	12	3.4	2.18	9	0.49	0.13	6	*2.33*	0.22	7	1.77	0.24	8
$CD8^+CD4^+$ T cells	0.68	0.3	18	0.14	0.04	12	0.89	0.38	9	*0.34*	0.12	6	0.11	0.05	7	0.15	0.07	8
$NK1.1^+Ly6c^-$ NK cells	0.87	0.12	18	0.82	0.16	12	1.6	0.8	9	0.99	0.36	6	0.67	0.17	7	0.47	0.14	8
NK T cells	0.51	0.1	18	0.13	0.03	12	**0.17**	0.14	9	0.05	0.01	6	0.34	0.09	7	0.29	0.13	8
B cells	21.12	5.21	18	18.41	4	12	36.01	5.8	9	22.68	5.84	6	13.45	7.11	7	16.83	6.47	8
activiated Monocytes	0.91	0.33	18	0.16	0.07	12	0.02	0.01	9	0.03	0.01	6	0.44	0.22	7	0.15	0.04	8
Monocytes	4.96	0.63	18	5.32	0.52	12	*5.61*	1.74	9	5.44	0.64	6	6.1	0.79	7	5.48	0.57	8
$CD80^+CD11b^+$ Monocytes	7.46	1.55	18	9.33	3.7	12	**5.16**	3.34	9	3.98	0.94	6	20.13	7.08	7	14.59	5.64	8
$CD14^+CD11b^+$ Monocytes	1.53	0.27	18	1.15	0.17	12	1.83	0.69	9	1.46	0.47	6	1.46	0.45	7	0.92	0.35	8
DCs	0.08	0.03	18	0.09	0.02	12	0.09	0.03	9	0.11	0.03	6	0.09	0.02	7	0.13	0.02	8
Neutrophiles	12.71	1.8	18	**27.76**	5.73	12	9.43	0.94	9	**44.55**	8.02	6	8.54	1.62	7	**20.75**	7.71	8

TABLE 3.4: Flow Cytometry analysis of the immune cells isolated from the spleen of control (Ctrl) and DSS treated (DSS) WT mice (WT), CerS4 KO mice (KO) and CerS4 LCK/Cre mice (LCK/Cre). Data are mean ±SEM with distinct group sizes. Statistical analysis was performed by one-way ANOVA, significant differences were highlighted bold and tendencies italic.

Spleen	WT Ctrl			WT DSS			KO Ctrl			KO DSS			LCK/Cre Ctrl			LCK/Cre DSS		
	Mean	SEM	n	Mean	SEM	n	Mean	SEM	n	Mean	SEM	n	Mean	SEM	n	Mean	SEM	n
Immune cells	76.75	4.67	17	**65.36**	4.19	12	69.14	6.65	11	**90.47**	1.119	6	**46.06**	6.3	9	**54.76**	4.61	8
Single Cells	85.14	1.86	17	**80.21**	2.35	12	**76.64**	6.64	11	80.1	0.672	6	87.37	0.86	9	**86.84**	0.97	8
Living immune cells	90.92	0.65	17	88.75	1.02	12	**88.09**	3.24	11	89.57	0.685	6	**84.29**	2.68	9	85.91	1.1	8
$CD3^+$ T cells	25.86	1.3	17	25.68	1.25	12	27.77	5.08	11	**23.4**	2.793	6	26.8	4.05	9	**20.11**	1.82	8
$CD4^+$ T cells	13.48	0.68	17	13.36	0.96	12	**10.01**	1.29	11	**10.2**	1.772	6	10.93	0.61	9	10.63	1.35	8
$CD25^+GITR^+$ T_{regs}	0.95	0.1	17	1.06	0.19	12	0.78	0.15	11	0.9	0.111	6	1.15	0.1	9	1.42	0.19	8
$CD8^+$	10.3	0.78	17	9.39	0.7	12	**7.43**	1.31	11	9.54	0.929	6	**3.86**	0.62	9	**7.28**	1.28	8
$CD8^-CD4^-$ T cells	1.53	0.39	17	1.57	0.28	12	**9.45**	5.3	11	**0.52**	0.078	6	**11.77**	4.6	9	**2.08**	0.74	8
$NK1.1^+$ cells	0.87	0.07	17	0.9	0.13	12	1.04	0.26	11	1.09	0.143	6	**2.21**	0.56	9	*1.07*	0.12	8
Monocytes/Macrophages	4.02	2.63	17	**8.89**	4.01	13	4.51	3.03	8	8.48	3.58	7	**8.07**	8.26	9	10.05	4.46	5
$CD11b^+MHCII^-Ly6C^+$ Monocytes	0.45	0.59	17	1.7	1.56	13	0.41	0.3	8	0.66	0.43	7	1.13	1.12	9	3.5	2.46	5
$F4/80^+$ Macrophages	0.13	0.09	17	0.52	0.58	13	0.31	0.46	8	1.43	0.86	7	0.52	0.86	9	0.19	0.08	5
$F4/80^+CD36^+$ Makrophages	0.07	0.05	17	0.28	0.27	13	0.25	0.19	8	0.75	0.39	7	0.18	0.21	9	0.08	0.08	5
$MHCII^+CD11c^+$ DC	0.13	0.08	17	0.26	0.14	13	0.15	0.14	8	0.28	0.09	7	0.39	0.4	9	0.12	0.1	5
cDC1	0.04	0.04	17	0.13	0.08	13	0.08	0.12	8	0.22	0.1	7	0.09	0.1	9	0.05	0.05	5
cDC2	0.22	0.17	17	0.33	0.17	13	0.21	0.22	8	0.43	0.33	7	0.41	0.37	9	0.22	0.18	5
Neutrophiles	2.15	0.21	17	2.71	0.54	12	1.56	0.38	11	3.5	0.77	6	1.74	0.63	9	**8.21**	3.78	8

In sum, higher susceptibility of CerS4 KO mice towards DSS induced inflammation was not due a barrier defect, but these DSS treated mice had a higher immune cell infiltration than DSS treated WT mice. The acute inflammation in the colon of CerS4 KO mice was ascribed to an increase in neutrophils and monocytes differentiating into macrophages. The increase in neutrophils was also detected in the blood of CerS4 KO mice, and a higher abundance of cDC1 and F4/80$^+$CD36$^+$ macrophages was quantified in the spleen. The number of circulating T cells (mainly CD8$^+$ T cells in WT mice and CD4$^+$ T cells in CerS4 KO mice) also decreased under DSS treatment. CerS4 deficiency in T cells did not affect the total number of T cells in the blood and spleen. However, in the CerS4 LCK/Cre control mice, the frequency of CD8$^+$ T cells was decreased. CerS4 LCK/Cre mice showed a delayed response to DSS treatment compared with DSS treated CerS4 KO mice and did not respond with a strong immune response to DSS treatment like CerS4 KO mice.

3.2 Impact of tissue specific CerS4 deficiency in AOM/DSS colon cancer model

The results of the AOM/DSS model were very similar to the acute DSS treatment. During each DSS induced inflammation cycle, body weight decreased and recovered over time (Figure 3.8 A) and the score increased, indicating a poor health status (Figure 3.8 B). The "clinical course" was worse in the first DSS treatment cycle, in which many WT mice and CerS4 KO mice already reached a "human endpoint", and the mouse experiment was aborted. $61.54\,\%$ of CerS4 KO mice and $12.9\,\%$ of WT mice reached this human endpoint after the first DSS cycle. Nevertheless, survival of the first DSS cycle did not mean that the mice survived to the end: Overall, $84.61\,\%$ CerS4 KO mice and $19.35\,\%$ WT mice were killed prematurely. When calculating AUC over time, the decrease in body weight was significantly greater in CerS4 KO mice compared with WT mice, CerS4 Vil/Cre mice and CerS4 LCK/Cre mice, respectively, after AOM/DSS treatment (Figure 3.8 A). In contrast, a higher score described a severer disease progression in the mice and thus a larger area could indicate a more severe disease progression. AUC is influenced by body weight or score course and time. As can be seen with in the body weight progression (Figure 3.8 A), the weight change in the CerS4 KO mice was less than $100\,\%$, resulting in a lower area. However, time is also included in the AUC calculation. When a mouse died, the integral was computed from time point zero to its endpoint. Therefore, mice aborted prior day 72 also resulted in a smaller AUC (Figure 3.8 A2 and B2). Exclusion of aborted mice resulted in a higher AUC in CerS4 KO mice, but it was still 0.8-fold lower than the other mice (p= 0.002, p=0.005, p=0.0008) (Figure 3.8 A). During DSS cycles, the score increased, indicating poor health during AOM/DSS treatment in mice (Figure 3.8 B). AUC measurements of all mice, including aborted mice, revealed higher score in CerS4 LCK/Cre mice compared to WT mice (2.1-fold change, p=0.01) or CerS4 KO mice (2.3-fold increase, p=0.014) (Figure 3.8 A2 and B2). When the severely diseased mice were excluded from the events, the AUC of CerS4 KO mice increased. Thus, the difference between WT mice and CerS4 LCK/Cre

mice remained significant (p= 0.01) and the AUC of CerS4 KO mice was 1.9-fold (ns) higher than AUC of WT mice. This indicates a higher score of CerS4 KO mice and CerS4 LCK/Cre mice compared to WT mice or CerS4 Vil/Cre mice (Figure 3.8 B). The tissue specific CerS4 KO mice did not suffer as much as the CerS4 KO mice but were also not statistically significantly different from the WT mice, although the lethal rate of CerS4 Vil/Cre mice and CerS4 LCK/Cre mice were 0 %. These different results in the AOM/DSS treated mice already indicate a major influence of the tissue specific deficiency of CerS4. Whereas CerS4 Vil/Cre mice had little effect on disease progression, CerS4 LCK/Cre mice appeared to be more susceptible towards AOM/DSS than WT mice (Figure 3.8 B).

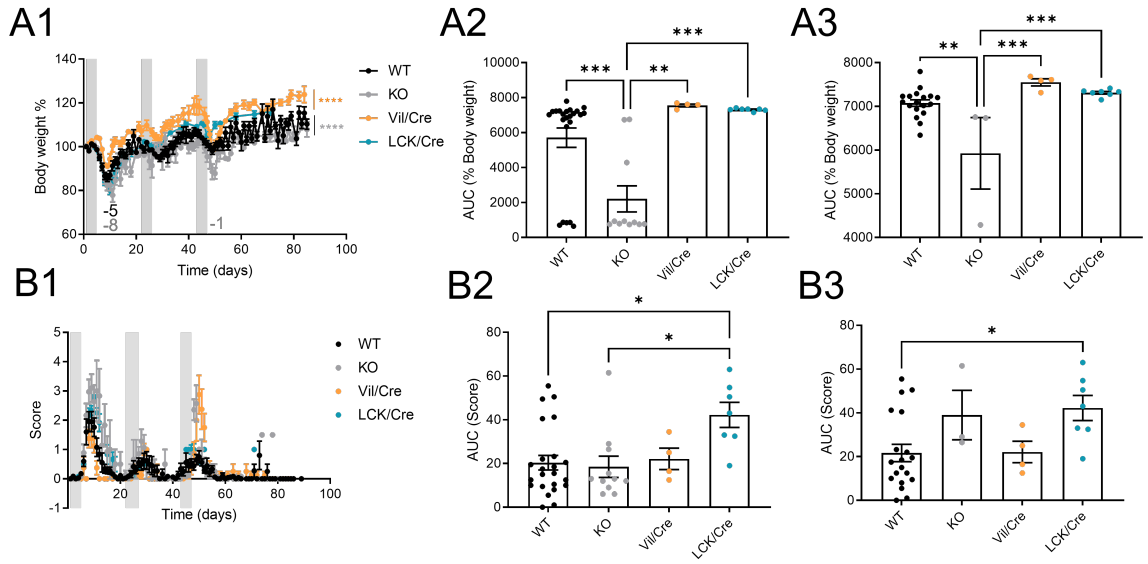

FIGURE 3.8: Tissue specific effect of CerS4 deficiency in AOM/DSS induced CAC model. Disease monitoring of WT mice (WT), CerS4 KO mice (KO), CerS4 Vil/Cre mice (Vil/Cre) and CerS4 LCK/Cre mice (LCK/Cre) during AOM/DSS treatment by detecting body weight (A1) or score (B1). (A2 and B2) AUC calculation of body weight change and score contains all mice, including those that could not continue because of the human endpoint. (A3 and B3) AUC calculation of body weight change and score includes only mice that survived almost to the end. Data are mean±SEM. Statistical analysis was performed by one-way ANOVA. Group size of control mice WT mice n=18 CerS4 KO mice n=9 CerS4 Vil/Cre mice n=2 and CerS4 LCK/Cre mice n=12 and for AOM/DSS treated group WT mice n=23, CerS4 KO mice n=11, CerS4 Vil/Cre mice n=4 and CerS4 LCK/Cre mice n=7. Data, A1 and B1 previously published in [204].

Tumor development was examined 6 weeks after the last DSS induced inflammation. The colon length was recorded with hand camera shots (Figure 3.9 A) and analyzed. The upper area of the colon is referred to as proximal and is characterized by a herringbone structure, whereas alongside downward the distal colon is aligned with the rectum. At most, larger tumors have been found in the distal part of the colon and smaller tumors in the middle part of the colon. Figure 3.9 A2 shows the colon of a CerS4 KO mouse, which was aborted after 58 days of AOM/DSS treatment. The colon was extremely truncated, but no obvious tumors were visible (Figure 3.9 A2). The AOM/DSS treatment resulted in shorter colon lengths. While the colon length of the uncleaned colon (not shown), cleaned colon (not shown) and longitudinal cut colon (Figure 3.9 B1) were measured, the colon length

was reduced in WT mice, CerS4 KO mice and CerS4 LCK/Cre mice. Pooling all measurements with the mean values indicated a shortening in all mouse strains after AOM/DSS treatment (calculated with a Kruskal-Wallis test, not shown). Tumor incidence and tumor volume were opposite between CerS4 Vil/Cre mice and CerS4 LCK/Cre mice after AOM/DSS treatment. Judging by the visible tumors, CerS4 LCK/Cre mice had a tumor incidence of $100\,\%$, whereas it was approximately $52\,\%$ for WT mice, $33\,\%$ for CerS4 KO mice, and $17\,\%$ for CerS4 Vil/Cre mice. CerS4 Vil/Cre mice had fewer and smaller tumors, while CerS4 LCK/Cre mice had more tumors. Overall, WT mice had larger tumors than CerS4 LCK/Cre mice (Figure 3.9 B2+B3). These results suggest that CerS4 deficiency has a differential impact on tumor outcome. CerS4 Vil/Cre mice had a reduced incidence and volume, whereas CerS4 LCK/Cre mice resulted in a higher incidence, but tumor volume was still smaller than WT mice. However, no statistically significant differences were detected when WT mice and CerS4 KO mice were compared (Figure 3.9 B2+3).

3.2.1 Histological analysis of tumor growth

In Figure 3.10, a section of the colon of a WT mouse after AOM/DSS treatment is shown. Throughout the colon, some regions were characterized by inflammation, either by an increased LP infiltrate or by destroyed crypts indicative of erosion (Figure 3.10 a+b). During tissue restauration, hyperplastic growth (h) occurred evidenced by enlarged crypts, increased proliferation, and glandular growth. However, it was limited to overgrowth, while the tissue morphology was not altered. In the example Figure 3.10 c, the hyperplasia is indicated by an arrow. In the hyperplastic region, the numbers of glands are increased, the nuclei are located basally, and the mucin is located apically. Cell size and shape are not altered, and these patterns are thought to return to normal in response to specific stimulus, which is not the case in dysplasia. At the arrow indicating hyperplasia, the glands are characterized by denser nuclear staining and an increased nuclear-to-cytoplasmic ratio, which is referred to as hyperchromatic nuclei. Immediately adjacent to the arrow area, the star indicates a villous (*) adenomas structure (Figure 3.10 c). Since also above the arrow the lower crypts show more hyperchromatic nuclei and there is more basophilic cytoplasm at the surface, these regions could also be a sessile (serrated) adenoma. This already counts as a dysplastic tumor. In contrast to hyperplasia, the cells in dysplasia are densely packed and have a polymorphic structure, i.e., the size and shape of the cells deviate from normal condition. The nuclear size is enlarged relative to the cytoplasm and because the DNA content is increased, the nuclei appear darker (hyperchromatic) [258]. Dysplastic growth also refers to large, crowding cells that stratify toward the apical surface, away from the basement membrane, which can be seen in Figure 3.10 d. Pedunculated adenoma (#) is marked by tubular growth of crypts originating from a peduncle (arrows) of increased cellular infiltrate of the LP. The crypts grow granularly back to back way (the dotted line shows that the tubules are connected to each other and not to the basement membrane), and polarity has been lost within the glands. In this irregular arrangement of cells, hardly any mucin-producing cells are seen. On the apical surface, the cells are flattened or partially

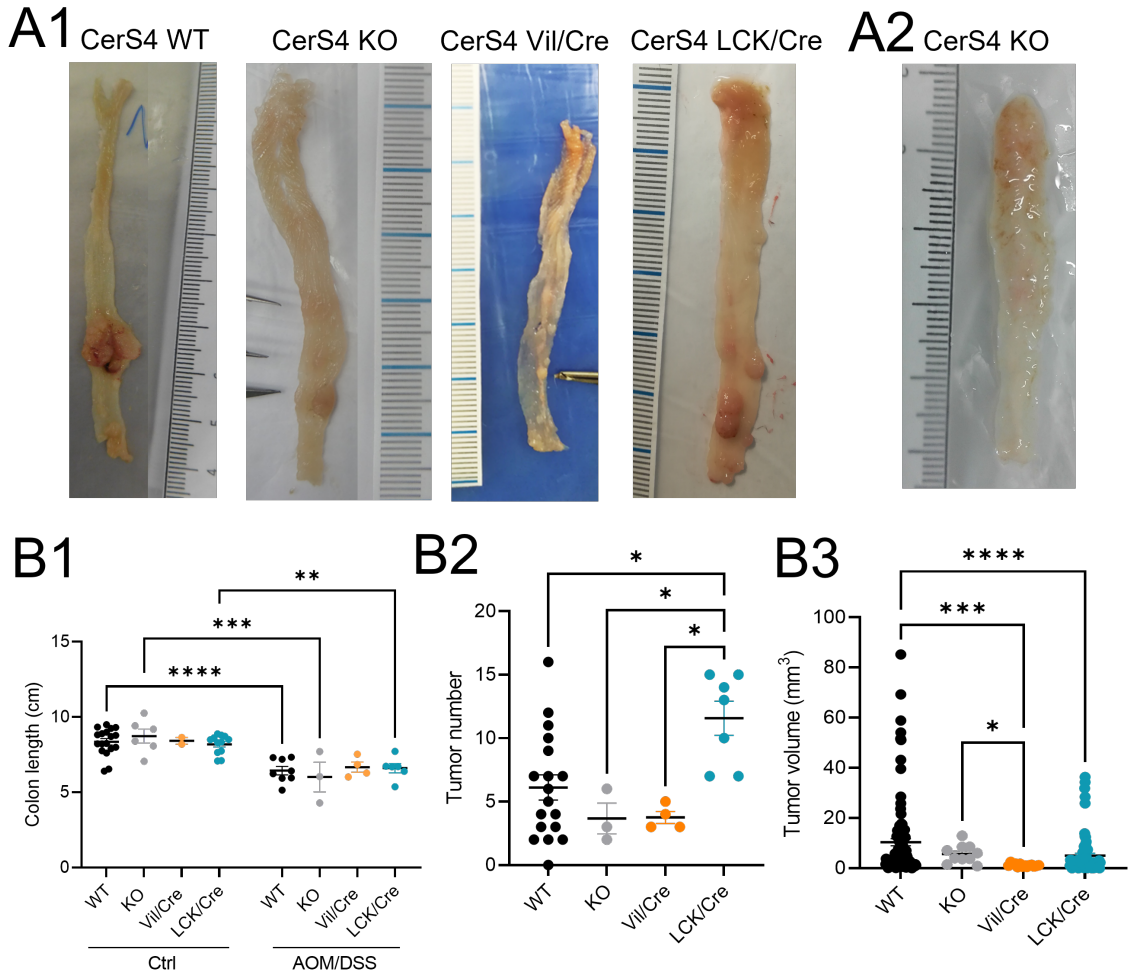

FIGURE 3.9: Tissue specific effect of CerS4 deficiency in tumor growth upon AOM/DSS tumor model. At the end of the experiment, the length of the colon and tumor development were examined. (A) Hand camera shots of colon after preparation, washing and longitudinally cut of WT mice (WT), CerS4 KO mice (KO), CerS4 Vil/Cre mice (Vil/Cre) and CerS4 LCK/Cre mice (LCK/Cre). (A2) Colon of an aborted CerS4 KO mice at day 58 after suffering from severe disease progression. (B1) Measurements of colon length of control mice (Ctrl) and AOM/DSS treated (AOM/DSS) WT mice, CerS4 KO mice, CerS4 Vil/Cre mice and CerS4 LCK/Cre mice. (B2) visible tumors of colon shots from (A) were counted, indicating a higher tumor number in CerS4 LCK/Cre mice. (B3) Approximately calculation of tumor volume by length $\times$ width $\times$ $\frac{\text{width}}{2}$ indicating bigger tumors in WT mice. Data are mean $\pm$SEM. Statistical analysis was performed by one-way ANOVA. Group size of control mice WT mice n=18, CerS4 KO mice n=9, CerS4 Vil/Cre mice n=2 and CerS4 LCK/Cre mice n=12 and for AOM/DSS treated group WT mice n=23, CerS4 KO mice n=3, CerS4 Vil/Cre mice n=4 and CerS4 LCK/Cre mice n=7. Data and B previously published in [204].

lost (erosion, E) and the light pink area indicates a necrotic region (N) (Figure 3.10 d). This dysplastic growth results in neoplasia. Due to the loss of connection to the basement membrane, the growth lost polarity and is characterized by a disordered growth pattern. Even the existing glands are deformed in shape, with hyperchromatic and enlarged cells and hardly any goblet cells in between (white circle indicating the deformed gland) (Figure 3.10

e). As described in Figure 3.10 d, the apical side is marked by erosion (E), and the arrowheads indicate highly acidophilic bodies with condensed cytoplasm and absent nucleus, suggesting apoptotic bodies (Figure 3.10 e).

The histology of the CerS4 KO mice, CerS4 Vil/Cre mice and CerS4 LCK/Cre mice was different. Figure 3.11 represents a colon roll of each mouse strain treated with AOM/DSS. In Figure 3.11 A is the continuation of the neoplasia in WT mouse shown in Figure 3.10 d, which arose from pedunculated dysplasia. In the upper left corner of the image section, hyperplastic growth with increased LP infiltrate leads to an increasingly dysplastic growth. Although many goblet cells (g) are still present, the lower crypts are more hyperchromatic and leading to two main pedunculated adenomas (white arrow) (Figure 3.11 A). The pedunculated adenomas exhibited back-to-back- glandular growth, hyperchromatic cells, loss of polarity, shed and erosive regions, and necrotic areas (N). The white circles do not indicate invasion of the mucosa by the colon wall, but the submucosa breaches the muscularis mucosae through its connection to arteries, veins or the lymphatic system that supply the colon. This indicates a strong blood and lymphatic supply in these dysplastic regions. In addition to pedunculated adenoma, a sessile serrated adenoma in which the gland grows tubular-villous. This sessile adenoma was surrounded by another neomorphism: a stratified squamous epithelium (st) growing on the LP and was characterized by a complete loss of crypts in these regions (Figure 3.11 A, III). Hyperplastic and dysplastic growth was also observed in CerS4 KO mouse. The adenomas were mainly pedunculated (white arrow) and a few crypts were villous (*) but mainly tubular or tubular-villous in growth (Figure 3.11 A, I, II). The dysplasia in the lower-left corner was a tissue growth upon an enlarged lymphatic nodule (L) (Figure 3.11 B, VI). Lymphatic nodules are covered by cuboidal cells or shortened villi with a flattened epithelium on the surface. However, with no direct contact to the basal lamina a pedunculated adenoma derives upon those lymphoid aggregates (Figure 3.11 B, VI). The neoplasia on the lower right-hand side had necrotic areas (N). Overall, the polarity of most of the dysplastic/neoplastic regions partially preserved polarity. Many goblet cells (g) were present in and around the dysplastic areas. Some villi were almost completely lined by goblet cells, indicating a hypercrinia (hc) (Figure 3.11 B, IV). This was also observed in the CerS4 Vil/Cre mice (Figure 3.11 C, IV). Although tumor growth was restricted to hyperplasia in CerS4 Vil/Cre mice, the remaining crypts showed signs of long-term damage. Thus, crypts in some regions were smaller (crypt atrophy, A) or branched instead of growing long and straight (crypt branching, B) (Figure 3.11 C, V). This crypt distortion indicates that DSS cycles in those mice indeed induced inflammation, but tumor growth was limited in these CerS4 Vil/Cre mice compared with WT mice or even CerS4 LCK/Cre mice.

Figure 3.11 D represents a CerS4 LCK/Cre AOM/DSS treated mouse rolled from distal to proximal. Thus, in the middle, the distal colon was enrobed with dysplastic growth. In contrast to the other mice, more (tubular-) villous adenoma (*) were present in the distal colon, whereas pedunculated, branched adenomas (#) grew in the middle and proximal colon. The remaining crypts were either hyperplastic or distorted in growth. Although many inferior crypts maintained polarity, no hypercrinia was observed (Figure 3.11 D).

However, other AOM/DSS treated WT mice and other AOM/DSS treated CerS4 LCK/Cre mice showed hypercrinia, and the phenotype of 'goblet cell rich crypts' was not restricted to AOM/DSS treated CerS4 KO mice or AOM/DSS treated CerS4 Vil/Cre mice.

Quantification and comparison of slides from different layers of the colon rolls confirmed the different histology of the mice. To simplify the analysis, inflamed areas (infiltrating immune cells as well as destructive crypts) and tumors (hyperplasia + dysplasia/neoplasia) were related to the absolute colon length of each slice. Thus, the area still inflamed in the colon of the AOM/DSS treated mice remained below $10\,\%$. However, in CerS4 KO mice, the inflammation in the colon was more than twice that in the WT mice. After inflammation and tissue damage, crypts are restored and during this process mutagenic cells can drive tumor growth. Total tumor growth occupied approximately $40\,\%$ of the total colon length (Figure 3.12 A1). The tumor area measured was significantly higher in WT mice than in CerS4 KO mice, CerS4 Vil/Cre mice and CerS4 LCK/Cre mice (Figure 3.12 A2). Although CerS4 LCK/Cre mice had smaller tumors, the extent of neoplasia was similar in WT mice, CerS4 KO mice and CerS4 LCK/Cre mice. While dysplastic regions were more than twice as high in CerS4 LCK/Cre mice as WT mice and Cer4 KO mice, no dysplasia and neoplasia were detected in CerS4 Vil/Cre mice Figure 3.12 A3).

Because classic UC is limited to the colon originating from the rectum and extending proximally, the anatomic extent of involvement is used to classify the manifestation of UC, distinguishing between procolitis, left side colitis and pancolitis [259]. For histological analysis the anatomy has been simplified into distal, middle and proximal inflammation of the colon. When inflammation was confined to the distal part of the colon, it was termed distal colitis. Inflammation that extend from the distal to the middle part of the colon, was termed extensive colitis, and whenever inflammation was also present in the proximal colon it was termed pan colitis (Figure 3.12 B). The localization of inflammation was significantly different in WT mice and CerS4 Vil/Cre mice. In WT mice, $26\,\%$ of the colitis was confined to the distal colon, $58\,\%$ of the cases were extensive colitis, and $5\,\%$ of the slices examined had pan colitis, whereas $10\,\%$ had no inflammation. Thus, there was a significant difference between extensive colitis and pan colitis (p=0.007) or lack of inflammation (p=0.003). Global CerS4 deficiency had a massive impact on inflammation, with extensive or pan inflammation manifesting in half of slices of CerS4 KO mice. With tissue specific knockout of CerS4, the ratio shifted. In CerS4 Vil/Cre mice, inflammation was extensive in all slices and in CerS4 LCK/Cre mice, $\sim 50\,\%$ of the colitis was pan, $19\,\%$ was extensive, only $6\,\%$ was distal inflammation, and no inflammation was observed in $25\,\%$. These different patterns raised the question of whether a particular colitis was more common in a particular mouse line, and indeed the percentage of pan-colitis was significantly different between WT mice and CerS4 LCK/Cre mice (p=0.01)(Figure 3.12 B1).

Damaged epithelium is normally restored, and tumorigenic growth likely occurs during the inflammatory process and mutagenic uptake of AOM. Here, the location showed a similar pattern of inflammation. Hyperplastic growth was present in all mice. In WT mice, hyperplastic growth was mainly extensive ($56\,\%$) with a small amount of distal ($11\,\%$) or pan ($17\,\%$) hyperplasia. In analyzed slides of CerS4 KO mice, hyperplasia was extensive,

while in CerS4 Vil/Cre mice and CerS4 LCK/Cre mice, as in WT mice, it was mainly extensive (60 % to 64 %) with a small amount of distal (14 % to 20 %) or pan (∼20 % and 21 %) localized. Overall, the localizations of hyperplasia were not statistically different. CerS4 KO mice showed a significant difference between extensive and absent, distal and pan growth (p<0.0001). In CerS4 LCK/Cre mice, absent hyperplasia was significantly different from the extensive hyperplasia (p=0.016) (Figure 3.12 B2).

Dysplasia and neoplasia are the main polyps that can lead to cancer. Therefore, a more detailed analysis of this growth may provide valuable insights. In WT mice, the ratio was quite heterogeneously: No dysplasia was detected in 15 % of the slices, half of the dysplastic growth was limited to the distal part, whereas ¼ was extensive and only 10 % were pan. Thus, the distal portion of dysplasia was significantly different compared to absent dysplasia (p=0.01) and extensive dysplasia (p=0.002). In CerS4 KO mice, dysplasia was detected distally in half of the slices and no dysplasia was spotted histologically in CerS4 Vil/Cre mice. Thus, the missing percentage was significantly different from all other locations (p<0.0001). Colonic slices of CerS4 LCK/Cre mice had fewer distal (28 %) but more than half extensive (64 %) tumors, with a fewer pan located tumors (∼7 %). Overall, these data showed that the percentage of absent dysplasia was higher in CerS4 Vil/Cre mice than in WT mice (p=0.0005) and CerS4 LCK/Cre mice (p<0.0001). Distal dysplasia was more prominent in WT mice than CerS4 Vil/Cre mice (p=0.006) and extensive dysplasia was found more frequently in CerS4 LCK/Cre mice than in WT mice (p=0.0008), CerS4 KO mice (p=0.087) and CerS4 Vil/Cre mice (p=0.04) (Figure 3.12 B3).

In summary, histological analysis showed that in addition to CerS4 KO mice, CerS4 LCK/Cre mice was also sensitive to AOM/DSS induced CAC compared to WT mice, resulting in more severe pan colitis and extensive dysplastic growth, while WT mice developed larger tumors. Although extensive colitis occurred in all sections, CerS4 Vil/Cre mice developed smaller tumors and only hyperplastic tumors.

The high inflammation rate of CerS4 KO mice in Figure 3.12 A1 is due to an aborted mouse that reached its endpoint after the third cycle of DSS – 27.5 % before the planned end of the study. The colon length, shown in Figure 3.9 A2, already indicated severe inflammation. Histological evaluation confirmed that this mouse suffered from massive ulcerative colitis (Figure 3.13). The whole colon roll showed that a large part of the colon, crypts were massively destroyed and the missing crypts were replaced by a dense inflammatory infiltrate (U). The ulcerations were extensive, starting from the distal colon, and affected other parts of the middle colon to varying degrees (Figure 3.13 A). The black rectangle shows an area where the crypts are damaged by immune cells, alongside bulldozed regions (U). Figure 3.13 B was imaged with a 10x objective and C with a 20x objective. Around the remaining epithelial cells and the crypts indicated by the black arrows were mainly myeloid immune cells with granules. An enlarged view with at 400x magnification presents the neutrophils (n) and other granulocytes (g) destroying epithelial cells (Figure 3.13 C). In general, a huge infiltrate of immune cells crosses the mucosa from the blood (white arrows) and the lymphatic system (yellow arrows) located in the submucosa (Figure 3.13 D). Lymphocytes were also involved in the inflammation. Lymphoid aggregates were not only observed in

lymphatic nodules (L) but also appeared to accumulate (*) in the immune cells infiltrate of the ulceration near the lymphoid nodules (Figure 3.13 E). Remaining epithelial cells from previous crypts were present and indicated by black arrowheads. In addition, the immune cells in the submucosa infiltrated from the blood circulation in this area and crossing the muscularis mucosae into the mucosa, as indicated by the black arrows (Figure 3.13 E). These data suggest that CerS4 KO mice reached the human endpoint due to severe ulcerative colitis.

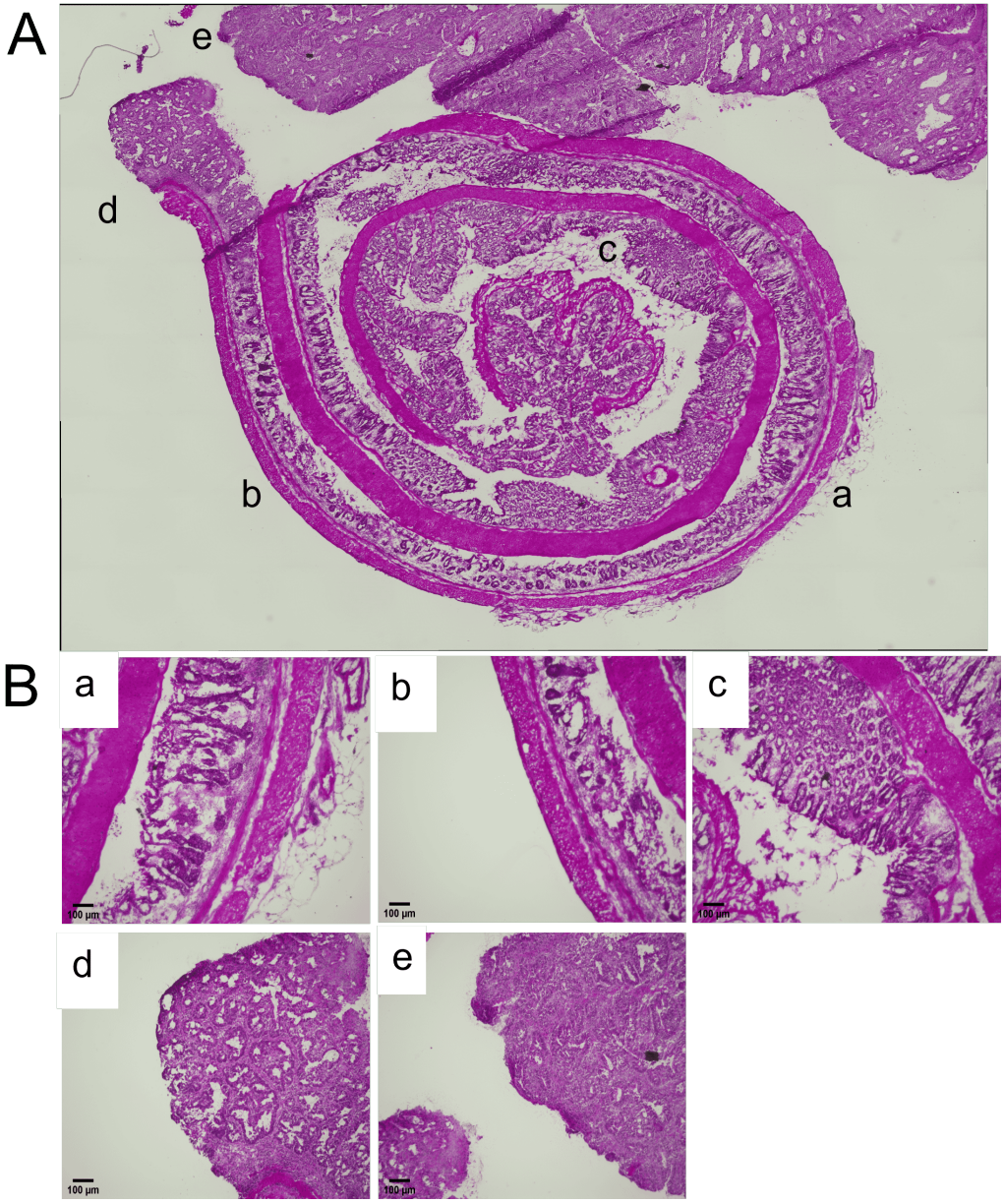

FIGURE 3.10: Representative colon role of a WT mouse after AOM/DSS treatment. (A) A HE-stained colon rolled from proximal (center of role) to distal (fringe of role). Merged picture from 10x magnification. Inflammation characterized (B.a) by a thicker LP filled with immune cells and (B.b) destructed crypts indicated by the arrows. Tumor growth starts with (B.c) hyperplasia, in which the glands are increased in numbers. The villous enlargement indicated by an asterisk (*) might also lead to a non-reversible dysplasia ending to a neoplasia. (B.d) dysplastic growth of a pedunculated serrated adenoma. From the increased LP infiltrate, many strands form a pedunculi from which glands growth in a back-to-back pattern (indicated by the white dotted lines). The polarity between the hyperchromatic lower crypts and the flattened epithelium on the surface is mostly lost. The flattened epithelium and the loss of epithelium marks erosion on the apical side of the adenoma. The bright pink staining indicates necrotic area (N). (B.e) a section from a neoplasia, in which cells are arranged irregularly, indicating mostly a loss of polarity. Existing glands are irregular shaped with hyperchromatic cells and little goblet cells, bordered with a white line. Black arrowheads indicate acidophil bodies with a condensed, dark pink staining of the cytosol and an absent nucleus. Hyperplasia (h), tubular growth (#), Erosion (E), Lamina Propria (LP), villous growth (*), necrosis (N). Scale bar 100 µM.

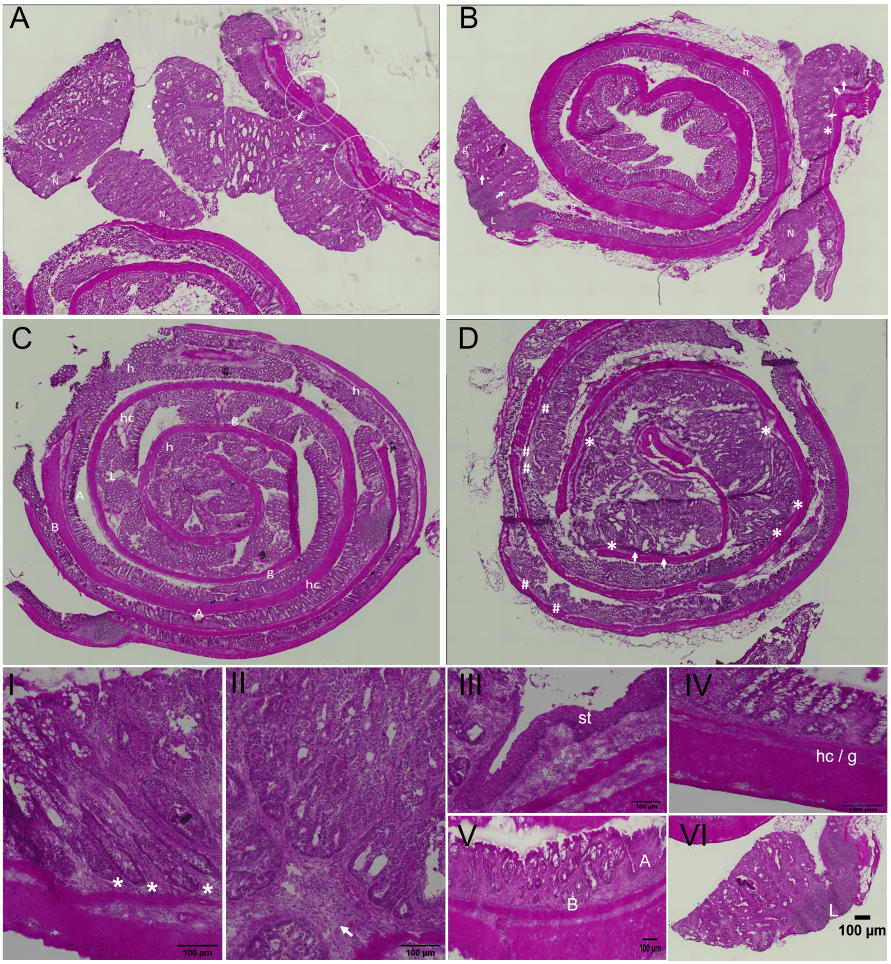

FIGURE 3.11: Histological analysis of a representative colon role after AOM/DSS treatment of (A) WT mouse, (B) CerS4 KO mouse, (C) CerS4 Vil/Cre mouse and (D) CerS4 LCK/Cre mouse.(A) Continuation of the section of WT mouse in Figure 3.10. Predominantly dysplastic and neoplastic growth originated from pedunculated serrated adenoma (peduncle is indicated by a white arrow) and sessile serrated adenoma growing in a distorted glandular pattern without a pedicle. White circles highlight an invasion of the submucosa. Besides hyperplastic growth (h), villous enlargments are indicated by an asterisk (*). Crypts suffering from long term damage are indicated by a loss of crypts (l), shortening of crypts (atrophy, A) or branching of crypts (B). Villi, wich almost lined with goblet cells (g) were referred hypercrinia (hr). Villous growth of a sessile adenoma in distal part of the colon was highlighted by asterisks (*) and tubular growth by a number sign (#). In addition, peduncular serrated adenomas grew in the mouse indicated by a white arrow. (I) Villous growth (*), (II) peduncular dysplastic growth indicated by a white arrow. (III) Stratified squamous epithelium (st) with complete loss of crypts, indicating either metaplasia (when cells are of mucinous origin) or neoplasia. This stratified epithelium was also observed in other slides of mice. (IV) Region with a high presence of goblet cells (g), mucosa that are mainly lined up with goblet cells are referred to as hypercrinia (hr). (V) Long term damage assigned by either a crypt atrophy (A) or crypt branching (B). (VI) Dysplastic growth upon an enlarged lymphatic nodule (L). Abbreviation: hyperplasia (h), necrosis (N), crypt atrophy (A), crypt branching (B), hypercrinia (hc), goblet cells (g), enlarged lymphatic nodules (L). Scale bar $100\,\mu m$. II and IV previously published in [204].

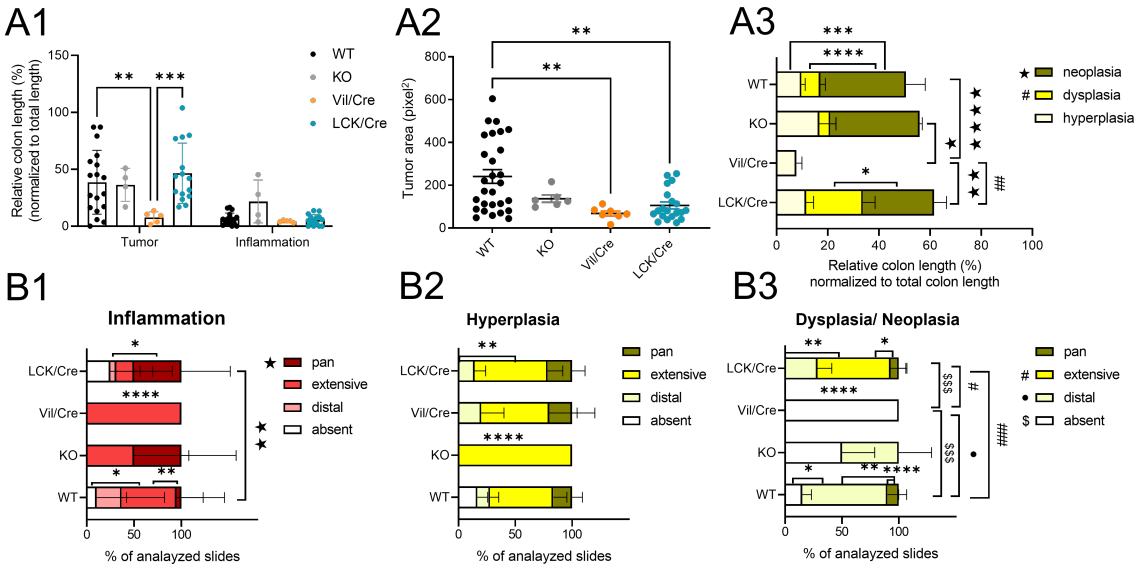

FIGURE 3.12: Quantitative analysis of HE staining WT mice (WT), CerS4 KO mice (KO), CerS4 Vil/Cre mice (Vil/Cre) and CerS4 LCK/Cre mice (LCK/Cre) treated with AOM/DSS. (A1) Inflamed areas and tumor areas were based on total colon length %. (A2) WT mice showed the largest tumor areas. Statistical analysis was performed by one-way ANOVA. (A3) Differentiation of tumor type shown from A1. (B) Analysis of localization in (1) inflamed areas (2) hyperplasic areas and (3) dysplastic areas confined to the distal part of the colon or extensive or entire colon (pan) in different sections. Data are mean±SEM. Statistically analysis was performed using two-way ANOVA (** p<0.01, *** p<0.001). Statistically significant differences within a mouse strain are indicated by asterisks(*), whereas differences between different mouse strains are indicated by symbols ($\star$, #, • and $) in the legend. Data published in [204].

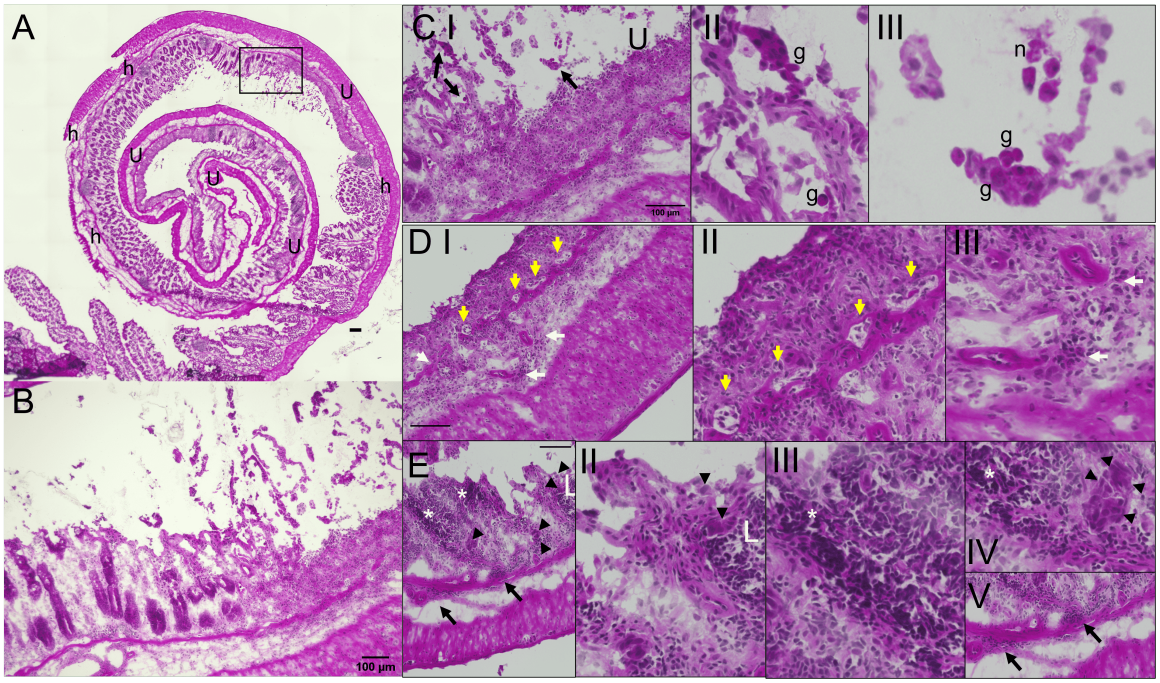

FIGURE 3.13: Histological analysis of a colon role from an aborted CerS4 KO mouse that reached clinical endpoint during AOM/DSS treatment. (A) HE-staining imaged with a 10x objective. The CerS4 KO mouse suffered from extensive ulcerative colitis (U) while the proximal colon was normal, the other areas that did not suffer from ulceration showed hyperplastic growth (h). The black outlined rectangle highlights the transition from healthy/aligning crypts and complete loss of crypts after inflammation-induced destruction. (B) This area was imaged with a 10x/0.25 objective and (CI) with a 20x/0.3 objectives BIOREVO (Keyence). The black arrows indicate the presence of myeloid cells near the crypts. These areas were magnified at 400x magnification. Granulocytes (g) and especially neutrophils (n) were present around the crypts and the remaining epithelial cells (II+III). (D) The blood and lymphatic system vessels supply the submucosa and serve as a transport channel for immune cells. The yellow arrows indicate the lymphatic source, while the white arrows indicate immune cells coming from the blood system (D I). The 400x magnification shows the presence of cells (II) and the accumulating azure blue lymphocytes (III) along the vessel, which appear to infiltrate the colon from these vessels. A reservoir of lymphocytes is also present in lymphatic nodes (L). Lymphocytes are accumulated in these follicles and primed for the adaptive response (II) Further aggradation of lymphocytes (*) outside the follicle was also observed in the crypts near the remaining crypts (arrowheads) (IV). This indicates that the lymphocytes source are not only the blood and lymphatic vessel (V), from which lymphocytes infiltrate towards the mucus indicated by the arrows (V), but also the from the lymphatic nodules. Scale bar in all shots is $100\,\mu m$.

3.2.2 Immune cell profile after AOM/DSS treatment

Not only does the immune cell response play a crucial role in acute inflammation, but also in cancer development. The tumor microenvironment triggers the immune response of innate and adaptive immune response. In many neoplastic regions in the colon, the LP-infiltrate was increased, and even in dysplastic growth, some acidophil bodies indicative of apoptotic cells (white arrowheads) were surrounded by immune cells, suggesting that the immune response partially removes potential damaged tumor cells (Figure 3.14). Both innate (yellow arrowheads) and adaptive immune cells (black arrowheads) were present (Figure 3.14) in the example colon section of AOM/DSS treated WT mouse. The myeloid cells appeared to remove apoptotic cells that could derived from epithelial or neutrophil cells. In the lumen of the crypts the myeloid cells were clearly seen, whereas the lymphocytes appeared to be closer to the tissue (Figure 3.14 c).

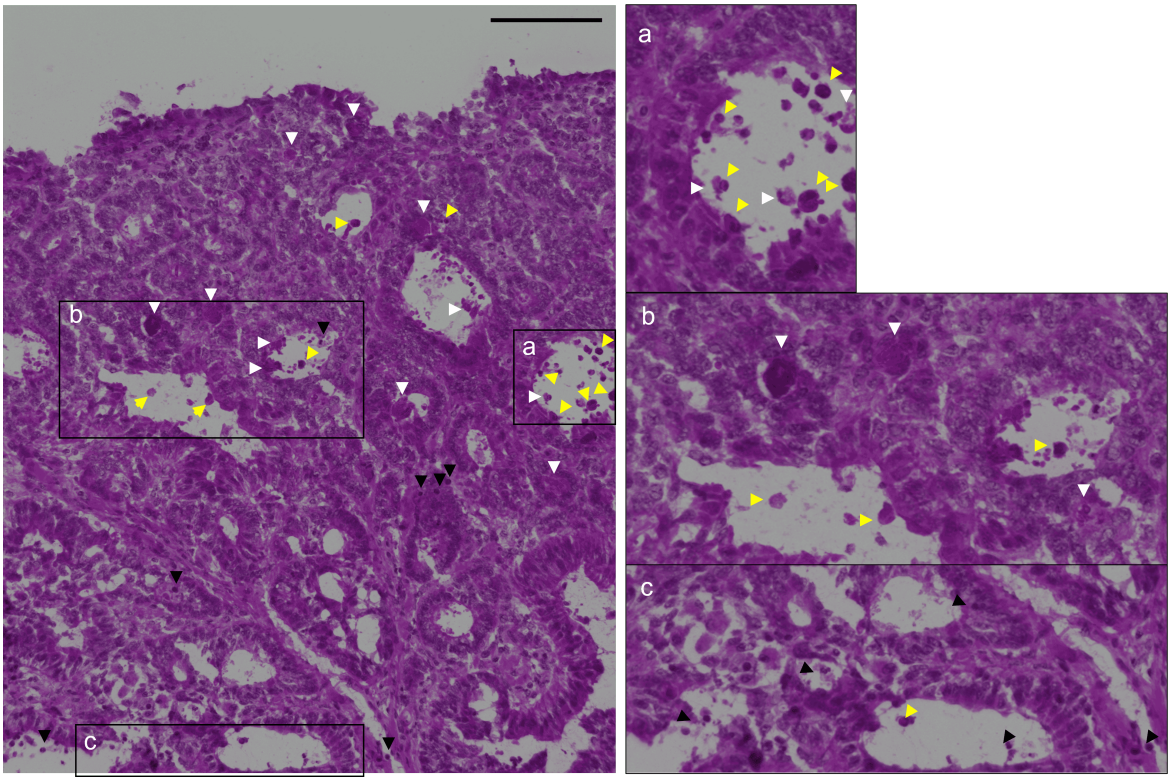

FIGURE 3.14: An image section of the neoplastic growth in the colon of AOM/DSS treated WT mice shown in Figure 3.11 A. Picture was taken with a plan achromat 20x/0.3 lens. The snapshots were taken with a 400x screen magnification. White arrowheads point to acidophil bodies, cells undergoing apoptosis with a dark cytoplasm and pyknotic nucleus (small, condensed nuclei) or absent nuclei. Yellow arrow heads point to myeloid cells, cells containing salmon pink granules or purple granules and segmented or bilobed nucleus. Dark arrow heads point to dark blue, spherical cells indicating lymphocytes. Scale bar is 100 µm.

The increased presence of immune cells was also demonstrated by flow cytometry. It exhibited a 15-fold increase of neutrophils in the LP fraction of the colon. In the IEL fraction of the colon, the abundance of neutrophils was 74-fold higher than in the control group. This increase was also observed in WT mice. In the IEL fraction, the increase was 24-fold

higher after AOM/DSS treatment of WT mice. In addition to neutrophils, monocytes differentiating to macrophages also increased. In WT mice the increase in this abundance was only 4.9 times higher after AOM/DSS treatment, whereas in CerS4 KO mice, this abundance increased 17-fold in LP fraction and 61-fold in IEL fraction (Figure 3.15, Table 3.5 and Table 3.6). It was found that already infiltrated undifferentiated monocytes were higher in the IEL fraction of CerS4 KO mice with an approximately 70-fold increase after AOM/DSS treatment, whereas in WT mice it was only a twofold increase Table 3.5. Consistent with the histological findings, lymphocytes determined by flow cytometry were also increased after AOM/DSS treatment. T cell levels were significantly increased in both WT mice and CerS4 KO mice, but with a difference in the location. In the WT mice more T cells were detected in the IEL fraction of the colon, while in the CerS4 KO mice T cells were more abundant in the LP fraction of the colon. Differences in $CD8^+$ T cells occurred in the IEL fraction, whereas levels were equally increased in the LP fraction, with no difference between WT mice and CerS4 KO mice. Double negative $CD4^-CD8^-$ T cells were also more prevalent in the WT mice than in the CerS4 KO mice. In the IEL fraction, no further differences were observed between WT mice and CerS4 KO mice in the $CD4^+CD8^+$ T cells, T_{reg} and $CD4^+$ T cells. Because no T_{regs} could be detected in the CerS4 KO control mice, the 0.5-fold increase after AOM/DSS treatment was significant. Another investigated cytotoxic immune population besides $CD8^+$ T cells in the WT mice were the NK T cells, which also increased significantly in WT mice after AOM/DSS treatment. In LP fraction of the colon, B cells were also increased 3-fold and 11-fold in WT mice and CerS4 KO mice, respectively. DC levels did not change by AOM/DSS treatment. Overall, in the AOM/DSS treated colon of WT mice and CerS4 KO mice, there was a tremendous increase in T cells, especially $CD8^+$ cells and myeloid cells such as neutrophils and monocytes, that differentiate to macrophages.

Analysis of blood from WT mice, CerS4 KO mice, CerS4 Vil/Cre mice and CerS4 LCK/Cre mice by flow cytometry showed only some overall differences in CerS4 LCK/Cre mice. The frequency of $CD8^+$ and $CD8^-CD4^-$ T cells in control CerS4 LCK/Cre mice was altered compared with the other mice. Thereby the control LCK/Cre mice had less $CD8^+$ T cells and more $CD8^-CD4^-$ T cells (Figure 3.16 A). AOM/DSS treatment also induced alterations in circulating immune cells. Peripheral DCs increased after AOM/DSS treatment (WT mice p=0.008, CerS4 KO mice p=0.007, CerS4 Vil/Cre mice ns, and CerS4 LCK/Cre mice p=0.068), and the increase was significant in CerS4 KO mice after AOM/DSS treatment. Many differences were also observed in CerS4 LCK/Cre mice, which already had fewer single immune cells. T cell levels were decreased and among T cell subtypes the $CD8^+$ T cells were decreased (p=0.064), while the amount of $CD4^+CD8^+$ T cells and T_{regs} increased in CerS4 LCK/Cre mice after AOM/DSS treatment. $CD8^-CD4^-$ T-cells were as reported in the literature between 1-3 % [260] (Figure 3.16 A). Many others immune cell types were altered after AOM/DSS treatment: Neutrophils, monocytes and NK cells were increased two- to threefold Table 3.7) and B cell level was significantly reduced in AOM/DSS treated CerS4 LCK/ Cre mice compared with WT mice and CerS4 KO mice (Figure 3.16 B). Thus, like the increased immune cell populations in the colon tissue, differences were also detected in the blood (Figure 3.16).

TABLE 3.5: Summary of flow cytometrically determined immune cell in the IEL fraction of WT mice (WT) and CerS4 KO mice (KO) treated with AOM/DSS. Data are mean, SD and number of analyzed mice. Significant differences were calculated by two-way ANOVA and highlighted in bold. MΦ, Macrophages; diff., differentiating; undiff., undifferentiated.

IEL	WT Ctrl			WT AOM/DSS			KO Ctrl			KO AOM/DSS		
	Mean	SD	n	Mean	SD	n	Mean	SD	n	Mean	SD	n
Immune cells	2.96	0.32	11	4.34	0.45	2	3.34	1.11	5	4.29	0.19	4
Single Cells	56.79	7.36	11	**98.5**	0	2	44.69	15	5	**97.45**	0.51	4
Living immune cells	60.44	4.58	11	74.65	2.85	2	67.4	3.77	5	70.43	3.35	4
$CD3^+$ T cells	26.36	3.2	11	**69.7**	5.9	2	16.48	3.55	5	**41.9**	2.81	4
$CD4^+$ T cells	1.15	0.25	11	2.1	0.46	2	0.42	0.12	5	**2.35**	0.58	4
$CD25^+GITR^+$ T_{regs}	0.24	0.09	11	0.14	0.14	2	0	0	5	0.51	0.18	4
$CD8^+$ T cells	11.9	1.94	11	**31**	0.8	2	7.61	1.76	5	**14.18**	1.21	4
$CD8^-CD4^-$ T cells	12.41	1.36	11	**23.95**	5.85	2	8.19	2.22	5	9.75	2.34	4
$CD8^+CD4^+$ T cells	0.98	0.35	11	0.68	0.41	2	0.24	0.08	5	0.15	0.06	4
$NK1.1^+$ T cells	1.06	0.11	11	**2.33**	0.15	2	0.67	0.21	5	1.4	0.35	4
B cells	3.44	0.69	11	3.28	1.09	2	1.96	0.86	5	1.11	0.28	4
Monocytes/Makrophages	4.15	1.94	11	7.61	1.43	2	8.93	4.27	5	15.08	0.35	4
Monocytes diff. to MΦ	0.05	0.04	11	0.28	0.28	2	0.01	0.01	5	**0.45**	0.22	4
Monocytes/Makrophages	1.77	0.66	11	2.51	1.06	2	2.85	0.91	5	2.6	0.37	4
Undiff. Monocytes	0.29	0.27	11	0.69	0.69	2	0.01	0.01	5	0.53	0.26	4
Neutrophiles	0.16	0.08	11	3.84	2.75	2	0.42	0.24	5	**5.3**	2.77	4
$CD11c^+MHCII^+$ DCs	0.48	0.2	6	1.23	0.14	2	1.12	0.49	5	0.78	0.02	4

TABLE 3.6: Summary of flow cytometrically determined immune cells in the LP of AOM/DSS treated WT mice (mice) and CerS4 KO mice (KO). Data are mean, SD and number of analyzed mice. Significant differences were calculated by two-way ANOVA and highlighted in bold. MΦ, Macrophages; diff., differentiating; undiff., undifferentiated.

LP	WT Ctrl			WT AOM/DSS			KO Ctrl			KO AOM/DSS		
	Mean	SD	n	Mean	SD	n	Mean	SD	n	Mean	SD	n
Immune cells	7.87	2.08	11	9.81	3.39	2	8.88	2.36	5	6.8	2.06	4
Single Cells	57.36	3.05	11	**96.4**	2.6	2	46.08	10.12	5	**90.98**	2.74	4
Living immune cells	55.86	5.79	11	82.75	2.95	2	66.64	4.09	5	72.95	1.48	4
$CD3^+$ T cells	10.17	1.83	11	15.3	1	2	4.05	1.18	5	**21.65**	1.23	4
$CD4^+$ T cells	4.96	0.84	11	6.54	1.08	2	2.36	1.05	5	6.39	1.1	4
$CD25^+GITR^+$ T_{regs}	0.15	0.06	11	0.39	0.22	2	0	0	5	0.47	0.19	4
$CD8^+$ T cells	2.11	0.41	11	3.2	0.66	2	0.58	0.22	5	**3.02**	0.3	4
$CD8^-CD4^-$ T cells	2.93	0.78	11	2	0.62	2	1	0.26	5	2.68	0.74	4
$CD8^+CD4^+$ T cells	0.18	0.07	11	0.02	0.02	2	0.11	0.05	5	0.05	0.03	4
$NK1.1^+$ T cells	0.75	0.18	11	0.22	0.04	2	0.21	0.06	5	0.47	0.13	4
B cells	5.75	2.64	11	17.64	13.26	2	1.05	0.62	5	12.27	3.36	4
Monocytes diff. to MΦ	0.27	0.08	11	**1.3**	0.87	2	0.28	0.11	5	0.51	0.2	4
Monocytes/Macrophages	7.84	4.8	11	5.76	3.96	2	**30.46**	11.77	5	6.18	1.73	4
undiff. Monocytes	0.21	0.15	11	0.29	0.09	2	0.16	0.08	5	0.4	0.13	4
Neutrophiles	0.2	0.1	11	0.71	0.01	2	0.17	0.04	5	**2.76**	1.61	4
$CD11c^+MHCII^+$ DCs	0.19	0.04	6	0.21	0	2	0.64	0.28	5	0.47	0.08	4

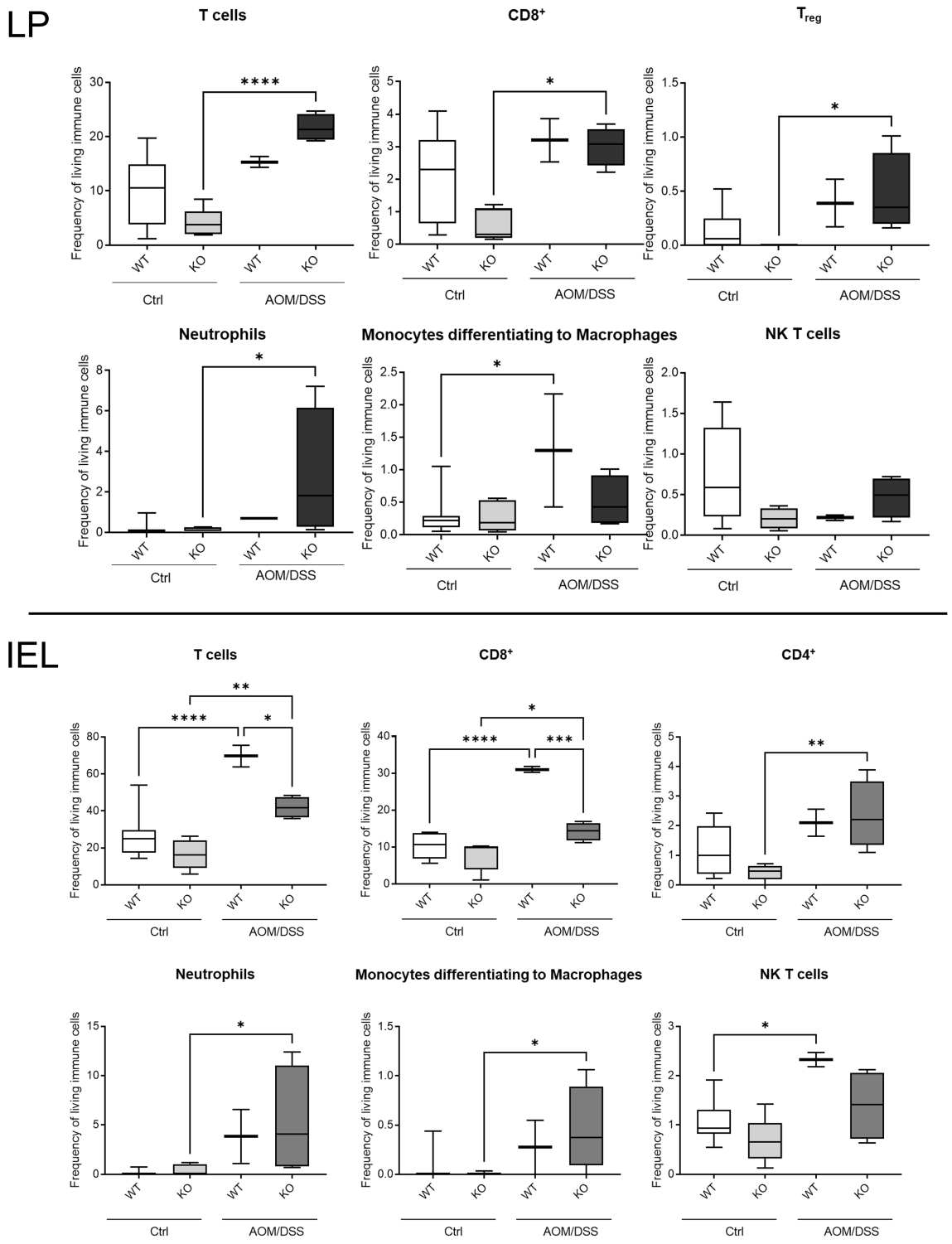

FIGURE 3.15: Flow Cytometry analysis of LP fraction and IEL fraction of control (Ctrl) and AOM/DSS treated (AOM/DSS) WT mice (WT) and CerS4 KO mice (KO). Data are median ± Min/Max of control WT mice. n=11, AOM/DSS treated WT mice n=2, control CerS4 KO mice n=5, AOM/DSS treated CerS4 KO mice n=4. Data published in [204].

In the spleen, frequency of DCs did not change but the subtypes. CDC1 was found in low abundance. After AOM/DSS treatment, a significant increase in cDC1 was detected

only in WT mice and cDC2 increased fourfold in WT mice and CerS4 KO mice and by threefold in AOM/DSS treated CerS4 LCK/Cre mice, which was threefold higher than in AOM/DSS treated CerS4 Vil/Cre mice (Figure 3.17, Table 3.8). However, the T cell population and subpopulations did not alter by AOM/DSS treatment. In control CerS4 LCK/Cre mice, the decreased amount of $CD8^+$ T cells was also observed in the spleen (Figure 3.17 A). As a possible compensation, NK cells were increased in control CerS4 LCK/Cre mice compared to the other control WT mice and CerS4 KO mice (1.99-fold increase, p=0.0016; 2.1-fold increase p=0.005). Further differences were observed after AOM/DSS treatment in CerS4 LCK/Cre mice. The frequency of monocytes, monocytes/macrophages, $F4/80^+CD36^+$ macrophages, neutrophils and NK cells was increased in CerS4 LCK/Cre mice and partially in WT mice. Mostly, the levels were higher in CerS4 LCK/Cre mice than in other AOM/DSS treated mice. After AOM/DSS treatment, neutrophil levels in CerS4 LCK/Cre mice increased 6.9-fold ($p<0.0001$) and consequently, neutrophil level of CerS4 LCK/Cre mice was between 2.4 and 3.4-fold higher than those of the other mice strains (p=0.001, $p<0.0001$). As for NK cells, the frequency in AOM/DSS treated CerS4 LCK/Cre mice was 3.5-fold higher than in AOM/DSS treated CerS4 Vil/Cre mice (p=0.0047), 2.2 -fold higher than AOM/DSS treated WT mice (p=0.004) and 2.1-fold higher than AOM/DSS treated CerS4 KO mice (p=0.097). $F4/80^+CD36^+$ macrophage levels also increased by 8.7-fold (p=0.0045) in WT mice and 28-fold ($p<0.0001$) in CerS4 LCK/Cre mice after AOM/DSS treatment. This huge increase in AOM/DSS treated CerS4 LCK/Cre mice was significantly different from AOM/DSS treated WT mice (3.7-fold , $p<0.0001$), AOM/DSS treated CerS4 KO mice (10-fold , $p<0.0001$) and AOM/DSS treated CerS4 Vil/Cre mice (15-fold, $p<0.0001$). As for the pooled monocytes/macrophage population, the difference between AOM/DSS treated CerS4 LCK/Cre mice and the other mice strains was between two-fold and four-fold (p=0.0004 and $p<0.0001$), and the AOM/DSS treated CerS4 LCK/Cre mice had more monocytes, resulting in monocyte levels that were between 6-fold and 23-fold higher than in the other AOM/DSS treated groups ($p<0.0001$) (Figure 3.17 B).

In summary, the immune status of the mice altered depending on the genotype after AOM/DSS treatment. CerS4 LCK/Cre mice did not have fewer $CD3^+$ T cells at all but had less $CD8^+$ T cells, both in blood and spleen under control condition. In general, the AOM/DSS treatment increased DC levels in blood. However, most immune cell populations did not alter after chronic inflammation and tumor development, only in CerS4 LCK/Cre mice many myeloid immune cells were upregulated, and T and B lymphocytes were downregulated after AOM/DSS treatment. The elevated level in CerS4 LCK/Cre mice indicated persistent inflammation in these mice.

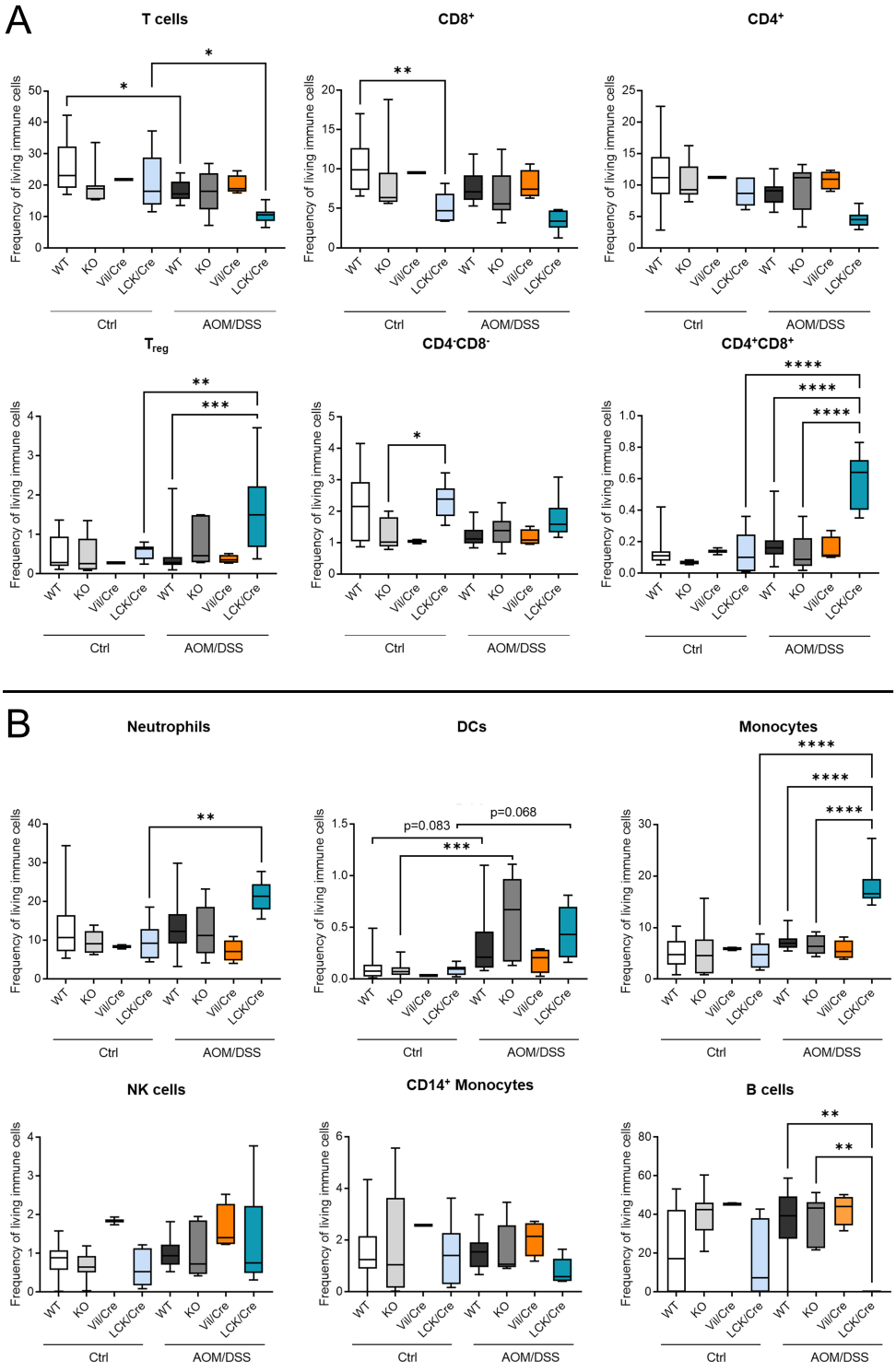

FIGURE 3.16: Immune cell populations in blood after CerS4 depletion and AOM/DSS treatment analyzed by flow cytometry. (A) T cell populations in WT mice (WT), CerS4 KO mice (KO), CerS4 Vil/Cre mice (Vil/Cre) and CerS4 LCK/Cre mice (LCK/Cre) at control condition (Ctrl) and after AOM/DSS treatment (AOM/DSS). CerS4 depletion did not alter T cell population. AOM/DSS treatment itself affected lymphocyte populations in the blood of CerS4 LCK/Cre mice. (B) Other immune cell populations were altered in blood of CerS4 LCK/Cre mice after AOM/DSS treatment. Data are presented as the median with Min to Max. Statistical analysis was performed by one-way ANOVA. Group size of control mice: WT mice n=17, CerS4 KO mice n=8, CerS4 Vil/Cre mice n=2 and CerS4 LCK/Cre mice n=9 and for AOM/DSS treated group: WT mice n=12, CerS4 KO mice n=6, CerS4 Vil/Cre mice n=4 and CerS4 LCK/Cre mice n=8. Data are published in [204].

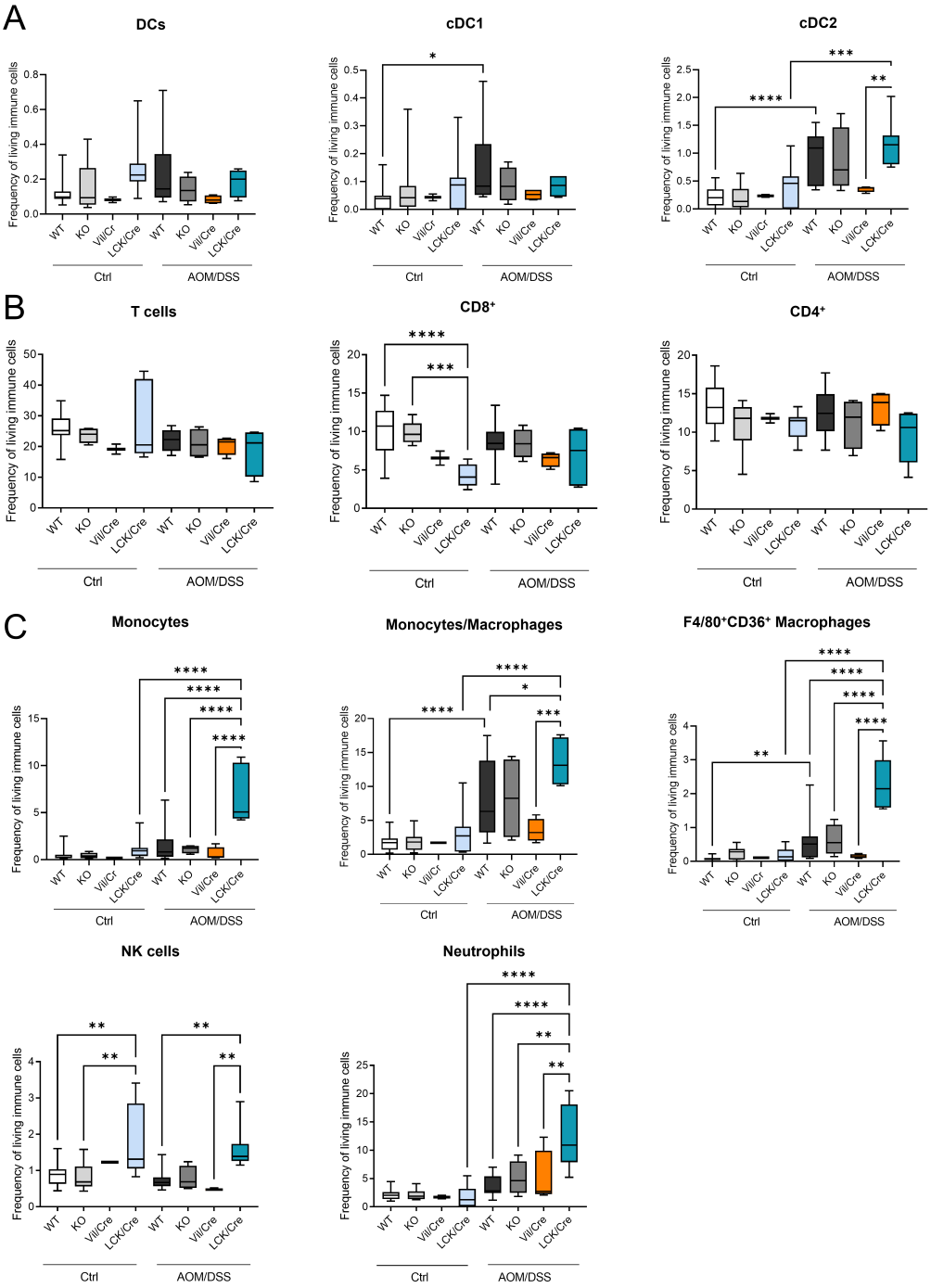

FIGURE 3.17: Immune cell status in the spleen of control (Ctrl) and AOM/DSS treated (AOM/DSS) WT mice (WT), CerS4 KO mice (KO), CerS4 Vil/Cre mice (Vil/Cre) and CerS4 LCK/Cre mice (LCK/Cre) measured by flow cytometry. (A) DC and DC subpopulations cDC1 and cDC2 did not increase equally after AOM/DSS treatment. (B) T cells and T subpopulation did not change, but CerS4 LCK/Cre mice had fewer $CD8^+$ T cells under control conditions. (C) Myeloid cell populations Monocytes, monocytes/macrophages, $F4/80^+CD36^+$ macrophages, neutrophils an NK cells were increased in CerS4 LCK/Cre mice after AOM/DSS treatment. Data are median ±Min/Max. Statistical analysis was performed with one-way ANOVA. Group size of control mice: WT mice n=17, CerS4 KO mice n=8, CerS4 Vil/Cre mice n=2 and CerS4 LCK/Cre mice n=9, and for DSS treated groups: WT mice n=12 CerS4 KO mice n=6, CerS4 Vil/Cre mice n=4 and CerS4 LCK/Cre mice n=8. Data are published in [204].

TABLE 3.7: Flow cytometry analysis of the immune cells isolated from the blood of control (Ctrl) and AOM/DSS treated (AOM/DSS) WT mice (WT), CerS4 KO mice (KO), CerS4 Vil/Cre mice (Vil/Cre) and CerS4 LCK/Cre mice (LCK/Cre). Data are mean ±SEM with distinct group sizes. Statistical analysis was performed by one-way ANOVA; significant differences were highlighted in bold and trends in italics.

	WT Ctrl			WT AOM/DSS			KO Ctrl			KO AOM/DSS			Vil/Cre Ctrl			Vil/Cre AOM/DSS			LCK/Cre Ctrl			LCK/Cre AOM/DSS		
	Mean	SEM	n	Mean	SEM	n	Mean	SEM	n	Mean	SEM	n	Mean	SEM	n	Mean	SEM	n	Mean	SEM	n	Mean	SEM	n
Single cells	80.18	5.46	18	92.91	6.01	12	89.41	4.12	9	99.28	0.32	6	98.85	0.15	2	99.33	0.15	4	**82.23**	6.08	7	**38.13**	1.74	7
Living immune cells	67.14	8.96	18	40.35	9.04	12	42.35	13.05	9	32.15	15.49	6	63	5.6	2	29.45	16.59	4	62.25	17.16	7	90.89	1.2	7
$CD3^+$ T cells	27.46	2.05	18	17.95	0.98	12	22.99	3.75	9	**17.84**	2.8	6	21.9	0	2	20	1.53	4	16.13	1.25	7	10.54	1.05	7
$CD4^+$ T cells	11.53	1.25	18	8.85	0.54	12	10.56	0.97	9	9.59	1.51	6	11.2	0	2	10.78	0.73	4	8.7	0.76	7	4.63	0.52	7
T_{regs}	0.55	0.1	18	0.48	0.16	12	0.46	0.16	9	0.75	0.24	6	0.29	0.02	2	0.37	0.05	4	0.57	0.07	7	1.69	0.42	7
$CD8^+$ T cells	10.49	0.79	18	7.53	0.59	12	8.19	1.51	9	6.69	1.33	6	9.54	0.04	2	7.94	0.93	4	5.02	0.7	7	3.34	0.47	7
$CD8^-CD4^-$ T cells	4.74	1.51	18	1.24	0.11	12	3.4	2.18	9	1.38	0.22	6	1.04	0.07	2	1.16	0.13	4	**2.33**	0.22	7	1.83	0.24	7
$CD8^+CD4^+$ T cells	0.68	0.3	18	0.26	0.09	12	0.89	0.38	9	0.13	0.05	6	0.14	0.02	2	0.15	0.04	4	0.11	0.05	7	0.74	0.16	7
$NK1.1^+Ly6c^-$ NK cells	0.87	0.12	18	1	0.1	12	1.6	0.8	9	1.02	0.28	6	1.84	0.11	2	1.65	0.3	4	**0.67**	0.17	7	**1.44**	0.48	7
NK T cells	0.51	0.1	18	0.38	0.04	12	0.17	0.14	9	0.35	0.07	6	0.28	0.03	2	0.3	0.05	4	0.34	0.09	7	0.72	0.22	7
B cells	21.12	5.21	18	**36.97**	4.77	12	36.01	5.8	9	37.93	5.04	6	45.4	0.6	2	42.5	3.96	4	13.45	7.11	7	**0.03**	0.01	7
activiated Monocytes	0.91	0.33	18	0.19	0.11	12	0.02	0.01	9	0.04	0.02	6	0.01	0	2	0.02	0.01	4	0.44	0.22	7	**0.82**	0.18	7
Monocytes	4.96	0.63	18	6.56	0.59	12	5.61	1.74	9	6.58	0.77	6	5.86	0.29	2	5.67	0.92	4	6.1	0.79	7	18.33	1.63	7
$CD80^+CD11b^+$ Monocytes	7.46	1.55	18	6.71	1.4	12	5.16	3.34	9	4.58	1.5	6	1.7	0.17	2	5.8	1.75	4	20.13	7.08	7	**4.2**	0.93	7
$CD14^+CD11b^+$ Monocytes	1.53	0.27	18	1.59	0.2	12	1.83	0.69	9	1.62	0.42	6	2.57	0	2	2.06	0.34	4	1.46	0.45	7	**0.82**	0.18	7
DCs	0.08	0.03	18	0.51	0.18	12	0.09	0.03	9	0.61	0.16	6	0.03	0.01	2	0.18	0.06	4	0.09	0.02	7	**0.44**	0.09	7
Neutrophiles	12.71	1.8	18	13.01	2.06	12	9.43	0.94	9	12.4	2.83	6	8.32	0.49	2	7.28	1.4	4	8.54	1.62	7	**23.86**	2.95	7

TABLE 3.8: Flow cytometry analysis of the immune cells isolated from the spleen of control (Ctrl) and AOM/DSS treated (AOM/DSS) WT mice (WT), CerS4 KO mice (KO), CerS4 Vil/Cre mice (Vil/Cre) and CerS4 LCK/Cre mice (LCK/Cre). Data are mean ± SEM with distinct group sizes. Statistical analysis was performed by one-way ANOVA; significant differences were highlighted in bold and trends in italics.

	WT Ctrl			WT AOM/DSS			KO Ctrl			KO AOM/DSS			Vil/Cre Ctrl			Vil/Cre AOM/DSS			LCK/Cre Ctrl			LCK/Cre AOM/DSS		
	Mean	SEM	n	Mean	SEM	n	Mean	SEM	n	Mean	SEM	n	Mean	SEM	n	Mean	SEM	n	Mean	SEM	n	Mean	SEM	n
Immune cells	76.7	4.7	17	**61.7**	6.9	12	**69.1**	6.7	11	71.4	5.7	5	**84.8**	0.2	2	**67**	4.5	4	**46.1**	6.3	9	**18.7**	1.1	7
Single Cells	85.1	1.9	17	83.5	1.5	12	**76.6**	6.6	11	**77.7**	10.2	5	86.6	1.3	2	83	2.2	4	87.4	0.9	9	**80**	2.8	7
Living immune cells	90.9	0.6	17	92.3	0.6	12	88.1	3.2	11	**69.2**	15.7	5	94.4	0.4	2	91.7	0.7	4	**84.3**	2.7	9	**94.6**	0.7	7
$CD3^+$ T cells	25.9	1.3	17	**22**	1	12	27.8	5.1	11	**16.8**	4.6	5	19.2	1.7	2	20.5	1.5	4	26.8	4.1	9	**18.5**	2.5	7
$CD4^+$ T cells	13.5	0.7	17	12.5	0.8	12	10	1.3	11	9	2.6	5	11.8	0.6	2	13.2	1.1	4	10.9	0.6	9	9.5	1.3	7
$CD25^+GITR^+$ T_{regs}	1	0.1	17	1.2	0.1	12	0.8	0.1	11	1.2	0.5	5	0.7	0.1	2	0.9	0.1	4	1.2	0.1	9	1.5	0.2	7
CD8+	10.3	0.8	17	8.3	0.8	12	7.4	1.3	11	6.7	1.8	5	6.5	0.9	2	6.4	0.5	4	**3.9**	0.6	9	6.8	1.2	7
$CD8^-CD4^-$ T cells	1.5	0.4	17	0.9	0.1	12	**9.5**	5.3	11	**0.9**	0.3	5	0.6	0.1	2	0.6	0	4	**11.8**	4.6	9	**2**	0.4	7
NK1.1+ cells	0.9	0.1	17	0.7	0.1	12	1	0.3	11	0.6	0.2	5	1.2	0	2	0.5	0	4	**2.2**	0.6	9	**1.6**	0.2	7
Monocytes/Macrophages	4	2.6	17	**18.4**	12.8	12	4.5	3	11	18.3	13.1	4	3.7	0.1	2	**7.8**	4.2	4	**8.1**	8.3	9	**37.4**	9.5	7
$CD11b^+MHCII^-Ly6C^+$ Monocytes	0.5	0.6	17	1.6	1.9	18	0.4	0.3	8	1.1	0.4	4	0.2	0	2	0.6	0.7	4	1.1	1.1	9	**6.9**	2.9	7
F4/80 Macrophages	0.1	0.1	17	1.4	1.3	18	0.3	0.5	8	2	2.1	4	0.2	0	2	0.5	0.3	4	0.5	0.9	9	1.7	0.5	7
Makrophagen $F4/80^+CD36^+$	0.1	0.1	17	**0.6**	0.7	18	0.3	0.2	8	0.6	0.5	4	0.1	0	2	0.1	0.1	4	0.2	0.2	9	**2.3**	0.8	7
$MHCII^+CD11c^+$DCs	0.1	0.1	17	0.2	0.2	18	0.2	0.1	8	0.1	0.1	4	0.1	0	2	0.1	0	4	0.4	0.4	9	0.2	0.1	7
cDC1	0	0	17	**0.1**	0.1	18	0.1	0.1	8	0.1	0.1	4	0	0	2	0.1	0	4	0.1	0.1	9	0.1	0	7
cDC2	0.2	0.2	17	**0.9**	0.4	18	0.2	0.2	8	0.9	0.6	4	0.2	0	2	0.4	0.1	4	0.4	0.4	9	**1.2**	0.4	7
Neutrophiles	2.2	0.2	17	3.5	0.5	12	1.6	0.4	11	4	1.5	5	1.7	0.3	2	5	2.5	4	1.7	0.6	9	**12**	2.1	7

3.3 Disease induced shift in sphingolipid homeostasis

The following section deals with the question of the disease driven alterations in sphingolipid profile of colon tissue but also in other tissues like the small intestine, liver, plasma and lymphoid tissues as spleen and thymus. To get an impression of the sphingolipid distribution, all tables included the same sphingolipid analytes (even if some were not detectable) and within one sample the abundance of the sphingolipids was highlighted by color scale to obtain an overview of the sphingolipid profile in different tissues.

3.3.1 Impact of DSS induced inflammation

3.3.1.1 In the colon tissue

In the colon of WT control mice, the most abundant sphingolipid was Cer d18:1/16:0 ($\sim 40{,}000\,\mathrm{pg\,mg^{-1}}$), followed by Cer d18:1/24:1 ($\sim 8{,}000\,\mathrm{pg\,mg^{-1}}$). The remaining sphingolipids were mainly composed of Cer d18:1/18:0 ($\sim 4{,}000\,\mathrm{pg\,mg^{-1}}$), GlcCer d18:1/16:0 ($3{,}500\,\mathrm{pg\,mg^{-1}}$) and Cer d18:1/20:0, Cer d18:1/22:0 and Cer d18:1/24:0 ($\sim 3{,}000\,\mathrm{pg\,mg^{-1}}$). This means, that Cer and GlcCer constitute mainly the sphingolipid profile of the colon, among the dhCer dhCer d18:0/C16:0 ($\sim 2{,}500\,\mathrm{pg\,mg^{-1}}$) is more predominant than the other dhCer. Sphingoid bases (sphingosine and sphinganine) also ranged from $\sim 300\,\mathrm{pg\,mg^{-1}}$ to $500\,\mathrm{pg\,mg^{-1}}$, representing $0.34\,\%$ and $0.73\,\%$ of the sphingolipids. CerS4 deficiency shifted the sphingolipid composition already under basal conditions. In CerS4 KO mice, the Cer d18:1/20:0 was decreased by 0.3-fold (ns) and the GlcCer d18:1/18:0 by half compared with control WT mice (ns). In contrast Cer d18:1/16:0 increased 1.2-fold (ns) and dhCer d18:0/16:0 increased 1.6-fold (ns).

DSS-induced colitis had a vast impact on colon shrinking, and histological pictures also indicated a massive tissue remodeling and damage. Consequently, the sphingolipid composition also changed. All sphingolipids increased after DSS treatment: GlcCer d18:1/24:1 increased 3.7-fold (p=0.0006), sphingosine increased 3-fold (ns), GlcCer d18:1/18:0 by 2.5-fold (ns), both GlcCer d18:1/16:0- and LacCer d18:1/24:0 by 2.3-fold (ns, p=0.0006) and also Cer d18:1/20:0 by twofold (p<0.0001). In addition to GlcCer d18:1/18:0 and Cer d18:1/C20:0, the other sphingolipids with stearic acid as a side chain also increased upon DSS, such as LacCer d18:1/C18:0 (1.9-fold, ns), GlcCer d18:1/C18:1, Cer d18:1/C18:0-Cer (1.7-fold, p=0.1) and Cer d18:1/18:1 (1.2-fold, ns) after DSS treatment.

Similar increases as seen in WT mice after DSS treatment were observed in CerS4 KO mice, but LacCer d18:1/18:0 did not increase as in WT DSS treated mice and GlcCer d18:1/16:0 increased threefold (p<0.0001) compared to control CerS4 KO mice (Table 3.9).

These data indicate that CerS4 plays an important role in Cer d18:1/20:0 and GlcCer d18:1/ C18:0 in the colon. They increased under DSS in the same way as in the WT mice, but still remained at half the level compared with the WT mice. Another effect of CerS4 appeared to be stress-dependent: LacCer d18:1/18:0 did not increase in CerS4 KO mice compared to WT mice after DSS treatment.

This suggests that the increase in GlcCer d18:1/24:1, GlcCer d18:1/16:0 and Cer d18:1/20:0 may be caused by DSS. However, CerS4 deficiency in mice inhibited the increase of Cer d18:1/20 Cer by 71.5 % (p<0.0001). Although dhCer d18:0/18:0 content was decreased by 25 % at baseline, the reduction after DSS treatment was up to 41.5 % (p=0.02) in the colon of DSS treated CerS4 KO mice, and the same was observed in LacCer d18:1/18:0 content, which was also 40 % (p=0.01) lower than in DSS treated WT mice. This indicates the importance of CerS4 under stress stimuli for the synthesis of sphingolipids with stearic acid (Table 3.9).

TABLE 3.9: Sphingolipid levels in the colon of control (Ctrl) and DSS treated (DSS) WT mice (WT) and KO mice (KO). Proximal and distal part of the colon were pooled. Concentrations in $\mathrm{pg\,mg^{-1}}$ tissue, empty cells represent levels of certain sphingolipids that were below the detection limit and could not be detected. Data are mean ±SEM, n=4-7. Statistically significant differences were determined with a two-way ANOVA with a Tukey multiple comparison test and highlighted in bold and trends (p= 0.09-0.05) in italics. Data already published in [204].

Colon DSS	WT Ctrl			CerS4 KO Ctrl			WT DSS			CerS4 KO DSS		
	Mean	SEM	n	Mean	SEM	n	Mean	SEM	n	Mean	SEM	n
SPH d18:1	242.9	65	4	314.3	48	4	752.3	158	16	726.7	99	18
SPH d18:0	524.2	127	4	537.9	136	4	436.0	57	16	485.1	68	18
S1P d18:1	646.2	-	1	609.1	-	1						
S1P d18:0												
dhCer d18:0/16:0	2,516.4	626	4	4,082	1,819	4	2,029	224	16	2,586	356	18
dhCer d18:0/18:0	144.4	15	4	108.7	17	4	211.3	23	16	123.5	9	17
dhCer d18:0/24:0	166.5	-	1	180.8	16	2	215.0	22	12	287.6	35	10
dhCer d18:0/24:1	203.9	-	1	202.3	46	2	231.3	24	14	328.7	59	15
Cer d18:1/14:0	219.8	30	4	266.0	92	4	167.4	29	16	154.2	22	18
Cer d18:1/16:0	38,388	6,372	4	47,258	12,043	4	**64,181**	10,915	16	**59,931**	8,819	18
Cer d18:1/18:0	4,227.1	1,097	4	3,637.5	1,317	4	7,349.5	962	16	6,156.5	796	18
Cer d18:1/18:1	553.0	90	4	646.1	43	3	714.7	63	14	662.9	62	18
Cer d18:1/20:0	3,236.4	676	4	*998.3*	333	4	**6,739.7**	866	16	**1,921.5**	204	18
Cer d18:1/22:0	2,899.3	588	4	2,984.7	678	4	5,076.0	444	16	*4,894.9*	407	18
Cer d18:1/24:0	2,653.6	467	4	2,999.9	605	4	3,888.0	243	16	4,449.3	267	18
Cer d18:1/24:1	8,219	1,499	4	8,395	1,270	4	11,151	797	16	**13,034**	936	18
GlcCer d18:1/16:0	3,480.7	617	4	3,477.8	533	4	7,900.3	903	16	**10,717.8**	1,584	17
GlcCer d18:1/18:0	1,003.8	219	4	516.0	102	4	2,520.2	388	16	1,268.0	135	18
GlcCer d18:1/18:1							23.4	-	1	39.9	10	6
GlcCer d18:1/24:1	1,619.9	45	3	1,720.5	26	3	**6,027.1**	740	16	**5,875.8**	855	18
LacCer d18:1/16:0							1,567.9	81	4	1,404.4	32	5
LacCer d18:1/18:0	93.4	3	2	110.8	-	1	176.4	16	14	104.7	9	14
LacCer d18:1/24:0	312.9	10	2	329.4	13	3	721.9	105	16	584.9	52	16

To analyze whether the sphingolipid changes is also reflected on CerS expression level, CerS expression was detected in the colon of WT mice and CerS4 KO mice at control conditions and after DSS treatment. CerS1 and CerS3 had the lowest expression (-12.9 $\pm 0.26\Delta$CT and -12.1 ± 0.5 ΔCT, respectively), whereas all other CerS were expressed twice as much as CerS1 and CerS3. CerS5 expression was -6.8 ± 1 ΔCT, CerS4 -6.2 ± 0.85 ΔCT, CerS6 -5.7 ± 0.8 ΔCT and CerS2 num-5.7 ± 0.85 ΔCT. CerS4 KO mice exhibited significantly reduced CerS4 mRNA levels, and this remained so after DSS treatment (Figure 3.18). This decrease in CerS4 mRNA could theoretically be compensated by upregulation of another

CerS such as CerS1. However, this was not the case, because the other CerS expression levels did not change compared with the WT mice. CerS1 level was increased in one mouse, but this was not the case in the remaining CerS4 KO mice. The DSS treatment tended to decrease CerS4 mRNA expression (0.32-fold, p=0.096), in the WT mice. Both CerS2 and CerS6 expression were significantly decreased by 0.1- and 0.3-fold, respectively compared to control mice. In the DSS treated mice, CerS3 expression ranged from a 0.2-fold decrease to a 7.1-fold increase, making it difficult to evaluate the DSS induced effect and CerS5 and CerS6 did not change significantly. The same was also observed in CerS4 KO mice after DSS treatment. Most CerS mRNA levels decreased compared with control CerS4 KO mice. CerS1 decreased 0.3-fold (p=0.003), CerS2 decreased 0.1-fold (p<0.0001), and CerS6 decreased 0.2-fold (p=0.0016). However, no significant reduction was observed for CerS4 mRNA, CerS5 mRNA and CerS3 mRNA after DSS treatment. Therefore, CerS mRNA transcript levels could not explain the higher sphingolipid levels, indicating that the salvage pathway might contribute to the higher sphingolipid levels.

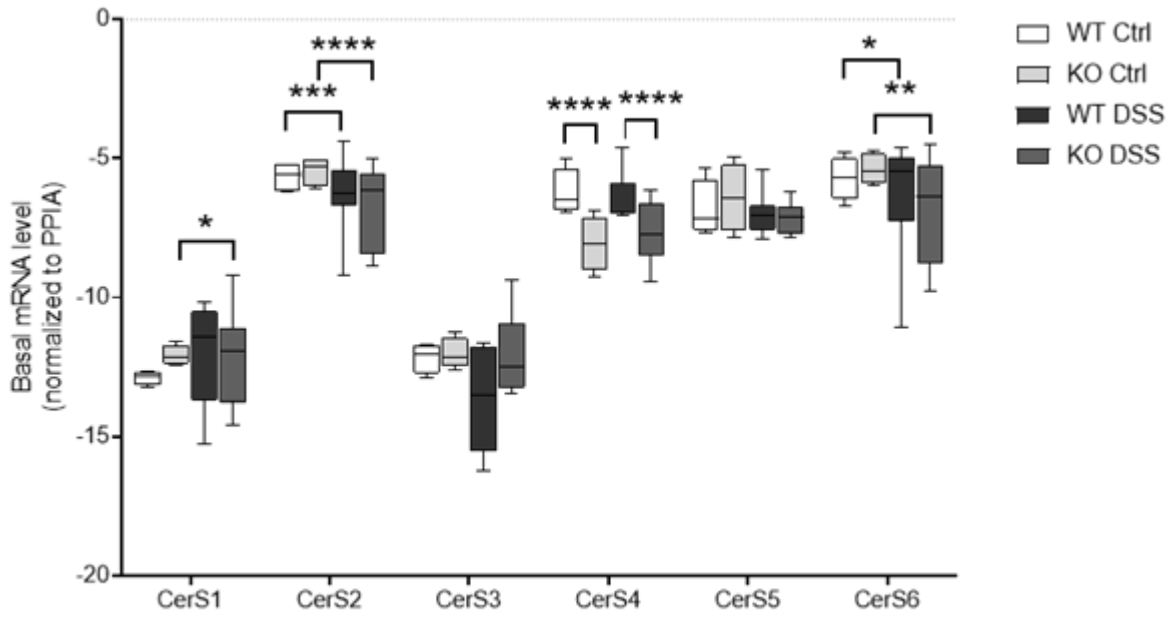

FIGURE 3.18: Basal mRNA expression of CerS in the colon tissue of control (Ctrl) and DSS treated (DSS) WT mice (WT) and CerS4 KO mice (KO). Basal mRNA levels were normalized to PPIA. The values of proximal and distal colon were pooled and plotted as median±CI95. Group size was as follows: control WT mice (n=2), control CerS4 KO mice (n=2) and for the acute DSS treated group: WT DSS treated mice(n=6) and KO DSS treated mice (n=-7). Statistically significant differences were determined by a one-way ANOVA and a Sidak's multiple comparison post-test of the $\Delta\Delta$CT, in which the mRNA levels were related to control WT mice. (* p<0.05, *** p<0.001, *** p<0.0001). Data published in [204].

3.3.1.2 In the small intestine

The small intestine was also affected by colitis. This directed interest to sphingolipid composition in the small intestine, how it was affected by DSS treatment, and the effects of

CerS4 deficiency in this adjacent tissue. Sphingolipid composition in control WT mice was similar to that in the colon: Cer d18:1/16:0 was the most abundant Cer ($\sim$70,000 pg mg^{-1}), followed by Cer d18:1/24:1 (14,000 pg mg^{-1}). GlcCer d18:1/C16:0 ($\sim$10,000 pg mg^{-1}), dhCer d18:0/16:0 ($\sim$8,000 pg mg^{-1}), Cer d18:1/18:0 ($\sim$8,000 pg mg^{-1}), Cer d18:1/22:0, Cer d18:1/24:0 ($\sim$6,000 pg mg^{-1}) and Cer d18:1/20:0 ($\sim$4,000 pg mg^{-1}) (Table 3.10). Interestingly, CerS4 deficiency was more pronounced in the small intestine. Thus, in CerS4 KO mice, Cer d18:1/20:0 was significantly reduced (about 75 % compared to control WT mice, p=0.06), GlcCer d18:1/18:0 decreased 0.7-fold (ns). LacCer d18:1/18:0 was detectable in the small intestine and was half of levels in WT mice (ns). In the small intestine, Cer d18:1/18:0 was reduced by 0.6-fold (ns) and dhCer d18:0/18:0 also dropped by 0.6-fold (ns). In contrast to the colon, dhCer d18:0/16:0, which was increased in the colon of CerS4 KO mice, was also downregulated in the small intestine (0.4-fold, p=0.006) (Table 3.10). DSS-induced inflammation had an opposite effect in the small intestine than in the colon. While all sphingolipids increased in the colon, the sphingolipid levels either did not change or decreased in the small intestine: LacCer d18:1/18:0 (0.3-fold, p=0.004), GlcCer d18:1/16:0 (0.5-fold, p=0.0026), Cer d18:1/14:0 (0.6-fold, ns) and Cer d18:1/16:0 (0.6-fold, ns). In contrast, sphingolipid levels changed differently in CerS4 KO mice. While GlcCer d18:1/16:0 (0.6-fold, p=0.01) and LacCer d18:1/18:0 (0.4-fold, ns) decreased to a lesser extent than in the WT mice, GlcCer d18:1/24:1 decreased 0.4-fold (ns) and GlcCer d18:1/18:0 decreased by half (ns). Similarly, in the colon, Cer d18:1/16:0 (p<0.0001) and all dhCer increased 3- to 2-fold in CerS4 KO mice (p<0.001 for dhCer d18:0/16:0, remaining dhCer ns) (Table 3.10). These data suggest that although DSS treatment affects colon tissue, DSS induced inflammation shifts sphingolipid level in the small intestine and CerS4 deficiency leads to a significant decrease in dhCer d18:0/18:0 level as in the colon.

3.3.1.3 In the liver

Since all blood leaving the gastrointestinal tract passes through the liver, sphingolipids were analyzed in the liver. The sphingolipid composition differed clearly from the intestine, whereas in the intestine Cer d18:1/16:0 was the most abundant sphingolipid very long chain ceramides Cer d18:1/24:1 ($\sim$25,000 pg mg^{-1}), Cer d18:1/24:0 ($\sim$11,000 pg mg^{-1}), GlcCer d18:1/24:1 ($\sim$9,000 pg mg^{-1}) and Cer d18:1/22:0 (6,500 pg mg^{-1}) were the most common sphingolipids in the liver of WT mice. CerS4-releated sphingolipids made up for only 10.8 % in total. Of these, Cer d18:1/20:0 accounted for $\sim$5.9 % of the total sphingolipids detected, Cer d18:1/18:0 accounted for only $\sim$1.7 %, GlcCer d18:1/18:0 accounted for $\sim$2.6 % and dhCer d18:0/18:0 ($\sim$0.3 %) and LacCer d18:1/18:0 LacCer ($\sim$0.2 %) were of a minor relevance (Table 3.11).

Although CerS4 relevant sphingolipids compromised approximately 10 %, CerS4 deficiency resulted in a shift in liver composition of CerS4 KO mice. GlcCer d18:1/18:0 and LacCer d18:1/18:0 decreased by 0.6-fold (ns). Accompanied by a 0.6-fold (ns) decrease in LacCer d18:1/24:1 and a 0.5-fold decrease (ns) in dhCer d18:0/16:0. In turn, very long

TABLE 3.10: Sphingolipid levels of WT mice (WT) and CerS4 KO mice (KO) determined by LC-MS/MS in the small intestine of control (Ctrl) and DSS treated mice (DSS). Concentrations in $\mathrm{pg\,mg^{-1}}$ tissue. Blank cells are sphingolipids that were below the detection limit and could not be measured. Data are mean ± SEM, n=4-7. Statistically significant differences were determined by a two-way ANOVA and highlighted in bold. Data published in [204]. Colored cells represent the distribution of the single lipids in the tissue: red high expression, yellow: middle expression, green-low expression.

Small Intestine DSS	WT Ctrl			KO Ctrl			WT DSS			KO DSS		
	Mean	SEM	n	Mean	SEM	n	Mean	SEM	n	Mean	SEM	n
SPH d18:1	1,011.8	618	4	1,030.3	207	7	918.4	100	6	1,035.6	197	7
SPH d18:0	642.6	159	4	636.6	77	7	546.1	178	6	460.5	119	7
S1P d18:1												
S1P d18:0												
dhCer d18:0/16:0	7,969.4	1,598	3	3,393.7	755	7	4,958.0	418	6	10,590.5	4,596	6
dhCer d18:0/18:0	181.0	13	3	114.3	26	4	171.4	6	6	211.3	37	6
dhCer d18:0/24:0	660.4	157	3	600.0	76	7	518.0	42	6	1,938.8	645	7
dhCer d18:0/24:1	685.2	58	3	560.4	119	7	586.9	51	6	1,446.1	516	7
Cer d18:1/14:0	400.5	153	3	334.0	53	7	233.0	16	6	184.5	32	7
Cer d18:1/16:0	64,287	25,205	3	69,692	16,446	7	79,460	13,925	2	123,835	35,365	2
Cer d18:1/18:0	7,192.7	3,339	3	**4,314.7**	474	7	6,128.6	728	6	**3,120.6**	404	7
Cer d18:1/18:1	799.8	10	2	816.9	98	2	907.5	27	6	783.1	90	7
Cer d18:1/20:0	3,528.1	1,021	3	**905.2**	104	7	**6,289.1**	773	6	**1,108.9**	174	7
Cer d18:1/22:0	6,214.7	746	3	5,334.2	578	7	5,419.7	421	6	4,663.2	578	7
Cer d18:1/24:0	6,962.3	1,051	3	5,429.5	417	7	4,170.1	252	6	4,548.3	410	7
Cer d18:1/24:1	13,978	4,363	3	12,989	1,069	7	11,160	713	6	9,259	1,067	7
GlcCer d18:1/16:0	9,934.5	2,205	3	8,865.5	1,339	7	**4,847.5**	855	6	**5,506.1**	1,093	7
GlcCer d18:1/18:0	1,098.9	45	3	721.1	68	7	849.9	133	6	394.7	54	7
GlcCer d18:1/18:1												
GlcCer d18:1/24:1	2,442.6	584	3	3,497.6	389	7	2,460.9	686	6	1,306.7	289	7
LacCer d18:1/16:0	711.9	-	1									
LacCer d18:1/18:0	282.5	-	1	154.1	54	5	82.8	6	5	62.1	7	6
LacCer d18:1/24:0	306.3	6	2	397.6	16	4	299.5	34	6	338.2	54	7

chain dhCer (dhCer d18:0/24:0 and dhCer d18:0/24:1, ns) and Cer d18:1/22:0 (p=0.0012) increased 1.5-fold to 3-fold; indicating an important role of CerS4 in the synthesis of complex ceramides and may also influence the synthesis of other chain length specific sphingolipids (Table 3.11).

As in the small intestine, the DSS treatment affected the sphingolipid composition in the liver. As in the colon, Cer d18:1/22:0 increased twice as much in DSS treated mice as in control mice (p=0.07). Interestingly, either the salvage pathway or the *de novo* synthesis pathway may have been affected by DSS treatment, as sphingosine levels increased threefold (ns) and all other dihydroceramides decreased sharply (ns). dhCer d18:0/16:0 decreased 0.5-fold, dhCer d18:0/18:0 had 0.7-fold decrease, dhCer d18:0/24:0 decreased 0.2-fold and dhCer d18:0/24:1 0.1-fold. Because the Cer levels did not increase, the increased sphingosine levels and decreased dhCer levels may indicate an activation of the salvage pathway. In addition, the Cer d18:1/14:0 content decreased by $99.6\,\%$ (ns) and LacCer d18:1/18:0 LacCer content by $\sim 60\,\%$ (ns), indicating a potential involvement of CerS4 (Table 3.11).

In the livers of CerS4 KO mice, sphingosine level increased twofold after DSS treatment compared with the control group. In contrast, the total dhCer level in the liver decreased after DSS treatment and was 0.77-fold lower in CerS4 KO mice treated with DSS than WT mice treated with DSS. Here, dhCer d18:0/16:0 did not change, but all other dhCers decreased more in the DSS treated CerS4 KO mice than in the DSS treated WT mice: dhCer d18:0/18:0 exhibited a 0.3-fold decrease (ns), dhCer d18:0/24:0 showed a 0.05-fold decrease (p=0.04) and dhCer d18:0/24:1 showed a 0.06-fold decrease (p=0.04). The decrease in LacCer d18:1/18:0 was similar to that of the WT mice, but the decrease in Cer was greater in DSS: Cer d18:1/14:0 was below the detection limit, Cer d18:1/18:0 decreased to half (ns) and both Cer d18:1/20:0 (ns) and Cer d18:1/22:0 Cer decreased by 0.6-fold (p=0.0041) after DSS treatment (Table 3.11). This decrease in long chain sphingolipids (especially C18 and C20) suggests a potential stress-driven synthesis by CerS4 that cannot be compensated by other CerS.

3.3.1.4 In the plasma

Sphingolipid levels were also be detected in plasma. However, the composition was quite different compared to the other tissues. Mainly complex sphingolipids could be detected: LacCer d18:1/16:0 ($\sim 900\,\mathrm{pg\,mL^{-1}}$), GlcCer d18:1/18:0 ($\sim 700\,\mathrm{pg\,mL^{-1}}$) and GlcCer d18:1/16:0 ($\sim 500\,\mathrm{pg\,mL^{-1}}$) were detected, followed by dhCer d18:0/16:0 ($\sim 500\,\mathrm{pg\,mL^{-1}}$) and GlcCer d18:1/18:1, GlcCer d18:1/24:1, Cer d18:1/24:0, Cer d18:1/24:1 and also S1P and SA1P were between $100\,\mathrm{pg\,mL^{-1}}$ and $300\,\mathrm{pg\,mL^{-1}}$. Other Cer or dhCer were found to a lesser extend in the plasma of WT mice but had no statistical significance. CerS4 deficiency increased sphinganine and S1P levels as well as Cer d18:1/18:0 (2.23-fold), very long chain sphingolipids as Cer d18:1/22:0 (5.3-fold), Cer d18:1/24:0 (2.8-fold) and GlcCer d18:1/24:1 (1.6-fold), but these increases were not significantly different from those in plasma of WT mice. As in the previous tissues, Cer d18:1/18:0 and GlcCer d18:1/18:1 were reduced by 0.4-fold compared with the WT mice, but dhCer d18:0/C16:0 and LacCer d18:1/ 16:0 were also

TABLE 3.11: Sphingolipid levels of WT mice (WT) and CerS4 KO mice (KO) determined by LC-MS/MS in the liver of control (Ctrl) and DSS treated mice (DSS). Sphingolipids below the detection limit could not be detected and are therefore blank. Concentrations in $\mathrm{pg\,mg^{-1}}$ tissue. Data are mean ±SEM, n=4-7. Statistically significant differences were determined by two-way ANOVA and highlighted in bold. Colored cells represent the distribution of the single lipids in the tissue: red high expression, yellow: middle expression, green-low expression. Data published in [204].

Liver DSS	WT Ctrl			KO Ctrl			WT DSS			KO DSS		
	Mean	SEM	n	Mean	SEM	n	Mean	SEM	n	Mean	SEM	n
SPH d18:1	376.6	137	4	534.5	173	7	1,186.0	225	6	1,207.6	253	7
SPH d18:0	465.0	171	4	494.5	161	5	681.6	206	6	537.2	124	7
dhCer d18:0/16:0	462.6	194	4	239.1	26	7	250.0	30	6	237.7	35	7
dhCer d18:0/18:0	206.3	103	2	279.4	158	3	137.6	33	4	82.3	-	1
dhCer d18:0/24:0	1,770.5	1,404	4	5,528.6	3,383	7	299.6	35	6	**275.2**	32	7
dhCer d18:0/24:1	3,856.0	2,927	4	5,596.1	3,128	7	542.6	60	6	**348.7**	48	7
Cer d18:1/14:0	5,086.2	5,051	4	5,942.6	3,959	7	19.4	3	3			
Cer d18:1/16:0	5,465.8	1,464	4	4,816.8	648	7	4,381.4	646	6	4,926.3	591	7
Cer d18:1/18:0	1,040.4	245	4	1,311.6	881	7	814.2	158	6	590.6	129	7
Cer d18:1/18:1							183.7	-	1	173.6	-	1
Cer d18:1/20:0	3,520.3	2,422	4	3,426.9	1,208	7	3,145.8	653	6	1,968.3	388	7
Cer d18:1/22:0	6,486.4	241	3	**17,364.5**	6,421	5	13,312.4	4,038	6	9,695.1	1,996	6
Cer d18:1/24:0	10,996.8	3,695	4	13,095.7	2,666	6	13,739.2	1,719	6	**19,795.0**	1,920	7
Cer d18:1/24:1	26,694.1	1,200	3	27,978.7	2,816	5	22,856.3	865	6	22,727.4	2,464	7
GlcCer d18:1/16:0	7,956.4	2,688	4	10,545.5	2,103	5	13,437.5	3,554	6	10,003.9	1,613	7
GlcCer d18:1/18:0	1,574.9	378	4	871.8	265	5	1,745.1	611	6	1,425.8	796	7
GlcCer d18:1/18:1							35.5	10	3	36.0	13	2
GlcCer d18:1/24:1	8,874.0	177	3	10,126.5	1,100	5	12,034.6	1,043	6	9,789.9	1,078	7
LacCer d18:1/16:0							1,548.1	-	1	1,432.2	65	2
LacCer d18:1/18:0	142.6	-	1	97.5	32	2	57.9	17	4	33.4	4	5
LacCer d18:1/24:0	353.0	10	2	405.0	24	5	621.6	79	6	632.1	82	7
LacCer d18:1/24:1	1,220.5	-	1	784.9	-	1						

reduced by 50 % to 32 % in control CerS4 KO mice. However, these changes were not statistically significant from plasma of control WT mice (Table 3.12). As in liver, very long chain Cer, Cer d18:1/22:0, Cer d18:1/24:0 and sphinganine were increased after DSS treatment in the plasma. This was in contrast to the reduction in S1P (0.2-fold), dhCer d18:0/16:0 (0.6-fold) and GlcCer d18:1/18:1 (0.4-fold) in DSS treated WT mice. CerS4 deficiency resulted in a shift in the sphingolipid composition. As in WT mice, sphinganine level was increased, but no further increase was observed after DSS treatment; instead, sphingolipid content decreased. The decrease in S1P was after DSS treatment approximately 97 % (p=0.006) compared to the control CerS4 KO mice. The halved reduction of dhCer d18:0/16:0 and GlcCer d18:1/18:0 (p=0.015) was also observed in the plasma of CerS4 KO mice, but other sphingolipid levels were also reduced: GlcCer d18:1/24:1 decreased by 98.6 % (p=0.0124), GlcCer d18:1/16:0, Cer d18:1/22:0 showed a 0.5-fold (ns) decrease and Cer d18:1/18:0 showed a 0.6-fold change (ns) (Table 3.12).

TABLE 3.12: Sphingolipid levels of WT mice (WT) and CerS4 KO mice (KO) determined by LC-MS/MS in the plasma of control (Ctrl) and DSS treated mice (DSS). Concentrations in $\mathrm{pg\,mL^{-1}}$ plasma. Colored cells represent the distribution of the single lipids in the tissue: red high expression, yellow: middle expression, green-low expression. Sphingolipid levels below the detection limit, could not be detected. Data are mean ±SEM, n=4-7. Statistically significant differences were determined by two-way ANOVA and highlighted in bold. Data published in [204].

Plasma DSS	WT Ctrl			KO Ctrl			WT DSS			KO DSS		
	Mean	SEM	n	Mean	SEM	n	Mean	SEM	n	Mean	SEM	n
SPH d18:0	6.4	1	4	10.1	5	7	14.1	4	6	12.8	3	6
S1P d18:1	313.3	177	4	464.7	116	7	67.6	54	6	**10.5**	2	6
S1P d18:0	202.2	19	4	239.4	19	7	289.8	50	6	359.0	63	6
dhCer d18:0/16:0	498.6	76	2	253.3	141	4	291.3	90	5	241.6	64	6
dhCer d18:0/18:0	12.2	3	2	14.3	5	2	10.5	-	1	10.0	1	2
dhCer d18:0/24:0				25.0	10	3	17.9	-	1			
dhCer d18:0/24:1	26.7	-	1	36.4	10	3	23.4	3	2	25.9	1	2
Cer d18:1/14:0				1.8	-	1				16.2	-	1
Cer d18:1/16:0	44.1	-	1	49.5	23	4	47.2	-	1			
Cer d18:1/18:0	33.0	7	3	73.8	21	4	25.0	6	5	20.2	6	5
Cer d18:1/18:1				20.5	-	1						
Cer d18:1/20:0				52.1	19	2	58.6	-	1			
Cer d18:1/22:0	67.0	48	2	352.8	201	5	148.9	90	3	35.0	10	2
Cer d18:1/24:0	118.8	32	4	330.0	102	7	255.1	97	6	170.8	77	5
Cer d18:1/24:1	262.3	52	4	378.3	86	7	300.8	53	5	470.0	116	3
GlcCer d18:1/16:0	476.8	223	4	471.4	83	6	465.2	158	5	262.3	61	3
GlcCer d18:1/18:0	680.0	270	4	276.9	90	7	650.1	281	6	**760.3**	325	6
GlcCer d18:1/18:1	111.6	23	3	44.5	23	5	45.2	16	5	50.1	21	6
GlcCer d18:1/24:1	282.5	276	3	457.4	152	4	253.6	246	5	6.6	3	4
LacCer d18:1/16:0	895.3	324	3	612.0	152	4	741.2	199	5	606.8	203	6

3.3.1.5 Sphingolipid levels in CerS4 LCK/Cre mice

Sphingolipid levels in the plasma

Since CerS4 deficiency in T cells does not leverage sphingolipid composition in colon, small intestine and liver were not measured. However, plasma and also solid tissues rich in T cells, such as spleen and thymus, were measured by LC-MS/MS. The sphingolipid composition in the plasma of control WT and CerS4 LCK/Cre mice was as follows: S1P content was 30-40 %, SPH 10 %, Cer d18:1/24:0 10 %, Cer d18:1/24:1 9-10 % and GlcCer d18:1/24:0 20 % of total sphingolipids. The only difference between both genotypes was in Cer d18:1/22:0 content, which was 10 % in the control CerS4 LCK/Cre mice and 4 % in the untreated WT mice. Because the number of mice measured was small, this difference had no statistical relevance. However, this difference was also observed in CerS4 KO mice. In the plasma of the WT mice, Cer d18:1/22:0 represented only 2 % of the total sphingolipids, while in the plasma of the CerS4 KO mice, this proportion increased to 8 %. Whereas in plasma from CerS4 KO mice we cannot be certain which cells contribute to plasma sphingolipid composition, the increased Cer d18:1/22:0 level in CerS4 LCK/Cre mice suggests that sphingolipids from T cells contribute to plasma sphingolipids and the increase in Cer d18:1/22:0 is attributable to CerS4 deficiency in the T cells. The residual composition was similar but with a slight increase in very long chain Cer and GlcCer. The plasma of the CerS4 KO mice showed further differences from the plasma of the control WT mice. While in the plasma of WT mice GlcCer account for ∼40 % of total sphingolipids, their proportion was reduced to 30 % in plasma of CerS4 KO mice, representing a huge decrease in GlcCer d18:1/18:0. GlcCer d18:1/18:1 represented 40 % of the GlcCer and was reduced to 22 % in plasma of the CerS4 KO mice. Instead, GlcCer d18:1/24:1 accounted for 37 % of total GlcCer, compared with 18 % in the WT mice . This pattern was not observed in CerS4 LCK/Cre mice, where the amount of GlcCer was approximately 20 % of the total sphingolipids and only GlcCer d18:1/18:0 (1 %) and GlcCer d18:1/24:0 (20 %) were detectable and were found in the same proportions in the plasma of both WT mice and CerS4 LCK/Cre mice (Table 3.13).

The most remarkable effect of DSS treatment is the change in S1P level in the plasma. In CerS4 KO mice, it was reduced by 0.2-fold after DSS treatment. This decrease was also observed in WT mice and CerS4 LCK/Cre mice, but only by 10 % and was not statistically relevant. In both WT mice and CerS4 LCK/Cre mice, dhCer d18:0/C24:0 increased up to three times more than in control (ns). The fact that CerS4 deficiency leads to more very long-chain ceramides was also evident with DSS treatment. In CerS4 LCK/Cre mice, the increase in Cer d18:1/24:0 was 1.7-fold (p=0.07) higher than in DSS treated WT mice, the same was observed for Cer d18:1/24:1 Cer (ns) (Table 3.13).

3.3.1.6 Sphingolipid levels in the spleen

In the spleen, T cells constitute around 25 % of all splenocytes. The sphingolipid composition differed slightly from previously described tissues and plasma. GlcCer account for

TABLE 3.13: Sphingolipid levels of WT mice (WT) and CerS4 LCK/Cre mice (LCK/Cre) determined by LC-MS/MS in the plasma of control (Ctrl) and DSS treated mice (DSS). Concentrations in $\mathrm{pg\,mL^{-1}}$ plasma. Colored cells represent the distribution of the single lipids in the tissue: red high expression, yellow: middle expression, green-low expression. Not detectable sphingolipids were kept empty. Data are mean ±SD, n=2-5. Statistically significant differences determined by a multiple unpaired t test and highlighted in bold. Data published in [204].

Plasma DSS	WT Ctrl			LCK/Cre Ctrl			WT DSS			LCK/Cre DSS		
	Mean	SD	n	Mean	SD	n	Mean	SD	n	Mean	SD	n
SPH d18:1	9.1	3	2	10.2	2	2	12.0	5	5	16.3	12	5
SPH d18:0	6.2	2	2	7.1	2	2	9.0	4	5	**9.1**	5	5
S1P d18:1	630.6	46	2	705.3	180	2	567.3	55	5	**615.4**	126	5
S1P d18:0	169.3	9	2	216.6	65	2	134.9	28	5	141.8	25	5
dhCer d18:0/16:0							30.4	-	1	30.4	-	1
dhCer d18:0/18:0												
dhCer d18:0/24:0	15.9	-	1	16.1	-	1	51.9	36	2	39.9	23	5
dhCer d18:0/24:1												
Cer d18:1/14:0												
Cer d18:1/16:0	37.1	14	2	48.1	30	2	50.4	48	5	74.0	44	5
Cer d18:1/18:0				7.5	-	1	8.5	-	1			
Cer d18:1/20:0				30.2	-	1	10.5	-	1	8.8	-	1
Cer d18:1/22:0	70.9	13	2	245.5	260	2	80.3	50	5	128.1	81	5
Cer d18:1/24:0	184.3	116	2	253.6	214	2	239.3	225	5	408.7	234	5
Cer d18:1/24:1	139.8	48	2	252.9	207	2	166.2	74	5	287.7	198	5
GlcCer d18:1/16:0							363.6	72	4	496.2	50	2
GlcCer d18:1/18:0	21.2	14	2	30.1	2	2	32.8	15	5	20.9	8	5
GlcCer d18:1/24:1	322.7	34	2	506.8	227	2	500.2	162	5	542.4	194	5

half of the total sphingolipids detected. Followed by very long chain ceramides, which accounted for 30 % of total sphingolipids. While Cer d18:1/16:0 accounted for only 7 % of total sphingolipids, the amount of LacCer was 6 % in the WT mice and 9 % in the CerS4 LCK/Cre mice. Thus, under control conditions, no decrease in Cers4 relevant sphingolipids was observed; instead, the increase of very long chain sphingolipids, especially GlcCer d18:1/24:1 (1.5-fold, p=0.0015) was of statistical relevance (Table 3.14).

Interestingly, DSS treatment altered sphingolipid composition in the spleen. In WT mice, Cer levels decreased 0.6- to 0.4-fold, with 0.4-fold decreases in Cer d18:1/16:0, Cer d18:1/24:0 and Cer d18:1/24:1 being statistically significant (Cer d18:1/16:0, p= 0.0038; Cer d18:1/24:0, p=0.0002 and Cer d18:1/24:1, p=0.0003). GlcCer d18:1/24:1 was also reduced by ∼20 % compared to control (p=0.023). The other changes such as the slight increase in LacCer and the decrease in other GlcCer were not statistically significant. In contrast, sphingolipid composition in DSS treated CerS4 LCK/Cre mice was characterized by a greater increase, especially in the very long chain species. dhCer d18:0/24:0 and dhCer d18:0/24:1 changed 1.5-1.7-fold (ns) and GlcCer d18:1/24:1 increased by 22 % (p=0.046). The 0.7 to 0.6-fold reduction in Cer was also observed in the spleen of CerS4 LCK/Cre mice after DSS treatment (Cer d18:1/24:1 (p=0.0054), other changes ns). However, Cer with lignoceric acid as a side chain behaved differently. Although the increases in Cer d18:1/24:0 (p=0.0037) and GlcCer d18:1/24:1 were 10 % to 20 %, they were statistically significant (Table 3.14).

Sphingolipid levels in the thymus

The thymus is crucial for T cell development, in which T cells differentiate to various phenotypes such as $CD4^+$ T cells, $CD8^+$ T cells, γδ T cells, NK T cells, T_{regs} and IEL progenitors. S1P is an important modulator of T cell emigration from the thymus into the blood. To date, no impairment of T cell trafficking has been observed. $CD3^+$ T cells were present in CerS4 KO mice and WT mice in both blood and tissue. As in the spleen, GlcCer accounted for 60 % of total sphingolipids in the thymus: In contrast to the spleen, in which GlcCer d18:1/16:0 accounted 1/5, GlcCer d18:1/18:0 was 1/12.5, and GlcCer d18:1/24:1 was 60 % to 70 %, in the thymus GlcCer d18:1/16:0 made up 40 %, GlcCer d18:1/24:1 was about half, and Cer d18:1/18:1 was only 3 % of the glucosylceramides. Very long chain ceramides accounted for 25 % and Cer d18:1/16:1 for 10 % to 12 % of total sphingolipids. As observed in the spleen, CerS4 deficiency in T cells did not alter the amount of CerS4 related sphingolipids in the thymus (Table 3.15).

Similar to spleen, DSS induced colitis decreased Cer and GlcCer levels: Cer d18:1/16:0 decreased 0.77-fold (ns), Cer d18:1/14:0 0.6-fold (ns) and Cer d18:1/24:1 0.7-fold (p=0.0048), also GlcCer d18:1/16:0 and GlcCer d18:1/24:1 also decreased by 0.6 and 0.7-fold, respectively (p=0.018, p=0.0048). In CerS4 LCK/Cre mice, the decrease in GlcCer d18:1/24:1 (0.58-fold, p<0.0001) was greater than in WT mice (p=0.01). In DSS treated CerS4 LCK/Cre mice, more Cer and LacCer increased (ns) after DSS treatment, e.g., double increase of LacCer d18:1/24:0 (ns) (Table 3.15).

TABLE 3.14: Sphingolipid levels of WT mice (WT) and CerS4 LCK/Cre mice (LCK/Cre) determined by LC-MS/MS in the spleen of control (Ctrl) and DSS treated mice (DSS). Concentrations in $\mathrm{pg\,mg^{-1}}$ tissue. Data are mean ±SD, n=2-5. Statistically significant differences were determined by multiple unpaired t test and highlighted in bold. Colored cells represent the distribution of the single lipids in the tissue: red high expression, yellow: middle expression, green-low expression. Statistically significant differences were determined by two-way ANOVA and highlighted in bold. Data published in [204].

Spleen DSS	WT Ctrl			LCK/Cre Ctrl			WT DSS			LCK/Cre DSS		
	Mean	SD	n	Mean	SD	n	Mean	SD	n	Mean	SD	n
SPH d18:1	1,139.1	70	2	1,410.4	122	3	1,259.6	224	5	1,287.2	678	5
SPH d18:0	300.3	35	2	352.5	25	3	321.9	46	5	379.2	214	5
S1P d18:1	42.9	5	2	44.9	13	3	59.2	32	5	66.5	19	5
S1P d18:0	34.6	0	2	33.1	3	3	39.2	12	5	33.6	8	5
dhCer d18:0/16:0	383.1	-	1	315.0	23	3	264.7	12	3	374.4	103	4
dhCer d18:0/18:0	124.1	-	1	107.9	11	3	79.2	17	3	89.8	24	5
dhCer d18:0/24:0	303.1	66	2	347.4	57	3	398.8	115	5	540.4	119	5
dhCer d18:0/24:1	868.1	-	1	779.8	147	3	826.5	163	5	1,349.1	523	5
Cer d18:1/14:0	26.4	14	2	17.6	4	3	16.1	-	1	17.0	1	4
Cer d18:1/16:0	7,530.9	6,474	2	5,793.9	1,544	3	**3,287.8**	791	5	4,179.3	1,856	5
Cer d18:1/18:0	1,343.1	744	2	1,062.2	143	3	656.1	243	5	626.9	279	5
Cer d18:1/20:0	1,349.4	958	2	837.0	141	3	568.5	178	5	552.7	297	5
Cer d18:1/22:0	3,667.1	1,626	2	3,281.4	459	3	2,661.9	522	5	3,377.8	1,307	5
Cer d18:1/24:0	10,353.6	9,090	2	6,622.2	1,563	3	**6,228.3**	1,997	5	7,364.6	2,159	5
Cer d18:1/24:1	16,570	8,086	2	15,247	964	3	**11,487**	2,735	5	**11,653**	4,135	5
GlcCer d18:1/16:0	11,668.5	1,697	2	9,569.4	4,713	3	9,318.7	2,403	5	8,252.1	2,650	5
GlcCer d18:1/18:0	4,102.7	790	2	2,423.7	817	3	3,219.3	665	5	2,817.6	1,191	5
GlcCer d18:1/24:1	35,151	5,081	2	25,388	5,576	3	**28,380**	10,635	5	**30,925**	13,498	5
LacCer d18:1/16:0	941.4	-	1	782.5	120	3	889.0	247	5	958.1	482	5
LacCer d18:1/24:0	1,536.1	237	2	2,086.0	687	3	2,111.3	942	5	2,117.3	733	5
LacCer d18:1/24:1	3,262.8	1,196	2	4,832.9	1,285	3	4,063.1	2,651	5	5,726.2	2,631	5

In conclusion, CerS4 deficiency restricted to T cell could not be represented in sphingolipid levels of the lymphoid tissue. The heterogeneity was still too high to detect changes in CerS4 relevant substrates such as C18:0, C18:1 and C20:0 FA. Instead, in CerS4 LCK/Cre mice and CerS4 KO mice an increase of GlcCer d18:1/24:1 and very long chain Cer could be detected as clear phenomenon after DSS treatment (Table 3.15).

TABLE 3.15: Sphingolipid levels of WT mice (WT) and CerS4 LCK/Cre mice (LCK/Cre) determined by LC-MS/MS in the thymus of control (Ctrl) and DSS treated mice (DSS). Concentrations in $\mathrm{pg\,mg^{-1}}$ tissue. Data are mean ±SD n=2-5. Statistically significant differences were determined by multiple unpaired t test and highlighted in bold. Colored cells represent the distribution of the single lipids in the tissue: red high expression, yellow: middle expression, green-low expression. Statistically significant differences were determined by two-way ANOVA and highlighted in bold. Data published in [204].

Thymus DSS	WT Ctrl			LCK/Cre Ctrl			WT DSS			LCK/Cre DSS		
	Mean	SD	n	Mean	SD	n	Mean	SD	n	Mean	SD	n
SPH d18:1	311.9	62	2	388.5	58	3	465.5	270	5	563.8	363	5
SPH d18:0	63.1	15	2	105.1	39	3	96.6	63	5	141.2	124	5
S1P d18:1							63.3	-	1	73.9	37	2
S1P d18:0							33.8	14	2	34.1	9	2
dhCer d18:0/16:0	853.8	126	2	681.1	319	3	677.4	250	5	787.2	542	5
dhCer d18:0/18:0	74.7	19	2	111.4	-	1	117.1	78	4	133.2	55	3
dhCer d18:0/24:0				183.1	-	1	313.0	186	2	316.4	17	2
dhCer d18:0/24:1				650.4	-	1	607.6	-	1	850.8	-	1
Cer d18:1/14:0	103.4	11	2	72.8	12	3	62.9	18	5	67.6	22	5
Cer d18:1/16:0	14,498.0	148	2	11,208.6	4,327	3	11,032.6	3,553	5	11,074.6	6,483	5
Cer d18:1/18:0	1,303.6	431	2	1,092.4	1,008	3	1,333.2	558	5	1,734.3	1,077	5
Cer d18:1/20:0	552.9	227	2	400.0	286	3	691.3	171	5	773.2	604	5
Cer d18:1/22:0	3,220.7	267	2	2,661.7	1,531	3	3,397.4	674	5	3,318.1	1,677	5
Cer d18:1/24:0	3,793.4	812	2	3,621.1	1,756	3	5,502.7	4,561	5	6,274.9	4,614	5
Cer d18:1/24:1	19,555.1	3,293	2	19,153.4	8,557	3	**17,031.7**	7,364	5	**14,291.3**	5,971	5
GlcCer d18:1/16:0	31,169.3	1,937	2	24,764.9	12,385	3	**18,072.4**	9,268	5	**14,358.7**	7,496	4
GlcCer d18:1/18:0	2,779.9	453	2	1,668.3	679	3	1,956.5	482	4	1,892.3	904	4
GlcCer d18:1/24:1	39,567.8	3,870	2	35,490.0	16,805	3	**29,027.7**	8,769	5	**20,640.2**	10,542	5
LacCer d18:1/16:0	776.2	125	2	955.5	164	3	891.3	269	4	1,186.2	330	3
LacCer d18:1/24:0	265.0	46	2	243.5	125	3	417.6	316	5	509.9	466	4
LacCer d18:1/24:1	1,333.2	538	2	1,787.4	807	3	2,130.0	813	5	1,842.0	1,522	4

3.3.2 Sphingolipid composition upon AOM/DSS treatment

The changes in the DSS treated mice compared to the control indicated disease-related changes in sphingolipid levels. Therefore, sphingolipid composition was compared in the colon, liver and plasma of AOM/DSS treated WT mice, CerS4 KO mice and CerS4 Vil/Cre mice.

3.3.2.1 In the colon

Tissue specific deficiency of CerS4 in Vil/Cre mice did not result in a shift in sphingolipid composition. While most sphingolipid levels were comparable between CerS4 Vil/Cre control mice and WT control mice, sphinganine was reduced by ∼37 % and sphingolipids

containing saturated or unsaturated stearic acid were reduced between 25 % and 35 %: Cer d18:1/18:0 (31 %), Cer d18:1/18:1 (25 %), GlcCer d18:1/18:0 (35 %), LacCer d18:1/18:0 (25 %) with no statistical relevance in control CerS4 Vil/Cre mice compared to control WT mice. This indicated that in the cell mixture of the colon, other cell types besides epithelial cells contribute to the sphingolipid pool. Compared to tissue specific deficiency, total knockout resulted in 65 % to 91 % decrease in sphingolipids with stearic acid: dhCer d18:0/18:0 were reduced by ∼84 % (p=0.002), Cer d18:1/18:1 by 91 % (p=0.04), GlcCer d18:1/ 18:0 by 76 % and GlcCer d18:1/18:1 by 91 % (p=0.05) and LacCer d18:1/18:0 by 65 % (p=0.5) under basal conditions in CerS4 KO mice. Cer d18:1/20:0 was also significantly reduced by 87 % (p=0.016) in control CerS4 KO mice. In these measurements, GlcCer d18:1/16:0 increased 1.6-fold and Cer d18:1/24:1 increased 2.5-fold, while dhCer d18:0/24:1 decreased 0.06-fold, indicating a possible higher conversion of very long chain, unsaturated dihydroceramides to ceramides by DEGS in the CerS4 KO mice or because Cer d18:1/24:1 level changed compared with WT mice, lower *de novo* synthesis of dhCer d18:0/24:1 may also be possible. However, these changes were not statistically different and might be only due to fluctuations (Table 3.16).

Sphingolipid data between chronic inflammation and acute inflammation differed for some sphingolipids and were comparable for other sphingolipids. The 3-fold increase in sphingosine appeared to be an acute inflammatory effect; no increase was observed in AOM/DSS treated mice. In AOM/DSS treatment, unsaturated very long chain sphingolipids increased. dhCer d18:0/24:1 (p=0.015), Cer d18:1/24:1 (p=0.001) and GlcCer d18:1/24:1 increased from 1.6-fold to 2.8-fold in AOM/DSS treated mice. The highest increase was a 3-fold change in levels of GlcCer d18:1/16:0 and LacCer d18:1/16:0 in the colon of AOM/DSS treated WT mice and CerS4 KO mice, respectively, which also were increased in DSS treated mice but had no statistical significance. In contrast, AOM/DSS treatment resulted in a decrease in unsaturated Cer d18:1/18:1 (0.3-fold change, p=0.03), GlcCer d18:1/18:1 by 70 % (p=0.05) and saturated dhCer d18:0/18:0 (p=0.002) as well as LacCer d18:1/18:0 by 50 % (ns) in WT mice. Cer d18:1/14:0 also decreased by 0.6-fold after AOM/DSS treatment in WT mice and CerS4 KO mice. The decrease level of unsaturated dhCer d18:0/24:1 (0.3-fold change, ns) and the 2.4-fold increase of Cer d18:1/24:1 (p=0.03) might indicate a higher activity of DEGS for unsaturated dhCer. In summary, only the decrease in Cer d18:1/18:1, Cer d18:1/24:1 and dhCer d18:0/18:0 were regarded as discoveries (FDR analysis), which were altered due to AOM/DSS treatment in WT mice (Table 3.16).

In CerS4 Vil/Cre mice, not many sphingolipids could be quantified, but half of the sphingolipids detected either did not change or increased after AOM/DSS treatment. As in the AOM/DSS treated WT mice, Cer d18:1/24:1 also increased in AOM/DSS treated Vil/Cre mice (1.7-fold, p=0.002). The other increases were opposite to the reduction in WT mice. Thus, Cer d18:1/18:1 increased 1.8-fold, GlcCer d18:1/18:0 increased 2.3-fold, and LacCer d18:1/18:0 increased 2-fold compared with control CerS4 Vil/Cre mice but had no statistical significance. These increases were not detected in the AOM/DSS treated CerS4 KO mice. In AOM/DSS treated CerS4 KO mice, GlcCer d18:1/18:0 also increased twofold and dhCer d18:0/C18:0 increased slightly by 1.6-fold compared with the CerS4 KO control mice (ns).

The remaining stearic acids, especially the unsaturated lipids, did not change, as the levels in the control were already lower. However, the very long-chain ceramides (Cer d18:1/24:0, GlcCer d18:1/24:1 and LacCer d18:1/24:0, LacCer d18:1/24:1) and GlcCer d18:1/16:0 also increased 1.7 to 2.7-fold in the CerS4 KO mice compared with the control CerS4 KO mice (Table 3.16).

In summary, AOM/DSS treatment appeared to result in a reduction in Cer d18:1/14:0 and an increase in glucosylceramides in the colon but was no statistical significant. Whereas all stearic acids were significantly reduced in the WT mice, the remaining stearic acid ceramides and glucosylceramides remained at low levels in the CerS4 KO mice. Another contrast with acute inflammation was higher sphingosine levels, which did not change under AOM/DSS treatment, and the significant reduction of dihydroceramides in AOM/DSS treated WT mice (Table 3.16).

3.3.2.2 In the liver

As previously described, the CerS4 KO mice had increased levels of very long chain ceramides (1.4 to 3.7-fold increase) and reduced levels of GlcCer d18:1/18:0 (0.03-fold decrease) and LacCer d18:1/18:0 (0.005-fold change) in the liver. Unfortunately, the CerS4 Vil/Cre mice also had a different sphingolipid composition compared the control group. No sphingolipid level was increased, most sphingolipid species remained the same as in the WT mice group, but especially the very long chain sphingolipids were reduced in AOM/DSS treated WT mice, such as Cer d18:1/24:1 (0.1-fold, $p<0.0001$), Cer d18:1/22:0 (0.12-fold, $p=0.005$), GlcCer d18:1/24:1 (0.2-fold, $p=0.056$) and both Cer d18:1/16:0 and Cer d18:1/18:0 significantly reduced by 0.3-fold ($p<0.0001$) compared to control WT mice (Table 3.17).

Despite the lack of statistical significance, DSS treatment increased sphingosines levels (3-fold), Cer d18:1/22:0 (2-fold), LacCer d18:1/24:0 (1.8-fold) and GlcCer d18:1/16:0 (1.7-fold), while LacCer d18:1/18:0 (0.4-fold), Cer d18:1/14:0 (0.004-fold) and dhCers decreased in the liver of WT mice. Under AOM/DSS treatment, the very long chain sphingolipids Cer d18:1/24:1 (3.6-fold, $p<0.0001$), Cer d18:1/22:0 (2.5-fold, ns), GlcCer d18:1/24:1 (2.8-fold, $p=0.03$) and both Cer d18:1/16:0 ($p=0.034$) and LacCer d18:1/16:0 increased twofold larger in the liver of AOM/DSS treated WT mice than the control WT mice. DhCer did not decrease under AOM/DSS treatment. As in DSS treated mice, Cer d18:1/14:0 was reduced by $90.8\,\%$ (ns) and LacCer d18:1/18:0 by $99.5\,\%$ ($p=0.008$). In contrast to DSS treatment, GlcCer d18:1/18:0 and GlcCer d18:1/C18:1 were also reduced by $96.2\,\%$ and $99.8\,\%$, respectively, in the liver after AOM/DSS treatment, but without statistical significance (Table 3.17).

Beyond statistical significance, these comparisons suggested that some sphingolipid cha-nges in the liver were induced by inflammation and remained over time, such as the decrease in Cer d18:1/14:0, LacCer d18:1/18:1 and increase in Cer d18:1/22:0, whereas others appear to be induced by tumor progression (increase in Cer d18:1/24:1 and GlcCer d18:1/24:1 and decrease in other GlcCer chain lengths). The decrease in saturated and unsaturated glycosphingolipids with stearic acid could also be a tumor induced shift. FDR

statistics showed that Cer d18:1/24:1, GlcCer d18:1/18:0 and LacCer d18:1/18:1 were altered by AOM/DSS treatment in the liver of WT mice (Table 3.17).

In the DSS model, CerS4 KO mice showed a similar sphingolipid shift as WT mice. After AOM/DSS treatment, sphinganine content increased 4-fold compared with control and also 3.4-fold compared with AOM/DSS treated WT mice, but this had no statistical effect. In contrast to the DSS model, in which dhCer decreased, dhCer increased 1.7 to 3.3 times in the AOM/DSS model compared with the control. Cer d18:1/14:0 counteracts the rest of observation and was increased 3.6-fold (p=0.06). Surprisingly, Cer d18:1/18:0, GlcCer d18:1/18:0 and LacCer d18:1/18:0 increased up to 4-fold compared to control, but were not significantly increased and remained at the same level as the AOM/DSS treated WT mice. This indicated that the liver tissue adjusted stearic FA sphingolipids within a certain range during tumor progression.

Histologically, CerS4 Vil/Cre mice were found to suffer from chronic inflammation, but tumor development was reduced. Only sphingosine and sphinganine levels were 0.3 times significantly reduced compared to control CerS4 Vil/Cre mice and AOM/DSS treated WT mice (p=0.047). The notion that a specific DSS induced shift persisted in the liver was not the case. Cer d18:1/14:0 increased 1.6-fold (ns) compared to the control and 17.1-fold (p=0.078) compared to AOM/DSS treated WT mice, as did LacCer d18:1/18:0 (p<0.0001), Cer d18:1/22:0 (p=0.0057), which did not change in CerS4 Vil/Cre mice under AOM/DSS treatment. However, the suggestion of GlcCer d18:1/24:1 and Cer d18:1/24:1 as a possible tumor marker, could still be considered. Although GlcCer d18:1/24:1 increased twofold (ns) compared to control CerS4 Vil/Cre mice , it remained 0.2-fold lower than AOM/DSS treated WT mice (p=0.056) and AOM/DSS treated CerS4 KO mice (p=0.017). Cer d18:1/24:1 also did not increase in AOM/DSS treated CerS4 Vil/Cre mice, remaining 0.03 times lower than in AOM/DSS treated WT mice (p<0.0001) and AOM/DSS treated KO mice (p=0.055) (Table 3.17).

Comparison of AOM/DSS treated Vil/Cre mice with AOM/DSS treated WT mice and AOM/DSS treated KO mice showed further differences sphingolipid-composition in liver. LacCer d18:1/18:1, GlcCer d18:1/18:1, GlcCer d18:1/18:0 and Cer d18:1/18:0 did not decrease, indicating that this decrease is first not caused by CerS4 depletion in intestinal epithelial cells and secondly could be a tumor-related phenomenon. FDR statistics showed that in all cases control WT mice vs AOM/DSS treated WT mice, AOM/DSS treated WT mice vs AOM/DSS treated CerS4 Vil/Cre mice and AOM/DSS treated CerS4 KO mice vs AOM/DSS treated CerS4 Vil/Cre mice, GlcCer d18:1/18:0, LacCer d18:1/18:0, Cer d18:1/24:1, and Cer d18:1/16:0 were tumor-related changes (discoveries), because dysplasia was not observed in either AOM/DSS treated CerS4 Vil/Cre mice or control WT mice. Between AOM/DSS treated WT mice and AOM/DSS treated CerS4 Vil/Cre mice, GlcCer d18:1/16:0 and very long chain sphingolipids (Cer d18:1/22:0, Cer d18:1/24:0, dhCer d18:0/24:1, GlcCer d18:1/24:1) were also increased (Table 3.17).

3.3.2.3 In the plasma

Fewer sphingolipids ($5{,}886.86 \pm 2{,}022\,\mathrm{pg\,mL^{-1}}$) were detectable in plasma than in tissues (colon $46{,}379 \pm 6{,}086\,\mathrm{pg\,mg^{-1}}$, liver: $86{,}492.3 \pm 16{,}911\,\mathrm{pg\,mg^{-1}}$), Cer levels were mostly below the detection limit, but S1P was present at higher levels than in tissues. In tissue, level of S1P and S1AP amounted $0.525\,\%$ or even $0.053\,\%$ in liver and less than $0.003\,\%$ to $0\,\%$ in colon, whereas S1P content in plasma was $7\,\%$ and S1AP content was $\sim 3.75\,\%$ of the total sphingolipids measured. GlcCer were most abundant ($9\,\%$ to $30\,\%$), followed by very long chain Cer $5\,\%$ to $9\,\%$ in the plasma. Control CerS4 KO mice had higher levels of very long ceramides compared to control WT mice (Cer d18:1/22:0 9.5-fold increase p=0.0023; Cer d18:1/24:1 10-fold increase, p<0.0001; and Cer d18:1/24:1 11.5-fold increase p<0.0001). Sphingolipids with a stearic acid as a side chain did not change in the plasma of CerS4 KO mice. Although GlcCer d18:1/18:0 decreased 0.2-fold and GlcCer d18:1/18:1 decreased 0.6-fold in the plasma of CerS4 KO mice compared to WT mice, this was not significant.

After DSS treatment, sphinganine increased while complex ceramide GlcCer 18:1/18:1 decreased. After AOM/DSS treatment, very long chain Cer were significantly decreased in the plasma (both Cer d18:1/24:0 and Cer d18:1/24:1 0.6-fold (p<0.0001, p=0.014) and GlcCer showed a 0.2 to 0.6-fold reduction (GlcCer d18:1/16:0 0.3-fold (ns), GlcCer d18:1/18:0 0.3-fold (ns), GlcCer 18:1/18:1 0.6-fold (ns) and GlcCer d18:1/24:1 0.2-fold (p=0.039)). This decrease was not observed in the AOM/DSS treated CerS4 KO mice; instead, levels increased for GlcCer d18:1/16:0 (3-fold, p=0.01) and GlcCer 18:1/18:0 (5-fold, ns) and did not change in GlcCer d18:1/24:1. Thus, sphingolipid levels of the plasma of WT mice and CerS4 KO mice differed after AOM/DSS treatment: CerS4 KO mice had more GlcCer d18:1/24:1 (p<0.0001) and GlcCer d18:1/16:0 (p<0.0001) than AOM/DSS treated WT mice, and very long chain Cer were increased after AOM/DSS treatment: Cer d18:1/24:1 (p<0.001), Cer d18:1/24:0 (p<0.0001).

In control CerS4 Vil/Cre mice, sphingolipid levels in the plasma did not differ from control WT mice, but Cer d18:1/18:0 (0.3-fold, ns), Cer d18:1/18:1 (0.4-fold, p=0.004) and Cer d18:1/24:1 (0.1, ns) tended to decrease. After AOM/DSS treatment, sphingolipid levels did not change significantly.

Comparison of AOM/DSS treatments showed no significant difference between WT mice and CerS4 Vil/Cre mice. Thus, as in the plasma of WT mice treated with AOM/DSS, the levels of Cer d18:1/24:0 and Cer d18:1/24:1 were elevated in the plasma of CerS4 KO mice compared with CerS4 Vil/Cre mice after AOM/DSS treatment.

AOM/DSS treatment did not result in any discoveries that could be induced by the treatment. However, the very long chain ceramides Cer d18:1/24:1 and Cer d18:1/24:0 Cer were significantly different between AOM/DSS treated WT mice and AOM/DSS treated CerS4 KO mice, indicating a phenotype specific response. This is also independent from the Cers4 deficiency in the colon since the same difference was discovered between AOM/DSS treated CerS4 KO mice and AOM/DSS treated CerS4 Vil/Cre mice.

TABLE 3.16: Sphingolipid levels of WT mice (WT), CerS4 KO mice (KO) and CerS4 Vil/Cre mice (Vil/Cre) determined by LC-MS/MS of the colon of control (Ctrl) and AOM/DSS treated (AOM/DSS) mice. Concentrations in $\mathrm{pg\,mg^{-1}}$ tissue. Distal and proximal colon were measured and pooled because no difference was detected between distal and proximal colon. Data are mean ±SEM, n=2-12. Statistically significant differences were determined by a multiple unpaired comparison test with a FDR correction and highlighted in bold. P values that were not discoveries but were ranged between 0.09 and 0.0015 were highlighted in italics. While no differences were detected between WT mice and CerS4 Vil/Cre mice, differences between CerS4 KO mice and CerS4 Vil/Cre mice after AOM/DSS treatment are marked in blue. Data published in [204].

Colon AOM/DSS	WT Ctrl			KO Ctrl			Vil/Cre Ctrl			WT AOM/DSS			KO AOM/DSS			Vil/Cre AOM/DSS		
	Mean	SEM	n	Mean	SEM	n	Mean	SEM	n	Mean	SEM	n	Mean	SEM	n	Mean	SEM	n
SPH d18:1	982.5	81	24	1,042.7	95	6	1,026.2	206	4	1,095.5	57	22	1,009.1	162	6	1,186.2	122	7
SPH d18:0	161.1	25	22	284.1	42	6	101.7	12	4	213.1	23	22	274.9	81	6	137.9	13	7
S1P d18:1																		
S1P d18:0	852.5	-	1	*28.9*	-	1							71.2	-	1	819.7	-	1
dhCer d18:0/16:0	1,398.9	332	9	1,784.9	268	6				1,825.2	224	18	1,840.2	502	6	*382.1*	-	1
dhCer d18:0/18:0	556.0	56	18	**91.0**	9	6	762.5	126	4	**264.7**	49	14	*142.0*	28	4	**633.2**	57	7
dhCer d18:0/24:0	187.7	25	2	167.1	10	2				297.3	33	6	292.2	89	2			
dhCer d18:0/24:1	4,161.5	700	24	*247.1*	34	5	6,274.3	1,065	4	*1,359.8*	473	19	301.3	59	6	**7,970.1**	1,328	7
Cer d18:1/14:0	274.3	92	8	492.7	114	6				172.8	15	18	*151.9*	41	6			
Cer d18:0/16:0	1,398.9	332	9	1,784.9	268	6				1,825.2	224	18	*1,840.2*	502	6	382.1	-	1
Cer d18:1/18:0	3,564.3	367	24	*5,861.2*	1,381	6	2,461.2	257	4	*4,979.3*	610	22	4,553.3	1,413	6	*3,437.8*	306	7
Cer d18:1/18:1	2,901.3	252	16	**272.6**	0	2	2,185.5	231	4	**999.2**	328	12	274.0	11	2	3,992.4	618	7
Cer d18:1/20:0	7,820.3	897	24	**1,020.8**	319	6	9,674.0	1,097	4	6,291.2	615	22	1,455.9	404	6	**12,230.0**	946	7
Cer d18:1/22:0	3,769.4	310	8	3,682.3	533	6				*4,946.9*	319	18	3,975.8	795	6			
Cer d18:1/24:0	4,055.3	407	24	3,342.0	216	6	2,904.2	282	4	4,156.6	272	22	3,786.3	523	6	5,289.1	422	7
Cer d18:1/24:1	4,760.6	986	24	**11,832.0**	1,037	6	1,167.6	180	4	**11,390.0**	1,225	22	*12,320.0*	1,728	6	**2,024.3**	110	7
GlcCer d18:1/16:0	2,079.8	348	7	*3,372.2*	527	6				*6,431.3*	1,356	18	8,973.1	3,688	6			
GlcCer d18:1/18:0	2,605.6	414	24	*622.3*	84	6	1,706.7	114	4	2,085.5	394	15	1,366.8	246	6	3,986.8	466	7
GlcCer d18:1/18:1	673.0	55	3	**62.3**	1	2				186.7	88	10	55.3	3	2	*580.9*	-	1
GlcCer d18:1/24:1	2,317.7	160	8	2,780.2	442	6				*6,390.4*	1,016	18	6,707.6	1,992	6			
LacCer d18:1/16:0	684.7	84	7							*2,137.5*	439	14	1,187.0	184	4			
LacCer d18:1/18:0	529.8	98	20	*180.4*	31	6	394.7	48	3	*275.7*	46	22	221.2	72	6	**810.0**	87	7
LacCer d18:1/24:0	1,022.6	269	12	343.7	16	2				750.9	102	20	636.6	114	6	1,590.6	143	4
LacCer d18:1/24:1	1,020.3	128	2	*753.4*	26	3				*1,490.7*	115	7	2,055.7	147	2			

TABLE 3.17: Sphingolipid levels of WT mice (WT), CerS4 KO mice (KO) and CerS4 Vil/Cre mice(Vil/Cre) determined by LC-MS/MS in the liver of control (Ctrl) and AOM/DSS treated mice (AOM/DSS). Concentrations in $\mathrm{pg\,mg^{-1}}$ tissue. Data are mean ±SEM, n=2-13. Statistically significant differences were determined by two-way ANOVA with a Tukey' multiple comparison test and highlighted in bold. Data are published in [204].

Liver AOM/DSS	WT Ctrl			KO Ctrl			Vil/Cre Ctrl			WT AOM/DSS			KO AOM/DSS			Vil/Cre AOM/DSS		
	Mean	SEM	n	Mean	SEM	n	Mean	SEM	n	Mean	SEM	n	Mean	SEM	n	Mean	SEM	n
SPH d18:1	1,004.5	115	12	1,011.0	63	3	1,402.9	286	2	1,241.8	192	5	1,708.7	319	3	370.7	63	4
SPH d18:0	216.0	22	12	165.3	25	3	338.4	78	2	355.6	50	9	661.1	242	3	97.3	21	4
S1P d18:1	21.9	9	3													29.5	12	3
S1P d18:0	17.8	5	3													16.7	4	2
dhCer d18:0/16:0	223.6	0	1	149.0	24	3				207.6	16	9	365.3	163	3			
dhCer d18:0/18:0	82.2	0	1							76.2	0	1	262.5	0	1			
dhCer d18:0/24:0	182.1	25	9	170.0	11	2	128.2	1	2	255.4	19	4	295.7	55	2	144.0	15	4
dhCer d18:0/24:1	296.8	65	7	196.9	25	3				494.9	71	9	642.7	116	3	93.1	11	3
Cer d18:1/14:0	186.4	52	7	22.4	0	2	182.1	4	2	17.0	0	1	79.9	0	1	290.7	35	4
Cer d18:1/16:0	1,491.0	380	6	4,119.9	655	3	391.2	56	2	2,964.2	225	9	3,429.5	497	3	761.1	70	4
Cer d18:1/18:0	268.2	105	12	311.7	87	3	79.7	1	2	416.4	78	9	1,213.4	713	3	105.7	6	4
Cer d18:1/18:1	6,047.5	571	8				5,232.3	378	2							7,103.8	381	4
Cer d18:1/20:0	1,166.9	199	12	749.8	48	3	861.7	99	2	1,330.8	218	9	1,155.2	418	3	1,313.7	177	4
Cer d18:1/22:0	3,836.6	1,746	12	**14,206.6**	4,528	3	470.2	60	2	**9,768.5**	1,240	9	10,341.3	5,387	3	552.0	15	4
Cer d18:1/24:0	11,788.2	1,207	4	16,701.3	1,020	3				12,566.6	1,191	9	15,530.4	3,977	3			
Cer d18:1/24:1	7,474.7	2,779	12	**20,855.9**	2,882	3	716.9	56	2	**26,741.7**	2,110	9	**30,974.7**	7,548	3	851.2	75	4
GlcCer d18:1/16:0	9,719.8	1,256	12	4,725.3	532	3	14,487.8	598	2	6,102.4	988	9	9,211.1	2,455	3	13,797.2	984	4
GlcCer d18:1/18:0	16,578.8	3,170	11	**459.0**	228	3	25,471.3	320	2	**638.3**	141	8	1,334.8	155	3	24,830.9	689	4
GlcCer d18:1/18:1	9,367.6	1,593	9				8,805.8	1,274	2	**20.4**	0	2	18.2	0	1	12,918.2	1,654	4
GlcCer d18:1/24:1	5,976.1	1,556	12	7,234.1	1,215	3	1,287.6	279	2	**16,654.6**	3,112	9	13,848.1	3,248	3	2,734.5	504	4
LacCer d18:1/16:0	402.4	122	4							786.8	81	5	797.4	139	2			
LacCer d18:1/18:0	8,908.2	1,831	11	**48.2**	22	2	11,748.5	2,515	2	**47.0**	6	8	74.5	39	3	13,223.8	1,155	4
LacCer d18:1/24:0	340.8	103	4	459.6	0	1				384.7	31	9	612.3	158	3			
LacCer d18:1/24:1	894.5	0	1	915.8	0	1				1,427.8	0	1	1,705.2	0	1			

TABLE 3.18: Sphingolipid levels in plasma of WT mice (WT), CerS4 KO mice (KO) and CerS4 Vil/Cre mice (Vil/Cre) determined by LC-MS/MS of control (Ctrl) and AOM/DSS treated mice (AOM/DSS). Concentrations in $\mathrm{pg\,mL^{-1}}$. Data are mean ±SEM, n=2-13. Statistically significant differences were determined by two-way ANOVA with a Tukey's multiple comparison test and highlighted in bold. While WT mice and CerS4 Vil/Cre mice did not differ after AOM/DSS treatment, differences between CerS4 KO mice and CerS4 Vil/Cre mice after AOM/DSS treatment were marked in a blue bold font. Data are published in [204].

Plasma AOM/DSS	WT Ctrl			KO Ctrl			Vil/Cre Ctrl			WT AOM/DSS			KO AOM/DSS			Vil/Cre AOM/DSS		
	Mean	SEM	n	Mean	SEM	n	Mean	SEM	n	Mean	SEM	n	Mean	SEM	n	Mean	SEM	n
SPH d18:1	9.2	1	5	15.8	3	2				9.5	1	9	17.8	13	3	7.2	-	1
SPH d18:0	7.5	1	5	6.8	2	3				9.9	2	9	15.6	10	3			
S1P d18:1	428.4	102	5	180.2	143	3				533.7	36	9	343.4	183	3			
S1P d18:0	146.9	27	6	203.9	21	3				235.3	26	9	259.3	39	3			
dhCer d18:0/16:0				10.8	-	1							22.8	-	1			
dhCer d18:0/18:0													11.2	-	1			
dhCer d18:0/24:0	40.0	9	10	30.6	13	2	35.2	12	2	48.9	41	2	103.9	-	1	26.9	12	4
dhCer d18:0/24:1	17.8	2	3										161.5	-	1			
Cer d18:1/14:0																		
Cer d18:1/16:0	35.2	6	7	81.3	31	2				25.9	9	3	201.4	-	1			
Cer d18:1/18:0	152.9	67	7				38.6	11	2	174.4	159	2	250.8	-	1	32.8	11	4
Cer d18:1/18:1	220.6	55	6				96.0	17	2	400.8	-	1				113.1	24	2
Cer d18:1/20:0	185.0	59	10	309.9	-	1	142.0	28	2	195.6	130	3	483.7	-	1	160.9	54	2
Cer d18:1/22:0	496.9	117	5	**4,725.1**	2,601	2				120.7	64	7	**2,472.5**	2,451	2			
Cer d18:1/24:0	540.3	75	12	**5,432.2**	2,667	2	337.1	30	2	333.5	69	4	**9,566.6**	-	1	**376.1**	90	4
Cer d18:1/24:1	307.9	90	13	**3,562.6**	949	2	44.7	2	2	194.0	89	5	**9,883.8**	-	1	**88.9**	25	4
GlcCer d18:1/16:0	820.3	540	6	1,603.1	702	3				236.2	36	7	**5,091.2**	4,906	3			
GlcCer d18:1/18:0	548.1	139	13	121.7	50	3	462.8	104	2	147.4	102	11	722.7	692	3	436.1	109	4
GlcCer d18:1/18:1	4.1	1	2	2.7	-	1				2.3	0	4	2.3	0	2			
GlcCer d18:1/24:1	1,790.1	724	5	**4,542.8**	2,210	3				330.7	79	9	**5,192.4**	4,971	3			
LacCer d18:1/16:0	135.8	6	2															

3.4 Results-Part II

3.4.1 Role of CerS in patient derived organoids

Yet 21 control samples, 20 tumor samples and 10 diverticulitis samples were isolated, but not all of them grew or were successfully grown and used for mRNA isolation. The average age of tumor biopsies was originated from patients in the age of 66.8 $\pm$ 6.5 years, control biopsies originated from patients in the age of 68 years $\pm$ 6 years and diverticulitis from an average patient age of 68,5 $\pm$ 3.5 years.

CerS mRNA expression in organoids isolated from control samples (termed as control organoids) was similar to basal CerS expression in murine colon. The most abundant CerS level was CerS2 with -4.9 ± 0.66 ΔCT and CerS6 -5.8 ± 0.68 ΔCT, followed by CerS5 with -8.4 ± 1.06 ΔCT. Combining all controls, CerS3 had -11.5 ± 0.68 ΔCT, CerS4 mRNA with -14.4 ± 1.09 ΔCT, and CerS1 -14.1 ± 1.9 ΔCT. In organoids isolated from tumor samples (termed as tumor organoids), average mRNA expression did not change, in contrast to CerS1, which was 0.89-fold (p=0.047) more altered than in control. Organoids derived from diverticulitis samples (termed as diverticulitis organoids) altered CerS mRNA expression. CerS4 expression increased by $25\,\%$ to -10.8 ΔCT (p=0.1) compared to control organoids. Although CerS1 and CerS3 were expressed at low levels, they decreased even further, by $14\,\%$ (p=0.7) and $43\,\%$ (p=0.09), respectively. The mRNA expression of the more abundant CerS did not change compared to control organoids (Figure 3.19 A). A two-way ANOVA with a Tukey's multiple comparison test showed an opposite change in CerS1 and CerS3 expression in tumor organoids and diverticulitis organoids (p=0.04 and p=0.001) (Figure 3.19 B).

CerS expression in the murine colon included more cell types and was not restricted to colon epithelial cells. In contrast to the human data, DSS induced colitis decreased rather than increased CerS4 expression. Nevertheless, it should be kept in mind that diverticulitis is not a colitis and therefore not comparable.

3.4.2 Interaction between CerS and stem cell/ differentiation markers

While basal expression of stem cell marker LGR5 was -10.6 ± 2.4 ΔCT in control organoids, higher expression levels of SMOC2 -6.5 ± 4.4 ΔCT and Olfm4 -5.1 ± 1.64 were detected in control organoids. In organoids obtained from tumor tissue, Lgr5 did not change, and the other stem cell factors were surprisingly reduced to a small extend (Olfm4 by 0.75-fold and SMOC-2 by $9.1\,\%$) (Figure 3.20 A).

In general, differentiation markers were much more highly expressed than stem cell marker or even CerS isoforms. The highest average of mRNA expression was found in TFF -1.13 ± 1.3 ΔCT, fatty acid uptake also played an important role, and FABP1 had high expression with -1.27 ± 1.17 ΔCT in control organoids, followed by KRT20 -2.34 ± 0.84 ΔCT. Markers more relevant for mucus production were found at lower expression level: CA2 was -5.1 ± 1.54 ΔCT, MUC2 -9.43 ± 1.35 ΔCT, and ALPI -10.4 ± 1.33 ΔCT. In organoids derived from tumor tissue, differentiation markers were reduced compared with control,

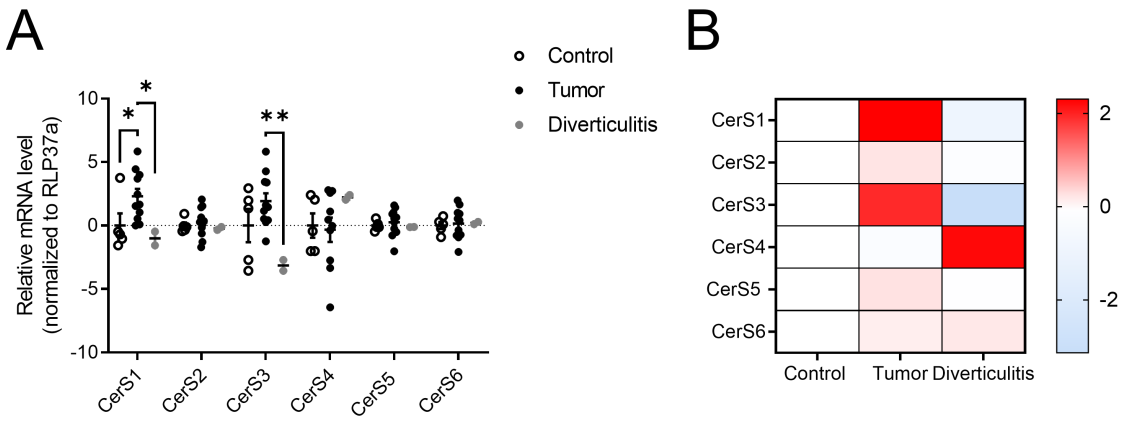

FIGURE 3.19: Basal mRNA expression of CerS measured by qRT-PCR in organoids derived from control, tumor or diverticulitis samples. Basal mRNA level was calculated as ΔCT value. Data are mean±SEM. Statistically significant changes were detected by two-way ANOVA and Tukey's multiple comparison test (* $p<0.05$, ** $p<0.01$). (B) Pearson correlation shows a correlation between CerS expression in organoids and tissue origin. Heatmap legend represents correlation factor of 3 variables compared to control.

indicating a less differentiated organoid. Stem cell markers such as Lgr5 did not change, Olfm4 was reduced by 0.74-fold (ns), and SMOC-2 was reduced 0.91-fold (ns) in tumor organoids compared to control organoids. Changes in differentiation markers were much higher: TFF1 changed by 0.22-fold times ($p=0.01$), FABP1 by 0.3-fold (ns) and KRT20 by the half (ns) in tumor organoids compared to control organoids. Mucin-related genes were either downregulated less or not at all. CA2 reduced by 0.7-fold (ns), ALPI by 0.84 (ns) and MUC2 did not change in tumor organoids. Organoids derived from diverticulitis tissue increased Lgr5 levels 1.4-fold, and this increase was significantly different compared with tumor. Olfm4 also increased by 1.39-fold and SMOC-2 1.6-fold but had no significant effect. Differentiation markers were reduced in these organoids compared with control. TFF1 was 3.3-fold (ns) higher control organoids than diverticulitis organoids, FABP1 was 2.8-fold higher (ns), KRT20 was 2.2-fold (ns). Similar to tumor organoids, the difference was less pronounced in mucin-related genes. In organoids obtained from diverticulitis tissue, CA2 was 0.63-fold, ALPI 0.9-fold and MUC2 0.85-fold lower than in control organoids, but with no statistical difference (Figure 3.20 A). Pearson correlation of fold changes compared with control tissue and the stem cell and differentiation marker showed that stem cell marker such as Lgr5, Olfm4, SMOC-2 were positively associated with diverticulitis, while differentiation markers were negatively associated. Quite surprising were the tumor data. In contrast, most marker in tumor organoids were less expressed than in the control organoids, but only MUC2 was positively associated with tumor derived organoids (Figure 3.20 B).

Comparison of basal mRNA values indicated that CerS expression was much lower than some differentiation marker. Even the high basal mRNA expression of CerS2 was much

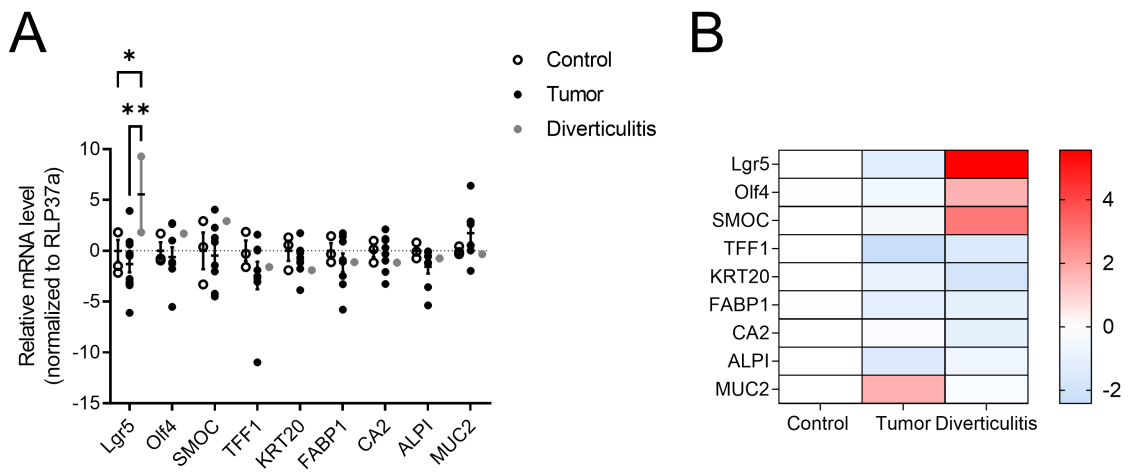

FIGURE 3.20: Measurement of basal mRNA expression of stem cell and differentiation markers by qRT-PCR in organoids derived from control, tumor or diverticulitis samples. Basal mRNA level was calculated as ΔCT value. Data are mean±SEM. Statistically significant changes were determined by two-way ANOVA and Tukey's multiple comparison post-test (* p<0.05, ** p<0.01). (B) Pearson's correlation indicated a relationship between marker expression in organoids and tissue origin. Calculations were carried out after first calculating the mean of side-by-side replicates and then analyzing the means. The heat map legend shows the changes of marker expression compared to the control.

lower than the differentiation marker. Interestingly, the basal expression of CerS4 was already lower than in the differentiated murine tissue. To determine whether the changes in stem cell and differentiation markers and the changes in CerS were associated and Pearson correlation analysis was performed with the ΔΔCT values, which revealed some correlations. Although the differences between CerS expression was significant (CerS3 - CerS1 p=0.0002 R=0.77, CerS1 - CerS5 p=0.04, CerS3 - CerS4 p=0.08), CerS2 - CerS5 p=0.00018, R=0.77, CerS6 - CerS5 p=0.02) there was a low correlation between the CerS isoforms, despite CerS5 and CerS2 (R=-1, p=0.005). However, some CerS correlated with differentiation marker. CerS4 and Lgr5 showed significant correlation (R=0.997, p=0.047). CerS1 and Olfm4 were associated with each other (R=-0.993, p=0.07). While CerS3 and MUC2 were associated (R=0.995, p=0.065), FABP1 correlated with CerS2 (R=0.999, p=0.03) and with CerS5 (R=-0.998, p=0.036). Since CerS2 is important for TJ integrity, it also appears to be important for mediating structure. CerS2 and KRT20 correlated with each other (R=0.997, p=0.049). In contrast to CerS2 and KRT20, CerS5 was negatively correlated with KRT20 (R=-0.998, p=0.044). CerS2 also correlated with ALPI (p=0.079, R=0.992). Differentiation markers were also associated with each other: for example, KRT20 correlated with ALPI (R=0.999, p=0.03) and TFF1 correlated with CA2 (R=1, p=0.007), and KRT20 correlated with FABP1 (R=0.959, p=0.079). In addition, the stem cell marker SMOC-2 was negatively associated with differentiation marker such as CA2 (R=-0.996, p=0.053) and TFF1 (R=-0.996, p=0.06). Heatmap in Figure 3.21 depicts positive associations in red shading and negative ones in blue shading. High correlation factor R combined with p<0.05 were marked with an asterisk, while strong correlations with a p-value <0.1 were marked with a white circle.

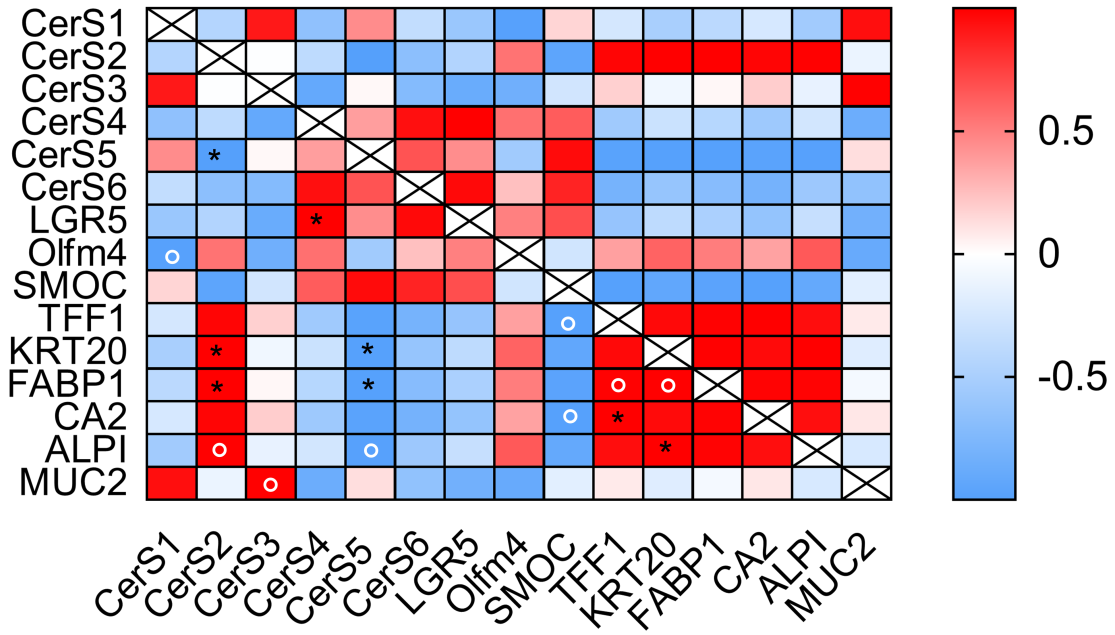

FIGURE 3.21: Pearson correlation of ΔCT values of total organoid measurements from control, tumor and diverticulitis biopsies. CerS mRNA expression of CerS1-CerS6 with stem cell marker and differentiation marker were analyzed. Values with high R and statistical significance are marked with an asterisk *, and correlations with statistical significance of p<0.1-0.05 indicating association with high R were labeled with a white circle °. Wells with a cross indicate a correlation of 1 of the primer with itself (R=1, and significant). The legend represents the R values.

Organoid morphology is divers. Cystic organoids were characterized by circularly organized flat epithelial cells with a clear lumen. These organoids are typically undifferentiated with a high proliferative and self-renewal capacities [261, 262]. Thicker epithelial cells that have a columnar shape are referred to as columnar organoids. These organoids undergo both proliferation and differentiation. Their lumen can be either clear or filled with debris. Once debris has accumulated, the organoids release the intraluminal debris through a crater. Budding organoids are fully differentiated organoids that have both proliferative and differentiation capacities and exhibit protrusions of new crypts.

The morphology of organoids derived from control and tumor samples was quite diverse and could not be classified because many morphologies were present in a single sample. In some cases, the control organoids were more budding, indicating a more differentiated structure (1/4), while the tumor organoids also had budding and releasing structures, but most of them were cystic (1/2) or columnar (2/9). In Figure 3.22, a representative pair of organoids derived from control and tumor tissues from the same patient. While more budding organoids were seen in the control organoids in this section, the organoids from the tumor tissue were more columnar. Both had larger organoids filled with apoptotic cells or debris and therefore have a darker core.

Pooling all data was necessary because it was difficult to culture control organoids and

tumor organoids from the same patient. However, the difference between the more differentiated organoids from the control biopsy compared with the tumor biopsy was better seen when only paired samples were compared. Although individual differences were more present in the stem cell and differentiation marker of control organoids. Expression levels of stem cell marker tended to change in tumor, i.e., Lgr5 (1.3-fold increase, ns) and Olfm4 (0.54-fold decrease, p=0.05). That tumor loses differentiation and prevents stem cell status was observed by the significant decrease of TFF1 by 88 % (p<0.001) compared to the paired control. The other differentiation markers did not decrease significantly (KRT20 0.63-fold, FABP1 0.25-fold, CA2 0.63-fold, ALPI 0.78-fold, MUC2 0.97-fold reduction) (Figure 3.22 B). Comparison of CerS level in organoids with paired samples revealed no change in CerS isoforms, only CerS4 level increased by 1.39-fold (p<0.0001). However, data distribution of the control organoids indicated that in patients CerS4, CerS5 and CerS6 had stronger individual differences than the other CerS isoforms (Figure 3.22 C).

The discrepancies in one patient were not only between the control and the tumor, but also between the tumor types. An adenocarcinoma and another colon tumor were dissected from the patient #23. Isolations of organoids from control tissue did not work, so only the two tumors organoids were compared from this patient. Already the morphology of the two tumor organoids was different. Many cystic organoids with a high proliferation and self-renewal capacity arose from #23 1. While in the organoids derived from the tumor tissue, there were more columnar and budding organoids (#23 2) in passage 1 (Figure 3.23 A). Already between tumor types from the same patient, CerS expression levels were different despite CerS2. CerS1 was 1.4-fold (p=0.0013), CerS2 (1.45-fold, ns), CerS3 1.47-fold (p=0.0002), CerS4 1.22-fold, (p=0.09), CerS5 1.52-fold (p=0.004) and CerS6 1.76-fold (p=0.026) (Figure 3.23 B).

To get a more accurate idea of the role of CerS in organoids, organoids derived from diverticulitis biopsies were stained because they were abundant in culture, very fast growing, and maintained for a long period of time. CerS antibodies were co-stained with occludin or claudin (CLDN)-4 and DAPI to gain better insight into the structural location of the enzymes. CerS2 was ubiquitously expressed throughout the cytoplasm. It would be expected to be found on membrane side as well, but that was not the case (Figure 3.24). CerS4 was more strongly expressed on the apical side of the cells, and co-expression of occludin indicated that this it was localized apically rather than basolaterally (Figure 3.25). CerS6 was mainly located in the cytosol and either on the nucleus or in the nucleus and compared to the other CerS the staining was fainter. Between the different organoids the localization was generally seen with different intensities in different patients (Figure 3.26).

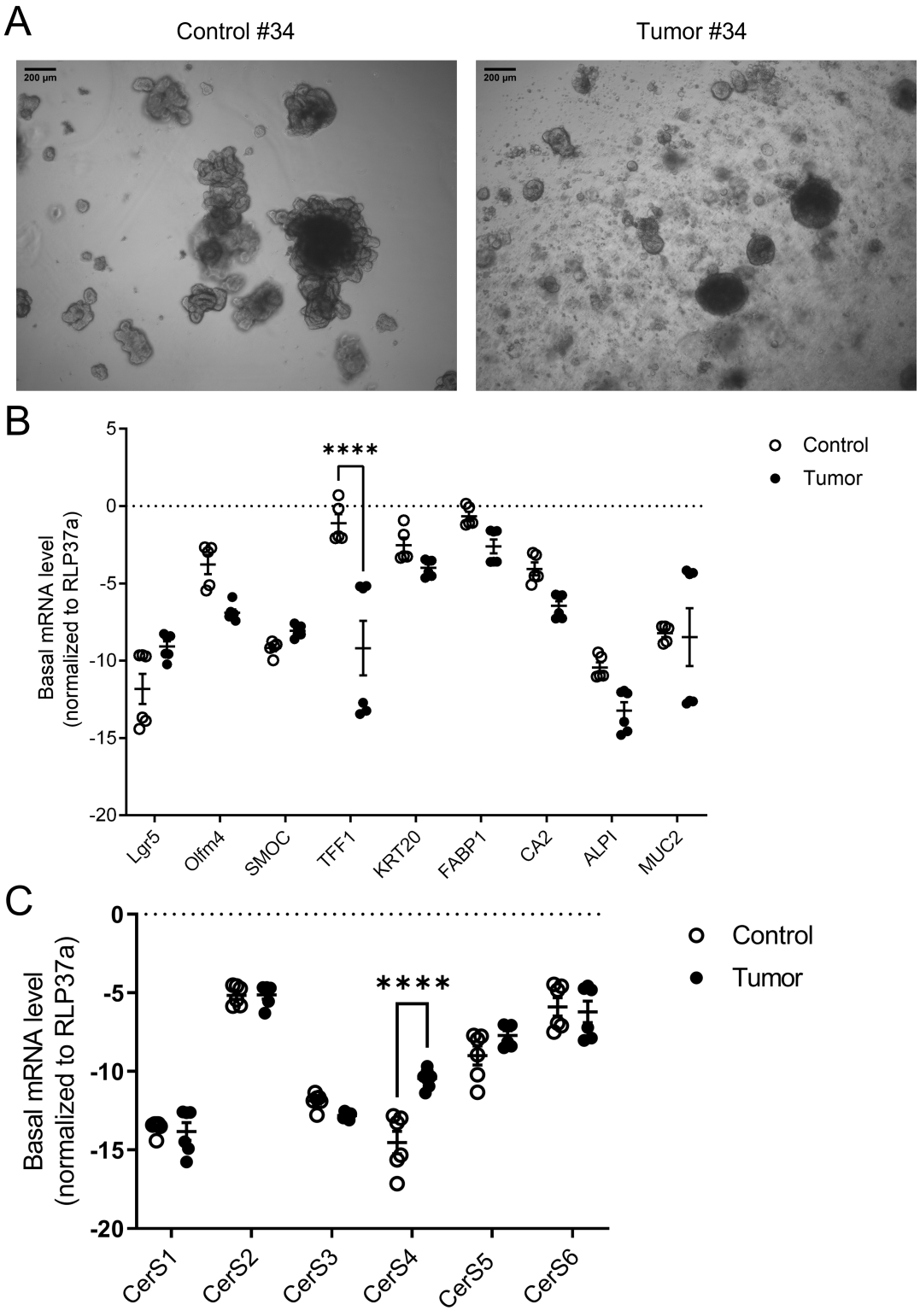

FIGURE 3.22: Organoids derived from control and tissue samples from the same patient were compared. (A) Representative transmitted light-field microscopy of organoids of passage 1 isolated from control and tumor tissue of patient No.34 after the cultivation period of 5 days (control organoids) and 7 days (tumor organoids). The scale bar is 200 µm. (B) Basal mRNA expression of stem cells and differentiation markers calculated as ΔCT value. (C) Basal mRNA expression of CerS1 to CerS6. Data are mean ±SEM, n=2.

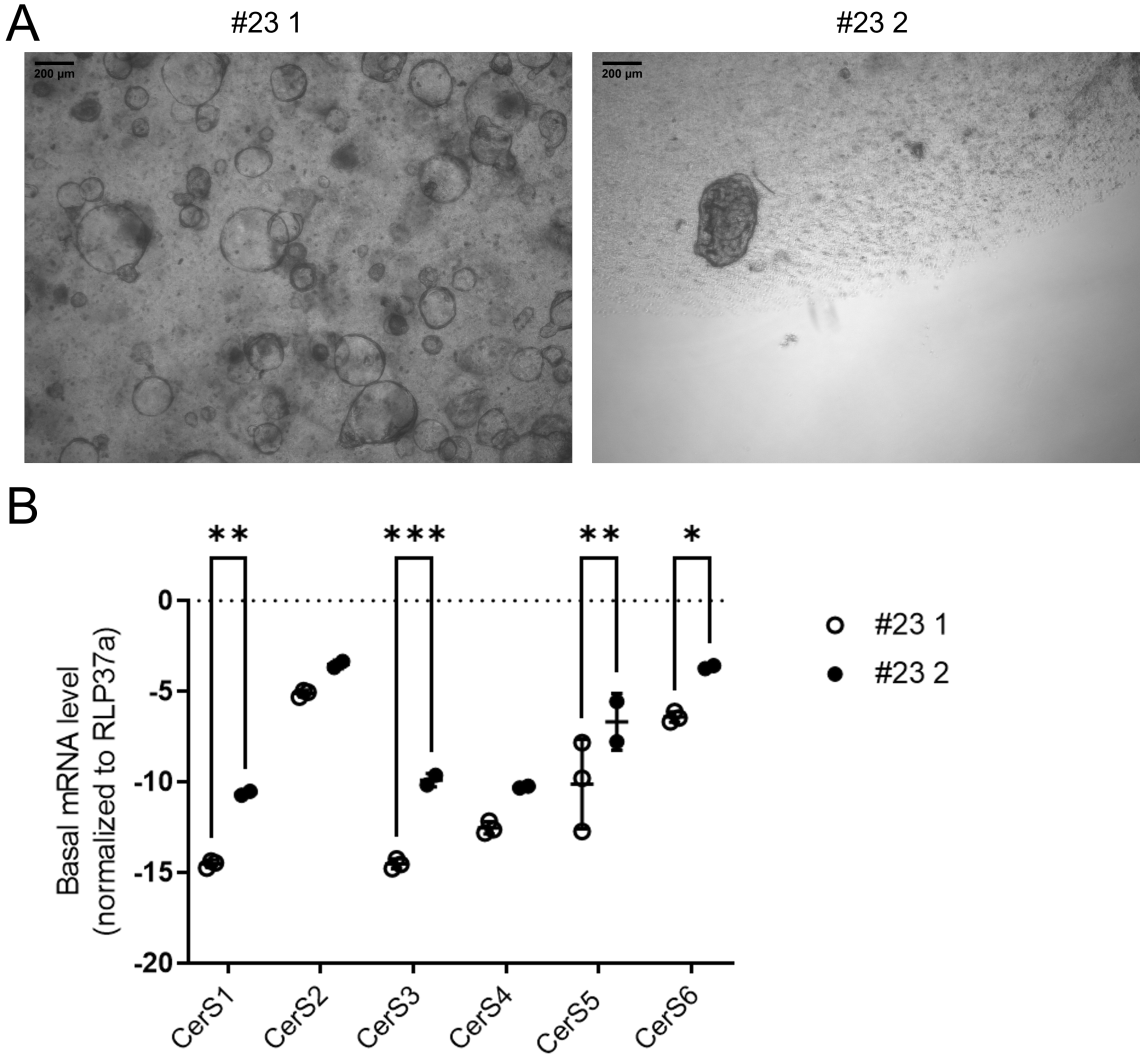

FIGURE 3.23: Tumor heterogenicity in one patient: Changes in morphology of organoids but also in CerS expression. (A) Representative phase contrast image of morphological differences between organoids isolated from two different tumors from the same patient. Scale bar 200 µm. (B) Basal mRNA level of Cers1 - CerS6 from two different tumors from the same sample (#23 1 adenocarcinoma and #23 2 tumor). Data are median ±CI95 and mean ±SEM, n=1.

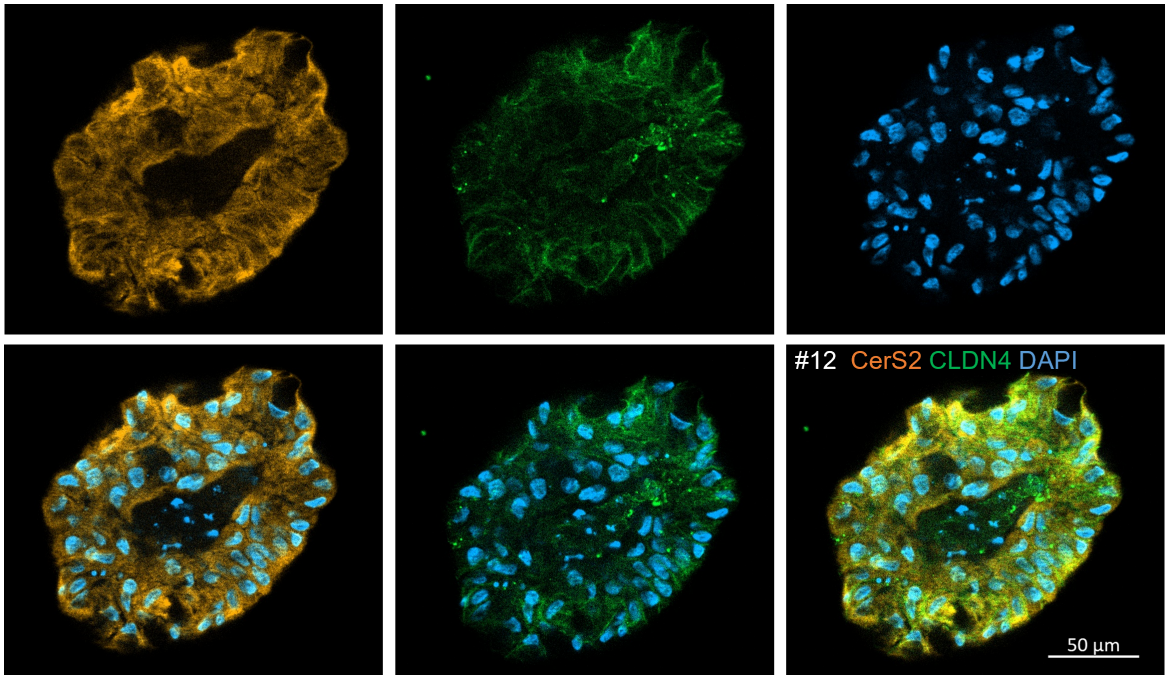

FIGURE 3.24: Immunofluorescence staining of CerS2 Cy3 (orange), claudin 4 (CLDN4)-Alexa Fluor® 488 (green) and DAPI (blue) in a patient-derived organoid. Images were taken using Axio Observer with an LD Plan-achromat 20x/0.3 lens. Scale bar in 50 µm.

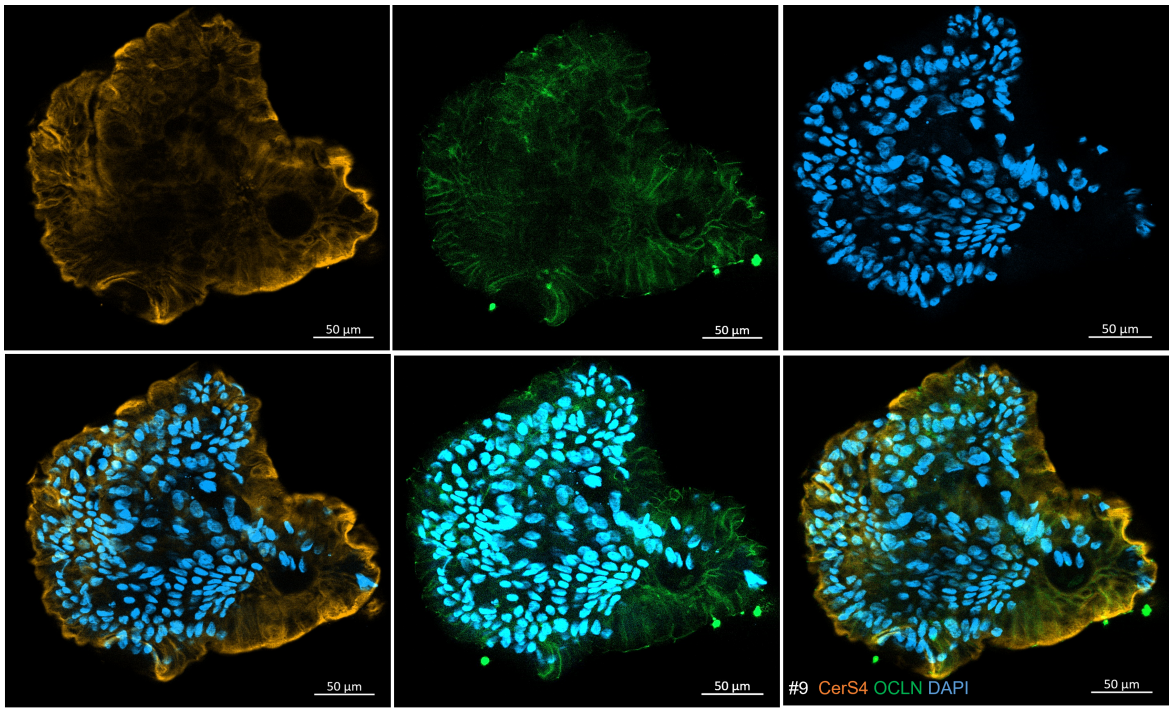

FIGURE 3.25: Immunofluorescence staining of CerS4 (Cy3-orange), occludin (OCLN) - (Alexa Fluor® 488-green) and DAPI (blue) in the organoid derived from patients. Images were taken using Axio Observer with an LD Plan-Achromat 20x/0.3 lens. Scale bar in 50 µm.

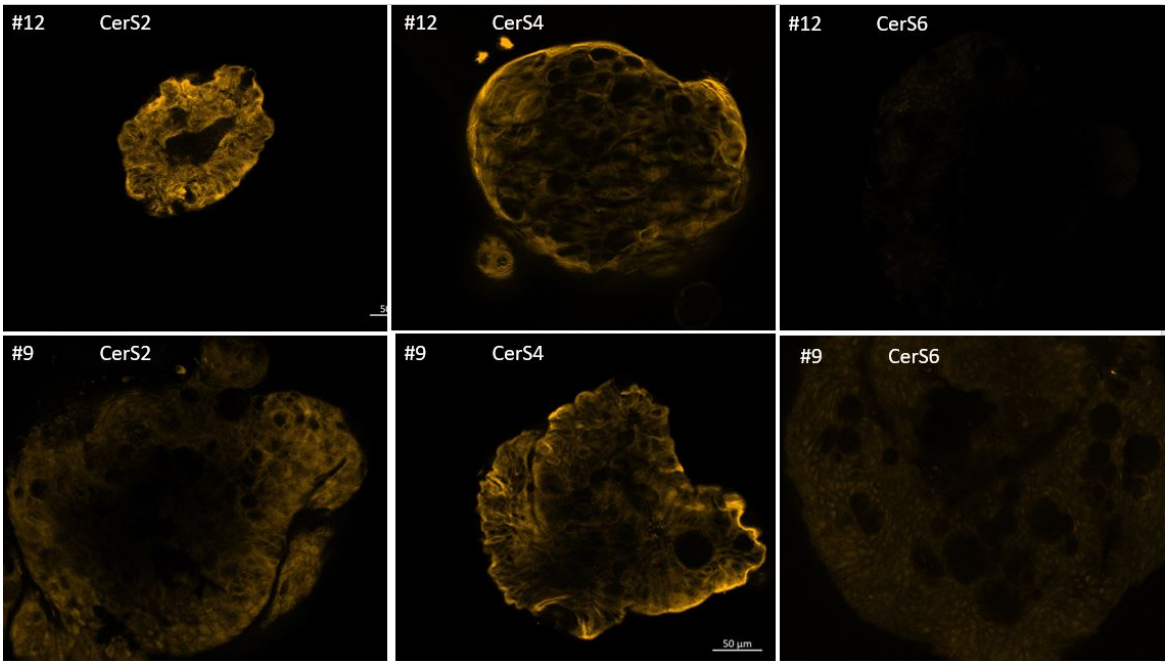

FIGURE 3.26: Immunofluorescence staining of CerS 2, CerS4 and CerS6 orange in the organoid derived from patients #9 and #12. Images were acquired using an Axio Observer microscope with an LD Plan-Achromat 20x/0.3 objective. Scale bar in $50\,\mu\mathrm{m}$.

3.5 Part III

3.5.1 Basal CerS and sphingolipid profile of HCT116 cells, HCT15 cells and Caco-2 cells

Caco-2 cells, differed from HCT116 cells and HCT15 cells in morphology and growth behavior (Figure 3.27 A). Both HCT116 cells and HCT15 cells formed outgrowths, showed no contact inhibition, and grew quite rapidly, whereas Caco-2 cells were larger, exhibited marked contact inhibition, and, once confluent, shrank in size and presumably differentiated (Figure 3.27 A). These differences may also be associated with a different CerS expression profile. In general, CerS2 mRNA was the most abundantly expressed CerS in CRC cell lines, as previously observed in organoids or mouse tissues, followed by CerS6 mRNA and CerS5 mRNA expression. Finally, CerS1 mRNA and CerS3 mRNA were only weakly expressed (-10 and -14 ΔCT, respectively). Both HCT116 cells and HCT15 cells expressed 0.8-fold less CerS1 and CerS3 than Caco-2 cells (p=0.0083/0.065 and p=0.017/0.075, respectively), but exhibited a 1.3-fold increase in CerS2 (p=0.035/ns). CerS5 and CerS6 mRNA show similar expression levels between -6 and -9 ΔCT and no significant changes between the three cell lines. However, the most striking difference was the 0.75-fold decrease in CerS4 expression in HCT15 cells compared to Caco-2 cells (p=0.006) (Figure 3.27 B). Therefore, HCT15 cells was considered as a model cell line for CerS4 deficiency.

-

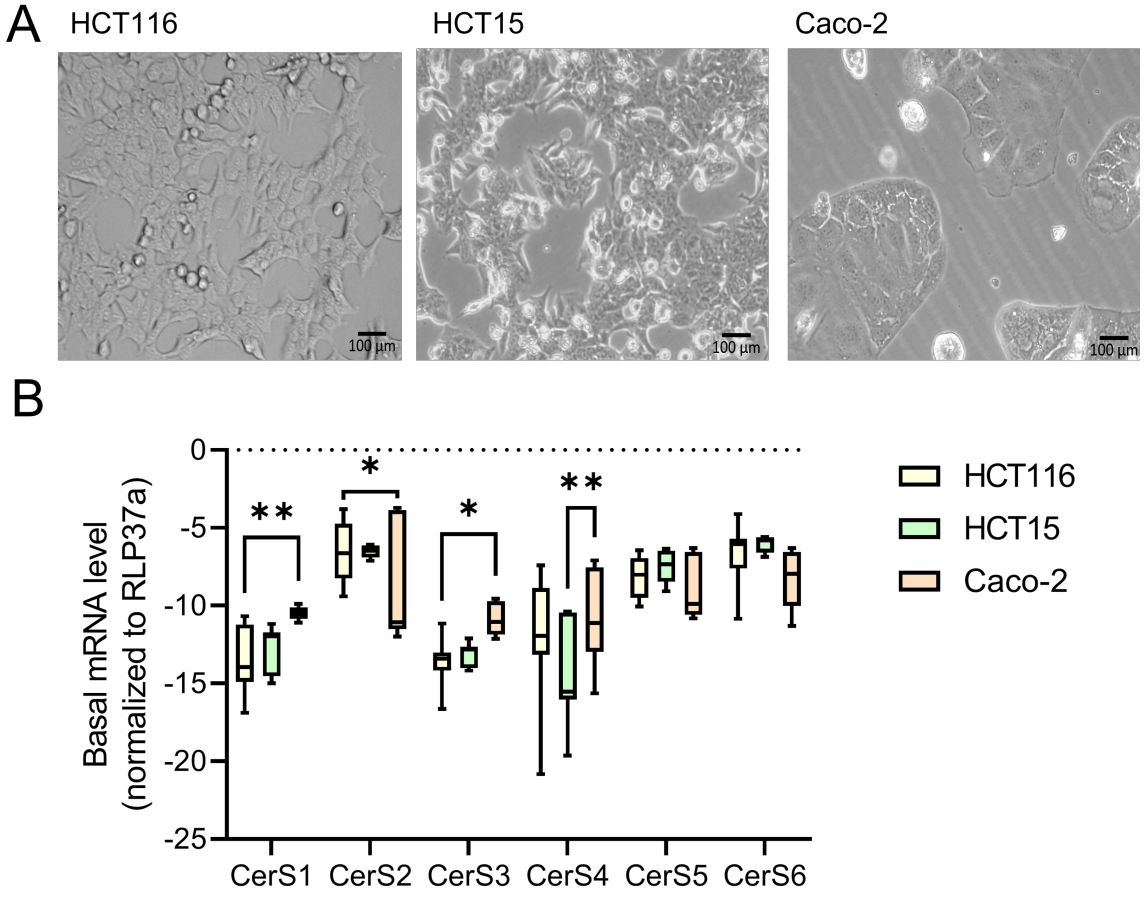

FIGURE 3.27: CRC cell lines examined in morphology and CerS expression: (A) Phase-contrast microscopy of non-confluent naïve HCT116 cells, naïve HCT15 cells and shNC Caco-2 cells 72 h after cell seeding. Scale bar, 100 µM. (B) Basal CerS mRNA expression shown in ΔCT values of naïve CRC cells normalized to RPL37A. Data are median ±CI95 from n=4 independent experiments. Statistical significance was assessed by two-way ANOVA/ Tukey's multiple comparison post-test. (* p<0.05, ** p<0.01, *** p<0.001, **** p<0.0001).

3.5.2 2D Cell line specific response to hypoxia

To exclude impairment due to chronic hypoxia exposure , the cell vitality was monitored using a CellTiterBlue® assay, in which living cells convert resazurin into the fluorescent product resorufin (Figure 3.28). Already the RFU levels of HCT116 cells and HCT15 cells were higher than Caco-2 cells (p<0.0001) and chronic hypoxic stimulation did not change the RFU values (p<0.0001 and p=0.0071) (Figure 3.28 B). With higher RFU, protein concentration also differed (Figure 3.28 C). Thus, calculating the cell viability showed no impairment of vitality by hypoxia, but it also showed that HCT116 cells have a higher metabolic capacity than Caco-2 cells (Figure 3.28 A).

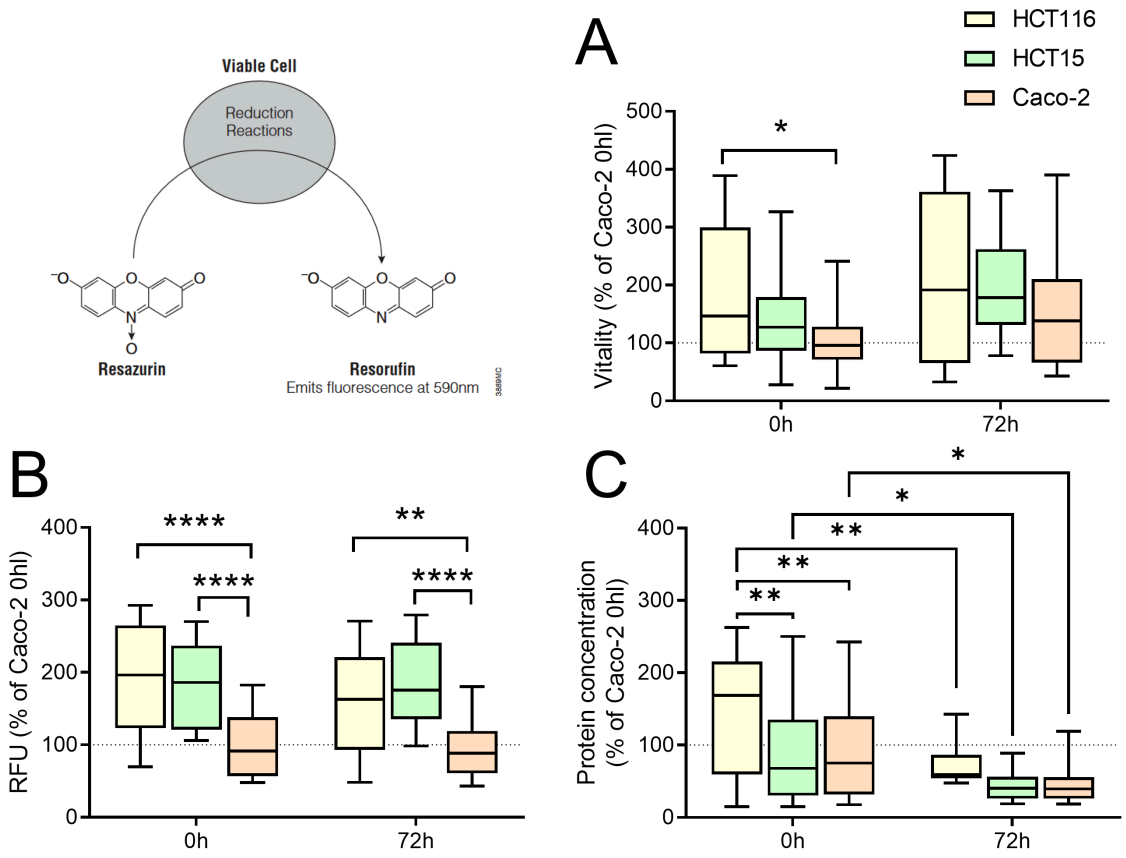

FIGURE 3.28: The viability of HCT116 cells, HCT15 cells and Caco-2 cells exposed to hypoxia for 72 h was determined using the CellTiterBlue® assay. A screenshot of the technical leaflet shows the theory of the measurement. Only viable cells can convert resazurin to resorufin, which in turn can be detected at 590 nm. (A). Cell viability was calculated by normalizing (B) RFU with (C) the protein concentration determined by the Bradford assay. All values were referenced to Caco-2 0 h (set as 100 %). Statistically significant differences were determined by one-way ANOVA with a Sidak's multiple comparison test: (* p<0.05, ** p<0.01,*** p<0.001,**** p<0.0001).

3.5.2.1 HIF1α regulation and metabolic adjustment

Already at basal levels, mRNA expression of PHD3 was increased by 1.22-fold in HCT116 cells compared to HCT15 cells (p=0.04) and Caco-2 cells (ns) (Figure 3.29 A1). However, PHD3 mRNA expression did not increase significantly in HCT116 cells, HCT15 cells and Caco-2 cells (Figure 3.29 A2). The 1.3- to 1.7-fold increase in PHD3 mRNA in CRC cells suggests feedback regulation probably by HIF1α. When CRC cells were cultured under hypoxia for 24 h, an increase of HIF1α was detected at protein level, and the highest expression was reached at 48 h. However, it decreased again after 72 h (Figure 3.29 B1). Detection of HIF1α in total protein lysate showed no difference between the response of Caco-2 cells and HCT116 cells to hypoxia. With increasing duration of hypoxic cultivation, HIF1α levels also increased (p=0.07), but after 48 h in HCT116 cells, HIF1α levels decreased after 72 h in HCT116 cells (p=0.0958), while those of Caco-2 cells and HCT15 cells were maintained. The increase in HIF1α protein level in the CerS4-deficient cell line, HCT15 cells, was much

lower than that in other CRC cell lines. After 48 h, HIF1α levels were significantly higher in HCT116 cells than in HCT15 cells (p=0.04), indicating that CerS4 may play a role in the HIF1α pathway (Figure 3.29 B).

To evaluate how the increase in cellular HIF1α upon hypoxia exposure also induced metabolic adaptation, mRNA expression of relevant metabolic enzymes GLUT1, PK, PDHA1 and LDHA was analyzed by qRT-PCR (Figure 3.30. Comparison of basal levels indicated that the three CRC cell lines did not differ in the mRNA expression of GLUT1, PK, PDHA1 (Figure 3.30 A). While GLUT1 had the lowest mRNA expression (p=0.0006 compared to PK, p=0.0175 to PDHA1 and p=0.0006 compared to LDHA), LDHA and PK were the most abundant and both tended to be more highly expressed than PDHA1 (p=0.077). Comparison of LDHA mRNA also showed a trend towards increased LDHA expression in HCT116 cells compared to Caco-2 cells (Figure 3.30 A). Hypoxia partially altered mRNA expression. The differences in GLUT1 mRNA expression increased at 24 h and 48 h and were higher in Caco-2 cells compared to HCT116 cells and HCT15 cells (24 h p=0.0018, p=0.0052; 48 h p=0.0041, p=0.04). At 72 h, GLUT1 levels decreased and were as high as the other CRC cell lines, indicating that Caco-2 cells increase the energy production in hypoxia by increasing glucose transport to the cells. Whether the increased glucose uptake is also translated into increased glycolysis could not be determined at the mRNA level. PK levels increased in HCT116 cells at 48 h and 72 h compared to HCT15 cells (p=0.03, p=0.0015) and Caco-2 cells (p=0.055, p=0.013). In addition to increased PK mRNA, LDHA mRNA also increased in HCT116 cells at 48 h and 72 h. LDHA mRNA levels in HCT116 cells were higher than in HCT15 cells (p=0.03, p=0.04) and Caco-2 cells (p=0.06, p=0.09) at both 48 h and 72 h. PDHA1 mRNA expression varied by up to 20 % but did not change significantly upon hypoxia or between the CRC cell lines (Figure 3.30 B). In summary, HCT15 cells showed no significant changes at the mRNA expression level, whereas Caco-2 cells increased Glut1 mRNA and HCT116 cells increased PK and LDHA expression level upon hypoxia (Figure 3.30 A).

3.5.3 Hypoxic effect on CerS mRNA expression level

As described previously, the expression of CerS isoform was variable (Figure 3.27). The CerS1 mRNA level of Caco-2 cells was approximately 1.2-fold higher than that of HCT116 cells and HCT15 cells. This difference was maintained during hypoxia stimulation, but CerS1 levels in the CRC cell lines did not change significantly due to hypoxia (Figure 3.31 A). CerS2 mRNA level was expressed more in HCT15 cells than in Caco-2 cells (p=0.013). Upon hypoxia, the CerS2 levels did not change significantly and remained in a range between 0.8- and 1.3-fold change, but the difference between the cell lines decreased (Figure 3.31 B). Expression of CerS3 was similar to that of CerS1: both had low basal mRNA levels and with highest expression level in Caco-2 cells (p=0.01, p=0.009). After hypoxia no significant changes could be detected at 48 h and 72 h (Figure 3.31 C). As described previously CerS4 mRNA level differed between CRC cell lines. In HCT15 cells CerS4 expression was barely detectable and decreased even further under hypoxia (p=0.002-0.001) (Figure 3.31 D). Hypoxia induced reduction of CerS4 expression in HCT15 cells, HCT116 cells

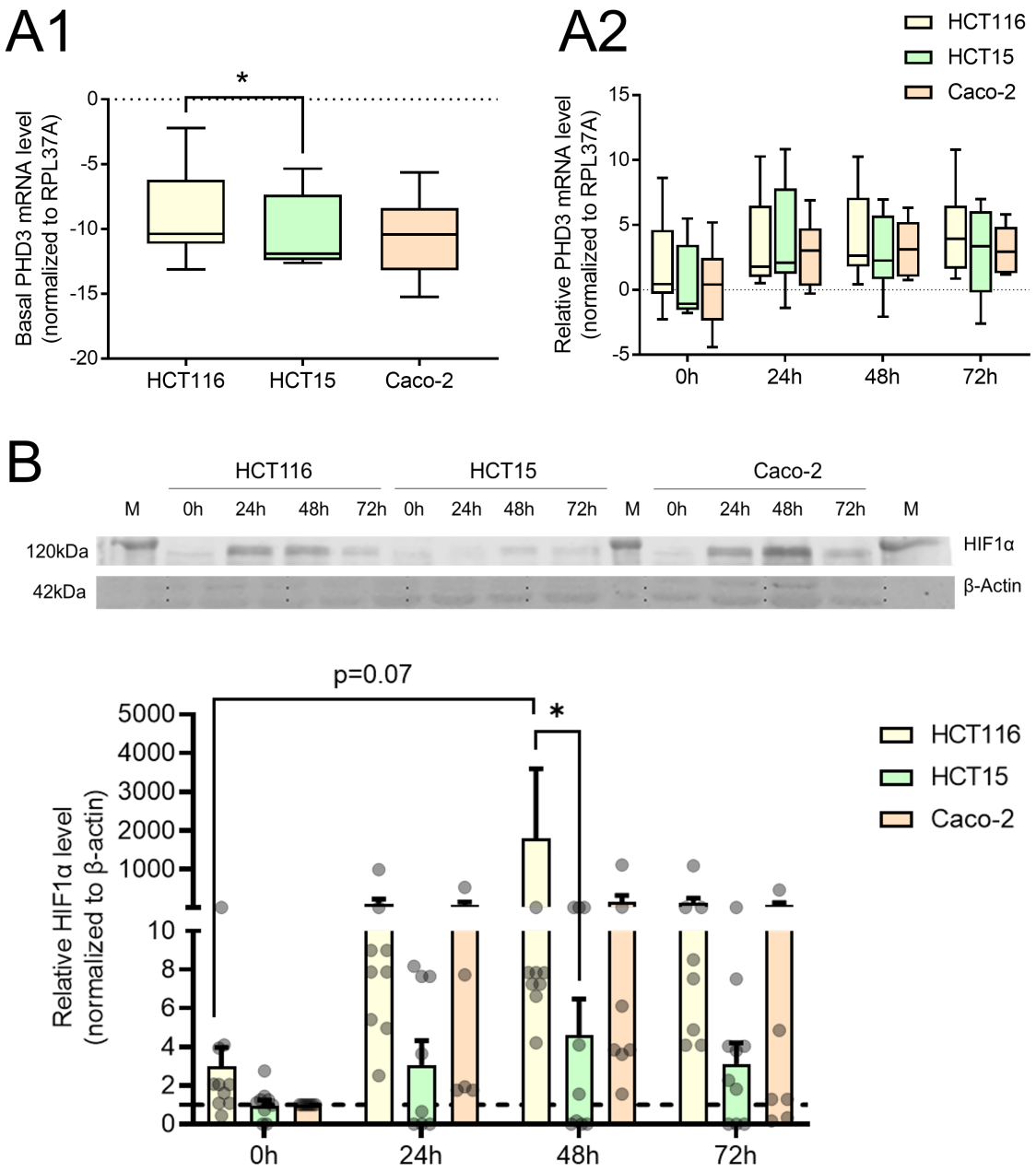

FIGURE 3.29: Differential rise in HIF1α protein expression in CRC cell lines to hypoxia. (A1) Basal cellular mRNA level of PHD3 shown as ΔCT values of HCT116 cells, HCT15 cells and Caco-2 cells. (A2) Cellular mRNA level of PHD3 was calculated as a relative expression (ΔΔCT) by normalization to the housekeeping gene RPL37A and the untreated Caco-2 cells. Caco-2 cells show a tendency to elevated PHD3 levels upon hypoxia exposure. (B) Western Blot analysis of HIF1α protein level in whole cell extracts from HCT116 cells, HCT15 cells and Caco-2 cells exposed to hypoxic conditions for 24 h to 72 h, normalized against β-actin expression and compared with untreated Caco-2 cells. Data of n=3-4 shown as median ±CI95 or interleaved scatter dot plot as mean ±SEM from 3 independent experiments. Statistically significant differences between cell lines were determined by two-way ANOVA with a Tukey's multiple comparison post-test (* p<0.05).

and Caco-2 cells. Whereas in HCT15 cells and HCT116 cells the significant reduction was detectable after 24 h, in Caco-2 cells it decreased significantly after 72 h. Thus, the significant

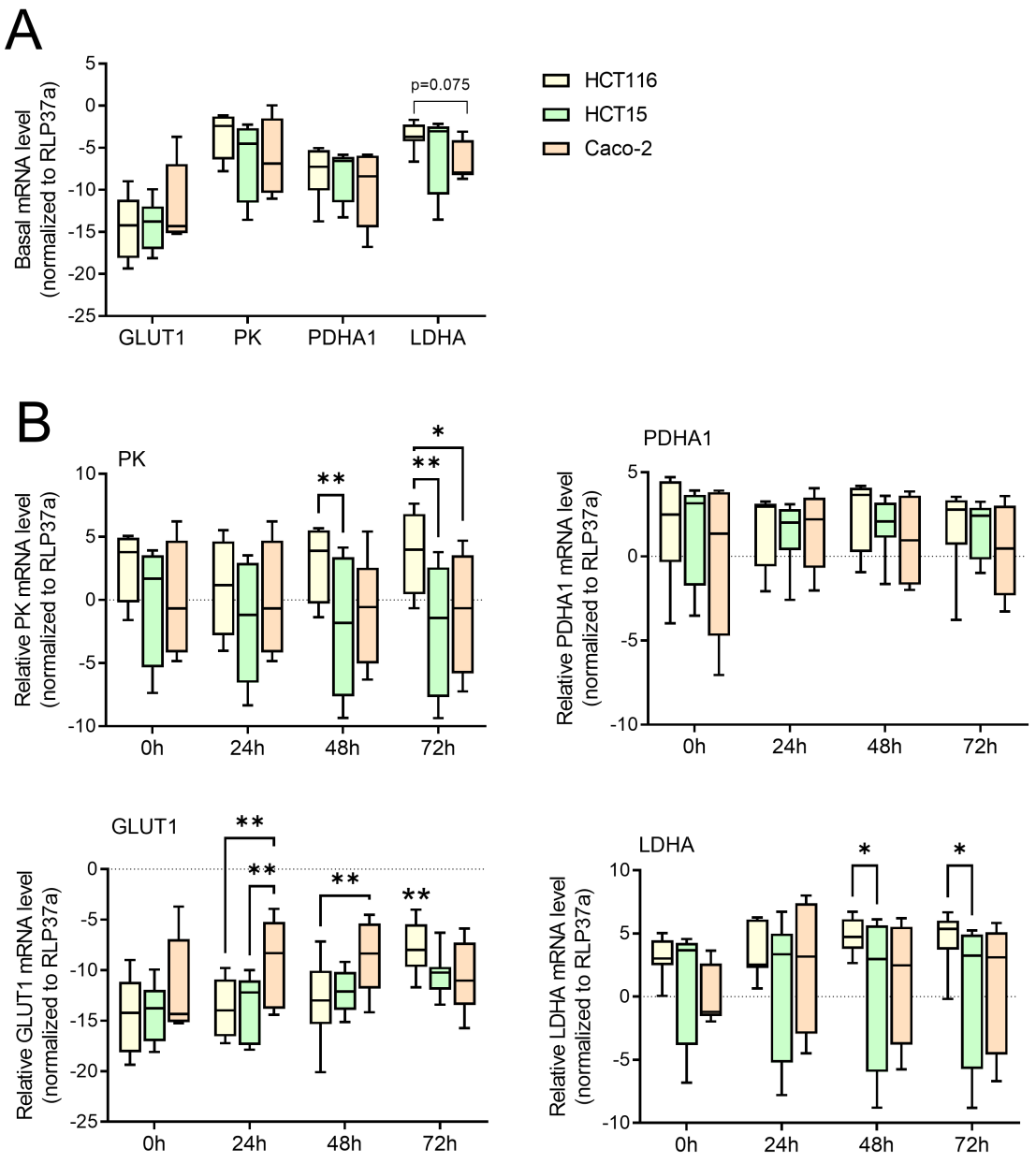

FIGURE 3.30: Differential metabolic responses of CRC cell lines to hypoxia. (A) Basal expression levels of GLUT1, PK, PDHA1 and LDHA in CRC cell lines. (B) HCT116 cells (HCT116), HCT15 cells (HCT15) and Caco-2 cells (Caco-2) were exposed to hypoxia for 24 h, 48 h and 72 h. Relative mRNA expression levels were computed as relative expression values ($\Delta\Delta$CT) by normalizing to housekeeping gene RPL37A and untreated Caco-2 cells (set to 0). Data from 3-4 independent experiments plotted as median ±CI95. Statistically significant differences between 3 different cell lines were determined by two-way ANOVA with a Tukey's multiple comparison post-test (* p<0.05, ** p<0.01).

difference between HCT116 cells and Caco-2 cells at 24 h (0.25-fold change, p=0.0013) diminished at later time points (Figure 3.31 E). Upon hypoxia, CerS5 mRNA level decreased only in HCT116 cells at 24 h (0.06-fold change, ns), 48 h (p=0.0049) and at 72 h (p=0.0016) compared to control HCT116 cells (Figure 3.31 F). CerS6 mRNA levels varied 0.8- to 1.2-fold upon hypoxia, and no significant differences were observed between the CRC lines

(Figure 3.31 G).

3.5.4 3D Cell line specific response to hypoxia

In a previous work of our group, the tumorigenic potential of CRC cell lines was investigated using a xenograft model. The growth of the CRC lines already differed in the xenograft tumor model. While the xenograft tumor volume of HCT116 cells was about $400\,\mathrm{mm}^3$ postmortem, the xenograft tumors of Caco-2 cells were about $100\,\mathrm{mm}^3$ and HCT15 cells about $600\,\mathrm{mm}^3$ [263]. This suggests that in xenograft model metabolic adaptation of CRC cell lines might influence the xenograft growth and should also be considered from a 3D perspective. Therefore, CRC cell lines were cultured in Matrigel, and a single clone grew into a 3D colony in the form of a spheroid-like structure. And since the CRC cell lines were phenotypically different in the 2D culture, this was also the case in 3D culture. The lost contact inhibition of HCT116 cells was also observed in the 3D culture. The 3D colonies of HCT116 cells were enate (excess formation) and 5-fold larger than 3D cultures of HCT15 cells or 3D cultures of Caco-2 cells ($p<0.0001$) (Figure 3.32 A, B). The core was dark due to the filled apoptotic cells, as was the case with human organoid structure (Figure 3.22). Completely different was the growth of Caco-2 cells, which grew in an ordered, clear, spherical structure. HCT15 cells grew in Matrigel as a mixture between Caco-2 cells and HCT116 cells, they did not enate, but their structure was also not as clearly outlined as Caco-2 cells. In contrast to the xenograft model, in which HCT15 cells had developed large-volume tumors, the 3D colonies were smaller than HCT116 cells (3.4-fold change, $p<0.0001$) (Figure 3.32 A, B). After one week of culture, 3D cultures were cultured under hypoxic conditions for up to $72\,\mathrm{h}$. Measurement of the area after hypoxic stimulation had no effect on the growth of Caco-2 cells (Figure 3.32 C).

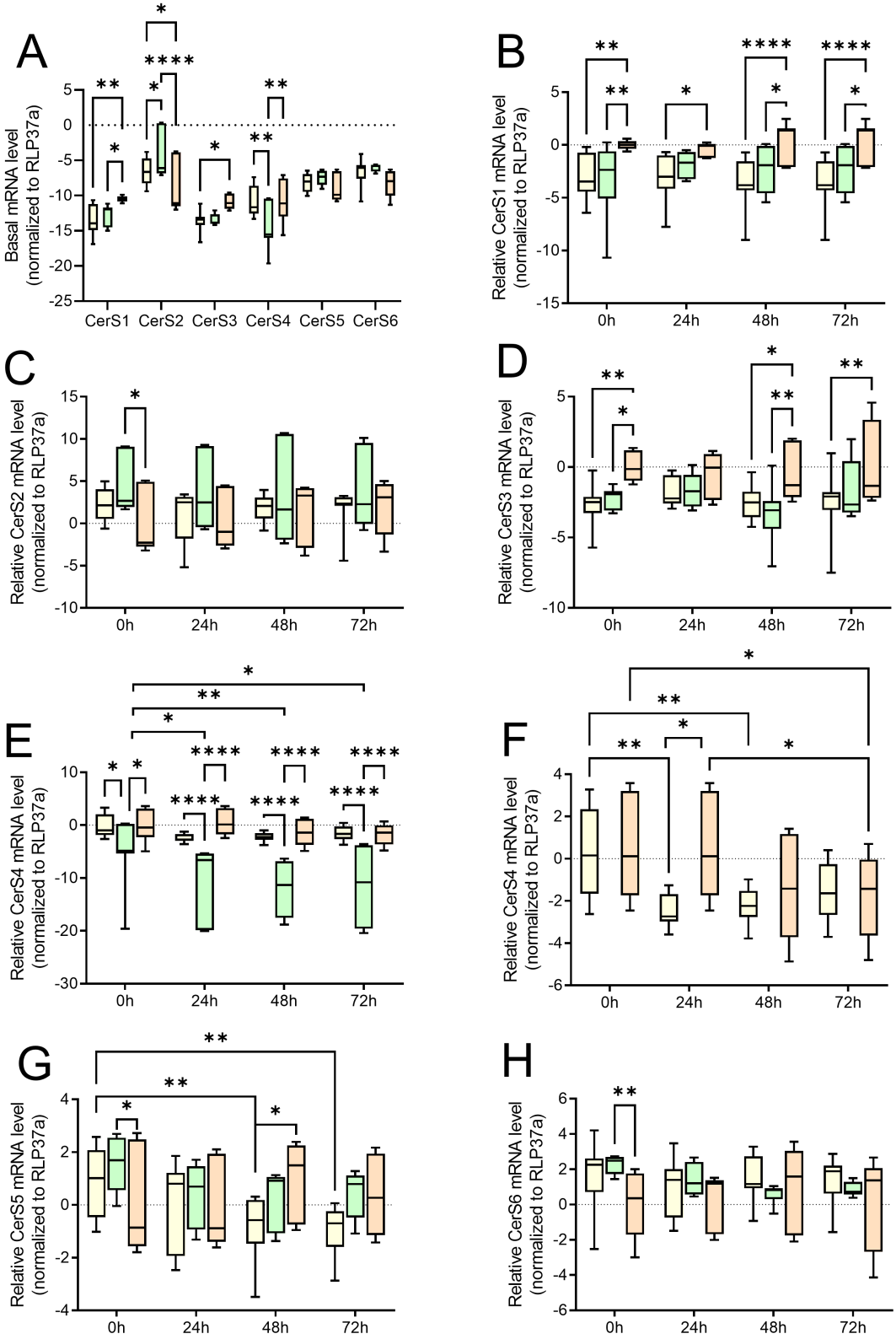

FIGURE 3.31: Hypoxia induced downregulation of CerS4 mRNA and Cers5 mRNA expression, respectively. (A) Basal cellular CerS1 - CerS6 mRNA levels in untreated HCT116 cells (HCT116), HCT15 cells (HCT15) and Caco-2 cells (Caco-2) were determined by qRT-PCR and calculated as ΔCT normalized to RPL37A. (B-H) Relative cellular CerS1 - CerS6 mRNA levels were calculated as ΔΔCT values by normalization to housekeeping gene RPL37A and Caco-2 0 h (set to 0). Data are median ±CI95 of n=3 to 4 independent experiments. Statistically significant differences between three different cell lines were determined by two-way ANOVA and Tukey's multiple comparison test (* $p<0.05$, ** $p<0.01$).

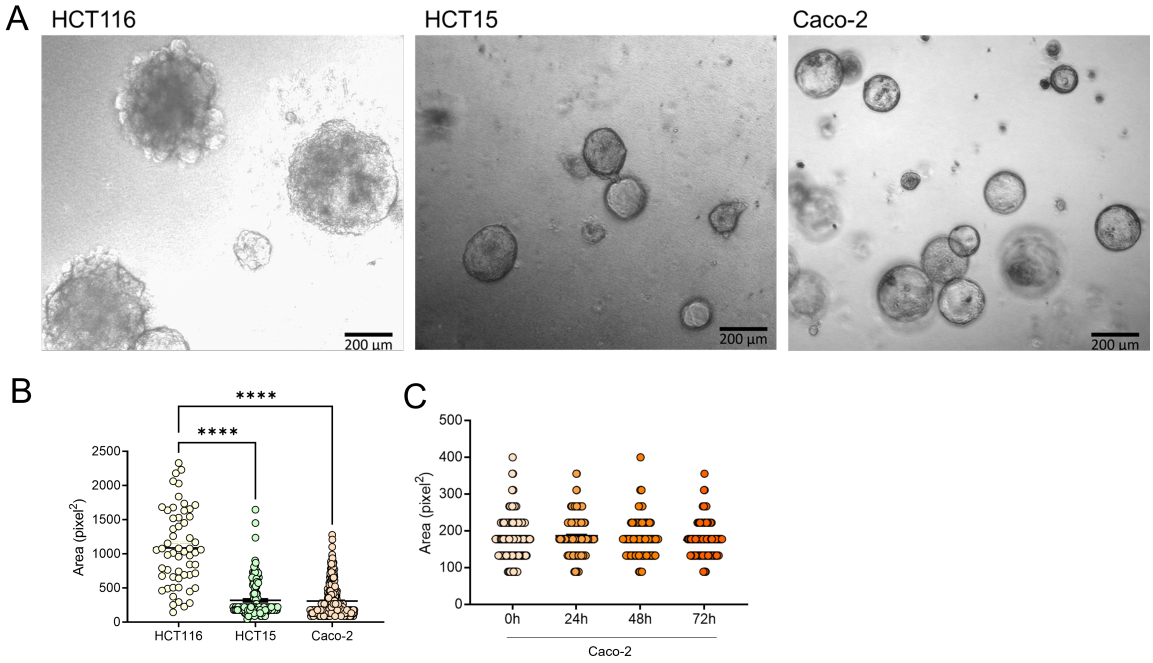

FIGURE 3.32: 3D-Culturing of CRC cell lines HCT116 cells (HCT116), HCT15 cells (HCT15) and Caco-2 cells (Caco-2) in Matrigel results in a different phenotypic outcome. (A) Phase contrast image of HCT116 cells, HCT15 cells and Caco-2 cells cultured in 3D for 10 days. Phase contrast images were acquired using Axio Primovert inverted microscope with Plan-Achromat 4x/0.10 objective. Scale bar $200\,\mu\mathrm{m}$. (B) Cell area of 3D cultured cells were determined manually with FIJI analyze tool. Data are shown in mean ±SEM. A statistically significant difference between cell areas was determined by one-way ANOVA and a Tukey's multiple comparison post-test. (C) 3D grown cell lines were incubated under hypoxic conditions for $24\,\mathrm{h}$, $48\,\mathrm{h}$ and $72\,\mathrm{h}$. Statistical difference of the cell area was determined by one-way ANOVA and a Dunnett's multiple comparison test.

3.5.4.1 HIF1α regulation and metabolic adjustment

To analyze whether chronic hypoxia affects the viability of the 3D cultures, the same assay as in subsection 3.5.2) was performed. Based on the protein isolation, viability showed some discrepancies but did not differ between CRC cell lines at both $0\,\mathrm{h}$ and $72\,\mathrm{h}$ hypoxia. This indicates that hypoxia did not tarnish the metabolic capacity of the 3D cultured cells even after $72\,\mathrm{h}$ of hypoxia (Figure 3.33 A).

The mRNA level of PHD3 in HCT15 cells, HCT116 cells and Caco-2 cells did not differ at basal level (Figure 3.33 B). Under hypoxia, PHD3 mRNA did not change significantly in CRC cell lines; only after $72\,\mathrm{h}$, HCT116 cells had higher PHD3 mRNA expression than Caco-2 cells (Figure 3.33 C).

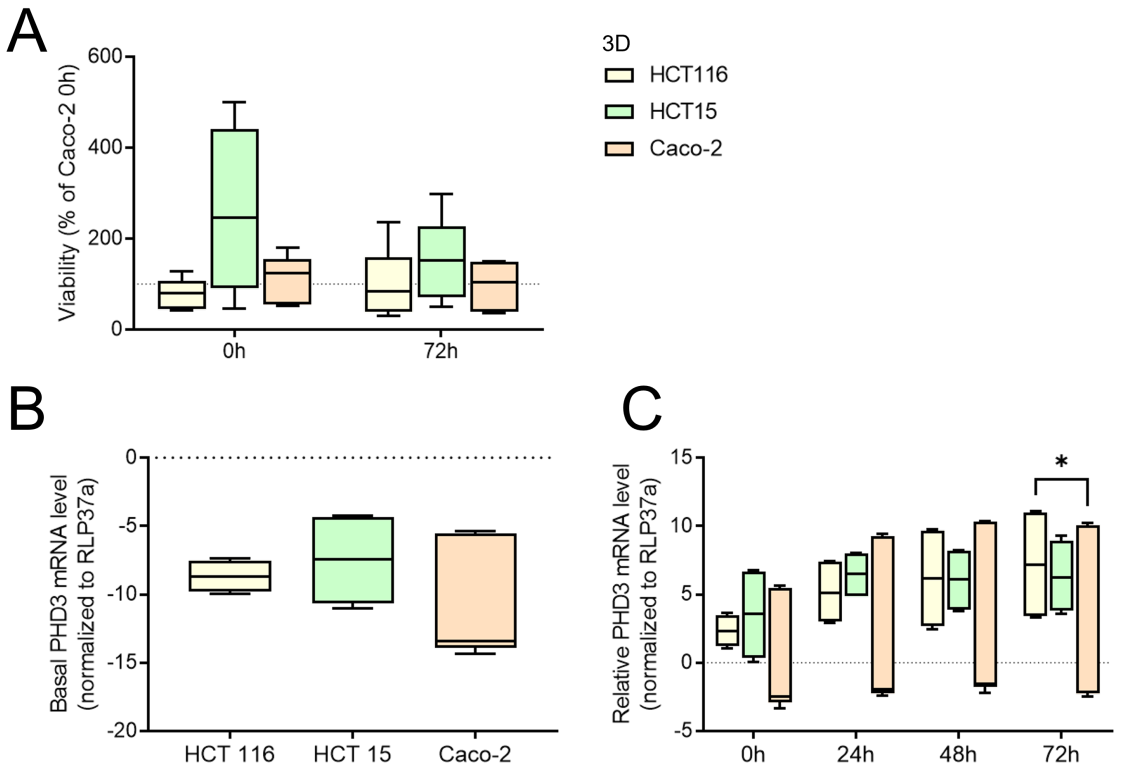

FIGURE 3.33: Cultivation of CRC lines in 3D and the hypoxic influence on the cell viability and mRNA level of the O_2- responsive enzyme PHD3. (A) Cell viability of 3D cells under normoxia and $72\,\mathrm{h}$ hypoxia was referenced to control Caco-2 cells at $0\,\mathrm{h}$ (set as $100\,\%$). (B) Basal cellular PHD3 mRNA levels in ΔCT were determined after normalization to housekeeping gene RPL37A. (C) Relative mRNA levels of PHD3 after normalization to control Caco-2 cells $0\,\mathrm{h}$ (set as 0). Data are median $\pm$CI95 of n=3-4 independent experiments. Statistically significant differences were determined by two-way ANOVA or one-way ANOVA and Tukey's multiple comparison test: (* $p<0.05$).

To determine whether the morphological differences also had an effect on metabolism, the mRNA levels of GLUT1, PK, PDHA1 and LDHA from control 3D cultures of CRC cell lines were compared. No significant difference was found at the mRNA level in two 3D cultures HCT116 cells and HCT15 cells (Figure 3.34 A). A basal difference was already detected in the 2D culture: Caco-2 cells had slightly higher GLUT1 levels and lower levels of

PK and LDHA compared with HCT116 cells (see Figure 3.30 A). Culturing the cells in Matrigel altered the expression of metabolic enzymes. The larger 3D colonies of HCT116 cells had significantly higher mRNA levels of GLUT1 and PK but did not differ in PDHA1 and LDHA levels (Figure 3.34 A). The comparison of 2D and 3D culture suggested that HCT116 cells in 3D culture could increase glycolysis more compared with Caco-2 cells. Next, it was analyzed how environmental hypoxia alters the metabolic pathway of cells, even some 3D cultures may suffer from hypoxic conditions in their inner core. Upon hypoxia, GLUT1 mRNA levels increased in HCT15 cells and Caco-2 cells at $72\,\mathrm{h}$. 3D cultures of HCT116 cells already showed higher GLUT1 levels, which were significantly higher than in 3D cultures of HCT15 cells not only at baseline but also after $48\,\mathrm{h}$. The increase in GLUT1 mRNA in 3D cultured Caco-2 cells also exceeded the GLUT1 mRNA of 3D cultured HCT15 cells after $48\,\mathrm{h}$ and $72\,\mathrm{h}$ of hypoxic exposure (Figure 3.34 B). Higher GLUT1 mRNA levels could indicate higher translation of the glucose transporter and thus induce a higher glycolysis metabolism. Analysis of the last key enzyme of the glycolysis, PK, showed that 3D cultured HCT116 cells indeed had more PK mRNA levels compared to 3D cultured Caco-2 cells (p=0.025) (Figure 3.34 B). The difference between 3D cultured HCT116 cells and 3D cultured HCT15 cells even increased up to a 6-fold change (p=0.0125) after $72\,\mathrm{h}$ of hypoxia. Hypoxic stimulation did not change PDHA1 mRNA levels of 3D cultured HCT116 cells, HCT15 cells and Caco-2 cells. As in 2D culture (see Figure 3.30 A), LDHA mRNA increased in the 3D culture under hypoxia. Whereas in 2D culture only HCT116 cells showed a significant increase of LDHA mRNA, in 3D culture both HCT116 cells and Caco-2 cells significantly increased LDHA mRNA (Figure 3.34 B). This suggests that cells such as HCT116 cells, which might suffer from internal hypoxia, also elicit LDHA signaling in response to external hypoxia, as did all other 3D cultured CRC cells exposed to external hypoxia. In summary, PDHA did not change under hypoxia in 3D cultures, whereas the other enzymes either increased or did not increase, depending on the 3D cultured CRC cell line. Chronic hypoxia resulted in the maintenance of GLUT1 and PK levels in 3D cultured HCT116 cells, which already had high expression of these enzymes at basal expression level. After hypoxia, LDHA mRNA levels also increased significantly in 3D cultured HCT116 cells. In 3D cultured Caco-2 cells and HCT15 cells, chronic hypoxia resulted in an increase in mRNA expression of GLUT1 and LDHA.

So far, the 3D culture seems to enhance the hypoxic effect. To analyze whether the 3D system also had an effect on CerS isoforms, the basal level of the 3D control cultures was compared and showed a significant difference only for CerS4. As in 2D culture, CerS1, CerS3, and CerS4 mRNA level had low expression levels (CerS1 mRNA $-10\ \pm 1.9\ \Delta$CT, CerS3 mRNA $-9.2\ \pm 4\ \Delta$CT, CerS4 mRNA $-9\ \pm 1.7\ \Delta$CT). Moreover, CerS2 mRNA was expressed twice as much ($-4.1\ \pm 2\ \Delta$CT), followed by CerS6 mRNA ($-5.6\ \pm 0.8\ \Delta$CT), CerS5 mRNA ($-5.6\ \pm 1.1\ \Delta$CT) in these 3D cultures. As seen in 2D and 3D culture, CerS4 deficient HCT15 cells had lower CerS4 mRNA than HCT116 cells (p=0.01) and Caco-2 cells (p<0.0001).

Hypoxia in the environment did not alter CerS1 or CerS2 mRNA expression in all three CRC cell lines Figure 3.36). In contrast to 2D culture of HCT116 cells, in 3D culture CerS3

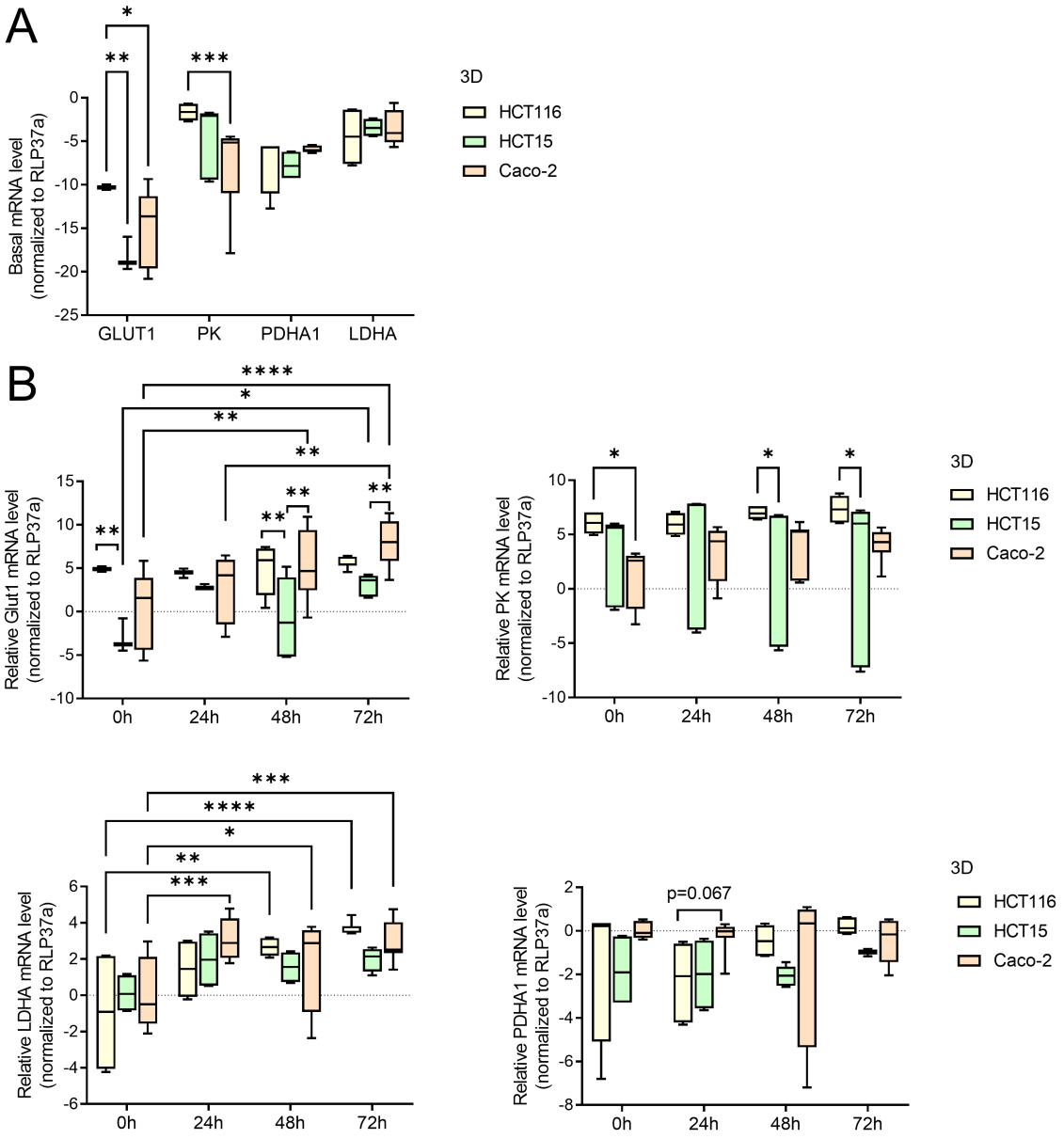

FIGURE 3.34: Metabolic changes in 3D cultures during ambient hypoxia. The 3D culture of CRC cell lines HCT116 cells (HCT116), HCT15 cells (HCT15) and Caco-2 cells (Caco-2) were cultured in Matrigel for 7 days and exposed to hypoxia for 24 h, 48 h or 72 h. (A) Basal cellular mRNA expression levels were determined by qRT-PCR and normalized to the housekeeping gene RPL37A. (B) Relative mRNA expression after hypoxia exposure was calculated by normalization to the housekeeping gene RPL37A and control Caco-2 cells (Caco-2 0 h set as 0). Data are median ±CI95. Statistically significant differences between the untreated and hypoxia-exposed cell lines were determined by two-way ANOVA with Tukey's multiple comparison post-test (* p<0.05, ** p<0.01, *** p<0.001, **** p<0.0001).

levels were 3-fold higher than in HCT15 cells at 0 h and an additional 2.3 times higher than Caco-2 cells at 24 h. However, after 48 h, CerS3 levels decreased significantly (p=0.003) in HCT116 cells. 3D cultured HCT15 cells also reduced CerS3 levels by 0.3-fold (Figure 3.36). CerS4 level was comparable in 3D to 2D culture. The CerS4-deficient cell line HCT15 had much less CerS4 mRNA than HCT116 cells (p=0.001) or Caco-2 cells (p<0.0001). However,

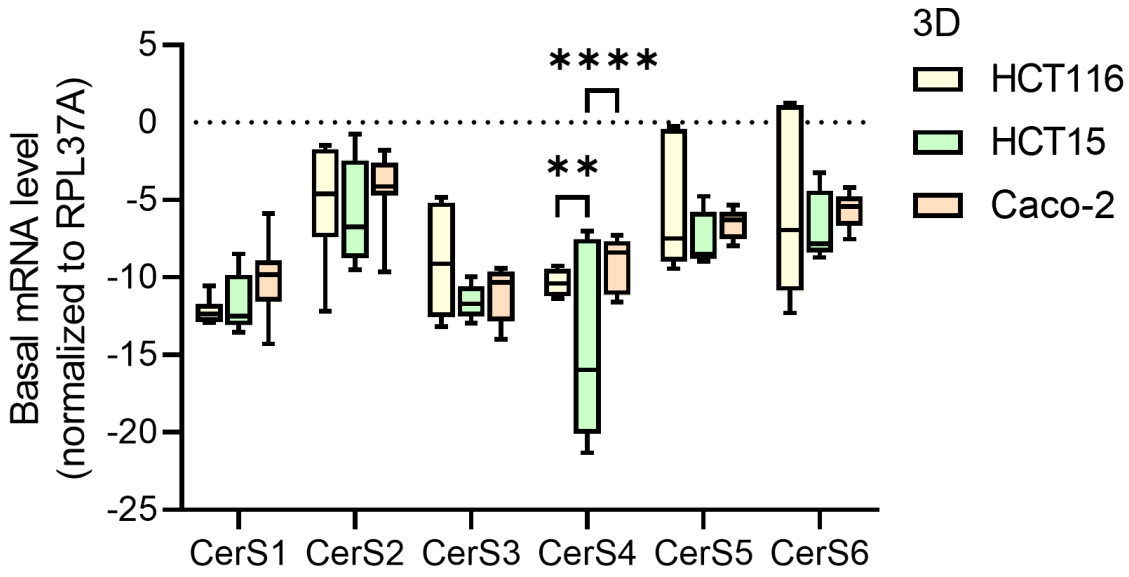

FIGURE 3.35: 3D cultures of HCT116 cells (HCT116), HCT15 cells (HCT15) and Caco-2 cells (Caco-2) differ in their CerS4 status. HCT116 cells, HCT15 cells and Caco-2 cells were cultured in Matrigel for 1 week and exposed to hypoxia for 24 h, 48 h and 72 h. (A) Basal mRNA levels of untreated 3D CRC cells were determined by qRT-PCR and calculated as ΔCT by normalization to the housekeeping gene RPL37A. Data are median ±CI95. Statistically significant differences between the untreated and hypoxia exposed cell lines were determined by two-way ANOVA with a Tukey's multiple comparison post-test (** p<0.01, **** p<0.0001).

CerS4 mRNA expression also decreased 0.8-fold in 3D cultured HCT116 cells after hypoxia. The difference in CerS4 mRNA levels also increased between 3D cultured Caco-2 cells and HCT116 cells at 48 h and 72 h (3-fold change and 11-fold change, p=0.015) (Figure 3.36). In contrast to 2D culture, 3D cultures of HCT116 cells had 1.3-fold higher CerS5 mRNA levels than 3D cultured HCT15 cells. In hypoxia, this difference was no longer observed, and only after 72 h 3D cultured Caco-2 cells had higher CerS5 expression than 3D cultured HCT15 cells. A similar pattern was observed for CerS6 mRNA levels. CerS6 mRNA level did not change under hypoxia, and only after 72 h CerS6 expression was significantly higher in 3D cultured Caco-2 cells than in 3D cultured HCT15 cells (Figure 3.36). In summary, CerS expression did not change under hypoxia in 3D cultured CRC cell lines, except for CerS3 mRNA.

Overall, analysis of naïve CRC lines in 2D culture showed a common reduction of CerS4 mRNA, even when CRC cells already had low CerS4 mRNA level, as in HCT15 cell line. In HCT116 cells, CerS3 and CerS5 mRNA levels additionally reduced after hypoxia (Figure 3.37 A). In response to hypoxia, GLUT1 mRNA levels and LDHA mRNA levels increased, particularly in 3D cultures, whereas PHD3 mRNA, PK mRNA and PDHA1 mRNA levels did not change significantly (Figure 3.37 B).

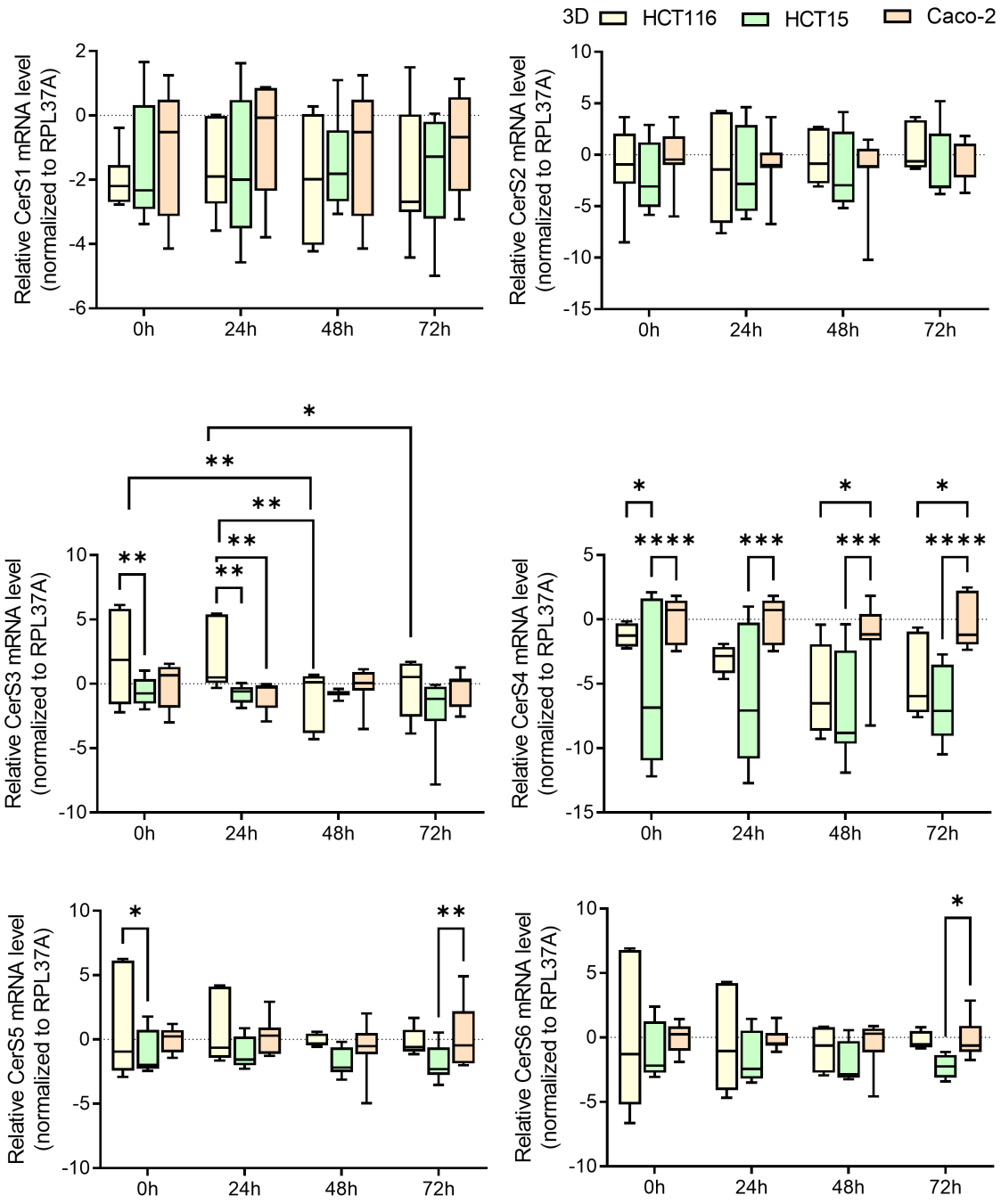

FIGURE 3.36: Hypoxia induced CerS4 and CerS5 downregulation in 3D culture of HCT15 cells and HCT116 cells, respectively. HCT116 cells (HCT116), HCT15 cells (HCT15) and Caco-2 cells (Caco-2) were exposed to hypoxia for 24 h, 48 h and 72 h. Relative cellular CerS1 - CerS6 mRNA levels were calculated as $\Delta\Delta$CT values by normalization to the housekeeping gene RPL37A and control Caco-2 cells (Caco-2 0 h set to 0). Data are median $\pm$CI95 from n=3 to 4 independent experiments. Statistically significant differences between three different cell lines were determined by two-way ANOVA and Tukey's multiple comparison post-test (* p<0.05, ** p<0.01, *** p<0.001, **** p<0.0001).

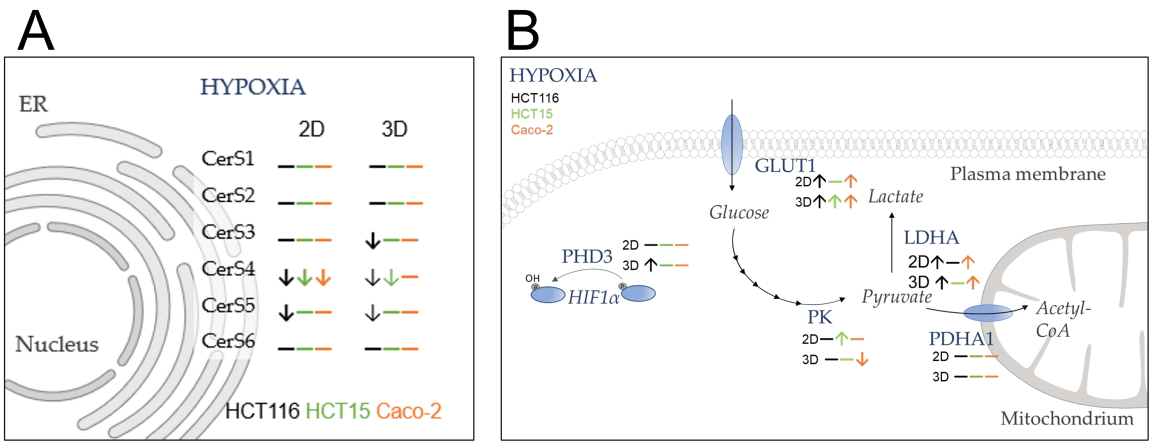

FIGURE 3.37: Comparison of 2D culture and 3D culture between HCT116 cells (black), HCT15 cells (green) and Caco-2 cells (orange). (A) indicates differences in CerS mRNA expression between the cell lines and (B) their response to hypoxia compared to 0 h of the respective cell line. Schematic overview of some metabolic responses to hypoxia. After glucose is transported by GLUT1, it is metabolized through many steps until PK catalyzes pyruvate. Under normoxia, pyruvate is metabolized to acetyl-CoA by PDHA1 and loaded into mitochondria. Under hypoxia, pyruvate is more likely to be metabolized to lactate by LDHA and transported out of the cell. This switch is mediated by HIF1α that is stabilized under hypoxia and act as a transcription factor after the inhibition of the PHD activity. Changes in mRNA expression upon hypoxia are indicated by arrows and stagnation is indicated by a line. Significant changes were marked with bold arrows.

3.5.5 Hypoxic response in CerS4 and CerS5 downregulated cells

So far, the data indicated a downregulation of CerS4 mRNA and partially CerS5 mRNA after hypoxia. CerS4 deficient cells responded more weakly to hypoxia-induced metabolic adaptation. Therefore, the potential influence of CerS4 or CerS5 expression on hypoxia induced metabolic adaptation was investigated using CerS4 and CerS5 downregulated HCT116 cells and Caco-2 cells cultured in 2D. CerS4 downregulation was significant in HCT116 cells (p=0.047) and Caco-2 cells (p=0.01) compared to shNC cell line. CerS5 mRNA was downregulated 0.84-fold (p<0.001) and 0.76-fold (p<0.0001) in HCT116 and Caco-2 cells, respectively (Figure 3.38 A, B). As seen in subsection 3.5.2, cells differed in mRNA expression levels of some CerS isoforms. At baseline, CerS1 mRNA expression was -14.43 $\pm$1.4 ΔCT in shNC HCT116 cells and -9.9 $\pm$2.7 ΔCT in shNC Caco-2 cells. The remaining CerS isoforms were similarly expressed in HCT116 cells and Caco-2 cells. The highest mRNA expression level showed CerS2 with -4.8 $\pm$1.4 ΔCT, followed by CerS6 with -5.7 $\pm$0.53 ΔCT, CerS5 with -6.9 $\pm$0.54 ΔCT, CerS4 with -11.42 $\pm$1.9 ΔCT and CerS3 with -12.56 $\pm$0.8 ΔCT (Figure 3.38 C).

In HCT116 cells, hypoxia itself did not increase CerS1 mRNA levels except after 48 h. Here, the difference in CerS1 mRNA expression between shCerS5 HCT116 cells was higher than in shNC HCT116 cells or shCerS4 HCT116 cells after 48 h (Figure 3.39). In contrast, hypoxia decreased CerS2 mRNA expression in in shCerS4 HCT116 cells at 72 h (p=0.02) and in shCerS5 HCT116 cells at 48 h and 72 h (p=0.002 and p<0.0001, respectively), while CerS2 expression did not change in shNC HCT116 cells. This resulted in significantly different CerS2 mRNA expression between shCerS5 HCT116 cells and shNC HCT116 cells or shCerS4 HCT116 cells after 48 h and 72 h. CerS3 mRNA expression did not change significantly in shNC HCT116 cells, shCerS4 HCT116 cells, and shCerS5 HCT116 cells. After 48 h, CerS3 mRNA expression was significantly higher in shCerS5 HCT116 cells than in shNC HCT116 cells (p=0.01) (Figure 3.39). In contrast, CerS4 expression decreased in hypoxia. Hypoxia induced a decrease in CerS4 mRNA in shNC HCT116 cells at 24 h (p=0.02). In shCerS4 HCT116 cells, CerS4 mRNA decreased 0.2-fold at 24 h (p=0.08) and after 72 h (p=0.006) compared to 0 h, while CerS4 mRNA expression did not change in shCerS5 HCT116 cells under hypoxia. Thus, CerS4 mRNA expression was significantly higher in shCerS5 HCT116 cells than in shNC HCT116 cells at 24 h (p=0.016) and 48 h (p=0.002) and at all time points compared to shCerS4 HCT116 cells (0 h p=0.07, 24 h p=0.004, 48 h p=0.007 and 72 h p<0.0001). Hypoxia did not alter CerS5 mRNA expression except in shCerS5 HCT116 cells at 72 h, where CerS5 mRNA expression significantly decreased. Among the different transduced HCT116 cells, shCerS5 HCT116 cells had significantly lower CerS5 mRNA expression compared with shNC HCT116 cells and shCerS4 HCT116 cells at all time points. No changes were observed in CerS6 mRNA expression: Neither did hypoxia induce changes in CerS6 mRNA levels nor was a significant difference observed between shNC HCT116 cells, shCerS4 HCT116 cells and shCerS5 HCT116 cells (Figure 3.39).

Downregulation of CerS4 and CerS5 in Caco-2 cells had differential effects on hypoxia.

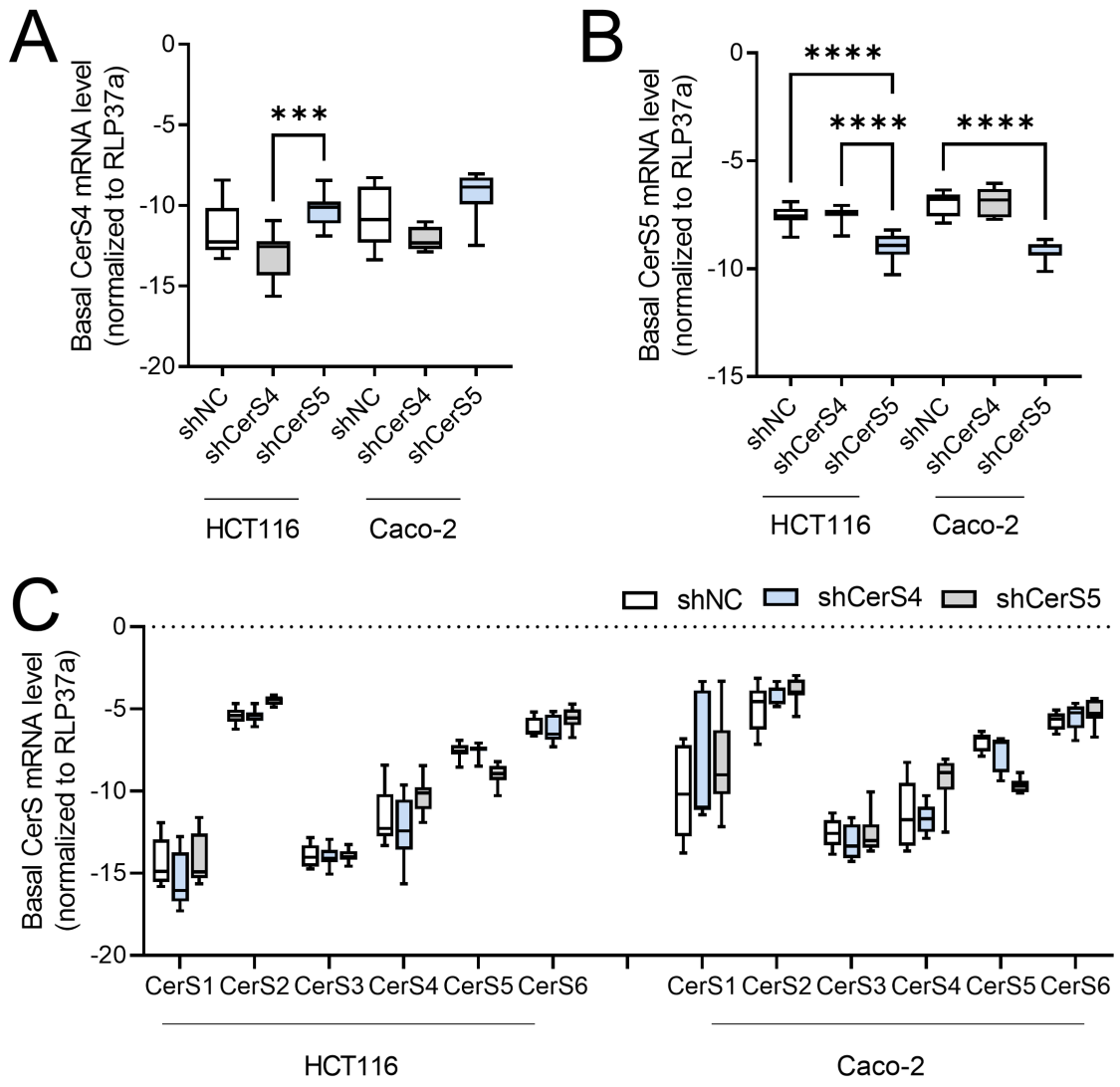

FIGURE 3.38: Downregulation of CerS4 and CerS5 in HCT116 cells (HCT116) and Caco-2 cells (Caco-2) by lentiviral transduction with shRNAs and its influence on CerS levels. Basal expression level of CerS mRNA of cellular extracts from shNC-, shCerS4- and shCerS5-downregulated HCT116 cells and Caco-2 cells determined by qRT-PCR and calculated as ΔCT by normalization to the housekeeping gene RPL37A. (A) Measurement of CerS4 mRNA, (B) of CerS5 mRNA, and (C) of all CerS isoforms in both CRC lines. Statistically significant differences between 3 different cell lines were determined by two-way ANOVA and Tukey's multiple comparison post-test (*** $p<0.001$, **** $p<0.0001$).

Hypoxia had no effect on CerS1 mRNA expression in all transduced Caco-2 cell lines (Figure 3.39). CerS2 mRNA expression decreased after 24 h in shNC Caco-2 cells compared to 0 h (p=0.005) or to shCerS4 Caco-2 cells (p=0.04) and shCerS5 Caco-2 cells (p=0.002) at 24 h, while CerS2 mRNA expression decreased by 0.8-fold in shCerS4 HCT116 cells (p=0.02) and by 0.02-fold in shCerS5 HCT116 cells (p=0.02) at 72 h compared to 0 h. Similar to CerS1 mRNA expression, CerS3 mRNA expression did not change in Caco-2 cells except after 48 h, when CerS3 mRNA expression decreased 0.95-fold compared to 24 h (p=0.006). Under hypoxia, CerS4 expression in shNC Caco-2 cells at 24 h (p=0.01) and at 48 h (p=0.06)

compared to 0 h and at 72 h compared to 24 h (p=0.04), whereas CerS4 mRNA expression also decreased in shCerS4 Caco-2 cells at all time points compared to 0 h (0.06-fold decrease at 24 h p<0.0001, 0.08-fold decrease at 48 h p=0.003 and 0.06-fold decrease at 72 h p<0.0001). The same decrease was also observed in shCerS5 Caco-2 cells: CerS4 mRNA expression significantly decreased by 0.4-fold at 24 h (p=0.02), by 0.06-fold at 48 h (p=0.04) and by 0.4-fold at 72 h (p=0.004) compared to 0 h shCerS5 Caco-2 cells (Figure 3.39). Although CerS4 mRNA expression decreased in all Caco-2 cell lines, CerS4 mRNA expression was significantly lower in shCerS4 Caco-2 cells than in shNC Caco-2 cells and shCerS5 Caco-2 cells at all time points. A similar pattern was observed for CerS5 mRNA expression, which decreased in shNC Caco-2 cells under hypoxia at 24 h (p=0.001), and 48 h (p=0.06). CerS5 mRNA expression also decreased in shCerS4 Caco-2 cells at 72 h (p=0.0007). Although CerS5 mRNA did not decrease after hypoxia in shCerS5 Caco-2 cells, CerS5 mRNA levels were significantly lower in shCerS5 Caco-2 cells than in shNC Caco-2 cells or shCerS4 Caco-2 cells at all time points. In contrast to HCT116 cells, CerS6 expression decreased in Caco-2 cells. In shNC Caco-2 cells, CerS6 mRNA expression decreased after 24 h (p=0.01) compared to 0 h. At 72 h, CerS6 mRNA expression declined in shCerS4 Caco-2 cells (p=0.0007) or shCerS5 Caco-2 cells (p=0.09) compared to 0 h (Figure 3.39).

In summary, hypoxia further downregulated CerS4 mRNA and partially downregulated CerS5 mRNA in shCerS4 and shCerS5 HCT116 cells or Caco-2 cells. The effects on the expression level of the other CerS depended on the CRC cell line used. While the expression of CerS1, CerS3 and CerS6 mRNA in HCT16 cells did not change after hypoxia, the expression of CerS2, CerS4 and CerS5 mRNA was decreased in HCT116 cells, whereas in Caco-2 cells hypoxia caused an additional decrease in CerS6 mRNA levels in shCerS4 and shCerS5 Caco-2 cells but not in shNC Caco-2 cells.

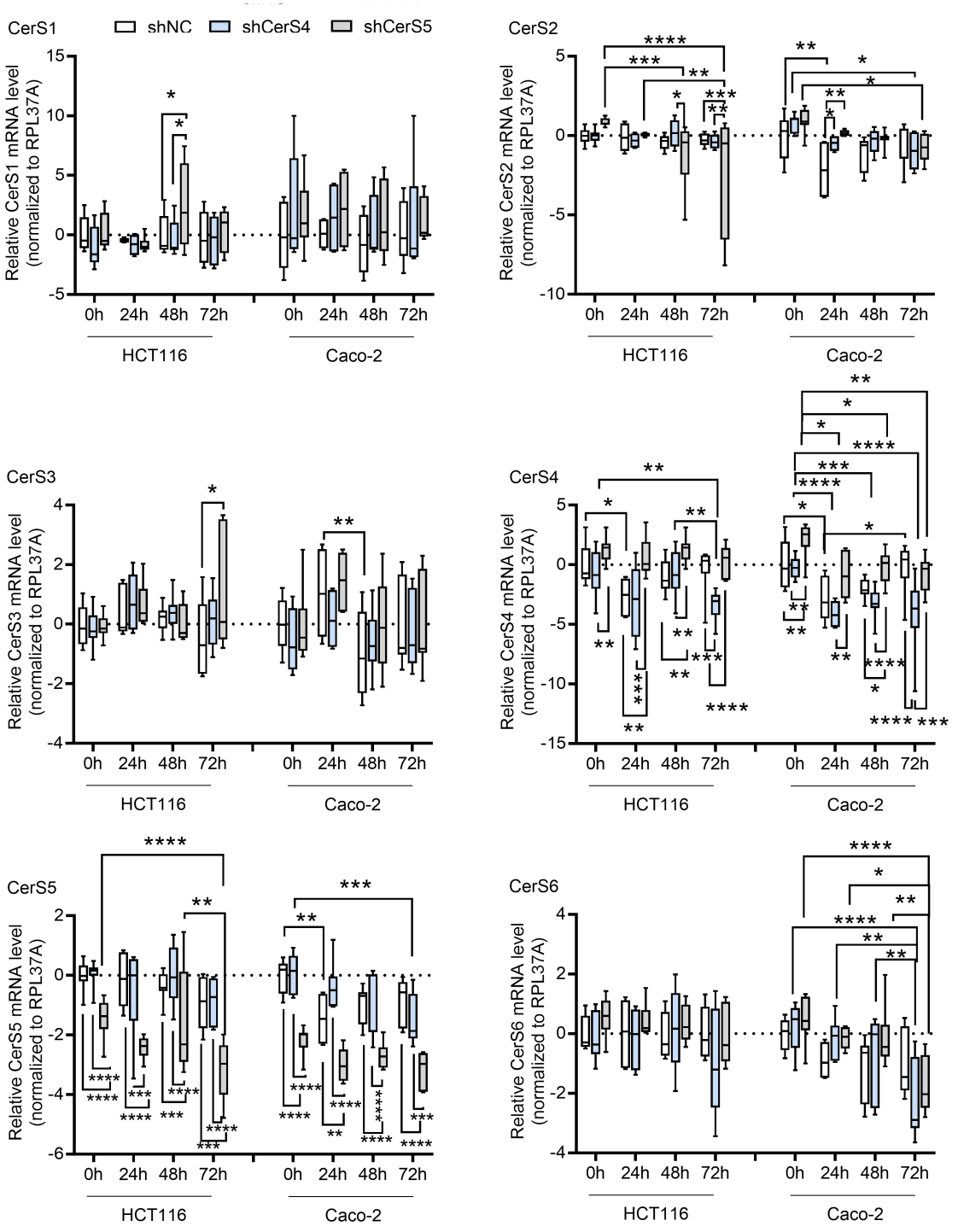

FIGURE 3.39: Effect of downregulation of CerS4 and CerS5 in HCT116 cells and Caco-2 cells on CerS expression level after hypoxia exposure. HCT116 cells (HCT116) and Caco-2 cells (Caco-2) transduced with shNC, shCerS4 or shCerS5 were exposed to hypoxia for 24 h, 48 h and 72 h. Relative CerS1 - CerS6 mRNA expression levels ($\Delta\Delta$CT) were normalized by the housekeeping gene RPL37A and untreated shNC HCT116 cells or untreated shNC Caco-2 cells (set to 0). Data are presented as median $\pm$CI95 of n= 2 (24 h), 3 (72 h) and 4 (0 h, 48 h) independent experiments. Statistically significant differences between the untreated and hypoxia exposed cell lines were determined by two-way ANOVA and Tukey's multiple comparison post-test (* p<0.05, ** p<0.01, *** p<0.001, **** p<0.0001).

To further analyze whether downregulation of CerS4 or CerS5 in CRC cell lines might interfere with the hypoxic response pathway, PHD3 mRNA levels and HIF1α were detected. PHD3 mRNA was similar in shNC, shCerS4, and shCerS5 HCT116 cells and Caco-2 cells, indicating that downregulation of CerS4 or CerS5 in HCT116 and Caco-2 cells did not affect the basal expression level of PHD3 (Figure 3.40 A). However, exposure to hypoxia increased PHD3 mRNA levels in both HCT116 cells and Caco-2 cells independent of transduced shRNA (Figure 3.40 B). At each time point, PHD3 expression increased significantly compared with 0 h in shNC HCT116 cells. In shCerS5 HCT116 cells, PHD3 mRNA levels also increased at each time point (significances not plotted in Figure 3.40 B), and PHD3 expression increased significantly at 48 h ($p<0.0001$) and 72 h ($p=0.0078$), but not at 24 h in shCerS4 HCT116 cells. Thus, shCerS4 HCT116 cells had significantly lower PHD3 mRNA levels than shNC HCT116 cells and shCerS5 HCT116 cells at 24 h (0.2-fold decrease, $p=0.0001$; 0.18-fold decrease, $p<0.0001$) and 72 h (0.4-fold decrease, $p=0.0096$), respectively.

This difference was not observed in shCerS4 Caco-2 cells (Figure 3.40 B). In shNC Caco-2 cells and in shCerS5 Caco-2 cells, PHD3 mRNA levels significantly increased at each time point compared with 0 h, and similar to shCerS4 HCT116 cells, PHD3 mRNA level did not significantly increase in shCerS4 Caco-2 cells until 48 h (Figure 3.40 B). This suggest that the deficiency in CerS4 delayed the hypoxia-induced increase in PHD3 mRNA CerS4 deficient CRC cells.

HIF1α also increased at protein level under hypoxia. In particular, HIF1α increased after 24 h and 48 h in shNC, shCerS4, and shCerS5 HCT116 cells but declined after 72 h regardless of the cell line (Figure 3.40 C). Densitometric analysis exhibited no significant increase in HIF1α content as early as 24 h in shNC HCT116 cells (8-fold, ns) and in shCerS5 HCT116 cells (2-fold, ns). At 48 h, the increase in HIF1α was significantly higher in shCerS4 HCT116 cells and shCerS5 HCT116 cells compared with 0 h, and HIF1α signal was higher in shCerS5 HCT116 cells compared with shNC HCT116 cells (Figure 3.40 D).

In Caco-2 cells, HIF1α signal was much weaker than in HCT116 cells (Figure 3.40 C). As in HCT116 cells, basal differences in Caco-2 cells were not significant: downregulation of CerS4 and CerS5 in Caco-2 cells did not increase basal protein HIF1α levels. Although variations within individual Caco-2 cell lines ranged from 0.4- and 5.4-fold after hypoxia, no statistical significant difference in HIF1α was detectable at any time point after hypoxia (Figure 3.40 D). Basal protein levels of HIF1α suggested that they might be associated with CerS4 expression levels. To investigate whether CerS4 downregulation mimics hypoxia, HIF1α was detected in nuclear fractions of CerS4 and CerS5 downregulated HCT116 cells and Caco-2 cells. No significant change in nuclear HIF1α level was detected between shCerS4 and shCerS5 Caco-2 cells or HCT116 cells compared with the shNC control (data not shown). These results thus refute the hypothesis that downregulation of CerS4 or CerS5 in HCT116 cells or Caco-2 cells alone could induce HIF1α stimulation or stabilization or nuclear translocation.

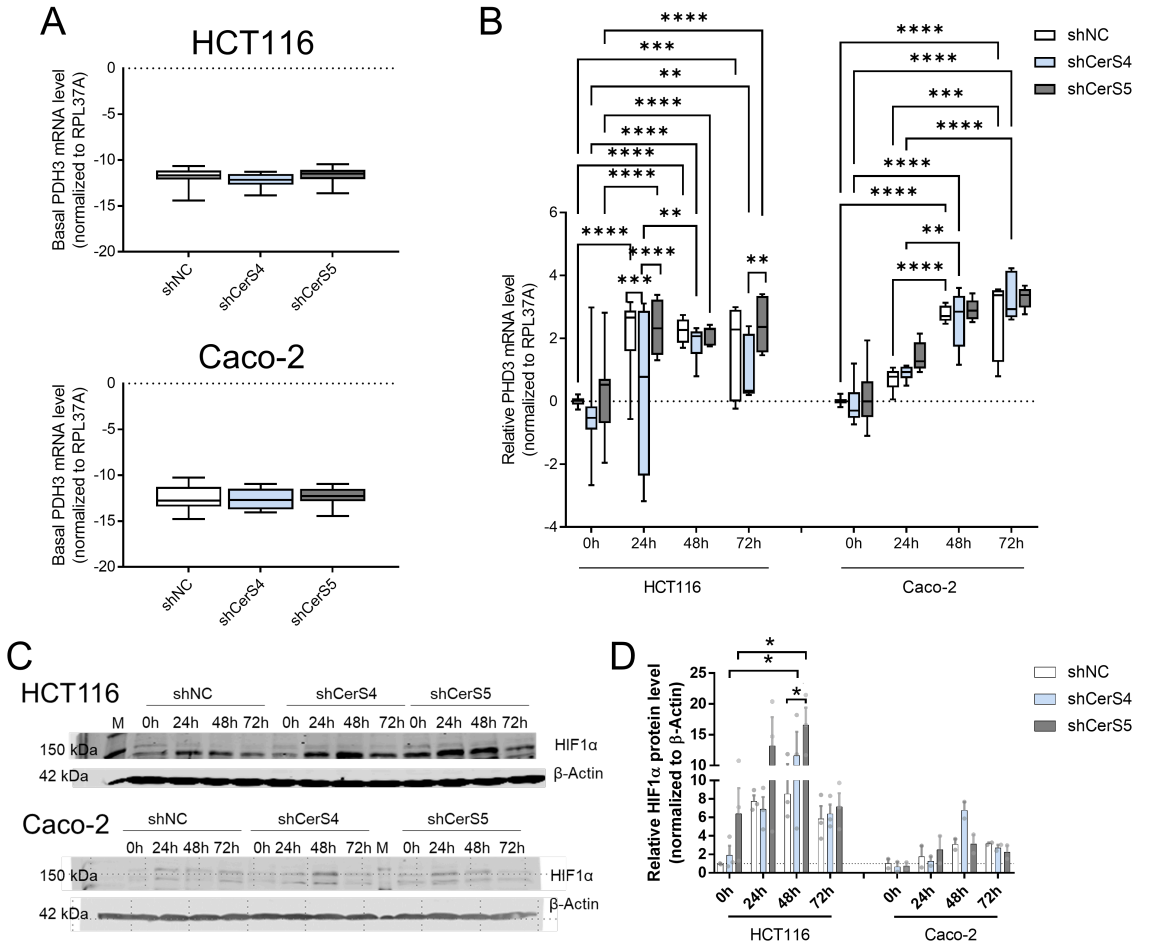

FIGURE 3.40: Downregulation of CerS4 or CerS5 in HCT116 cells or Caco-2 cells affects the response to hypoxia. HCT116 cells (HCT16) and Caco-2 cells (Caco-2) stably transduced with CerS4 or CerS5 targeting shRNA constructs or non-silencing (NC) shRNA cells were exposed to hypoxia for 24 h, 48 h and 72 h. (A) Basal PHD3 mRNA levels were determined by qRT-PCR and calculated as ΔCT values by normalization to the housekeeping gene RPL37A. (B) Relative PHD3 mRNA expression was calculated as relative values (ΔΔCT) by normalization to RPL37A and shNC Caco-2 cells (shNC Caco-2 0 h set to 0). (C) Representative blot of Western blot analysis of HIF1α protein levels and β-actin levels in whole cell extracts of hypoxia treated HCT116 cells and Caco-2 cells. (D) Densitometric analysis of relative HIF1α protein levels was calculated by normalizing the HIF1α signal to the β-actin signal and to the signal in shNC Caco-2 cells at 0 h (set to 1). Data are median ±CI95 of n=3-8. Statistically significant differences were determined by two-way ANOVA and Tukey's multiple comparision post-test (* p<0.05, ** p<0.01, *** p<0.001, **** p<0.0001).

Although HIF1α protein levels did not change in shCerS4 and shCerS5 CRC cells compared to shNC CRC cells, CerS4 and CerS5 may be involved in downstream hypoxia adaptation. To understand the potential of CerS4 and CerS5 in hypoxia adaptation, metabolic pathways, mitochondrial health, and also enzymes involved in PPP were investigated at the transcriptional level in shCerS4 and shCerS5 HCT116 cells or Caco-2 cells and compared with shNC HCT116 cells or Caco-2 cells.

Downregulation of CerS4 and CerS5 in HCT116 cells had no effect on basal expression of PK, PDHA1 and LDHA expression. Only GLUT1 mRNA showed higher expression in shCerS5 HCT116 cells compared with shNC HCT116 cells (p<0.0001) or shCerS4 HCT116

cells (p=0.055) (Figure 3.41 A).

A similar effect was also observed in Caco-2 cells: In shCerS4 Caco-2 cells and shCerS5 Caco-2 cells, basal mRNA expression of PK, PDHA1 and LDHA was similar compared with shNC Caco-2 cells, but in shCerS5 Caco-2 cells, GLUT1 expression was 1.2-fold higher than in shNC Caco-2 cells (p=0.03) (Figure 3.41 B). This suggests that downregulation of CerS5 affects basal expression of GLUT1 in both HCT116 cells and Caco-2 cells.

Culturing CRC cells under hypoxia altered the expression levels of GLUT1, PK, PDHA1 and LDHA. GLUT1 mRNA expression significantly increased in shNC HCT116 cells at 24 h (p=0.003) and at 72 h (p=0.001) compared with 0 h. In shCerS4 HCT116 cells and shCerS5 HCT116 cells, GLUT1 mRNA did not increase in hypoxia. Therefore, GLUT1 mRNA level was significantly higher in shNC HCT116 cells than in shCerS4 HCT116 cells (p=0.004) and shCerS5 HCT116 cells after 24 h (p=0.01) (Figure 3.41 C).

In contrast, GLUT1 mRNA increased in Caco-2 cells, independently of transduced shRNA. In shNC Caco-2 cells, GLUT1 mRNA levels increased significantly at 48 h (p<0.0001, p=0.001) and 72 h (p<0.0001, p=0.01) compared with 0 h and 24 h. In shCerS4 Caco-2 cells, GLUT1 mRNA increased 7-fold (p=0.003) at 24 h and 18.5-fold (p=0.001) at 48 h and 72 h (p=0.01) compared to 0 h. In shCerS5 Caco-2 cells, GLUT1 mRNA increased significantly at 48 h (p<0.0001) and 72 h (p=0.01) compared to 0 h (Figure 3.41 C). Therefore, no differences were observed between transduced Caco-2 cells, suggesting that downregulation of CerS4 and CerS5 only interferes with the increase of GLUT1 mRNA in HCT116 cells but not in Caco-2 cells after hypoxia.

Hypoxia also induced the decrease of PDHA1 mRNA in HCT116 cells. In shNC HCT116 cells and shCerS4 HCT116 cells, PDHA1 mRNA levels decreased significantly at 24 h compared with 0 h (p=0.003), whereas in shCerS5 HCT116 cells PDHA1 mRNA04 levels decreased significantly at 72 h compared with 0 h (p<0.0001), 24 h (p=0.004) and 48 h (p=0.02). PDHA1 mRNA level was significantly lower in shCerS5 HCT116 cells compared with shCerS4 HCT116 cells at 24 h (p=0.04) and 72 h (p=0.02) and with shNC HCT116 cells at 72 h (p=0.003).

However, in Caco-2 cells, PDHA1 expression levels did not change with hypoxia in shNC, shCerS4 and shCerS5 Caco-2 cells (Figure 3.41 D) and no differences in PDHA1 mRNA were observed between shNC, shCerS4 and shCerS5 Caco-2 cells. This suggests that the reduction of PDHA1 mRNA levels after hypoxia was restricted to HCT116 cells and not Caco-2 cells.

PK expression did not change in shNC HCT116 cells treated with hypoxia, but increased significantly in shCerS4 HCT116 cells at 24 h (p=0.002) and 48 h (p=0.0002) compared with 0 h. In shCerS5 HCT116 cells, PK mRNA levels increased significantly at 24 h (p=0.003) compared to 0 h but decreased significantly at 48 h (p=0.004) and 72 h (p=0.0.006, p<0.0001) compared with 24 h and 0 h. Therefore, PK mRNA level was significantly lower in shCerS5 HCT116 cells compared with shCerS4 HCT116 cells at 48 h (p=0.01) and 72 h (p=0.0004), respectively, and also significantly lower compared with shNC HCT116 cells at 72 h (p<0.0001) (Figure 3.41 E).

In Caco-2 cells, no difference in PK mRNA levels was observed between shNC, shCerS4 and shCerS5 Caco-2 cells. Furthermore, hypoxia exposure did not alter the PK mRNA levels in shNC, shCerS4, or shCerS5 Caco-2 cells compared with 0 h (Figure 3.41 E).

A clear increase in LDHA mRNA concentration due to hypoxia was observed: In shNC HCT116 cells, a significant increase in LDHA mRNA concentration was observed after 24 h (p=0.0003), 48 h (p=0.0001) and 72 h (p=0.01) compared with 0 h. In shCerS4 Caco-2 cells, LDHA mRNA levels increased 30-fold at 24 h (p<0.0001) , 38-fold at 48 h (p<0.0001), and 30-fold at 72 h (p=0.0002) compared with 0 h. This increase in LDHA mRNA was much smaller in shCerS5 HCT116 cells: after 24 h, LDHA mRNA levels increased significantly by 20-fold (p<0.0001), whereas the 10-fold increase after 48 h (p=0.09) and the 5-fold increase after 72 h were not statistically significant compared with 0 h. Comparison of transduced HCT116 cells at different time points, revealed no difference at 0 h and 24 h, but at 48 h, LDHA mRNA levels were significantly lower in shCerS5 HCT116 cells than in shCerS4 HCT116 cells, and at 72 h, LDHA mRNA levels were significantly higher in shNC HCT116 cells and shCerS4 HCT116 cells compared with shCerS5 HCT116 cells (Figure 3.41 F).

In Caco-2 cells, LDHA mRNA also increased upon hypoxia. In shNC Caco-2 cells, a significant increase in LDHA mRNA was observed at 48 h (p=0.0004) compared with 0 h, whereas in shCerS4 HCT116 cells, LDHA mRNA increased 16-fold at 24 h (p<0.0001) and 18-fold at 48 h (p<0.0001). In shCerS5 Caco-2 cells, the significant increase in LDHA expression lasted up to 72 h: LDHA mRNA increased 20-fold after 24 h (p<0.0001), 11-fold after 48 h (p=0.09), and 5-fold after 72 h (ns) compared with 0 h. Between the different time points, LDHA mRNA expression did not differ in shNC, shCerS4 and shCerS5 Caco-2 cells (Figure 3.41 F).

In conclusion, downregulation of CerS4 in HCT116 cells had no effect on the expression of GLUT1, PDHA1, PK and LDHA mRNA level during hypoxia compared to shNC HCT116 cells. In contrast, shCerS5 HCT116 cells already differed in the basal expression of GLUT1 but also differed during hypoxia compared with shNC HCT116 cells and shCerS4 HCT116 cells at different time points. However, this effect was restricted to HCT116 cells. In Caco-2 cells, the expression levels of GLUT1, PDHA1, PK and LDHA were not significantly different from shNC Caco-2 cells or shCerS4 Caco-2 cells. This suggests that the effect of CerS5 downregulation is not causal but restricted to CRC cell line.

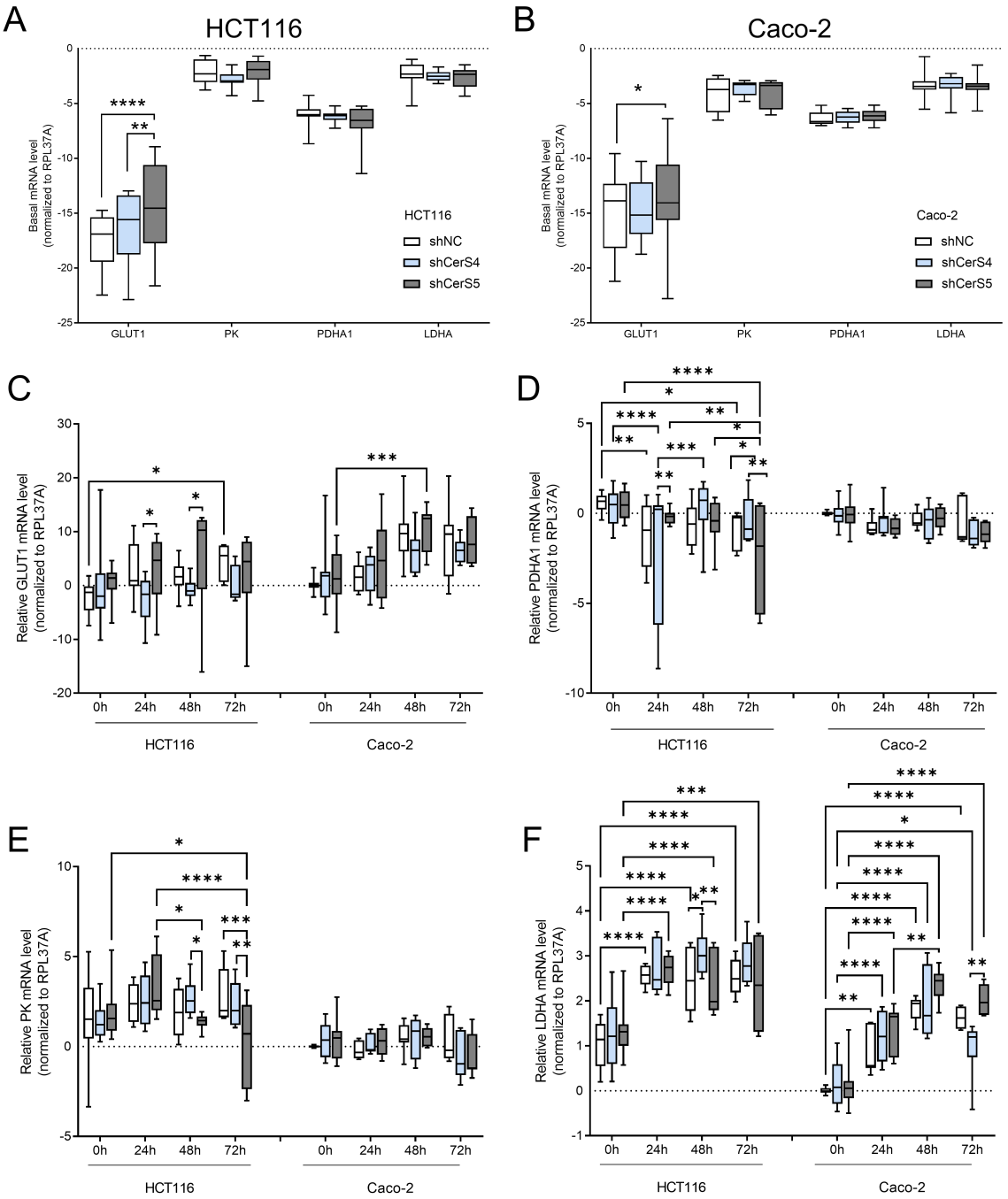

FIGURE 3.41: Effect of CerS4 or CerS5 downregulation in HCT116 cells (HCT116) and Caco-2 cells (Caco-2) towards certain mRNA expression of glycolysis enzymes after hypoxia. (A) Basal expression levels of GLUT1, PK, PDHA1 and LDHA determined by qRT-PCR normalized to housekeeping gene RPL37A (ΔCT) in shNC, shCerS4 and shCerS5 HCT116 cells and (B) Caco-2 cells. (C) Relative expression levels as $\Delta\Delta$CT values of HCT116 cells and Caco-2 cells exposed to hypoxia for 24 h, 48 h and 72 h normalized to housekeeping gene RPL37A and control shNC HCT116 cells or control shNC Caco-2 cells (set to 0). Data from n=3 (72 h), 4 (48 h, 24 h), and 7-9 (0 h) presented as median $\pm$CI95. Statistically significant differences between untreated and hypoxia exposed cells and shNC, shCerS4 and shCerS5 transduced cells were determined by two-way ANOVA with Tukey's multiple comparison post-test. (* p<0.05, ** p<0.01, *** p<0.001, **** p<0.0001).

As seen in Figure 3.41, the switch from aerobic to anaerobic energy production at the transcriptional level occurred more rapidly in HCT116 cells than in Caco-2 cells. The difference in PK levels was also clear. The PK gene can give rise to two splice variants: pyruvate kinase isoform (PKM)1 and PKM2. Basal expression of PKM1 and PKM2 revealed that Caco-2 cells (-11.5 ± 0.98 ΔCT) already had lower mRNA level than HCT116 cells (-5.7 ± 0.7 ΔCT). However, downregulation of CerS4 or CerS5 did not affect the basal expression of PK isoforms: Basal expression of PKM1 and PKM2 was similar in shNC, shCerS4 and shCerS5 HCT116 cells (Figure 3.42 A), and mRNA levels of PKM1 and PKM2 were also similar in shNC, shCerS4 and shCerS5 Caco-2 cells (Figure 3.42 B).

After hypoxia, PKM1 mRNA level increased in shNC HCT116 cells after $48\,\mathrm{h}$ (p=0.028). In shCerS4 HCT116 cells, PKM1 mRNA level increased 5-fold after $24\,\mathrm{h}$ (p=0.03), 6-fold after $48\,\mathrm{h}$ (p=0.04) and 7-fold after $72\,\mathrm{h}$ (p=0.09). PKM1 mRNA level significantly increased in shCerS5 HCT116 cells at $24\,\mathrm{h}$, but at $72\,\mathrm{h}$ PKM1 mRNA level tended to decrease compared to $0\,\mathrm{h}$ (p=0.09) (Figure 3.42 C). This resulted in a significantly lower PKM1 mRNA level in shCerS5 HCT116 cells compared to shNC and shCerS4 HCT116 cells at $72\,\mathrm{h}$ (Figure 3.42 C). Although PKM2 mRNA levels did not change in shCerS4 Caco-2 cells and shCerS5 HCT116 cells compared with shNC HCT116 cells, PKM2 levels increased differently under hypoxia. PKM2 levels did not significantly increase in shNC HCT116 cells, but PKM2 levels significantly increased in shCerS4 HCT116 cells at $24\,\mathrm{h}$, and PKM2 levels also increased in shCerS5 HCT116 cells at $24\,\mathrm{h}$ (p<0.0001) and $48\,\mathrm{h}$ (p=0.015) compared to $0\,\mathrm{h}$ (Figure 3.42 D).

In Caco-2 cells, PKM1 also increased, especially in shCerS4 Caco-2 cells. In shNC Caco-2 cells, PKM1 level increased significantly at $48\,\mathrm{h}$ compared to $0\,\mathrm{h}$. In shCerS4 Caco-2 cells, PKM1 level increased 8-fold after $24\,\mathrm{h}$ (p=0.003) and 14-fold after $48\,\mathrm{h}$ (p<0.0001). PKM1 expression level significantly decreased after $72\,\mathrm{h}$ compared to $48\,\mathrm{h}$. In shCerS5 Caco-2 cells, the 10- to 16-fold increase in PKM1 was significant at $24\,\mathrm{h}$, $48\,\mathrm{h}$, and $72\,\mathrm{h}$ compared to $0\,\mathrm{h}$. No difference was observed in PKM1 levels between shNC, shCerS4 and shCerS5 Caco-2 cells at different time points (Figure 3.42 C). Although basal PKM2 levels did not differ between shNC, shCerS4 and shCerS5 Caco-2 cells, PKM2 levels increased significantly in hypoxia only in shCerS5 Caco-2 cells at $48\,\mathrm{h}$ compared with $0\,\mathrm{h}$ (Figure 3.42 D).

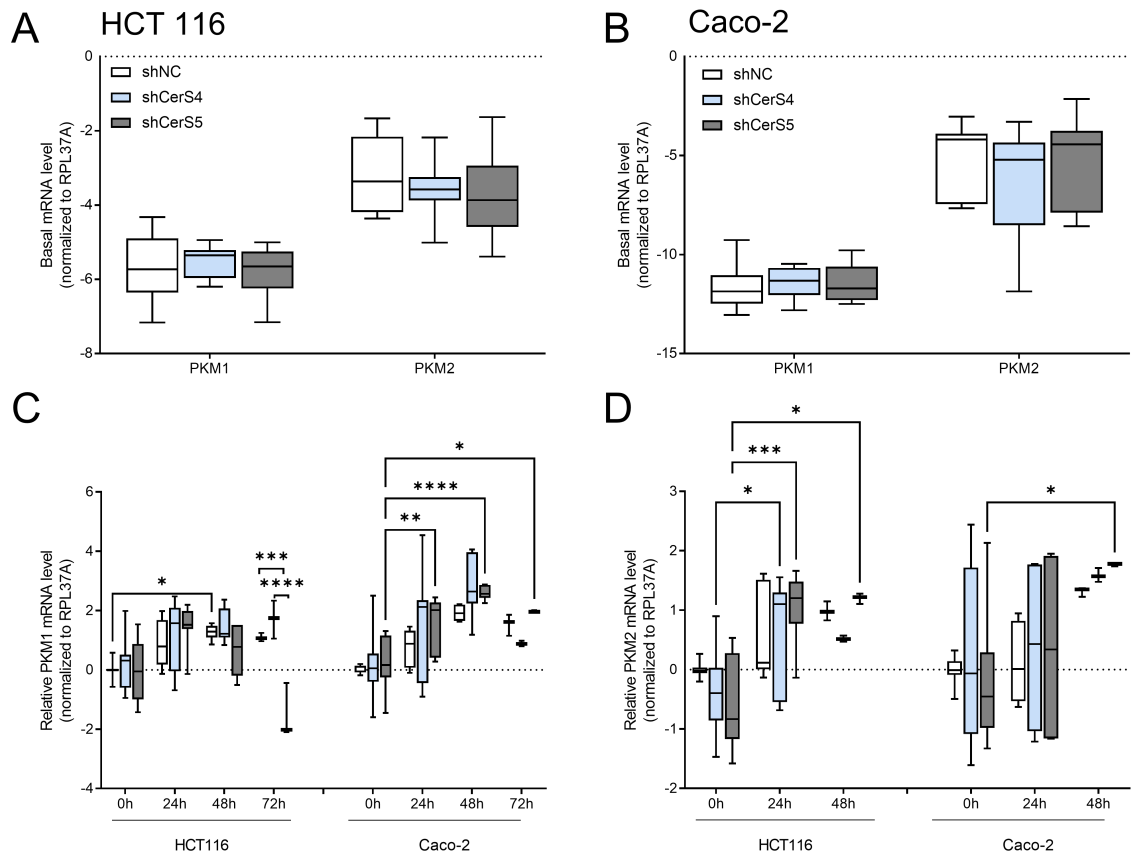

FIGURE 3.42: PKM isoform profile in HCT116 cells and Caco-2 cells and change in their expression upon hypoxia. HCT116 cells (HCT116) and Caco-2 cells (Caco-2) stably transduced with CerS4- or CerS5- targeting shRNA constructs or with non-silencing (NC) shRNA were exposed to hypoxia for 24 h, 48 h and 72 h. (A) Basal mRNA levels of PKM1 and PKM2 mRNA in HCT116 cells or (B) Caco-2 cells were determined by qRT-PCR and calculated as ΔCT values by normalization to the housekeeping gene RPL37A. (C) Relative mRNA expression of PKM1 and (D) PKM2 were calculated as relative values (ΔΔCT) by normalization to 0 h control shNC HCT116 cells or control 0 h shNC Caco-2 (set as 0). Data are median ±CI95 of n=1 (72 h)-8. Statistically significant differences were determined by two-way ANOVA and Tukey's multiple comparison post-test (* p<0.05, ** p<0.01, *** p<0.001, **** p<0.0001).

To understand whether downregulation of CerS4 or CerS5 may interfere with PPP during hypoxia, mRNA levels of TKT and transketolase-like 1 (TKTL1) were quantified. HCT116 cells expressed three times as much TKT as TKTL1. Downregulation of CerS4 or CerS5 in HCT116 cells did not affect basal expression of TKT (Figure 3.43 A). TKTL1 mRNA was significantly lower in shCerS5 HCT116 cells than in shNC HCT116 cells and shCerS4 HCT116 cells (Figure 3.43 A). Hypoxia did not significantly alter TKT expression. Only in shCerS5 HCT116 cells did TKT levels increase at 72 h compared with 0 h (p=0.01) and 24 h (p=0.02) (Figure 3.43 C). Hypoxia itself did not further reduce TKTL levels, but the significant difference between shCerS5 HCT116 cells and shNC HCT116 cells or shCerS4 HCT116 cells persisted after 24 h (Figure 3.43 D).

In Caco-2 cells, basal expression of TKT was also threefold higher than that of TKTL1. While no basal differences in TKT mRNA levels were observed in shNC Caco-2 cells, shCerS4

Caco-2 cells, and shCerS5 Caco-2 cells, TKTL1 mRNA levels were significantly lower in shCerS4 Caco-2 cells compared with shNC Caco-2 cells or shCerS5 Caco-2 cells (Figure 3.43 B). During hypoxia, the expression level of TKT did not change significantly in Caco-2 cells (Figure 3.43 C). Only the expression of TKTL1 was affected by hypoxia: in shNC HCT116 cells, TKTL1 expression increased significantly at 24 h (p<0.0001) and 48 h (p<0.0001) compared with 0 h. A significant increase in TKTL1 was also observed in shCerS4 Caco-2 cells and in shCerS5 Caco-2 cells after 24 h (p<0.0001) and 48 h (p<0.0001) compared with 0 h, but the increase in shCerS5 Caco-2 cells was higher than in shCerS4 Caco-2 cells, resulting in a 1.6 higher TKTL1 level in shCerS5 Caco-2 cells compared with shCerS4 Caco-2 cells after 24 h (p=0.017) (Figure 3.43 D).

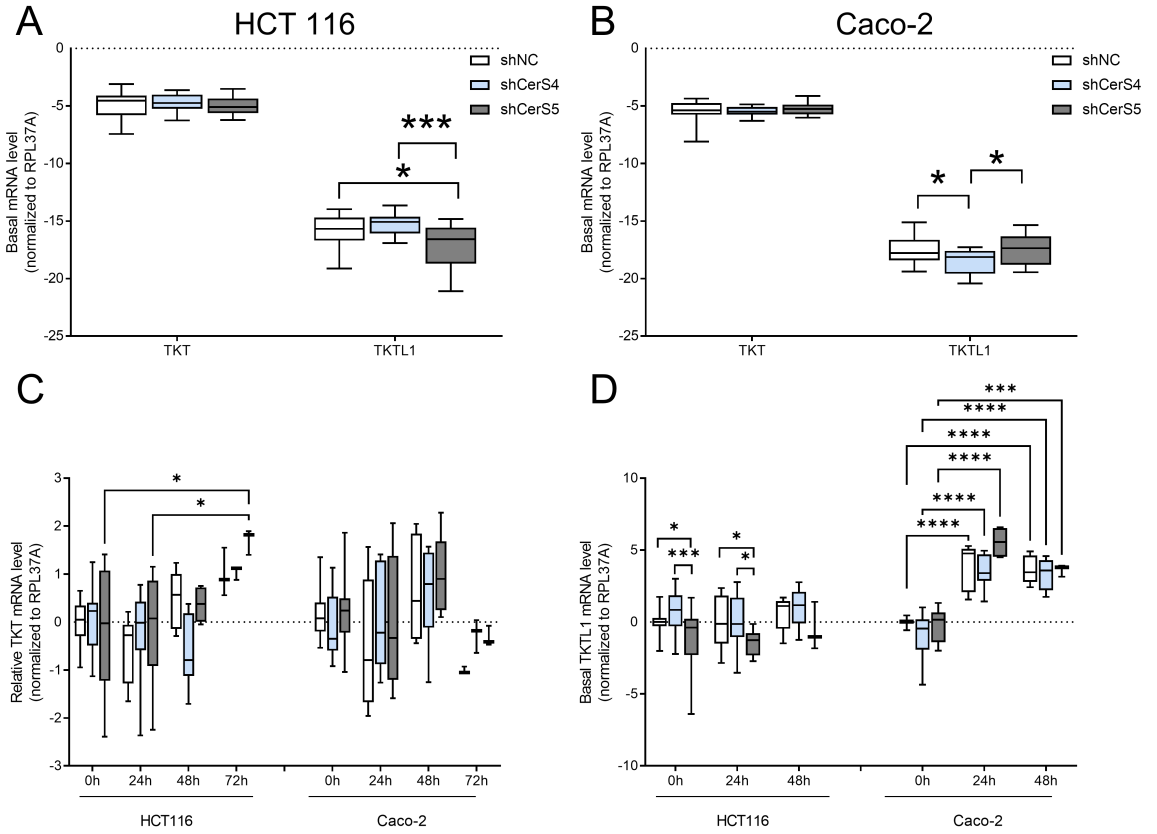

FIGURE 3.43: The profile of pentose phosphate transketolase in HCT116 cells and Caco-2 cells and its expression change upon hypoxia. HCT116 cells (HCT116) and Caco-2 cells (Caco-2) stably transduced with CerS4- or CerS5-targeting shRNA constructs or non-silencing (NC) shRNA were exposed to hypoxia for 24 h, 48 h and 72 h. (A) Basal mRNA levels of the pentose phosphate way enzymes TKT and TKTL1 were determined by qRT-PCR and calculated as ΔCT values by normalization to the housekeeping gene RPL37A in HCT116 cells and (B) in Caco-2 cells. (C) Relative mRNA expression of TKT and (D) TKTL-1 were calculated as relative values (ΔCT) by normalization to control 0 h shNC HCT116 cells or control 0 h Caco-2 (set as 0). Data are median ±CI95 of n=1 (72 h)-8. Statistically significant differences were determined by two-way ANOVA and Tukey's multiple comparison post-test (* p<0.05, ** p<0.01, *** p<0.001, **** p<0.0001).

Metabolic pathway switching is an adaptation to stress, and another important mechanism for cells is the change in mitochondrial dynamics. Mitochondrial fusion is controlled by MFN1 and MFN2 "for the outer membrane and OPA1 for the inner membrane" [264,

265] (Figure 3.44 F). The median of MFN1 mRNA level in HCT116 cells ranged from -7.4 ΔCT to -7.9 ΔCT, the median of MFN2 mRNA level ranged from -6.9 ΔCT to -7.7 ΔCT, whereas OPA1 mRNA level was less expressed and ranged from -10.9 ΔCT to -11.4 ΔCT.

Downregulation of CerS4 or CerS5 in HCT116 cells did not affect these levels Figure 3.44 A). When HCT116 cells were exposed to hypoxia, MFN1 levels decreased significantly in shNC HCT116 cells at $72\,\mathrm{h}$ (p<0.0001) and also in shCerS5 HCT116 cells at $48\,\mathrm{h}$ (p=0.01) and $72\,\mathrm{h}$ (p<0.0001). In shCerS4 HCT116 cells, MFN1 levels decreased significantly at $72\,\mathrm{h}$ compared to $0\,\mathrm{h}$ (p=0.0002), to $24\,\mathrm{h}$ (p=0.007) and to $48\,\mathrm{h}$ (p=0.0002). Downregulation of CerS4 appeared to affect the reduction of MFN1 level in HCT116 cells after hypoxia. At $48\,\mathrm{h}$, shCerS4 HCT116 cells had higher MFN1 mRNA expression than shCerS5 HCT116 cells (p=0.02), but this decreased at $72\,\mathrm{h}$ (Figure 3.44 C). As MFN1 expression decreased with hypoxia, MFN2 expression also decreased with hypoxia, but not in all HCT116 cells (Figure 3.44 C). In shNC HCT116 cells, MFN2 expression did not decrease significantly under hypoxia. In shCerS4 HCT116 cells, MFN2 levels decreased after $24\,\mathrm{h}$ (p=0.007) and after $72\,\mathrm{h}$ (p=0.08) compared with $0\,\mathrm{h}$. The decrease was much greater in shCerS5 HCT116 cells than in shCerS4 HCT116 cells: After $48\,\mathrm{h}$, MFN2 level was 4.6 times higher in shCerS4 HCT116 cells than in shCerS5 HCT116 cells. In shCerS5 HCT116 cells, MFN2 levels significantly decreased after $48\,\mathrm{h}$ (p=0.009) and after $72\,\mathrm{h}$ (p=0.0003) compared to $0\,\mathrm{h}$, and MFN2 mRNA expression also decreased after $72\,\mathrm{h}$ compared to $24\,\mathrm{h}$ (p=0.01) (Figure 3.44 D). Consistent with the decline in MFN1 and MFN2, OPA1 levels also decreased under hypoxia: OPA1 mRNA expression decreased at $24\,\mathrm{h}$ (p=0.02) and $72\,\mathrm{h}$ (p=0.006) in shNC HCT116 cells and in shCerS4 HCT116 cells at $24\,\mathrm{h}$ (p=0.03) and $72\,\mathrm{h}$ (p=0.008), but not in shCerS5 HCT116 cells. However, no differences in OPA1 mRNa levels were observed between the transduced HCT116 cell lines at any time point (Figure 3.44 E).

In Caco-2 cells, the basal mRNA levels of MFN1 (-8 ± 1.2 ΔCT), MFN2 (-7.3 ± 1.6 ΔCT) and OPA1 (-11.3 ± 1 ΔCT) were in a similar range as in HCT116 cells and the downregulation of CerS4 or CerS5 did not affect the mRNA expression of these fusion proteins (Figure 3.44 B). Hypoxia significantly reduced MFN1 levels in shNC Caco-2 cells as early as $24\,\mathrm{h}$ (p=0.02, p=0.003, p=0.03) compared to $0\,\mathrm{h}$, while MFN1 levels decreased in shCerS4 Caco-2 cells (p=0.01, p=0.0002) and shCerS5 Caco-2 cells (p=0.001, p=0.006) as early as $48\,\mathrm{h}$ compared with $0\,\mathrm{h}$. No difference in MFN1 mRNA level was observed between transduced Caco-2 cells (Figure 3.44 C). However, MFN2 mRNA levels did not decrease. In shNC Caco-2 cells and shCerS5 Caco-2 cells, MFN2 levels did not change upon hypoxia, but in shCerS4 Caco-2 cells they decreased at $72\,\mathrm{h}$ (p=0.04) compared to $24\,\mathrm{h}$ and $48\,\mathrm{h}$. No differences were observed between shNC, shCerS4 and shCerS5 Caco-2 cells at each time point (Figure 3.44 D). The expression of OPA1 also decreased in hypoxia. In shNC Caco-2 cells and shCerS4 Caco-2 cells, OPA mRNA levels decreased significantly at $24\,\mathrm{h}$, $48\,\mathrm{h}$ and $72\,\mathrm{h}$ compared with $0\,\mathrm{h}$. In shCerS5 Caco-2 cells, OPA levels decreased significantly at $24\,\mathrm{h}$ and $48\,\mathrm{h}$. No differences in OPA1 expression were observed between shNC, shCerS4 and shCerS5 Caco-2 cells at each time point (Figure 3.44 E).

In summary, hypoxia reduced mitochondrial fusion: MFN1 mRNA levels dropped in HCT116 cells and Caco-2 cells, OPA1 levels in all Caco-2 cells and shCerS4 HCT116 cells

also decreased, and MFN2 mRNA levels declined after hypoxia in shCerS5 HCT116 and shCerS4 Caco-2 cells (Figure 3.44 F).

Thus, hypoxia led to a reduction in some components of the mitochondrial fusion machinery such as MFN1 and OPA1, but mitochondrial dynamics also include mitochondrial fission. Detection of FIS1 at mRNA level was used to investigate whether mitochondrial fission is affected by either CerS downregulation or hypoxia. At the basal level, no difference in FIS1 levels was detected between shNC, shCerS4 and shCerS5 HCT116 cells (Figure 3.45 A). Under hypoxia, FIS1 levels decreased significantly only in shCerS5 HCT116 cells at $48\,\mathrm{h}$ (0.09-fold , p=0.004) and $72\,\mathrm{h}$ (0.4-fold, p=0.0004) compared to $0\,\mathrm{h}$ (Figure 3.45 C). Since FIS1 mRNA levels did not significantly decrease in shNC and shCerS4 HCT116 cells, FIS1 levels were higher in shCerS5 HCT116 cells than in shNC HCT116 cells (4.6-fold increase, p=0.002) but lower than in shCerS4 HCT116 cells (0.1-fold decrease, p<0.0001) at $48\,\mathrm{h}$. At $72\,\mathrm{h}$, FIS1 levels were significantly lower in shCerS5 HCT116 cells than in shNC HCT116 cells (0.3-fold, p=0.009) (Figure 3.45 C).

In Caco-2 cells, basal expression of FIS1 was similar in shNC, shCerS4 and shCerS5 Caco-2 cells (Figure 3.45 B). Similar to HCT116 cells, FIS1 levels decreased in response to hypoxia in Caco-2 cells. FIS mRNA expression decreased significantly in shNC Caco-2 cells at $72\,\mathrm{h}$ compared to $0\,\mathrm{h}$ (p=0.04) while they did not change in shCerS4 Caco-2 cells. In shCerS5 Caco-2 cells, FIS1 levels decreased after $24\,\mathrm{h}$ compared with $0\,\mathrm{h}$ (p=0.005) (Figure 3.45 C). However, there were no differences between shNC, shCerS4 and shCerS5 Caco-2 cells at different time points (Figure 3.45 C).

In conclusion, mRNA expression of FIS1 was higher in HCT116 cells than Caco-2 cells and hypoxia reduced the mRNA level of FIS1 in all Caco-2 cells and only in shCerS5 HCT116 cells (Figure 3.45 D).

Previously, downregulation of CerS4 and CerS5 could affect mitochondrial dynamics during hypoxia, but mitochondrial quality control could also be influenced by hypoxia. To analyze whether downregulation of CerS4 or CerS5 affects mitochondrial quality control under hypoxic stress, PINK and PARK levels were examined by qRT-PCR. The mRNA levels of PINK and PARK already differed at a basal level: the mRNA expression level of PINK was approximately twice that of PARK in HCT116 cells. Downregulation of CerS4 and CerS5 in HCT116 cells did not affect the expression of PINK level. The expression of PARK was significantly lower in shCerS4 HCT116 cells compared to shNC HCT116 cells (Figure 3.46 A). Hypoxia had no effect on PARK levels in shNC HCT116 cells, in shCerS4 HCT116 cells, and in shCerS5 HCT116 cells (Figure 3.46 C). However, the PARK expression level was different in HCT116 cells. Thus, shCerS4 HCT116 cells had lower PARK mRNA levels compared with shNC at $0\,\mathrm{h}$ and $48\,\mathrm{h}$ and compared to shCerS5 HCT116 cells at $0\,\mathrm{h}$, $48\,\mathrm{h}$, and $72\,\mathrm{h}$ (Figure 3.46 C). The expression of PINK did not change with hypoxia in shNC HCT116 cells or shCerS4 HCT116 cells, but in shCerS5 HCT116 cells, PINK mRNA levels decreased significantly at $48\,\mathrm{h}$ compared with $0\,\mathrm{h}$ and $24\,\mathrm{h}$, and after $72\,\mathrm{h}$, PINK mRNA levels decreased significantly compared with $24\,\mathrm{h}$ (0.58-fold, p=0.0049) (Figure 3.46 D).

In Caco-2 cells, downregulation of CerS4 and CerS5 affected the expression of PARK only, but not PINK. No differences were observed between the basal expression of PINK

among shNC, shCerS4, and shCerS5 Caco-2 cells (Figure 3.46 B). PARK expression in shNC Caco-2 cells was also not different from shCerS4 Caco-2 cells or shCerS5 Caco-2 cells, but PARK expression was significantly lower in shCerS4 Caco-2 cells than in shCerS5 Caco-2 cells (Figure 3.46 B). During hypoxia, the expression of PINK and PARK changed. The expression of PARK increased significantly in shNC Caco-2 cells at 72 h compared with 0 h, 24 h and 48 h. In shCerS4 Caco-2 cells, the level of PARK decreased after 24 h (0.1-fold, p=0.04) compared with 0 h and increased at 72 h (2-fold, p=0.004) compared with 0 h , whereas the expression of PARK did not change in shCerS5 Caco-2 cells under hypoxia (Figure 3.46 C). Expression of PINK declined significantly at 48 h and 72 h compared with 0 h in shNC Caco-2 cells. However, the expression of PINK in shCerS4 Caco-2 cells did not alter under hypoxia. In shCerS5 Caco-2 cells, PINK expression also decreased significantly at 24 h (0.15-fold, p=0.006) and 48 h (0.12-fold, p<0.0001) compared with 0 h (Figure 3.46 D). No difference in PARK level was observed between shNC, shCerS4, and shCerS5 Caco-2 cells at any time point (Figure 3.46 D).

Overall, downregulation of CerS4 and CerS5 in both HCT116 cells and Caco-2 cells resulted in a decreased expression of PARK but not PINK. Notably, in shCerS5 HCT116 cells and shCerS5 Caco-2 cells, the expression level decreased during hypoxia, whereas in shCerS4 HCT116 cells and shCerS4 Caco-2 cells, the PINK level did not decrease with hypoxia. The difference in PARK expression between shCerS4 and shCerS5 HCT116 cells and Caco-2 cells persisted during hypoxia, indicating a slowed increase in PARK mRNA in shCerS4 Caco-2 cells or HCT116 cells and a more rapid increase in shCerS5 Caco-2 cells or HCT116 cells (Figure 3.46 E).

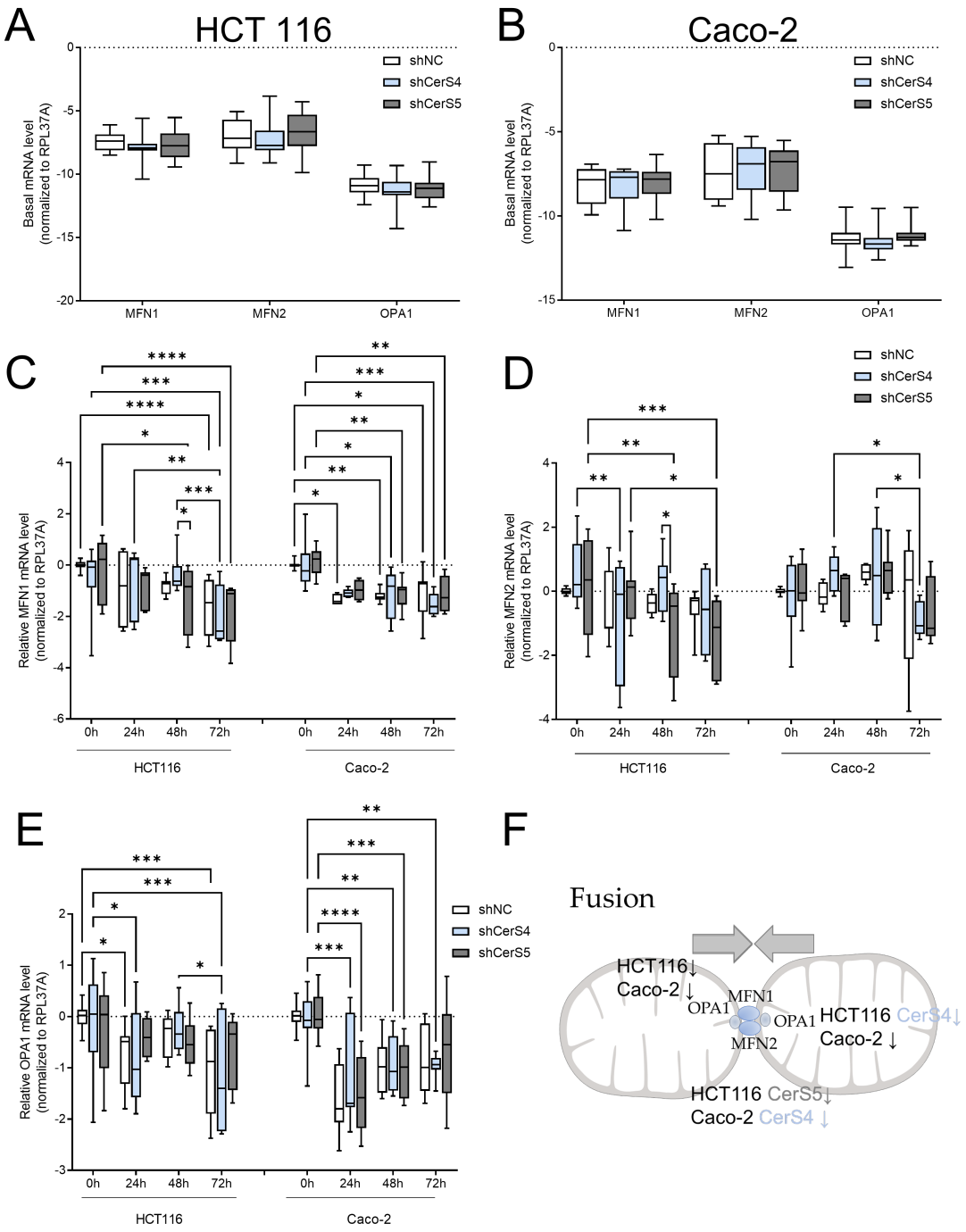

FIGURE 3.44: Mitochondrial fusion dynamic in HCT116 cells and Caco-2 cells during hypoxia. (A) Basal mRNA expression levels of shNC, shCerS4, shCerS5 HCT116 cells, and (B) Caco-2 cells calculated as ΔCT after normalization to the housekeeping gene RPL37A. ShNC, shCerS4 and shCerS5 HCT116 cells or Caco-2 cells were exposed to hypoxia for 24 h, 48 h and 72 h. Relative mRNA expression levels of (C) MFN1 (D) MFN2 and (E) OPA1 normalized to housekeeping gene RPL37A and control shNC HCT116 cells 0 h or control shNC Caco-2 cells 0 h (set to 0). (F) Mitochondrial fusion is regulated by MFN1 and MFN2 for the outer membrane fusion and OPA1 for inner mitochondrial membrane. Major changes in mRNA levels after chronic hypoxia are indicated by arrows. Data from n=3-8 independent experiments presented as median ±CI95. Statistically significant differences between the untreated and hypoxia exposed cell lines were determined by two-way ANOVA and Tukey's multiple comparison post-test (* p<0.05, ** p<0.01, *** p<0.001, **** p<0.0001).

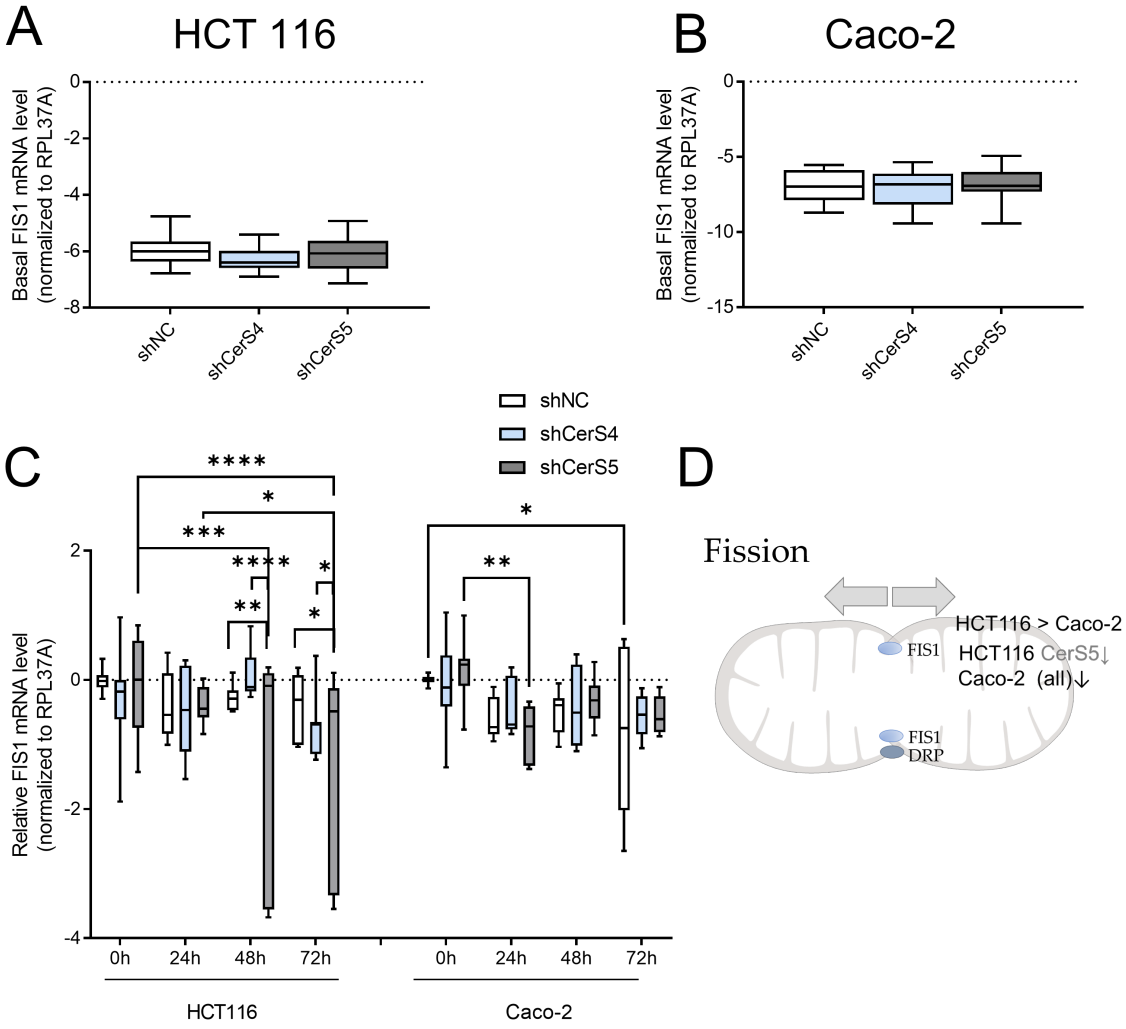

FIGURE 3.45: Mitochondrial fission in HCT116 cells and Caco-2 cells upon hypoxia. (A) Basal expression levels of FIS1 in HCT116 cells and (B) Caco-2 cells as ΔCT value after the normalization to housekeeping gene RPL37A. (C) Relative FIS1 mRNA levels (ΔΔCT value) normalized to RPL37A and control shNC HCT116 cells 0 h or control shNC Caco-2 cells 0 h (set to 0). (D) The major players of mitochondrial fission are DRP for the outer membrane and FIS1 for the inner membrane. Summary of FIS levels in HCT116 cells and Caco-2 cells. Major changes in mRNA levels after chronic hypoxia are indicated by arrows. Data from n=3-8 independent experiments, presented as median ±CI95. Statistically significant differences between the untreated and hypoxia-exposed cell lines were determined by two-way ANOVA and a Tukey's multiple comparison post-test (* p<0.05, ** p<0.01, *** p<0.001, **** p<0.0001).

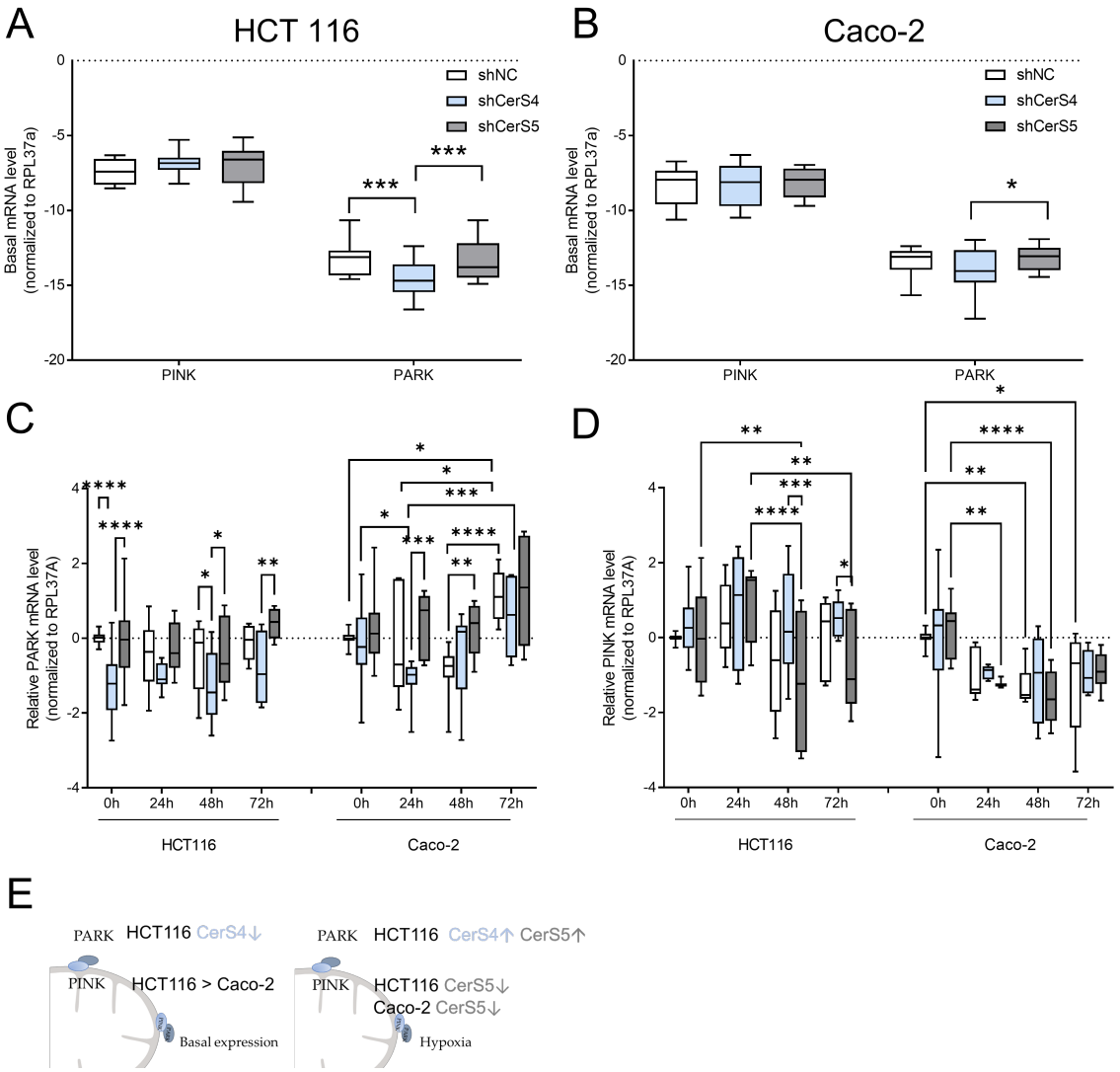

FIGURE 3.46: Downregulation of CerS4 or CerS5 in HCT116 cells and Caco-2 cells impedes mRNA expression of mitochondrial quality system. (A) Basal cellular mRNA levels of PINK and PARK calculated as ΔCT values after normalization to the housekeeping gene RPL37A in HCT116 cells and (B) Caco-2 cells. (C) Cells were exposed to hypoxia for 24 h, 48 h and 72 h. Relative PARK and (D) PINK mRNA expression was determined by qRT-PCR and calculated as relative values (ΔCT) by normalization to RPL37A and shNC HCT116 cells 0 h or shNC Caco-2 cells 0 h (set to 0). (E) Mitochondrial quality is sensored by PINK and PARK, which can induce mitochondrial degradation or regeneration. Summary overview of how CRC lines differed on basal expression (left) and in their response to hypoxia (right) are indicated by arrows. Data are median±CI95 of n=3-8. Statistically significant differences were determined by two-way ANOVA and Tukey's multiple comparison post-test (* p<0.05, ** p<0.01, *** p<0.001, **** p<0.0001).

In sum, analysis of the effects of CerS4 and CerS5 downregulation had different effects depending on the CRC cell line and metabolic pathway. In general, downregulation of CerS4 and CerS5 had no effect on basal metabolic pathway expression, despite GLUT1 mRNA. Here, basal GLUT1 mRNA expression was already higher in shCerS5 HCT116 cells than in shNC or shCerS4 HCT116 cells, but GLUT1 mRNA expression was lower than in shCerS5 Caco-2 cells than in shNC Caco-2 cells. Remarkably, during hypoxia, GLUT1 mRNA increased in all Caco-2 cell lines and shNC HCT116 cells, except for shCerS4 and shCerS5 HCT116 cells, in which GLUT1 levels did not increase significantly. The expression of the other enzymes such as LDHA, PDHA1 and PK showed no significant difference between the shNC, shCerS4 and shCerS5 HCT116 cells and Caco-2 cells, but at some time points, the expression was mostly higher in shCerS5 than in shCerS4 or lower depending on the cell line. For example, the increase in LDHA levels was greater in shCerS4 HCT116 cells than in shCerS5 HCT116 cells, whereas in Caco-2 cells, LDHA levels peaked at $48\,\mathrm{h}$ but did not differ between shCerS4 or shCerS5 Caco-2 cells. Similarly, PKM isoforms did not differ after CerS4 or CerS5 downregulation in CRC cells, but during hypoxia PKM2 expression increased in shCerS4 and shCerS5 HCT116 cells but not in shNC HCT116 cells, whereas in Caco-2 cells, PKM2 levels increased after hypoxia only in shCerS5 Caco-2 cells but not in shNC Caco-2 cells or shCerS4 Caco-2 cells. This suggests that expression changes during hypoxia depending on the gene and cell line, even if the basal expression was not affected. Thus, in shCerS5 HCT116 cells, the peak expression of PDHA or PK was reached after $24\,\mathrm{h}$ and further decreased at $48\,\mathrm{h}$ and $72\,\mathrm{h}$, such that the expression of LDHA, PK or PDHA were lowest in shCerS5 HCT116 cells at $72\,\mathrm{h}$, whereas the increase was inhibited in shCerS4 HCT116 cells compared with shNC HCT116 cells or shCerS5 HCT116 cells, and the expression levels of LDHA, PDHA PK and GLUT peaked at $48\,\mathrm{h}$ and then declined at $72\,\mathrm{h}$ (Figure 3.41). However, this difference in expression level was not due to a different upstream response to hypoxia, because PHD3 mRNA levels were not affected by CerS4 or CerS5 downregulation in the baseline state or during hypoxia (Figure 3.40). Interestingly, shCerS5 also showed a different response to hypoxia in other signaling pathways. In contrast, Caco-2 cells showed no major differences in the expression levels of LDHA, PK, PDHA or GLUT between shNC, shCerS4 ,and shCerS5 Caco-2 cells. The course of expression level was during hypoxia quite similar in the enzymes involved in the glucose-pathway (Figure 3.41). With regard to PPP, downregulation of CerS4 and CerS5 in HCT116 cells and Caco-2 cells did not affect basal expression of TKT and TKTL or expression of TKT and TKTL after hypoxia; only TKT levels increased in hypoxia in shCerS5 HCT116 cells compared with shNC HCT116 cells and shCerS4 HCT116 cells (Figure 3.43). Similar effects were also observed in the mitochondrial dynamics. In general, basal mRNA expression of fission and fusion proteins did not differ significantly in shCerS4 and shCerS5 HCT116 cells or Caco-2 cells, but after hypoxia, shCerS5 HCT116 cells and shCerS4 Caco-2 cells in particular showed difference in the expression. Thus, downregulation of CerS5 in HCT116 cells resulted in downregulation of FIS and MFN2 levels, whereas in shNC HCT116 cells, FIS and MFN2 levels did not decline after hypoxia. In contrast, the mRNA expression of OPA1 declined after hypoxia in shNC HCT116 cells and shCerS4 HCT116 cells but not in shCerS5 HCT116

cells. This indicates that downregulation of CerS5 in HCT116 cells affects the mitochondrial dynamics in hypoxia. In Caco-2 cells, shCerS5 Caco-2 cells did not differ from shNC Caco-2 cells with respect to expression levels in hypoxia, but in shCerS4 Caco-2 cells, FIS1 levels did not decrease as in shNC Caco-2 cells. Moreover, MFN2 levels decreased after hypoxia in shCerS4 Caco-2 cells and shCerS4 HCT116 cells compared with shNC Caco-2 cells and shNC HCT116 cells, respectively (Figure 3.44, Figure 3.45). Proteins regulating mitochondrial health showed a difference already on basal level: basal expression of PARK was much lower in shCerS4 HCT116 cells and shCerS4 Caco-2 cells compared to shNC HCT116 cells or shCerS5 HCT116 cells and shCerS5 Caco-2 cells. After hypoxia, PARK expression did not change in HCT116 cells, whereas it declined in Caco-2 cells, except in shCerS5 Caco-2 cells, where PARK levels did not decrease. A similar effect was also observed for PINK levels, which decreased in Caco-2 cells under hypoxia but not in shCerS4 Caco-2 cells. In HCT116 cells, shCerS5 HCT116 cells showed greater dynamics in the expression of PINK: Whereas PINK levels did not change with hypoxia in shNC HCT116 cells and shCerS4 HCT116 cells, they increased in shCerS5 HCT116 cells at $24\,\mathrm{h}$ but then declined at $48\,\mathrm{h}$ and $72\,\mathrm{h}$, resulting in lower PINK mRNA expression compared to shCerS4 HCT116 cells (Figure 3.46). This suggest that the absence of CerS5 may influence the regulation of mitochondrial quality.

3.5.6 Transcriptional regulation of CerS4

The CerS4 gene is located on chromosome 19p13.2, and the putative promotor region for human CerS4 is assumed to be located in a region approximately $1{,}300\,\mathrm{bp}$ upstream of the transcription start site [188]. To better understand the reduced CerS4 levels in HCT15 cells, direct transcriptional regulation of CerS4 was analyzed by luciferase reporter gene assay. Transfection of HCT15 cells and HCT116 cells with an empty pGL3 basic vector did not alter the basal luciferase activity in HCT15 cells and HCT116 cells, which is measured in RLU. However, RLU increased 183-fold ($p<0.0001$) with the CerS4 promotor in HCT116 cells, while RLU increased 45-fold ($p=0.04$) in HCT15 cells transfected with the full length CerS4 promotor compared to the pGL3 basic promotor. The 0.25-fold lower RLU in HCT15 cells compared to HCT116 cells was significant ($p<0.0001$), indicating a basal difference in CerS4 transcription (Figure 3.47 A). Once CerS4 is transcribed to an mRNA, further post transcriptional regulation may occur by the 3'UTR to regulate the CerS4 translation. Transfecting the CRC cells with CerS4 3'UTR promotor construct affected the luciferase activity. RLU increased 60-fold in HCT116 cells compared to the empty vector pGL3 promotor ($p=0.0017$). In HCT15 cells, this increase was only by 8.5-fold ($p=0.02$) compared to control and 0.14-fold compared to HCT116 cells ($p=0.008$) (Figure 3.47 B). These data indicate that in HCT15 cells CerS4 is repressed at transcriptional and post-transcriptional levels.

Whether epigenetic regulatory mechanism are involved in CerS regulation was investigated by adding the HDAC inhibitors TSA and SAHA to HCT116 cells and HCT15 cells (Figure 3.48 A). Treatment of CRC cells with HDAC inhibitors and analysis of CerS mRNA transcription revealed that CerS1, CerS4 and CerS5 genes were regulated by (histone) acetyl modulation depending on the CRC cell line (Figure 3.48 B). Because HDAC inhibitors were

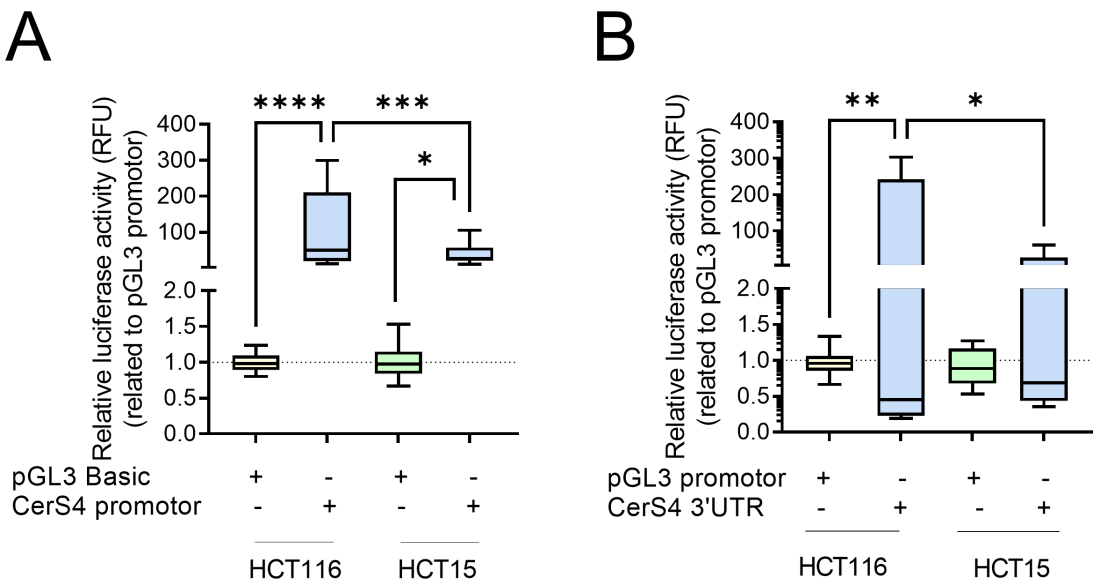

FIGURE 3.47: Difference in transcriptional regulation of CerS4 expression through (A) CerS4 promotor activity or (B) mRNA stabilization by 3'UTR region determined by firefly luciferase activity. (A) The full length CerS4 promotor increased RLU in both HCT116 cells (HCT116) and in HCT15 cells (HCT15) . (B) Also, the insertion of CerS4 3'UTR increased RLU. However, in both cases, the activity was much lower in HCT15 cells than in HCT116 cells. Data from n=4-6 independent experiments shown as median ±CI95. Statistically significant differences were calculated by one-way ANOVA with a Sidak's multiple comparison post-test (* p<0.05, ** p<0.01, *** p<0.001, **** p<0.0001).

dissolved in DMSO, HCT15 cells and HCT116 cells treated with DMSO were used as controls. DMSO treatment induced an increase in CerS1 mRNA and CerS4 mRNA in HCT15 cells, whereas no other changes were detected with DMSO treatment (Figure 3.48 B). Comparison of SAHA treatment with the DMSO control revealed a significant increase in CerS1 mRNA and CerS5 mRNA in HCT116 cells (Figure 3.48 C) In HCT116 cells, treatment with SAHA and TSA did not alter the mRNA expression of CerS4 and CerS6. In contrast, treatment with SAHA and TSA had a different effect on HCT15 cells: The expression level of CerS1, CerS2 and CerS3 did not change significantly after SAHA or TSA treatment. Treatment with $50\,\mu M$ SAHA induced a 3-fold increase in CerS4 compared to DMSO control (p=0.06) and a 10-fold increase compared to HCT15 cells treated with $50\,nM$ TSA. Treatment with $50\,nM$ TSA significantly increased CerS5 mRNA level. In contrast, CerS6 mRNA level in HCT15 cells decreased significantly after treatment with $100\,nM$ TSA (Figure 3.48 C). Thus, all in all, treatment with HDAC inhibitors has different effects depending on the CRC cell line: it significantly increases the expression of CerS1 and CerS5, whereas treatment with HDAC inhibitors in HCT15 cells increases the expression of CerS4 and CerS5 but decreases the expression level of CerS6.

To sum up, CerS4 mRNA expression is as variable in CRC cell lines as in tumor patients. As shown by the luciferase activity assay, CerS4 is regulated at the transcriptomic and post-transcriptional levels. Treatment of CRC cells with HDAC inhibitors resulted in a 3-fold

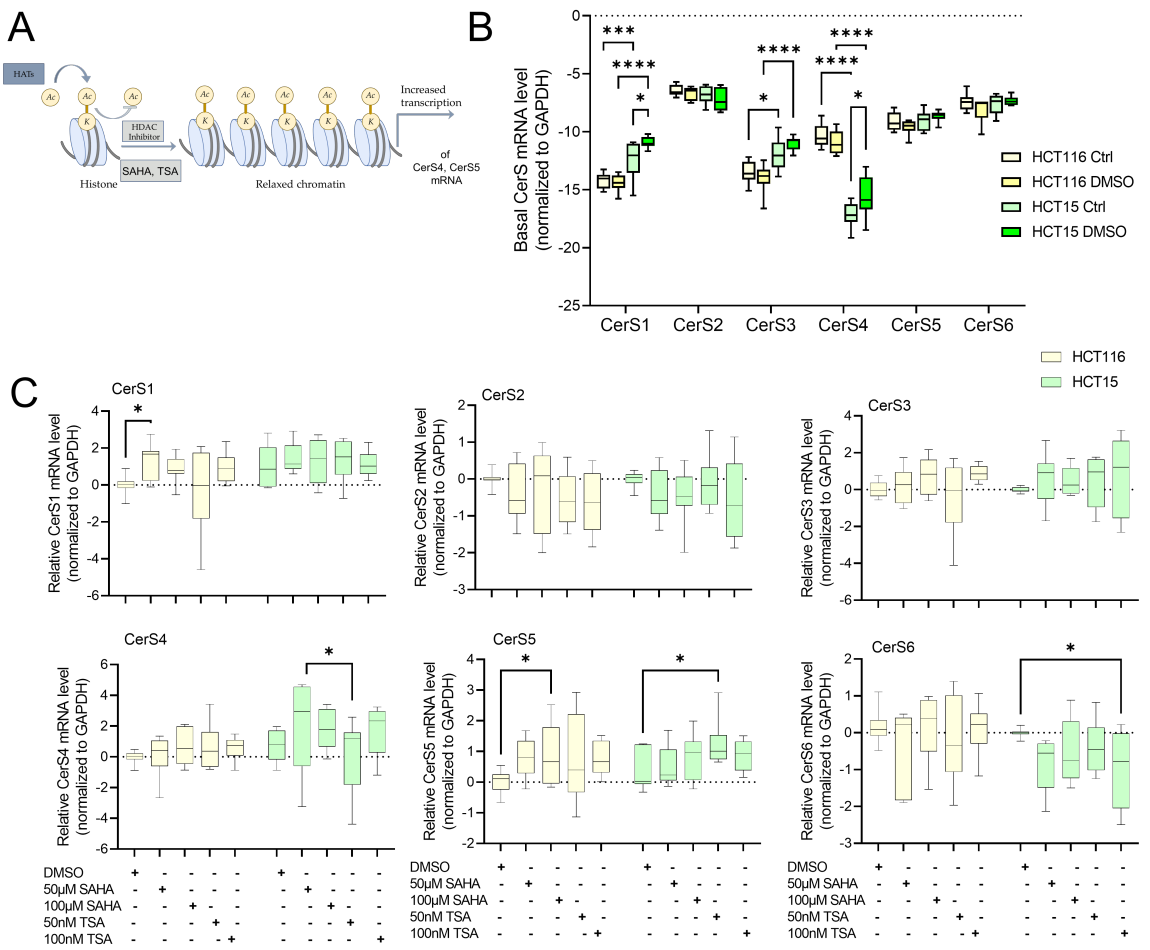

FIGURE 3.48: Epigenetic regulation of CerS by HDACs inhibitors. (A) Schematic cartoon after [227]. Histone acetylation (Ac) at specific lysine (K) residues by HATs. HDACs "remove acetyl groups from lysine amino acids on histones" [266]. HDAC inhibitors increase acetylation and lead to a relaxed chromatin, which enhances gene transcription. HDAC inhibitors such as SAHA and TSA block the deacetylation. (B) Basal CerS mRNA levels normalized to GAPDH comparing the effects of DMSO to control HCT116 cells and HCT15 cells. For CerS1, CerS3 and CerS4, DMSO treatment increased their expression. (C) CerS mRNA expression level in HCT116 cells and HCT15 cells after treatment with $50\,\mu M$ and $100\,\mu M$ SAHA and $50\,nM$ and $100\,nM$ TSA for $4\,h$. The relative CerS mRNA level normalized to GAPDH was compared with the corresponding DMSO control. Median with CI95 is given for data from four independent experiments. Statistical analysis was performed by two-way ANOVA with Tukey's multiple comparison post-test tests (* $p<0.05$, ** $p<0.01$).

increase of CerS4 but this did not provide clear evidence that CerS4 mRNA expression is also regulated by the acetylation pattern of histones.

After finding a significant difference between HCT116 and HCT15 in full-length CerS4 promotor, CerS4 promoter deletion constructs were used to identify specific transcription factors based on predicted binding sites: CerS4 construct F started at $979\,bp$ upstream of the transcription start site near the predicted NFκB binding site. CerS4 construct D started at $607\,bp$ upstream of the transcription start site and still contained the putative binding sites for SP1 and AP-1 (Figure 3.49 A). The luciferase activity assay with these constructs also showed an increased RLU, suggesting that, particularly in HCT15, an important regulatory

region may be located directly upstream of the transcription start site between $607\,\mathrm{bp}$ and the transcription start. Here, the CerS4 full promotor was set to 1 in both cell lines. In HCT116 cells, CerS4 constructs D and F increased the RLU threefold ($p<0.0001$). In HCT15 cells, only construct CerS4 F increased RLU threefold ($p<0.0001$), and this increase was also significantly different from construct D ($p<0.0001$). The RLU difference in construct CerS4 D between HCT116 cells and HCT15 cells was also significant ($p<0.0001$) (Figure 3.49 B). This suggests that a marked difference between HCT116 cells and HCT15 cells is due to the region between $607\,\mathrm{bp}$ and the transcription start site.

As seen in Figure 3.48, treatment with HDAC inhibitors, particularly $50\,\mu\mathrm{M}$ SAHA, increased CerS4 mRNA levels. Therefore, HCT116 cells and HCT15 cells transfected with CerS4 constructs were treated with HDAC inhibitors, and the luciferase activity was quantified. Similar to Figure 3.48, HDAC treatment had a stronger effect on HCT15 cells than on HCT116 cells. However, construct D also showed a greater difference compared to full length promotor or construct F in HCT116 cells. While RLU did not significantly change in HCT116 cells transfected with the full length promotor and treated with HDAC inhibitors, HCT116 cells transfected with construct D and treated with $100\,\mathrm{nM}$ TSA significantly increased RLU compared to control (untreated) HCT116 cells (3-fold, $p<0.0001$), HCT116 cells treated with $50\,\mu\mathrm{M}$ SAHA (4-fold, $p=0.0002$) or with $50\,\mathrm{nM}$ TSA (2.3-fold, $p=0.007$). Furthermore, $100\,\mathrm{nM}$ TSA treatment increased luciferase activity in HCT116 cells transfected with construct D by 2.7-fold ($p=0.03$) compared to the full length promotor treated with $100\,\mathrm{nM}$ TSA. In HCT116 cells transfected with construct F, the luciferase activity did not change significantly after treatment with SAHA or with $100\,\mathrm{nM}$ TSA (Figure 3.49 C).

In HCT15 cells, SAHA treatment had a greater effect on HCT15 cells transfected with CerS4 D construct. In HCT15 cells, as little as $50\,\mu\mathrm{M}$ SAHA increased the RLU of the CerS4 full-length promotor by sixfold ($p=0.02$), while luciferase activity did not change after treatment with TSA. In HCT15 cells transfected with the CerS4 D construct, treatment with $50\,\mu\mathrm{M}$ SAHA increased RLU by 10-fold ($p<0.0001$). RLU was also significantly different for CerS4 D constructs compared to the full-length promotor in HCT15 cells ($p=0.03$). Luciferase activity was also significantly higher after SAHA treatment of HCT15 cells transfected with CerS4 D than after $50\,\mathrm{nM}$ TSA ($p=0.0002$) and $100\,\mathrm{nM}$ TSA ($p=0.007$). Treatment with TSA did not significantly alter RLU in HCT15 cells (Figure 3.49 C). This suggest that $50\,\mathrm{nM}$ SAHA induced the luciferase activity greater in HCT15 cells than in other constructs or treatments.

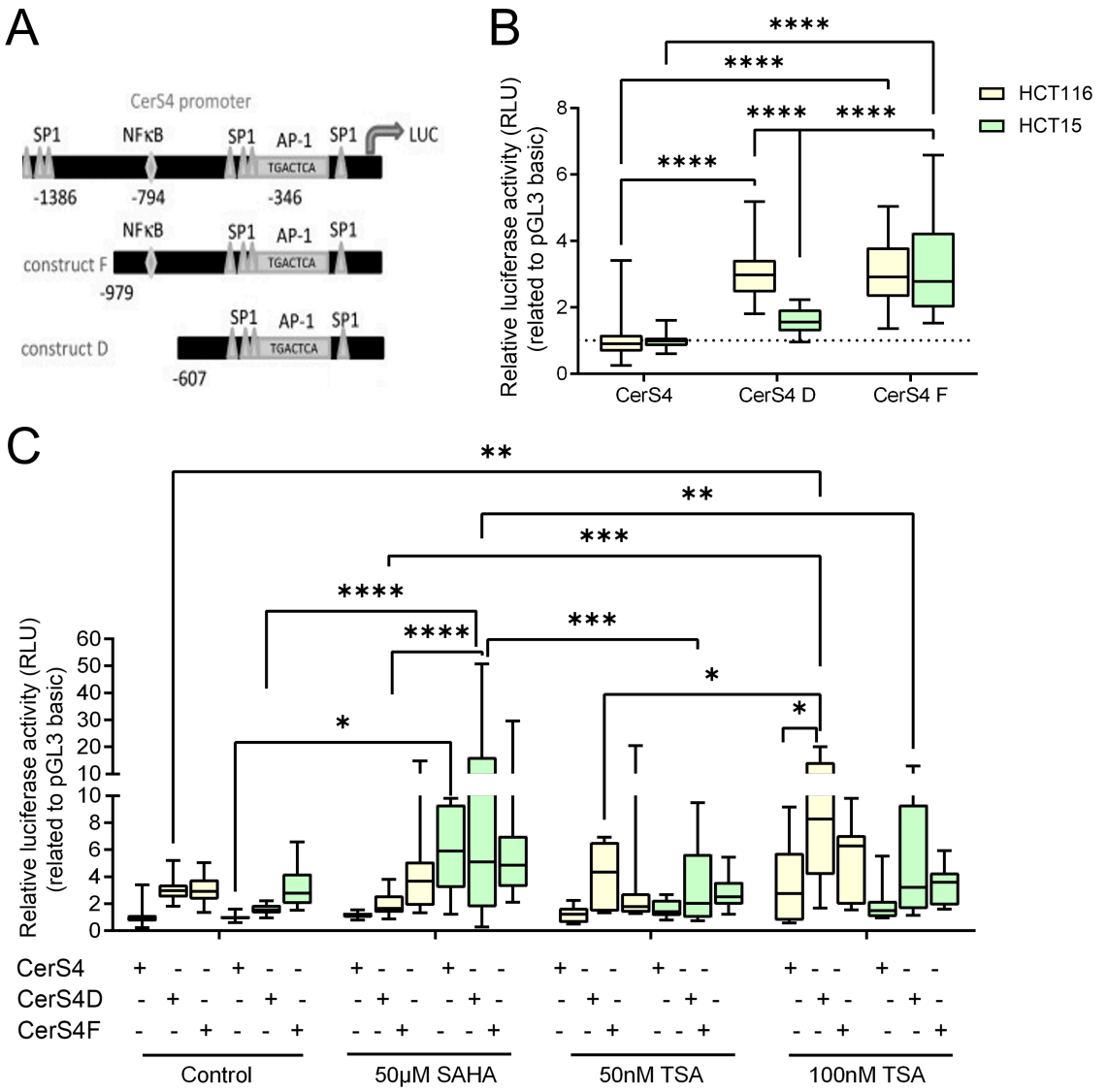

FIGURE 3.49: Luciferase activity assay with CerS4 promoter deletion constructs can be amplified with HDACS inhibitors. Overview of CerS4 promotor constructs previously published in [188]: In addition to the full-length CerS4 promotor, a 979 bp long promotor (construct CerS4 F) and a 607 bp bp long promotor (construct CerS4 D) were used for transfection in HCT116 cells and HCT15 cells. (B) Relative luciferase activity of HCT116 cells and HCT15 cells transfected with full-length CerS4 promoter (CerS4), CerS4 D construct (CerS4 D), and CerS4 F construct (CerS4 F). RLU was referenced to the full-length CerS4 promoter for each CRC line (set to 1). (C) Relative luciferase activity after transfection of HCT116 cells and HCT15 with full-length CerS4, CerS4 D and CerS4 F promotor constructs and treatment with HDAC inhibitors. Data from n=3 independent experiments shown as median ±CI95. Statistically significant differences were calculated using a two-way ANOVA with a Sidak's multiple comparison post-test (* p<0.05, ** p<0.01, *** p<0.001, **** p<0.0001).

3.5.7 Hypoxia reduces CerS4 promotor activity

As shown in subsection 3.5.2, hypoxia reduced CerS4 mRNA levels in CRC cells. To further analyze the relationship between hypoxia and CerS4, the luciferase-based CerS4 promotor assay (see subsection 3.5.6) was performed under normal conditions and under hypoxia.

HCT116 cells infected only with the Renilla luciferase construct showed no difference in the RLU after 24 h. The same was observed for Caco-2 cells transfected with Renilla construct only: RLU did not differ after 24 h hypoxia (data not shown). Only the difference in RLU between HCT116 cells and Caco-2 cells was significantly different. In HCT116 cells, the RLU was 1.2-fold higher than in Caco-2 cells at 0 h. The difference between the two cell lines persisted after 24 h: A 0.6-fold higher RLU (p=0.06) was observed in HCT116 cells compared to Caco-2 cells, indicating that hypoxia itself does not interfere with Renilla expression, but promotor activity is different in the two cell types. Thus, RLU of HCT116 cells transfected with the CerS4 promotor increased significantly compared with the empty control vector (pGL2 basic). Luciferase activity was 1.88-fold greater in HCT116 cells transfected with the CerS4 promotor than in Caco-2 cells (p<0.0001) (Figure 3.50 A). However, after 24 h of hypoxia, the RLU of the CerS4 promotor decreased by 0.16-fold in HCT116 cells and Caco-2 cells (p<0.0001). With the significant decrease in promotor activity in HCT116 cells and Caco-2 cells under hypoxia, no difference was detected between the pGL3 basic control vector and CerS4 promotor under hypoxia anymore (Figure 3.50 A). This suggests that CerS4 expression is inhibited by hypoxia already at the transcriptional level (see subsection 3.5.2).

To further specify the relationship between hypoxia and CerS4 promotor activity, HCT116 cells and HCT15 cells were transfected with different CerS4 promoter constructs and exposed to hypoxia. Here, 24 h of hypoxia resulted in the same decrease as in HCT116 cells and Caco-2 cells, and the effect was enhanced after 48 h of hypoxia. The luciferase activity of CerS4 promoter constructs under normal conditions was previously described in Figure 3.49. In all CRC cells, hypoxia exposure reduced the RLU of HCT116 cells and HCT15 cells regardless of the transfected CerS4 promoter construct: In HCT116 cells, hypoxia exposure reduced the luciferase activity of full-length CerS4 promotor by 0.17-fold at 24 h (p<0.0001) and by 0.11-fold at 48 h (p<0.0001). Hypoxia also reduced the RLU of CerS4 deletion constructs in HCT116 cells: CerS4 F in HCT116 cells decreased 0.08-fold at 24 h (p<0.0001) and 0.048-fold at 48 h (p<0.001). Construct CerS4 D in HCT116 cells was decreased 0.13-fold after 24 h (p<0.0001) and 0.08-fold after 48 h (p<0.0001) (Figure 3.50 B). There was no significant difference between 24 h and 48 h and also the difference between the constructs and the full-length promotor lost this difference after hypoxia and no difference was detected between the CerS4 constructs in HCT116 cells. The decrease in luciferase activity after hypoxia was independent of promotor constructs in HCT116 cells, as RLU also decreased 0.7-fold after 48 h in HCT116 cells (p=0.02), indicating that luciferase activity is reduced after 48 h in HCT116 cells (Figure 3.50 B).

A similar pattern was observed in HCT15 cells as in HCT116 cells. After 24 h, RLU decreased significantly by 0.3-fold (p<0.0001) only in HCT15 cells transfected with the CerS4 F construct, while RLU declined by 0.46-fold in HCT15 cells transfected with the full length CerS4 promotor and by only 0.7-fold in HCT15 cells transfected with CerS4 D. After 48 h, RLU reduced significantly in all HCT15 cells transfected with the full-length CerS4 promotor (0.25-fold decrease, p=0.03), CerS4 D construct (0.53-fold decrease, p=0.03) and CerS4 F

construct (0.08-fold decrease, p<0.0001). Since RLU was already high in HCT15 cells transfected with the CerS4 F construct under control conditions, it was significantly different from control HCT15 cells transfected with the CerS4 F construct at 48 h (p<0.0001) and 24 h (p=0.02). Luciferase activity was significantly higher in HCT15 cells transfected with the CerS4 D constructs compared to the full-length promotor at 24 h (2.5-fold increase, p=0.04) and after 48 h (3.4-fold increase, p=0.098) (Figure 3.50 B). However, the RLU of HCT15 cells transfected with Renilla construct alone was not significantly different after 24 h and 48 h of hypoxia (data not shown). This suggests that it was not the luciferase activity *per se* that was sensitive, but the regulation of the promotor constructs that was more sensitive to hypoxia.

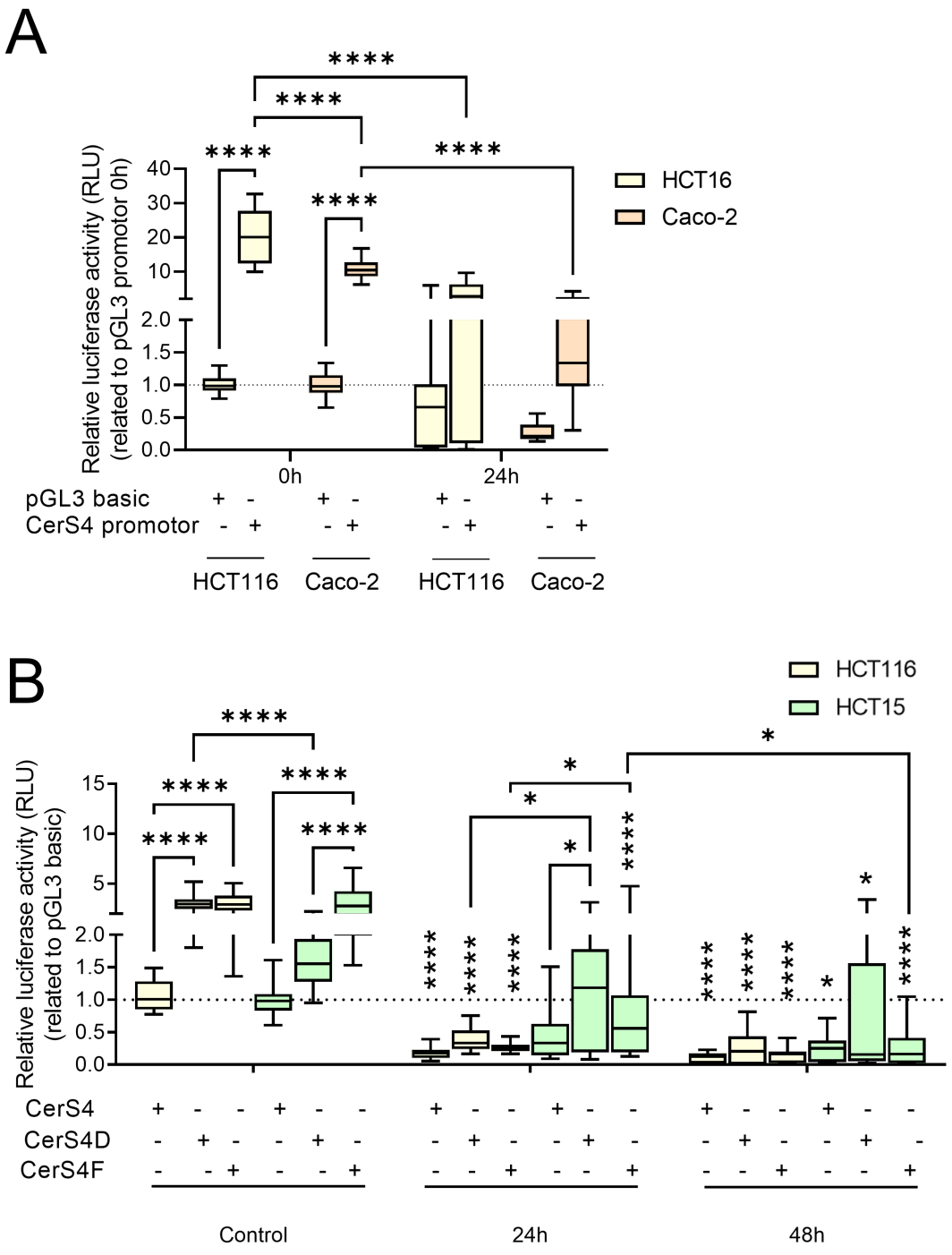

FIGURE 3.50: Hypoxia affects transcriptional regulation of CerS4 expression. (A) Naive HCT116 cells (HCT116) and Caco-2 cells (Caco-2) were transfected with the pGL3 basic firefly luciferase reporter plasmid, either containing the full-length promotor of CerS4 or pGL3 basic promotor and incubated for 24 h under hypoxia. RLU was determined by normalizing to each empty pGL3 basic plasmid (set to 1). (B) HCT116 cells (HCT116) and HCT15 cells (HCT15) were transfected with different CerS4 promotor constructs and exposed to hypoxia for 24 h and 48 h. Relative RLU was normalized to each CerS4 full length promotor under normoxia (control). Data are means ±SEM from 3 independent experiments. Statistically significant differences between the untreated and hypoxia-exposed cell lines were determined by two-way ANOVA/ Tukey's multiple comparison post-test (* $p<0.05$, **** $p<0.0001$).

Chapter 4

Discussion

4.1 Part I

Cer play an important role in CRC and colitis progression. Measurements of sphingolipids in plasma of CRC patients revealed that Cer d18:1/16:0, Cer d18:1/18:1, Cer d18:1/20:0 and Cer d18:1/24:1 distinguish between early and advanced cancer [267, 268]. Previously, different CerS KO mice were studied in the DSS and AOM/DSS induced model and highlighted a chain length specific effect. Each KO (CerS2, CerS5, CerS6) aggregated disease progression but due to different mechanisms [189, 192, 269, 220]. Further lipidomic changes in patients show that CerS4 and Cer d18:1/18:0 or Cer d18:1/20:0 decreases in CRC patients [270, 271] and in plasma of colitis patients [272].

This project demonstrated that CerS4 deficiency has a tissue-specific impact on disease progression in colitis and CAC, and was published along with other collaborative studies in [204]. In both disease models, CerS4 deficiency resulted in acceleration of disease progression, although it was usually fatal in CAC model. Tissue-specific CerS4 deficiency (CerS4 LCK/Cre mice or CerS4 Vil/Cre mice) had less impaired DSS-induced colitis or AOM/DSS-induced CAC. Thus, CerS4 LCK/Cre mice were sensitive only to AOM/DSS-induced CAC but not in the acute DSS induced colitis, and CerS4 Vil/Cre mice were not vulnerable towards AOM/DSS induced CAC. Differences were also observed in tumor development, which were significant: While CerS4 LCK/Cre mice had significantly more tumors, especially extensive tumors, WT mice had larger tumors in the distal colon. The role of CerS4 was not restricted to tumor development, but showed a central role in inflammation, especially its role in T cells for resolution of inflammation, which was evident in the pan-colitis of CerS4 LCK/Cre mice and even in the severe ulcerative colitis of aborted CerS4 KO mouse.

CerS4 impact on intestinal barrier

The DSS induced colitis model is thought to trigger inflammation due to permeabilization of the intestinal barrier [273, 274, 275]. The integrity of the intestinal barrier plays a critical role in progression of IBD. Already impaired sphingolipid homeostasis affects intestinal barrier integrity, as shown in CerS2 deficient mice [189, 192]. In the intestine, basal knockdown of CerS4 reduced Cer d18:1/18:0 and Cer d18:1/20:0 but did not alter other

sphingolipids in CerS4 KO mice. This decrease does not affect TJs proteins, as indicated by the immunohistostaining of occludin and ZO-1 in colon or TEER and FITC permeability in Caco-2 cells. This suggests that CerS4 deficiency does not impair the barrier function of colon. However, a barrier effect could be anticipated because Cer d18:1/18:1 regulates PKCζ [276]. PKCζ activation is involved in barrier integrity. While localization of PKCζ in membrane increases its activity, cytosolic PKCζ decreases its activity. In addition, PKCζ affects ZO-1 distribution, and inhibiting PKCζ protects the disruption of TJs caused by *E.coli* [277]. Sphingolipid measurement of Cer d18:1/18:1 in the colon did not differ between CerS4 KO mice and WT mice, explaining the missing effect on barrier function due to other compensated mechanisms. Because CerS4 deficiency does not affect barrier integrity, the sensitive response to DSS induced colitis in CerS4 KO mice is attributed to immune cells.

CerS4 impact on immune response

CerS4 KO mice and CerS4 LCK/Cre mice suffered from neutrophil leukocytosis (high number of neutrophils) in the colon and blood. The same increase is observed in CerS6-deficient mice after DSS treatment [269]. Therefore, CerS6 and Cer d18:1/16:0 are assumed to have an anti-inflammatory effect by suppressing neutrophil migration or deactivating them [193]. Although neutrophil recruitment is essential for modulation of the inflammatory response, resolution, and healing of the mucosa, excessive recruitment in IBD patients leads to mucosal injury [278, 279, 280]. Notably, in UC, accumulation of neutrophils correlates with the severity of colitis [281]. Also, in CerS4 KO mice, large number of neutrophils led to severe inflammation, which was manifested by severe shortening of the colon. Indeed, the specific chain length of Cer and different CerS isoforms are involved in the regulation of neutrophils. CerS2 and consequently very long chain Cer mediate proinflammatory responses in neutrophils and monocytes. CerS2 and its very long chain Cer have been shown to affect the chemokine receptor CXCR2 in neutrophils and are essential for proper translocation of granulocyte colony stimulating factor receptor into lipid rafts. Therefore, deletion of CerS2 resulted in reduced neutrophil infiltration in experimental autoimmune encephalomyelitis and multiple sclerosis models [282, 283].CXCR2 is also involved in the neutrophil chemotaxis in IBD and AOM/DSS-induced cancer progression [284, 285]. Since the very long-chain ceramides were mainly upregulated in various tissues such as intestine, liver, spleen, and thymus, it could be that the very long-chain Cer were also compensatory upregulated in neutrophils and caused an enhanced immune response in CerS4 KO mice. Therefore, the increase in very long chain Cer in tissues may have increased the chemotaxis, and caused the severe ulcerative colitis that resulted in a human end point with late AOM/DSS treatment in CerS4 KO mice.

The balance between pro-inflammatory and anti-inflammatory immune cells is important for resolution of inflammation. In the colon of CerS4 KO mice, neutrophile leukocytosis was observed after AOM/DSS treatment, but the number of Tregs also increased. Similarly, in AOM/DSS treated CerS4 LCK/Cre mice, the frequency of neutrophils and Tregs in the

blood increased, whereas T cells and B cells decreased. This is very similar to the lymphocyte populations of CD patients with long disease duration. These patients also have elevated Tregs, decreased T cells and very low B cells [286]. In tumor patients, frequencies of DCs, $CD8^+$ and $CD4^+$ T cell are decreased and altered in function, whereas regulatory lymphocytes such as Tregs are increased because Tregs proliferate in the periphery before entering the tumor microenvironment [287]. Tregs are important immune modulators for the resolution of inflammation and tissue regeneration. They "secrete IL-13, which stimulates IL-10 production in macrophages", which in turn activate the engulfment of apoptotic cells (effector cytosis) [288]. The Polarization to M2 like macrophages in the colon tissue is stimulated by the interaction with Tregs. M2 polarized macrophages promote tissue remodeling, angiogenesis and tumor progression [289, 290]. Although this function helps to resolve inflammation, it may also support tumor formation. In [204], CerS4 LCK/Cre mice had a high frequency of M2 macrophages in colon tissue after AOM/DSS treatment. Therefore, the abundance of M2 like macrophages may have contributed to the higher tumor incidence observed in AOM/DSS treated CerS4 LCK/Cre mice. In another study, an increase of Tregs was also observed in late stages of AOM/DSS induced CAC in mice. The Tregs displayed an activated phenotype, which in turn had a suppressive capacity toward $CD4^+$ and $CD8^+$ T cells, "which was also associated with a tumor-promoting function in CAC [291]" [204]. Dysregulation in T cell homeostasis also influences the mutation suppression in stem cells. Cancer incidence increases not only with increased mutation frequency but also with survived damaged stem cells [292, 293]. The use of TCRβ knockout mice shows less mutation frequencies and tumor incidences in the AOM/DSS treatment, indicating that T cells, likely immunosuppressive Tregs or the absence of cytotoxic T cells due to the TCRβ knockout, may support survival of DNA damaged stem cells [292].

Role of CerS4 in T cells

This severe effect of AOM/DSS in CerS4 LCK/Cre mice suggests an important role of CerS4 in T cell function. In addition to the reduced $CD8^+$ T cells in the blood, $CD8^+$ T cells are absent in the colon of CerS4 LCK/Cre mice [204]. The absence of the important cytotoxic T cells was compensated by increased eosinophils, neutrophils and monocytes in blood and colon [204] after AOM/DSS treatment. In analyzing the effect of CerS in T cell response, Chao et al. (2019) observed that downregulation of CerS4 tend to an increase FoxP3 in $CD4^+$ T cells [294]. This suggests that CerS4 may be involved in T cell development. Sofi et al. (2017) have shown that T cell development is similar in WT mice and CerS4 KO mice, and only CerS6 KO mice show increased proliferation [196]. In contrast to their study, we demonstrate that CerS4 deficiency in $CD4^+$ Jurkat T cells impairs T cell function. CerS4 deficiency leads to prolonged cytokine secretion and constitutive CD28 signaling [204]. The increased secretion of IL-10, IL-6, TNF-α and IFN-γ from activated CerS4 LCK/Cre thymocytes fits well with the observed pan colitis in AOM/DSS treated CerS4 LCK/Cre mice. The pathway behind this dysregulation could be attributed to the interaction of CerS4 produced Cer d18:1/18:0 and Cer d18:1/20:0 and the TGF-β signaling

pathway [295]. In human T cells, TGF-β inhibits T cell proliferation by increasing the ratio of cyclin-dependent kinase inhibitor and cyclin, but enhances cytokine signaling after stimulation [296]. TGF-β signaling is fine-tuned by the intracellular inhibitor TβRI/SMAD7 complex, which prevents phosphorylation of SMAD2 and SMAD3 and thus complex formation with SMAD4 and subsequent translocation to the nucleus. Both Cer d18:1/18:0 and Cer d18:1/20:0 are shown to stabilize this inhibitory TβRI/SMAD7 complex. Thus, downregulation of CerS4 enhances TGF-β signaling in primary cilia [295], suggesting a similar role for CerS4-produced ceramides in stabilizing SMAD7 in T cells. SMAD7 has a double-edged role in inflammation and tumor development. On the one hand, it is a target in IBD treatment to resolve inflammation; on the other hand, overexpression of SMAD7 reduces tumor development in AOM/DSS model. Anti-SMAD7 antisense oligonucleotides are also used in IBD patients to restore TGF-β activity and constrains cytokine production [297]. Also, in animal models, inhibition of SMAD7 by antisense inhibitor ameliorates DSS induced colitis in mice [298]. In contrast, overexpression of SMAD7 in $CD4^+$ T cell raises IFN-γ levels, accumulates cytotoxic $CD8^+$ T cells and results in a less tumor development in AOM/DSS induced CAC model [299]. This is consistent with increased tumor incidence in CerS4 LCK/Cre mice, suggesting that CerS4 ablation reduces the TβRI/SMAD7 complex and likely enhances TGF-β signaling.

The importance of CerS in T cell function in AOM/DSS induced CAC and DSS induced inflammation is also seen in CerS5 KO mice, in which T cell numbers are also reduced and CerS5 deficient T cells have reduced NFκB activation after stimulation [220]. However, not only the CerS5 derived Cer d18:1/16:0 is important for T cell function, CerS6 derived Cer d18:1/16:0 is also required for TCR signal transduction and T cell proliferation [196]. The impact on colitis is opposite, while adoptive transfer of CerS6 deficient splenocytes attenuates colitis progression [300], it increases the sensitivity against DSS induced colitis in CerS5 KO mice [220].

Increased AOM toxicity via CerS4 deficiency

The high susceptibility towards AOM/DSS in CerS4 KO mice is related to AOM in combination with DSS. Although the initial dose of $10\,\mathrm{mg\,kg^{-1}}$ AOM one day before the start of DSS treatment was reduced to an injection of $5\,\mathrm{mg\,kg^{-1}}$ twice, subsequent administration of DSS via drinking water resulted in a higher lethality in CerS4 KO mice ($84.61\,\%$) than in WT mice ($19.35\,\%$) or CerS4 Vil/Cre mice ($0\,\%$) and CerS4 LCK/Cre mice ($0\,\%$). The analysis of the late aborted mouse showed that severe ulceration resulted in death. However, because the lethality was higher during the first DSS cycle ($64.54\,\%$ for CerS4 KO mice and $12.9\,\%$ for WT mice) than after the second cycle, this suggests that CerS4 KO mice had a higher intolerance to AOM. AOM is a methylating agent that forms O6-methylguanine and leads to mismatch mutations during replication [301], causing preneoplastic lesions in the colon [302], but also long-term renal and liver tumors [303]. In the liver, it is metabolized by CYP2E1 [304] and causes progressive liver injuries and fulminant hepatic failure [305]. Although a twofold lower dose of AOM was injected, yet CerS4 KO mice, but not CerS4

Vil/Cre mice or CerS4 LCK/Cre mice, were highly sensitive to the toxic effect. In the liver generated AOM-metabolits are important factors that may influence susceptibility to the AOM/DSS induce CAC model.

As in the colon, disruption of sphingolipid homeostasis contributes to hepatocellular death and liver injury. In particular, Cer d18:1/24:0 increases with hepatoxicity and appears to be a sensitive biomarker [306]. Very long chain Cer is important for the lipids raft formation, and any disturbance in the sphingolipid balance impairs the biophysical membrane function [189, 307, 308, 309]. Thus, CerS2 knockout mice exhibit mislocalization in intercellular junctions such as the Tjs in the intestine [192, 189] and gap junctions in the liver [307]. In CerS2 knockout mice, mislocalization of connexin 32 protects the liver from hepatoxic agents [307], suggesting that the absence of very long chain Cer may also have beneficial side effects. In this project, CerS4 deficiency was best seen in the liver. The reduced levels of dhCer, GlcCer and LacCer d18:1/d18:0 were compensated by increased levels of very long chain Cer, namely Cer d18:1/22:0 and Cer d18:1/24:1. While Cer d18:1/18:0 was not altered, Cer d18:1/18:1 was also reduced in the liver. Overall, despite Cer 18:1/18:0, all CerS4-related sphingolipids were reduced. Cer d18:1/18:0 is important for a proper signaling function. Matsuzuka et al. (2020) have shown that CerS4-produced Cer d18:1/18:0 (and to a lesser extend Cer d18:1/20:0) interacts with I2PP2A, thereby activating the PP2A. Activation of PP dephosphorylates and deactivates AKT and inhibits insulin signaling [310]. However, Cer d18:1/18:0 was not altered in the liver. Matsuzuka et al. have shown that ELPVL fatty acid elongate 6 (ELovl6) elongates Cer d18:1/16:0 to Cer18:1/18:0. Thus, it is possible that ELovl6 elongates the slightly elevated Cer d18:1/16:0 levels to Cer d18:1/18:0 in the liver of CerS4 KO mice, compensating for a possible deficiency of Cer d18:1/18:0, whereas the decreased dhCer d18:0/20:0 levels persist [310]. This pathway may be relevant to severe susceptibility because PP2A plays an important role in responses to environmental chemicals by regulating CYP2E1. Deletion of PP2A Aα inhibits the induction of CYP2E1 and thus reduces benzene-induced hepatoxicity [311]. However, the normal d18:1/18:0 levels indicate that the interaction between PP2A and Cer d18:1/18:0 was still maintained in CerS4 KO mice. Thus, this cannot explain the high susceptibility of CerS4 KO mice to AOM or it indicates that Cer d18:1/20:0 plays a major role in the signaling cascade and its absence triggers such a severe response. Another study shows that the enzyme CerS4 itself is also associated with protein phosphatase 2A (PP2A). The sensitivity of CRC cell lines towards PP2A inhibitor, FTY720, which induces apoptosis, depends on the sphingolipid pathway, including CerS4 [312]. Another signaling pathway that may be involved in the AOM toxicity is the TGF-β signaling. Jefferson et al. (2020) have shown that AOM administration increases thrombospodin-1 (TSP-1) which activates TGF-β and thus contributes to acute liver failure and hepatic encephalopathy [313, 314]. Inhibition of TGF-β signaling and associated pathways such as SMAD3 prevents hepatic necrosis and reduces neurological decline and neuroinflammation. Knockdown of TSP-1 and induction of non-alcoholic fatty liver disease reduces hepatic fibrosis and downregulates fatty acid β oxidation pathways [314]. CerS4 transcripts were also detected in the RNA sequence data but did not alter ([314], NCBI Gene Expression Omnibus Profile GSE120977). This suggests that CerS4

indeed plays an important role in the liver, although it is not associated with either TSP-1 deficiency or nonalcoholic steatohepatitis.

Role of Sphingolipids in the tissue: sphingolipids in gut-liver-homeostasis

Sphingolipid changes in the liver after DSS and AOM/DSS indicate a gut-liver-interaction. The treatment of DSS increased GlcCer d18:1/16:0 in the colon of the WT mice, and the same increase was observed in the liver. In contrast, in CerS4 KO mice, Cer d18:1/24:1 and GlcCer d18:1/16:0 increased in the intestine, whereas in the liver, very long chain sphingolipids such as dhCer d18:0/24:0, dhCer d18:0/24:1, Cer d18:1/22:0 and Cer d18:1/24:0 increased. This suggests that inflammation in the intestine also affects the liver, at least in WT mice. Chronic inflammation through the AOM/DSS model also altered sphingolipid homeostasis. In WT mice, AOM/DSS treatment increased very long chain Cer d18:1/24:1 in the colon but in the liver Cer d18:1/22:0 and Cer d18:1/24:1 increased and GlcCer d18:1/18:0 and LacCer d18:1/18:0 decreased. In contrast, in the CerS4 KO mice, Cer d18:1/16:0 decreased in the colon, whereas Cer d18:1/24:1 increased significantly in the liver. No lipid alterations were observed in CerS4 Vil/Cre mice. This indicates that the effect of CerS4 on sphingolipids is not limited to epithelial cells. Moreover, it exposes that mild disease progression does not affect tissue sphingolipid homeostasis, indicating the involvement of sphingolipids in pathogenesis. It has been shown that DSS treatment combined with a high-fat diet (HFD) has effects on liver metabolism [315, 316], suggesting that the intestine contributes to the bioactive Cer level of liver metabolism [317, 318, 319, 320]. Since the portal vein is straightway outflow of the intestine, the liver is steadily exposed to bacterial components or factors from the intestine. Hence, the liver's resident macrophages, Kupffer cells, get rid of bacterial components through phagocytosis, secretion of proinflammatory cytokines and ROS production. Bacterial components are recognized by TLR4 activating a signaling cascade, which is associated with NFκB and AP-1 transcription factor (reviewed by [321]). Such TLR4 mediated inflammation exacerbates liver injury in fatty liver [322]. With the secretion of TGFβ1 by Kupffer cells, TGF-β receptor signaling stimulates fibrogenesis [322] and increases the sensitivity of injured liver by gut-endotoxins [321]. In an initial review of liver sections, AOM/DSS treated mice did not show any signs of fibrogenesis or fatty liver (data not shown). Reduction of GlcCer in plasma membrane of macrophages has been reported to reduce the TLR4 signaling, but not by affecting the LPS/TLR4 complex instead by modifying the orientation and conformation of LPS/TLR4 dimers. Through this conformation change, reduction of GlcCer influences downstream signaling of macrophages [323]. In their study, all GlcCer were examined, and no distinction was made between GlcCer chain length. Therefore, further analysis should be performed to understand the impact of the CerS4 produced ceramides in the liver, as GlcCer d18:1/18:0 decreased in WT liver after AOM/DSS treatment.

The gut liver axis draws attention to obesity and type 2 diabetes melitus as potential triggers for IBD. The gut liver axis regulates not only glucose homeostasis and body weight, but also the hepatocytes health status. Luo et al. (2021) show that intestinal cMYC drives

CerS4 transcription, and the *de novo* synthesized Cer enhance lipid uptake and impairs mitochondrial fatty acid β oxidation, leading to fibrosis, inflammation and liver injury. Therefore, CerS4 expression enhances steatosis in a HFD induced obesity. Ablation of Myc in the intestine already lowers CerS4 expression and the corresponding Cer in serum, liver and adipose tissue, which improves metabolism in mice [324, 325]. Insulin resistance was also induced by Cer d18:1/16:0 and Cer d18:1/18:0 either by CerS6 in liver and in brown adipose tissue or by accumulation of CerS1 derived Cer d18:1/18:0 in skeletal muscle [326, 327, 328]. Glucose homeostasis was also improved by CerS5 deficiency in a HFD diet [329]. This indicates an important role of CerS in IBD models, not only directly in IBD disease progression, but also as a major factor in IBD risk factors.

The liver is also the tissue that clears endothelial cell- and erythrocyte-derived S1P from plasma [330, 331]. The S1P gradient is essential for the maintenance of endothelial vascular integrity and locally regulates immune cell trafficking [332, 333, 334]. In the LC-MS/MS data, S1P levels in the plasma were higher in the CerS4 KO control mice than in the WT control, and levels decreased after DSS treatment. The clearing of S1P occurs in a loop: First, hepatocytes absorb S1P by converting it to sphingosine, and then the SphK re-converts the sphingosine back to S1P. Finally, the hepatocytes degrade S1P by SPL [335, 333]. SPL knockout mice also exhibit elevated levels of S1P in the serum and in the liver, with Cer d18:1/18:0 and Cer d18:1/18:1 elevated in these mice [336]. However, ablation of SPL in hepatocytes (Sgpl1HepKo) does not increase plasma S1P levels, but ceramide levels are increased in liver of 8 weeks old mice, including Cer 18:1/18:0 and Cer 18:1/20:0, and after 8 months, Cer 18:1/20:0 levels were remained elevated. However, CerS4 mRNA level did not differ between WT mice and Sgpl1HepKo mice [250]. This suggests that the high S1P level in CerS4 KO mice is not due to SPL activity in hepatocytes. Another explanation is the activity of SPHK, which shows opposite effects depending on the isoform. Whereas mice lacking SPHK2 have increased levels of S1P in plasma [333], SPHK1 KO mice have decreased S1P levels in the liver but no alterations in sphingosine or Cer [337]. However, the increased S1P levels in plasma of CerS4 KO mice did not cause an increase of immune cells in control mice, and after DSS treatment, the levels returned to the S1P levels of WT mice. Therefore, the important function of S1P gradient for lymphocyte egress was preserved in CerS4 KO mice.

Sphingolipid as biomarker for disease

Comparison of S1P levels in plasma of DSS treated mice revealed an interesting association between clinical score and S1P levels. While CerS4 KO mice had the highest disease score and inflammation, plasma S1P levels were significantly lower than DSS treated WT mice and DSS treated CerS4 LCK/Cre mice. DSS treated CerS4 LCK/Cre mice, on the other hand, were less susceptible and showed significant lower neutrophil levels in colon and plasma than DSS treated CerS4 KO mice. This observation supports approaches to detect sphingolipids as markers for IBD disease. Since sphingolipid balance is shifted in IBD patients (in stool samples [338], colon biopsies and plasma [272, 339, 340], attempts have been

made to identify some biomarkers. For example, Bazarganipour et al. (2019) show that sphingoid levels, dhCer d18:0/C24:0 and dhCer d18:0/24:1 are decreasing in UC patients, while Cer d18:1/22:0 tends to increase as well as LacCer d18:1/16:0 and LacCer d18:1/24:0 in the colon tissue of inflamed patients [272]. In terms of sphingolipid levels in the human plasma, Sph, dhCer, Cer, GlcCer and most LacCer were evaluated in UC patients at moderate to severe stage, whereas LacCer d18:1/24:1 was decreased at severe stages [272]. Cer d18:1/16:0, Cer d18:1/24:1, GlcCer d18:1/16:0 and GlcCer d18:1/C24:1 were also increased in patients with other inflammatory diseases as multiple sclerosis compared with controls [283, 282]. This increase is similar to the DSS-induced increase in mice, estimating its usability as a biomarker in inflammatory diseases [283].

So far, some CerS KO models have been used to study DSS induced colitis and AOM/DSS induced CAC [189, 192, 269, 220, 204]. The discovery of a common pattern in sphingolipid levels that is also detected in the plasma may help to detect specific markers or targets for treatment. Comparison of murine data indicates a difference not only between human and mice but also between different mouse line and even the LC-MS/MS measurements. The increase in very long chain ceramides and long chain GlcCer in the colon is restricted to WT mice and CerS4 KO mice. This increase is partially reflected in the plasma but without significant difference between mouse lines (Figure 4.1). The DSS treated CerS4 KO mice shows CerS distinct differences that appears to be due to knockout in the colon but not in plasma (Figure 4.2). Therefore, sphingolipids circulating in plasma may indicate disease but do not necessarily indicate the tissue source of the change. The decrease in GlcCer d18:1/16:0 and GluCer d18:1/24:1 in the thymus and the decrease in Cer d18:1/16:0, Cer d18:1/24:0 and Cer 18:1/24:1 and GluCer d18:1/24:1 in the spleen indicate the extent of sphingolipid changes in DSS induced colitis. Ceramide levels also change in lymphatic organs and could affect the immune cells residing there.

While diagnostic biomarkers indicate the presence of disease, predictive biomarkers indicate response to a particular treatment and supports the treatment strategy [341]. Therapeutic management of IBD patients has shifted to a targeted treatment strategy to control intestinal inflammation, promote remission and prevent long- term damage (reviewed in [342]). In this context, remission is determined by invasive methods such as examination of wound healing by endoscopy or non-invasive methods such as radiologic status or biomarkers. To prevent disease relapse, treatment must be adjusted to the needs of patients, even though they are in remission phases. Therefore, biomarkers could provide insights about the stability of remission and potential risk of relapse [342]. A clinical trial investigated that treatment of CD patients improves when treatment is not only based on symptoms but also monitored by fecal biomarkers such as calprotectin and C-reactive protein (CRP) [343]. However, the predictive power of serum biomarkers for IBD is challenging, as depending on the CD or UC, certain biomarkers may be better than others [338, 344, 342]. To date, inflammatory parameters such as S100 A9/A9, CRP, and albumin can predict escalation in IBD [344, 342]. Other proinflammatory mediators (a range of ILs, IFNβ, CXC chemokine ligands, Granulocyte-Colony Stimulating Factor or Galectin-1) that regulate innate and adaptive immune response were also predicted to be serum biomarkers, as

levels were elevated in patients with later onset relapses [342]. Since inflammation increases the ceramide synthesis [345, 346, 192], combining such diverse biomarkers with potential sphingolipids could be beneficial. In a study by Mathews et al. (2017), the majority of circulating sphingolipids are found not to correlate with proinflammatory cytokines, only Cer d18:1/24:0 and GlcCer d18:1/24:0 correlated with IFN-γ and IL-10 [347]. A previous study by our group also investigated the therapy-induced effect on sphingolipids in human plasma. According to this, monotherapy with aminosalicylate increased Cer d18:1/18:0 in the human plasma compared to monotherapy treatment with TNF-α or no medication [272]. This effect must be immune cell independent because TNF-α alters the phenotype of the peripheral immune cells, whereas the anti-inflammatory aminosalicylate does not [286]. In this study, plasma from CerS4 LCK/Cre mice treated with AOM/DSS was not measured. So far, the measured immune cell profile, the prolonged cytokine profile and the fact that CerS4 mRNA is downregulated in white blood cells of colitis patients [272] suggest a high similarity of CerS4 LCK/Cre mice with IBD patients. CerS4 LCK/Cre mice should be considered as a good mouse model for exploring new therapeutics in the AOM/DSS model. The delayed colitis and the pan colitis in CerS4 LCK/Cre mice indicate a serious immunological role of CerS4 in disease progression.

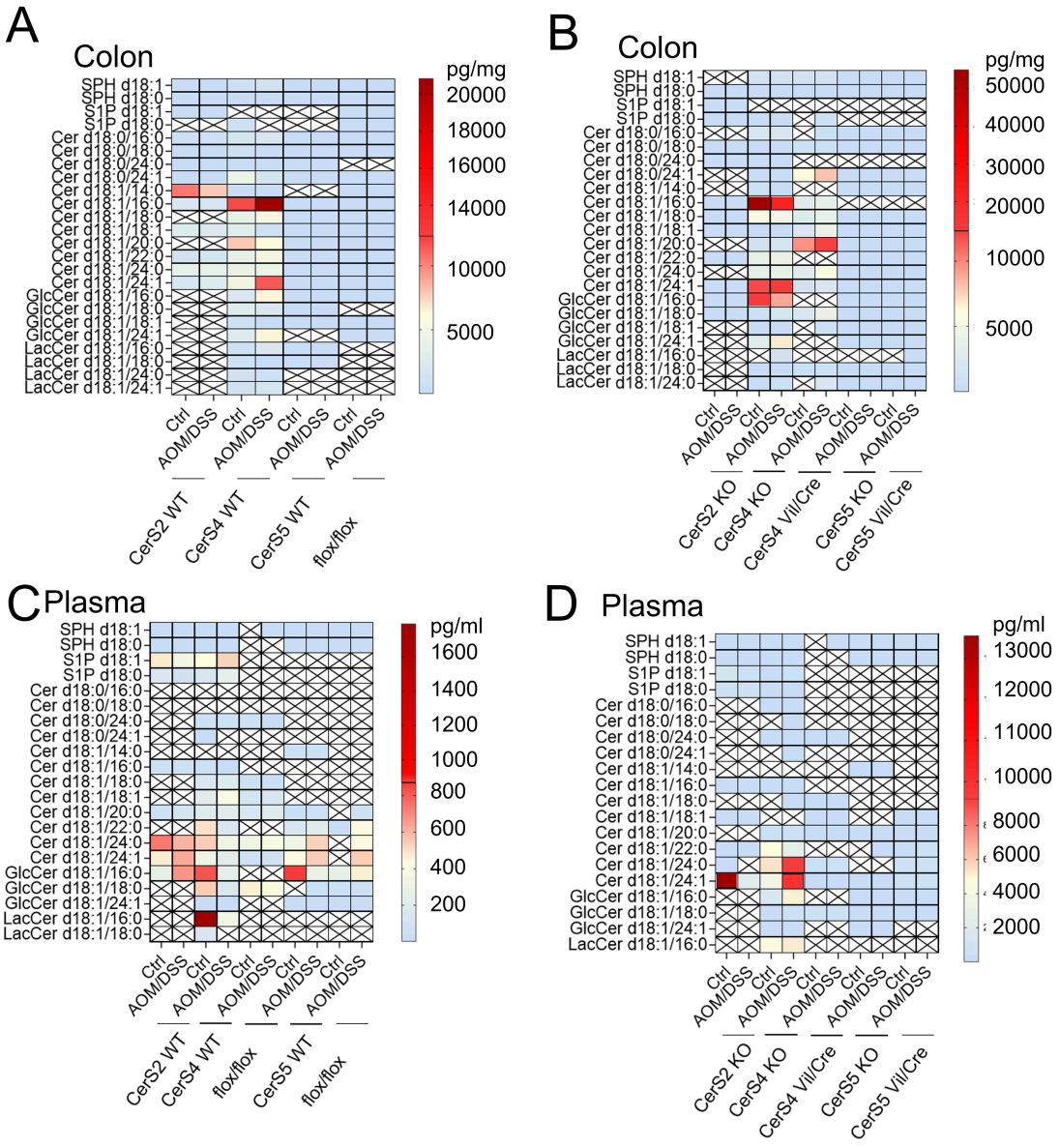

FIGURE 4.1: Overview of the sphingolipid measurement of colon (pg/mg) and plasma (pg/ml) from CerS2 [189], CerS4 [204] and CerS5 mice [220]. On the left side the WT mice are summarized (A, C) and on the right side the KO mice, including Vil/Cre mice (B, D).

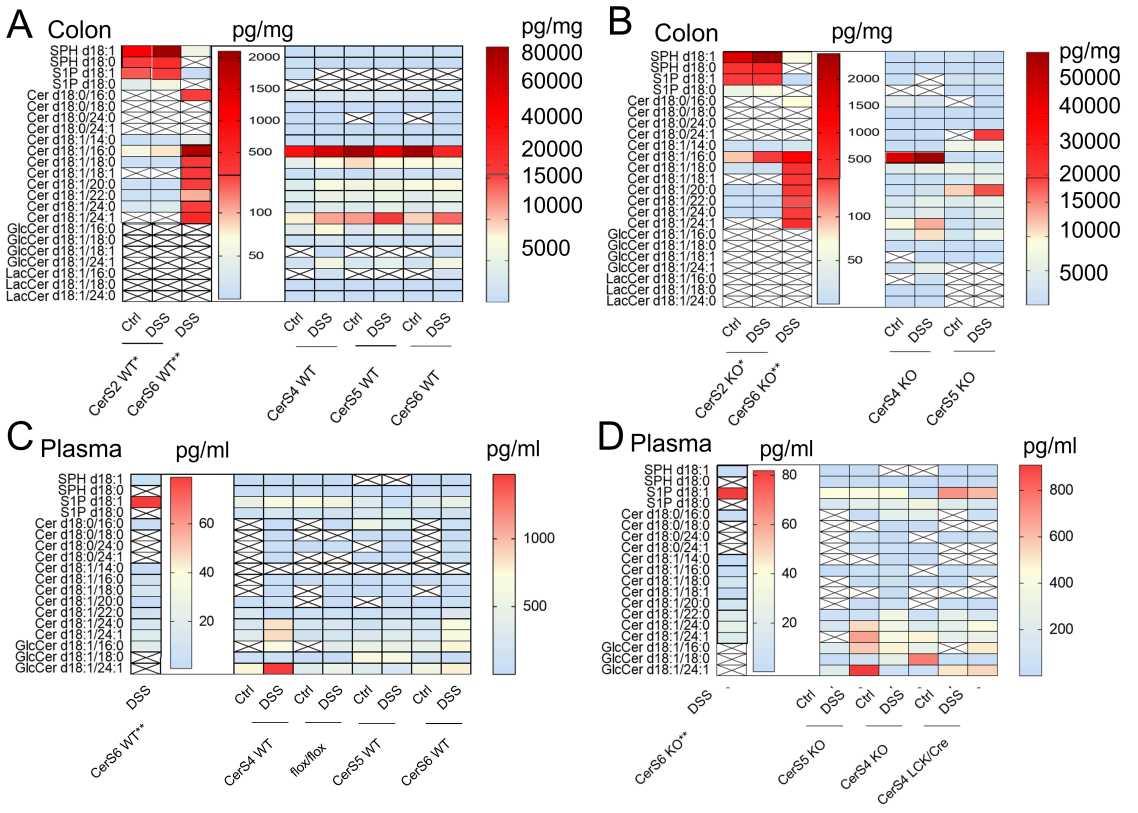

FIGURE 4.2: Overview of the sphingolipid measurement of colon and plasma from DSS treated mice CerS2* from [192] **CerS6[269], CerS4 [204], CerS5 [220] and unpublished data of CerS6 WT mice. On the left side the WT mice are summarized (A, C) and on the right side the CerS4 KO mice (B, D) and CerS4 LCK/Cre mice (D).

CerS4 in tissue healing

Mucosal healing in IBD patients is associated with the absence of acute and chronic inflammation and with a long term remission [46]. Thus, while high immune status in blood and prolonged cytokine secretion maintained the inflammation in the CerS4 LCK/Cre mice [204], the CerS4 KO mice also failed to abolish inflammation, especially during severe disease progression when they reached a human endpoint (Score$\geq$3). Histologically, CerS4 Vil/Cre mice suffered long-term tissue damage induced from DSS treatment, and the weight loss during the DSS cycle in the AOM/DSS model suggests a difference in tissue restauration. Because increased TGF-β signaling due to the absence of CerS4 in immune cells increases cytokine secretion, a similar role in epithelial cells can be hypothesized, leading to increased proliferation of epithelial cells. Beck et al. (2003) have shown that TGF-β is required for intestinal healing. In their DSS model, overexpression of truncated TGFβ Receptor II (TGFβ R II) in mice results in greater susceptibility to DSS-induced mucosal injury and shows impaired wound healing leading to death [348]. This is consistent with the CerS4 Vil/Cre model, in which the absence of CerS4 possibly promotes TGF-β signaling, resulting in better tissue healing. However, downregulation of TGF-β by overexpression of truncated TGFβ RII does not increase dysplasia and neoplasia [348]. This suggests that TGF-β signaling is not the sole regulator of intestinal epithelial cell proliferation and differentiation and cannot explain the lack of dysplasia and neoplasia in CerS4 Vil/Cre mice after AOM/DSS treatment.

Based on CerS4 function of *in vitro* data suggesting a tumor promoting effect of CerS4 [180], CerS4 Vil/Cre mice with the protective phenotype showed quite unexpected results. This discrepancy may be related to the AOM/DSS model or to the fact, that downregulation of CerS4 may have opposite effects at different cancer stages [204].

Human CRC data shows a decrease of CerS4 in already early stages of CRC and CerS5 in late stages (manuscript in preparation). It is not known whether this decline contributed to carcinogenesis or was induced by cancer. To approach this question, further *in vitro* studies were conducted to investigate the role in early-stage cancer using human organoids and CRC cell lines.

4.2 Part II

Expression profile of CerS in organoids

This thesis provides, for the first time, insights into the expression profile of CerS in organoids that have not been published previously. Similar to the mouse colon and human CRC cell lines, CerS2 was the most abundant CerS, followed by CerS6 and CerS5. CerS1 and CerS3 both showed the lowest expression, whereas the expression of CerS4 varied depending on the tissue origin. This dependence was also observed for CerS1 and CerS3. In organoids obtained from tumor biopsies, CerS1 and CerS3 were more highly expressed than in control biopsies or diverticulitis. The increase in CerS1 and CerS3 is also observed in colitis patients not only at the mRNA level but also by immunohistochemistry [272]. CerS4 was

more highly expressed in organoids obtained from diverticulitis biopsies. When samples were paired, i.e., when organoids derived from the same patient were compared, the expression of CerS1 and CerS3 was not different, but that of CerS4 was. It was more highly expressed in the organoids derived from the tumor.

CerS4 and stem cell homeostasis

Moreover, the different cancer stages (adenocarcinoma and colon cancer) showed that CerS expression changes with different stages. The correlation of CerS with differentiation marker or stem cell marker also suggests that cell differentiation and epithelial-mesenchymal transformation (EMT) affects the CerS profile. In particular, the correlation of CerS4 with the stem cell marker Lgr5 is very interesting. Peters et al. (2014) have shown that the distinct phenotype of age related alopecia (hair loss) in CerS4 KO mice [205] is due to the involvement of CerS4 in the stem cell homeostasis and the hair follicle cycle [203]. CerS4 is localized in various stem and progenitor cells. In Lgr1 positive cells, CerS4 is highly expressed, indicating that it regulates the cell fate of a stem cell towards the hair follicle cell or sebaceous gland. Loss of CerS4 resulted in both an enlargement of Lgr1-positive compartments and enlargement of sebaceous glands. In addition, CerS4 is thought to regulate the quiescence or activation of the hair follicle stem cell niche. Therefore, CerS4 deficiency results in premature activation of the hair follicle stem cell niche and contributes to stem cell depletion leading to age-related hair loss in mice [203]. These results suggest that low CerS4 levels can maintain stem cell in organoids. In contrast, correlation analysis between CerS, stem cell marker and differentiation marker exhibited that CerS4 was positively correlated with Lgr5 in the colon organoids. In diverticulitis patients both Lgr5 expression and CerS4 expression were higher than in controls, and the paired control-tumor comparison also showed the same pattern: in tumor-derived organoids, Lgr5 expression was slightly higher and CerS4 expression was significantly higher than in controls. To analyze this further, both the sample size needs to be increased and immunofluorescence analysis of co-staining of CerS4 with Lgr5 could provide further insight into whether CerS4 is positively or negatively associated with Lgr5.

Lgr5 expression is found in adult intestinal stem cells and are highly proliferative [349, 350]. This stem cell marker is also upregulated in hair follicle stem cells, [351]. Peters et al. (2015) have not shown whether Lgr5 is also associated with CerS4 mediated stem cell activation, but it would be of interest to find out whether the CerS4 interaction is restricted to Lgr1 or includes other family members. Lgr5 is a general stem cell marker that is also found in colon cancer cells, ovarian primary tumors, hepatocellular carcinomas, and also in malignant cells [349, 352, 353]. It is a receptor for R-spondin and activates the canonical Wnt signaling pathway by incorporation of the coreceptor into the Frizzled-Lrp complex [354, 355, 356]. It is also possible that CerS4 expression depends on these factors and continuous supply of these factors could trigger CerS4 downregulation or that the ceramides such as Cer d18:1/18:1 and Cer d18:1/18:0 or Cer d18:1/20:0 could be involved in the receptor interaction. To analyze the interaction of CerS4 with stem cell factors, the culture

medium can be altered to either contain more Wnt, R-spondin or the BMP inhibitor Noggin, or to be less concentrated and thus screened for CerS4 expression or checked for localization of CerS4 or CerS4 produced ceramides with a co-expression of Wnt and BMP receptors. Deprivation of R-spondin leads to the downregulation of the Wnt target signature [350]. That is, if CerS4 is also a target signature of Wnt, this change in media composition should mirror this. Blocking Wnt prevents stem cell renewal and results in a stem cell loss. However, tumor organoids with APC mutations or APC loss results in constitutive intrinsic Wnt activation and can grow independently of Wnt supply [357]. Thus, Wnt deprivation for tumor organoids and the effects on CerS4 could be verified. This study design was already performed by Michels et al. (2019). In their study, they distinguish between oncogenic and physiological Wnt activity by culturing organoids with or without exogenous Wnt and CRISPR/Cas9-induced APC loss to distinguish between extrinsic and intrinsic receptor-mediated signaling. In their analysis, they identify in total 4,051 proteins, including CerS. At the transcriptome level, Wnt stimulation with extrinsic Wnt altered CerS profile, particularly CerS4. Without Wnt, CerS4 expression in organoids decreases 4.67 log2 fold change (FC) ($p<0.0001$). At the same time, the expression of Wnt responsive genes such as Lgr5 and Lgr6 expression also drop by 6 log2 FC ($p<0.0001$) and 4 log2 FC ($p<0.0001$), respectively. Other Wnt responsive targets such as tyrosine-protein kinase-like 7 (PTK7) and ephrin type-B receptor 2 (EPHB2) also decrease twofold ($p<0.0001$). The other CerS RNA expressions are less affected but also have significant adjusted p values: CerS2 -0.23 log2 FC ($p=0.009$), CerS5 0.39 log2 FC, $p=0.0017$ and CerS6 $p=0.007$). While CerS4 RNA levels are detected barely in the complete absence of Wnt, CerS4 RNA also increases with increasing Wnt concentration. When comparing WT organoids cultured without Wnt and at low Wnt concentrations, CerS4 expression increases 2.67 FC ($p<0.0001$). A comparison between low and high level of Wnt concentrations results in a 1.55 log2 FC ($p<0.0001$) in CerS4 expression. This Wnt-dependent effect is also observed in other CerS, but none of them is affected as much as CerS4. When low Wnt levels are compared to high Wnt levels, only CerS5 RNA shows a difference (0.24 log2 FC, $p=0.0059$), while the other CerS RNAs do not change significantly. However, once no Wnt levels are compared to low Wnt levels, RNA expression of other CerS such as CerS2 (-0.21 log2 FC, $p=0.014$) and CerS6 (-0.151 log2 FC, $p=0.02$) decreases. With increasing Wnt concentration, Lgr5 and Lgr6 also increase 3.75-fold and twofold ($p<0.0001$) when the concentration increases from zero to low Wnt levels, and twofold ($p<0.0001$) when low Wnt level increases to high level Wnt levels. This effect on CerS4 is not limited to extrinsic Wnt, the intrinsic stimulation of the Wnt receptor through APC loss, also results in a higher CerS4 expression when Wnt is withdrawn: CerS4 mRNA increased 3.9 log2 FC ($p<0.0001$) in APC-mutant organoids cultured in no Wnt medium. However, once low Wnt concentration are present in the medium, the increase attenuated (0.45 log2 FC, adjusted $p=0.18$). When Wnt content in the medium is high, CerS4 expression is reduced compared to WT organoids (-0.71 log2 FC, $p=0.0002$). That CerS4 expression is more dependent on extrinsic than intrinsic stimulation of Wnt receptor is also evident when both extrinsic and intrinsic effects are combined. Comparison of APC mutants with low level and high level of Wnt no longer alters CerS4 expression.

Furthermore, CerS2 expression decreases in APC-mutant organoids cultured without Wnt (-0.26 log2 FC, p=0.014), while the other CerS mRNA show no significant change. Addition of Wnt to the medium in APC-mutant organoids results in no change (Figure 4.3 A).

Wnt responsive genes are more responsive to Wnt concentration than CerS but shows the same pattern as CerS4: as Wnt increases, their expression increase, and compared with APC-mutant organoids that activated an intrinsic Wnt response, Lgr genes are higher in WT organoids than in APC mutant organoids, regardless of whether no or little Wnt is present in the medium. Comparison between WT organoids and APC-mutant organoids at high Wnt levels does not alter Lgr expression. This suggests that oncogenic Wnt activity stimulates Wnt responsive genes once Wnt is absent or at low levels. At high Wnt levels, the canonical response is saturated [357]. Correlation of Wnt responsive genes with CerS shows a positive correlation of CerS4 with Lgr5 (R=0.972, p<0.0001), Lgr6 (R=0.921, p=0.003) and also with other Wnt responsive targets such as PTK7 (R=0.971, p<0.0001) and EPHB2 (R=0.972, p<0.0001). In contrast, CerS2 correlates negatively with Wnt responsive targets such as Lgr5 (R=-0.92, p=0.004), PTK7 (R=-0.94, p=0.002), EPHB2 (R=-0.93, p=0.003). This negative correlation is consistent with the correlation of CerS2 with differentiation marker as observed in own results.

Proteomic profiling by Michels et al. (2019) also detected CerS expression. The CerS profile of the proteom analysis is similar to the measured mRNA levels [357]. CerS6 is the most abundant protein detected ($5{,}088.7 \pm 1{,}940.8$), followed by CerS2 ($2{,}247.3 \pm 625.9$) and CerS5 (665.3 ± 348.7). CerS4 was 175.3 ± 190.9, much higher than CerS1 (2.3 ± 2.5) and CerS3, which is not detected (Table 4.1 B). Pairwise analysis of physiological Wnt response and oncogenic Wnt response reveals no changes in CerS expression, except for CerS4. In WT organoids, the physiological Wnt response exhibits a 0.92 FC with an adjusted p value of 0.08 (p-value 0.014). In contrast to the transcriptomics, the oncogenic Wnt response is independent from CerS4 and generally of any CerS protein detection. The log2 fold changes after APC mutation are small and not significant. Also, the combined effect of oncogenic and extrinsic Wnt responses do not induce any discovers of total proteins [357]. As observed in the transcriptomics, the oncogenic Wnt response saturates the Wnt response and therefore there is no difference in the CerS4 expression whether APC mutants are cultured in presence of Wnt or in absence of Wnt (both 0.2 FC (n.s)). Comparison of WT and APC deleted organoids cultured in Wnt-free medium increase by 0.7 FC, but is no longer significant (p=0.5) (Figure 4.3 B). In transcriptomics, CerS isoforms show weaker correlation and changes, especially CerS4, suggesting that CerS4 is induced by physiological Wnt response (4-fold increase), whereas in proteomics it decreases to 0.9-fold. This weak correlation between transcriptomics and proteomics indicates that in CerS, post-transcriptomic regulation plays an important role in tumor progression [357]. Because the response in the proteomic profile is much weaker than in the transcriptomic profile, CerS4 and Lgr5 no longer correlated, but CerS4 is still associated with PTK7 (R=0.93, p=0.069). This strong association of CerS4 and Lgr5 on mRNA level explains the intensive apical staining of CerS4 in organoids. The weaker induction of CerS4 expression by APC truncation and the activation of the intrinsic pathway compared to the physiological Wnt response suggests that

CerS4 is upstream rather than downstream in the Wnt signaling pathway.

TABLE 4.1: Extrinsic and intrinisic Wnt response and their influence on CerS expression. Proteomics data (PXD012650) from [357] of detected CerS peptides and their altered expression in response to extracellular Wnt receptor response (+/- Wnt in WT) and intrinsic Wnt receptor response by APC mutants. APC mutants activate an intrinsic pathway for Wnt response. This oncogenic Wnt response saturated the canonical pathway and did not change with the presence of Wnt. Abbreviations: Ceramide Synthase (CerS), Adenoma polyposis coli (APC), Wingless (Wnt), Wildtype (WT) human organoids without APC mutation

	WT +Wnt			WT -Wnt			APC+Wnt			APC-Wnt		
	Mean	SD	N	Mean	SD	N	Mean	SD	N	Mean	SD	N
CerS1	2,3	2,5	3	0,7	1,2	3	1,3	0,6	3	2,3	0,6	3
CerS2	2247,3	625,9	3	1916,0	580,1	3	2224,7	572,7	3	2048,7	521,7	3
CerS3	0,0	0,0	3	0,0	0,0	3	0,0	0,0	3	0,0	0,0	3
CerS4	175,3	190,9	3	88,3	128,4	3	186,0	28,1	3	133,7	29,5	3
CerS5	665,3	348,7	3	519,3	386,5	3	525,0	179,5	3	494,7	114,7	3
CerS6	5088,7	1940,8	3	3742,7	1459,7	3	5341,3	701,3	3	5113,7	1045,1	3

Wnt is among many signaling molecules a main regulator for stem cell maintenance, regeneration and differentiation. This development can be easily investigated in organoids, which can have various phenotypes, either enriched with stem cells or with more differentiated cells. In the study of Lindeboom et al. (2018), stem cell rich mouse organoids cultured in organoid culture medium supplemented with CHIR99021 and valporic acid (ENR+CV) are compared with normal mouse organoids cultured in organoid culture medium (EGF, Noggin, R-spondin) (ENR) and with enterocytes-rich mouse organoids cultured in organoid culture medium (EGF, Noggin) (EN) [358]. Stem cell enriched organoids exhibit a corresponding shift in sphingolipids in addition to shifted CerS mRNA expression. Their study shows that as CerS increases in stem cell-rich cultures, the corresponding ceramides also increase, but not dihydroceramides: Cer d18:1/24:0 increases 5-fold ($p<0.0001$) and Cer d18:1/18:0 increases 2.8-fold ($p<0.0001$) (Figure 4.4 A). Among the dihydroceramides dhCer d18:0/16:0 is abundant and increases 1.7-fold ($p<0.0001$) in organoid culture enriched with stem cells (Figure 4.4 B). Differentiation of mouse organoids into enterocytes rich mouse organoids does not significantly alter sphingolipids, only Cer d18:1/18:0 decreases by 0.47-fold ($p=0.01$) (Figure 4.4 B). At the RNA level, differentiation leads to a decrease in Lgr5 ($p<0.0001$) and Lgr4 ($p=0.003$), accompanied by a decrease in CerS2 ($p<0.0001$) (Figure 4.4 A). While the online transcriptome data provide transcripts per kilobase million (TMP), Lindeboom et al. (2018) also report copy numbers of selected genes and proteins, including CerS2, CerS4 and CerS6, as well as integration of transcriptomics and proteomics in their supplement data. CerS2 mRNA expression is significantly increased in differentiated organoids, as it is in human organoids (Figure 4.4 C). CerS6 mRNA is also increased upon organoid differentiation. The relation between protein copies and mRNA copies provides insight on posttranscriptional regulation. Comparing the fold change of differentiated organoids (EN) with normal organoid culture (ENR), CerS2 is increased 4.7-fold at mRNA level, but the protein/mRNA ratio is 7.6, indicating that posttranscriptional mechanisms

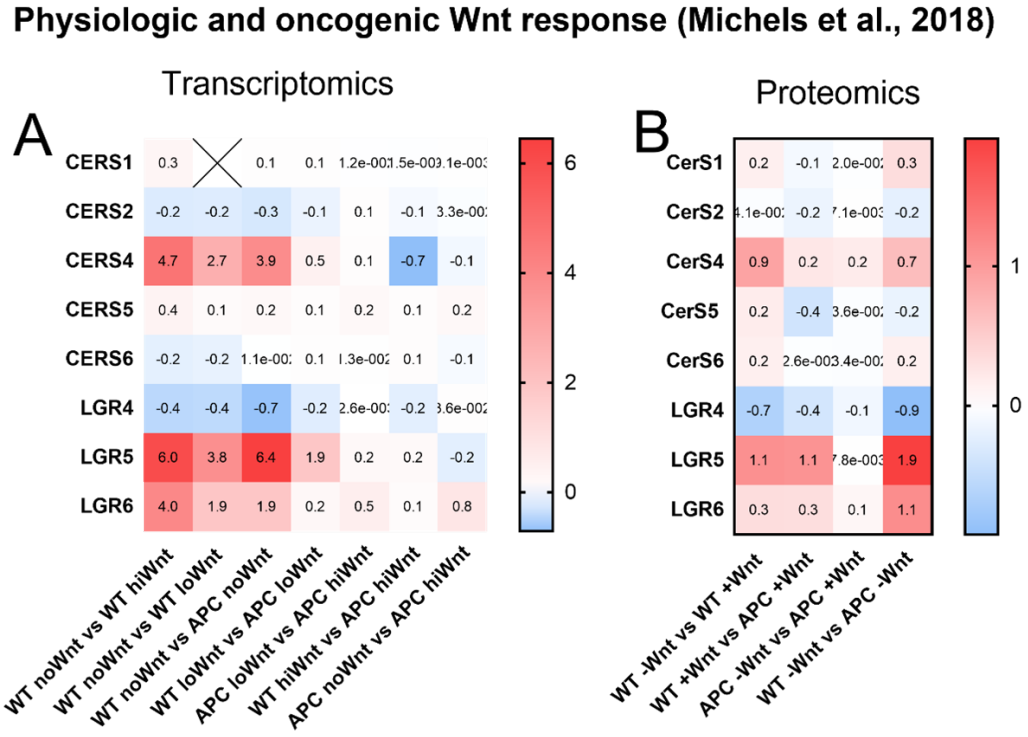

FIGURE 4.3: Log2 fold exchange of organoids compared physiologic Wnt response and oncogenic Wnt response. (A) Transcriptomics analysis of organoids cultured in absence of Wnt, at low Wnt concentration, or at high Wnt concentrations. Stimulation of the oncogenic Wnt receptor was achieved by APC truncation, which resulted in APC loss in the organoids. (B) Proteomics data of extrinsic Wnt response analyzed after the culturing in the presence or absence of Wnt and intrinsic Wnt response induced by CRISPR/CAS induced APC mutations/ APC loss. In the heatmap, 2 log fold changes of n=3 treated organoids are plotted. Data were extracted from the dataset available online. Transcriptomics were extracted from the NCBI Gene Expression Omnibus (Series Matrix file: GSE125578_20190114_Stim_Wnt) and proteomics from the ProteomXchange Consortium PRIDE (ID: PXD012650). Abbreviations: Ceramide Synthase CerS, Leucine-rich repeat-containing G-protein coupled receptor (LGR), Wingless (Wnt). No Wnt (noWnt), low WNt (loWnt), highWNt (hiWnt), Wiltype human organoids without APC mutation (WT), Adenoma polyposis coli (APC), APCmutant organoids (APC). Heatmap legends reflects log2 fold changes.

stabilize and upregulate CerS2 translation. In regard to CerS4 and CerS6, this stabilization is also present but not as upregulated as CerS2 in the EN culture. In the stem cell rich organoid culture (ENR+CV), this regulation is stronger for CerS4 and CerS6: at the mRNA level, the change is between 1.2 and 1.6-fold, but increases to 2-fold (CerS2), 3.4-fold (CerS6) and even 5.3-fold (CerS4) in ENR+CV culture compared with the ENR culture. This suggest that in a Wnt-supported environment, posttranscriptional regulation is stronger than in differentiated mouse organoids.

Although both studies come to contradictory results regarding CerS change, they highlight that the CerS profile depends on organoid differentiation, which can be controlled through the addition of growth factors. Therefore, organoids represent an interesting model for CerS function, but can only be compared under the same culture conditions, which may vary from laboratory to laboratory.

The involvement of CerS4 in stem cell maintenance and differentiation may explain

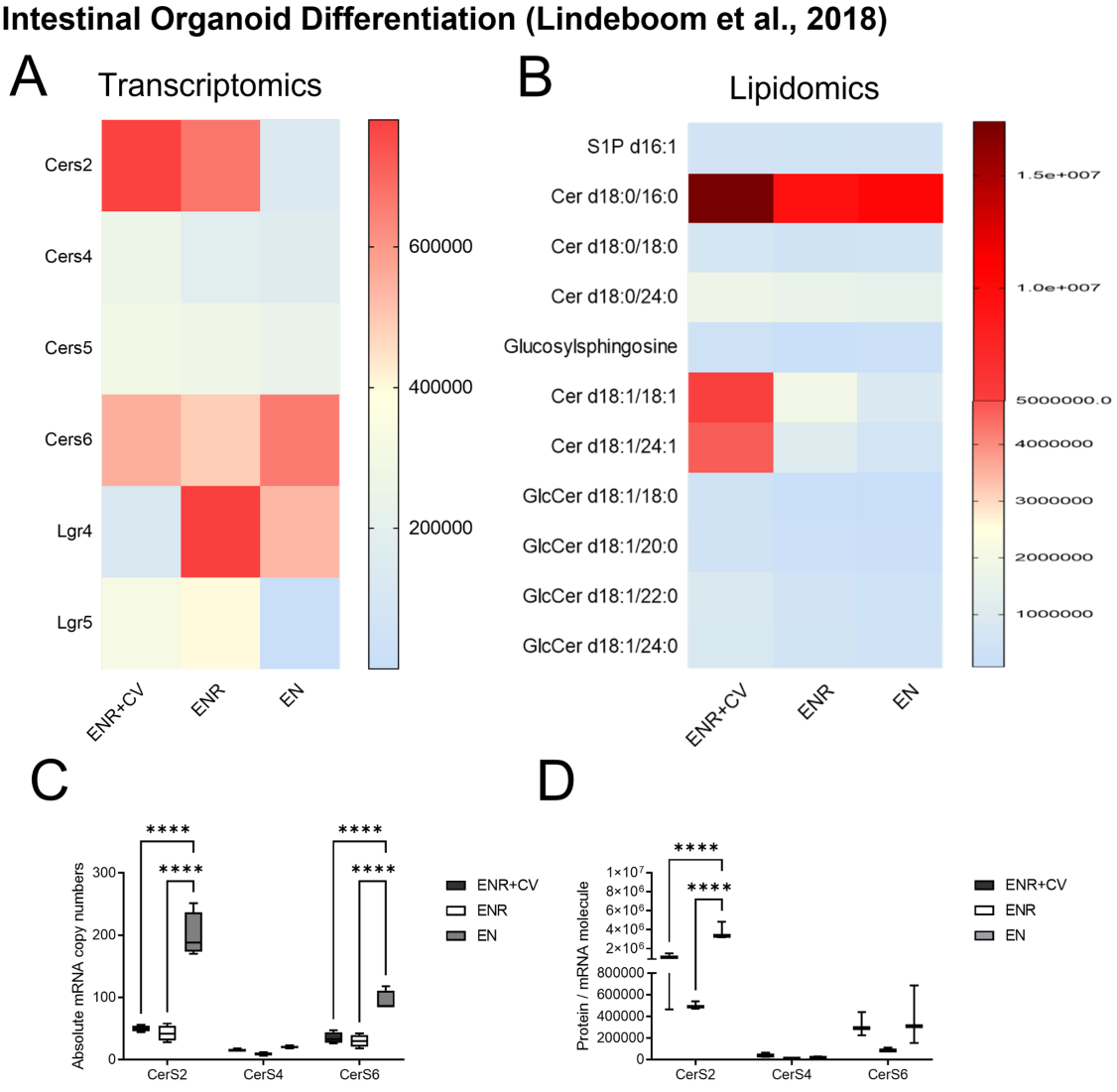

FIGURE 4.4: Integrative multi-omics analysis of intestinal organoid differentiation, online available data from [358] are analyzed with respect to CerS and sphingolipid changes after differentiation. Mouse organoids enriched in stem cells (CV) were cultured with the addition of CHIR99021 and valproic acid (ENR+CV). Normal mouse organoids were cultured in ENR medium (containing EGF, Noggin and R-Spondin, ENR) and to induce mouse organoids to a more differentiated phenotype, R-Spondin was withdrawn (EN). Organoids were pooled and used to determine absolute mRNA abundance in an RNA Seq (A) and in an LC-MS/MS metabolic analysis from which lipidomic data are extracted (B). Data set from [358]. For transcriptomics, transcripts per kilobase million (TPM) from the GeoProfiles ID dataset are compared: GSE114113 is screened, and metabolic data are from the ProteomXchange Consortium PRIDE (PXD009700). (C) Absolute mRNA copies quantified by Lindeboom et al. (2018) and (D) protein abundance was calculated as a ratio to mRNA molecules to investigate posttranscriptional gene regulation.

why CerS4 downregulation is one of the first events in tumor patients. Especially for mutations in APC, the dependence from physiological Wnt is not required and hence CerS4 is downregulated.

4.3 Part III

Already in Part I, the CRC model showed that the tumors were larger in the WT mice than in the CerS4 deficient mice. In some cases, giant tumors were found in the WT mice. Both mouse model and the downregulation of CerS4 in patients (manuscript in preparation), raise the hypothesis that CerS4 may be associated with hypoxia. However, the increase in tumors in WT mice suggests that CerS4 is involved in either cell proliferation or the tumor microenvironment. Elevated levels of hypoxia in tumor tissue not only alters metabolism but also promote metastasis of invasive cancer cells [359]. Metastasis is a hallmark of the UICC stage IV [360, 98, 361]. And since CerS4 and CerS5 are downregulated at these late stages (manuscript in preparation), CerS5 might also be associated with hypoxia. Since cells respond to hypoxia through HIF1α activity [362], comparison of CRC lines and their metabolic response to hypoxia revealed differences. HCT116 cells grew faster in 2D and 3D and increased glycolysis after hypoxia by increased PK mRNA level and LDHA mRNA level. In contrast, Caco-2 cells increased glycolysis by upregulating GLUT1 mRNA, and even more in 3D culture. Downregulation of CerS4 and CerS5 in HCT116 cells and Caco-2 cells affected not only the glycolysis pathway, but also single enzyme of the pentose phosphate way TKTL1 and proteins involved in mitochondrial dynamic and quality control as PARK. The decrease of CerS4 was observed in all CRC cells (HCT116 cells, HCT15 cells and Caco-2 cells) exposed to hypoxia, indicating that oxygen deprivation represses CerS4 transcription.

2D and 3D culture

The CerS profile of CRC lines is in accordance with that of murine colon [143, 142] and human organoids. CerS2 is the most abundant CerS, followed by CerS6 and CerS5 and then CerS4 and the lowest expression was usually found in CerS1 and CerS3. The equilibrium between sphingolipid levels in tissues is not limited to CerS expression [143], but also to CerS activity. It has been shown that the balance of CerS is also important for CerS activity and that dimerization of CerS isoforms modulates activity [148, 149]. The cell system is expected to compensate for the absence of one particular specific chain length with another Cer, but does not necessarily alter CerS mRNA expression [189, 220, 204]. However, at the level of mRNA expression, no significant compensation was observed in shCerS4 HCT116 and shCerS4 Caco-2 cells, only CerS5 mRNA tended to increase. Conversely, shCerS5 HCT116 and shCerS5 Caco-2 cells had decreased CerS5 mRNA levels but increased CerS4 mRNA levels. In HCT15 cells, CerS4 expression was very low, and CerS2 content was higher in 2D culture but not in 3D culture, suggesting that CerS expression is dynamic and depends on the environment. With the changes in CerS expression levels, CRC cells differed metabolically. Caco-2 cells were characterized by a lower reduction of resazurin, which was higher in HCT116 cells and HCT15 cells than in Caco-2 cells. This difference was also observed in other studies, in which HCT116 cells have a higher RFU compared to Caco-2 cells [363]. 3D cultures as screening platforms are already known and

established as spheroids. In contrast to 2D colony forming assays, spheroids establish cell-cell-interactions such as TJs and adherens junctions. The difference of resazurin reduction in 3D culture between HCT116 cells and Caco-2 cells decreased. One mechanism explaining this is the establishment of TJ on the surface of spheroids, which prevents penetration of resazurin in other CRC cell lines, but as seen in the TEER data, HCT116 cells do not form as strong a barrier as Caco-2 cells [220, 364] and even in spheroids they tend to be more loose cell aggregates with a leaky phenotype [364]. In Matrigel, the morphology of 3D HCT116 cells was similar to that in spheroids. The "solid tumor" cell formation of Caco-2 cells is previously described in [365], HCT15 cells grew similarly to 3D-DLD-1 cells and 3D-HCT29 cells cultured in Laminin-Rich-extracellular matrix as "mass-like" spheroids, and HCT116 cells as a mixture of "grape-like" and "mass-like" spheroids [365]. Culturing CRC cell lines in Matrigel induces the initiation of tumor growth and enables a growth as xenografts, as observed in mammary cell lines [366, 367]. However, Matrigel is not only important for the growth of tumors in nude mice but can also be considered a mirror tumor or xenograft growth in cell culture although the tumor microenvironment is missing. Similar to the shCerS4 HCT116 xenografts and shCerS5 HCT116 xenografts or shCerS4 Caco-2 xenografts and shCerS5 Caco-2 xenografts [263], the size of 3D HCT116 cells is larger than that of 3D Caco-2 cells. Only HCT15 cells are the largest xenografts in the xenograft model, but not in Matrigel, indicating, that metabolic and nutritional support was better *in vivo* than *in vitro*. 3D culture did not differ from 2D culture in cell viability, except for HCT116 cells. With increased cell number, RFU normally increases in spheroids of HCT116 cells [364], suggesting that the increased necrotic core in 3D cultured HCT116 cells may explain the decreased viability. However, chronic hypoxia did not affect the viability of 2D culture or 3D culture of CRC cell lines. This is consistent with other studies, in which hypoxia does not interfere with the viability [368, 369, 370]. Knoll et al. (2016) even describe that hypoxia prevents apoptosis in CRC cells by inhibiting mitophagy or Caspase 3 activation [370]. However, Chiang et al (2021) reported a reduced growth rate of HCT116 cells under hypoxia and decreased further if HCT116 cells were cultured on collagen [371]. In addition, the necrotic core of 3D cultured HCT116 cells may have already induced transcriptional increase of glycolytic enzymes such as PK or GLUT1 mRNA levels in 3D cultured HCT116 cells compared to 3D cultured Caco-2 cells. This change in glycolysis metabolism is also observed in other cell types and increases similarity to primary cells [372]. Glycolytic activity in 3D cultured fibroblasts shows lower glucose uptake and lactate secretion in 3D culture compared to 2D culture. However, with increasing cell density, glycolytic activity also increases in 3D cultured fibroblast [373], which let assume a similar increase in glycolytic activity of 3D cultured HCT116 cells compared to 3D cultured Caco-2 cells.

Cell metabolism

Monitoring of energetic enzymes expression indicated that CerS4 downregulation in Caco-2 cells did not affect the increase of GLUT1 or LDHA after hypoxia; only in shCerS4 HCT116

cells did GLUT1 mRNA not increase in hypoxia compared with shNC HCT116 cells. Moreover, active downregulation of mitochondrial consumption might be stronger in HCT116 cells than in Caco-2 cells. Although the increase in GLUT1 mRNA is greater in Caco-2 cells at $48\,\mathrm{h}$, HCT116 cells appear to regulate energy consumption in a different manner. PK mRNA levels were significantly higher in HCT116 cells than Caco-2 cells, which may indicate a better glycolysis. Subsequently, the mRNA expressions indicate that the pyruvate produced is used more for anaerobic energy production. LDHA mRNA levels and PDHA1 mRNA levels were significantly higher in HCT116 cells than Caco-2 cells.This suggest that HCT116 cells grow larger both in Matrigel and xenograft model by differently adapting to nutrient deprivation. In contrast, 3D Caco-2 cells had a greater increase in GLUT1 mRNA and unlike HCT116 cells and HCT15 cells, PDHA1 was not actively reduced. These differences also persist in shCerS4 and shcerS5 transduced HCT116 cells and Caco-2 cells. In general, the difference between low CerS4 expression (shCerS4) and high CerS4 expression (shCerS5) showed the largest differences. The mRNA expression data suggest that downregulation of shCerS4 inhibits the increase in GLUT1 after chronic hypoxia, which remains to be confirmed at the protein level and in glycolytic activity. While shCerS5 HCT116 had higher basal GLUT1 levels, PDHA1, PK and LDHA levels were lower, but TKT levels were higher, indicating that the transported glucose may be used more in PPP or induce more mitochondrial stress to the cells, because FIS1, MFN1/2 and PINK levels decreased, and PARK levels increased after hypoxia in shCerS5 HCT116 cells. These observations are consistent with the role of CerS4 and glucolipotoxicity in pancreatic β-cells. With upregulation of CerS4 and CerS4 related sphingolipids, apoptosis is enhanced, and treatment with ceramide inhibitor Fumonisin-B1 inhibits glucolipotoxicity induced apoptosis [374].

Moreover, PK mRNA levels increase with hypoxia in HCT116 cells but not in Caco-2 cells suggesting a basal difference in glycolysis between HCT116 cells and Caco-2 cells. Accordingly, both PKM1 and PKM2 are less strongly expressed in Caco-2 cells. The increased expression of PKM2 relative to PKM1 is consistent with the literature (reviewed by [375]). However, mRNA expression cannot imply translation adaptation because PK activity depends on its quaternary structure and is allosterically regulated. As a tetramer, PK has its highest activity and as monomer or dimer it has low activity. The allosteric regulation stabilizes or destabilize the assembly into a homotetramer. For example, PKM2 can be phosphorylated by PKC. Therefore, glycolytic activity might indicate whether CerS4 downregulated cells have less glycolysis. If so, it may be possible, that Cer also influence PKC activity, as PKCζ is regulated by Cer d18:1/18:1 [276], Cer d18:1/16:0 and arachnoid acid [157, 276]. In addition, PKM2 has been shown to translocate to the nucleus and induce cell death [376], promotes angiogenesis by acting as a co-factor for HIF1α [377] or interact with p65 [378]. While hypoxia increased PKM1 levels, PKM2 levels no longer changed. PKM2 was already highly expressed in CRC lines because it thought to alter glucose metabolism and contribute to tumorigenesis. Therefore, it may be better for future studies to analyze the location of PKM2. However, PKM1 is also required for cell proliferation depending on the tissue and cell line. In human small cell lung cancer cells, PKM1 activates glucose catabolism and promotes PKM2 assembly in its active tetrameric form [379]. Upon isotopically 13C-labeled

glucose loading, Morita et al. (2018) show that PKM1 enhances the conversion of pyruvate to lactate [379]. Moreover, in HCT116 cells, PKM1 was reported to indirectly promote apoptosis through the regulation of HNF4α and miR124. In shCerS5 HCT116 cells, the PK levels increases upon hypoxia but decreases after $72\,\mathrm{h}$. CerS5 and its products Cer d18:1/14:0 and Cer d18:1/16:0 are linked to autophagy and apoptosis pathways [380, 381]. Therefore, energetic stress could be a link between CerS5 induced autophagy and PKM1 induced autophagy [379].

Mitochondrial regulation

In this regard, autophagy supports cell death [382] or cell survival [252]. This mechanisms is particularly important as a survival mechanism for hypoxic cells under hypoxia [383]. This was also seen in the mitochondrial dynamics: mRNA level of mitochondrial fission and -fusion mRNA were reduced in CRC cells. Enlargement of mitochondria is a mechanism to elude hypoxia induced apoptosis [384]. Mitochondrial proteins as MFN1/2 can either interfere with apoptosis proteins [385, 386] or like OPA1, avoid apoptosis by forming the cristae structure and redistributing cytochrome C [387]. Therefore, hypoxic stress triggers fusion to avoid apoptosis [384]. The decreased MFN2 and FIS1 levels are also observed in a HIF1α dependent manner in other studies (Appendix B Figure B.2,B.1). Because shCerS5 (and to a lesser extend shCerS4) exhibited reduced levels of mitochondrial morphology proteins depending on the cell line, further studies should be performed to test the viability and apoptosis of shCerS5 CRC cell lines. Another striking feature was the decreased PINK levels in shCerS5 HCT116 cells and increased PARK levels at $48\,\mathrm{h}$ and $72\,\mathrm{h}$, respectively. Because shNC HCT116 cells tends to have elevated PINK levels, this increase was observed in [388] and is HIF1α dependent (Appendix B Figure B.2, B.1). The only striking feature was the decrease in shCerS5 HCT116 cells after $48\,\mathrm{h}$ and $72\,\mathrm{h}$ hypoxia. This decrease was also observed in Caco-2 cells and in shCerS5 Caco-2 cells earlier than in shNC caco-2 cells and shCerS4 Caco-2 cells. PARK mRNA increased with hypoxia in shCerS5 HCT116 cells and shCerS5 Caco-2 cells with the same pattern, although the increase was faster in shCerS5 Caco-2 cells than in shNC Caco-2 cells and shCerS4 Caco-2 cells. The interaction of PINK and PARK regulates mitophagy. This important recycling process responds to mitochondrial stress and is based on the ubiquitylation of mitochondrial proteins as Mfn1, Mfn2 and VDAC. However, under hypoxia, a receptor-mediated pathway induces mitophagy [389]. The elevated PARK levels may indicate slower proliferation in CRC cells, because upregulation of PARK inhibits proliferation and downregulation promotes it in various cancer cell types (reviewed in [389]). These mechanisms may have contributed to the growth of xenograft tumors. Depending on the cell line, this may explain the reduced shCerS5 Caco-2 xenografts, but not the increased shCerS5 HCT116 xenografts [263]. The reduced expression of PARK in shCerS4 HCT116 cells is interesting. PARK is thought to increase oxidative metabolism by removing dysfunctional mitochondria and inhibiting the Warburg effect. Although shCerS4 HCT116 cells had increased mRNA levels of LDHA levels after $48\,\mathrm{h}$, glycolytic experiments need to confirm whether these cells have a higher lactate production. A

proper regulation of mitochondria under high ROS levels is important to prevent cell apoptosis and induce mitophagy. It is interesting to observe that mitochondrial defects triggers metastatic transformation in cancer progression [390, 391, 392] and that these damages are tightly associated with the metabolism, especially the increased glycolysis [393].

Warburg effect

The increase of LDHA mRNA expression in HCT116 cells compared with Caco-2 cells may explain the enhanced in tumor growth of HCT116 xenografts. HCT116 cells actively direct the metabolic pathway from aerobic to anaerobic energy production. HCT116 cells exhibited higher GLUT1 levels, resulting in higher glucose uptake. The increased PK mRNA level suggest that HCT116 cells had a higher pyruvate production. The increased PKM2 levels indicate that pyruvate is used as a substrate for lactate production by LDHA, whose mRNA expression is also increased. The increase in both CRC line is essential because it maintains the high glycolytic influx into the cell. The lactate produced can then either be converted back to pyruvate by LDHA5 or transported out of the cell by MCTs. These transporters can export and import pyruvate or lactate, thereby regulating pH. The efflux of lactate by MCT4 prevents cytosolic acidification, which triggers cell death, and in turn acidifies the extracellular environment, inhibiting cytotoxic immune cells and attracting immunosuppressive Tregs [394, 92, 395, 396, 397]. Both MCT1 and MCT4 are associated with the plasma membrane glycoprotein CD147 [398, 399, 400]. The profile of MTC1 and MTC4 in CRC cell lines has been was studied by Pereira-Vieira et al. (2019). HCT15 cells show higher protein expression levels of MCT1 and the chaperone CD147 than Caco-2 cells, but less MCT4. Under chemical induced hypoxia, HCT15 cells increase extracellular lactate levels and both HIF1α and MCT4 increase, whereas MCT1 and CD147 remained unchanged. The increase in MCT4 in hypoxia is also observed in myocardial cells after prolonged hypoxia [401]. Immunofluorescence shows that both transporters are located in the junctions between cells of Caco-2 cells. In HCT15 cells, MCT1 is more expressed than MCT4 and located in the whole plasma membrane [396]. Pereira-Vieira et al. (2019) also show that HCT15 cells have a higher glycolytic profile than Caco-2 cells. HCT15 cells are more dependent on glucose and are more sensitive to glucose deprivation, leading to a decrease in CD147 [396]. Knockdown of CD147 has been shown to decrease lactate efflux in astrocytes [294]. If CerS5 affects lipid rafts and these transporters are in these microdomains, this may explain the reduced xenograft growth of shCerS5 Caco-2 cells, although LDHA and GLUT levels were increased. Thus, the proteomics data of shCerS4 and shCerS5 CRC cells may provide better insight and show whether CD147 or MCTs are altered in these cells.

PPP

While glycolysis is upregulated by hypoxia, the PPP pathway behaves in the opposite way: it is upregulated by acute oxygenation and downregulated by hypoxia in glioblastoma stem-like cells [402]. Depending on the cell line hypoxia increases or decreases PPP expression [403, 404]. In HCT116 cells and Caco-2 cells, only trends in TKT levels were

evident: expression levels remained essentially the same. The increase at 48 h hypoxia in shNC HCT116 cells and shCerS5 HCT116 cells was not significant, as were the fluctuations in Caco-2 cells. However, the increase in TKT was also observed in HCT116 cells (Appendix B Figure B.2, B.3). In contrast, TKTL1 was downregulated in shCerS5 HCT116 cells and further decreased during hypoxia, whereas in Caco-2 cells, TKTL1 levels increased and shCerS5 Caco-2 cells reached a higher expression level compared to 0 h and 24 h shCerS4 Caco-2 cells. The upregulation of TKTL1 is also observed in LNT-299 glioma cells after hypoxia (16 h and 36 h), but this increase is depended on HIF1α [402]. "TKTL1 knockdown enhances glucose consumption and lactate production under hypoxic conditions", but has no effect under normoxia in LNT-229 cells [402]. Heller et al. (2018) observe the same effect of TKTL1 knockdown in HCT116 cells: It increased glucose uptake and lactate production, but also increased the ROS levels and cell death especially under hypoxia [402]. Therefore, they suggest that TKTL1 does not impact ROS level and survival under normoxia but is upregulated under hypoxia, and the increased PPP lowers ROS level and prevent cell death. Another study shows that downregulation of TKTL1 in HCT116 cells reduces cell growth but does not significantly alter glucose uptake and lactate production under normoxic conditions [405]. The impaired increase of TKTL1 in shCerS5 HCT116 cells raises the need to investigate the ROS levels in those cells and whether CerS5 may be directly or indirectly involved in PPP pathway. Since PPP influences ROS, it also affects the mitochondrial quality. Future studies are needed to clarify the role of CerS5 in mitochondrial health, because so far, the mitochondrial quality control system with PINK and PARK as well as mitochondrial dynamics indicate a strong involvement of CerS4 and CerS5. Especially, under hypoxia an efficient mitochondrial regulation is important.

Hypoxia dependent effects

Hypoxia increased cellular HIF1α levels, which were much higher in HCT116 cells and Caco-2 cells than HCT15 cells. Although HIF1α levels increased with hypoxia, the increase was much greater in HCT116 cells and Caco-2 cells. This raised the question of whether CerS4 is associated with HIF. However, deficiency of CerS4 did not affect basal nuclear levels of HIF1α, cellular levels of HIF1α under hypoxia, or even after hypoxia. This indicates that CerS4 is not involved in stabilization of HIF1α. The main regulator of HIF1α is the PHD family. In 3D culture, HCT15 cells tended to decrease PHD3 after 48 h of hypoxia, but not in 2D culture. PHD3 levels in naïve HCT116 cells and Caco-2 cells also did not alter change after hypoxia. In contrast, levels in transduced HCT116 cells and Caco-2 cells gradually increased with hypoxia. This increase is consistent with the literature, as PHD2 and PHD3 are a HIF1α target (see section 1.5 and is also seen in HCT116 cells after 24 h of hypoxia (Appendix B Figure B.2). And only in shCerS4 HCT116 cells is this increase in PHD3 delayed compared with shNC HCT116 cells and shCerS5 HCT116 cells, but still increasing. However, no change was observed at the level of HIF1α.

In all CRC cell lines, and regardless of 2D cultureand 3D culture, hypoxia reduced CerS4 mRNA expression as early as 24 h of hypoxia, whereas all other CerS did not alter after

chronic hypoxia exposure. In addition to mRNA levels, luciferase promotor studies showed a clear reduction in CerS4 promotor activity after hypoxia. Both the full length CerS4 promotor and CerS4 deletion constructs exhibited significantly reduced activity, and the effect was even greater in HCT15 cells at $48\,\mathrm{h}$ than at $24\,\mathrm{h}$.

Andrysik et al. (2021) characterized the transcriptional changes in acute hypoxia in HCT116 cells exposed to $90\,\mathrm{min}$ of hypoxia ($1\,\%\ O_2$). They identified that HIF1α induces an early transcriptional response, and that HCT116 cells with HIF1α knockdown, prominent HIF targets such as Enolase 1 (ENO1), PKM1, HK1 and GLUT1 were repressed and failed to increase in hypoxia. In their data, CerS4 was also downregulated upon hypoxia as early as after $90\,\mathrm{min}$ [388]. Screening of the deposited data (geo profile: GSE68297) also detected the other CerS isoforms [388, 406]. Similar to the results in this project, hypoxia only reduces CerS4 mRNA after hypoxia (Figure 4.5). This suggests that CerS4 downregulation is an early hypoxia response, and because chromatin binding patterns are stable over time [407], CerS4 downregulation is persistent under chronic hypoxia. Interestingly, the significant decrease in CerS4 by 0.64 FC ($p<0.0001$) after hypoxia is not dependent on HIF1α. Ablation of HIF1α in HCT116 cells (shHIF1a HCT116 cells) shows a significant decrease in CerS4 transcripts after hypoxia, indicating that other O2-sensing factors besides HIF1α, such as HIF2α, or lysine demethylases, could be responsible for the downregulation and that in the case of CerS4, HIF1α is not responsible for the downregulation. This explains why the detection of HIF1α at protein level was not significantly different between shCerS4 HCT116 cells and shCerS5 HCT116 cells or shCerS4 Caco-2 cells and shCerS5 Caco-2 cells. It also shows that most CerS under normoxia are no HIF1α targets. Only CerS2, CerS3 and CerS5 levels are reduced under hypoxia without HIF1α compared with shHIF1a HCT116 cells under normoxia (Figure 4.5) indicating that these genes may be potential HIF targets. Genes upregulated under hypoxia exhibit increased histone modifications associated with enhancers and increased accessibility for DNase I [388]. Most HIF1α binding sites are associated with acute transactivation but not transcriptional repression [388]. Therefore, downregulation could occur via induction of MAX interactor 1 (MXI1) and indirect transcriptional repression of MYC. Further predictive analysis suggests that HIF1α induces signaling pathways such as TGF-β signaling (strong induction of SMAD3 and SMAD9), FOXO3 and KDM3A, which in turn might inhibit CerS4 expression. FOXO3 inhibits the mammalian target of rapamycin complex 1 (mTORC1) and activates protein kinase B (AKT) (PKB), affecting cellular energy homeostasis [408]. CerS4 plays an important role in adipose and liver tissue, suggesting that it may be also involved in stabilizing other signaling pathways, such as PKB and mTORC1. However, HIF1α targets require cofactor activity such as histone acetyltransferase tat-interactive protein-60 (TIP60) (human KAT5) or CDK8 for full transcription [409, 410, 406, 388]. While depletion of TIP60 did not alter CerS4 expression, but only CerS2 and CerS6 transcript levels, inhibition of CDK8 mediator significantly reduced CerS4 and CerS1 transcription already under normoxia. Hypoxia, on the other hand, did not decrease CerS4 mRNA levels, as they were already at a low level in CDK8-inactivated HCT116 cells and are comparable to the hypoxia-induced downregulation of WT HCT116

cells, suggesting that CDK8 is crucial for CerS4 transcription (Figure 4.5). The kinase activity CDK8 itself has both repressive and activating function, its interaction with RNA pol II and the mediators Med12, Med13, and Cyclin C regulates RNAPII binding known as Cdk8 kinase module (CKM) [325, 411].

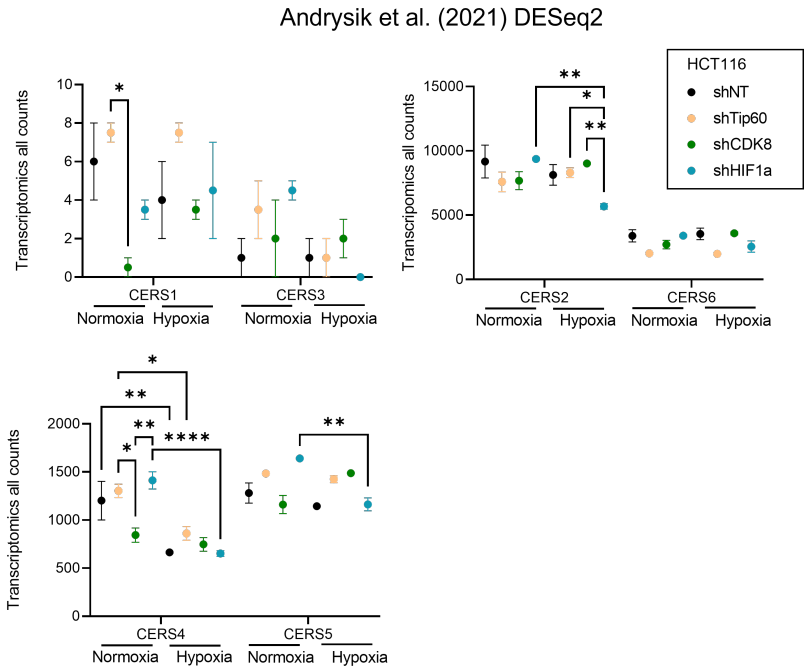

FIGURE 4.5: Transcriptomics by [388, 406] was analyzed in respect of CerS levels HCT116 cells were exposed to 24 h hypoxia and compared with normoxia. Additionally, downregulation of the transcription factors and co-factors such as HIF1α and TIP60 or CDK8, indicated a transcriptional regulation of some factors with distinct CerS isoforms under normal conditions and hypoxic conditions. Both CerS1 and CerS4 are dependent on CDK8. Transcriptomics data were extracted from the NCBI Gene Expression Omnibus (GSE68297) and analyzed by 2way ANOVA with a Tukey's multiple comparison test (* p<0.05, ** p<0.01, *** p<0.001, **** p<0.0001).

Inhibition of CDK8 also impairs glycolysis [412, 388] and reduces productive elongation, but has lesser effects on transcription start site (TSS) [388], suggesting that all CerS4 deletion constructs were reduced under hypoxia because the dependent factor was neither at the TSS nor at the 3'UTR, but within the gene body. This dovetails nicely with the HDAC inhibitor treatment, which indicated that SAHA treatment increased CerS4 mRNA level in HCT15 cells. It is reported that histone demethylases sense oxygen and control histone methylation. Through this pathway, oxygen controls cellular differentiation and cell fate [413, 414]. This pathway also explains the repression of the CerS4 promotor in the promotor deletion constructs after hypoxia. And indicate an epigenetic regulation of CerS4 already at the TSS site.

HDAC inhibitor treatment with SAHA 50 µM and TSA 50 nM in HCT15 cells showed that both CerS4 and CerS5 are epigenetically regulated. A similar effect is obtained by the synthetic S1P analog fingolimod (FTY720), which can enter the nucleus after phosphorylation by SPHK2 and inhibits HDACs in the hippocampus [415]. It is also reported that inhibition by FTY720-P is as effectively as SAHA. As little as 2 µM of SAHA is efficient to

reduce the activity of HDAC1, HDAC2, HDAC3 and HDAC8 [415]. Treatment of mice with FTY720 also increases CerS4 mRNA expression levels [416]. Burg et al. (2021) also showed that HDAC inhibition regulates lipid homeostasis. Treatment with the HADC inhibitor ACY-738 reduced glycerophospholipids, sphingolipids and cholesterol esters. However, Cer d18:1/20:0 was significantly increased in spinal cords after ACY-738 treatment [417]. Burg et al. (2021) suggest that the ACY-738 treatment is mediated by class I HDAC. HDAC1 and HDAC2 or HDAC3, as they are linked to lipid metabolism in intestinal cells and hepatocytes and adipose tissue, respectively [418, 419, 420, 421]. Indeed, the class I HDAC expression differs between HCT116 cells and HCT15 cells (Appendix B Figure B.4). Treatment with SAHA and TSA increased only HDAC3 transcripts but not HDAC1 and HDAC2. Because HDAC inhibitors acetylate the protein, further studies need to test this interaction at the protein level rather than the mRNA level.

Transcriptional regulation is not limited to acetylation and deacetylation, but another important mechanism is DNA or histone methylation. Environmental toxins can alter DNA methylation such as the genotoxic carcinogen aflatoxin B1 (AFB1), which influences CerS4 methylation in hepatocytes [422]. After 3 days wash out period, CerS4 gene is still hypermethylated in hepatocytes. The treatment itself decreases CerS4 expression after 5 days of exposure to $0.3\,\mu\mathrm{M}$ AFB1 [423]. Also, in several human bronchial cell lines, CerS4 is hypermethylated at the TSS1500 site or hypomethylated at the TSS1500 and 5'-untranslated region (5'UTR) site upon toxic exposure of benzopyrene [424]. Among the CerS isoforms, CerS4 is both hypermethylated and hypomethylated in many cells, but unlike CerS2 and CerS3, which also shows methylation at TSS200, DNA methylation of CerS4 is restricted to either TSS1500 or 5'UTR [424], which were not included in the luciferase assays of this thesis. These studies support the presumption that oxygen-sensitive demethylases trigger transcriptional inhibition of CerS4. Future studies could further investigate the JmjC lysine demethylase 5 (KDM5) family, as some of these enzymes are oxygen-sensitive (reviewed in [425]), particularly KDM5A, as its depletion mimics a hypoxia-induced response [413].

A further observation consistent with this hypothesis is the predictive transcription factor binding sites on the CerS4 promotor as NFκB, AP-1 or SP1 [188], which are activated directly or indirectly in response to hypoxia [105]. However, none of them appeared to upregulate CerS4 transcription. Luciferase activity of both the full-length promotor and construct D was less active in HCT15 cells compared with HCT116 cells, suggesting that either SP1 or AP-1 are less strongly activated in HCT15 cells than in HCT116 cells to induce CerS4 promotor activity or that the region is modified such that the transcription factor cannot bind. To analyze this, HCT116 cells and HCT15 cells transfected with luciferase plasmids were also treated with HDACs inhibitors. Like HDAC treatment, CerS4 D construct activity was higher after treatment with SAHA and TSA. In hypoxia, the CerS4 D construct had higher activity in HCT15 cells compared with the full-length promotor or HCT116 cells after $24\,\mathrm{h}$. However, after $48\,\mathrm{h}$, the activity decreased further and was no longer different than the other constructs. Construct D contains both an SP1 and AP-1 binding site. Wegner et al. (2014) have shown that estradiol and G protein-coupled estrogen receptor 1 increase CerS4 expression because they activate the transcription factor AP-1 [188]. Construct D

contains the AP-1 DNA binding site, and c-Jun and c-Fos have shown to bind to it, but that binding does not correlate with transcriptional effects [426, 427]. Interestingly, both CerS4 and SP1 are associated with insulin resistance. There, PKC and PPA activates SP1 through phosphorylation, which in turn regulates gene transcription in response to insulin [428].

Hypoxia effect on sphingolipid metabolism

The hypoxia-dependent decrease in CerS4 raises the question of how sphingolipid metabolism relates to hypoxia. As suggested by Burg et al. (2021), lipid metabolism is altered, but in their sphingolipid analysis only Cer d18:1/20:0 significantly increases and GlcCer d18:0/18:0 significantly decreases. The other differences in Cer, GlcCer and sphingomyelin are not significantly altered [417]. This is in line with CerS expression not being altered, despite CerS4 on mRNA level. However, transcriptomics by Andrysik et al. (2021) also reveals further insights into sphingolipid metabolism. The first step of the *de novo* synthesis, SPTLC transcript level, is not significantly affected by hypoxia. DEGS1, but not DEGS2, is significantly decreased by hypoxia, and its downregulation depends on TIP60 and CDK8 (Appendix B Figure B.5). Only one SMS isoform, SMPD4, is significantly affected by hypoxia, but not the other SMS isoforms and SMases. This suggests an important role of CerS in the Cer homeostasis. The degradation of Cer to sphingosine by ASAH is also downregulated by hypoxia and independent from HIF1α, TIP60 or CDK8. The metabolic pathway from sphingosine to S1P is also affected by hypoxia. Interestingly, SPHK is not only significantly downregulated by hypoxia, but HIF1α also appears to regulate it under normoxic conditions (Appendix B Figure B.5). Cleavage of S1P by SGPL is not affected. Although UGCG is not affected by hypoxia, TIP60 appears to repress its expression under hypoxic conditions (Appendix B Figure B.5). In summary, hypoxia seems to influence the lysosomal pathway of sphingolipids stronger than the synthesis pathway.

Role of hypoxia

In all three parts, CerS4 was studied in murine intestinal model, human organoids and *in vitro* under hypoxia. All these aspects may explain the outcome of CerS4 Vil/Cre mice after AOM/DSS treatment. The absence of neoplasia and dysplasia in CerS4 Vil/Cre mice may be due to better tissue restauration, but this needs further confirmation. The *in vitro* studies are partially in line with the observed *in vivo* results. Homeostasis between microbiota and intestine is not only important in preventing inflammation, but also maintains a hypoxic environment in "the intestine that is critical for nutrient absorption, intestinal barrier function", and immune response [429]. Adaptation to hypoxia is important to prevent chronic hypoxia, which aggravates intestinal injury, inflammation and CRC (reviewed in [429]). The intestinal mucosa exhibits an oxygen-poor environment with a vertical oxygen gradient, i.e., 7 - 10 % O_2 in the colonic muscle, 6 % in the vascularized submucosa, 0.7 - 1.5 % at the crypt- lumen interface, decreasing from $\sim$1.5 % in the ascending colon to 0.4 % in the sigmoid colon [429, 430]. A similar pattern is measured in the small intestine, where

oxygen concentration is $3\,\%$ at the villous tip and $2\,\%$ in the lumen. In comparison, oxygen concentration is higher in well-oxygenated tissues such as lung ($\sim$15 %) and liver ($\sim$9 %). Lymphoid tissues such as the spleen have lower oxygen levels (3.6 - 5 %). For adaptation to hypoxia, HIF is well known to be the master regulator, which, as seen, is not directly linked to CerS4. The HIF regulator PHD3 is unlikely to be affected by CerS4. Although HCT15 cells had lower PHD3 expression levels than HCT116 cells in 2D culture, downregulation of CerS4 did not affect PHD3 expression levels but indicated a slower increase in hypoxia compared with CerS4-rich shCerS5 HCT116 cells and shNC HCT116 cells. Both PHD2 and PHD3 are target genes of HIF [100, 101] and therefore are increased in hypoxia. In IBD patients, PHD1 is upregulated in UC patients and CD patients and correlates with cytokines such as IL-8 and TNF-α and caspase 3 [431]. Both PHD1 and PHD3 play an important role in DSS induced colitis. While inhibition of PHD1 protects against colitis [432, 433], PHD3 protects intestinal epithelial barrier by stabilizing Occludin [434]. In Caco-2 cells, downregulation of CerS4 did not alter PHD3 levels, consistent with observed TEER measurements, and did not alter TJ expression in the tissue. In both blood-brain barrier models and Caco-2 cells, hypoxia "has been shown to increase the tightness of the barrier" [435] with the increase of TJ proteins such as CLDN5 [436, 437]. In addition to upregulation of various TJ by HIF1α [438], it regulates transcription of several mucins [439, 440], which in turn add to barrier integrity. Interestingly, the expression of Muc5ac is regulated by both HIF1α and SMAD4, suggesting that loss of CerS4 may increase SMAD4 expression and thus contributes to mucus formation. Therefore, CerS4 Vil/Cre mice likely did not benefit from an increased barrier compared with WT mice but may had a better mucus which may have ameliorated disease progression. In IBD patients, the mucus layer is altered because the mucus-producing goblet cells are depleted and concentrations of phosphatidylcholine, which is incorporated into mucus, is reduced. Administration of phosphatidylcholine to patients restores the mucus layer [441, 442]. Another modulator of goblet cells is the IL18/IL18-R signaling pathway. Hyperactivation of IL18 produced by epithelial cells may lead to goblet cell depletion during colitis, whereas prior colitis prevents goblet cell maturation [443]. To clarify this, goblet cells should be detected in the colon tissue of AOM/DSS treated mice. HE staining showed no obvious differences. No goblet cells were seen in ulcerative regions after acute DSS treatment, as well as in neoplastic regions regardless of mice strain (Figure 3.11). For a more in-depth analysis, detection of mucin with periodic acid-Schiff [444] or staining of fucosylated glycoproteins with the lectin Ulex europeus agglutin-1 and the rich mucin secreted by mature goblet cells with MUC2 [443] would be useful. Another aspect that should also be investigated is whether CerS4 is involved in goblet maturation. To this end, IL18 and goblet cell differentiation transcriptional factors such as Gfi1, Spdef and Klf4 could be detected, as they are inhibited in IL18bp$^{-/-}$ mice [443]. Thus, CerS4 deficiency in epithelial cells could influence IL18, which is a mechanism that promotes colitis by inhibiting goblet cell maturation. To further investigate the role of CerS4 in intestinal differentiation, CerS4 should be downregulated, and intestinal differentiation analyzed in organoids from patients.

The metabolic program and mitochondrial activity of intestinal cells depend on the cell

type. Any imbalance in these mechanisms can affect epithelial homeostasis. Lgr5 stem cells and Paneth cells have different metabolic programs. Stem cells have a higher mitochondrial activity, whereas Paneth cells are characterized by a higher rate of glycolysis. Secreted lactate is taken up by Lgr5 stem cells and converted to pyruvate to increase mitochondrial OXPHOS [445]. Inhibition of glycolysis in Paneth cells decreases crypt maturation [445]. *In vitro* data from CRC cells already suggest that CerS4 deficiency influence the glycolysis in hypoxia, which remains to be confirmation by the seahorse assay. The possible role of CerS4 in lactate transporters also needs further investigation. Together with the organoid data indicating a correlation of CerS4 and Lgr5 or the function of CerS4 in hair follicle stem cells, CerS4 deficiency may have influenced stem cells in CerS4 Vil/Cre mice. The exact role of CerS4 in intestinal stemness needs further investigation; initial organoid data suggest that organoids with less CerS4 are more differentiated. Hypoxic conditions are present in early development, and hypoxia can induce pluripotent stem cells [446, 447]. CerS6 has previously been reported to play a role in early embryonic development and cancer differentiation [448, 449]. Hence, the downregulation of CerS4 after hypoxia may also indicate a role of CerS4 in cell differentiation. Consistent with this are the *in vitro* results of TEER measurements: The decreased capacity of shCerS4 Caco-2 cells in CellZscope measurements did not differ in electrical resistance but in capacitance, indicating that shNC develops longer and more densely packed microvilli on their apical surface than shCerS4 Caco-2 cells [217]. This suggest that CerS4 is involved in the differentiation process and is in agreement with data from the literature [450, 203] and from organoids. The role of CerS4 in stemness renewal and differentiation could explain why CerS4 Vil/Cre mice lacked tumor formation.

In addition, the increase in capacitance in shCerS4 Caco-2 cells indicates a role for CerS4 in vesicle formation and fusion. When vesicles fuse with the PM and form a pore on the outside, the capacitance increases [253]. This process occurs during exocytosis and endocytosis, and is particularly striking in immune cells with large vesicles such as mast cells [451, 452], in neutrophils [453] and during phagocytosis in macrophages [454, 455, 456], but is also an important mechanism in intestinal epithelium in the release of granular contents such as mucin [457]. However, it remains to be elucidated whether CerS4-produced sphingolipids are important for vesicle formation [458, 459] or in regulating the mechanism, since the release of mucin is mediated by PKCϵ [460]. As described previously, Cer d18:1/18:1 regulates PKCζ activity [276], it may also be involved in other PCK isoforms and thus affect mucin exocytosis. Mucin is not only important for barrier function, but several studies have also shown that the profile of mucin and mucin-associated glycans changes during the progression of CRC [461, 462, 463, 464, 465]. Furthermore, some mucin as Muc5AC are also directly regulated by HIF1α, explaining the increase of Muc5A in adenomas and carcinomas of CRC (reviewed in [466]).

Furthermore, the absence of dysplasia and the lack of tumor formation in CerS4 Vil/Cre is in accordance with the inhibitory function of CerS4 for TGF-β signaling. As mentioned previously, hypoxia increases TGF-β signaling [388], and TGF-β can act tumor suppressive and limit tumorigenesis by decreasing the dedifferentiation of intestinal cells in the villi of

APC- and KRAS- deficient mice. These mice (TGFbR1-, KRAS- and APC- deficient) develop more intestinal tumors from the villi and are sensitive to MEK1/2 inhibition [467]. CerS4 deficiency may increase TGF-β signaling in the intestine, which in turn has a tumor suppressive function and leads to less tumor development.

During tumor development, hypoxia contributes to genomic instability by downregulating numerous DNA repair pathways, developing resistance to radiotherapy and chemotherapy, and promoting EMT [359]. In particular, HCT116 cells are described to have a malignant phenotype [371] and the ability to metastasize in immunodeficient mice, whereas Caco-2 cells do not [468, 371]. As indicated by the loose spheroid morphology in 3D culture of HCT116 cells and the lack of barrier formation in 2D culture of HCT116 cells, HCT116 cells are less differentiated than Caco-2 cells [371]. Treatment of HCT116 cells and Caco-2 cells with TNF-α strongly induces EMT in HCT116 cells through activation Snail and pGSK-3β pathways [469]. In contrast, Caco-2 cells can differentiate further [470, 471, 472] and both high barrier formation and the solid spheroid formation in Matrigel reveal a differentiated CRC cell line. Therefore, Caco-2 cells with a still differentiated CRC cell line reflect tumors in the early stages of CRC progression, whereas the aggressive HCT116 cells reflects tumors of UICC stage IV of CRC that are malignant. This may explain why downregulation of CerS4 or CerS5 in HCT116 cells and Caco-2 cells did not always result in the same changes, and explains the differential metabolic activity of the naïve CRC cells as metabolic pathways alters during tumor progression (reviewed in [473]). Further studies are needed to determine the effects of downregulation of CerS4 or CerS5 during CRC development and cannot be limited to observation of single CRC cell lines.

Conclusion

As a conclusion, CerS4 deficiency in different tissues has opposite effects on progression of CAC due to different functions. In general, CerS4 appears to play an important role in fine-tuning signaling pathways: In the absence of CerS4, T cells prolong their cytokine secretion, which impairs resolution of inflammation and leads to severe ulcers with fatality in mice. The absence of CD8 T cells in CerS4 LCK/Cre mice and increased Tregs resulted in a high frequency of tumor formation in the CAC model. The role of CerS4 in fine-tuning is also seen in stem cells, such as hair follicle stem cells, but organoid data also show a correlation of CerS4 with Lgr5 in intestinal stem cells associated with the physiological Wnt pathway. Based on the present data, CerS4 appears to play a tumor stage-dependent role. At early stage, it is pro-tumorigenic and its absence in intestinal cells mitigate tumor formation, but at advanced tumor stage it has anti-tumorigenic features, and its downregulation enhances the Warburg effect. Mechanistically, CerS4 is downregulated by hypoxia. This suppression already occurs in acute hypoxia and persists in chronic hypoxia and is independent from HIF1α but is epigenetically regulated. This could explain the different properties of CerS4 in different tumor stages. In addition, CerS5 also exhibits important tumor suppressive functions, and its suppression affects mitochondrial dynamic and health. Therefore, downregulation of CerS5 is consistent with increased mitochondrial damage in late tumor

stages with metastasis. Hence, CerS4 is an interesting target for colitis and CRC. Future therapeutics may act indirectly on CerS4 by targeting epigenetic regulators.

Chapter 5

Outlook

The tissue specific function of CerS4 in colitis and CAC progression drives future studies in many directions. First, the inhibitory effect of CerS4 on TGF-β signaling is the most striking interaction that theoretically explains the observed *in vivo* results. Of note, in the CAC model, various TGF-β or anti-SMAD7 models are concordant with CerS4 deficient mice. Therefore, SMAD staining of existing histological staining should verify this interaction and the CerS4 TGF-β signaling both in intestinal cells and in T cells and should be further investigated.

In this sense, elucidation of molecular mechanisms of CerS in immune cells and particularly T cells requires further investigation. The fine-tuning function of CerS4 in T cell activation draws attention not only to common signaling mechanisms that need further investigation, but also the potential of CerS4 derived Cer in cytokine secretion. Both compartment-specific enzyme activity and lipid localization could be analyzed with bi-or trifunctional lipid probes that allow microscopical localization and lipid-interacting proteome by photo-cross linking [474]. The T cell specific deletion of CerS isoforms would also provide a better understanding of the role of CerS in T cells. Therefore, the residual CerS crossed with LCK/Cre system would be an interesting mouse model. In addition, the increased neutrophilia and macrophage polarization draws attention to CerS4 in other immune cells. Future studies should further investigate the progression of colitis with CerS4 deficient macrophages or neutrophils by crossing CerS4$^{flox/flox}$ mice with Lys/Cre mice allowing the studies on myeloid cell lineage.

The high sensitivity of AOM/DSS in CerS4 KO mice draws the attention to CerS4 in the liver. Besides gut-liver axis observed in the sphingolipid alteration in liver after CerS4 deficiency and inflammation, many other studies showed the important role of CerS4 in hepatocytes and adipose cells and how CerS4 is involved in metabolic diseases [450, 374]. Here, CerS4 seems to be involved only under high fat diets and to a lesser extend under normal conditions [325, 324, 346, 475]. This is a worthwhile observation as obesity and metabolic syndrome such as diabetes are potential risk factors for IBD and CRC. Therefore, further studies using CerS4 KO mice could be performed to elucidate the effect on the liver and to analyze metabolic markers or syndromes in these mice. In accordance with these studies, CerS4 KO mice may show differences under high fat diets.

Moreover, the established organoids are a promising model for future studies. The data set needs to be enlarged, and the complex dynamics of CerS in intestinal differentiation

and stemness and needs further verification. First, the correlation of CerS4 with Lgr5 is consistent with the co-localization of CerS4 with Lgr1 in hair follicle stem cells, so the co-localization of CerS4 and Lgr5 in organoids requires further verification and investigation. Second, CerS4 appears to be involved in physiological Wnt signaling rather than intrinsic Wnt signaling in an environment without or with little Wnt. Therefore, whether CerS4 or CerS4 derived Cer can amplify the Wnt signaling should be further investigated. Third, the influence of CerS4 on the metabolic pathway may also be involved in stem cell maintenance and differentiation. It has been reported that lactate produced by Paneth cells is used by stem cell to increase OXPHOS. Hence, defects in mitochondrial respiration may affect stemness, and such the implications for CRC progression remain to be investigated.

Downregulation of CerS4 showed altered regulation of glycolysis metabolism after hypoxia. Although CerS4 downregulation did not alter HIF1α levels or its translocation to the nucleus, CerS4 downregulation may be associate with the glycolysis pathway. Hence, differences in GLUT and LDHA proteins should be examined on protein level, and seahorse assays should be performed to analyze oxygen consumption and extracellular acidification rate to determine glucose metabolism and lactate production of shNC, shCerS4, shCerS5 HCT116 cells or Caco-2 cell lines. The mitochondrial expression levels in shCerS4 HCT116 cells and Caco-2 cells and even more impressively of shCerS5 HCT116 cells and Caco-2 cells already indicate an important role of CerS4 and CerS5 in mitochondrial respiration. Therefore, proteomic analysis of CRC cell lines and a verification at protein levels should provide better insights. In shCerS4 CRC cells, OPA expression was reduced and it has been reported that reduction of OPA by shRNA increases apoptosis and mitochondrial fragmentation [114]. Therefore, analyzing CerS4 impact on mitochondrial function should also include apoptosis and necrosis assays.

This thesis provided insight into CerS4 regulation and confirmed that hypoxia downregulates CerS4 expression in intestinal cells. The mechanism behind this needs further investigation, as this downregulation is independent of HIF1α [388]. This downregulation is also likely independent of HIF2, as CerS4 levels are not significantly altered in DSS treated mice deficient in HIF2 [476, 477, 478]. It is more likely that this is an epigenetically determined process. Trimethylation of lysine 9 of histone 3 (H3K9me3) and trimethylation of lysine 27 of histone 3 (H3K27me3) are common modifications that condense chromatin structure and block gene expression [479]. H3K9me3 is catalyzed by histone methyltransferase SUV39H1 and SUV39H2. SUV39H has previously been shown to be activated by hypoxia in human fetal lung type II cells and repressing chromatin status [480]. In a PhD thesis by Anne Rademacher (University of Heidelberg), Rademacher discovered CerS4 among the genes that are repressed by SUV39H, alluding that CerS4 is a promising target for epigenetic drug development [481]. Methylation pattern is also altered by lysine methyltransferases (KTM). It is reported that methyltransferase KMT2A is overexpressed in hypoxic regions of the tumor [482]. During neuronal trans differentiation, CerS4 was highly expressed in control cells and downregulated in KTM2B-deficient cells, indicating that CerS4 is a target of

KTM2B that plays a role in maturation [483]. KMT2A is responsible for trimethylating Histone H3 lysine 4 (H3K4me3) in gene promotors and can mark active promotors [484]. Additional methylation and acetalization patterns of the CerS4 gene and the enzymes involved should be investigated by DNA-Protein Interaction (Chip-Seq) or chromatin accessibility analysis (ATAC-Seq, EpiQ™ chromatin analysis kit).

CerS4 likely has an impact on the cell cycle because of its role in hair follicle stem cells and hepatocytes and its correlation with E2 factor (E2F) transcriptional factors, which are important regulators of S-phase entry and control of cell division (Appendix C Figure C.1). Cell cycle control is an important mechanism for cancer cells to prevent elimination by immune cell and enter senescence [485, 486]. A PhD thesis by Flora Lucy Dix (University of Edinburgh) showed that lipid metabolism is altered in oncogene-induced senescence and that CerS4 is linked to the cell cycle via PP1-RB-E2F axis [487]. Similar to the signaling function of Cer d18:1/18:0 with PP2A [312] CerS4 derived Cer binds directly to PP1 [487], which can then bind to RB. It dephosphorylates the phosphorylated RB, thereby activating it. Activated RB in turn assembly with E2F and prevents transcription of E2F targets [488, 489]. The observation of Dix (2018) needs further verification, as hypoxia downregulates CerS4 and should decrease PP1 activation, but depending on the cell line, hypoxia increases PP1-mediated pRB dephosphorylation [490]. Similar to the CerS5 and CerS6 involvement in p53 [252, 491], this resembles another sphingolipid metabolism involved in tumor suppression that should be investigated further.

CerS4 cannot be clearly assigned to a tumor suppressive or proto-oncogene function. Its ubiquitously expression suggests that it plays an important role in various cell types and in different signaling pathways. The metabolic effect of CerS4 may not only contribute directly to the progression of IBD and CRC, but also indirectly, even before the onset of disease, as a potential risk factor. This work elaborated that CerS4 can be used as a therapeutic target, but it should be inhibited or increased in a tissue specific manner to prevent off-target effects. Therefore, research on tissue-specific drug delivery using small molecules, nucleic acids, peptides, antibodies, and cell-based strategies targeting CerS4 should be considered [492]. Also, analysis of the effect of CerS4 after treatment with drugs targeting epigenetic regulators (common in leukemia) could clarify whether CerS4 could also be specifically upregulated by these treatments to prevent pro-metastatic and protumor functions in late stage.

Appendix A

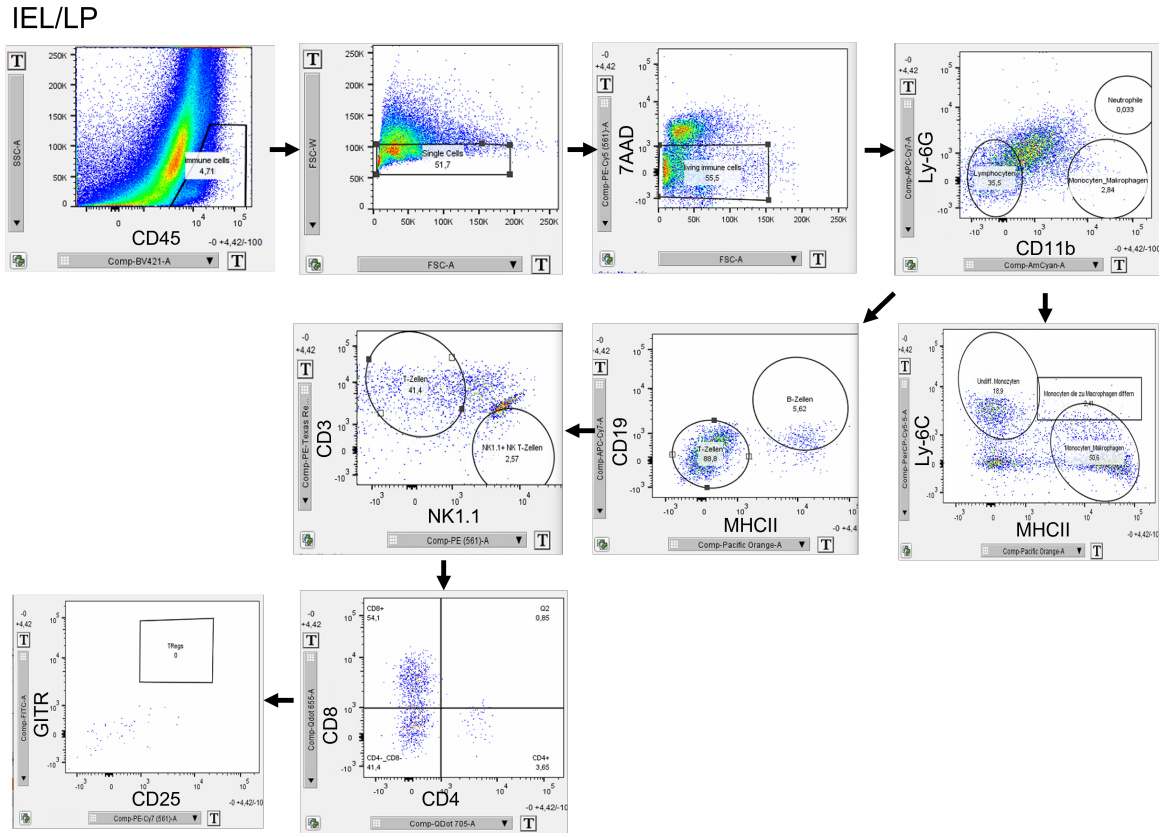

FIGURE A.1: Gating strategy of immune cells in colon (IEL/LP) analyzed with FlowJo software. Figure was previously published in [204] in the supplementary material.

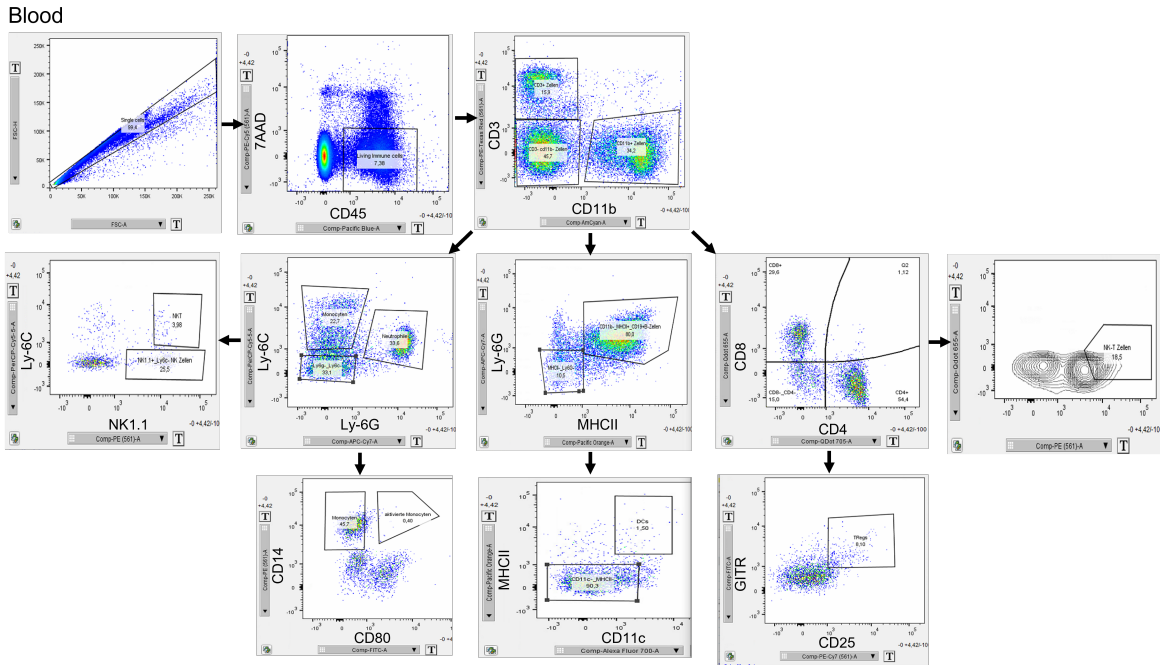

FIGURE A.2: Gating strategy of immune cells in blood analyzed with FlowJo software. Figure was previously published in [204] in the supplementary material.

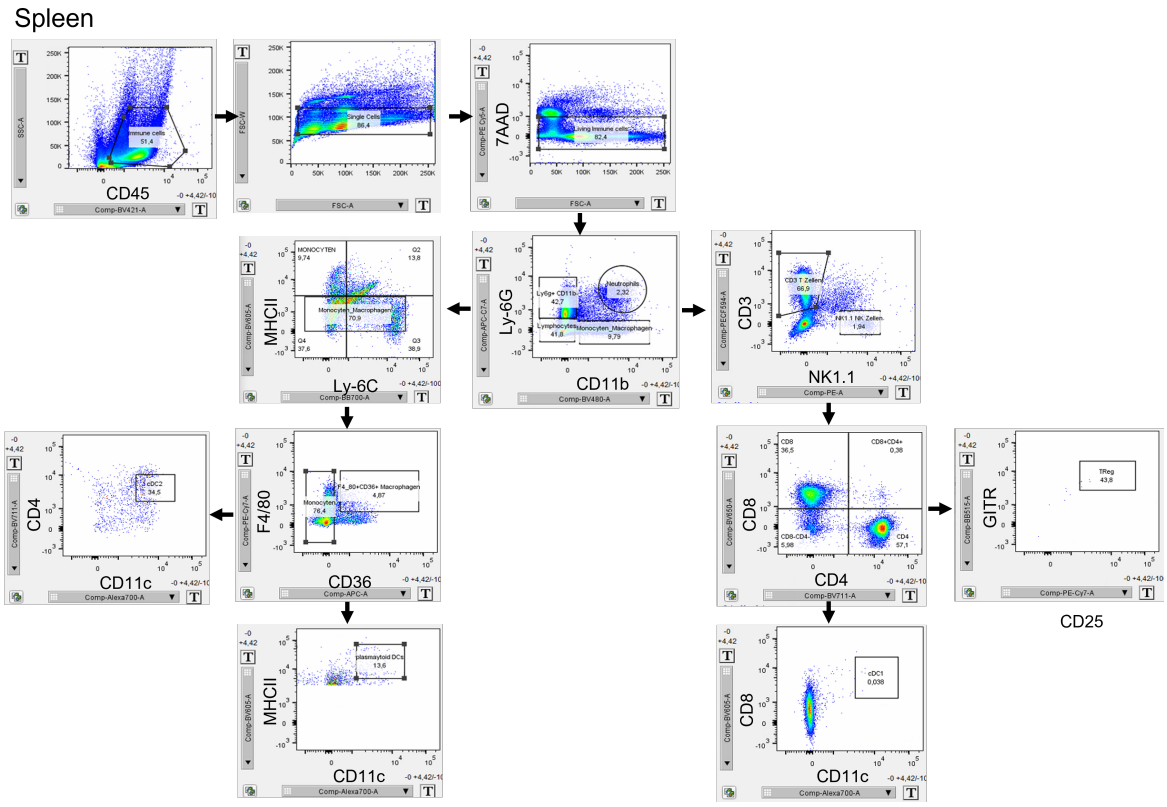

FIGURE A.3: Gating strategy of immune cells in the spleen was performed using FlowJo software. The figure was previously published in [204] in the supplementary material.

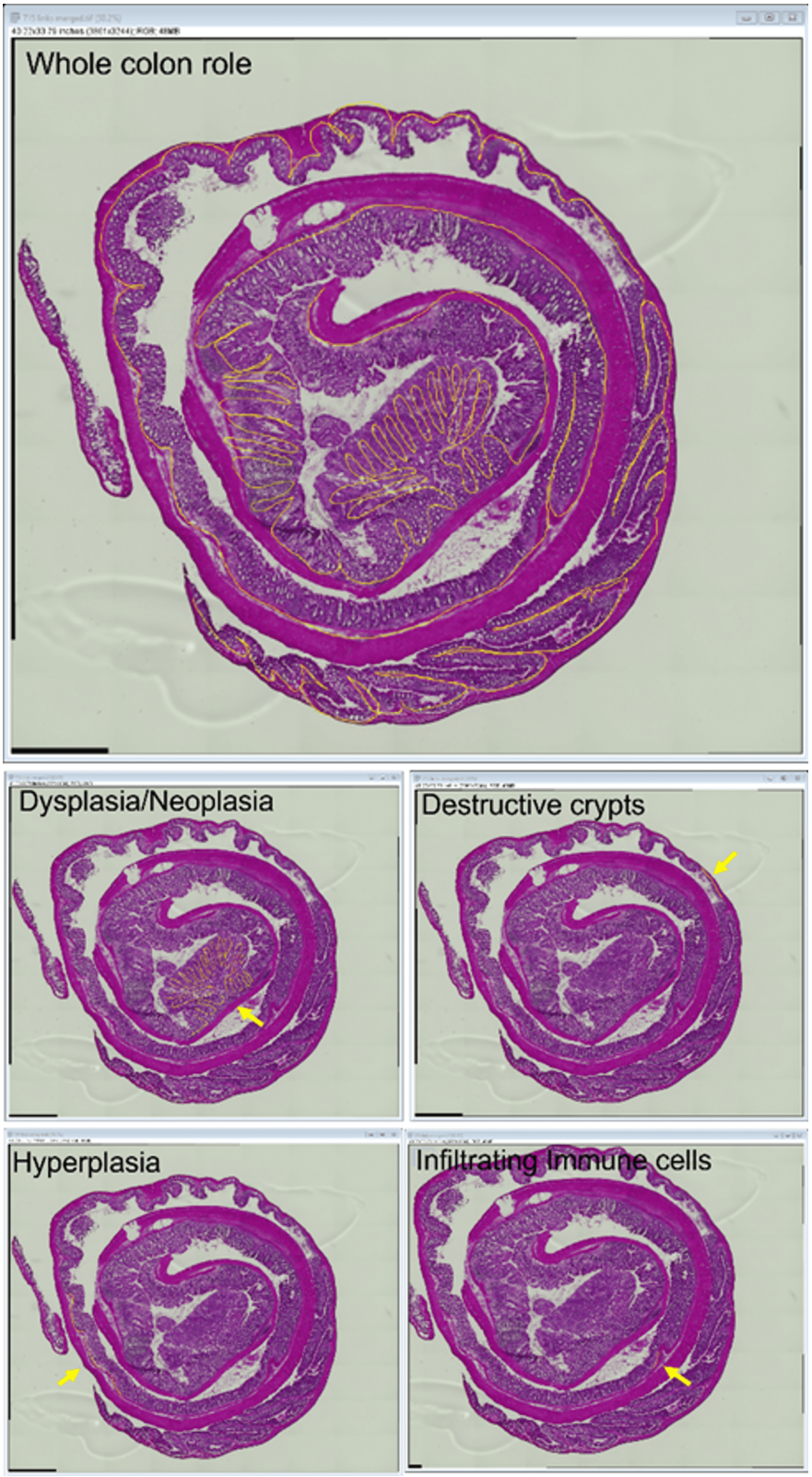

FIGURE A.4: Example screenshots of analysis of colon sections with Fiji freehand tool and dysplastic, neoplastic, hyperplastic, and inflamed regions (destructive and infiltrating immune cells) indicated by yellow lines and arrows were related to the total length of the colon (left image, yellow line

Appendix B

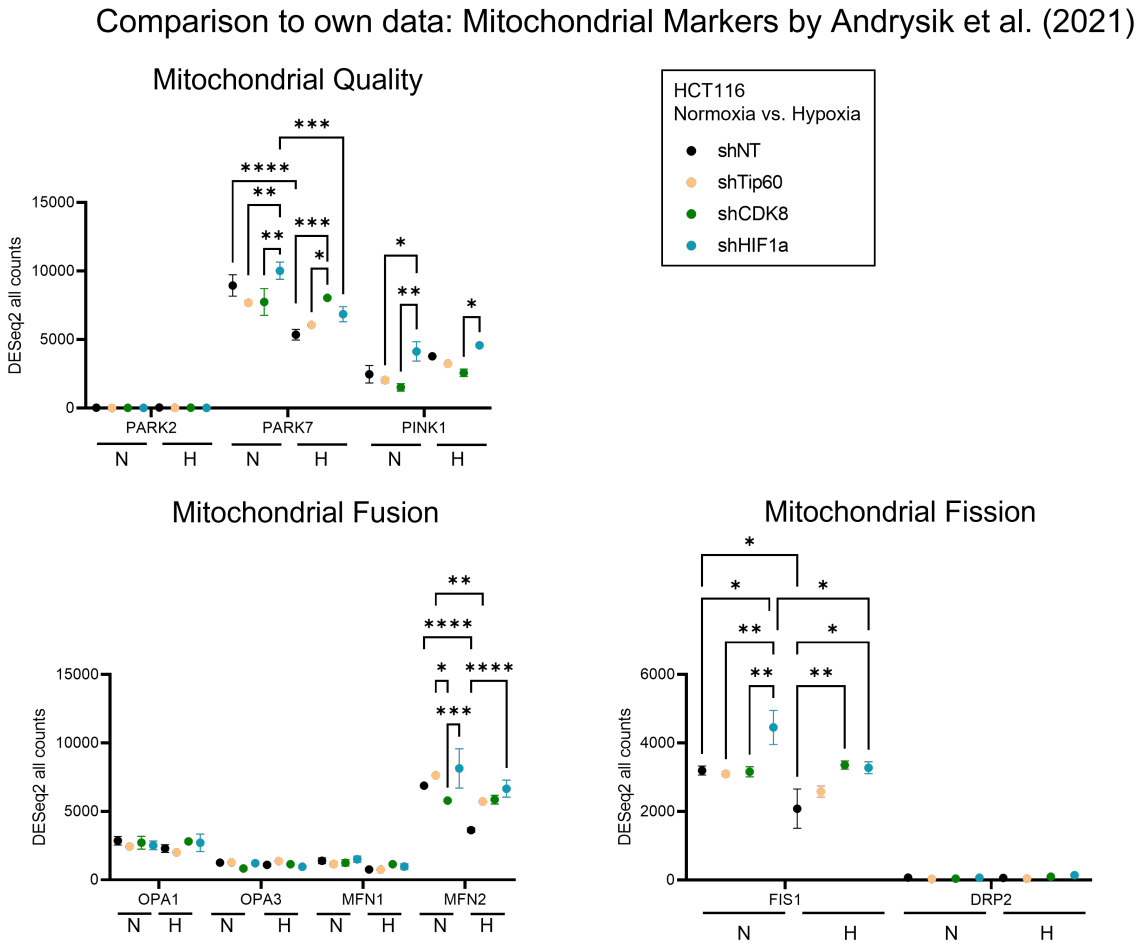

FIGURE B.1: Changes of expression of mitochondrial markers of mitochondrial quality, fission and fusion after 24 h of hypoxia in HCT116 cells. The study involved deletion of the transcription factor HIF1α and cofactors Tip60 and CDK8 in HCT116 cells. Downregulation of PARK7, MFN2 and FIS1 are mediated by HIF1α under normoxic (N) and hypoxic (H) conditions [388, 406]. Transcriptome data were extracted from the NCBI Gene Expression Omnibus (GSE68297) and analyzed by two-way ANOVA with a Tukey's multiple comparison test (* p<0.05, ** p<0.01, *** p<0.001, **** p<0.0001).

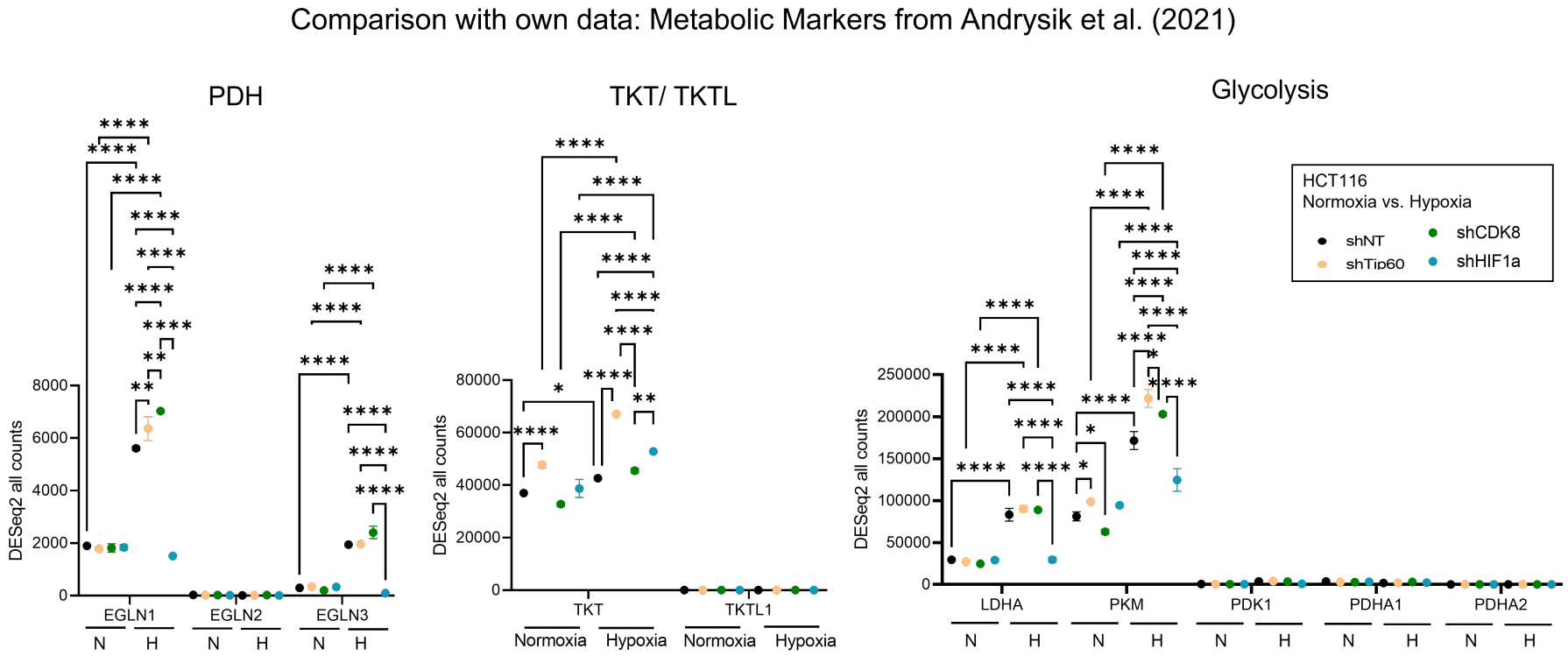

FIGURE B.2: Hypoxia increases PDH and glycolysis pathway in HCT116 cells. DeqSeq2 data from [388, 406]: HCT116 cells exposed to 1% O_2 for 24 h (Hypoxia, H) compared with normal oxygen condition (Normoxia, N). The markers used in this study were mapped. The increase in expression level is consistent with that observed in this study. In addition, transcription factor HIF1α and the cofactors Tip60 and CDK8 were downregulated in HCT116 cells, providing insight into whether the increase is dependent on these factors. Accordingly, PHD (gene name EGLN), LDHA and PKM are HIF1α targets and increase only in the presence of this transcription factor. EGLN1 corresponds to PDH2, EGLN2 corresponds to PDH1, and EGLN3 corresponds to PDH3. In addition to the PDHA, the PDK, which inhibits PDHA, did not increase as much as LDHA or PKM. Transcriptome data were extracted from the NCBI Gene Expression Omnibus (GSE68297) and analyzed by two-way ANOVA with a Tukey's multiple comparison test (* p<0.05, ** p<0.01, *** p<0.001, **** p<0.0001).

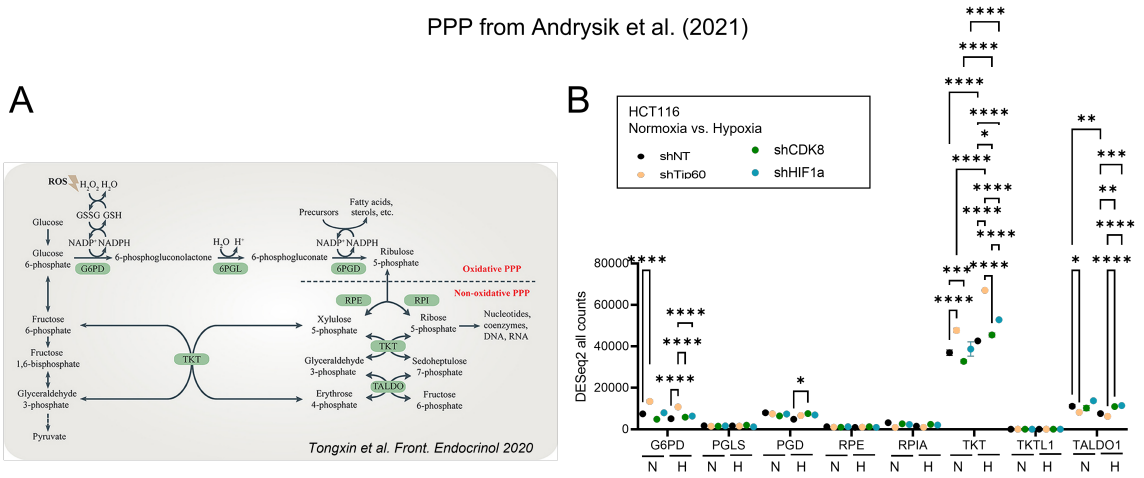

FIGURE B.3: Analysis of PPP in HCT116 cells. (A) Schematic representation of the enzymes involved in PPP: G6PD is responsible for the oxidative PPP, whereas RPE and RPI enable switching between oxidative and non-oxidative PPP. The figure is taken from Tongxin et al. (2020) [493]. (B) Because only TKT and TKTL were analyzed in this study, PPP enzymes do not increase after hypoxia, but Tip60 appears to repress some PPP enzymes. Transcriptome data were extracted from the NCBI Gene Expression Omnibus ((GSE68297)) and analyzed by two-way ANOVA with a Tukey's multiple comparison test (* p<0.05, ** p<0.01, *** p<0.001, **** p<0.0001).

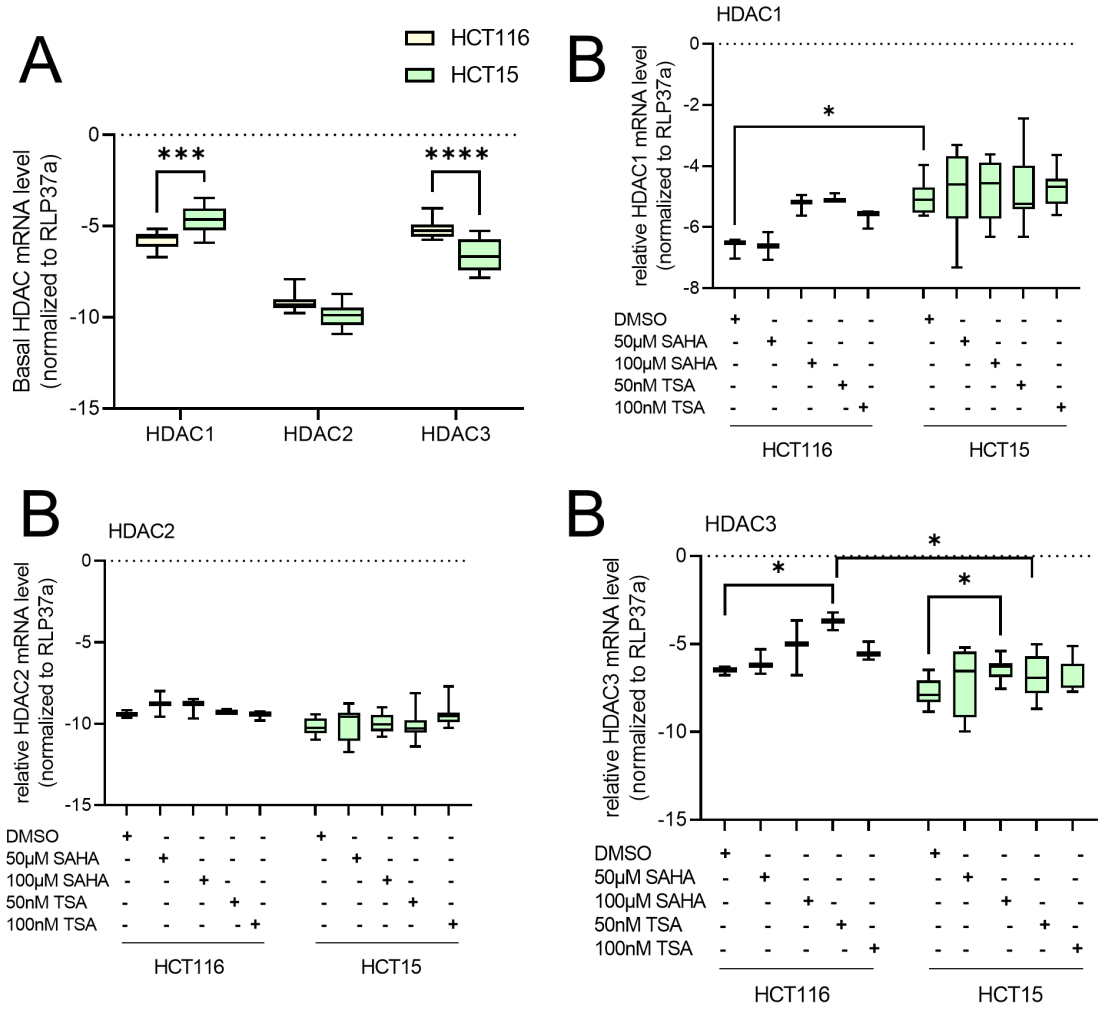

FIGURE B.4: HDAC profile in HCT116 and HCT15 cell lines differs. (A) Basal expression level of HDAC1, 2 and 3 mRNA level normalized to RLP37a in HCT116 and HCT15 cells were determined by qRT-PCR and calculated as ΔCT value. (B) HCT116 and HCT15 cells were treated with $50\,\mu M$ and $100\,\mu M$ SAHA and $50\,nM$ and $100\,nM$ TSA (both from TOCRIS) for $4\,h$. Cellular mRNA levels of HDAC1-HDAC3 were determined by qRT-PCR and calculated as relative expression levels ($\Delta\Delta$CT) by normalization to housekeeping gene RLP37a and to DMSO control. Data are presented as median $\pm$ CI95 from one (HCT116) and 4 independent experiments. Statistically significant differences between DMSO control and treatment were calculated by two-way ANOVA and Dunnett's multiple comparison post-tests (* p<0.05, ** p<0.01, *** p<0.001, **** p<0.0001).

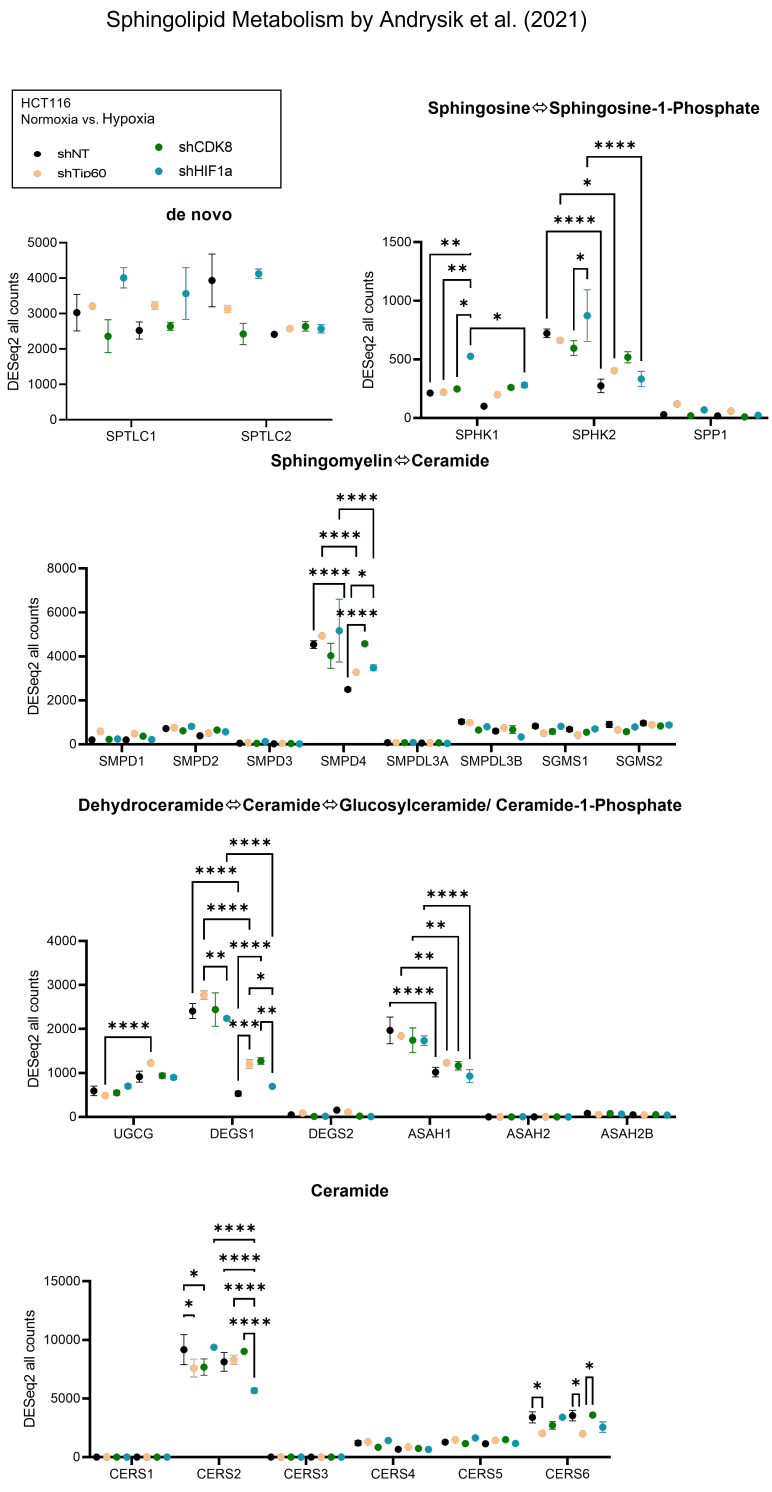

FIGURE B.5: Sphingolipid metabolism changes after acute hypoxia. (A) HCT116 cells were exposed to 24 h hypoxia and performed transcriptomics analysis. Knockdown of the transcription factor HIF1α and cofactors Tip60 and CDK8 revealed that some genes of the sphingolipid metabolism are regulated by these factors. Transcriptomics data were extracted from the NCBI Gene Expression Omnibus ((GSE68297)) and analyzed by two-way ANOVA with a Tukey's multiple comparison test (* p<0.05, ** p<0.01, *** p<0.001, **** p<0.0001). (B) Sphingolipid metabolism in a nutshell with the gene names (italics) to give a better overview. Schematic representation was adapted from [494].

Appendix C

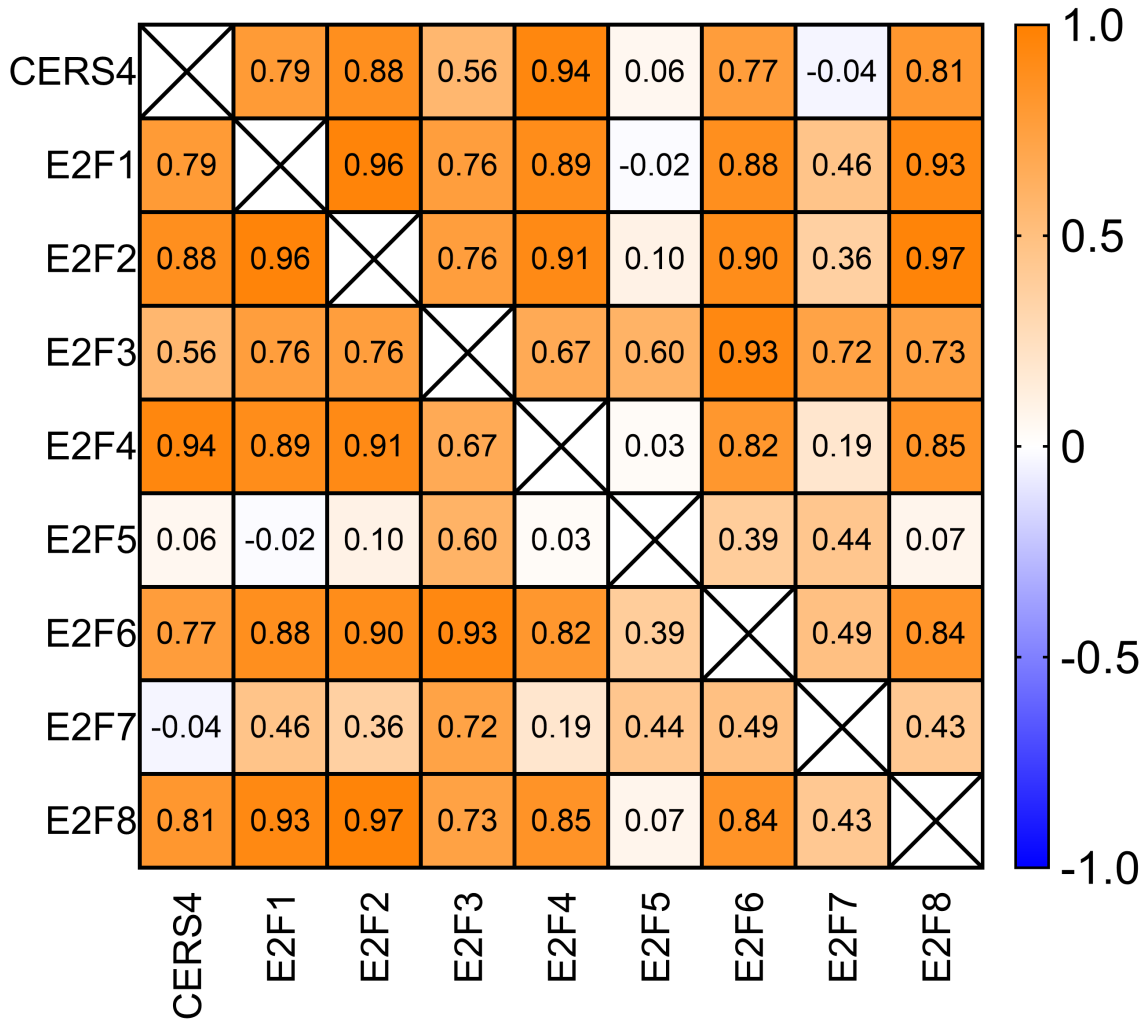

FIGURE C.1: CerS4 and E2F genes from transcriptomics were correlated ([388]). CerS4 shows the highest correlation with E2F4. Similar to CerS4, E2F4 expression decreases after hypoxia. Among the E2F genes, it is the most highly expressed isoform in HCT116 cells. In HIF1α-deficient HCT116 cells, expression is even higher, suggesting that HIF1α downregulates E2F4, consistent with the decrease during hypoxia (not shown). The least downregulation of E2F4 is observed in WT HCT116 cells, indicating that repression of E2F4 requires all cofactors Tip60, CDK8, and transcription factor HIF1α. Transcriptome data were extracted from the NCBI Gene Expression Omnibus (GSE68297) and analyzed by Pearson correlation after first calculating the mean of adjacent replicates and then analyzing these means.

Bibliography

[1] Deborah C. Rubin, Anisa Shaker, and Marc S. Levin. "Chronic intestinal inflammation: inflammatory bowel disease and colitis-associated colon cancer." In: *Frontiers in immunology* 3.107 (May 2012).

[2] Meenakshi Bewtra et al. "Crohn's Disease and Ulcerative Colitis Are Associated With Elevated Standardized Mortality RatiosA Meta-Analysis." In: *Inflammatory Bowel Diseases* 19.3 (Mar. 2013), pp. 599–613.

[3] Daniel C. Baumgart and Simon R. Carding. "Inflammatory bowel disease: cause and immunobiology." In: *The Lancet* 369.9573 (May 2007), pp. 1627–1640.

[4] Daniel C. Baumgart and William J. Sandborn. "Inflammatory bowel disease: clinical aspects and established and evolving therapies." In: *The Lancet* 369.9573 (May 2007), pp. 1641–1657.

[5] Ashwin N. Ananthakrishnan. "Epidemiology and risk factors for IBD." In: *Nature Reviews Gastroenterology & Hepatology 2015 12:4* 12.4 (Mar. 2015), pp. 205–217.

[6] Siddharth Singh et al. "Obesity in IBD: epidemiology, pathogenesis, disease course and treatment outcomes." In: *Nature Reviews Gastroenterology & Hepatology 2016 14:2* 14.2 (Nov. 2016), pp. 110–121.

[7] Paul Stephen Fitzmorris et al. "Impact of Metabolic Syndrome on the Hospitalization Rate of Crohn's Disease Patients Seen at a Tertiary Care Center: A Retrospective Cohort Study." In: *Digestion* 91.3 (May 2015), pp. 257–262.

[8] J A Eaden, K R Abrams, and J F Mayberry. "The risk of colorectal cancer in ulcerative colitis: a meta-analysis." In: *Gut* 48.4 (Apr. 2001), pp. 526–535.

[9] M D Rutter et al. "Cancer surveillance in longstanding ulcerative colitis: endoscopic appearances help predict cancer risk." In: *Gut* 53.12 (Dec. 2004), pp. 1813–1816.

[10] Matthew Rutter et al. "Severity of inflammation is a risk factor for colorectal neoplasia in ulcerative colitis." In: *Gastroenterology* 126.2 (Feb. 2004), pp. 451–459.

[11] Masakazu Yashiro. "Ulcerative colitis-associated colorectal cancer." In: *World Journal of Gastroenterology* 20.44 (Nov. 2014), pp. 16389–16397.

[12] Rebecca L. Siegel, Kimberly D. Miller, and Ahmedin Jemal. "Cancer statistics, 2017." In: *CA: A Cancer Journal for Clinicians* 67.1 (Jan. 2017), pp. 7–30.

[13] Rebecca L Siegel et al. "Colorectal cancer statistics, 2017." In: *CA: A Cancer Journal for Clinicians* 67.3 (May 2017), pp. 177–193.

[14] Eduardo Vilar and Stephen B. Gruber. "Microsatellite instability in colorectal cancer—the stable evidence." In: *Nature Reviews Clinical Oncology 2010 7:3* 7.3 (Feb. 2010), pp. 153–162.

[15] C. Richard Boland and Ajay Goel. "Microsatellite Instability in Colorectal Cancer." In: *Gastroenterology* 138.6 (May 2010), 2073–2087.e3.

[16] Odise Cenaj, Joanna Gibson, and Robert D Odze. "Clinicopathologic and outcome study of sessile serrated adenomas/polyps with serrated versus intestinal dysplasia." In: *Modern Pathology 2018 31:4* 31.4 (Dec. 2017), pp. 633–642.

[17] Ernst J. Kuipers et al. "Colorectal cancer." In: *Nature Reviews Disease Primers 2015 1:1* 1.1 (Nov. 2015), pp. 1–25.

[18] Eun Ran Kim and Dong Kyung Chang. "Colorectal cancer in inflammatory bowel disease: The risk, pathogenesis, prevention and diagnosis." In: *World Journal of Gastroenterology* 20.29 (Aug. 2014), pp. 9872–9881.

[19] T. Muto, H. J. R. Bussey, and B. C. Morson. "The evolution of cancer of the colon and rectum." In: *Cancer* 36.6 (Dec. 1975), pp. 2251–2270.

[20] Harith Rajagopalan et al. "The significance of unstable chromosomes in colorectal cancer." In: *Nature Reviews Cancer 2003 3:9* 3.9 (2003), pp. 695–701.

[21] P F Denoix. "Tumor, node and metastasis (TNM)." In: *Bull Inst Nat Hyg (Paris)* 1.6 (1944), pp. 1–69.

[22] PF Denoix. "The TNM staging system." In: *Bull Inst Nat Hyg* 7 (1952), pp. 743–748.

[23] Mahul B. Amin et al. "The Eighth Edition AJCC Cancer Staging Manual: Continuing to build a bridge from a population-based to a more "personalized" approach to cancer staging." In: *CA: A Cancer Journal for Clinicians* 67.2 (Mar. 2017), pp. 93–99.

[24] Peter Goldstraw. *New TNM classification: Achievements and hurdles*. 2013.

[25] Elena Sancho, Eduard Batlle, and Hans Clevers. "Live and let die in the intestinal epithelium." In: *Current Opinion in Cell Biology* 15.6 (Dec. 2003), pp. 763–770.

[26] Nick Barker, Marc Van De Wetering, and Hans Clevers. "The intestinal stem cell." In: *Genes & Development* 22.14 (July 2008), pp. 1856–1864.

[27] Laurens G. Van Der Flier and Hans Clevers. *Stem cells, self-renewal, and differentiation in the intestinal epithelium*. Feb. 2009.

[28] Phulwinder K. Grover, Jennifer E. Hardingham, and Adrian G. Cummins. "Stem cell marker olfactomedin 4: critical appraisal of its characteristics and role in tumorigenesis." In: *Cancer and Metastasis Reviews 2010 29:4* 29.4 (Sept. 2010), pp. 761–775.

[29] Laurens G. van der Flier et al. "OLFM4 Is a Robust Marker for Stem Cells in Human Intestine and Marks a Subset of Colorectal Cancer Cells." In: *Gastroenterology* 137.1 (July 2009), pp. 15–17.

[30] W. Liu et al. "Olfactomedin 4 deletion induces colon adenocarcinoma in ApcMin/+ mice." In: *Oncogene 2016 35:40* 35.40 (Mar. 2016), pp. 5237–5247.

[31] A. Shvab et al. "Induction of the intestinal stem cell signature gene SMOC-2 is required for L1-mediated colon cancer progression." In: *Oncogene 2016 35:5* 35.5 (Apr. 2015), pp. 549–557.

[32] Edward F. Rocnik et al. "The Novel SPARC Family Member SMOC-2 Potentiates Angiogenic Growth Factor Activity." In: *Journal of Biological Chemistry* 281.32 (Aug. 2006), pp. 22855–22864.

[33] Charles L. Bevins and Nita H. Salzman. "Paneth cells, antimicrobial peptides and maintenance of intestinal homeostasis." In: *Nature Reviews Microbiology 2011 9:5* 9.5 (Mar. 2011), pp. 356–368.

[34] Toshiro Sato et al. "Paneth cells constitute the niche for Lgr5 stem cells in intestinal crypts." In: *Nature* 469.7330 (Jan. 2011), p. 415.

[35] Brian F. Hinnebusch et al. "Enterocyte differentiation marker intestinal alkaline phosphatase is a target gene of the gut-enriched Krüppel-like factor." In: *American Journal of Physiology - Gastrointestinal and Liver Physiology* 286.1 49-1 (2004).

[36] Shinya Bekku et al. "Carbonic anhydrase I and II as a differentiation marker of human and rat colonic enterocytes." In: *Research in Experimental Medicine 1998 198:4* 198.4 (May 2014), pp. 175–185.

[37] Qin Zhou et al. "Keratin 20 helps maintain intermediate filament organization in intestinal epithelia." In: *Molecular Biology of the Cell* 14.7 (July 2003), pp. 2959–2971.

[38] Susan E. Schonhoff, Maryann Giel-Moloney, and Andrew B. Leiter. "Minireview: Development and Differentiation of Gut Endocrine Cells." In: *Endocrinology* 145.6 (June 2004), pp. 2639–2644.

[39] Takahiro Nagatake et al. "Enteroendocrine Cells Are Specifically Marked by Cell Surface Expression of Claudin-4 in Mouse Small Intestine." In: *PLOS ONE* 9.3 (Mar. 2014), e90638.

[40] K. A. Roth, J. M. Hertz, and J. I. Gordon. "Mapping enteroendocrine cell populations in transgenic mice reveals an unexpected degree of complexity in cellular differentiation within the gastrointestinal tract." In: *Journal of Cell Biology* 110.5 (May 1990), pp. 1791–1801.

[41] W. M. Wong, R. Poulsom, and N. A. Wright. "Trefoil peptides." In: *Gut* 44.6 (June 1999), pp. 890–895.

[42] Luca Pastorelli et al. "Central role of the gut epithelial barrier in the pathogenesis of chronic intestinal inflammation: Lessons learned from animal models and human genetics." In: *Frontiers in Immunology* 4.SEP (2013), p. 280.

[43] Malin E.V. Johansson, Henrik Sjövall, and Gunnar C. Hansson. "The gastrointestinal mucus system in health and disease." In: *Nature Reviews Gastroenterology & Hepatology 2013 10:6* 10.6 (Mar. 2013), pp. 352–361.

[44] Eugene D Weinberg. "Human lactoferrin: a novel therapeutic with broad spectrum potential." In: *Journal of Pharmacy and Pharmacology* 53.10 (Feb. 2010), pp. 1303–1310.

[45] Lena Antoni et al. "Human colonic mucus is a reservoir for antimicrobial peptides." In: *Journal of Crohn's and Colitis* 7.12 (Dec. 2013), e652–e664.

[46] Gerhard Rogler. "Resolution of inflammation in inflammatory bowel disease." In: *The Lancet Gastroenterology & Hepatology* 2.7 (July 2017), pp. 521–530.

[47] Takuya Suzuki. "Regulation of intestinal epithelial permeability by tight junctions." In: *Cellular and Molecular Life Sciences 2012 70:4* 70.4 (July 2012), pp. 631–659.

[48] Matthew A. Odenwald and Jerrold R. Turner. "The intestinal epithelial barrier: a therapeutic target?" In: *Nature Reviews Gastroenterology & Hepatology 2016 14:1* 14.1 (Nov. 2016), pp. 9–21.

[49] M. Furuse et al. "Occludin: a novel integral membrane protein localizing at tight junctions." In: *Journal of Cell Biology* 123.6 (Dec. 1993), pp. 1777–1788.

[50] Matthias Bruewer et al. "Proinflammatory Cytokines Disrupt Epithelial Barrier Function by Apoptosis-Independent Mechanisms." In: *The Journal of Immunology* 171.11 (Dec. 2003), pp. 6164–6172.

[51] Matthias Bruewer et al. "Interferon-γ induces internalization of epithelial tight junction proteins via a macropinocytosis-like process." In: *The FASEB Journal* 19.8 (June 2005), pp. 923–933.

[52] Takuya Suzuki, Naho Yoshinaga, and Soichi Tanabe. "Interleukin-6 (IL-6) regulates claudin-2 expression and tight junction permeability in intestinal epithelium." In: *Journal of Biological Chemistry* 286.36 (Sept. 2011), pp. 31263–31271.

[53] Linette E.M. Willemsen et al. "Polyunsaturated fatty acids support epithelial barrier integrity and reduce IL-4 mediated permeability in vitro." In: *European Journal of Nutrition* 47.4 (June 2008), pp. 183–191.

[54] Andreas Fischer et al. "Glucocorticoids regulate barrier function and claudin expression in intestinal epithelial cells via MKP-1." In: *American Journal of Physiology - Gastrointestinal and Liver Physiology* 306.3 (Feb. 2014), pp. 218–228.

[55] Karen L Madsen et al. "Interleukin-10 gene-deficient mice develop a primary intestinal permeability defect in response to enteric microflora." In: *Inflammatory bowel diseases* 5.4 (1999), pp. 262–270.

[56] Daniel R. Clayburgh, Le Shen, and Jerrold R. Turner. "A porous defense: the leaky epithelial barrier in intestinal disease." In: *Laboratory Investigation 2004 84:3* 84.3 (Jan. 2004), pp. 282–291.

[57] Karen L. Edelblum et al. "Dynamic migration of $\gamma\delta$ intraepithelial lymphocytes requires occludin." In: *Proceedings of the National Academy of Sciences of the United States of America* 109.18 (May 2012), pp. 7097–7102.

[58] M. Sun et al. "Regulatory immune cells in regulation of intestinal inflammatory response to microbiota." In: *Mucosal Immunology 2015 8:5* 8.5 (June 2015), pp. 969–978.

[59] Sarah L. Pull et al. "Activated macrophages are an adaptive element of the colonic epithelial progenitor niche necessary for regenerative responses to injury." In: *Proceedings of the National Academy of Sciences* 102.1 (Jan. 2005), pp. 99–104.

[60] Maria Rescigno et al. "Dendritic cells express tight junction proteins and penetrate gut epithelial monolayers to sample bacteria." In: *Nature Immunology 2001 2:4* 2.4 (Apr. 2001), pp. 361–367.

[61] Marcello Chieppa et al. "Dynamic imaging of dendritic cell extension into the small bowel lumen in response to epithelial cell TLR engagement." In: *Journal of Experimental Medicine* 203.13 (Dec. 2006), pp. 2841–2852.

[62] Gary Nace et al. "Dendritic Cells and Damage-Associated Molecular Patterns: Endogenous Danger Signals Linking Innate and Adaptive Immunity." In: *Journal of Innate Immunity* 4.1 (Dec. 2012), pp. 6–15.

[63] Francesca A.R. Silva et al. "The Immunological Basis of Inflammatory Bowel Disease." In: *Gastroenterology Research and Practice* 2016 (2016).

[64] Pieranna Fietta and Giovanni Delsante. "The effector T helper cell triade." In: *Biology Forum/Rivista di Biologia*. Vol. 102. 1. 2009.

[65] S. Al-Haddad and R. H. Riddell. "The role of eosinophils in inflammatory bowel disease." In: *Gut* 54.12 (Dec. 2005), pp. 1674–1675.

[66] John R. Grainger et al. "Inflammatory monocytes regulate pathologic responses to commensals during acute gastrointestinal infection." In: *Nature Medicine 2013 19:6* 19.6 (May 2013), pp. 713–721.

[67] L. J. Hall et al. "Natural killer cells protect mice from DSS-induced colitis by regulating neutrophil function via the NKG2A receptor." In: *Mucosal Immunology 2013 6:5* 6.5 (Jan. 2013), pp. 1016–1026.

[68] Andrés Vazquez-Terres et al. "Extraintestinal dissemination of Salmonella by CD18-expressing phagocytes." In: *Nature 1999 401:6755* 401.6755 (Oct. 1999), pp. 804–808.

[69] Birte Steiniger, Michael Bette, and Hans Schwarzbach. "The open microcirculation in human spleens: A three-dimensional approach." In: *Journal of Histochemistry and Cytochemistry* 59.6 (Apr. 2011), pp. 639–648.

[70] Vincenzo Bronte and Mikael J. Pittet. "The Spleen in Local and Systemic Regulation of Immunity." In: *Immunity* 39.5 (Nov. 2013), pp. 806–818.

[71] Andreas Schlitzer et al. "Identification of cDC1- and cDC2-committed DC progenitors reveals early lineage priming at the common DC progenitor stage in the bone marrow." In: *Nature Immunology 2015 16:7* 16.7 (June 2015), pp. 718–728.

[72] Miriam Merad et al. "The Dendritic Cell Lineage: Ontogeny and Function of Dendritic Cells and Their Subsets in the Steady State and the Inflamed Setting." In: *http://dx.doi.org/10.1146/annurev-immunol-020711-074950* 31 (Mar. 2013), pp. 563–604.

[73] Vivek Durai and Kenneth M. Murphy. "Functions of Murine Dendritic Cells." In: *Immunity* 45.4 (Oct. 2016), pp. 719–736.

[74] Nuruddeen D. Lewis et al. "Circulating Monocytes Are Reduced by Sphingosine-1-Phosphate Receptor Modulators Independently of S1P3." In: *The Journal of Immunology* 190.7 (Apr. 2013), pp. 3533–3540.

[75] Niklas Czeloth et al. "Sphingosine-1-Phosphate Mediates Migration of Mature Dendritic Cells." In: *The Journal of Immunology* 175.5 (Sept. 2005), pp. 2960–2967.

[76] Susan R. Schwab and Jason G. Cyster. "Finding a way out: lymphocyte egress from lymphoid organs." In: *Nature Immunology 2007 8:12* 8.12 (Nov. 2007), pp. 1295–1301.

[77] Paola Italiani and Diana Boraschi. *From monocytes to M1/M2 macrophages: Phenotypical vs. functional differentiation*. 2014.

[78] Deepak Mittal et al. "New insights into cancer immunoediting and its three component phases — elimination, equilibrium and escape." In: *Current Opinion in Immunology* 27.1 (Apr. 2014), pp. 16–25.

[79] Gavin P. Dunn, Catherine M. Koebel, and Robert D. Schreiber. "Interferons, immunity and cancer immunoediting." In: *Nature Reviews Immunology 2006 6:11* 6.11 (Nov. 2006), pp. 836–848.

[80] Vijay Shankaran et al. "IFNγ and lymphocytes prevent primary tumour development and shape tumour immunogenicity." In: *Nature 2001 410:6832* 410.6832 (Apr. 2001), pp. 1107–1111.

[81] Gavin P. Dunn et al. "Cancer immunoediting: from immunosurveillance to tumor escape." In: *Nature Immunology 2002 3:11* 3.11 (2002), pp. 991–998.

[82] Brian F. Zamarron and Wanjun Chen. "Dual roles of immune cells and their factors in cancer development and progression." In: *International Journal of Biological Sciences* 7.5 (2011), pp. 651–658.

[83] Michele W.L. Teng et al. "Opposing roles for IL-23 and IL-12 in maintaining occult cancer in an equilibrium state." In: *Cancer Research* 72.16 (Aug. 2012), pp. 3987–3996.

[84] Tyler J. Curiel. "Tregs and rethinking cancer immunotherapy." In: *The Journal of Clinical Investigation* 117.5 (May 2007), pp. 1167–1174.

[85] Maria A. Curotto de Lafaille and Juan J. Lafaille. "Natural and Adaptive Foxp3+ Regulatory T Cells: More of the Same or a Division of Labor?" In: *Immunity* 30.5 (May 2009), pp. 626–635.

[86] Stefanie R. Bailey et al. *Th17 cells in cancer: The ultimate identity crisis*. 2014.

[87] Muneo Numasaki et al. "Interleukin-17 promotes angiogenesis and tumor growth." In: *Blood* 101.7 (Apr. 2003), pp. 2620–2627.

[88] Andrea Facciabene et al. "Tumour hypoxia promotes tolerance and angiogenesis via CCL28 and Treg cells." In: *Nature 2011 475:7355* 475.7355 (July 2011), pp. 226–230.

[89] Ralph J. DeBerardinis et al. "The Biology of Cancer: Metabolic Reprogramming Fuels Cell Growth and Proliferation." In: *Cell Metabolism* 7.1 (Jan. 2008), pp. 11–20.

[90] Michael I. Koukourakis et al. "Comparison of Metabolic Pathways between Cancer Cells and Stromal Cells in Colorectal Carcinomas: a Metabolic Survival Role for Tumor-Associated Stroma." In: *Cancer Research* 66.2 (Jan. 2006), pp. 632–637.

[91] Andrew P. Halestrap and Marieangela C. Wilson. "The monocarboxylate transporter family—Role and regulation." In: *IUBMB Life* 64.2 (Feb. 2012), pp. 109–119.

[92] Nihed Draoui and Olivier Feron. "Lactate shuttles at a glance: from physiological paradigms to anti-cancer treatments." In: *Disease Models & Mechanisms* 4.6 (Nov. 2011), pp. 727–732.

[93] Nissim Hay. "Reprogramming glucose metabolism in cancer: can it be exploited for cancer therapy?" In: *Nature Reviews Cancer 2016 16:10* 16.10 (Sept. 2016), pp. 635–649.

[94] Krushna C. Patra and Nissim Hay. "The pentose phosphate pathway and cancer." In: *Trends in Biochemical Sciences* 39.8 (Aug. 2014), pp. 347–354.

[95] Marta Anna Kowalik, Amedeo Columbano, and Andrea Perra. *Emerging role of the pentose phosphate pathway in hepatocellular carcinoma*. May 2017.

[96] Sidney Weinhouse et al. "On respiratory impairment in cancer cells." In: *Science* 124.3215 (Aug. 1956), pp. 267–272.

[97] Rafael Moreno-Sánchez et al. "Energy metabolism in tumor cells." In: *The FEBS Journal* 274.6 (Mar. 2007), pp. 1393–1418.

[98] Barbara Muz et al. "The role of hypoxia in cancer progression, angiogenesis, metastasis, and resistance to therapy." In: *Hypoxia* 3 (Dec. 2015), pp. 83–92.

[99] Gregg L Semenza and Guang L Wang. "A nuclear factor induced by hypoxia via de novo protein synthesis binds to the human erythropoietin gene enhancer at a site required for transcriptional activation." In: *Molecular and Cellular Biology* 12.12 (Dec. 1992), pp. 5447–5454.

[100] Eric Metzen et al. "Regulation of the prolyl hydroxylase domain protein 2 (phd2/egln-1) gene: identification of a functional hypoxia-responsive element." In: *Biochemical Journal* 387.3 (May 2005), pp. 711–717.

[101] Nuria Pescador et al. "Identification of a functional hypoxia-responsive element that regulates the expression of the egl nine homologue 3 (egln3/phd3) gene." In: *Biochemical Journal* 390.1 (Aug. 2005), pp. 189–197.

[102] G. H. Fong and K. Takeda. "Role and regulation of prolyl hydroxylase domain proteins." In: *Cell Death & Differentiation 2008 15:4* 15.4 (Feb. 2008), pp. 635–641.

[103] Edurne Berra et al. "HIF prolyl-hydroxylase 2 is the key oxygen sensor setting low steady-state levels of HIF-1α in normoxia." In: *The EMBO Journal* 22.16 (Aug. 2003), pp. 4082–4090.

[104] Christopher J. Schofield and Peter J. Ratcliffe. "Signalling hypoxia by HIF hydroxylases." In: *Biochemical and Biophysical Research Communications* 338.1 (Dec. 2005), pp. 617–626.

[105] Eoin P. Cummins and Cormac T. Taylor. *Hypoxia-responsive transcription factors*. Sept. 2005.

[106] Veronica L. Dengler, Matthew D. Galbraith, and Joaquín M. Espinosa. *Transcriptional regulation by hypoxia inducible factors*. Jan. 2014.

[107] Cheng-Jun Hu et al. "Differential Roles of Hypoxia-Inducible Factor 1α (HIF-1α) and HIF-2α in Hypoxic Gene Regulation." In: *Molecular and Cellular Biology* 23.24 (Dec. 2003), pp. 9361–9374.

[108] Gregg L. Semenza. "Hypoxia-Inducible Factors in Physiology and Medicine." In: *Cell* 148.3 (Feb. 2012), pp. 399–408.

[109] Dominik C. Fuhrmann and Bernhard Brüne. *Mitochondrial composition and function under the control of hypoxia*. Aug. 2017.

[110] Benedikt Westermann. "Mitochondrial fusion and fission in cell life and death." In: *Nature Reviews Molecular Cell Biology 2010 11:12* 11.12 (Nov. 2010), pp. 872–884.

[111] Hyungsoo Kim et al. "Fine-Tuning of Drp1/Fis1 Availability by AKAP121/Siah2 Regulates Mitochondrial Adaptation to Hypoxia." In: *Molecular Cell* 44.4 (Nov. 2011), pp. 532–544.

[112] Dominic I. James et al. "hFis1, a novel component of the mammalian mitochondrial fission machinery." In: *Journal of Biological Chemistry* 278.38 (Sept. 2003), pp. 36373–36379.

[113] Yisang Yoon et al. "The Mitochondrial Protein hFis1 Regulates Mitochondrial Fission in Mammalian Cells through an Interaction with the Dynamin-Like Protein DLP1." In: *Molecular and Cellular Biology* 23.15 (Aug. 2003), pp. 5409–5420.

[114] Le Chen et al. "Mitochondrial OPA1, apoptosis, and heart failure." In: *Cardiovascular Research* 84.1 (Oct. 2009), pp. 91–99.

[115] Scott A. Detmer and David C. Chan. "Functions and dysfunctions of mitochondrial dynamics." In: *Nature Reviews Molecular Cell Biology 2007 8:11* 8.11 (Nov. 2007), pp. 870–879.

[116] Derek P. Narendra et al. "PINK1 Is Selectively Stabilized on Impaired Mitochondria to Activate Parkin." In: *PLOS Biology* 8.1 (Jan. 2010), e1000298.

[117] Alicia M. Pickrell and Richard J. Youle. "The Roles of PINK1, Parkin, and Mitochondrial Fidelity in Parkinson's Disease." In: *Neuron* 85.2 (Jan. 2015), pp. 257–273.

[118] Atsushi Tanaka et al. "Proteasome and p97 mediate mitophagy and degradation of mitofusins induced by Parkin." In: *Journal of Cell Biology* 191.7 (Dec. 2010), pp. 1367–1380.

[119] Matthew E. Gegg et al. "Mitofusin 1 and mitofusin 2 are ubiquitinated in a PINK1/parkin-dependent manner upon induction of mitophagy." In: *Human Molecular Genetics* 19.24 (Dec. 2010), pp. 4861–4870.

[120] Lori Buhlman et al. "Functional interplay between Parkin and Drp1 in mitochondrial fission and clearance." In: *Biochimica et Biophysica Acta (BBA) - Molecular Cell Research* 1843.9 (Sept. 2014), pp. 2012–2026.

[121] Gian Luca McLelland et al. "Parkin and PINK1 function in a vesicular trafficking pathway regulating mitochondrial quality control." In: *The EMBO Journal* 33.4 (Feb. 2014), pp. 282–295.

[122] Vincent Soubannier et al. "A Vesicular Transport Pathway Shuttles Cargo from Mitochondria to Lysosomes." In: *Current Biology* 22.2 (Jan. 2012), pp. 135–141.

[123] Agnieszka Chacinska et al. "Importing Mitochondrial Proteins: Machineries and Mechanisms." In: *Cell* 138.4 (Aug. 2009), pp. 628–644.

[124] Sarah T Pruett et al. "Thematic Review Series: Sphingolipids. Biodiversity of sphingoid bases ("sphingosines") and related amino alcohols *." In: *Journal of Lipid Research* 49.8 (Aug. 2008), pp. 1621–1639.

[125] Yusuf A. Hannun and Lina M. Obeid. "Principles of bioactive lipid signalling: lessons from sphingolipids." In: *Nature Reviews Molecular Cell Biology 2008 9:2* 9.2 (Feb. 2008), pp. 139–150.

[126] Alfred H. Merrill. "Sphingolipid and Glycosphingolipid Metabolic Pathways in the Era of Sphingolipidomics." In: *Chemical Reviews* 111.10 (Oct. 2011), pp. 6387–6422.

[127] Christopher R. Gault, Lina M. Obeid, and Yusuf A. Hannun. *An overview of sphingolipid metabolism: From synthesis to breakdown*. 2010.

[128] Michael E. Breimer et al. "Glycosphingolipid composition of epithelial cells isolated along the villus axis of small intestine of a single human individual." In: *Glycobiology* 22.12 (Dec. 2012), pp. 1721–1730.

[129] Kentaro Hanada. *Serine palmitoyltransferase, a key enzyme of sphingolipid metabolism*. June 2003.

[130] Alfred H. Merrill and D. Deborah Jones. "An update of the enzymology and regulation of sphingomyelin metabolism." In: *Biochimica et Biophysica Acta (BBA) - Lipids and Lipid Metabolism* 1044.1 (May 1990), pp. 1–12.

[131] Christoph Michel et al. "Characterization of Ceramide Synthesis: A Dihydroceramide Desaturase Introduces the 4,5-Trans-Double Bond of Sphingosine at the Level of Dihydroceramide." In: *Journal of Biological Chemistry* 272.36 (Sept. 1997), pp. 22432–22437.

[132] Toshiyuki Yamaji and Kentaro Hanada. *Sphingolipid Metabolism and Interorganellar Transport: Localization of Sphingolipid Enzymes and Lipid Transfer Proteins*. Feb. 2015.

[133] Kay Hofmann et al. "Cloning and characterization of the mammalian brain-specific, Mg2+-dependent neutral sphingomyelinase." In: *Proceedings of the National Academy of Sciences* 97.11 (May 2000), pp. 5895–5900.

[134] Fikadu Geta Tafesse et al. "Both Sphingomyelin Synthases SMS1 and SMS2 Are Required for Sphingomyelin Homeostasis and Growth in Human HeLa Cells." In: *Journal of Biological Chemistry* 282.24 (June 2007), pp. 17537–17547.

[135] Kazuyuki Kitatani, Jolanta Idkowiak-Baldys, and Yusuf A. Hannun. "The sphingolipid salvage pathway in ceramide metabolism and signaling." In: *Cellular Signalling* 20.6 (June 2008), pp. 1010–1018.

[136] Sabine Grösch, Alice V Alessenko, and Elisabetta Albi. "The Many Facets of Sphingolipids in the Specific Phases of Acute Inflammatory Response." In: (2018).

[137] Takafumi Kohama et al. "Molecular Cloning and Functional Characterization of Murine Sphingosine Kinase." In: *Journal of Biological Chemistry* 273.37 (Sept. 1998), pp. 23722–23728.

[138] Wilhelm Stoffel, Dac Lekim, and Guido Sticht. "Distribution and Properties of Dihydrosphingosine-1-phosphate Aldolase (Sphinganine-1-phosphate alkanal-lyase)." In: *Hoppe-Seyler's Zeitschrift fur Physiologische Chemie* 350.2 (Jan. 1969), pp. 1233–1241.

[139] Jianhui Zhou and Julie D. Saba. "Identification of the First Mammalian Sphingosine Phosphate Lyase Gene and Its Functional Expression in Yeast." In: *Biochemical and Biophysical Research Communications* 242.3 (Jan. 1998), pp. 502–507.

[140] Florence Bourquin, Guido Capitani, and Markus Gerhard Grütter. *PLP-dependent enzymes as entry and exit gates of sphingolipid metabolism*. Sept. 2011.

[141] Thomas D. Mullen, Yusuf A. Hannun, and Lina M. Obeid. "Ceramide synthases at the centre of sphingolipid metabolism and biology." In: *Biochemical Journal* 441.3 (Feb. 2012), pp. 789–802.

[142] Elad L. Laviad et al. "Characterization of Ceramide Synthase 2: Tissue Distribution, Substrate Specificity, and Inhibition by Sphingosine 1-Phosphate." In: *Journal of Biological Chemistry* 283.9 (Feb. 2008), pp. 5677–5684.

[143] Susanne Schiffmann et al. "Ceramide metabolism in mouse tissue." In: *International Journal of Biochemistry and Cell Biology* 45.8 (2013), pp. 1886–1894.

[144] Yukiko Mizutani, Akio Kihara, and Yasuyuki Igarashi. "LASS3 (longevity assurance homologue 3) is a mainly testis-specific (dihydro)ceramide synthase with relatively broad substrate specificity." In: *Biochemical Journal* 398.3 (Sept. 2006), pp. 531–538.

[145] Richard Jennemann et al. "Loss of ceramide synthase 3 causes lethal skin barrier disruption." In: *Human Molecular Genetics* 21.3 (Feb. 2012), pp. 586–608.

[146] Mariona Rabionet, Karin Gorgas, and Roger Sandhoff. "Ceramide synthesis in the epidermis." In: *Biochimica et Biophysica Acta (BBA) - Molecular and Cell Biology of Lipids* 1841.3 (Mar. 2014), pp. 422–434.

[147] Takayuki Sassa, Taisuke Hirayama, and Akio Kihara. "Enzyme Activities of the Ceramide Synthases CERS2–6 Are Regulated by Phosphorylation in the C-terminal Region." In: *Journal of Biological Chemistry* 291.14 (Apr. 2016), pp. 7477–7487.

[148] Elad L. Laviad et al. "Modulation of Ceramide Synthase Activity via Dimerization." In: *Journal of Biological Chemistry* 287.25 (June 2012), pp. 21025–21033.

[149] Daniela Hartmann et al. "The equilibrium between long and very long chain ceramides is important for the fate of the cell and can be influenced by co-expression of CerS." In: *The International Journal of Biochemistry & Cell Biology* 45.7 (July 2013), pp. 1195–1203.

[150] Sandra N. Pinto et al. "Effect of ceramide structure on membrane biophysical properties: The role of acyl chain length and unsaturation." In: *Biochimica et Biophysica Acta (BBA) - Biomembranes* 1808.11 (Nov. 2011), pp. 2753–2760.

[151] Mikko Karttunen et al. "Lipid domain morphologies in phosphatidylcholine-ceramide monolayers." In: *Langmuir* 25.8 (Apr. 2009), pp. 4595–4600.

[152] Heike Grassmé, Joachim Riethmüller, and Erich Gulbins. *Biological aspects of ceramide-enriched membrane domains*. May 2007.

[153] Yang Zhang et al. "Ceramide-enriched membrane domains—Structure and function." In: *Biochimica et Biophysica Acta (BBA) - Biomembranes* 1788.1 (Jan. 2009), pp. 178–183.

[154] Michael Heinrich et al. "Cathepsin D targeted by acid sphingomyelinase-derived ceramide." In: *The EMBO Journal* 18.19 (Oct. 1999), pp. 5252–5263.

[155] Yuhua Zhang et al. "Kinase Suppressor of Ras Is Ceramide-Activated Protein Kinase." In: *Cell* 89.1 (Apr. 1997), pp. 63–72.

[156] Andrea Huwiler et al. "Ceramide binds to the CaLB domain of cytosolic phospholipase A2 and facilitates its membrane docking and arachidonic acid release." In: *The FASEB Journal* 15.1 (Jan. 2001), pp. 7–9.

[157] Gertraud Müller et al. "PKC ζ is a molecular switch in signal transduction of TNF-α, bifunctionally regulated by ceramide and arachidonic acid." In: *EMBO Journal* 14.9 (1995), pp. 1961–1969.

[158] Kazuyuki Kitatani et al. "Protein Kinase C-induced Activation of a Ceramide/Protein Phosphatase 1 Pathway Leading to Dephosphorylation of p38 MAPK." In: *Journal of Biological Chemistry* 281.48 (Dec. 2006), pp. 36793–36802.

[159] Hailong Fu et al. *The emerging roles of exosomes in tumor–stroma interaction*. Sept. 2016.

[160] Clotilde Théry, Matias Ostrowski, and Elodie Segura. "Membrane vesicles as conveyors of immune responses." In: *Nature Reviews Immunology 2009 9:8* 9.8 (June 2009), pp. 581–593.

[161] Katarina Trajkovic et al. "Ceramide triggers budding of exosome vesicles into multivesicular endosomes." In: *Science* 319.5867 (Feb. 2008), pp. 1244–1247.

[162] Yael Pewzner-Jung, Shifra Ben-Dor, and Anthony H. Futerman. "When Do Lasses (Longevity Assurance Genes) Become CerS (Ceramide Synthases)?: INSIGHTS INTO THE REGULATION OF CERAMIDE SYNTHESIS *." In: *Journal of Biological Chemistry* 281.35 (Sept. 2006), pp. 25001–25005.

[163] Richard J. Hodes, Anna M. McCormick, and Marcia Pruzan. "Longevity Assurance Genes: How Do They Influence Aging and Life Span?" In: *Journal of the American Geriatrics Society* 44.8 (Aug. 1996), pp. 988–991.

[164] Björn Schumacher et al. "Delayed and Accelerated Aging Share Common Longevity Assurance Mechanisms." In: *PLOS Genetics* 4.8 (Aug. 2008), e1000161.

[165] Besim Ogretmen and Yusuf A. Hannun. "Biologically active sphingolipids in cancer pathogenesis and treatment." In: *Nature Reviews Cancer 2004 4:8* 4.8 (2004), pp. 604–616.

[166] Sabine Grösch, Susanne Schiffmann, and Gerd Geisslinger. "Chain length-specific properties of ceramides." In: *Progress in Lipid Research* 51.1 (Jan. 2012), pp. 50–62.

[167] Heike Grassmé, Heinz Schwarz, and Erich Gulbins. "Molecular mechanisms of ceramide-mediated CD95 clustering." In: *Biochemical and Biophysical Research Communications* 284.4 (June 2001), pp. 1016–1030.

[168] L. J. Siskind and M. Colombini. "The Lipids C2- and C16-Ceramide Form Large Stable Channels: Implications For Apoptosis." In: *Journal of Biological Chemistry* 275.49 (Dec. 2000), pp. 38640–38644.

[169] Leah J. Siskind, Richard N. Kolesnick, and Marco Colombini. "Ceramide Channels Increase the Permeability of the Mitochondrial Outer Membrane to Small Proteins." In: *Journal of Biological Chemistry* 277.30 (July 2002), pp. 26796–26803.

[170] Hamid Kashkar et al. "Acid Sphingomyelinase Is Indispensable for UV Light-induced Bax Conformational Change at the Mitochondrial Membrane." In: *Journal of Biological Chemistry* 280.21 (May 2005), pp. 20804–20813.

[171] Wenjing Zheng et al. *Ceramides and other bioactive sphingolipid backbones in health and disease: Lipidomic analysis, metabolism and roles in membrane structure, dynamics, signaling and autophagy*. Dec. 2006.

[172] R. David Sentelle et al. "Ceramide targets autophagosomes to mitochondria and induces lethal mitophagy." In: *Nature Chemical Biology 2012 8:10* 8.10 (Aug. 2012), pp. 831–838.

[173] Mototeru Yamane, Shota Moriya, and Hiroko Kokuba. "Visualization of ceramide channels in lysosomes following endogenous palmitoyl-ceramide accumulation as an initial step in the induction of necrosis." In: *Biochemistry and Biophysics Reports* 11 (Sept. 2017), pp. 174–181.

[174] Laura R Parisi, Nasi Li, and G. Ekin Atilla-Gokcumen. "Very Long Chain Fatty Acids Are Functionally Involved in Necroptosis." In: *Cell Chemical Biology* 24.12 (2017), 1445–1454.e8.

[175] Archana Mukhopadhyay et al. "Direct interaction between the inhibitor 2 and ceramide via sphingolipid-protein binding is involved in the regulation of protein phosphatase 2A activity and signaling." In: *The FASEB Journal* 23.3 (Mar. 2009).

[176] Mark A. Gregory, Ying Qi, and Stephen R. Hann. "Phosphorylation by Glycogen Synthase Kinase-3 Controls c-Myc Proteolysis and Subnuclear Localization." In: *Journal of Biological Chemistry* 278.51 (Dec. 2003), pp. 51606–51612.

[177] M. Caspi et al. "Nuclear GSK-3β inhibits the canonical Wnt signalling pathway in a β-catenin phosphorylation-independent manner." In: *Oncogene 2008 27:25* 27.25 (Jan. 2008), pp. 3546–3555.

[178] Veerle Janssens and Jozef Goris. "Protein phosphatase 2A : a highly regulated family of serine/threonine phosphatases implicated in cell growth and signalling." In: *Biochem. J* 353 (2001), pp. 417–439.

[179] Amin Rustom et al. "Nanotubular Highways for Intercellular Organelle Transport." In: *Science* 303.5660 (Feb. 2004), pp. 1007–1010.

[180] Daniela Hartmann et al. "Long chain ceramides and very long chain ceramides have opposite effects on human breast and colon cancer cell growth." In: *The International Journal of Biochemistry & Cell Biology* 44.4 (Apr. 2012), pp. 620–628.

[181] Rui Dong Duan and Åke Nilsson. "Metabolism of sphingolipids in the gut and its relation to inflammation and cancer development." In: *Progress in Lipid Research* 48.1 (Jan. 2009), pp. 62–72.

[182] Jean Francois Bouhours and Robert M. Glickman. "Rat intestinal glycolipids: II. Distribution and biosynthesis of glycolipids and ceramide in villus and crypt cells." In: *Biochimica et Biophysica Acta (BBA) - Lipids and Lipid Metabolism* 441.1 (July 1976), pp. 123–133.

[183] Michael E. Breimer et al. "Glycosphingolipids and the differentiation of intestinal epithelium." In: *Experimental Cell Research* 135.1 (Sept. 1981), pp. 1–13.

[184] J. F. Bouhours and H. Guignard. "Free ceramide, sphingomyelin, and glucosylceramide of isolated rat intestinal cells." In: *Journal of Lipid Research* 20.7 (Sept. 1979), pp. 897–907.

[185] Michael E. Breimer et al. "Studies on differentiating epithelial cells of rat small intestine: alterations in the lipophilic part of glycosphingolipids during cell migration from crypt to villus tip." In: *Biochimica et Biophysica Acta (BBA)-Lipids and Lipid Metabolism* 710.3 (Mar. 1982), pp. 415–427.

[186] Anders Kalén, Roy A. Borchardt, and Robert M. Bell. "Elevated ceramide levels in GH4C1 cells treated with retinoic acid." In: *Biochimica et Biophysica Acta (BBA) - Lipids and Lipid Metabolism* 1125.1 (Apr. 1992), pp. 90–96.

[187] T. R. Breitman, S. E. Selonick, and S. J. Collins. "Induction of differentiation of the human promyelocytic leukemia cell line (HL-60) by retinoic acid." In: *Proceedings of the National Academy of Sciences* 77.5 (May 1980), pp. 2936–2940.

[188] Marthe Susanna Wegner et al. "Ceramide synthases CerS4 and CerS5 are upregulated by 17β-estradiol and GPER1 via AP-1 in human breast cancer cells." In: *Biochemical Pharmacology* 92.4 (Dec. 2014), pp. 577–589.

[189] Stephanie Oertel et al. "Ceramide synthase 2 deficiency aggravates AOM-DSS-induced colitis in mice: role of colon barrier integrity." In: *Cellular and Molecular Life Sciences* 74.16 (2017), pp. 3039–3055.

[190] Ye-Ryung Kim et al. "Ablation of ceramide synthase 2 exacerbates dextran sodium sulphate-induced colitis in mice due to increased intestinal permeability." In: *Journal of Cellular and Molecular Medicine* 21.12 (Dec. 2017), pp. 3565–3578.

[191] Jacque N. Wilk, Janine Bilsborough, and Joanne L. Viney. "The mdr1a−/− mouse model of spontaneous colitis." In: *Immunologic Research 2005 31:2* 31.2 (2005), pp. 151–159.

[192] Min Hee Kim et al. "Hepatic inflammatory cytokine production can be regulated by modulating sphingomyelinase and ceramide synthase 6." In: *International journal of molecular medicine* 39.2 (Feb. 2017), pp. 453–462.

[193] Max Eberle et al. "Exacerbation of experimental autoimmune encephalomyelitis in ceramide synthase 6 knockout mice is associated with enhanced activation/migration of neutrophils." In: *Immunology and Cell Biology* 93.9 (Oct. 2015), pp. 825–836.

[194] Kacee Sims et al. "Kdo2-Lipid A, a TLR4-specific Agonist, Induces de Novo Sphingolipid Biosynthesis in RAW264.7 Macrophages, Which Is Essential for Induction of Autophagy." In: *Journal of Biological Chemistry* 285.49 (Dec. 2010), pp. 38568–38579.

[195] Sun-Young Chang et al. "Colonic Patches Direct the Cross-Talk Between Systemic Compartments and Large Intestine Independently of Innate Immunity." In: *The Journal of Immunology* 180.3 (Feb. 2008), pp. 1609–1618.

[196] M. Hanief Sofi et al. "Ceramide synthesis regulates T cell activity and GVHD development." In: *JCI Insight* 2.10 (May 2017).

[197] Markus Selzner et al. "Induction of apoptotic cell death and prevention of tumor growth by ceramide analogues in metastatic human colon cancer." In: *Cancer research* 61.3 (2001), pp. 1233–1240.

[198] T. E. Merchant et al. "Phospholipid profiles of human colon cancer using 31P magnetic resonance spectroscopy." In: *International Journal of Colorectal Disease 1991 6:2* 6.2 (May 1991), pp. 121–126.

[199] Erik Hertervig et al. "Alkaline sphingomyelinase activity is decreased in human colorectal carcinoma." In: *Cancer: Interdisciplinary International Journal of the American Cancer Society* 79.3 (1997), pp. 448–453.

[200] E. Hertervig et al. "Familial adenomatous polyposis is associated with a marked decrease in alkaline sphingomyelinase activity: A key factor to the unrestrained cell proliferation?" In: *British Journal of Cancer 1999 81:2* 81.2 (Aug. 1999), pp. 232–236.

[201] Rodrigo Mora et al. "Sphingolipid rheostat alterations related to transformation can be exploited for specific induction of lysosomal cell death in murine and human glioma." In: *Glia* 58.11 (Aug. 2010), pp. 1364–1383.

[202] Rasheena Edmondson et al. *Three-dimensional cell culture systems and their applications in drug discovery and cell-based biosensors*. May 2014.

[203] Franziska Peters et al. "Ceramide synthase 4 regulates stem cell homeostasis and hair follicle cycling." In: *Journal of Investigative Dermatology* 135.6 (2015), pp. 1501–1509.

[204] Khadija El-Hindi et al. "T-Cell-Specific CerS4 Depletion Prolonged Inflammation and Enhanced Tumor Burden in the AOM/DSS-Induced CAC Model." In: *International Journal of Molecular Sciences 2022, Vol. 23, Page 1866* 23.3 (Feb. 2022), p. 1866.

[205] Philipp Ebel et al. "Ceramide synthase 4 deficiency in mice causes lipid alterations in sebum and results in alopecia." In: *Biochemical Journal* 461.1 (2014), pp. 147–158.

[206] Richard Latt, Eileen Macallum, and Warner-Lambert Canada Inc. "CCAC guidelines on: choosing an appropriate endpoint in experiments using animals for research, teaching and testing." In: (1998).

[207] Johannes Schindelin et al. "Fiji: an open-source platform for biological-image analysis." In: *Nature Methods 2012 9:7* 9.7 (June 2012), pp. 676–682.

[208] John K.C. Chan. "The wonderful colors of the hematoxylin-eosin stain in diagnostic surgical pathology." In: *International Journal of Surgical Pathology* 22.1 (Feb. 2014), pp. 12–32.

[209] D Ahmed et al. "Epigenetic and genetic features of 24 colon cancer cell lines." In: *Oncogenesis 2013 2:9* 2.9 (Sept. 2013), e71–e71.

[210] Jørgen Fogh and Germain Trempe. "New Human Tumor Cell Lines." In: *Human Tumor Cells in Vitro* (1975), pp. 115–159.

[211] E. Grasset, M. Pinto, and E. Dussaulx. "Epithelial properties of human colonic carcinoma cell line Caco-2: Electrical parameters." In: *American Journal of Physiology - Cell Physiology* 16.2 (1984).

[212] Frederic D. Sigoillot and Randall W. King. "Vigilance and validation: Keys to success in RNAi screening." In: *ACS Chemical Biology* 6.1 (Jan. 2011), pp. 47–60.

[213] Jarno Tuimala and Aleksi Kallio. "RNA-induced Silencing Complex (RISC)." In: *Encyclopedia of Systems Biology* (2013), pp. 1876–1876.

[214] Chris B. Moore et al. "Short Hairpin RNA (shRNA): Design, Delivery, and Assessment of Gene Knockdown." In: *Methods in molecular biology (Clifton, N.J.)* 629 (2010), pp. 139–156.

[215] Richard I. Gregory et al. "Human RISC Couples MicroRNA Biogenesis and Posttranscriptional Gene Silencing." In: *Cell* 123.4 (Nov. 2005), pp. 631–640.

[216] Terry L Riss et al. "Cell Viability Assays." In: *Assay Guidance Manual* (July 2016).

[217] Joachim Wegener et al. "Automated multi-well device to measure transepithelial electrical resistances under physiological conditions." In: *BioTechniques* 37.4 (June 2004), pp. 590–597.

[218] Jitesh D. Kawedia et al. "Interaction between transcellular and paracellular water transport pathways through Aquaporin 5 and the tight junction complex." In: *Proceedings of the National Academy of Sciences of the United States of America* 104.9 (Feb. 2007), pp. 3621–3626.

[219] Ansgar Hakvoort et al. "The Polarity of Choroid Plexus Epithelial Cells In Vitro Is Improved in Serum-Free Medium." In: *Journal of Neurochemistry* 71.3 (Sept. 1998), pp. 1141–1150.

[220] Khadija El-Hindi et al. "Ceramide synthase 5 deficiency aggravates dextran sodium sulfate-induced colitis and colon carcinogenesis and impairs T-cell activation." In: *Cancers* 12.7 (2020).

[221] Manuela Martins-Green, Melissa Petreaca, and Min Yao. "Chapter 8 An Assay System for In Vitro Detection of Permeability in Human "Endothelium"." In: *Methods in Enzymology* 443 (Jan. 2008), pp. 137–153.

[222] Y. Fu and Wei Xiao. "Study of Transcriptional Regulation Using a Reporter Gene Assay." In: *Methods in molecular biology (Clifton, N.J.)* 313 (2006), pp. 257–264.

[223] Marlene DeLuca and William D. McElroy. "Kinetics of the firefly luciferase catalyzed reactions." In: *Biochemistry* 13.5 (Feb. 2002), pp. 921–925.

[224] Matt Carter and Jennifer Shieh. "Biochemical Assays and Intracellular Signaling." In: *Guide to Research Techniques in Neuroscience*. Academic Press, Jan. 2015, pp. 311–343.

[225] Yi Jin et al. "Evaluating the MicroRNA Targeting Sites by Luciferase Reporter Gene Assay." In: *Methods in Molecular Biology* 936 (2013), pp. 117–127.

[226] John C. Matthews, Kazuo Hori, and Milton J. Cormier. "Purification and properties of Renilla reniformis luciferase." In: *Biochemistry* 16.1 (Jan. 2002), pp. 85–91.

[227] Aleksey G. Kazantsev and Leslie M. Thompson. "Therapeutic application of histone deacetylase inhibitors for central nervous system disorders." In: *Nature Reviews Drug Discovery 2008 7:10* 7.10 (2008), pp. 854–868.

[228] Tamara Vanhaecke et al. "Trichostatin A - like Hydroxamate Histone Deacetylase Inhibitors as Therapeutic Agents: Toxicological Point of View." In: *Current Medicinal Chemistry* 11.12 (Nov. 2012), pp. 1629–1643.

[229] Shoichi Date and Toshiro Sato. "Mini-Gut Organoids: Reconstitution of the Stem Cell Niche." In: *http://dx.doi.org/10.1146/annurev-cellbio-100814-125218* 31 (Nov. 2015), pp. 269–289.

[230] Kai Kretzschmar and Hans Clevers. "Organoids: Modeling Development and the Stem Cell Niche in a Dish." In: *Developmental Cell* 38.6 (Sept. 2016), pp. 590–600.

[231] Hynda K. Kleinman and George R. Martin. "Matrigel: Basement membrane matrix with biological activity." In: *Seminars in Cancer Biology* 15.5 (Oct. 2005), pp. 378–386.

[232] Steven M. Frisch et al. "Control of adhesion-dependent cell survival by focal adhesion kinase." In: *Journal of Cell Biology* 134.3 (Aug. 1996), pp. 793–799.

[233] Flavio Cimadamore et al. "Nicotinamide rescues human embryonic stem cell-derived neuroectoderm from parthanatic cell death." In: *Stem Cells* 27.8 (Aug. 2009), pp. 1772–1781.

[234] Masayoshi Tojo et al. "The ALK-5 inhibitor A-83-01 inhibits Smad signaling and epithelial-to-mesenchymal transition by transforming growth factor-β." In: *Cancer Science* 96.11 (Nov. 2005), pp. 791–800.

[235] Samir P. Patel et al. "N-acetylcysteine amide preserves mitochondrial bioenergetics and improves functional recovery following spinal trauma." In: *Experimental Neurology* 257 (July 2014), pp. 95–105.

[236] Toshiro Sato and Hans Clevers. "SnapShot: Growing Organoids from Stem Cells." In: *Cell* 161.7 (June 2015), 1700–1700.e1.

[237] Jill A. McMahon et al. "Noggin-mediated antagonism of BMP signaling is required for growth and patterning of the neural tube and somite." In: *Genes & Development* 12.10 (May 1998), p. 1438.

[238] Betsy Frantz et al. "The activation state of p38 mitogen-activated protein kinase determines the efficiency of ATP competition for pyridinylimidazole inhibitor binding." In: *Biochemistry* 37.39 (Sept. 1998), pp. 13846–13853.

[239] Shuh Narumiya, Toshimasa Ishizaki, and Masayoshi Uehata. "Use and properties of ROCK-specific inhibitor Y-27632." In: *Methods in Enzymology* 325 (Jan. 2000), pp. 273–284.

[240] W. W. Cleland. "Dithiothreitol, a New Protective Reagent for SH Groups." In: *Biochemistry* 3.4 (Apr. 1964), pp. 480–482.

[241] Marion M. Bradford. "A rapid and sensitive method for the quantitation of microgram quantities of protein utilizing the principle of protein-dye binding." In: *Analytical Biochemistry* 72.1-2 (May 1976), pp. 248–254.

[242] Christos D. Georgiou et al. "Mechanism of Coomassie brilliant blue G-250 binding to proteins: a hydrophobic assay for nanogram quantities of proteins." In: *Analytical and Bioanalytical Chemistry 2008 391:1* 391.1 (Mar. 2008), pp. 391–403.

[243] O. H. Lowry et al. "Protein Measurement with the Folin Phenol Reagent." In: *Journal of Biological Chemistry* 193.1 (Nov. 1951), pp. 265–275.

[244] Rene Rizzoli, T Vinzenz Von Tscharnert, and Herbert Fleisch. *Increase of adenylate cyclase catalytic-unit activity by dexamethasone in rat osteoblast-like cells*. Tech. rep. 1986, pp. 447–454.

[245] U. K. Laemmli. "Cleavage of Structural Proteins during the Assembly of the Head of Bacteriophage T4." In: *Nature 1970 227:5259* 227.5259 (1970), pp. 680–685.

[246] Samantha L. Eaton et al. "A Guide to Modern Quantitative Fluorescent Western Blotting with Troubleshooting Strategies." In: *JoVE (Journal of Visualized Experiments)* 93 (Nov. 2014), e52099.

[247] Werner Luttmann et al. "Der Experimentator: Immunologie." In: *Der Experimentator: Immunologie* (2014).

[248] E. G. Bligh and W. J. Dyer. "A rapid method of total lipid extraction and purification." In: *Canadian journal of biochemistry and physiology* 37.8 (1959), pp. 911–917.

[249] Ana Reis et al. "A comparison of five lipid extraction solvent systems for lipidomic studies of human LDL." In: *Journal of Lipid Research* 54.7 (July 2013), pp. 1812–1824.

[250] Anna Katharina Spohner et al. "Mouse Liver Compensates Loss of Sgpl1 by Secretion of Sphingolipids into Blood and Bile." In: *International Journal of Molecular Sciences 2021, Vol. 22, Page 10617* 22.19 (Sept. 2021), p. 10617.

[251] George M. Patton, Joan M. Fasulo, and Sander J. Robins. "Analysis of lipids by high performance liquid chromatography: Part I." In: *The Journal of Nutritional Biochemistry* 1.9 (Sept. 1990), pp. 493–500.

[252] Sebastian Brachtendorf et al. "Chemosensitivity of human colon cancer cells is influenced by a p53-dependent enhancement of ceramide synthase 5 and induction of autophagy." In: *Biochimica et Biophysica Acta (BBA) - Molecular and Cell Biology of Lipids* 1863.10 (Oct. 2018), pp. 1214–1227.

[253] Reinhold Penner and Erwin Neher. "The patch-damp technique in the study of secretion." In: *Trends in Neuroscience* 12.4 (1989), pp. 159–163.

[254] Karsten Lollike, Niels Borregaard, and Manfred Lindau. "The exocytotic fusion pore of small granules has a conductance similar to an ion channel." In: *Journal of Cell Biology* 129.1 (Apr. 1995), pp. 99–104.

[255] Lisanne Lutter et al. "The elusive case of human intraepithelial T cells in gut homeostasis and inflammation." In: *Nature Reviews Gastroenterology & Hepatology 2018 15:10* 15.10 (July 2018), pp. 637–649.

[256] E. V. Russler-Germain, S. Rengarajan, and C. S. Hsieh. "Antigen-specific regulatory T-cell responses to intestinal microbiota." In: *Mucosal Immunology 2017 10:6* 10.6 (Aug. 2017), pp. 1375–1386.

[257] Kevin J. Maloy and Fiona Powrie. "Regulatory T cells in the control of immune pathology." In: *Nature Immunology 2001 2:9* 2.9 (2001), pp. 816–822.

[258] Chi Young Ok, Bruce Woda, and Elizabeth Kurian. "The Pathology of Cancer. Cancer Concepts: A Guidebook for the Non-Oncologist." In: *Cancer Concepts: A Guidebook for the Non-Oncologist*. Ed. by Richard S. Richard S. Pieters and James Liebmann. Worcester, MA: University of Massachusetts Medical School, 2018. Chap. The Pathol, p. 12.

[259] Karsten Conrad, Dirk Roggenbuck, and Martin W. Laass. "Diagnosis and classification of ulcerative colitis." In: *Autoimmunity Reviews* 13.4-5 (Apr. 2014), pp. 463–466.

[260] Karin Fischer et al. "Isolation and characterization of human antigen-specific TCR$\alpha\beta$+ CD4-CD8- double-negative regulatory T cells." In: *Blood* 105.7 (Apr. 2005), pp. 2828–2835.

[261] Morgane Sébert et al. "Thrombin modifies growth, proliferation and apoptosis of human colon organoids: a protease-activated receptor 1- and protease-activated receptor 4-dependent mechanism." In: *British Journal of Pharmacology* 175.18 (Sept. 2018), pp. 3656–3668.

[262] Matthias Stelzner et al. "A nomenclature for intestinal in vitro cultures." In: *American Journal of Physiology - Gastrointestinal and Liver Physiology* 302.12 (June 2012), pp. 1359–1363.

[263] Sebastian Brachtendorf. "The role of ceramide synthases in chemotherapy and pathogenesis of colorectal cancer." Doctor of Natural Science. Goethe University Frankfurt am Main, 2020.

[264] Renée Ventura-Clapier et al. "Mitochondria: a central target for sex differences in pathologies." In: *Clinical Science* 131.9 (May 2017), pp. 803–822.

[265] David Pla-Martin and Rudolf J. Wiesner. "Reshaping membranes to build mitochondrial DNA." In: *PLOS Genetics* 15.6 (June 2019), e1008140.

[266] C. Felice et al. "Review article: selective histone deacetylase isoforms as potential therapeutic targets in inflammatory bowel diseases." In: *Alimentary Pharmacology & Therapeutics* 41.1 (Jan. 2015), pp. 26–38.

[267] Duska Separovic et al. "Altered Levels of Serum Ceramide, Sphingosine and Sphingomyelin Are Associated with Colorectal Cancer: A Retrospective Pilot Study." In: *Anticancer research* 37.3 (Mar. 2017), p. 1213.

[268] Adam R. Markowski et al. "Ceramides profile identifies patients with more advanced stages of colorectal cancer." In: *Biomolecules* 10.4 (Apr. 2020), p. 632.

[269] Kristi Helke et al. "Ceramide Synthase 6 Deficiency Enhances Inflammation in the DSS model of Colitis." In: *Scientific Reports* 8.1 (Dec. 2018).

[270] Josef Ecker et al. "The Colorectal Cancer Lipidome: Identification of a Robust Tumor-Specific Lipid Species Signature." In: *Gastroenterology* 161.3 (Sept. 2021), 910–923.e19.

[271] Sung Won Jang et al. "Altered mRNA expression levels of the major components of sphingolipid metabolism, ceramide synthases and their clinical implication in colorectal cancer." In: *Oncology Reports* 40.6 (Dec. 2018), pp. 3489–3500.

[272] Sarah Bazarganipour et al. "The Lipid Status in Patients with Ulcerative Colitis: Sphingolipids are Disease-Dependent Regulated." In: *Journal of Clinical Medicine 2019, Vol. 8, Page 971* 8.7 (July 2019), p. 971.

[273] Hamed Laroui et al. "Dextran sodium sulfate (dss) induces colitis in mice by forming nano-lipocomplexes with medium-chain-length fatty acids in the colon." In: *PLoS ONE* 7.3 (Mar. 2012), e32084.

[274] Benoit Chassaing et al. "Dextran sulfate sodium (DSS)-induced colitis in mice." In: *Current Protocols in Immunology* 104.SUPPL.104 (2014), Unit.

[275] Isao Okayasu et al. "A novel method in the induction of reliable experimental acute and chronic ulcerative colitis in mice." In: *Gastroenterology* 98.3 (1990), pp. 694–702.

[276] Nicole A. Bourbon, Jong Yun, and Mark Kester. "Ceramide Directly Activates Protein Kinase C ζ to Regulate a Stress-activated Protein Kinase Signaling Complex *." In: *Journal of Biological Chemistry* 275.45 (Nov. 2000), pp. 35617–35623.

[277] V. Dodane and B. Kachar. "Identification of Isoforms of G Proteins and PKC that Colocalize with Tight Junctions." In: *The Journal of Membrane Biology 1996 149:3* 149.3 (1996), pp. 199–209.

[278] Mel Pilar Espaillat, Richard R. Kew, and Lina M. Obeid. "Sphingolipids in neutrophil function and inflammatory responses: Mechanisms and implications for intestinal immunity and inflammation in ulcerative colitis." In: *Advances in Biological Regulation* 63 (Jan. 2017), pp. 140–155.

[279] B M Fournier and C A Parkos. "The role of neutrophils during intestinal inflammation." In: *Mucosal Immunology 2012 5:4* 5.4 (Apr. 2012), pp. 354–366.

[280] Odile Wéra, Patrizio Lancellotti, and Cécile Oury. "The Dual Role of Neutrophils in Inflammatory Bowel Diseases." In: *Journal of Clinical Medicine 2016, Vol. 5, Page 118* 5.12 (Dec. 2016), p. 118.

[281] Aude Bressenot et al. "Comparing histological activity indexes in UC." In: *Gut* 64.9 (Sept. 2015), pp. 1412–1418.

[282] Julia Barthelmes et al. "Lack of ceramide synthase 2 suppresses the development of experimental autoimmune encephalomyelitis by impairing the migratory capacity of neutrophils." In: *Brain, Behavior, and Immunity* 46 (May 2015), pp. 280–292.

[283] Jennifer Kurz et al. "Ceramides as Novel Disease Biomarkers." In: *Trends in Molecular Medicine* 25.1 (Jan. 2019), pp. 20–32.

[284] Hiroshi Katoh et al. "CXCR2-Expressing Myeloid-Derived Suppressor Cells Are Essential to Promote Colitis-Associated Tumorigenesis." In: *Cancer Cell* 24.5 (Nov. 2013), pp. 631–644.

[285] C. T. Murphy et al. "Use of bioluminescence imaging to track neutrophil migration and its inhibition in experimental colitis." In: *Clinical and Experimental Immunology* 162.1 (Oct. 2010), p. 188.

[286] Roman Kosoy et al. "Deep Analysis of the Peripheral Immune System in IBD Reveals New Insight in Disease Subtyping and Response to Monotherapy or Combination Therapy." In: *CMGH* 12.2 (Jan. 2021), pp. 599–632.

[287] Kamir J. Hiam-Galvez, Breanna M. Allen, and Matthew H. Spitzer. "Systemic immunity in cancer." In: *Nature Reviews Cancer 2021 21:6* 21.6 (Apr. 2021), pp. 345–359.

[288] Jonathan D. Proto et al. "Regulatory T Cells Promote Macrophage Efferocytosis during Inflammation Resolution." In: *Immunity* 49.4 (Oct. 2018), 666–677.e6.

[289] Gilaad G. Kaplan and Joseph W. Windsor. "The four epidemiological stages in the global evolution of inflammatory bowel disease." In: *Nature Reviews Gastroenterology & Hepatology 2020 18:1* 18.1 (Oct. 2020), pp. 56–66.

[290] Subhra K. Biswas and Alberto Mantovani. "Macrophage plasticity and interaction with lymphocyte subsets: cancer as a paradigm." In: *Nature Immunology 2010 11:10* 11.10 (Sept. 2010), pp. 889–896.

[291] Jonadab E. Olguín et al. "Early and partial reduction in CD4+Foxp3+ regulatory T cells during colitis-associated colon cancer induces CD4+ and CD8+ T cell activation inhibiting tumorigenesis." In: *Journal of Cancer* 9.2 (2018), pp. 239–249.

[292] Ryan D. Whetstone and Barry Gold. "T-cells enhance stem cell mutagenesis in the mouse colon." In: *Mutation Research/Fundamental and Molecular Mechanisms of Mutagenesis* 774 (Apr. 2015), pp. 1–5.

[293] Ryan D. Whetstone et al. "Colon carcinogenesis in wild type and immune compromised mice after treatment with azoxymethane, and azoxymethane with dextran sodium sulfate." In: *Molecular Carcinogenesis* 55.7 (July 2016), pp. 1187–1195.

[294] Chun Cheih Chao et al. "Metabolic Control of Astrocyte Pathogenic Activity via cPLA2-MAVS." In: *Cell* 179.7 (Dec. 2019), 1483–1498.e22.

[295] Salih Gencer et al. "No Title." In: *Science Signaling* 10.502 ().

[296] Lopamudra Das and Alan D. Levine. "TGF-β Inhibits IL-2 Production and Promotes Cell Cycle Arrest in TCR-Activated Effector/Memory T Cells in the Presence of Sustained TCR Signal Transduction." In: *The Journal of Immunology* 180.3 (Feb. 2008), pp. 1490–1498.

[297] Giovanni Monteleone et al. "Blocking Smad7 restores TGF-β1 signaling in chronic inflammatory bowel disease." In: *The Journal of Clinical Investigation* 108.4 (Aug. 2001), pp. 601–609.

[298] Lucien P Garo et al. "Smad7 Controls Immunoregulatory PDL2/1-PD1 Signaling in Intestinal Inflammation and Autoimmunity." In: *Cell Reports* 28.13 (2019), 3353–3366.e5.

[299] Angelamaria Rizzo et al. "Smad7 Expression in T cells Prevents Colitis-Associated Cancer." In: *Cancer Research* 71.24 (Dec. 2011), pp. 7423–7432.

[300] Matthew J. Scheffel et al. "Adoptive Transfer of Ceramide Synthase 6 Deficient Splenocytes Reduces the Development of Colitis." In: *Scientific Reports 2017 7:1* 7.1 (Nov. 2017), pp. 1–10.

[301] Emerich S. Fiala. "Investigations into the metabolism and mode of action of the colon carcinogens 1,2-dimethylhydrazine and azoxymethane." In: *Cancer.* 40.5 (1977), pp. 2436–45.

[302] Nasir H. Zaidi et al. "Transgenic expression of human mgmt protects against azoxymethane-induced aberrant crypt foci and g to a mutations in the k-ras oncogene of mouse colon." In: *Carcinogenesis* 16.3 (Mar. 1995), pp. 451–456.

[303] Gert L. Laqueur et al. "Carcinogenic Properties of Nuts From Cycas Circinalis L. Indigenous to Guam." In: *JNCI: Journal of the National Cancer Institute* 31.4 (Oct. 1963), pp. 919–951.

[304] Ock Soon Sohn et al. "Differential Effects of CYP2E1 Status on the Metabolic Activation of the Colon Carcinogens Azoxymethane and Methylazoxymethanol." In: *Cancer Research* 61.23 (2001), pp. 8435–40.

[305] Kristina A. Matkowskyj et al. "Azoxymethane-induced fulminant hepatic failure in C57BL/6J mice: Characterization of a new animal model." In: *American Journal of Physiology - Gastrointestinal and Liver Physiology* 277.2 40-2 (1999).

[306] Linhao Li, Hongbing Wang, and Jace W. Jones. "Sphingolipid metabolism as a marker of hepatotoxicity in drug-induced liver injury." In: *Prostaglandins & Other Lipid Mediators* 151 (Dec. 2020), p. 106484.

[307] Woo Jae Park et al. "Protection of a Ceramide Synthase 2 Null Mouse from Drug-induced Liver Injury: Role of Gap Junction Dysfunction and Connexin 32 Mislocalization." In: *Journal of Biological Chemistry* 288.43 (Oct. 2013), pp. 30904–30916.

[308] Joo Won Park et al. "Ablation of very long acyl chain sphingolipids causes hepatic insulin resistance in mice due to altered detergent-resistant membranes." In: *Hepatology* 57.2 (Feb. 2013), pp. 525–532.

[309] Yael Pewzner-Jung et al. "A Critical Role for Ceramide Synthase 2 in Liver Homeostasis: II. Insights Into Molecular Changes Leading To Hepatopathy*." In: *The Journal of Biological Chemistry* 285.14 (Apr. 2010), p. 10911.

[310] Takashi Matsuzaka et al. "Hepatocyte ELOVL Fatty Acid Elongase 6 Determines Ceramide Acyl-Chain Length and Hepatic Insulin Sensitivity in Mice." In: *Hepatology* 71.5 (May 2020), pp. 1609–1625.

[311] Liping Chen et al. "Benzene-induced mouse hematotoxicity is regulated by a protein phosphatase 2A complex that stimulates transcription of cytochrome P4502E1." In: *Journal of Biological Chemistry* 294.7 (Feb. 2019), pp. 2486–2499.

[312] Peter Sciberras, Laura Grech, and Godfrey Grech. "Differential expression of the sphingolipid pathway is associated with sensitivity to the pp2a activator fty720 in colorectal cancer cell lines." In: *Journal of Clinical Medicine* 10.21 (Oct. 2021), p. 4999.

[313] Brandi Jefferson et al. "Thrombospondin-1 Exacerbates Acute Liver Failure and Hepatic Encephalopathy Pathology in Mice by Activating Transforming Growth Factor β1." In: *The American Journal of Pathology* 190.2 (Feb. 2020), pp. 347–357.

[314] Jessica Min-DeBartolo et al. "Thrombospondin-I is a critical modulator in non-alcoholic steatohepatitis (NASH)." In: *PloS one* 14.12 (Dec. 2019).

[315] Jeonghyeon Kwon et al. "DSS-induced colitis is associated with adipose tissue dysfunction and disrupted hepatic lipid metabolism leading to hepatosteatosis and dyslipidemia in mice." In: *Scientific Reports 2021 11:1* 11.1 (Mar. 2021), pp. 1–16.

[316] Sou Hyun Kim et al. "Metabolomic Analysis of the Liver of a Dextran Sodium Sulfate-Induced Acute Colitis Mouse Model: Implications of the Gut–Liver Connection." In: *Cells* 9.2 (Feb. 2020).

[317] Changtao Jiang et al. "Intestinal farnesoid X receptor signaling promotes nonalcoholic fatty liver disease." In: *The Journal of Clinical Investigation* 125.1 (Jan. 2015), pp. 386–402.

[318] Changtao Jiang et al. "Intestine-selective farnesoid X receptor inhibition improves obesity-related metabolic dysfunction." In: *Nature Communications 2015 6:1* 6.1 (Dec. 2015), pp. 1–18.

[319] Cen Xie et al. "An Intestinal Farnesoid X Receptor–Ceramide Signaling Axis Modulates Hepatic Gluconeogenesis in Mice." In: *Diabetes* 66.3 (Mar. 2017), pp. 613–626.

[320] Elizabeth L. Johnson et al. "Sphingolipids produced by gut bacteria enter host metabolic pathways impacting ceramide levels." In: *Nature Communications* 11.1 (May 2020), pp. 1–11.

[321] Takaomi Kessoku et al. "The Role of Leaky Gut in Nonalcoholic Fatty Liver Disease: A Novel Therapeutic Target." In: *International Journal of Molecular Sciences 2021, Vol. 22, Page 8161* 22.15 (July 2021), p. 8161.

[322] Ekihiro Seki and David A. Brenner. "Toll-like receptors and adaptor molecules in liver disease: Update." In: *Hepatology* 48.1 (July 2008), pp. 322–335.

[323] Edouard Mobarak et al. "Glucosylceramide modifies the LPS-induced inflammatory response in macrophages and the orientation of the LPS/TLR4 complex in silico." In: *Scientific Reports 2018 8:1* 8.1 (Sept. 2018), pp. 1–11.

[324] Yuhong Luo et al. "Intestinal MYC modulates obesity-related metabolic dysfunction." In: *Nature Metabolism 2021 3:7* 3.7 (July 2021), pp. 923–939.

[325] Ying Li, Scott A. Summers, and William L. Holland. "Gutting out Myc to decrease ceramides." In: *Nature Metabolism 2021 3:7* 3.7 (July 2021), pp. 890–891.

[326] Sarah M. Turpin et al. "Obesity-Induced CerS6-Dependent C16:0 Ceramide Production Promotes Weight Gain and Glucose Intolerance." In: *Cell Metabolism* 20.4 (Oct. 2014), pp. 678–686.

[327] Sarah M. Turpin-Nolan and Jens C. Brüning. "The role of ceramides in metabolic disorders: when size and localization matters." In: *Nature Reviews Endocrinology 2020 16:4* 16.4 (Feb. 2020), pp. 224–233.

[328] Sarah M. Turpin-Nolan et al. "CerS1-Derived C18:0 Ceramide in Skeletal Muscle Promotes Obesity-Induced Insulin Resistance." In: *Cell Reports* 26.1 (Jan. 2019), 1–10.e7.

[329] Dominic Gosejacob et al. "Ceramide synthase 5 is essential to maintain C16:0-Ceramide pools and contributes to the development of diet-induced obesity." In: *Journal of Biological Chemistry* 291.13 (2016), pp. 6989–7003.

[330] Deepa Jonnalagadda et al. "Granule-mediated release of sphingosine-1-phosphate by activated platelets." In: *Biochimica et Biophysica Acta (BBA) - Molecular and Cell Biology of Lipids* 1841.11 (Nov. 2014), pp. 1581–1589.

[331] Rajita Pappu et al. "Promotion of lymphocyte egress into blood and lymph by distinct sources of sphingosine-1-phosphate." In: *Science* 316.5822 (Apr. 2007), pp. 295–298.

[332] Eric Camerer et al. "Sphingosine-1-phosphate in the plasma compartment regulates basal and inflammation-induced vascular leak in mice." In: *The Journal of Clinical Investigation* 119.7 (July 2009), pp. 1871–1879.

[333] Yugesh Kharel et al. "Mechanism of sphingosine 1-phosphate clearance from blood." In: *Biochemical Journal* 477.5 (Mar. 2020), pp. 925–935.

[334] Mehrdad Matloubian et al. "Lymphocyte egress from thymus and peripheral lymphoid organs is dependent on S1P receptor 1." In: *Nature 2004 427:6972* 427.6972 (Jan. 2004), pp. 355–360.

[335] Timothy Hla, Krishnan Venkataraman, and Jason Michaud. "The vascular S1P gradient—Cellular sources and biological significance." In: *Biochimica et biophysica acta* 1781.9 (Sept. 2008), p. 477.

[336] Meryem Bektas et al. "Sphingosine 1-phosphate lyase deficiency disrupts lipid homeostasis in liver." In: *Journal of Biological Chemistry* 285.14 (Apr. 2010), pp. 10880–10889.

[337] Jinbiao Chen et al. "Deletion of sphingosine kinase 1 ameliorates hepatic steatosis in diet-induced obese mice: Role of PPARγ." In: *Biochimica et Biophysica Acta (BBA) - Molecular and Cell Biology of Lipids* 1861.2 (Feb. 2016), pp. 138–147.

[338] Eric A. Franzosa et al. "Gut microbiome structure and metabolic activity in inflammatory bowel disease." In: *Nature Microbiology 2018 4:2* 4.2 (Dec. 2018), pp. 293–305.

[339] Joseph Diab et al. "Lipidomics in Ulcerative Colitis Reveal Alteration in Mucosal Lipid Composition Associated With the Disease State." In: *Inflammatory Bowel Diseases* 25.11 (Oct. 2019), pp. 1780–1787.

[340] Jung H Suh et al. "Sphingosine-1-Phosphate Signaling and Metabolism Gene Signature in Pediatric Inflammatory Bowel Disease: A Matched-case Control Pilot Study." In: *Inflammatory Bowel Diseases* 24.6 (May 2018), pp. 1321–1334.

[341] Bruno Augusto Alves Martins et al. "Biomarkers in Colorectal Cancer: The Role of Translational Proteomics Research." In: *Frontiers in Oncology* 0 (Nov. 2019), p. 1284.

[342] Christoph Kessel et al. "Serum biomarkers confirming stable remission in inflammatory bowel disease." In: *Scientific Reports 2021 11:1* 11.1 (Mar. 2021), pp. 1–10.

[343] Jean Frederic Colombel et al. "Effect of tight control management on Crohn's disease (CALM): a multicentre, randomised, controlled phase 3 trial." In: *The Lancet* 390.10114 (Dec. 2017), pp. 2779–2789.

[344] Rahul Kalla et al. "Serum Calprotectin: A Novel Diagnostic and Prognostic Marker in Inflammatory Bowel Diseases." In: *American Journal of Gastroenterology* 111.12 (Dec. 2016), pp. 1796–1805.

[345] James Boon et al. "Ceramides Contained in LDL Are Elevated in Type 2 Diabetes and Promote Inflammation and Skeletal Muscle Insulin Resistance." In: *Diabetes* 62.2 (Feb. 2013), p. 401.

[346] William L. Holland et al. "Lipid-induced insulin resistance mediated by the proinflammatory receptor TLR4 requires saturated fatty acid–induced ceramide biosynthesis in mice." In: *The Journal of Clinical Investigation* 121.5 (May 2011), p. 1858.

[347] Alice T. Mathews et al. "Efficacy of nutritional interventions to lower circulating ceramides in young adults: FRUVEDomic pilot study." In: *Physiological Reports* 5.13 (July 2017), p. 13329.

[348] Paul L. Beck et al. "Transforming Growth Factor-β Mediates Intestinal Healing and Susceptibility to Injury in Vitro and in Vivo Through Epithelial Cells." In: *The American Journal of Pathology* 162.2 (Feb. 2003), pp. 597–608.

[349] Nick Barker et al. "Identification of stem cells in small intestine and colon by marker gene Lgr5." In: *Nature 2007 449:7165* 449.7165 (Oct. 2007), pp. 1003–1007.

[350] Wim de Lau et al. "Lgr5 homologues associate with Wnt receptors and mediate R-spondin signalling." In: *Nature 2011 476:7360* 476.7360 (July 2011), pp. 293–297.

[351] Rebecca J Morris et al. "Capturing and profiling adult hair follicle stem cells." In: *Nature Biotechnology 2004 22:4* 22.4 (Mar. 2004), pp. 411–417.

[352] Terrill McClanahan et al. "Identification of overexpression of orphan G Protein-Coupled Receptor GPR49 in human colon and ovarian primary tumors." In: *Cancer Biology and Therapy* 5.4 (2006), pp. 419–426.

[353] Yoshiya Yamamoto et al. "Overexpression of orphan G-protein–coupled receptor, Gpr49, in human hepatocellular carcinomas with β-catenin mutations." In: *Hepatology* 37.3 (Mar. 2003), pp. 528–533.

[354] Ju-Suk Nam et al. "Mouse Cristin/R-spondin Family Proteins Are Novel Ligands for the Frizzled 8 and LRP6 Receptors and Activate β-Catenin-dependent Gene Expression *." In: *Journal of Biological Chemistry* 281.19 (May 2006), pp. 13247–13257.

[355] Qiou Wei et al. "R-spondin1 Is a High Affinity Ligand for LRP6 and Induces LRP6 Phosphorylation and β-Catenin Signaling *." In: *Journal of Biological Chemistry* 282.21 (May 2007), pp. 15903–15911.

[356] Francesca Fallarino et al. "Ligand and cytokine dependence of the immunosuppressive pathway of tryptophan catabolism in plasmacytoid dendritic cells." In: *International Immunology* 17.11 (Nov. 2005), pp. 1429–1438.

[357] Birgitta E. Michels et al. "Human colon organoids reveal distinct physiologic and oncogenic Wnt responses." In: *Journal of Experimental Medicine* 216.3 (Mar. 2019), pp. 704–720.

[358] Rik GH Lindeboom et al. "Integrative multi-omics analysis of intestinal organoid differentiation." In: *Molecular Systems Biology* 14.6 (June 2018), e8227.

[359] J. Martin Brown and William R. Wilson. "Exploiting tumour hypoxia in cancer treatment." In: *Nature Reviews Cancer 2004 4:6* 4.6 (2004), pp. 437–447.

[360] A Casazza et al. "Tumor stroma: a complexity dictated by the hypoxic tumor microenvironment." In: *Oncogene 2014 33:14* 33.14 (Apr. 2013), pp. 1743–1754.

[361] Varvara Petrova et al. "The hypoxic tumour microenvironment." In: *Oncogenesis 2018 7:1* 7.1 (Jan. 2018), pp. 1–13.

[362] Emily R. Watts and Sarah R. Walmsley. "Inflammation and Hypoxia: HIF and PHD Isoform Selectivity." In: *Trends in Molecular Medicine* 25.1 (Jan. 2019), pp. 33–46.

[363] Annie Lauzier et al. "Colorectal cancer cells respond differentially to autophagy inhibition in vivo." In: *Scientific Reports 2019 9:1* 9.1 (Aug. 2019), pp. 1–16.

[364] Angelika Walzl et al. "The resazurin reduction assay can distinguish cytotoxic from cytostatic compounds in spheroid screening assays." In: *Journal of Biomolecular Screening* 19.7 (Apr. 2014), pp. 1047–1059.

[365] Anna C. Luca et al. "Impact of the 3D Microenvironment on Phenotype, Gene Expression, and EGFR Inhibition of Colorectal Cancer Cell Lines." In: *PLOS ONE* 8.3 (Mar. 2013), e59689.

[366] Peter Mullen et al. "Effect of Matrigel on the tumorigenicity of human breast and ovarian carcinoma cell lines." In: *International journal of cancer* 67.6 (1996), pp. 816–820.

[367] Peter Mullen. "The use of Matrigel to facilitate the establishment of human cancer cell lines as xenografts." In: *Methods in molecular medicine* 88 (2004), pp. 287–292.

[368] Camila Bárbara Cantalupo Lima, Sânia Alves dos Santos, and Dahir Ramos de Andrade Junior. "Hypoxic Stress, Hepatocytes and Caco-2 Viability and Susceptibility to Shigella Flexneri Invasion." In: *Revista do Instituto de Medicina Tropical de São Paulo* 55.5 (Sept. 2013), p. 341.

[369] Teona Ontikatze et al. "Dihydroartemisinin is a Hypoxia-Active Anti-Cancer Drug in Colorectal Carcinoma Cells." In: *Frontiers in Oncology* 4 (2014).

[370] Gertrud Knoll et al. "Hypoxia regulates TRAIL sensitivity of colorectal cancer cells through mitochondrial autophagy." In: *Oncotarget* 7.27 (July 2016), p. 41488.

[371] Chun Te Chiang et al. "High-throughput microscopy reveals the impact of multifactorial environmental perturbations on colorectal cancer cell growth." In: *GigaScience* 10.4 (Apr. 2021), pp. 1–9.

[372] Simon Lagies et al. "Cells grown in three-dimensional spheroids mirror in vivo metabolic response of epithelial cells." In: *Communications Biology 2020 3:1* 3.1 (May 2020), pp. 1–10.

[373] Damian Hertig et al. "Live monitoring of cellular metabolism and mitochondrial respiration in 3D cell culture system using NMR spectroscopy." In: *Analyst* 146.13 (June 2021), pp. 4326–4339.

[374] Julien Véret et al. "Ceramide synthase 4 and de novo production of ceramides with specific N-acyl chain lengths are involved in glucolipotoxicity-induced apoptosis of INS-1 β-cells." In: *Biochemical Journal* 438.1 (Aug. 2011), pp. 177–189.

[375] Talya L Dayton, Tyler Jacks, and Matthew G Vander Heiden. "PKM2, cancer metabolism, and the road ahead." In: *EMBO reports* 17.12 (Dec. 2016), pp. 1721–1730.

[376] Attila Steták et al. "Nuclear Translocation of the Tumor Marker Pyruvate Kinase M2 Induces Programmed Cell Death." In: *Cancer Research* 67.4 (Feb. 2007), pp. 1602–1608.

[377] Ninel Azoitei et al. "PKM2 promotes tumor angiogenesis by regulating HIF-1aα through NF-κB activation." In: *Molecular Cancer* 15.1 (Jan. 2016), pp. 1–15.

[378] Q. Xu et al. "Regulatory circuit of PKM2/NF-κB/MIR-148a/152-modulated tumor angiogenesis and cancer progression." In: *Oncogene* 34.43 (Feb. 2015), pp. 5482–5493.

[379] Mami Morita et al. "PKM1 Confers Metabolic Advantages and Promotes Cell-Autonomous Tumor Cell Growth." In: *Cancer Cell* 33.3 (Mar. 2018), 355–367.e7.

[380] Seán Fitzgerald et al. "High CerS5 expression levels associate with reduced patient survival and transition from apoptotic to autophagy signalling pathways in colorectal cancer." In: *The Journal of Pathology: Clinical Research* 1.1 (Jan. 2015), p. 54.

[381] Sebastian Brachtendorf, Khadija El-Hindi, and Sabine Grösch. "Ceramide synthases in cancer therapy and chemoresistance." In: *Progress in Lipid Research* 74 (Apr. 2019), pp. 160–185.

[382] Mototeru Yamane et al. "D,L-Threo-1-phenyl-2-decanoylamino-3-morpholino-1-propanol (DL-PDMP) increases endoplasmic reticulum stress, autophagy and apoptosis accompanying ceramide accumulation via ceramide synthase 5 protein expression in A549 cells." In: *Biochimie* 93.9 (Sept. 2011), pp. 1446–1459.

[383] Qian Tan et al. "Role of Autophagy as a Survival Mechanism for Hypoxic Cells in Tumors." In: *Neoplasia (New York, N.Y.)* 18.6 (June 2016), p. 347.

[384] Johanna Chiche et al. "Hypoxic enlarged mitochondria protect cancer cells from apoptotic stimuli." In: *Journal of Cellular Physiology* 222.3 (Mar. 2010), pp. 648–657.

[385] Der Fen Suen, Kristi L. Norris, and Richard J. Youle. "Mitochondrial dynamics and apoptosis." In: *Genes & Development* 22.12 (June 2008), pp. 1577–1590.

[386] Rie Sugioka, Shigeomi Shimizu, and Yoshihide Tsujimoto. "Fzo1, a Protein Involved in Mitochondrial Fusion, Inhibits Apoptosis." In: *Journal of Biological Chemistry* 279.50 (Dec. 2004), pp. 52726–52734.

[387] Christian Frezza et al. "OPA1 Controls Apoptotic Cristae Remodeling Independently from Mitochondrial Fusion." In: *Cell* 126.1 (July 2006), pp. 177–189.

[388] Zdenek Andrysik et al. "Multi-omics analysis reveals contextual tumor suppressive and oncogenic gene modules within the acute hypoxic response." In: *Nature Communications 2021 12:1* 12.1 (Mar. 2021), pp. 1–18.

[389] Yigang Wang et al. *The Role of Mitochondrial Dynamics and Mitophagy in Carcinogenesis, Metastasis and Therapy*. June 2020.

[390] Paolo E. Porporato et al. "A mitochondrial switch promotes tumor metastasis." In: *Cell Reports* 8.3 (Aug. 2014), pp. 754–766.

[391] Nicoletta Guaragnella, Sergio Giannattasio, and Loredana Moro. "Mitochondrial dysfunction in cancer chemoresistance." In: *Biochemical Pharmacology* 92.1 (Nov. 2014), pp. 62–72.

[392] Reyniel Hernández-López et al. "Mitochondrial Function Differences between Tumor Tissue of Human Metastatic and Premetastatic CRC." In: *Biology 2022, Vol. 11, Page 293* 11.2 (Feb. 2022), p. 293.

[393] Jennifer S. Carew and Peng Huang. *Mitochondrial defects in cancer*. Dec. 2002.

[394] Mehdi Damaghi, Jonathan W. Wojtkowiak, and Robert J. Gillies. *pH sensing and regulation in cancer*. 2013.

[395] Yasumasa Kato et al. "Acidic extracellular microenvironment and cancer." In: *Cancer Cell International 2013 13:1* 13.1 (Sept. 2013), pp. 1–8.

[396] Joana Pereira-Vieira et al. "MCT1, MCT4 and CD147 expression and 3-bromopyruvate toxicity in colorectal cancer cells are modulated by the extracellular conditions." In: *Biological Chemistry* 400.6 (May 2019), pp. 787–799.

[397] Pawel Swietach, Richard D. Vaughan-Jones, and Adrian L. Harris. "Regulation of tumor pH and the role of carbonic anhydrase 9." In: *Cancer and Metastasis Reviews 2007 26:2* 26.2 (Apr. 2007), pp. 299–310.

[398] P. Kirk et al. "CD147 is tightly associated with lactate transporters MCT1 and MCT4 and facilitates their cell surface expression." In: *The EMBO Journal* 19.15 (Aug. 2000), pp. 3896–3904.

[399] Masaaki Nakai, Li Chen, and Romana A. Nowak. "Tissue distribution of basigin and monocarboxylate transporter 1 in the adult male mouse: A study using the wild-type and basigin gene knockout mice." In: *The Anatomical Record Part A: Discoveries in Molecular, Cellular, and Evolutionary Biology* 288A.5 (May 2006), pp. 527–535.

[400] Denise K. Walters, Bonnie K. Arendt, and Diane F. Jelinek. "CD147 regulates the expression of MCT1 and lactate export in multiple myeloma cells." In: *Cell Cycle* 12.19 (2013), pp. 3364–3372.

[401] Sarika Saraswati et al. "Prolonged Hypoxia Induces Monocarboxylate Transporter-4 Expression in Mesenchymal Stem Cells Resulting in a Secretome that is Deleterious to Cardiovascular Repair." In: *Stem Cells* 33.4 (Apr. 2015), pp. 1333–1344.

[402] Sonja Heller et al. "Gene Suppression of Transketolase-Like Protein 1 (TKTL1) Sensitizes Glioma Cells to Hypoxia and Ionizing Radiation." In: *International Journal of Molecular Sciences 2018, Vol. 19, Page 2168* 19.8 (July 2018), p. 2168.

[403] Lin Gao et al. "Induction of the glucose-6-phosphate dehydrogenase gene expression by chronic hypoxia in PC12 cells." In: *FEBS Letters* 569.1-3 (July 2004), pp. 256–260.

[404] Annegret Kathagen-Buhmann et al. "Glycolysis and the pentose phosphate pathway are differentially associated with the dichotomous regulation of glioblastoma cell migration versus proliferation." In: *Neuro-Oncology* 18.9 (Sept. 2016), pp. 1219–1229.

[405] Xu Xiaojun et al. "Transketolase-like protein 1 (TKTL1) is required for rapid cell growth and full viability of human tumor cells." In: *International Journal of Cancer* 124.6 (Mar. 2009), pp. 1330–1337.

[406] Joel I. Perez-Perri et al. "The TIP60 Complex Is a Conserved Coactivator of HIF1A." In: *Cell Reports* 16.1 (June 2016), pp. 37–47.

[407] James A Smythies et al. "Inherent DNA-binding specificities of the HIF-1α and HIF-2α transcription factors in chromatin." In: *EMBO reports* 20.1 (Jan. 2019), e46401.

[408] Chia Chen Chen et al. "FoxOs Inhibit mTORC1 and Activate Akt by Inducing the Expression of Sestrin3 and Rictor." In: *Developmental Cell* 18.4 (Apr. 2010), pp. 592–604.

[409] Matthew D. Galbraith et al. "XHIF1A employs CDK8-mediator to stimulate RNAPII elongation in response to hypoxia." In: *Cell* 153.6 (June 2013), p. 1327.

[410] Matthew T. Knuesel et al. "The human CDK8 subcomplex is a molecular switch that controls Mediator coactivator function." In: *Genes & Development* 23.4 (Feb. 2009), pp. 439–451.

[411] Sara Osman et al. "The Cdk8 kinase module regulates interaction of the mediator complex with RNA polymerase II." In: *Journal of Biological Chemistry* 296 (Jan. 2021).

[412] Matthew D. Galbraith et al. "CDK8 Kinase Activity Promotes Glycolysis." In: *Cell Reports* 21.6 (Nov. 2017), pp. 1495–1506.

[413] Michael Batie et al. "Hypoxia induces rapid changes to histone methylation and reprograms chromatin." In: *Science* 363.6432 (Mar. 2019), pp. 1222–1226.

[414] Abhishek A. Chakraborty et al. "Histone demethylase KDM6A directly senses oxygen to control chromatin and cell fate." In: *Science* 363.6432 (Mar. 2019), pp. 1217–1222.

[415] Nitai C. Hait et al. "Active, phosphorylated fingolimod inhibits histone deacetylases and facilitates fear extinction memory." In: *Nature Neuroscience 2014 17:7* 17.7 (May 2014), pp. 971–980.

[416] Henryk Jeśko et al. "Fingolimod Affects Transcription of Genes Encoding Enzymes of Ceramide Metabolism in Animal Model of Alzheimer's Disease." In: *Molecular Neurobiology* 57.6 (June 2020), pp. 2799–2811.

[417] Thibaut Burg et al. "Histone Deacetylase Inhibition Regulates Lipid Homeostasis in a Mouse Model of Amyotrophic Lateral Sclerosis." In: *International Journal of Molecular Sciences Article* (2021).

[418] Alexis Gonneaud et al. "HDAC1 and HDAC2 independently regulate common and specific intrinsic responses in murine enteroids." In: *Scientific Reports 2019 9:1* 9.1 (Mar. 2019), pp. 1–15.

[419] Andrea Galmozzi et al. "Inhibition of Class I Histone Deacetylases Unveils a Mitochondrial Signature and Enhances Oxidative Metabolism in Skeletal Muscle and Adipose Tissue." In: *Diabetes* 62.3 (Mar. 2013), pp. 732–742.

[420] Xiaoting Jiang et al. "Inhibition of HDAC3 promotes ligand-independent PPARγ activation by protein acetylation." In: *Journal of Molecular Endocrinology* 53.2 (Oct. 2014), pp. 191–200.

[421] Sarah K. Knutson et al. "Liver-specific deletion of histone deacetylase 3 disrupts metabolic transcriptional networks." In: *EMBO Journal* 27.7 (Apr. 2008), pp. 1017–1028.

[422] Volodymyr Tryndyak et al. "Effect of aflatoxin B1, benzo[a]pyrene, and methapyrilene on transcriptomic and epigenetic alterations in human liver HepaRG cells." In: *Food and Chemical Toxicology* 121 (Nov. 2018), pp. 214–223.

[423] Linda Rieswijk et al. "Aflatoxin B1 induces persistent epigenomic effects in primary human hepatocytes associated with hepatocellular carcinoma." In: *Toxicology* 350-352 (Mar. 2016), pp. 31–39.

[424] Cheng-Lan Jiang et al. "Air pollution and DNA methylation alterations in lung cancer: A systematic and comparative study." In: *Oncotarget* 8.1 (Nov. 2016), pp. 1369–1391.

[425] Rebecca L. Hancock et al. *Epigenetic regulation by histone demethylases in hypoxia*. Aug. 2015.

[426] E. M. Nolan et al. "Transcriptional regulation of the human chromogranin A gene by its 5′ distal regulatory element: novel effects of orientation, structure, flanking sequences, and position on expression." In: *Molecular and Cellular Endocrinology* 124.1-2 (Nov. 1996), pp. 51–62.

[427] A. L. Boutillier et al. "Corticotropin-releasing hormone stimulates proopiomelanocortin transcription by cFos-dependent and -independent pathways: characterization of an AP1 site in exon 1." In: *Molecular Endocrinology* 9.6 (June 1995), pp. 745–755.

[428] S. L.A. Samson and Norman C.W. Wong. "Role of Sp1 in insulin regulation of gene expression." In: *Journal of Molecular Endocrinology* 29.3 (Dec. 2002), pp. 265–279.

[429] Rashi Singhal and Yatrik M. Shah. "Oxygen battle in the gut: Hypoxia and hypoxia-inducible factors in metabolic and inflammatory responses in the intestine." In: *Journal of Biological Chemistry* 295.30 (July 2020), pp. 10493–10505.

[430] Guanglong He et al. "Noninvasive measurement of anatomic structure and intraluminal oxygenation in the gastrointestinal tract of living mice with spatial and spectral EPR imaging." In: *Proceedings of the National Academy of Sciences of the United States of America* 96.8 (Apr. 1999), pp. 4586–4591.

[431] Sophie Van Welden et al. "Differential expression of prolyl hydroxylase 1 in patients with ulcerative colitis versus patients with Crohn's disease/infectious colitis and healthy controls." In: *Journal of Inflammation (United Kingdom)* 10.1 (Nov. 2013), pp. 1–6.

[432] Eoin P. Cummins et al. "The Hydroxylase Inhibitor Dimethyloxalylglycine Is Protective in a Murine Model of Colitis." In: *Gastroenterology* 134.1 (Jan. 2008), 156–165.e1.

[433] Murtaza M. Tambuwala et al. "Loss of Prolyl Hydroxylase-1 Protects Against Colitis Through Reduced Epithelial Cell Apoptosis and Increased Barrier Function." In: *Gastroenterology* 139.6 (Dec. 2010), pp. 2093–2101.

[434] Ying Chen et al. "PHD3 Stabilizes the Tight Junction Protein Occludin and Protects Intestinal Epithelial Barrier Function." In: *Journal of Biological Chemistry* 290.33 (Aug. 2015), pp. 20580–20589.

[435] Susanne M. Krug et al. "Charge-selective claudin channels." In: *Annals of the New York Academy of Sciences* 1257.1 (June 2012), pp. 20–28.

[436] Burak Ozgür et al. "Hypoxia increases expression of selected blood-brain barrier transporters GLUT-1, P-gp, SLC7A5 and TFRC, while maintaining barrier integrity, in brain capillary endothelial monolayers." In: *Fluids and barriers of the CNS* 19.1 (Dec. 2022).

[437] Puqiao Lian et al. "Hypoxia and heat stress affect epithelial integrity in a Caco-2/HT-29 co-culture." In: *Scientific Reports 2021 11:1* 11.1 (June 2021), pp. 1–14.

[438] Bejan J. Saeedi et al. "HIF-dependent regulation of claudin-1 is central to intestinal epithelial tight junction integrity." In: *Molecular Biology of the Cell* 26.12 (June 2015), pp. 2252–2262.

[439] Hays W.J. Young et al. "Central role of Muc5ac expression in mucous metaplasia and its regulation by conserved 5′ elements." In: *American Journal of Respiratory Cell and Molecular Biology* 37.3 (Dec. 2007), pp. 273–290.

[440] Nancy A. Louis et al. "Selective induction of mucin-3 by hypoxia in intestinal epithelia." In: *Journal of Cellular Biochemistry* 99.6 (Dec. 2006), pp. 1616–1627.

[441] Annika Braun et al. "Alterations of phospholipid concentration and species composition of the intestinal mucus barrier in ulcerative colitis: A clue to pathogenesis." In: *Inflammatory Bowel Diseases* 15.11 (Nov. 2009), pp. 1705–1720.

[442] W Stremmel et al. "Retarded release phosphatidylcholine benefits patients with chronic active ulcerative colitis." In: *Gut* 54.7 (July 2005), p. 966.

[443] Roni Nowarski et al. "Epithelial IL-18 Equilibrium Controls Barrier Function in Colitis." In: *Cell* 163.6 (Dec. 2015), pp. 1444–1456.

[444] Joseph M. Amann et al. "Mtgr1 Is a Transcriptional Corepressor That Is Required for Maintenance of the Secretory Cell Lineage in the Small Intestine." In: *Molecular and Cellular Biology* 25.21 (Nov. 2005), pp. 9576–9585.

[445] Maria J. Rodríguez-Colman et al. "Interplay between metabolic identities in the intestinal crypt supports stem cell function." In: *Nature* 543.7645 (Mar. 2017), pp. 424–427.

[446] Yoshinori Yoshida et al. *Hypoxia Enhances the Generation of Induced Pluripotent Stem Cells*. Sept. 2009.

[447] Catherine E. Forristal et al. "Hypoxia inducible factors regulate pluripotency and proliferation in human embryonic stem cells cultured at reduced oxygen tensions." In: *Reproduction* 139.1 (Jan. 2010), pp. 85–97.

[448] Michal Levy and Anthony H. Futerman. "Mammalian Ceramide Synthases." In: *IUBMB life* 62.5 (May 2010), p. 347.

[449] Arndt Weinmann, Peter R. Galle, and Andreas Teufel. "LASS6, an additional member of the longevity assurance gene family." In: *International journal of molecular medicine* 16.5 (Nov. 2005), pp. 905–910.

[450] Jinwu Chen et al. "Ceramide synthase-4 orchestrates the cell proliferation and tumor growth of liver cancer in vitro and in vivo through the nuclear factor-κB signaling pathway." In: *Oncology Letters* 14.2 (2017), pp. 1477–1483.

[451] N. Fidler and J. M. Fernandez. "Phase tracking: an improved phase detection technique for cell membrane capacitance measurements." In: *Biophysical journal* 56.6 (1989), pp. 1153–1162.

[452] J. Zimmerberg et al. "Simultaneous electrical and optical measurements show that membrane fusion precedes secretory granule swelling during exocytosis of beige mouse mast cells." In: *Proceedings of the National Academy of Sciences of the United States of America* 84.6 (1987), pp. 1585–1589.

[453] Karsten Lollike and Manfred Lindau. "Membrane capacitance techniques to monitor granule exocytosis in neutrophils." In: *Journal of Immunological Methods* 232 (1999), pp. 111–120.

[454] Kathleen O. Holevinsky and Deborah J. Nelson. "Membrane capacitance changes associated with particle uptake during phagocytosis in macrophages." In: *Biophysical Journal* 75.5 (1998), p. 2577.

[455] Anke Di, Boris Krupa, and Deborah J. Nelson. "Calcium-G Protein Interactions in the Regulation of Macrophage Secretion." In: *Journal of Biological Chemistry* 276.40 (Oct. 2001), pp. 37124–37132.

[456] Anke Di et al. "Dynamin regulates focal exocytosis in phagocytosing macrophages." In: *Molecular Biology of the Cell* 14.5 (May 2003), pp. 2016–2028.

[457] C. A. Bertrand, C. L. Laboisse, and U. Hopfer. "Purinergic and cholinergic agonists induce exocytosis from the same granule pool in HT29-Cl.16E monolayers." In: *American Journal of Physiology - Cell Physiology* 276.4 45-4 (1999).

[458] Takeshi Harayama and Howard Riezman. "Understanding the diversity of membrane lipid composition." In: *Nature Reviews Molecular Cell Biology 2018 19:5* 19.5 (Feb. 2018), pp. 281–296.

[459] Tore Skotland et al. "An emerging focus on lipids in extracellular vesicles." In: *Advanced Drug Delivery Reviews* 159 (Jan. 2020), pp. 308–321.

[460] D. H. Hong, J. F. Forstner, and G. G. Forstner. "Protein kinase C-ϵ is the likely mediator of mucin exocytosis in human colonic cell lines." In: *American Journal of Physiology - Gastrointestinal and Liver Physiology* 272.1 35-1 (1997).

[461] Kohei Fujita et al. "Mucin core protein expression in serrated polyps of the large intestine." In: *Virchows Archiv : an international journal of pathology* 457.4 (Oct. 2010), pp. 443–449.

[462] Xiao Dong Bu et al. "Altered expression of MUC2 and MUC5AC in progression of colorectal carcinoma." In: *World Journal of Gastroenterology : WJG* 16.32 (Aug. 2010), p. 4089.

[463] Anne Eve Biemer-Hüttmann et al. "Immunohistochemical staining patterns of MUC1, MUC2, MUC4, and MUC5AC mucins in hyperplastic polyps, serrated adenomas, and traditional adenomas of the colorectum." In: *The journal of histochemistry and cytochemistry : official journal of the Histochemistry Society* 47.8 (1999), pp. 1039–1047.

[464] Shantibhusan Senapati et al. "Expression of intestinal MUC17 membrane-bound mucin in inflammatory and neoplastic diseases of the colon." In: *Journal of clinical pathology* 63.8 (Aug. 2010), p. 702.

[465] Shiv Ram Krishn et al. "Mucins and associated glycan signatures in colon adenoma-carcinoma sequence: prospective pathological implication(s) for early diagnosis of colon cancer." In: *Cancer letters* 374.2 (May 2016), p. 304.

[466] Ramesh Pothuraju et al. "Mechanistic and Functional Shades of Mucins and Associated Glycans in Colon Cancer." In: *Cancers* 12.3 (Mar. 2020).

[467] Patrizia Cammareri et al. "TGFβ pathway limits dedifferentiation following WNT and MAPK pathway activation to suppress intestinal tumourigenesis." In: *Cell Death & Differentiation 2017 24:10* 24.10 (June 2017), pp. 1681–1693.

[468] Kenji Hamada et al. "Liver metastasis models of colon cancer for evaluation of drug efficacy using NOD/Shi-scid IL2Rγnull (NOG) mice." In: *International Journal of Oncology* 32.1 (Jan. 2008), pp. 153–159.

[469] Hao Wang et al. "Epithelial–Mesenchymal Transition (EMT) Induced by TNF-α Requires AKT/GSK-3β-Mediated Stabilization of Snail in Colorectal Cancer." In: *PLoS ONE* 8.2 (Feb. 2013).

[470] Anita Ferraretto et al. "New methodological approach to induce a differentiation phenotype in Caco-2 cells prior to post-confluence stage." In: *Anticancer Research* 27.6 B (2007), pp. 3919–3925.

[471] M J Engle, G S Goetz, and D H Alpers. "Caco-2 cells express a combination of colonocyte and enterocyte phenotypes." In: *Journal of Cellular Physiology* 174.3 (1998), pp. 362–369.

[472] Qing Ming Ding, Tien C. Ko, and B. Mark Evers. "Caco-2 intestinal cell differentiation is associated with G1 arrest and suppression of CDK2 and CDK4." In: *American Journal of Physiology - Cell Physiology* 275.5 44-5 (1998), pp. 1193–1200.

[473] Sofia La Vecchia and Carlos Sebastián. "Metabolic pathways regulating colorectal cancer initiation and progression." In: *Seminars in Cell & Developmental Biology* 98 (Feb. 2020), pp. 63–70.

[474] Doris Höglinger et al. "Trifunctional lipid probes for comprehensive studies of single lipid species in living cells." In: *Proceedings of the National Academy of Sciences of the United States of America* 114.7 (Feb. 2017), pp. 1566–1571.

[475] Charmi Shah et al. "Protection from high fat diet-induced increase in ceramide in mice lacking plasminogen activator inhibitor 1." In: *Journal of Biological Chemistry* 283.20 (May 2008), pp. 13538–13548.

[476] Daniel Triner et al. "Epithelial Hypoxia-Inducible Factor 2α Facilitates the Progression of Colon Tumors through Recruiting Neutrophils." In: *Molecular and Cellular Biology* 37.5 (Mar. 2017).

[477] Xiang Xue et al. "Endothelial PAS domain protein 1 activates the inflammatory response in the intestinal epithelium to promote colitis in mice." In: *Gastroenterology* 145.4 (Oct. 2013), pp. 831–841.

[478] Yousra Ajouaou et al. "The oxygen sensor prolyl hydroxylase domain 2 regulates the in vivo suppressive capacity of regulatory T cells." In: *eLife* 11 (June 2022), p. 2021.03.23.436597.

[479] Nariaki Nakamura et al. *Hypoxia in Cell Reprogramming and the Epigenetic Regulations*. Jan. 2021.

[480] Houda Benlhabib and Carole R. Mendelson. "Epigenetic Regulation of Surfactant Protein A Gene (SP-A) Expression in Fetal Lung Reveals a Critical Role for Suv39h Methyltransferases during Development and Hypoxia." In: *Molecular and Cellular Biology* 31.10 (May 2011), pp. 1949–1958.

[481] Anne Rademacher. "Silencing and activating heterochromatin." Doctor of Natural Science. The Ruperto-Carola Univeryity of Heidelberg, 2017.

[482] Rajesh C. Rao and Yali Dou. *Hijacked in cancer: The KMT2 (MLL) family of methyltransferases*. May 2015.

[483] Giulia Barbagiovanni et al. "KMT2B Is Selectively Required for Neuronal Transdifferentiation, and Its Loss Exposes Dystonia Candidate Genes." In: *Cell Reports* 25.4 (Oct. 2018), pp. 988–1001.

[484] Sergei Denissov et al. "Mll2 is required for H3K4 trimethylation on bivalent promoters in embryonic stem cells, whereas Mll1 is redundant." In: *Development (Cambridge)* 141.3 (Feb. 2014), pp. 526–537.

[485] Branca I. Pereira et al. "Senescent cells evade immune clearance via HLA-E-mediated NK and CD8+ T cell inhibition." In: *Nature Communications* 10.1 (June 2019), pp. 1–13.

[486] Maximilian Rentschler et al. *Cytokine-Induced Senescence in the Tumor Microenvironment and Its Effects on Anti-Tumor Immune Responses*. Mar. 2022.

[487] Flora Lucy Dix. "Ceramide synthase 4: a novel metabolic regulator of oncogene-induced senescence." Doctor of Philosophy (PhD). The University of Edinburgh, 2018, p. 242.

[488] Eva M. Verdugo-sivianes and Amancio Carnero. *Role of the holoenzyme pp1-spn in the dephosphorylation of the rb family of tumor suppressors during cell cycle*. May 2021.

[489] Victoria Kolupaeva and Veerle Janssens. *PP1 and PP2A phosphatases - Cooperating partners in modulating retinoblastoma protein activation*. Jan. 2013.

[490] Ana Krtolica, Nancy A. Krucher, and John W. Ludlow. "Hypoxia-induced pRB hypophosphorylation results from downregulation of CDK and upregulation of PP1 activities." In: *Oncogene* 17.18 (Oct. 1998), pp. 2295–2304.

[491] Ping Lu et al. "Ceramide synthase 6 maximizes p53 function to prevent progeny formation from polyploid giant cancer cells." In: *Cancers* 13.9 (May 2021), p. 2212.

[492] Zongmin Zhao et al. *Targeting Strategies for Tissue-Specific Drug Delivery*. Apr. 2020.

[493] Tongxin Ge et al. *The Role of the Pentose Phosphate Pathway in Diabetes and Cancer*. June 2020.

[494] Alexander C. Lewis et al. "Targeting sphingolipid metabolism as an approach for combination therapies in haematological malignancies." In: *Cell Death Discovery 2018 4:1* 4.1 (June 2018), pp. 1–11.

Publications

Papers

Brachtendorf S, **El-Hindi K**, Grösch S. Ceramide synthases in cancer therapy and chemoresistance. Prog Lipid Res. 2019 Apr;74:160-185.

Bazarganipour S, Hausmann J, Oertel S, **El-Hindi K**, Brachtendorf S, Blumenstein I, Kubesch A, Sprinzl K, Birod K, Hahnefeld L, Trautmann S, Thomas D, Herrmann E, Geisslinger G, Schiffmann S, Grösch S. The Lipid Status in Patients with Ulcerative Colitis: Sphingolipids are Disease-Dependent Regulated. J Clin Med. 2019 Jul 4;8(7):971.

El-Hindi K, Brachtendorf S, Hartel JC, Oertel S, Birod K, Trautmann S, Thomas D, Ulshöfer T, Weigert A, Utermöhlen O, Krönke M, Grösch S. Ceramide Synthase 5 Deficiency Aggravates Dextran Sodium Sulfate-Induced Colitis and Colon Carcinogenesis and Impairs T-Cell Activation. Cancers (Basel). 2020 Jul 1;12(7):1753.

Spohner AK, Jakobi K, Trautmann S, Thomas D, Schumacher F, Kleuser B, Lütjohann D, **El-Hindi K**, Grösch S, Pfeilschifter J, Saba JD, Meyer Zu Heringdorf D. Mouse Liver Compensates Loss of Sgpl1 by Secretion of Sphingolipids into Blood and Bile. Int J Mol Sci. 2021 Sep 30;22(19):10617.

El-Hindi K, Brachtendorf S, Hartel JC, Oertel S, Birod K, Merz N, Trautmann S, Thomas D, Weigert A, Schäufele TJ, Scholich K, Schiffmann S, Ulshöfer T, Utermöhlen O, Grösch S. T-Cell-Specific CerS4 Depletion Prolonged Inflammation and Enhanced Tumor Burden in the AOM/DSS-Induced CAC Model. Int J Mol Sci. 2022 Feb 7;23(3):1866.

Talks

“CerS5 deficiency worsens DSS induced colitis and impairs T cell function”, 11th Interntaional Ceramide Conference, (2021)